NASA TECHNICAL MEMORANDUM

NASA TM X-3428

NASA TM X-3428

NASTRAN: USERS' EXPERIENCES

Fifth Colloquium held at
Ames Research Center
Moffett Field, California
October 5-6, 1976

NATIONAL AERONAUTICS AND SPACE ADMINISTRATION • WASHINGTON, D. C. • OCTOBER 1976

1. Report No.	2. Government Accession No.	3. Recipient's Catalog No.
NASA TM X-3428		

4. Title and Subtitle	5. Report Date
NASTRAN: USERS' EXPERIENCES	October 1976
	6. Performing Organization Code
7. Author(s)	8. Performing Organization Report No. A-6709
9. Performing Organization Name and Address NASA Ames Research Center Moffett Field, California 94035	10. Work Unit No. 020-02-00
	11. Contract or Grant No.
12. Sponsoring Agency Name and Address National Aeronautics and Space Administration Washington, D.C. 20546	13. Type of Report and Period Covered Technical Memorandum
	14. Sponsoring Agency Code

15. Supplementary Notes

Compendium of papers prepared for the Fifth NASTRAN Users' Colloquium, October 5-6, 1976, NASA Ames Research Center

16. Abstract

This Technical Memorandum is comprised of selected papers prepared for the Fifth NASTRAN Users' Colloquium held at the NASA Ames Research Center, October 5-6, 1976. The authors discuss the application of NASTRAN to a wide variety of static and dynamic structural problems. Specifically, the papers focus on the following topics:

I. Methods of Analysis
II. Hydroelastic Methods
III. Complete Analysis of Structures
IV. Elements and Material Studies
V. Critical Comparisons With Other Programs
VI. Pre- and Post-Processor Operations

17. Key Words (Suggested by Author(s))	18. Distribution Statement
NASTRAN, structures, finite element, NASTRAN Colloquium	Unlimited STAR Category — 39

19. Security Classif. (of this report)	20. Security Classif. (of this page)	21. No. of Pages	22. Price*
Unclassified	Unclassified	587	Domestic-$13.25 Foreign -$15.75

*For sale by the National Technical Information Service, Springfield, Virginia 22161

NASTRAN: USERS' EXPERIENCES

Compendium of papers prepared for the Fifth NASTRAN Users' Colloquium

October 5-6, 1976

NASA Ames Research Center

FOREWORD

NASTRAN (NASA STRUCTURAL ANALYSIS) is a large, comprehensive, non-proprietary, general purpose finite element computer code for structural analysis which was developed under NASA sponsorship and became available to the public in late 1970. It can be obtained through COSMIC (Computer Software Management and Information Center), Athens, Georgia, and is widely used by NASA, other government agencies, and industry.

NASA currently provides continuing maintenance and improvement of NASTRAN through a NASTRAN Systems Management Office (NSMO) located at Langley Research Center. Because of the widespread interest in NASTRAN, NSMO organized the Fifth NASTRAN Users' Colloquium at Ames Research Center, October 5-6, 1976. (Papers from previous colloquia held in 1971, 1972, 1973, and 1975 are published in NASA Technical Memorandums X-2378, X-2637, X-2893, and X-3278, respectively.) The Fifth Colloquium provides a comprehensive review of the future NASA plans for NASTRAN, some critical comparisons with the other approaches, unique applications, pre- and post-processing operations, and new methods of analysis with NASTRAN.

Individuals actively engaged in the use of NASTRAN were invited to prepare papers for presentations at the colloquium. These papers are included in this volume. No editorial review was provided by NASA, but detailed instructions were provided each author to achieve reasonably consistent format and content. The opinions and data presented are the sole responsibility of the authors and their respective organizations.

Deene J. Weidman, Manager
NASTRAN Systems Management Office
Langley Research Center
Hampton, VA 23665
October, 1976

CONTENTS

1. NASA'S PLANS FOR FUTURE NASTRAN CAPABILITY 1
Deene J. Weidman (NASA Langley Research Center)

I. METHODS OF ANALYSIS

2. ON MODELING AND THE USE OF THE NASTRAN THERMAL ANALYZER 3
Hwa-Ping Lee (NASA Goddard Space Flight Center)

3. EFFICIENT REANALYSIS OF STRUCTURES BY A DIRECT MODIFICATION METHOD 21
A. I. Raibstein, I. Kalev and A. Pipano (Israel Aircraft Industries Ltd.)

4. AUTOMATED FULLY-STRESSED DESIGN WITH NASTRAN 53
D. V. Wallerstein and G. W. Haggenmacher (Lockheed-California Company)

5. APPLICATION OF NASTRAN TO LARGE DEFLECTION SUPERSONIC FLUTTER OF PANELS 67
Chuh Mei (Vought Corporation) and James L. Rogers, Jr. (NASA Langley Research Center)

6. THERMAL ANALYSES OF THE INTERNATIONAL ULTRAVIOLET EXPLORER (IUE) SCIENTIFIC INSTRUMENT USING THE NASTRAN ANALYZER ($\bar{N}$TA) — A GENERAL PURPOSE SUMMARY 99
Clifton E. Jackson, Jr. (Goddard Space Flight Center)

7. THE GSFC NASTRAN THERMAL ANALYZER NEW CAPABILITIES 119
Hwa-Ping Lee (NASA Goddard Space Flight Center) and Robert L. Harder (The MacNeal-Schwendler Corporation)

8. REAL EIGENVALUE ANALYSIS IN NASTRAN BY THE TRIDIAGONAL REDUCTION (FEER) METHOD 127
Malcolm Newman and Paul F. Flanagan (Analytical Mechanics Associates, Inc.) and James L. Rogers, Jr. (NASA Langley Research Center)

9. A COMPARISON OF THE TWO NASTRAN DIFFERENTIAL STIFFNESS TECHNIQUES . 149
John R. McDonough (Computer Sciences Corporation)

10. DEFORMATIONS OF THICK TWO-MATERIAL CYLINDER UNDER AXIALLY VARYING RADIAL PRESSURE 161
Yakub A. Patel (Sargent & Lundy)

II. HYDROELASTIC METHODS

11. A NUMERICALLY EFFICIENT FINITE ELEMENT HYDROELASTIC ANALYSIS . . . 177
Robert N. Coppolino (The Aerospace Corporation)

12. A NASTRAN IMPLEMENTATION OF THE DOUBLY ASYMPTOTIC APPROXIMATION FOR UNDERWATER SHOCK RESPONSE 207
Gordon C. Everstine (David W. Taylor Naval Ship Research and Development Center)

13. A SUMMARY OF NASTRAN FLUID/STRUCTURE INTERACTION CAPABILITIES . . 229
Anthony J. Kalinowski and Jayant S. Patel (Naval Underwater Systems Center)

14. A FINITE ELEMENT-ANALYTICAL METHOD FOR MODELING A STRUCTURE IN AN INFINITE FLUID 251
P. Richard Zarda (David W. Taylor Naval Ship Research and Development Center)

III. COMPLETE ANALYSIS OF STRUCTURES

15. DEVELOPMENT, DOCUMENTATION AND CORRELATION OF A NASTRAN VIBRATION MODEL OF THE AH-1G HELICOPTER AIRFRAME 273
J. D. Cronkhite (Bell Helicopter Textron)

16. APPLICATION OF NASTRAN TO LARGE SPACE STRUCTURES 295
T. Balderes, J. Zalesak, V. DyReyes and E. Lee (Grumman Aerospace Corporation)

17. ANALYSIS OF THE LEARJET 35/36 WING AND CORRELATION WITH EXPERIMENTAL RESULTS 331
Mike H. Abla and Robert R. Boroughs (Gates Learjet Corporation) and Everett L. Cook (Wichita State University)

18. THERMAL AND STRUCTURAL ANALYSIS OF HELICOPTER TRANSMISSION HOUSINGS USING NASTRAN 353
R. W. Howells and J. J. Sciarra (Boeing Vertol Company) and G. Shek Ng (USAAMRDL, Eustis Directorate)

IV. ELEMENTS AND MATERIAL STUDIES

19. NASTRAN AS AN ANALYTICAL RESEARCH TOOL FOR COMPOSITE MECHANICS AND COMPOSITE STRUCTURES 381
C. C. Chamis, J. H. Sinclair, and T. L. Sullivan (Lewis Research Center)

20. THE QUARTER-POINT QUADRATIC ISOPARAMETRIC ELEMENT AS A SINGULAR ELEMENT FOR CRACK PROBLEMS 419
M. A. Hussain, W. E. Lorensen and G. Pflegl (Department of the Army, Watervliet Arsenal)

21. ADDITION OF HIGHER ORDER PLATE ELEMENTS TO NASTRAN 439
R. Narayanaswami (Old Dominion University) and Chuh Mei (Vought Corporation)

22. IMPLEMENTATION ON A NONLINEAR CONCRETE CRACKING ALGORITHM IN NASTRAN 479
David N. Herting, David L. Herendeen and Richard L. Hoesly (Universal Analytics, Inc.) and H. Chang (Ebasco Services, Inc.)

V. CRITICAL COMPARISONS WITH OTHER PROGRAMS

23. SOME APPLICATIONS OF THE NASTRAN LEVEL 16 SUBSONIC FLUTTER ANALYSIS CAPABILITY 495
Robert V. Doggett, Jr. and Herbert J. Cunningham (NASA Langley Research Center)

24. AUTOMATED MULTI-STAGE SUBSTRUCTURING ANALYSIS COMPARED WITH SUPERELEMENT ANALYSIS 513
Lalit C. Shah (Rockwell International)

25. MODAL SEISMIC ANALYSIS OF A NUCLEAR POWER PLANT CONTROL PANEL AND COMPARISON WITH SAP IV 515
M. R. Pamidi (Sargent and Lundy) and P. R. Pamidi (Computer Sciences Corporation)

VI. PRE- AND POST-PROCESSOR OPERATIONS

26. NASTRAN USED IN A PRODUCTION ENVIRONMENT 531
R. F. Wilkinson, J. W. Kelley, and N. K. Snead (Lockheed-Georgia Company)

27. A POSTPROCESSOR SYSTEM FOR THE DATA REDUCTION AND POST ANALYSIS OF NASTRAN RESULTS 555
A. I. Raibstein, S. Emil, and A. Pipano (Israel Aircraft Industries Ltd.)

28. APPLICATION OF LEVEL 15.9 NASTRAN TO A LARGE MODEL OF B-1 WING . . 581
Lalit C. Shah and Ronald Breznak (Rockwell International)

NASA's Plans for Future NASTRAN Capability

by Deene J. Weidman

NASA-Langley Research Center

INTRODUCTION

NASA has developed and maintained the NASTRAN System over the past eleven years. During this period, the system has evolved into one of the most versatile and widely used structural analysis systems currently available to the public. In order for the many users to plan their future use of the system, the present and future contents of NASTRAN are essential information. This paper presents the planned future additions to NASTRAN as defined by July 1976, and eventually leading to Level 17.

NEW CAPABILITIES

Recently, NASTRAN Level 16 was released through COSMIC. With that release, a large number of improvements being developed by NASA were made available to the U.S. public. This level has already been defined (ref. 1), and will not be reviewed again here.

However, some additional improvements are currently being pursued in the NASTRAN Systems Management Office (NSMO) for later inclusion in Level 16. Among these items are (1) the FEER eigenmethod and its extension to complex eigenvalue problems, (2) the addition of a "supersonic flutter package" which allows gust response calculations and active control effects as well, (3) the provision for a general purpose data generator, and (4) some additional advanced rigid, membrane, plate and shell elements. All of these improvements are in varying stages of contractual development, and their availability will define the release date for the new level.

NASTRAN MAINTENANCE

In addition to these new capabilities, the correction of reported NASTRAN errors has been continuing as a primary effort and should result in Level 17 being the version of NASTRAN with the fewest errors. The Error Correction Information System (ECIS) is available on the CYBERNET system, and is up-dated every two weeks on a

routine basis including Level 16 error information. A "User Info." file has also been added, and current rush information is placed on this file as soon as it is available. Users access this file with a single instruction. This activity indicates that NASA has been attempting to provide support to individual users as directly as possible.

NASA currently supplies direct contract maintenance support on only one computer program (NASTRAN) as a so-called "Class I" program. Some steps to allow users better direct maintenance on their own have already been made by the NSMO:

(1) Utility programs for NASTRAN maintenance have been announced as available in the newsletter and have been freely distributed to a number of user facilities to allow self maintenance and improvement.

(2) User groups have been formed by NSMO for programmers using each of the three major computers now being supported.

(3) Leasing of the NASTRAN program has also been initiated with funds being used for maintenance.

(4) More and more maintenance activity is being handled directly by the maintenance contractor.

CONCLUDING REMARKS

The activities in the NSMO at Langley Research Center are still continuing, directed to development of a sound, advanced NASTRAN Level 17. Additions to NASTRAN for this specific level have been described briefly. Also additional maintenance tools for users have been developed and are discussed herein.

REFERENCES

1. Weidman, D. J.: NASTRAN Status and Plans, pp. 1-10, NASTRAN Users' Experiences, TMX-3278, Sept. 1975.

ON MODELING AND THE USE OF THE NASTRAN THERMAL ANALYZER

Hwa-Ping Lee
NASA Goddard Space Flight Center

SUMMARY

Eight alternative modeling techniques to specify prescribed temperature at grid or scalar points for transient thermal analyses are presented. Four cases are for constant temperatures, and the others are time-varying temperature functions. Theoretical explications and detailed listing of input data cards used for illustrating different modelings are given. It is shown that the $\bar{N}$TA can be exploited to extend beyond its normal capabilities through innovative modeling techniques.

In addition, the effect of node valency on the energy distribution to grid points is illustrated and discussed. Guidelines to delineate this effect are given.

INTRODUCTION

The NASTRAN Thermal Analyzer ($\bar{N}$TA) is a finite-element based general purpose heat transfer computer program integrated in the NASTRAN system (refs. 1 and 2). Its development was intended to provide analytical analysis capabilities in the multiple disciplinary areas. Special attention was directed to the interface problem which interferes with reliable predictions of the thermo-stresses or deflections, especially for very large sized structures and complex configurations. The $\bar{N}$TA was developed by making an effective use of the functional modules available in NASTRAN to their fullest extent. In addition, new modules comprising new elements and solution algorithms to satisfy the unique requirements posed by thermal applications were added. The $\bar{N}$TA is indeed very versatile and flexible. Analysis capabilities, however can be further exploited by innovative modeling techniques to compensate for some of the apparent restrictions of the program, which were not implemented solely for economic reasons. Working around such restrictions through intelligent modeling is an achievable practice in engineering applications.

This paper deals with two essential subjects relevant to the $\bar{N}$TA modeling. The problems considered are:

(1) Alternative modeling techniques for specifying the prescribed temperatures at grid or scalar points in transient thermal analyses

A total of eight distinct modeling techniques are presented. Four cases concern with a constant temperature value, and the others, a time-varying temperature function. For the ease of reference and comparison, all cases are illustrated using a single basic physical problem. Details of altering the input data cards from case to case are given. Theoretical explications which amplify the basis of modeling techniques are included as necessary. Accuracy of solutions along with individual merits and disadvantages is discussed. While not attempting to be exhaustive, these illustrations will provide general $\bar{N}$TA users with a practical guide supplementing what has been documented and demonstrated in the two-volume set manuals (refs. 3 and 4).

(2) The effect of the node valency on energy distribution to grid points

The energy distribution to grid points attributed to the effect of the node valency is examplified by a unit surface of a rectangular area which is heated by an external heat flux. This rectangular surface is represented in six different models using two-dimensional triangular and quadrilateral elements. Users are reminded by facts to be cautious in a modeling process. Guidelines and suggestions to delineate this effect are given.

MODELING TECHNIQUES FOR PRESCRIBED TEMPERATURES

Unlike the steady-state linear and nonlinear cases (using the rigid formats APP HEAT, SOL 1 and SOL 3, respectively), for which the $\bar{N}$TA permits direct modeling of the prescribed temperature at grid or scalar points via the provided single-point-constraint (SPC1*) and temperature (TEMP and TEMPD) cards directly, the modeling to specify the prescribed temperatures in both linear and nonlinear transient thermal analyses (using the rigid format APP HEAT, SOL 9) requires indirect and more intricate techniques. A well adopted method to simulate the effect of a prescribed temperature T_i (i denotes grid or scalar point identification) is to connect a good thermal conductor between the point i and a datum of temperature at zero degree. The thermal conductor has a very large thermal conductance, K_{io}, where the subscripts i and o denote the terminals of connection. A power or rate of heat flow Q_i is then applied to that point to yield the desired value of a constrained temperature, according to

$$T_i = \frac{Q_i}{K_{io}} \tag{1}$$

*The names of actual $\bar{N}$TA cards are capitalized and underlined.

where $T_o = 0$ has been implied, and K_{io} is a thermal conductance defined by

$$K_{io} = \left(\frac{kA}{\ell}\right)_{io} \tag{2}$$

k, A and ℓ are thermal conductivity, cross-sectional area and length of the conductor, respectively. For instance, if a constant value of 512°C is prescribed at the point i, a conductor with a very large thermal conductance, say $K_{io} = 10^6$ W/°C is chosen, and a power, $Q_i = 512 \times 10^6$ W, is then applied to i, the desired value of the prescribed temperature is obtained from equation (1), i.e.

$$T_{io} = \frac{512 \times 10^6}{10^6} = 512°C \tag{3}$$

This method is due directly to an analogy between the thermal and structural systems, which is depicted in figure 1. A train of the NTA Bulk Data cards consisting of CELAS2 (to enter K_{io} and link between i and o), DAREA (to enter Q_i) and TLOAD2 (to apply Q_i to i and specify the transient loading conditions) is generally employed.

Based on the same principle, the modeling technique for a constant prescribed temperature at a grid point can be extended to the case of time-varying temperatures. This can be accomplished by a substitution of a time-dependent thermal load Q_i (t) for Q_i, a constant value, in equation (1), provided admissible quantities and connectable NTA Bulk Data cards are selected properly and referenced correctly. This approach is, by no means, the only modeling technique available to the NTA users. Eight options of modeling techniques to specify constant and time-varying temperatures at grid or scalar points will be systematically presented. All cases will be illustrated by a single simple physical problem which does not lose any generalities insofar as the thermal boundary conditions are concerned. Consequently, any alterations made to the input data cards for individual cases can be easily identified and compared, and the accuracy of solutions easily evaluated.

The physical problem is that of determining the transient temperature response of a composite slab of infinite extent during a 45-second period (see fig. 2). The rear surface of the insulation layer, having the value of $\epsilon = \alpha = 0.9$, dissipates heat radiatively to an environment of 0°C. The front surface of the metallic slab in contact with a hot flowing gas has a convective film coefficient of $h = 0.071$ W/cm^2-°C. The thermophysical properties and dimensions are tabulated in table 1. A uniform initial temperature of 20°C throughout the composite slab is assumed. Temperatures of the flowing hot gas are specified as:

(1) A constant prescribed value maintained at $T_f = 1927°C$.

(2) A time-varying temperature function $T_f(t)$ which is given in figure 3.

One-dimensional rod elements are sufficient to represent the described problem in a finite-element model. A sketch of the composite slab and its finite-element representation is shown in figure 2.

A listing of that portion of the input data deck, which describes the problem in the NTA model and is common to all eight cases is shown in figure 4. With comments appropriately added, functions of various sections of the Bulk Data Deck are self-explanatory. The blank space bounded by the two lines of dotted stars is reserved for inserting different packets of the NTA Bulk Data cards which model the prescribed temperatures for the hot flowing gas that is represented by GRID or SPOINT 200.* A description and discussion for each individual case is in order. Relevant Bulk Data cards will be listed.

For a Constant Prescribed Temperature

(1) To specify a constant temperature via CELAS2, DAREA, and TLOAD2

As described previously, this method is a common modeling technique. The Bulk Data cards which fill the blank space reserved in the input data deck (fig. 4) are shown in figure 5, Case (1) of the attached listing of computer printout excerpts.

A fictitious large thermal conductance $K_{io} = 10^6$ W/cm-°C is entered in the 3rd field of CELAS2. Its 4th field identifies the point which is numbered 200 and is of the SPOINT type as indicated by the 0 in the 5th field. The two blanks in the following two fields imply that the other end of the thermal conductor is connected to a datum of 0°C. The quantity of power, $Q_{io} = 1927 \times 10^6$ W, is entered in the 5th field in the thermal load card DAREA, whose identification 501 appearing in its 2nd field is referenced by TLOAD2 in the latter's third field. The set identification 401 of the TLOAD2 must be referenced by a DLOAD card in the Case Control Deck to activate the selection of an applied thermal load in the transient solution algorithm. Other filled data in these Bulk Data cards are obvious when the NTA manual (ref. 3) is consulted. No repetition need be made.

(2) To specify a constant temperature via CELAS2, SLOAD, and TLOAD2

To illustrate how a variety of other available thermal load cards may be substituted for DAREA in the preceding case, SLOAD is selected for its simplicity. The

*Unless otherwise noted to use GRID 200 as a restriction, GRID 200 and SPOINT 200 are interchangeable in all other cases where SPOINT 200 is explicitly indicated.

packet of Bulk Data cards for modeling a constant temperature at the SPOINT 200 is shown in figure 5, Case (2). Results are identical to that of the preceding case. Other thermal load cards such as QVECT, QBDY1, QBDY2, and QHBDY may also serve as the replacement for DAREA, but generally require the use of associated cards as an inherent requirement. Later cases will illustrate this point.

(3) To specify a constant temperature via CDAMP2

The apparent attractiveness of this modeling technique is attributed to its modeling simplicity. A CDAMP2 card loaded with an extremely large thermal mass would maintain a prescribed temperature at the applied point, as long as sufficient amount of thermal power is supplied. While achieving the intended boundary condition satisfactorily, the addition of a fictitious, very large thermal mass as a component in the corresponding matrix would produce an unstable solution. As a result, accuracy of the solution is questionable. Furthermore, there are restrictions associated with this technique: Only GRID is permitted to be referenced by CDAMP2 for adding a thermal mass. A restriction (defect) of the program code requires the presence of CELAS2, DAREA, and TLOAD2 in the input data deck even though they would not contribute to the result of solution. Although the use of this technique is not recommended, Bulk Data cards used in modeling are shown in figure 5, Case (3) for reference.

(4) To specify a constant temperature via EPOINT, DMIG, DAREA and TLOAD2

The demonstrated modeling techniques in the preceding cases are incapable of providing information on the amount of the heat of constraint required to sustain the prescribed temperature at a point. In each case, a very large fictitious thermal load or a thermal mass was applied to achieve the desired effect. The NTA permits a direct input to the conduction matrix through DMIG which can be utilized together with EPOINT, DAREA and TLOAD2 to enter a true value of the prescribed temperature and yet yield the value of the heat of constraint as a part of the solution. Some manipulations are required, however, to accommodate this scheme. It's theoretical basis will be discussed first.

In transient thermal analysis, the general differential equation in matrix form is

$$[C]\{\dot{T}\} + [K]\{T\} = \{Q_\ell\} + \{Q_r\} \tag{4}$$

where

[C] a symmetric matrix of heat capacitance

[K] a symmetric matrix of heat conduction

$\{Q_\ell\}$ a vector of applied thermal loads that are allowed to be time-dependent

$\{Q_r\}$ a vector of non-linear thermal loads that depend on temperature

$\{T\}$ a vector of temperatures at grid points

Equation (4) can be abridged as

$$[L]\{T\} = \{Q\} \tag{5}$$

where $[L]$, a nonlinear differential operator, is obtained by a comparison of equation (4) with equation (5), that gives

$$[L] = \left[[C] \cdot \frac{d}{dt} + [K]\right] \tag{6}$$

and

$$\{Q\} = \{Q_\ell\} + \{Q_r\} \tag{7}$$

Constraining a point to a constant temperature, we need to create one new unknown and one new equation. The new unknown representing the heat of constraint required to sustain the temperature to a prescribed level is defined as

$$T_{2001} = \text{heat of constraint} \tag{8}$$

Adding the quantity T_{2001} into equation (5) yields the following modified form

$$[L]\{T\} = \{Q\} + \begin{Bmatrix} 0 \\ 0 \\ \vdots \\ T_{2001} \\ 0 \end{Bmatrix} \begin{array}{l} \\ \\ \\ \leftarrow \text{row for the point 200} \\ \\ \end{array} \tag{9}$$

The new equation is defined as

$$T_{200} = q_{2001} \tag{10}$$

This quantity q_{2001} is an additional component in the vector $\{Q\}$ to be arranged in a row corresponding to that of the point 2001. The above equations can be merged to become

$$\left[\begin{array}{c|c} L & \begin{matrix} 0 \\ 0 \\ \vdots \\ 0 \\ -1.0 \end{matrix} \\ \hline 0\ 0 \cdots 0\ 1.0 & 0 \end{array}\right] \left\{\begin{array}{c} T \\ \hline T_{2001} \end{array}\right\} = \left\{\begin{array}{c} Q \\ \hline q_{2001} \end{array}\right\} \tag{11}$$

← row for the point 200

← row for the point 2001

column for the point 2001

column for the point 200

The Bulk Data cards used in modeling are given in figure 5, Case (4). An EPOINT is used to accommodate the new unknown T_{2001}. The two added quantities in the merged L-matrix are input through the DMIG cards. The prescribed temperature is entered by DAREA with its true value. As usual, a TLOAD2 again serves to reference the DAREA and provides an identification to be selected by the DLOAD card in the Case Control Deck to activate transient thermal loading conditions.

The use of DMIG for inputing components directly to the conduction matrix requires its function to be selected in the Case Control Deck by a K2PP card. Therefore, K2PP=THIXED, was added.

Since the modified L-matrix appearing on the left-hand side of equation (11) is asymmetric, an altering of the program code to the APP HEAT, SOL 9 is required. The DMAP-ALTER packet which was inserted in the Executive Control Deck is reproduced below for reference.

```
$ DMAP-ALTER FOR APP HEAT SOL 9 TO FACILITATE ASYMMETRIC CONDUCTION MATRIX
ALTER 53,53 $ FOR APP HEAT, SOL 9 TO ACCOMMODATE ASYMMETRIC MATRIX HKGG
MCE2      HUSET,HGM,HRGG,HBGG,,/HRNN,HBNN,, $
PARAM     //C,N,PREC/V,N,PREC $
UPARTN    HUSET,HKGG/HKNNB,HKMN,HKNM,HKMM/C,N,G/C,N,N/C,N,M $
MPYAD     HKMM,HGM,HKMN /HKM /C,N,0/C,N,1/C,N,1/V,N,PREC $
MPYAD     HKNM,HGM,HKNNB/HKN /C,N,0/C,N,1/C,N,1/V,N,PREC $
MPYAD     HGM ,HKM,HKN  /HKNN/C,N,1/C,N,1/C,N,1/V,N,PREC $
ENDALTER
```

Results of this method are identical to those of Case (1). In addition, the "Temperature Vector" output for the point 2001 should be interpreted as the heat of constraint (in the units of power, w) as defined by equation (10).

While the advantages of this modeling technique are self-evident, the disadvantages are: (A) An increase of the problem size, and (B) The nonstandard definition of output.

For a Time-Varying Temperature Function

(5) To specify a time-varying temperature function via CELAS2, QVECT, TABLED1, TLOAD2, etc.

A prescribed temperature at a point varied as a time function can be modeled by an extension of the basic technique shown in Case (1). The technique used is to replace DAREA with other admissible thermal load cards which would provide with the time-varying thermal power capability. QVECT permits its vector components of the directional thermal flux to be referenced by the TABLED1 cards where tabulated values of temperature vs. time functions can be entered.

The CELAS2 and TLOAD2 serve the same functions as described in Case (1).

Since QVECT can only input a thermal flux to a point through a boundary surface element, CHBDY is therefore required. To define the surface area of the provided CHBDY element as well as to specify the surface absorptivity to absorb the radiant flux, PHBDY must be included. Moreover, CHBDY can only be referenced by a GRID, which, therefore, must replace the SPOINT 200 in the packet of the Bulk Data cards as shown in figure 6, Case (5).

(6) To specify a time-varying temperature function via CELAS2, QVECT, TLOAD1, TABLED1, etc.

A variation of the modeling technique used in the last example is demonstrated. Although TLOAD2 is the only card that must be replaced, in this case by TLOAD1, the sequence of referencing from card to card to perform specific functions has altered substantially. The time-varying temperature function does not rely on the provision of the vector components of QVECT. Instead, QVECT serves only to facilitate a large fictitious thermal load, while tabulated values of a time-varying temperature function are entered in TABLED1 which, in turn, is referenced by TLOAD1. The packet of Bulk Data cards in figure 6, Case (6) shows the detail of inter-relationships among individual cards.

(7) To specify a time-varying temperature function via CELAS2, QHBDY, TLOAD1, TABLED1, etc.

The preceding case has shown that a temperature vs. time function can be modeled via TLOAD1 and TABLED1, and that a thermal load card is used merely to accommodata a constant value of thermal flux. In the present case, QHBDY is substituted for QVECT. Nothing else is altered and the packet of Bulk Data cards is shown in figure 6, Case (7).

(8) To specify a time-varying temperature function via EPOINT, DMIG, DAREA, TLOAD1 and TABLED1

As evidenced in Cases (6) and (7), a combination of TLOAD1 and TABLED1 is well suited to accommodate temperature vs. time functions.

Therefore, the modeling techniquss previously devised for a constant prescribed temperature can be modified easily if TLOAD2, which was used originally in the constant prescribed temperature case, is replaced by a combination of TLOAD1 and TABLED1. An application of this substitution to Case (4) has successfully demonstrated another method available to the users. The uniqueness and features of this modeling technique are identical to that of Case (4). A packet of relevant Bulk Data cards is shown in figure 6, Case (8).

Details of the illustrated cases with emphasis on the inter-relationships of the cards in the Bulk Data Deck and those between the Case Control and the Bulk Data Decks together with results are documented separately (ref. 5).

EFFECT OF THE NODE VALENCY

A node valency is the pattern of element arrangement in an assembled model in relation to an associated grid point. Since a number of factors could influence the solution accuracy of a finite-element model (ref. 6), the effect of the node valency can be controlled by modeling and is, therefore, considered and discussed herewith.

The input energy to an element, whether from an external thermal flux to the surface of an element or from an internal volumetric heating source, is evenly distributed to the vertices of the element according to the solution algorithm currently implemented in the NTA program. The effect of a node valency on the total energy distribution to grid points is essential to the eventual temperature results. As an illustration, without computation, six types of node valency available to model a constant area A of a rectangle are shown in figure 7. Each rectangular surface is assumed to be cut out from an assembled finite-element model along a boundary. The surface is heated by a constant uniform heat flux q. Then Q_i is the amount of energy being distributed to

that grid point i from all connected elements that define the node valency at i. For example, the rectangular surface is modeled by four equal quadrilateral elements as shown in figure 7(a). The distribution of energies at three noted grid points are $Q_1 = (1/4)Aq$, $Q_2 = (1/16)Aq$ and $Q_3 = (1/8)Aq$.

When the same rectangular surface is modeled differently by using triangular elements as shown in Cases (b) through (f) in figure 7, Q_i (i = 1, 2, 3, 4, wherever applicable) of each case shows that at the same location of the centers of these rectangles, Q_1 has varied from 1/3 to 1/6, Q_2 from 1/6 to 1/24, and Q_3 from 1/2 to 1/8 units. This is an indication of uneven distribution of a uniformly applied heat flux to a surface of the same area attributed to the node valency. In practice, a structure represented by a finite-element model usually employs sufficiently large number of elements arranged in a very regular pattern or patterns. This fact implies that those grid points, being fully surrounded by connected elements, would receive the same fraction of energy as long as the grid points have the node valency which would result in identical values of Q_i. It is also seen that the grid points that are isolated or located along boundary lines, where the grid points are not fully surrounded by adjacent elements, would be affected by the node valency more than their counterparts located on the interior of the surface. Therefore, to delineate temperature solution inaccuracy, when the existing software of the $\overline{N}$TA is used, the selection of uniformly sized and the similar type of elements arranged in a regular pattern for interior points is recommended. Using finer discretization or smaller elements along the boundary lines is also desirable but the engineering practice must trade-off with other considerations.

As a last resort, application of thermal loads manually to those isolated grid points or those along the boundary lines is a practical method of compensating for uneven energy distribution. The Bulk Data card QHBDY is employable for such an application.

REFERENCES

1. Lee, H. P., and Mason, J. B.: NASTRAN Thermal Analyzer — A General Purpose Finite-Element Heat Transfer Computer Program, The 2nd NASTRAN User's Colloquium, NASA TMX-2637, Sept. 1972, pp. 443-454.

2. Lee, H. P.: NASTRAN Thermal Analyzer — Status, Experience and New Developments, The 4th NASTRAN User's Colloquium, NASA TMX-3278, Sept. 1975, pp. 523-528.

3. Lee, H. P.: NASTRAN Thermal Analyzer — Theory and Application Including a Guide to Modeling Engineering Problems, Volume 1: The NASTRAN Thermal Analyzer Manual, NASA Goddard Space Flight Center, X-322-76-16, December 1975.

4. Jackson, C. E., Jr.: NASTRAN Thermal Analyzer — Theory and Application Including a Guide to Modeling Engineering Problems, Volume 2: A Guide to the GSFC NASTRAN Thermal Analyzer Sample Problem Library, NASA Goddard Space Flight Center, X-322-76-17, December 1975.

5. Lee, H. P.: Alternative Techniques for Modeling the Prescribed Temperatures in a Transient Thermal Analysis Using the NASTRAN Thermal Analyzer, NASA Goddard Space Flight Center, System Division, Greenbelt, Md., Sept. 1976.

6. Lee, H. P.: A Critical Analysis of Finite-Element Temperature Solution Accuracy, Presented at the Open-Forum, AIAA/ASME Thermophysics and Heat Transfer Conference, Boston, Mass., July 15-17, 1974.

TABLE 1. - THERMO-PHYSICAL PROPERTIES AND DIMENSIONS

Layer	Metallic Slab (a)	Insulation (b)
Thermal conductivity k (W/cm-°C)	2.25×10^{-3}	0.2×10^{-3}
Thermal capacitance ρC_p (Cal/cm^3-°C)	1.44×10^{-1}	1.163
Thickness ΔX (cm)	0.30	0.40

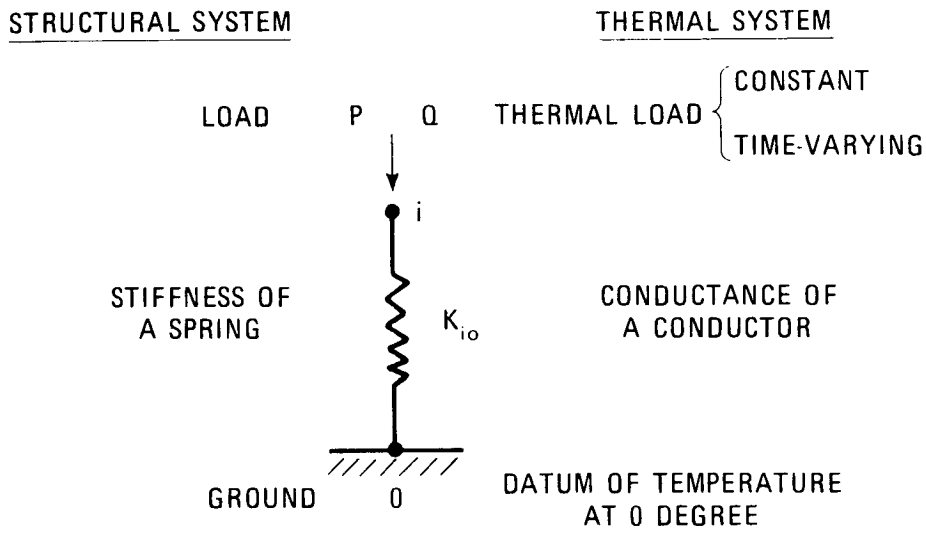

Figure 1. Analogy of a thermal conductor and a structural spring.

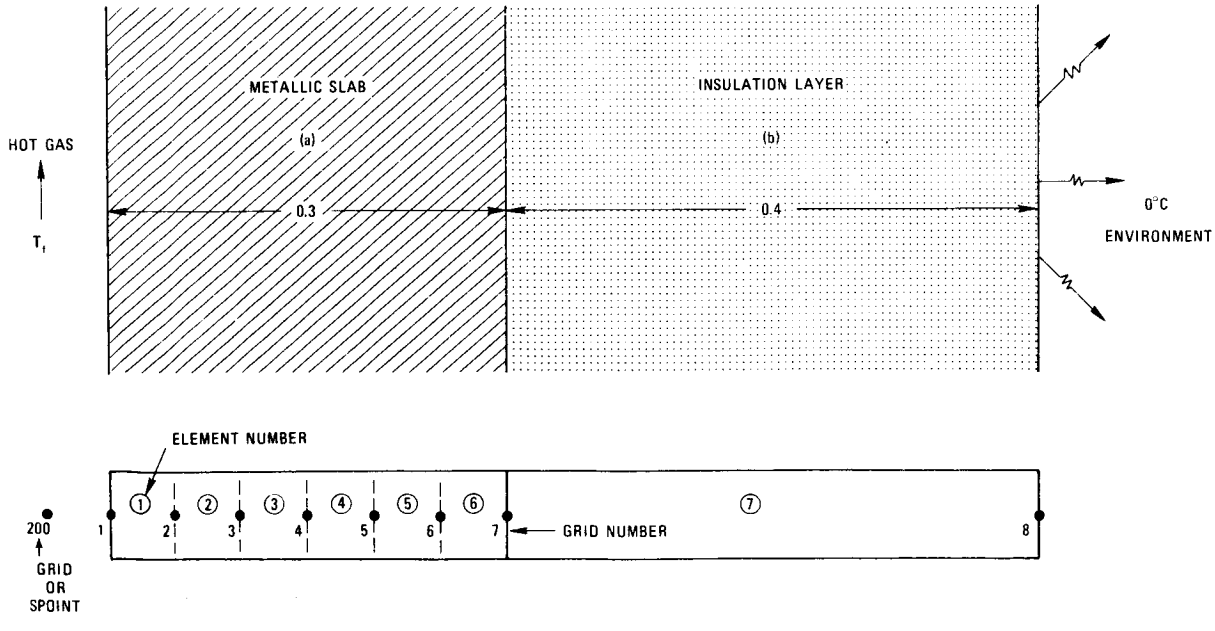

Figure 2. The composite slab and its finite-element representation.

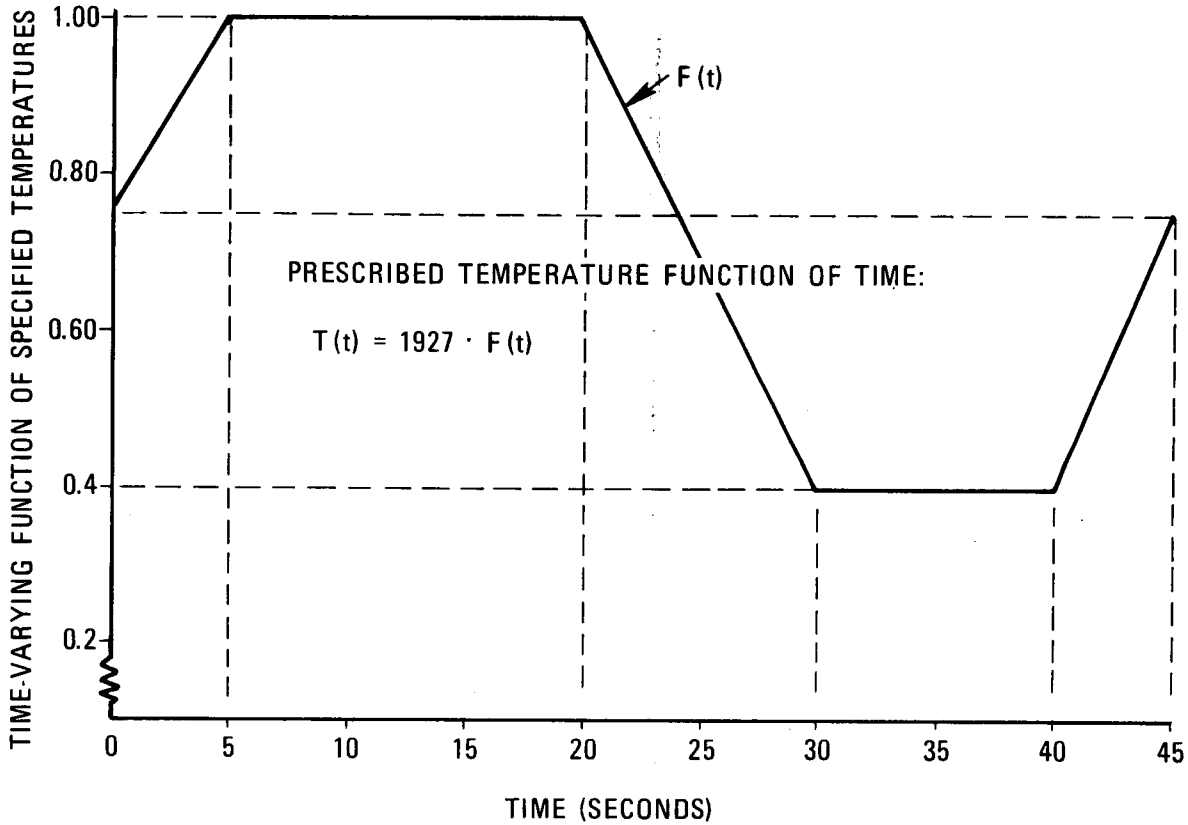

Figure 3. Time-dependent prescribed temperatures of the hot flowing gas.

```
$  EXECUTIVE CONTROL DECK
ID H P LEE, NASA-GSFC, SYSTEMS DIVISION, THERMAL SYSTEMS BRANCH
APP HEAT
SOL 9
TIME 5
DIAG 8,13,14
$  INSERT ALTER PACKET HERE IF USED
CEND

$  CASE CONTROL DECK
ECHO=BOTH
TITLE=DIFFERENT MODELING TECHNIQUES FOR PRESCRIBED TEMPERATURE
SUBTITLE=IN TRANSIENT THERMAL ANALYSIS
LABEL =    $***** A TITLE FOR THE CASE IDENTIFICATION ******
DLOAD=401
IC=701
TSTEP=601
TEMP(MATERIAL)=1
OUTPUT
ELFORCE=ALL
DLOAD=ALL
THERMAL=ALL
BEGIN BULK

.   1  ..   2  ..   3  ..   4  ..   5  ..   6  ..   7  ..   8  ..   9  ..  10  .
$  BULK DATA DECK
$  GRID POINTS
GRID    1                0.00    0.0     0.0
GRID    2                0.05    0.0     0.0
GRID    3                0.10    0.0     0.0
GRID    4                0.15    0.0     0.0
GRID    5                0.20    0.0     0.0
GRID    6                0.25    0.0     0.0
GRID    7                0.30    0.0     0.0
GRID    8                0.70    0.0     0.0
SPOINT  200
$  CONDUCTION ELEMENTS
CROD    1       101      1       2       2       101     2       3
CROD    3       101      3       4       4       101     4       5
CROD    5       101      5       6       6       101     6       7
PROD    101     102      1.0
MAT4    102     0.00225  0.144
CROD    7       1101     7       8
PROD    1101    1102     1.0
MAT4    1102    0.0002   1.163
$  CONVECTIVE BOUNDARY IN CONTACT WITH HOT GAS                          &1
CHBDY   1001    1002     POINT   1
&1      200
PHBDY   1002    1003     1.0
MAT4    1003    0.071
$  RADIATION TO AN ENVIRONMENT OF ZERO DEGREE                           &CY001
CHBDY   9001    9002     POINT   8
&CY001                                   1.0     0.      0.
PHBDY   9002             1.0     0.9
RADLST  9001
RADMTX  1       1.0
PARAM   SIGMA   5.67E-12
PARAM   TABS    273.16
$  INITIAL CONDITIONS
TEMP    701     200      1927.0
TEMPD   701     20.0
$  TIME INCREMENTS AND INTEGRATION STEPS                                 &3
TSTEP   601     15       1.0     2
&3              15       2.00    2
$  ESTIMATED TEMPERATURES
TEMPD   1       1927.0
$ ***************************************************************

$ ***************************************************************
ENDDATA
```

Figure 4. A listing of input data deck of the $\bar{N}$TA model.

```
LABEL= FIXED TEMPERATURE AT SPOINT 200 VIA CELAS2,DAREA & TLOAD2
$ ************************************************************************
$ CONSTANT PRESCRIBED TEMPERATURE APPLIED AT SPOINT 200
CELAS2  301     1.E6    200     0
DAREA   501     200     0       1927.E6
TLOAD2  401     501     0               0       1.E5    0.0     0.0     +TLD2
+TLD2   0.0     0.0
$ ************************************************************************
```

CASE (1)

```
LABEL= FIXED TEMPERATURE AT SPOINT 200 VIA CELAS2,SLOAD & TLOAD2
$ ************************************************************************
$ CONSTANT PRESCRIBED TEMPERATURE APPLIED AT SPOINT 200
CELAS2  301     1.E6    200     0
SLOAD   501     200     1927.E6
TLOAD2  401     501     0               0.0     1.E5    0.0     0.0     +TLD2
+TLD2   0.0     0.0
$ ************************************************************************
```

CASE (2)

```
$ ************************************************************************
$ CONSTANT PRESCRIBED TEMPERATURE APPLIED AT GRID 200
CDAMP2  301     1.E3    200     1
TEMP    1       200     1927.0                                          T-ESTIM
$  TO BYPASS PROGRAM RESTRICTION OF TRANSIENT LOAD INPUT
CELAS2  301     1.E6    8       1
DAREA   501     200     0       0.0
TLOAD2  401     501     0               0       1.E5    0.0     0.0     +TLD2
+TLD2   0.0     0.0
$ ************************************************************************
```

CASE (3)

```
LABEL= FIXED TEMPERATURE AT SPOINT 200 VIA EPOINT,DMIG,DAREA & TLOAD2
$ ************************************************************************
$ CONSTANT PRESCRIBED TEMPERATURE APPLIED AT SPOINT 200
EPOINT  2001
DMIG    TFIXED  0       1       1       1
DMIG    TFIXED  200     0               2001    0       1.0
DMIG    TFIXED  2001    0               200     0       -1.0
DAREA   501     2001    0       1927.0
TLOAD2  401     501     0               0       1.E5    0.      0.      +TL
+TL     0.      0.
$ ************************************************************************
```

CASE (4)

Figure 5. Bulk Data cards used in various modeling techniques for specifying constant prescribed temperatures.

```
LABEL= TIME-DEPENDENT PRESCRIBED TEMPERATURE VIA CELAS2,QVECT,TABLED1 & TLOAD2
$ ************************************************************************
$ TIME-DEPENDENT PRESCRIBED TEMPERATURE APPLIED AT GRID 200
CELAS2  301     1.E6    200     1
CHBDY   20001   20002   POINT   200                                     +CHBDY1
+CHBDY1                                 -1.0    0.0     0.0
PHBDY   20002           1.0     1.0
QVECT   501     1927.E6 5011                    20001
TABLED1 5011                                                            +TABL1
+TABL1  0.0     0.75    5.0     1.0     20.0    1.0     30.0    0.4     +TABL2
+TABL2  40.0    0.4     45.0    0.75    ENDT
TLOAD2  401     501                     0.0     1.E5    0.0     0.0     +TLD2
+TLD2   0.0     0.0
$ ************************************************************************
```

CASE (5)

```
LABEL= TIME-DEPENDENT PRESCRIBED TEMPERATURE VIA CELAS2,QVECT,TLOAD1 & TABLED1
$ ************************************************************************
$ TIME-DEPENDENT PRESCRIBED TEMPERATURE APPLIED AT GRID 200
CELAS2  301     1.E6    200     1
CHBDY   20001   20002   POINT   200                                     +CHBDY2
+CHBDY2                                 -1.0    0.0     0.0
PHBDY   20002           1.0     1.0
QVECT   501     1927.E6 1.0     0.0     0.0     20001
TLOAD1  401     501                     4011
TABLED1 4011                                                            +TABL1
+TABL1  0.0     0.75    5.0     1.0     20.0    1.0     30.0    0.4     +TABL2
+TABL2  40.0    0.4     45.0    0.75    ENDT
$ ************************************************************************
```

CASE (6)

```
LABEL= TIME-DEPENDENT PRESCRIBED TEMPERATURE VIA CELAS2,QHBDY,TLOAD1 & TABLED1
$ ************************************************************************
$ TIME-DEPENDENT PRESCRIBED TEMPERATURE APPLIED AT GRID 200
CELAS2  301     1.E6    200     1
CHBDY   20001   20002   POINT   200                                     +CHBDY2
+CHBDY2                                 -1.0    0.0     0.0
PHBDY   20002           1.0     1.0
QHBDY   501     POINT   1927.E6 1.0     200
TLOAD1  401     501                     4011
TABLED1 4011                                                            +TABL1
+TABL1  0.0     0.75    5.0     1.0     20.0    1.0     30.0    0.4     +TABL2
+TABL2  40.0    0.4     45.0    0.75    ENDT
$ ************************************************************************
```

CASE (7)

```
LABEL=TIME-DEPENDENT PRESCRIBED TEMPERATURE VIA EPOINT,DMIG,DAREA,TLOAD1,TABLED1
$ ************************************************************************
$ TIME-DEPENDENT PRESCRIBED TEMPERATURE APPLIED AT SPOINT 200
EPOINT  2001
DMIG    TFIXED  0       1       1       1
DMIG    TFIXED  200     1               2001            1.0
DMIG    TFIXED  2001    0               200             -1.0
DAREA   501     2001    0       1927.0
TLOAD1  401     501                     4011
TABLED1 4011                                                            +TABL1
+TABL1  0.0     0.75    5.0     1.0     20.0    1.0     30.0    0.4     +TABL2
+TABL2  40.0    0.4     45.0    0.75    ENDT
$ ************************************************************************
```

CASE (8)

Figure 6. Bulk Data cards used in various modeling techniques for specifying time-varying prescribed temperature functions.

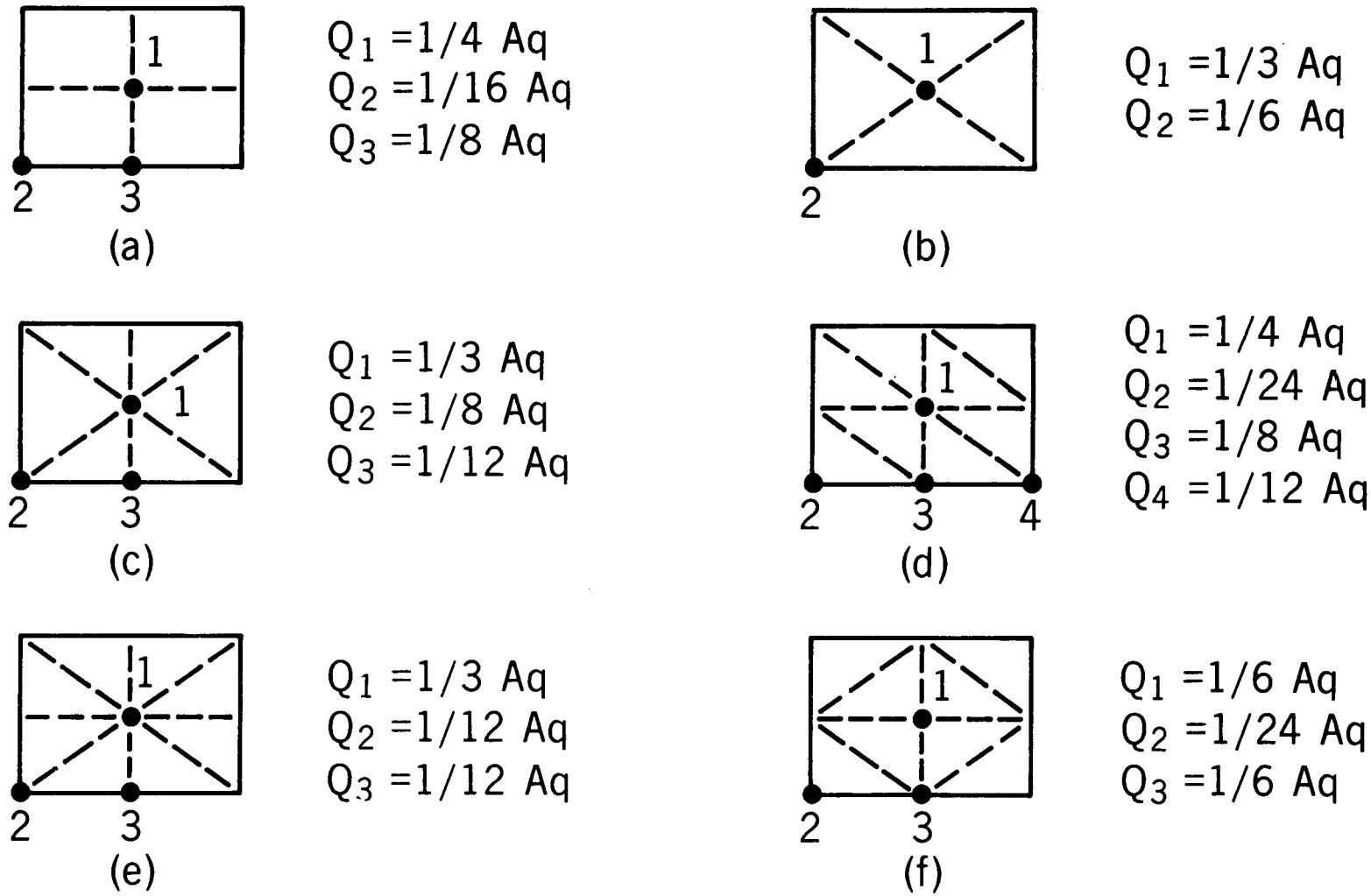

Q_i = Total thermal energy entering into the ith grid point
q = A uniform thermal flux applied to the plate of an area a

Figure 7. Typical patterns of the node valency of a constant Area A.

EFFICIENT REANALYSIS OF STRUCTURES BY A DIRECT MODIFICATION METHOD

A. I. Raibstein, I. Kalev and A. Pipano
Israel Aircraft Industries Ltd.

SUMMARY

A procedure for the local stiffness modifications of large structures is described. It enables structural modifications without an a priori definition of the changes in the original structure and without loss of efficiency due to multiple loading conditions. The solution procedure, implemented in NASTRAN, involves the decomposed stiffness matrix and the displacement vectors of the original structure. It solves the modified structure exactly, irrespective of the magnitude of the stiffness changes. In order to investigate the efficiency of the present procedure and to test its applicability within a design environment, several real and large structures were solved. The results of the efficiency studies indicate that the break-even point of the procedure varies between 8% and 60% stiffness modifications, depending upon the structure's characteristics and the options employed.

INTRODUCTION

For the efficient design of large and complex structures it is necessary to investigate several modified structural configurations. Frequently, structural modifications are made at a few discrete locations in the structure, affecting only a relatively small part of it. Consequently, it is desirable to apply a modification procedure which enables rapid re-analysis of the structure in a time step which is considerably less than that of the analysis of the regular structure. Furthermore, the procedure should be automated with minimum requirements of input data.

The various modifications procedures which have been developed so far can be subdivided into iterative and direct procedures. The iterative procedures are based either on a simple technique of successive approximations (reference 1), or on a version derived from the Gauss-Seidel technique (reference 2), or on a first order Taylor series expansion of design variables (references 3 and 4). The procedures become less efficient as more loading conditions are applied to the structure and more inaccurate as the magnitude of the stiffness changes increases. The advantage of using these procedures is that the efficiency of the procedure is not affected by the relative number of modified degrees of freedom. The direct procedures (references 1 and 5), are exact and their efficiency is mainly governed by the relative number of the modified degrees of freedom. Their efficiency is not affected by the number of loading conditions, and the accuracy of the analysis results is independent of the magnitude of the stiffness changes. Argyris and Roy (reference 6) have developed a general direct modification procedure which handles coupled combinations of three types of modifications, namely, changing stiffnesses of elements, adding degrees of freedoms and removing degrees of freedom.

To our knowledge, the direct procedures have not yet been investigated for large and complex structures and their applicability within a design environment has not been tested. In addition, operation counts alone, as it was done in references 1, 5 and 6, are not sufficient to predict the overall efficiency of the procedures. This is because, for large and real structures, the speed of in-core operations relative to the speed of out-of-core data transfer, the type of finite elements and the time required for the assembly of their stiffness matrices may have a considerable effect on the efficiency.

The present paper describes a direct procedure for the solution of structures with local stiffness modifications (reference 7). The basic concepts are similar to those of Argyris and Roy (reference 6). However, their procedure was modified and implemented in the static solution of NASTRAN (reference 8) by employing NASTRAN'S DMAP language (references 9 and 10). In order to reduce the burden of input data preparation, a NASTRAN preprocessor program, REAN, has been developed. This preprocessor, in addition to its other features, takes care of the characteristics of the modified and unmodified structure constructing the Boolean transformation matrices, which relate their corresponding degrees of freedom.

In order to investigate the efficiency of the modification procedure and to test its applicability within a design environment several real and large structures were solved. For each of the examples a number of modifications were made, including the addition or removal of elements and the investigation of regions with reduced stiffnesses in order to study the post-buckling behavior of these regions. The size of the different mathematical models varied between 60 and 1680 unconstrained degrees of freedom.

SYMBOLS

$[B]$	Boolean transformation matrix
$[F]$	inverse of $[K]$
G	modulus of rigidity
$[I]$	unit matrix
$[K]$	stiffness matrix
$[\bar{K}]$	modified stiffness matrix
$[L]$	lower triangularized stiffness matrix (figure 3)
$[LLL]$	lower triangularized stiffness matrix of original structure (figure 3)
$\{P\}$	load vector
$\{\bar{P}\}$	modified loading vector
$\{Q\}$	vector of reactions
$\{\bar{Q}\}$	modified vector of reactions
q	number of increments of stiffness changes (equation (39))
$[U]$	upper triangularized stiffness matrix (figure 3)
$\{U\}$	displacement vector
$\{\bar{U}\}$	modified displacement vector
a ; a_1 ; a_2	multiplication factors (equation (39))
Δ	increment
τ	shear stress

Subscripts

av	average
c	modified degrees of freedom
eff	effective
f	free degrees of freedom
max	maximum
r	modified constrained degrees of freedom
s	constrained degrees of freedom
u	unmodified degrees of freedom

Superscripts

(q)	indicator of the number of stiffness increments (figure 3)
T	transpose of a matrix

THE DIRECT MODIFICATION PROCEDURE

The Structural Equations

The usual governing equation for the static analysis of structures by the displacement method may be written as

$$[K]\ \{U\} = \{P\} \tag{1}$$

where [K] denotes the structural stiffness matrix. {U} the unknown displacement vector and {P} the applied load vector.

Equation (1), after elimination of the dependent equations (MPC) and including the forces of constraints, Qs, may be written in partitioned form as

$$\begin{bmatrix} K_{ff} & K_{fs} & 0 \\ K_{fs}^T & K_{ss} & -I \\ 0 & I & 0 \end{bmatrix} \begin{Bmatrix} U_f \\ U_s \\ Q_s \end{Bmatrix} = \begin{Bmatrix} P_f \\ P_s \\ U_s \end{Bmatrix} \tag{2}$$

where the subscripts

f denotes the unconstrained (free) set

and s denotes the constrained set.

Expanding the simultaneous set of equations (2) and assuming that the enforced displacement vector $\{U_s\} = 0$ gives us

$$[K_{ff}]\ \{U_f\} = \{P_f\} \tag{3}$$

$$\{Q_s\} = -\{P_s\} + [K_{fs}]^T\ \{U_f\} \tag{4}$$

Equation (3) is solved for the unknown displacement vector $\{U_f\}$ and then the forces of constraints $\{Q_s\}$, are computed using equation (4).

Preliminary Matrix Operations

We define that

c is the part of the f – set which is changed (modified)

and u is the part of the f – set which remains unmodified.

Equation (3) may be written in partitioned form as

$$\begin{bmatrix} K_{uu} & K_{uc} \\ K_{uc}^T & K_{cc} \end{bmatrix} \begin{Bmatrix} U_u \\ U_c \end{Bmatrix} = \begin{Bmatrix} P_u \\ P_c \end{Bmatrix} \tag{5}$$

Now if $[F_{ff}]$ is defined as the inverse of $[K_{ff}]$, then the following relation is valid

$$\begin{bmatrix} K_{uu} & K_{uc} \\ K_{uc}^T & K_{cc} \end{bmatrix} \begin{bmatrix} F_{uu} & F_{uc} \\ F_{uc}^T & F_{cc} \end{bmatrix} = \begin{bmatrix} I_{uu} & 0 \\ 0 & I_{cc} \end{bmatrix} \tag{6}$$

Expanding equation (6) gives

$$[K_{uu}]\,[F_{uc}] + [K_{uc}]\,[F_{cc}] = 0 \tag{7}$$

$$[K_{uc}]^T[F_{uc}] + [K_{cc}]\,[F_{cc}] = [I_{cc}] \tag{8}$$

By pre- and post-multiplying equation (7) by $[K_{uu}]^{-1}$ and $[F_{cc}]^{-1}$, respectively, the following is obtained

$$[K_{uu}]^{-1}[K_{uc}] = -\,[F_{uc}]\,[F_{cc}]^{-1} \tag{9}$$

By post-multiplying equation (8) by $[F_{cc}]^{-1}$ and substituting equation (9) gives

$$[F_{cc}]^{-1} = [K_{cc}] - [K_{uc}]^T[K_{uu}]^{-1}[K_{uc}] \tag{10}$$

The effect of element modifications will be transmitted into $[K_{ff}]$ through a symmetric Boolean transformation matrix. The part of $[K_{ff}]$ affected by element modifications is limited to the symmetric submatrix $[K_{cc}]$. Loading changes on the modified part of the structure are considered by the procedure. However, loading changes for the unmodified part of the structure should be considered through a usual restart job.

We now define the Boolean transformation matrices $[B_{cf}]$ and $[B_{uf}]$. Where

$[B_{cf}]$ is the Boolean transformation matrix relating

$$[K_{ff}] \quad \text{to} \quad [K_{cc}]$$

$[B_{uf}]$ is the Boolean transformation matrix relating

$$[K_{ff}] \quad \text{to} \quad [K_{uu}]$$

Each of the rows in $[B_{cf}]$ and $[B_{uf}]$ contain all zeros, except for one unit value in the column relating to the position of the corresponding row in $[K_{ff}]$ which is being changed or remains unmodified, respectively.

Due to basic algebraic considerations the following orthonormal equations are valid

$$[B_{cf}]\,[B_{cf}]^T = [I_{cc}] \tag{11}$$

$$[B_{uf}]\,[B_{uf}]^T = [I_{uu}] \tag{12}$$

$$[B_{cf}]^T[B_{cf}] + [B_{uf}]^T[B_{uf}] = [I_{ff}] \tag{13}$$

The inverse of $[K_{ff}]$ can now be related, via the Boolean transformation matrices, to its symmetric submatrices $[F_{uu}]$, $[F_{uc}]$ and $[F_{cc}]$ as follows

$$[F_{uu}] = [B_{uf}]\,[K_{ff}]^{-1}[B_{uf}]^T \tag{14}$$

$$[F_{uc}] = [B_{uf}]\,[K_{ff}]^{-1}[B_{cf}]^T \tag{15}$$

$$[F_{cc}] = [B_{cf}]\,[K_{ff}]^{-1}[B_{cf}]^T \tag{16}$$

The displacement vector $\{U_f\}$ is related, via the Boolean transformation matrices, to its subvectors $\{U_u\}$ and $\{U_c\}$ as follows

$$\{U_f\} = [B_{uf}]^T\{U_u\} + [B_{cf}]^T\{U_c\} \tag{17}$$

The Solution Procedure

The equilibrium equations of the modified structures can be written in an equivalent form to equation (5) as

$$\begin{bmatrix} K_{uu} & K_{uc} \\ K_{uc}^T & \bar{K}_{cc} \end{bmatrix} \begin{Bmatrix} \bar{U}_u \\ \bar{U}_c \end{Bmatrix} = \begin{Bmatrix} P_u \\ \bar{P}_c \end{Bmatrix} \tag{18}$$

where the element modifications in $[K_{cc}]$ are expressed as

$$[\bar{K}_{cc}] = [K_{cc}] + [\Delta K_{cc}] \tag{19}$$

$[\Delta K_{cc}]$ is the stiffness matrix of the changes and may be singular.

The final loading vector, $\{\bar{P}_c\}$, on the modified part is expressed as

$$\{\bar{P}_c\} = \{P_c\} + \{\Delta P_c\} \tag{20}$$

where $\{\Delta P_c\}$ defines the loading changes on the modified part of the structure.

The final displacement vectors of the modified degrees of freedom, $\{\bar{U}_c\}$, and the unmodified degrees of freedom, $\{\bar{U}_u\}$, are expressed as

$$\{\bar{U}_c\} = \{U_c\} + \{\Delta U_c\} \tag{21}$$

$$\{\bar{U}_u\} = \{U_u\} + \{\Delta U_u\} \tag{22}$$

Where $\{\Delta U_c\}$ and $\{\Delta U_u\}$ are the additional displacement vectors due to element modifications and loading changes.

Using equations (19) to (22), and substituting for $[\bar{K}_{cc}]$, $\{\bar{U}_c\}$, $\{\bar{U}_u\}$ and $\{\bar{P}_c\}$ in equation (18) and then subtracting equation (5) from it, yields

$$\begin{bmatrix} K_{uu} & K_{uc} \\ K_{uc}^T & K_{cc} + \Delta K_{cc} \end{bmatrix} \begin{Bmatrix} \Delta U_u \\ \Delta U_c \end{Bmatrix} = \begin{Bmatrix} 0 \\ \Delta P_c - \Delta K_{cc} \; U_c \end{Bmatrix} \tag{23}$$

Using the first of equation (23) we get

$$\{\Delta U_u\} = - [K_{uu}]^{-1} [K_{uc}] \{\Delta U_c\} \tag{24}$$

Using the second of equation (23) and eliminating $\{\Delta U_u\}$ yields

$$([\Delta K_{cc}] + [K_{cc}] - [K_{uc}]^T[K_{uu}]^{-1}[K_{uc}])\{U_c\} = \{\Delta P_c\} - [\Delta K_{cc}]\{U_c\} \tag{25}$$

By substituting equation (9) in equation (24) and equation (10) in equation (25) we obtain

$$\{\Delta U_u\} = [F_{uc}]\,[K_{cc}]^{-1}\{\Delta U_c\} \tag{26}$$

$$([\,\Delta K_{cc}] + [F_{cc}]^{-1})\,\{\Delta U_c\} = \{\Delta P_c\} - [\Delta K_{cc}]\,\{U_c\} \tag{27}$$

Using equation (17), the equivalent relation for the modified displacement vector $\{U_f + \Delta U_f\}$ is as follows

$$\{U_f + \Delta U_f\} = [B_{uf}]^T\,\{U_u + \Delta U_u\} + [B_{cf}]^T\,\{U_c + \Delta U_c\} \tag{28}$$

where $\{\Delta U_f\}$ is the change of the displacement vector in the f-set.

Subtracting equation (17) from equation (28) yields

$$\{\Delta U_f\} = [B_{uf}]^T\{\Delta U_u\} + [B_{cf}]^T\{\Delta U_c\} \tag{29}$$

Substituting $\{\Delta U_u\}$ from equation (26) in equation (29) yields

$$\{\Delta U_f\} = [B_{uf}]^T[F_{uc}][F_{cc}]^{-1}\,\{\Delta U_c\} + [B_{cf}]^T\{\Delta U_c\} \tag{30}$$

Using equation (15) and substituting for $[F_{uc}]$ in equation (30) we obtain

$$\{\Delta U_f\} = [B_{uf}]^T[B_{uf}][K_{ff}]^{-1}[B_{cf}]^T[F_{cc}]\{\Delta U_c\} + [B_{cf}]^T\{\Delta U_c\} \tag{31}$$

Using equation (13) and substituting for $([B_{uf}]^T[B_{uf}])$ in equation (31), yields

$$\{\Delta U_f\} = ([I_{ff}] - [B_{cf}]^T[B_{cf}])\,[K_{ff}]^{-1}[B_{cf}][F_{cc}]^{-1}\,\{U_c\} + [B_{cf}]^T\{\Delta U_c\} \tag{32}$$

From equation (16) we establish the identity

$$([B_{cf}][K_{ff}]^{-1}[B_{cf}]^T)[F_{cc}]^{-1} = [I_{cc}] \tag{33}$$

Using the identity of equation (33) we reduce equation (32) to obtain

$$\{\Delta U_f\} = [K_{ff}]^{-1}[B_{cf}]^T\,[F_{cc}]^{-1}\{\Delta U_c\} \tag{34}$$

Using equation (27) and substituting for $\{\Delta U_c\}$ in equation (34) we obtain the final equation for the change in the displacement vector of the f-set due to the modifications as follows

$$\{\Delta U_f\} = [K_{ff}]^{-1}[B_{cf}]^T \; [F_{cc}]^{-1} \; ([K_{cc}] + [F_{cc}]^{-1})^{-1} \; (\{\Delta P_c\} - [\Delta K_{cc}]\{U_c\}) \tag{35}$$

And the modified displacement vector, $\{\bar{U}_f\}$ is expressed as

$$\{\bar{U}_f\} = \{U_f\} + \{\Delta U_f\} \tag{36}$$

Using equation (4) we define the equivalent relations for the modified vector of constraints, $\{\bar{Q}_s\}$, as

$$\{\bar{Q}_s\} = -\{P_s\} + [\bar{K}_{fs}]^T \{\bar{U}_f\} \tag{37}$$

where the modified matrix $[\bar{K}_{fs}]$ is expressed as

$$[\bar{K}_{fs}]^T = [K_{fs}]^T + [B_{rs}]^T[\Delta K_{cr}]^T[B_{cf}] \tag{38}$$

where

$[\Delta K_{cr}]$ is the compacted change matrix of $[K_{fs}]$ and $[B_{rs}]$ is the Boolean transformation matrix relating $[K_{fs}]$ to $[\Delta K_{cr}]$, i.e., r denotes the part of the s-set which is changed.

Considering the final equation for the modified displacement vector, $\{\bar{U}_f\}$, (equation 36) we note that for the analysis of the modified structure, only $[\Delta K_{cc}]$ and $\{\Delta P_c\}$ have to be computed based on the modifications on the structure. However, the major computations are due to the following steps

* Performing a forward sweep and backward substitution, using the decomposed triangular matrices of $[K_{ff}]$ on the Boolean matrix $[B_{cf}]^T$.

* Decomposition and performing a forward sweep and backward substitution using $[F_{cc}]$ on a unit matrix $[I_{cc}]$. We note that $[F_{cc}]$ is a positive definite symmetric matrix.

* The remaining computations are involved with smaller computing time.

The efficiency of the procedure is further improved if, after computing $[K_{ff}]^{-1}[B_{cf}]^T$ and $[F_{cc}]^{-1}$ (first two terms of equation(35)), changes are made only to the c degrees of freedom. This is implemented in the procedure described here by increasing or decreasing the term $[\Delta K_{cc}]$ (last term of equation (35)) by a constant factor as shown below:

If

a_1 is an initial multiplication factor for $[\Delta K_{cc}]$ and $[\Delta K_{cr}]$

a_2 is an incremental multiplication factor

q is the number of incremental stiffness changes

Then

$$a = a_1 + q \cdot a_2 \tag{39}$$

Therefore if $[\Delta K_{cc}]$ is multiplied within the computational loop by the variable a, then only the term $([F_{cc}]^{-1} + a\,[\Delta K_{cc}])^{-1}$ will have to be recomputed for each increments of stiffness change. The factors a_1, a_2 and q are defined in the NASTRAN analysis of the modified structure by standard PARAM bulk data cards.

The generation of the Boolean transformation matrices $[B_{cf}]$ and $[B_{rs}]$ is tedious and error-prone. Therefore, a computer program, REAN, has been developed which generates those matrices automatically in a form suitable for NASTRAN.

An overall schematic diagram of the procedure is shown in figure 1.

DESCRIPTION OF PROGRAM REAN

The REAN (RE ANalysis) computer program is a preprocessor for NASTRAN. It performs the following main tasks

a) Updates MPT (Material Property Table) and EST (Element Summary Table) tables

b) Generates the Boolean transformation matrices $[B_{cf}]$ and $[B_{rs}]$

c) Generates the appropriate DMAP ALTER package for Rigid Format 1.

The execution of program REAN, illustrated in figure 2, is subdivided into the following steps.

* The input to the program consists of

  (a) a standard NASTRAN Data Deck defining the grid points, element connections, element properties, material properties for the structural modifications only and the values and number of incremental stiffness changes

  (b) the NASTRAN tables CSTM, YS, GPL, USET, OQG1, MPT and EST.

* The program then checks

  (a) if CBAR, CQDPLT, CQUAD2, CTRIA2 or CTRPLT elements are to be modified; if so, the EST tables are updated. This is done in order to obtain the correct stresses for the elements listed above.

  (b) if the material properties defined for the modified part of the structure are different from those defined for the original structure; if so, the MPT tables are updated.

* Using the grid points defined for the modified part of the structure in conjunction with the NASTRAN tables GPL, USET and OQG1 the program first checks if any of the modified elements are connected to degrees of freedom which are constrained. If this is the case, the Boolean transformation matrices $[B_{cf}]$ and $[B_{rs}]$ are generated. If none of the modified elements are connected to constrained degrees of freedom, then only $[B_{cf}]$ is generated; $[B_{cf}]$ and $[B_{rs}]$ are inserted via DMI card images.

* Using the information obtained via the NASTRAN files UT1 and UT2, the program then generates the appropriate DMAP Alter package and creates a NASTRAN input file.

After the execution of program REAN, NASTRAN is loaded and the analysis for the modified structure is performed.

DMAP ALTER PACKAGES

The modification procedure is effected in NASTRAN utilizing standard DMAP statements. The following two types of DMAP Alter Packages are required:

1) The first DMAP Alter package, inserted in the original deck, utilizes OUTPUT1 and OUTPUT2 modules only.

OUTPUT1 is used to save all the matrices and data blocks required to perform the analysis of the modified structure and the data recovery of nodal displacements, reactions, element forces and stresses. The OUTPUT2 module is used to save data blocks required for program REAN as explained in the previous section.

2) The second DMAP ALTER package, generated by program REAN and which effects the solution procedure, is automatically inserted into the data deck of the modified structure and performs the actual reanalysis procedure.

A flow diagram of the DMAP functional steps and their equivalent results is shown in figure 3. The DMAP statements for the first and second packages are listed and described in the Appendix. It should be noted that, according to the problem type, program REAN automatically chooses the appropriate form of inclusion of the optional data blocks CSTM, GM, KFSO, KSS, PS and YS in the SDR1 and SDR2 modules.

NUMERICAL EXAMPLES

The direct modification procedure has been applied to several real aircraft structures. Each of the examples described below is governed by different structural characteristics influencing the efficiency of the procedure. In order to achieve the minimum decomposition time for the regular analysis, resequencing of the grid points was performed. The examples were run on a CDC 6500 computer with 50000_{10} words of memory available for the execution of NASTRAN.

Wing Structure (model 1)

The wing structure was idealized using shear panels to represent the shear stiffness of the skins and webs, and rod elements representing their extensional stiffnesses. The mathematical model, figure 4, consisted of 6 BAR, 501 ROD, 288 SHEAR elements and 220 GRID points representing 1320 degrees of freedom of which 648 were unconstrained. The structure was subjected to two loading conditions and its stiffness matrix had 66 RMS column lengths.

Three structural modifications were investigated; (a) the stiffness properties of 40 elements were changed affecting 39 degrees of freedom; i.e. 6% of the structure; (b) the stiffness properties of 68 elements were changed affecting 85 degrees of freedom; i.e. 13% of the structure; and (c) the stiffness properties of 130 element were changed affecting 136 degrees of freedom; i.e. 21% of the structure. The changes were referenced as Regions "A", "B" and "C", respectively, on a plan view of the wing structure shown schematically in table 1. This table also presents comparisons of the CPU execution time for a regular analysis versus analysis by the modification procedure.

Wing Structure (model 2)

This wing structure was a highly idealized mathematical model, as shown in figure 5. The structural elements used were the same as those used in model 1. The mathematical model consisted of 26 BAR, 1200 ROD, 660 CSHEAR elements and 560 GRID points representing 3360 degrees of freedom, of which 1680 were unconstrained. The structure was subjected to two loading conditions and its stiffness matrix had 92 RMS column lengths.

Three structural modifications were investigated: (a) The stiffness properties of 60 elements were changed affecting 66 degrees of freedom, i.e. 4% of the structure; (b) the stiffness properties of 105 elements were changed affecting 132 degrees of freedom, i.e. 8% of the structure; and (c) the stiffness properties of 222 elements were changed affecting 231 degrees of freedom, i.e. 14% of the structure. The changes were referenced as regions "A", "B" and "C", respectively, on a plan view of the wing structure shown schematically in table 2. This table also presents comparison of the CPU execution time for a regular analysis versus analysis by the modification procedure.

Wing Structure (model 3)

This model is similar in size to the one described as model 2, as shown in figure 5. However instead of shear panels, isoparametric membrane elements, QDMEM1, were utilized. The mathematical model consisted of 42 CBAR elements, 662 QDMEM1, 860 ROD, and 500 GRID points representing 3000 degrees of freedom, of which 1580 were unconstrained. The structure was subjected to three loading conditions and its stiffness matrix had 114 RMS column lengths.

Three structural modifications were investigated: (a) The stiffness property of one element was changed affecting 6 degrees of freedom, i.e. 0.4% of the structure; (b) The stiffness properties of 22 elements were changed affecting 48 degrees of freedom, i.e. 3% of the structure; and (c) the stiffness properties of 130 elements were changed affecting 225 degrees of freedom, i.e. 14% of the structure. The changes are referenced as Regions "A", "B" and "C", respectively, on a plan view of the wing structure shown schematically in table 3. This table also presents comparisons of the CPU execution time for a regular analysis versus analysis by the modification procedure.

Fuselage Structure

The fuselage was idealized using shear panels to represent the skins, rod elements to represent the stringers and beam elements to represent the bulkheads. The mathematical model, (figure 6) consisted of 160 BAR, 590 ROD, 350 SHEAR elements and 404 GRID points representing 2424 degrees of freedom, of which 1293 were unconstrained. The structure was subjected to one loading condition and its stiffness matrix had 70 RMS column lengths.

Three structural modifications were investigated: (a) 3 elements were added to the structure affecting 28 degrees of freedom, i.e. 2.8% of the structure; (b) the properties of 12 elements were changed affecting 72 degrees of freedom, i.e. 6% of the structure; and (c) the properties of 90 elements were changed affecting 180 degrees of freedom i.e. 14% of the structure. The changes are referenced as Regions "A", "B" and "C", respectively, on an axonometric view of the fuselage structure shown schematically in table 4. This table also presents comparisons of the CPU execution time for a regular analysis versus analysis by the direct modification procedure.

Panel In Shear

Figure 7 shows the effect of reduced thickness at the center of a rectangular panel on the modulus of rigidity and on the maximum shear stress. The panel was idealized by 25 rectangular QDMEM elements and the thickness of the center element was reduced to zero in 10 increments.

This example demonstrates the procedure's capability of "one-shot" solution of several cases differing in stiffness (i.e. with varying $[\Delta K_{cc}]$ in equation (35)). In addition, the required CPU execution time utilizing the present procedure was 1/4 of the time required for 10 regular runs.

DISCUSSION

The efficiency studies for the solution times of the numerical examples solved, indicated the following intrinsic features of the direct modification procedure utilized.

(a) For large problems whose stiffness matrices have large RMS values for their semi-bandwidth, the forward sweep and back substitution using the triangularized stiffness matrix of $[K_{ff}]$ on $[B_{cf}]$ (First two terms of equation (35)) is the most time-consuming. Table 3 shows that for 3% modification, for example, the solution time for the modification procedure is equal to the solution time for the regular analysis. However, for a structure with lower RMS values, the break-even point in the solution time is reached at approximately 5% modifications, as can be seen from table 1.

(b) For modifications affecting a relatively large number of degrees of freedom, the decomposition and subsequent forward sweep and back substitution using $[F_{cc}]$ on the unit matrix $[I_{cc}]$ (third term of equation (35)) may take a considerable portion of the solution time needed for the modification procedure. For example in table 1, for modification "C", the computation of $[F_{cc}]^{-1}$ took 1/3 of the total solution time.

(c) The types of elements used in the finite element model may have a considerable effect on the efficiency of the procedure. Table 3 shows that when changing the stiffness property of one element only 1/20 of the total CPU execution time of the regular analysis was required to obtain the new displacement vector. However the same

change for the same mesh with different types of elements would require 1/12 of the execution time of the regular analysis, as can be deduced from table 2.

(d) When using the option of incremental stiffness changes, the efficiency of the procedure is increased substantially. The comparison between the regular analysis and the modification procedure (table 5) shows that for all the cases solved, the break-even CPU time for solution of the displacement vectors came to more than 30% modifications of degrees of freedom. For Wing model 1 the break-even point was approximately 60% modifications of degrees of freedom when including 4 additional stiffness increments.

CONCLUSIONS

A direct modification procedure has been presented and its implementation in NASTRAN has been described. The efficiency of the procedure has been investigated by solving several real and large structures. The study of the relative CPU execution times for the various problems indicated that the efficiency of the procedure is dependent on the following main structural characteristics: (a) Size of the original structure and the number of active columns in the stiffness matrix; (b) the number of stiffness modifications; (c) the types of finite elements used in the mathematical model; and (d) the number of required additional stiffness modifications.

The break-even point of the procedure varies between 8% to 60% modifications of the degrees of freedoms. However, the higher percentage can only be achieved when using the option of incremental stiffness modifications. It is therefore concluded that the direct modification procedure is highly efficient when investigating regions with continuous varying stiffness magnitudes, such as occurs during the post-buckling phenomena. Furthermore, the procedure was found to be very useful when studying the effect of removing or adding elements between existing grid points to a structure or changing the stiffness properties of elements at different locations.

APPENDIX

LISTING AND DESCRIPTION OF THE DMAP STATEMENTS

DMAP Alter Statements For The Original Structure

```
1.  ALTER      119
2.  OUTPUT1    LLL,ULV,KFS,,//C,N,-1/C,N,8/C,N,USERTPM  $
3.  OUTPUT1    USET,EQEXIN,SIL,BGPDT,//C,N,0/C,N,8  $
4.  OUTPUT1    GM,CSTM,YS,PS,KSS//C,N,0/C,N,8  $
5.  OUTPUT2    MPT,EST,,,//C,N,-1/C,N,11/C,N,USERTP2  $
6.  OUTPUT2    CSTM,YS,GPL,USET,OQG1//C,N,12/C,N,USERTP3  $
7.  ENDALTER
```

Description of DMAP Alter Statements

2. The lower triangularized stiffness matrix of $[K_{ff}]$, the displacement vector and $[K_{fs}]$, which are used in the modification procedure, are written on file INP8.

3, 4. NASTRAN tables to be used for the recovery of the nodal displacements, nodal reactions, element forces and stresses are written on file INP8.

5. The Element Summary Table (EST) and the Material Property Table (MPT) are written on file UT1 such that, if necessary, they can be updated by Program REAN.

6. Writes NASTRAN Tables on file UT2, with the help of which Program REAN computes the Boolean transformation matrices and generates the DMAP ALTER package for the subsequent analysis of the modified structure.

DMAP Alter Package For The Analysis Of The Modified Structure

```
1.  ALTER      78
2.  INPUTT1    /LLLO,ULVO,KFSO,,/C,N,-1/C,N,8/C,N,USERTP1  $
3.  INPUTT1    /USET1,EQEXIN1,SIL1,BGPDT1,/C,N,0/C,N,8  $
4.  INPUTT1    /GM1,CSTM1,YS1,PS1,KSS1//C,N,0/C,N,8  $
5.  INPUTT2    /MPT1,EST1,,,/C,N,-1/C,N,11/C,N,USERTP2  $
6.  FILE       KFF1=SAVE/KFF2=SAVE/Q1=SAVE/XB=SAVE/V=SAVE/
               BBT=SAVE/BS=SAVE/KFSA= SAVE /KFSB=SAVE  $
7.  PARAM      //C,N,NOP/V,N,NC=-1  $
```

```
 8.  PARAM      //C,N,NOP/V,N,NA=-1   $
 9.  PARAM      //C,N,SUB/V,Y,NCASES/V,Y,NCASES=1/C,N,1   $
10.  LABEL      W3   $
11.  COND       W7,NC   $
12.  COND       W1,NA   $
13.  LABEL      W7   $
14.  PARAM      //C,N,ADD/V,N,NC/C,N,1   $
15.  FBS        LLLO,,BBT/V/C,N,1/C,N,1/C,N,1/C,N,1   $
16.  MPYAD      BB,V,/Q/C,N,0/C,N,1/C,N,0/C,N,1   $
17.  MPYAD      BB,BBT,/DD/ C,N,0/C,N,1/C,N,0/C,N,1   $
18.  MPYAD      BB,ULVO,/XB/C,N,0/C,N,1/C,N,0/C,N,1   $
19.  DECOMP     Q/QL,QU/C,N,1/C,N,1   $
20.  FBS        QL,,DD/QI/C,N,1/C,N,1/C,N,1/C,N,1   $
21.  ADD        KFS,/KFSA/C,Y,FACA = (0.0,0.0)   $
22.  ADD        KFS,/KFSA/C,Y,FACB = (1.0,0.0)   $
23.  ADD        KFF,/KFF1/C,Y,FACA = (0.0,0.0)   $
24.  ADD        KFF,/KFF1/C,Y,FACB = (1.0,0.0)   $
$ ****  TOP OF DMAP LOOP FOR INCREMENTS OF STIFFNESS CHANGES  ****
25.  LABEL      W1   $
26.  ADD        KFSA,KFSB/KFSC   $
27.  EQUIV      KFSC,KFSA/NA   $
28.  ADD        KFF1,KFF2/KFF3   $
29.  EQUIV      KFF3,KFF1/NA   $
30.  PARAM      //C,N,ADD/V,N,NC/V,N,NC/C,N,1   $
31.  PRTPARM    //C,N,0/C,N,NC   $
32.  MPYAD      KFF3,XB,/XBB/C,N,0/C,N,1/C,N,0/C,N,1   $
33.  ADD        QI,KFF3/R   $
34.  DECOMP     R/RL,RU/C,N,1/C,N,1   $
35.  FBS        RL,,XBB/U1/C,N,1/C,N,1/C,N,1/C,N,1   $
36.  SMPYAD     V,QI,U1,,,/U2/C,N,3/C,N,-1/C,N,1   $
37.  ADD        U2,ULVO/ULVN   $
38.  JUMP       LBL9   $
39.  ALTER      110,119
40.  SMPYAD     BBT,KFSC,BS,,,KFSO/KFS1/C,N,3/C,N,1/C,N,1   $
```

```
41.  SDR1      USET1,,ULV1,,YS1,,GM1,PS1,KFS1,KSS1,/UGV,PGG,QG/
               V,N,NSKIP/C,N,STATICS  $
42.  SDR2      CASECC,CSTMM,MPT1,,EQEXIN1,SIL1,,,BGPDT1,PGG,QG,
               UGV,EST1,/OPG1,OQG1,OES1,OEF1,PUGV1/C,N,STATICS  $
43.  ALTER     121
44.  PARAM     //C,N,SUB/V,Y,NCASES/V,Y,NCASES/C,N,1  $
45.  COND      W3,15  $
$ ****  BOTTOM OF DMAP LOOP FOR INCREMENTS OF STIFFNESS CHANGES ****
46.  ENDALTER
```

Description Of DMAP ALTER Statements

1. The procedure starts after, the stiffness matrix for the modified structure, $[\Delta K_{cc}]$ has been assembled.

2. Retrieves the lower triangularized stiffness Matrix of $[K_{ff}]$, LLLO, Displacement vector, ULVO, and KFSO for the unmodified structure.

3, 4. Retrieves NASTRAN tables to be used for the recovery of the nodal displacements, reactions, element forces and stresses. It should be noted that not all the data block names saved via OUTPUT1 in the original analysis appear here. Program REAN checks if the files saved are empty, retrieving only those data blocks which contain information required for the analysis of the modified structure.

5. Retrieves the updated Material Property Table (MPT1) and Element Stiffness Table (EST1). The update of the tables is performed by REAN.

7–9. Defines the default values for α_1, α_2 and q.

15. Performs a forward sweep and backward substitution using the lower triangular matrix of $[K_{ff}]$, on $[B_{cf}]^T$ this yields $[K_{ff}]^{-1} \cdot [B_{cf}]^T$

16. Multiplies $[B_{cf}] \cdot [K_{ff}]^{-1} \cdot [B_{cf}]^T$ which yields the matrix $[F_{cc}]$.

18. Multiplies $[B_{cf}]$ by the displacement vector ULVO of the unmodified structure. This yields the displacement vector, $\{U_c\}$, for the part of the structure which is to be modified.

19. Decompose the matrix $[F_{cc}]$ into an upper and lower triangular matrix.

20. Performs a forward sweep and backward substitution using the lower triangularized matrix of $[F_{cc}]$ on a unit matrix, obtained by multiplying $[B_{cf}] \cdot [B_{cf}]^T$, this yields $[F_{cc}]^{-1}$

21–24. Initializes $[\Delta K_{cc}]$ and $[\Delta K_{cr}]$ of the modified structure.

25. Start of the DMAP loop for the specified increments of stiffness changes.

32. Multiplies $[\Delta K_{cc}] \cdot \{U_c\}$

33. Adds ($[\Delta K_{cc}] + [F_{cc}]^{-1}$)

34. Decomposes the matrix ($[\Delta K_{cc}] + [F_{cc}]^{-1}$) into upper and lower triangular matrices.

35. Performs a forward sweep and backward substitution using the lower triangular matrix of ($[\Delta K_{cc}] + [F_{cc}]^{-1}$) on ($[\Delta K_{cc}] \quad \{U_c\}$)
This yields ($[\Delta K_{cc}] + [F_{cc}]^{-1})^{-1} \cdot [\Delta K_{cc}] \cdot \{U_c\}$

36. Multiplies the results obtained in 15, 20 and 35. This yields the displacement vector, $\{\Delta U_f\}$, which represent the influence of the structural modification on the original structure.

37. Adds ULVO and $\{\Delta U_f\}$ and yields the final displacement vector ULVN of the modified structure.

40. Computes the nodal reaction (See equation (37)). The Boolean transformation matrix $[B_{rs}]$ is computed by REAN.

DMAP Statement 40 is not included by Program REAN if none of the modified elements are incident at degrees of freedom which are constrained.

41, 42. Recovers via SDR1 and SDR2 the nodal displacements, reactions element stresses and forces for the modified structure.

45. Bottom of DMAP loop.

REFERENCES

1. Kavlie, D.; and Powell, G.H. : Efficient reanalysis of modified structures, J. Struct. Div., ASCE, 97, ST 1, Jan. 1971, pp. 377-392.

2. Phansalkar, S.R. : Matrix iterative methods for structural reanalysis, Comp. & St., 4, 4, 1974, pp. 779-800.

3. Storaasli, O.O. ; and Sobieszczanski, J. : Design oriented structural analysis, AIAA paper 73-338, Willeamsburg, Va., 1973.

4. Noor, A.K.; and Lowder, H.E. : Approximate techniques of structural reanalysis, Comp. & St., 4, 4, 1974, pp. 801-812.

5. Argyris, J.H.; et al.: A direct modification procedure for the displacement method, AIAA J., 9, 9, Sept. 1971, pp. 1861-1964.

6. Argyris, J.H.; and Roy, J.R. : General treatment of structural modifications, J. Struct. Div., ASCE, 98, ST 2, Feb. 1972, pp. 465-492.

7. Kalev, I.; and Raibstein, A. : Reanalysis of structures due to stiffness modifications via NASTRAN, IAI TR 4842/10615, Feb. 1976.

8. MacNeal, R.H., ed.: The NASTRAN theoretical manual, NASA SP-221(01), April 1972.

9. McCormick, W., ed. : The NASTRAN user's manual, NASA SP-222 (01), June 1972.

10. Douglas, F.J., ed.: The NASTRAN programmer's manual, NASA SP-223, Sept. 1970.

Table 1 — Comparison of CPU Execution Times for Wing Model 1

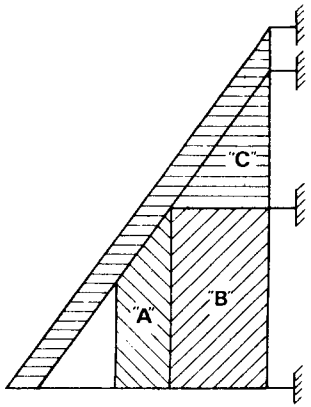

Wing Plan View

Model	characteristics
650	D.O.F.
220	Grid Points
800	Elements

Modification characteristics (Upper Skin)
Region "A" — 39 D.O.F.; 40 Elements
Region "B" — 85 D.O.F.; 70 Elements
Region "C" — 136 D.O.F.; 130 Elements

	Regular Analysis (sec.)	Analysis using the Direct Modification Procedure (sec.)					
		Region "A" — 6 % Modifications		Region "B" — 13 % Modifications		Region "C" — 21 % Modifications	
		First Stiffness Modification	Each Additional Modification	First Stiffness Modification	Each Additional Modification	First Stiffness Modification	Each Additional Modification
Input Data Processing, Generation and Partitioning of Stiffness Matrix	164	20	0	26	0	36	0
Solution	41	51	5	100	13	177	49
Data Recovery and Output of Results	27	27	27	27	27	27	27
Total	232	98	32	153	40	240	76

Table 2 – Comparison of CPU Execution Times for Wing Model 2

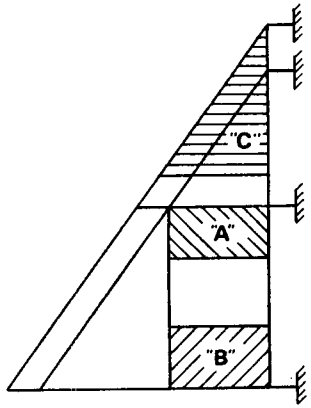

Wing Plan View

Model	characteristics
1650	D.O.F.
560	Grid Points
2150	Elements

Modification characteristics (Upper Skin)			
Region "A" –	66 D.O.F.:	60	Elements
Region "B" –	132 D.O.F.:	105	Elements
Region "C" –	231 D.O.F.:	222	Elements

	Regular Analysis (sec.)	Analysis using the Direct Modification Procedure (sec.)					
		Region "A" – 4% Modifications		Region "B" – 8% Modifications		Region "C" – 14% Modifications	
		First Stiffness Modification	Each Additional Modification	First Stiffness Modification	Each Additional Modification	First Stiffness Modification	Each Additional Modification
Input Data Processing, Generation and Partitioning of Stiffness Matrix	478	35	0	39	0	51	0
Solution	133	180	21	386	34	870	121
Data Recovery and Output of Results	79	79	79	79	79	79	79
Total	690	294	100	504	113	1000	200

Table 3 —Comparison of CPU Execution Times for Wing Model 3

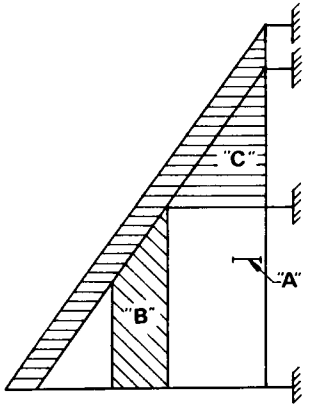

Wing Plan View

Model	characteristics
1580	D.O.F.
500	Grid Points
1570	Elements

Modification characteristics (Upper Skin)				
Region "A"—	6	D.O.F.:	1	Element
Region "B"—	48	D.O.F.:	22	Elements
Region "C"—	225	D.O.F.:	130	Elements

	Regular Analysis (sec.)	Analysis using the Direct Modification Procedure (sec.)					
		Region "A"—0.4% Modifications		Region "B" — 3% Modifications		Region "C"— 14% Modifications	
		First Stiffness Modification	Each Additional Modification	First Stiffness Modification	Each Additional Modification	First Stiffness Modification	Each Additional Modification
Input Data Processing, Generation and Partitioning of Stiffness Matrix	1190	15	0	17	0	170	0
Solution	230	58	5	233	13	900	121
Data Recovery and Output of Results	140	140	140	140	140	140	140
Total	1560	213	145	390	153	1210	261

Table 4 – Comparison of CPU Execution Times for Fuselage

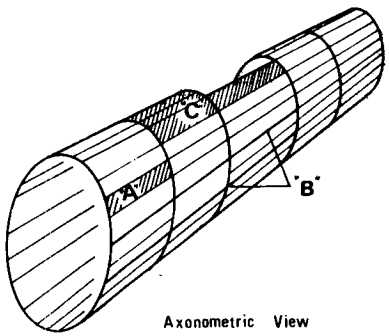

Axonometric View

Model	characteristics
1293	D.O.F.
404	Grid Points
1100	Elements

Modification characteristics			
Region "A" –	28 D.O.F.:	13	Elements
Region "B" –	72 D.O.F.:	12	Elements
Region "C" –	180 D.O.F.:	90	Elements

	Regular Analysis (sec.)	Analysis using the Direct Modification Procedure (sec.)					
		Region "A"–22% Modifications		Region "B" – 5 % Modifications		Region "C"– 14 % Modifications	
		First Stiffness Modification	Each Additional Modification	First Stiffness Modification	Each Additional Modification	First Stiffness Modification	Each Additional Modification
Input Data Processing, Generation and Partitioning of Stiffness Matrix	184	16	0	18	0	35	0
Solution	116	78	5	140	7	430	20
Data Recovery and Output of Results	46	46	46	46	46	46	46
Total	345	140	51	204	53	511	66

Table 5 - Comparison of Regular Analysis vs. The Direct Modification Procedure (*)

	Wing Model 1			Wing Model 2			Wing Model 3			Fuselage		
Magnitude of The Modified Part	6%	13%	21%	4%	8%	14%	0.4%	3%	14%	2.2%	5%	14%
Regular Run (%)	100	100	100	100	100	100	100	100	100	100	100	100
First Increment of Stiffness Modifications (%)	30	61	102	35	70	151	5	18	75	31	52	155
Four Additional Increments of Stiffness Modifications (%)	7	14	33	10	18	46	1	4	22	7	12	36

(*) The comparison is related to the computing time of the displacement vectors (i.e. the computing time for the stress recovery is not included)

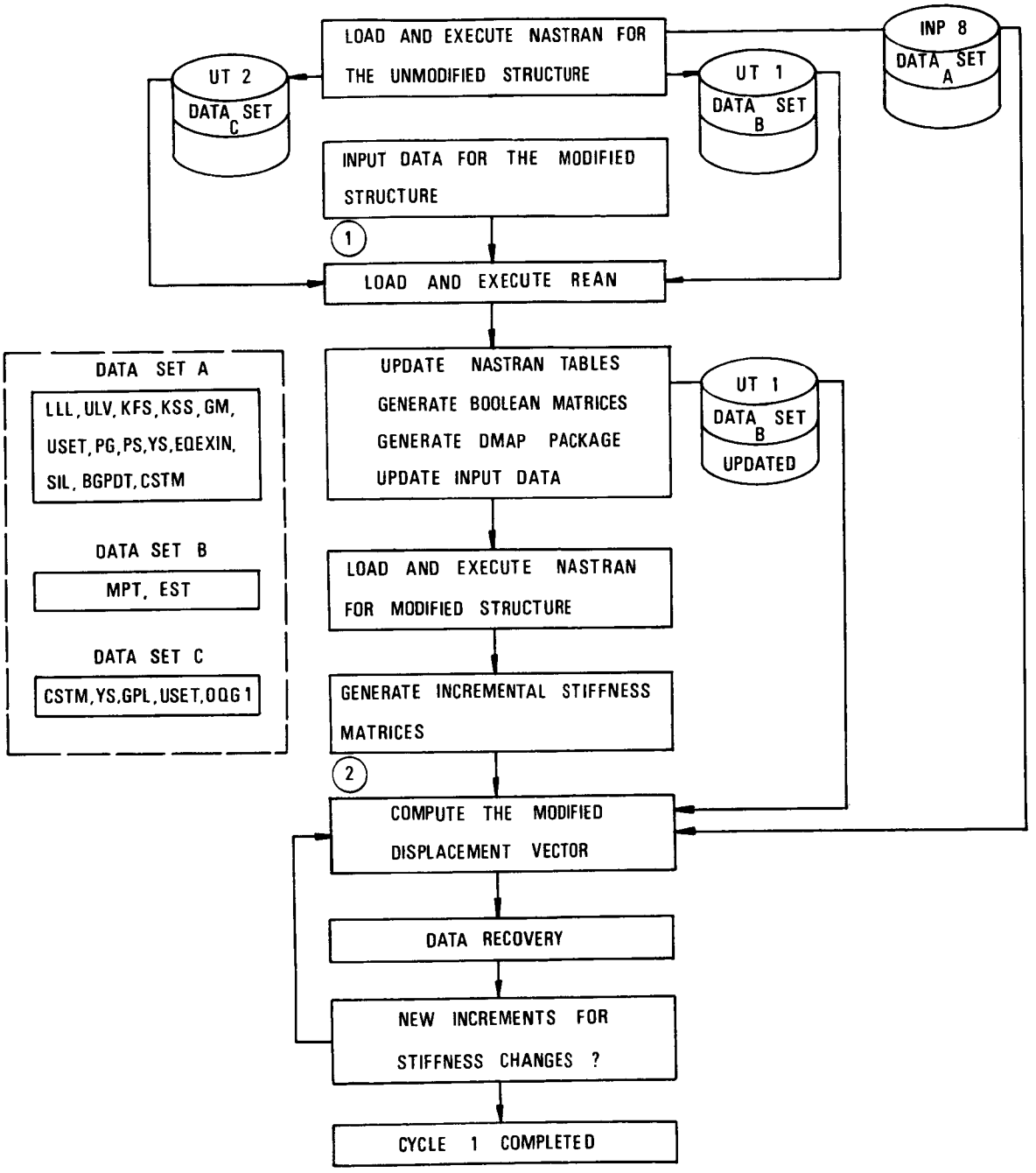

FIGURE 1: OVERALL SCHEMATIC DIAGRAM FOR 1 CYCLE REANALYSIS

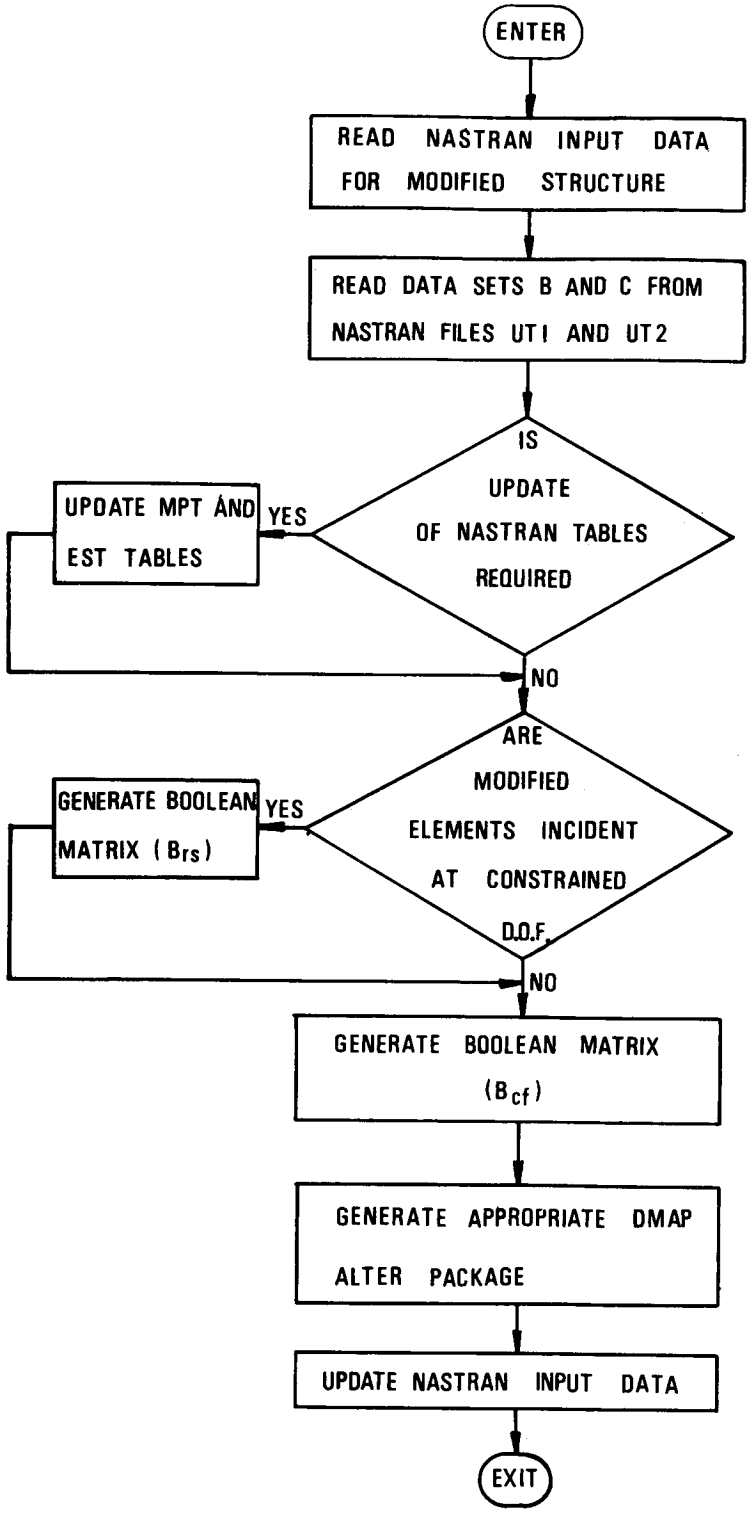

FIGURE 2:FLOW DIAGRAM FOR PROGRAM REAN

(BLOCK 1)

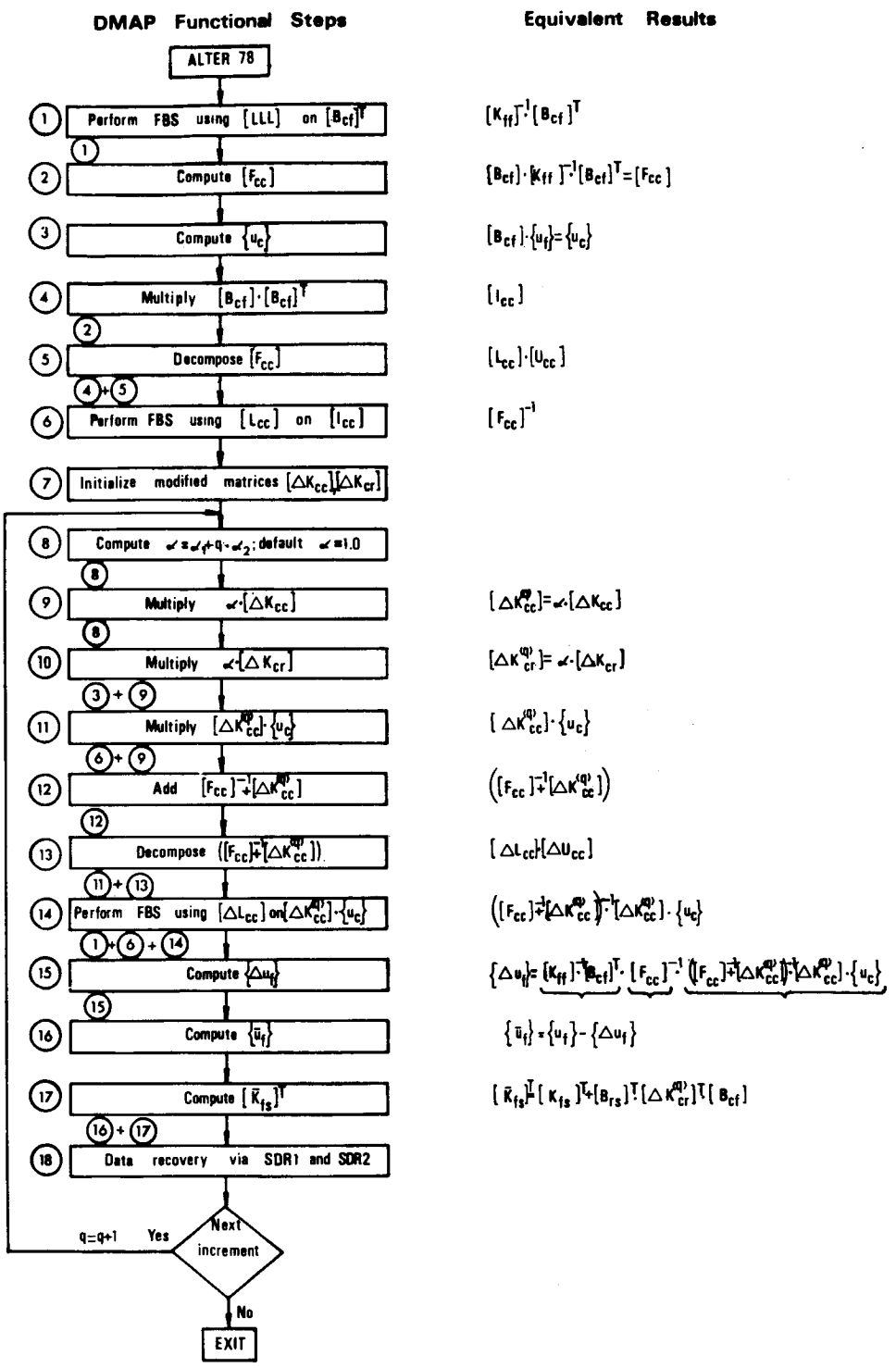

FIGURE 3 : FLOW DIAGRAM FOR BLOCK 2

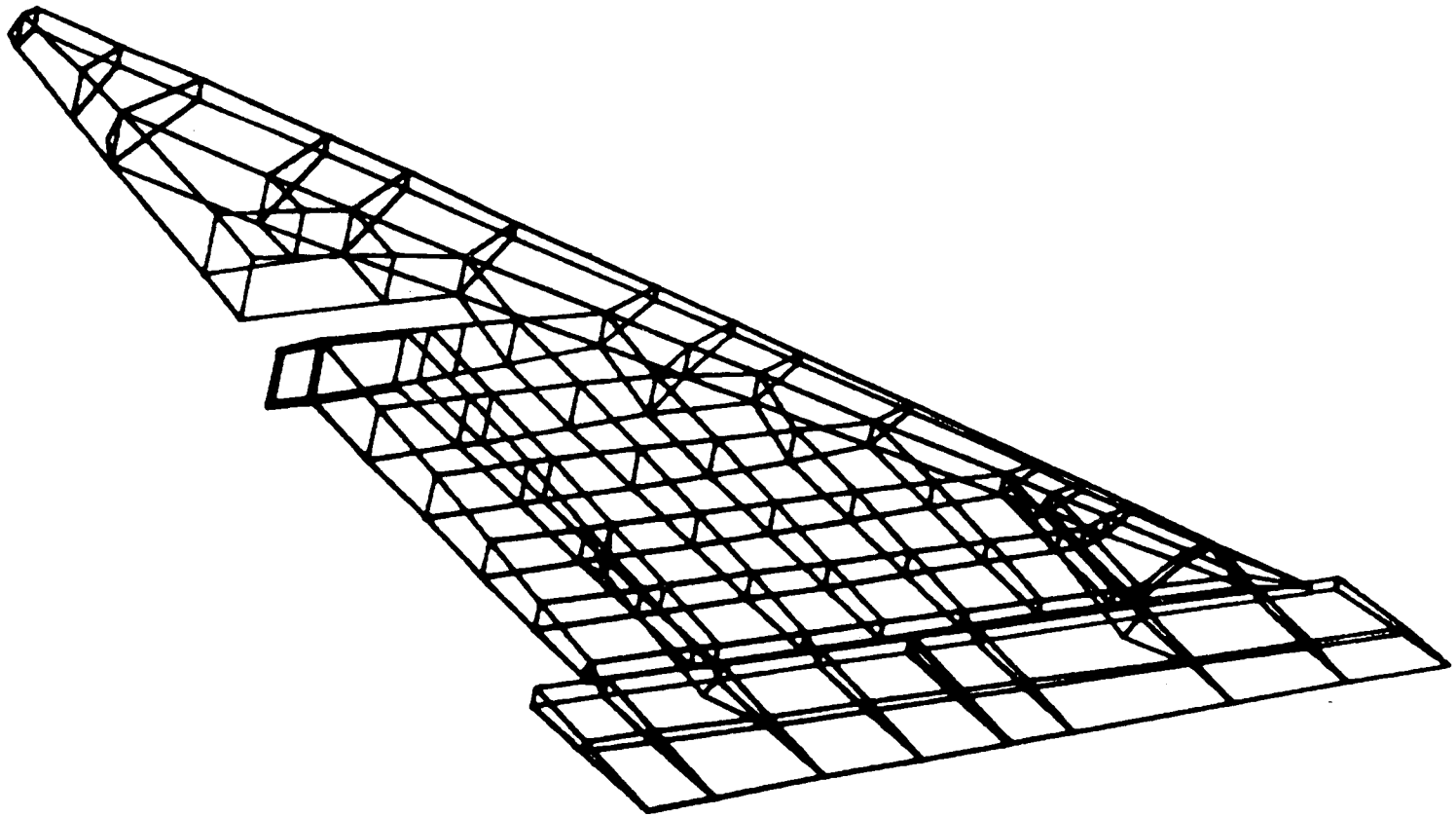

FIGURE 4: IDEALIZATION OF AIRCRAFT WING (MODEL 1)

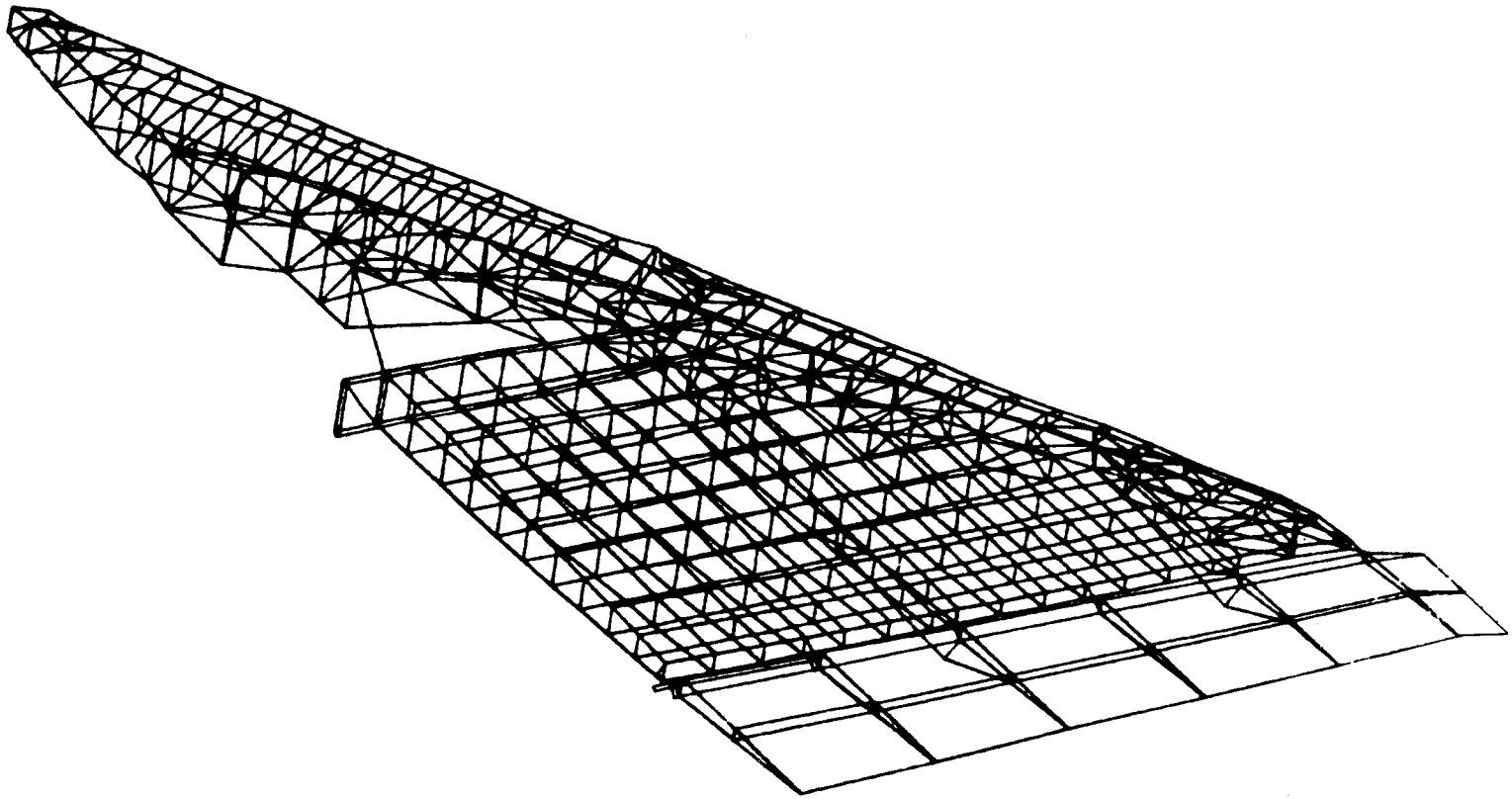

FIGURE 5: IDEALIZATION OF AIRCRAFT WING (MODELS 2 and 3)

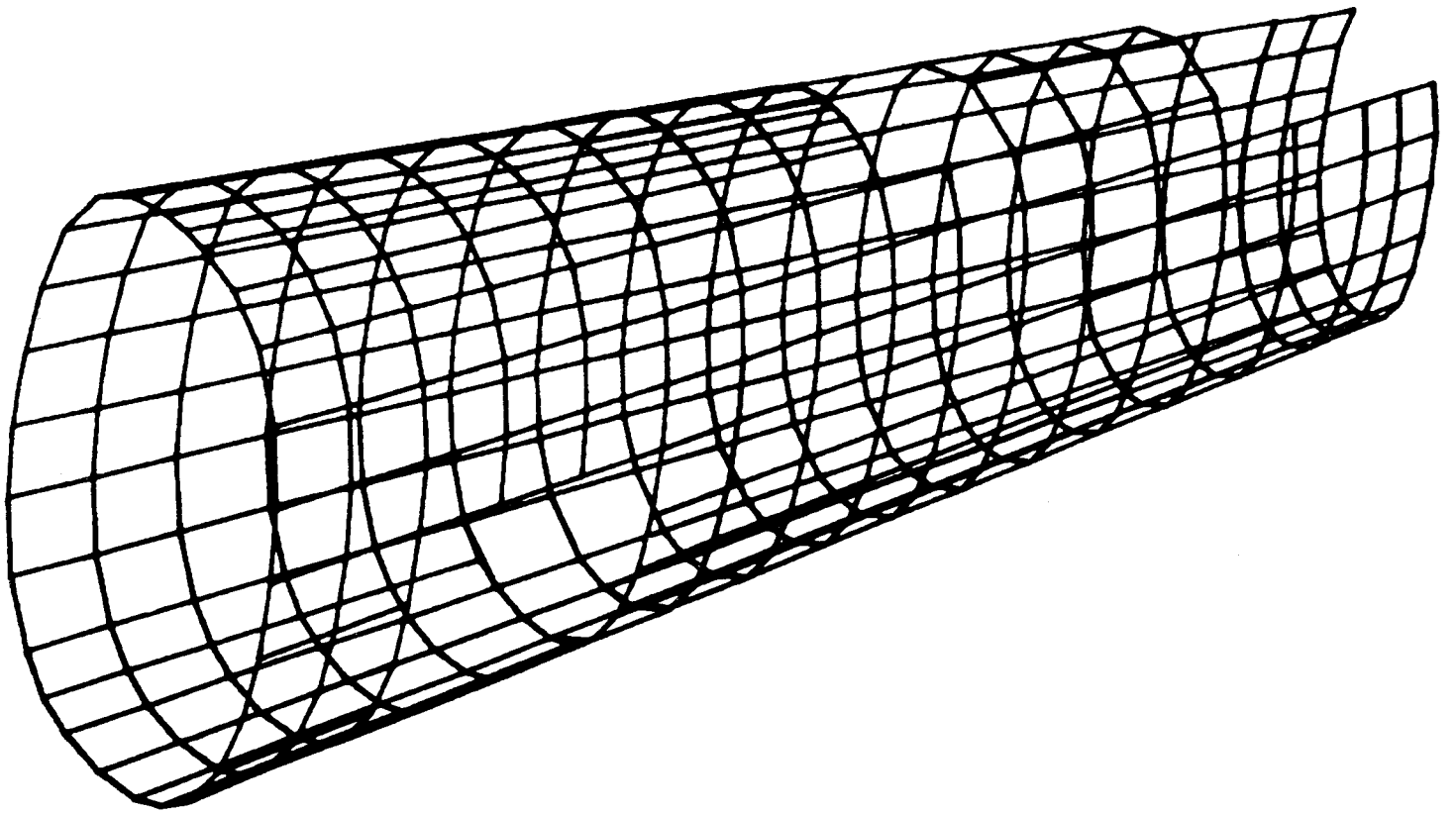

FIGURE 6: IDEALIZATION OF AIRCRAFT FUSELAGE

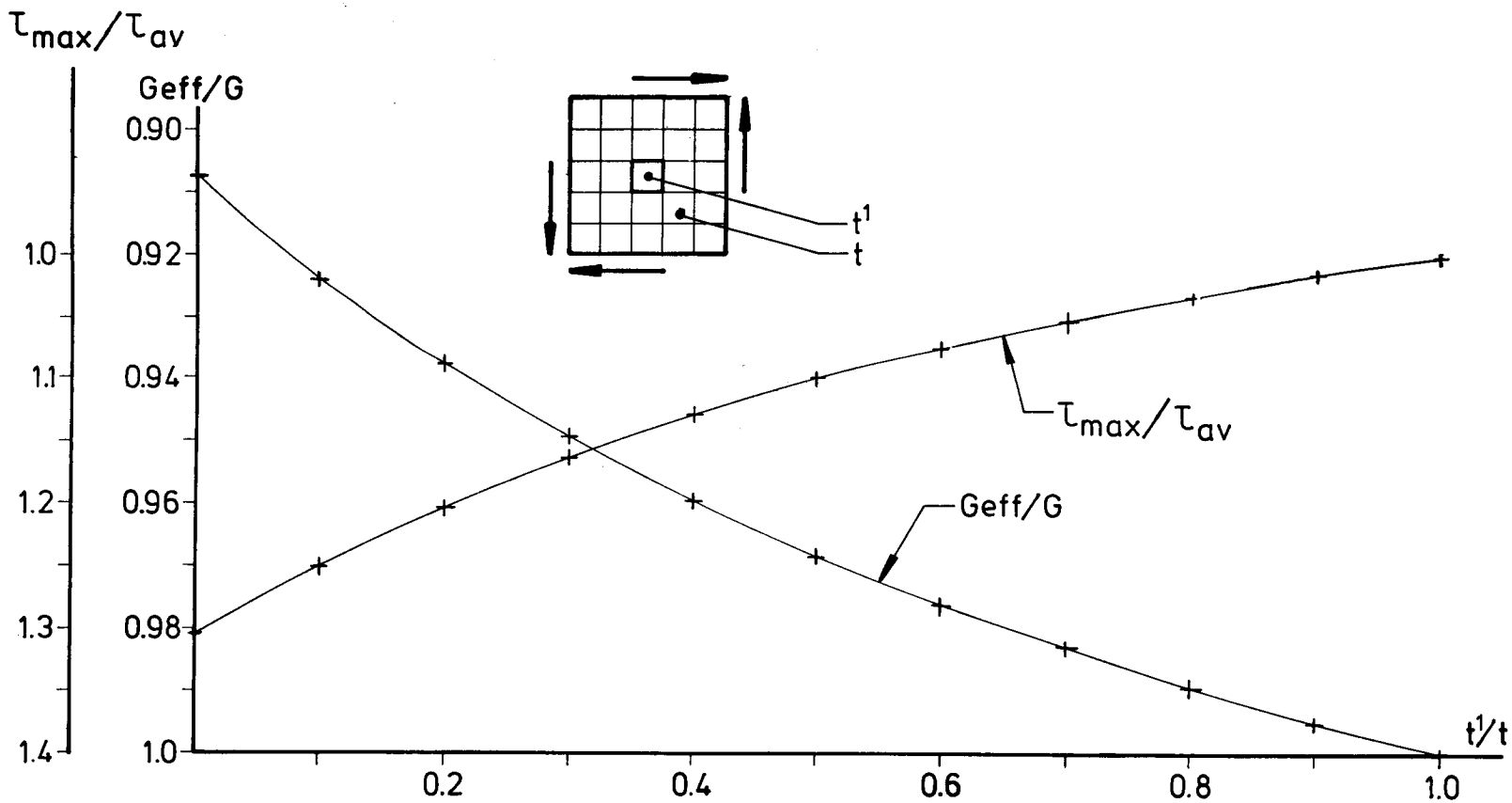

FIGURE 7: PANEL UNDER SHEAR – THE EFFECT OF LOCAL REDUCTION OF THE THICKNESS

AUTOMATED FULLY-STRESSED DESIGN WITH NASTRAN

D. V. Wallerstein and G. W. Haggenmacher
Lockheed-California Company

SUMMARY

An automated strength sizing capability which has been introduced into the Lockheed-California Company's modified version of NASTRAN Level 15.1 is described. The technique determines the distribution of material among the elements of a structural model. Presently, the sizing is based on either a fully-stressed design or a scaled-feasible fully-stressed design. Results obtained from the application of the strength sizing to the structural sizing of a composite material wing box using material strength allowables is presented. These results demonstrate the rapid convergence of the structural sizes to a usable design. Future developments for the generation of incremental stiffness matrices for lay-up studies of composite material structures, and for aeroelastic analyses, are indicated.

INTRODUCTION

Automated strength sizing of a structural finite element model is a very important facet in preliminary structural design. Preliminary design involves many other disciplines, such as aeroeleastic and flutter design. The involvement of many disciplines and their associated data emphasizes the need for a well integrated system which achieves the requirement of rapid response to design changes with a minimum of data communications, time and errors. Since the Lockheed-California Company has adopted a modified NASTRAN Level 15.1 (NASTRAN-LCC) as the primary finite element structural analysis system within its general integrated structural design analysis system, the decision was made to incorporate the strength sizing program within NASTRAN-LCC. This provides the sizing program with access to all facilities of the Company's integrated system, including the data checking of the NASTRAN-LCC system and the Company's integrated data management system. This latter feature, in turn, provides for direct interfacing with the analyses of related disciplines such as aeroelastic loads and flutter. The automated strength sizing capability has been designed to determine efficient structural material distributions which meet strength requirements while reducing the structural mass. This process provides the data for subsequent aeroelastic evaluation.

The automated structural sizing is controlled by DMAP looping within NASTRAN's Rigid Format 1. The actual sizing is accomplished by the introduction into NASTRAN-LCC of two new functional modules and their associated input and output data. The new modules consist of a scan module which identifies the critical load conditions for each element and their associated algebraic maximum and minimum stresses, and a module that performs the actual sizing. The input data required consist of tables for the specification of design element allowables and size constraints. Two kinds of output are provided: the first

is print output for use by the designer in evaluating the results of the automated structural sizing processes; the second is in the form of tables, containing the results of the sizing, which are stored into the data base for subsequent analyses.

SYMBOLS

Standard NASTRAN:

DMAP	Direct matrix abstraction approach
CASECC	Case control data table
ECT	Element connection table
EPT	Element property table
EST	Element summary table - a concatenation of ECT and EPT
g-Set	Grid point displacement set
KGGX	Stiffness matrix -g set
MAT2	Anisotropic material property definition input card
MPT	Material property table
OEF1	Output element force table
OES1	Output element stress table
PG	Static load vector -g set
SDR	Stress data recovery modules
SMA1	Structural matrix assembler module
SSG1	Static solution generator module
TA1	Table assembler module
UGV	Displacement vector matrix -g set

Nonstandard NASTRAN:

ECTC	Condensed element connection table
EPTC	Condensed element property table
EPTO	Original element property table

FCEOUT	Table of scanned forces
FSD	Fully-stressed design
FSDI	Structural sizing module
IEPTC	Incremental condensed element property table
KOLD	Stiffness matrix from previous iteration -g set
NASTRAN-LCC	Lockheed-California Company's version of NASTRAN
PIP	Element allowable and size constraint input card.
PIPT	Table formed from PIP cards
SFFSD	Scaled-feasible FSD
SR	Size ratio
STRSCN	Critical load determination module
STSOUT	Table of scaned stresses

INPUT DATA

To provide the input options for element redesign, a new Bulk Data Card (PIP) has been added to NASTRAN-LCC. The Property Input Parameter Table (PIPT) file is formed from these cards. The PIP input permits the following specifications for each element.

- Designation of an element as a design element.
- Two-directional stress allowables ($\bar{\sigma}xt$, $\bar{\sigma}xc$, $\bar{\sigma}yt$, $\bar{\sigma}yc$, $\bar{\tau}xy$).
- Minimum and maximum size constraints.
- Designation of the stress interaction curve to be used.

Only elements included in the PIPT table are design elements, all others are excluded from the sizing process.

In conjunction with two-directional stress allowables on the PIP card, the NASTRAN MAT2 card has been modified to include two-directional stress allowables.

THE SIZING PROCEDURE

A flow diagram of the pertinent features of the DMAP alter necessary for driving the sizing procedure is shown in figure 1. Except as otherwise noted, the main flow is vertical through the path marked A . Initially, path A performs a standard static internal loads solution. The STRSCN module then scans the resulting NASTRAN stress tables by load condition for each design element specified in the PIPT table. For each of these elements, a critical pair of load conditions and their corresponding stresses are determined and output in the STSOUT table. For example, the critical pair for a NASTRAN ROD element consists of the maximum tensile stress and its load condition number, and the maximum compressive stress and its load condition number.

The FSDI module then performs a comparison between the elements listed in the STSOUT table and those in the ECT table; and writes a new condensed connection table (ECTC) which contains only the design elements. Since the sizing logically requires a one-to-one correspondence between design element connection cards and design element property cards, a condensed property table (EPTC) is also formed. Next, the module performs the sizing of all design elements. The EPTC table is updated to reflect the new sizings; and an incremental condensed table (IEPTC) is formed. This latter table reflects the difference between the new and the old sizes.

Return to the top of the sizing loop is executed as shown by path B . Prior to entering TA1, however, the ECT table is equivalenced to the ECTC table and the EPT table is equivalenced to the incremental table IEPTC. As a result, SMA1 forms an incremental stiffness matrix which is added to the stiffness matrix from the previous iteration to form the new stiffness matrix for the current iteration.

When the conditional call to TA1 is entered at TA1-1, the ECT table is equivalenced to the ECTC table and the EPT table is now equivalenced to the condensed table EPTC. The looping continues in this fashion until the FSDI module determines that the solution has diverged or converged.

If convergence has been attained, the FSDI module outputs the last incremental table IEPTC and a full updated EPT table. The full table includes all of the element property information for those elements excluded from redesign, as well as all of the element property information (including final sizes) for the design elements. Path C is then followed.

Path B and Path C differ where they enter TA1-1. At this point, for path C , the ECT table is equivalenced to the original ECT table, which contains all elements; and the EPT table is equivalenced for the full, updated, EPT table, as output from FSDI. Path C then performs final stress recovery for all elements and prepares both standard NASTRAN and special FSD output.

If divergence has occured, the FSDI module outputs a full updated EPT table using the results from the previous iteration. Path D is then followed. Where Path D enters TA1 at TA1-1, the ECT table is equivalenced to the original ECT table and the EPT table is equivalenced to the previous complete and

updated EPT table. When SDR2 is entered, the displacement vector matrix UGV from the previous iteration is used. Path D then follows Path C for final stress recovery.

THE SCAN MODULE, STRSCN

The purpose of this module is to scan the NASTRAN OES1 and OEF1 tables, determine pairs of algebraic maximum and minimum stresses (or forces) and their corresponding load conditions, and write the results on the STSOUT (or FECOUT) file. Table I shows the input and output files and parameters required for this module. Figure 2 shows that the module can be used in two different ways depending on whether the PIPT table is purged or not purged.

If, in using the module, the PIPT table is purged, then the CASECC table is searched for the stress output element sets defined by the SET1 through SET5 parameters. The parameter PAIRS determines the number of pairs of algebraic maximum-minimum stresses (or forces) and their corresponding load conditions. These pairs are listed starting with the most critical pair, the next most critical pair, etc. If a PIPT table is an input to STRSCN, only the most critical pair of conditions and stresses is determined for the set of design elements defined in the PIPT table. The particular stress used for the scan procedure is of necessity dependent on the NASTRAN element type.

THE SIZING MODULE, FSDI

The FSDI module performs two major functions. Initially, the module prepares the condensed ECTC and EPTC tables containing only the design variable elements. Secondly, during each resizing iteration each design element is resized based on a selected sizing criterion; and the design parameter values in the EPTC table are updated. The module then checks various convergence criteria and decides whether to enter another sizing DMAP loop or to merge the EPTC and ECTC tables back into the complete tables and end with the final stress recovery. Table II gives the input and output files and parameters for the FSDI module.

The module flow, as demonstrated in figure 3, shows that in the first pass through the module, the condensed tables ECTC and EPTC are defined and the total mass of the structural model is computed. This mass is divided into two parts: the mass of the design elements (WD), and the mass of the remaining elements (WO). A table (WDO) containing the individual masses of the design elements is also written. In the first or any subsequent pass, the design elements are then resized.

The sizing of each of the design elements is currently based on either a Fully-Stressed Design (FSD) or a Scaled-Feasible Fully-Stressed Design (SFFSD) (ref. 1), depending on the value of the input parameter SCALE. Using the results of the STRSCN module and the allowable data and size constraints, a

stress ratio of the current active stress to allowable stress is determined along with the ratios of minimum size to current size and current size to maximum size. The maximum of these ratios (designated SR) is determined for each design element and the element sized by its SR ratio to determine its new size.

The SFFSD is similar to the FSD with the exception that all design elements are scaled by the largest of all the SR ratios. This ensures that at each step of redesign an acceptable design is available; that is, a design satisfying continuity and not exceeding any allowable stresses or constraings.

CONVERGENCE CRITERIA

Presently there are three ways to terminate execution (a fourth and unsatisfactory way is time):

- The permissible number of iteration loops specified by the user is reached.
- The total mass decrease between the (i-1) and i-th iteration is less than a user-defined fraction.
- The total mass between the (i-1) and i-th iteration increases.

For the latter case, the mass is currently allowed to increase through the first two (defaulted) iterations without termination.

STRESS ITERATION CRITERIA

The elements currently permitted for use with FSD include the standard NASTRAN BAR, ROD, and SHEAR elements and the Lockheed-California Company developed biaxially stiffened anistropic membrane element (BMEM). The ROD elements use the axial stress for the design stress. The SHEAR elements use the average value of shear for the design stress. Presently, the BAR elements can use only the axial stress for design. For this element type, a section-property smoothing process (to account for moment reversal in frames, for example) is being developed.

The BMEM element has available to it several options for the selection of the design stress or stresses. These options are user selected by a case control parameter. The two options which presently seem most useful are: the principal stresses at the center of the element, or a stress interaction criterion involving the two direct stresses, σx and σy, and the shear stress, τxy, all at the center of the element. This latter criterion also requires the corresponding two directional allowables; hence, the need for the allowables on the NASTRAN MAT2 Card. The BMEM element provides for the input of material property data relative to user-defined coordinate axes; such as the zero degree fiber orientation of a composite material. The element also provides for output of stresses along user-defined coordinate axes.

OUTPUT

At each iterative stage of the redesign, the scan and sizing modules print data which are useful to the designer in determining the acceptability of convergence to a reduced mass structure. Typically, the scan module outputs:

- Element identification.
- Maximum positive stress and the critical load condition identification.
- Maximum negative stress and its critical load condition.

The sizing module outputs:

- The maximum SR for each design element, along with its corresponding load condition number.
- The new size of each design element.

The scan module can also be used independently of the sizing module to scan for any desired number of critical load conditions and their corresponding critical stresses. This feature is of great use in standard stress analyses.

After the final sizing, the full EPT table is stored into the data base. From there, the table can be used by other disciplines, or used as initial input for continued strength sizing iterations or other NASTRAN analyses.

EXAMPLE

Figure 4 shows a plot of a finite element model of a composite material wing box to which the automated strength sizing procedure was applied. The truss structures on the leading edge and the trailing edge are for the purpose of transfering load from control surfaces to the wing box structures. The equations representing this transfer are automatically written by the NASTRAN-LCC rigid element multi-point constraint generator module during execution.

The structure was modeled with NASTRAN BAR elements for the fuselage frames and NASTRAN ROD elements for rib caps and fuselage longerons. The NASTRAN-LCC membrane element was used for all cover, spar, and rib panels. Since this element carries direct stress as well as shear, no rib or spar posts were used.

For the wing, unit panel thicknesses and cap areas were assigned arbitrarily for initial input properties. The fuselage frames had to be presized at this time. The rigid elements, used for external load introduction, and the fuselage frames were excluded from the design elements. Figure 5 demonstrates the total wing mass convergence after three iterations. A study of the resulting stress output for the wing showed that, for the given allowables, the resulting design was acceptable as a starting point for initial

flutter evaluations. Figure 6 illustrates the final sizing distributions of the upper surface panels adjacent to the rear beam after three iterations. The tip section is sized to minimum gauge; however, this section will probably require additional stiffening to meet flutter requirements.

CONCLUDING REMARKS

A scheme that permits the gross over-all distribution of material within a structure to be determined using NASTRAN has been presented. The basic sizing algorithm is a fully-stressed design approach which offers the advantage of arbritary initial size input; however, this method could easily be replaced by any other suitable algorithm. The basic manipulation of the ECT and EPT tables would remain the same. The sizing module concentrates on the modification of the EPT table; and, in particular, on the formulation of condensed ECT and EPT tables and on the formation of incremental stiffness matrices. This approach was selected because it offered several distinct advantages. Firstly, in most large structures, only part of the elements are to be sized. Thus, the formations of the relatively sparse incremental stiffness matrix for the design elements has advantages of operational flexibility. Secondly, the chosen approach lends itself to the formation of incremental stiffness matrices for selected sets of elements to be used as design variables in flutter and other aeroelastic design procedures. Along these same lines, by providing the basic capability to manipulate the EPT table, the material identification (MID) can be treated as a design variable; and the effect of different lay-ups on composite material structures response can be studied using an incremental approach. Finally, during the course of standard point design analyses, the FSDI module has been used to advantage to form condensed ECT and EPT tables representing sub-structure boundary coupling information.

REFERENCES

1. Berke, L.; and Khot, N. S." Use of Optimality Criteria Methods for Large Scale Systems. AGARD Lecture Series No. 70 on Structural Optimization, October 1974, pp 1-29.

TABLE I. - INPUT/OUTPUT DATA FOR STRSCN MODULE

Input Data Blocks

CASECC	-	Case Control Data Table
OES1	-	Output Element Stress Table
OEF1	-	Output Element Force Table
PIPT	-	Property Input Parameter Table

Output Data Blocks

STSOUT	-	A Table of Scanned Stresses
FCEOUT	-	A Table of Scanned Forces

Parameters

PAIRS	-	The number of maximum-minimum pairs to scan for in each element set.
SET1 SET2 SET3 SET4 SET5		Sets defining elements to be scanned

TABLE II. - INPUT/OUTPUT DATA FOR FSDI MODULE

Input Data Blocks

EST	-	Element Summary Table
ECT	-	Current Element Connection Table
EPT	-	Current Element Property Table
EPTO	-	Original Element Property Table
MPT	-	Material Property Table
STSOUT	-	Table of Scanned Stresses
WDIN	-	Table of Current Mass of Designated Design Elements

Output Data Blocks

ECTC	-	Extracted Element Connection Table
EPTC	-	Extracted Element Property Table
IEPTC	-	Extracted Incremental Element Property Table
WDO	-	Updated Mass of Designated Design Elements

Parameters

LOOP	-	Number of design iterations to be executed
SCALE	-	Type of sizing algorithm to be used
PERCENT	-	A weight convergence criteria
WO	-	Summed mass of all nondesignated design elements
WD	-	Summed mass of all designated design elements
FSDP	-	A DMAP control parameter

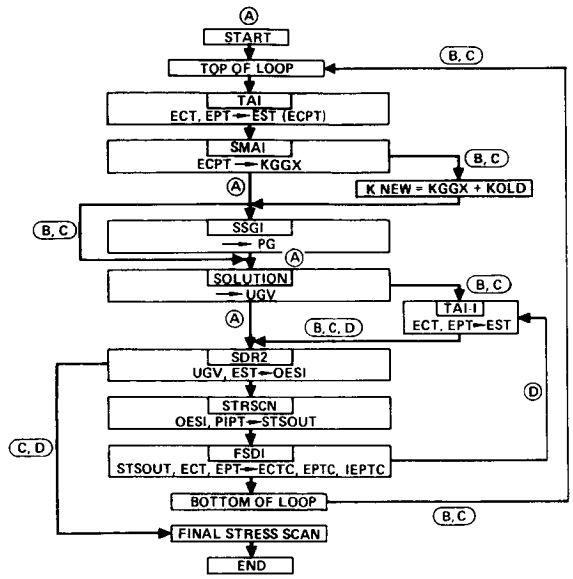

Figure 1. Flow of Sizing Procedure

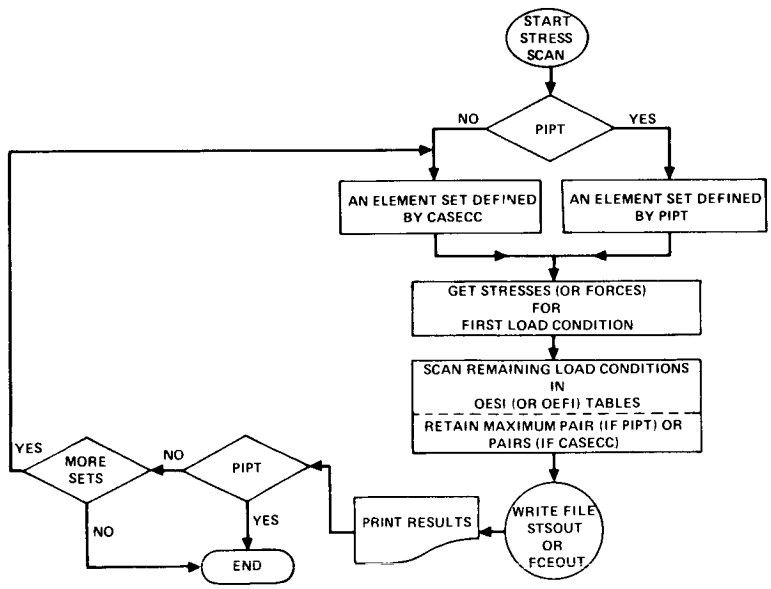

Figure 2. Stress-Scan Module Flow

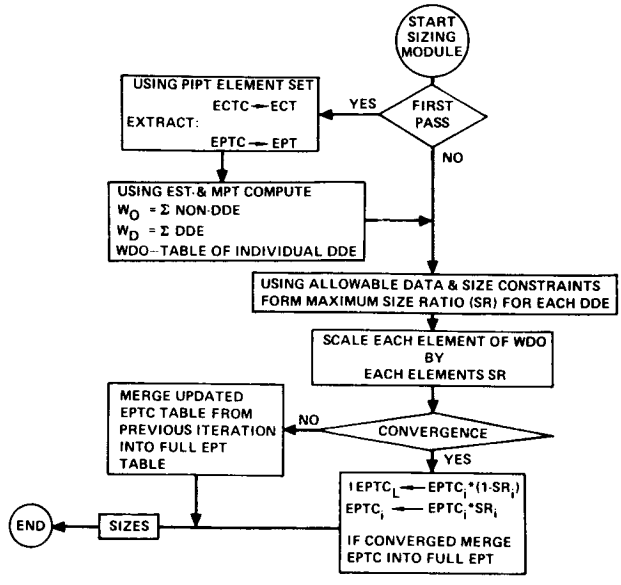

Figure 3. Sizing Module Flow

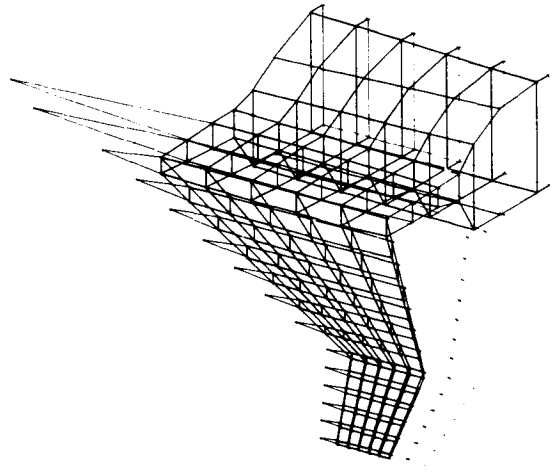

Figure 4. Wing Finite Element Model

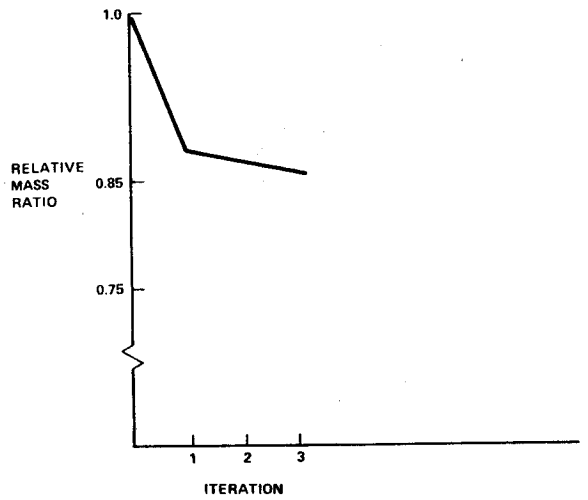

Figure 5. Total Wing Mass Convergence

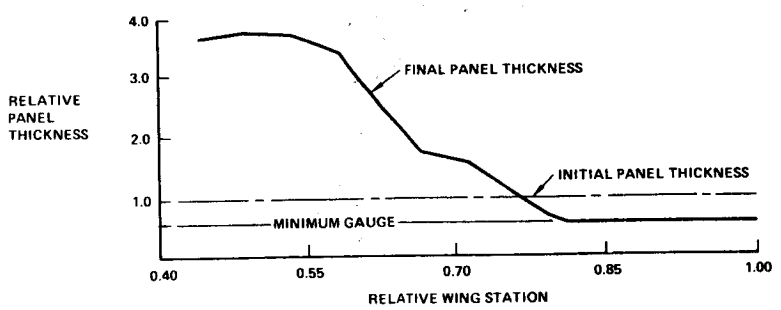

Figure 6. Sizing of Wing Upper Surface Panels Adjacent to Rear Beam

APPLICATION OF NASTRAN TO LARGE DEFLECTION SUPERSONIC FLUTTER OF PANELS

by

Chuh Mei
Vought Corporation, Hampton, Virginia

and

James L. Rogers, Jr.
NASA-Langley Research Center, Hampton, Virginia

SUMMARY

Flat panel flutter at high supersonic Mach number is analyzed using NASTRAN Level 16.0 by means of modifications to the code. Two-dimensional plate theory and quasi-steady aerodynamic theory are employed. The finite element formulation and solution procedure are presented. Modifications to the NASTRAN code are discussed. Convergence characteristics of the iteration processes are also briefly discussed. Effects of aerodynamic damping, boundary support condition and applied in-plane loading are included. Comparison of nonlinear vibration and linear flutter results with analytical solutions demonstrate that excellent accuracy is obtained with NASTRAN.

INTRODUCTION

Panel flutter is the self-excited oscillation of the external skin of a flight vehicle when exposed to an airflow along its surface. The classic approach using linear structural theory indicates that there is a critical (or flutter) dynamic pressure above which the panel motion becomes unstable. Since the linear theory does not account for structural nonlinearities, it can only determine the flutter boundary and can give no information about the flutter oscillation itself. A great quantity of literature exists on linear panel flutter (e.g. refs. 1 and 2 plus others too numerous to mention).

For large deflections, the nonlinear effects, mainly due to midplane stretching forces, restrain the panel motion to bounded limit cycle oscillations with increasing amplitude as dynamic pressure increases. Therefore, for realistic assessments and understanding of panel flutter, the nonlinear theory should be used. An excellent survey on both linear and nonlinear panel flutter through 1970 is given by Dowell (ref. 3).

To investigate large amplitude panel flutter, a number of approaches can be used. A modal approach with direct numerical integration has been used by Dowell (refs. 4 and 5). The major disadvantage in using this approach is its long computing time. The harmonic balance method can be used to determine limit cycles; see for example, Eastep and McIntosh (ref. 6) and Kuo et. al. (ref. 7). This approach, however, is quite complicated in mathematic manipulations. Morino (refs. 7 and 8) also used the pertubation method to obtain neighboring solutions to the linear problem.

The finite element method has been used successfully in investigating linear panel flutter (refs. 9 to 15). Because of its versatile applicability, effects of aerodynamic damping, complex panel configuration (e.g. delta planform in ref. 11, and rhombic planform in ref. 13), flow angularity, midplane forces, and anisotropic material properties can be conveniently included. Recently, the finite element method has been applied successfully in large amplitude vibrations of beam and plate structures (refs. 16 to 18). Thus, it is logical to extend the finite element application to study the limit cycle oscillations of panels.

The purpose of this paper is to describe a large deflection supersonic panel flutter capability available for NASTRAN Level 16.0 by means of DMAP sequences and modifications of the code. The paper includes a brief discussion of the theoretical formulation and solution procedure. Effects of aerodynamic damping, initial in-plane loading and boundary support condition are included. DMAP sequences required for nonlinear panel flutter analysis and an example of input bulk data are given in the Appendices.

SYMBOLS

a	length
$[a]$	nonsymmetric aerodynamic matrix
$c = (w)_{max}$	amplitude of oscillation
$D = \frac{Eh^3}{12(1-\nu^2)}$	bending rigidity
$[d]$	aerodynamic damping matrix
E	modulus of elasticity
$\{f\}$	interpolation function

g_A	aerodynamic damping parameter, equation (21)
h	thickness
$i = \sqrt{-1}$	
$[k]$	stiffness matrix
$[k^d]$	differential stiffness matrix
$[k^g]$	geometrical stiffness matrix
M	Mach number
$[m]$	mass matrix
N_x	inplane force due to deflection, tension positive
N_{xo}	applied inplane force, tension positive
p	aerodynamic force
$\{Q\}$	generalized aerodynamic force
q	dynamic pressure
t	time
$\{u\}$	nodal displacements
V	flow velocity
w	deflection
x,y,z	coordinates
α	damping factor
$\beta = \sqrt{M^2 - 1}$	
ε	norm
κ	complex eigenvalue, equation (19)
$\lambda = \frac{2qa^3}{\beta D}$	dynamic pressure parameter

SYMBOLS (CONT'D)

μ	aerodynamic damping coefficient, equation (8)
ν	Poisson's ratio
ρ	panel mass density
ρ_A	air mass density
$\{\phi\}$	eigenvector
$\Omega = \alpha + i\,\omega$	response of system
ω	frequency
ω_o	reference frequency

Subscripts:

aa	analysis
ee	element

THEORETICAL FORMULATION AND ITS SOLUTION

Formulation of Matrix Equation of Motion

The panel is represented by a flat thin plate of unit width in bending as shown in figure 1. The transverse dynamic equilibrium equation may be written as:

$$D \frac{\partial^4 w}{\partial x^4} - (N_x + N_{xo}) \frac{\partial^2 w}{\partial x^2} + \rho h \frac{\partial^2 w}{\partial t^2} = p \tag{1}$$

Where

$$N_x = \frac{Eh}{2a} \int_o^a \left(\frac{\partial w}{\partial x} \right)^2 dx \tag{2}$$

is the membrane force induced by large deflections, and N_{xo} is the initial in-plane loading. For sufficiently high supersonic speeds ($M > 1.6$), the aerodynamic pressure can be described by the two dimensional aerodynamic theory:

$$p(x,y,t) = -\frac{2q}{\beta}\left[\frac{\partial w}{\partial x} + \frac{1}{V}\,\frac{M^2-2}{M^2-1}\,\frac{\partial w}{\partial t}\right] \tag{3}$$

In the finite element method, the stiffness equations of motion for a plate element under the influence of elastic, initial in-plane, large deflection, and inertia forces (ref. 17) with the inclusion of aerodynamic forces may be written as:

$$([k_{ee}] + [k^d{}_{ee}] + [k^g{}_{ee}])\{u_e\} + [m_{ee}]\{\ddot{u}_e\} = \{Q(t)\} \tag{4}$$

The stiffness $[k_{ee}]$, differential stiffness $[k^d{}_{ee}]$, and mass $[m_{ee}]$ matrices have been well developed for almost every plate finite element available. The geometrical stiffness matrix $[k^g{}_{ee}]$ has been derived in references 16 and 17 for beam and rectangular plate elements. The development of the aerodynamic matrices follows the method proposed by Olson (refs. 9 and 11). The virtual work, U, of the aerodynamic force is

$$\begin{aligned} U &= Q_j u_j \\ &= \iint p(x,y,t)\, w\, dx\, dy \end{aligned} \tag{5}$$

Assuming the displacements are exponential functions of time

$$w(x,t) = w(x)e^{\Omega t} \tag{6}$$

where, in general, $\Omega = \alpha + i\omega$. Substituting expressions for the aerodynamic pressure, equation (3), and the displacement functions, equation (6), the virtual work becomes

$$U = \left\{ -\frac{2q}{\beta} \int \frac{dw}{dx} w \, dx - \mu \Omega \int w^2 \, dx \right\} e^{\Omega t} \tag{7}$$

$$\text{where } \mu = \frac{2q}{V} \frac{M^2-2}{\beta^3} \tag{8}$$

The deflection function for a particular element is usually assumed in the form:

$$w(x) = \sum_j f_j(x) \, u_j = \{f\}^T \{u\} \tag{9}$$

where f_j is the interpolation function corresponding to the element nodal degree-of-freedom u_j. Introducing the expression for w(x), equation (7) yields

$$U = \left\{ -\frac{2q}{\beta} \{u_e\}^T [a_{ee}] \{u_e\} - \mu \Omega \{u_e\}^T [d_{ee}] \{u_e\} \right\} e^{\Omega t} \tag{10}$$

where

$$[a_{ee}] = \int \left\{ \frac{\partial f}{\partial x} \right\} \{f\} \, dx \tag{11}$$

is the non-symmetric aerodynamic matrix and

$$[d_{ee}] = \int w^2 \, dx \tag{12}$$

is the aerodynamic damping matrix. The generalized aerodynamic forces are

$$Q_j = \frac{\partial U}{\partial u_j} = -\left(\frac{2q}{\beta}\,[a_{ee}] + \mu\,\Omega\,[d_{ee}]\right)\{u_e\}\,e^{\Omega t} \tag{13}$$

and their substitution into equation (4) yields the dynamic equilibrium of the panel in the form:

$$\begin{aligned}&([k_{ee}] + [k^d{}_{ee}] + [k^g{}_{ee}] + \frac{2q}{\beta}\,[a_{ee}] \\ &\quad + \Omega^2\,[m_{ee}] + \mu\Omega\,[d_{ee}])\,\{u_e\} = 0\end{aligned} \tag{14}$$

The aerodynamic damping matrix, equation (12), can be related to the mass matrix by the expression:

$$[d_{ee}] = \frac{1}{\rho h}\,[m_{ee}] \tag{15}$$

and equation (14) takes the final form for a finite element as,

$$\begin{aligned}&([k_{ee}] + [k^d{}_{ee}] + [k^g{}_{ee}] + \frac{2q}{\beta}\,[a_{ee}] \\ &\quad + \Omega^2\,[m_{ee}] + \frac{\mu\Omega}{\rho h}\,[m_{ee}])\,\{u_e\} = 0\end{aligned} \tag{16}$$

Solution Procedure

Assembling the finite elements, applying the kinematic boundary conditions, and dividing by $\left(\frac{D}{a^3}\right)$ equation (16) leads to a nondimensional eigenvalue problem of the form:

$$([k_{aa}] + [k^d_{aa}] + [k^g_{aa}] + \lambda\ [a_{aa}] - \kappa\ [m_{aa}])\ \{u_a\} = 0 \qquad (17)$$

where

$$\lambda = \frac{2qa^3}{\beta D} \qquad (18)$$

and

$$\kappa = -\frac{\rho h a^4}{D}\ \Omega^2 - \lambda\ \frac{M^2 - 2}{\beta^2}\ \frac{a}{V}\ \Omega \qquad (19)$$

are the nondimensional dynamic pressure parameter and eigenvalues, respectively. The eigenvalues can be put into more convenient form as

$$\kappa = -\frac{\Omega^2}{\omega_o{}^2} - g_A\ \frac{\Omega}{\omega_o} \qquad (20)$$

where

$$g_A = \frac{M^2 - 2}{\beta^3}\ \frac{\rho_A V}{\rho h \omega_o} \qquad (21)$$

is the nondimensional aerodynamic damping parameter, and

$$\omega_o = \sqrt{\frac{D}{\rho h a^4}} \qquad (22)$$

is a convenient frequency scale. For typical panels, g_A ranges from 0 to 50 approximately, as given in figure 2 of reference 2.

In determining the eigenvalues κ in equation (17) for a given dynamic pressure λ, the iterative procedure and equivalent linearization technique discussed in detail in reference 17 was employed. A simple flow diagram of the procedure is shown in figure 2. The solution procedure is illustrated briefly as follows. For a given λ, first the linear flutter problem is solved

$$\kappa[m_{aa}]\ \{\phi\}_0 = ([k_{aa}] + [k^d{}_{aa}] + \lambda\ [a_{aa}])\ \{\phi\}_0 \tag{23}$$

where $\{\phi\}_0$ represents the linear mode shape normalized by its maximum components. The first approximate displacement is then expressed in the form

$$\{u_a\}_1 = c\ \mathrm{Real}(\{\phi\}_0\ e^{(\alpha + i\omega)t}) \tag{24}$$

where c is a given amplitude of panel oscillations, and α and ω are the panel response parameters related to κ and g_A by equation (30). An equivalent geometrical stiffness matrix $[k^g{}_{aa}]_{eq}$ now can be obtained using $\{u_a\}_1$, and equation (17) is approximated by a linearized eigenvalue equation of the form

$$\kappa[m_{aa}]\ \{\phi\}_1 = ([k_{aa}] + [k^d{}_{aa}] + [k^g{}_{aa}]_{eq} + \lambda\ [a_{aa}])\ \{\phi\}_1 \tag{25}$$

where κ is the eigenvalue associated with amplitude c, and $\{\phi\}_1$ is the corresponding mode shape. The iterative process can be repeated until a convergence criterion is satisfied as shown in figure 2. The maximum displacement norm convergence criterion proposed in reference 19 was used in the present study and is defined as

$$\|\varepsilon\|_u = \max_j \left| \frac{\Delta u_j}{u_{j,ref}} \right| \tag{26}$$

where Δu_j is the change in displacement component j during iteration cycle n, and $u_{j,ref}$ is the reference displacement. The reference displacement is the largest displacement component of the corresponding "type". For instance in a panel flutter problem involving deflections and rotations, the reference displacement is the largest deflection component and the largest rotation, respectively. In addition a frequency norm is also introduced in the present study and is defined as

$$\|\varepsilon\|_f = \left|\frac{\Delta\kappa_n}{\kappa_n}\right| \tag{27}$$

where $\Delta\kappa_n$ is the change in eigenvalue during iteration cycle n. A typical plot of the maximum and frequency norms versus number of iterations for a simply supported panel is shown in figure 3. A modified absolute norm and a modified Euclidean norm defined in reference 19 were also calculated. They fall in between the maximum and frequency norms, and therefore, are not plotted on the figure. In the examples presented in the following section, convergence is considered achieved whenever any one of the norms reaches a value of 10^{-3}.

Equation (17) indicates that when $\lambda=0$ the problem degenerates into large amplitude vibrations of invacuo panels. The matrices [k], $[k^d]$, $[k^g]$, and [m] are all symmetric and the eigenvalues are real and positive. As λ is increased from zero, two of these eigenvalues will usually approach each other and coalesce to κ_{cr} at $\lambda = \lambda_{cr}$, and become complex conjugate pairs

$$\kappa = \kappa_R \pm i\,\kappa_I \tag{28}$$

for $\lambda > \lambda_{cr}$. Here λ_{cr} is considered to be the lowest value of λ for which coalescence occurs among all limit cycle amplitudes and usually corresponds to c = 0. A typical plot of κ versus λ is shown in figure 4. In the absence of aerodynamic damping ($g_A = 0$), the flutter boundary simply corresponds to λ_{cr}. When λ is below λ_{cr}, any disturbance to the panel decays and $(c/h) \to 0$.

For $\lambda > \lambda_{cr}$, a periodic limit cycle oscillation exists which increases in amplitude as λ increases. This can be seen more clearly by noting that the eigenvalue with a negative imaginary part leads to an instability (see ref. 13) and relating the complex eigenvalues to the panel response parameters α and ω as follows. Rewrite equations (20) and (28) as

$$\left(\frac{\Omega}{\omega_o}\right)^2 + g_A \frac{\Omega}{\omega_o} + (\kappa_R - i\,\kappa_I) = 0 \tag{29}$$

which can be solved for Ω to give

$$\frac{\Omega}{\omega_o} = \frac{\alpha}{\omega_o} + i\,\frac{\omega}{\omega_o}$$

$$= \left(-\frac{g_A}{2} + \psi\right) + i\left(\frac{\kappa_I}{2\psi}\right) \tag{30}$$

where

$$\psi = \pm\frac{1}{\sqrt{2}}\left\{\sqrt{\left[\left(\frac{g_A}{2}\right)^2 - \kappa_R\right]^2 + \kappa_I^{\,2}} + \left[\left(\frac{g_A}{2}\right)^2 - \kappa_R\right]\right\}^{1/2} \tag{31}$$

The complete panel behavior is characterized by plotting the variation of $\alpha + i\omega$ with increasing dynamic pressure λ. Amplitude increases when α becomes positive. A typical plot is shown in figure 5.

MODIFICATIONS TO THE NASTRAN CODE

To incorporate this new capability into NASTRAN, four existing NASTRAN subroutines must be modified. These subroutines are DBAR, KBAR, SDR1A (SDR1AZZ on CDC computers because of multiple entry points), and XMPLBD. DBAR was modified in the same way as shown in reference 17.

Subroutine KBAR was modified to calculate the aerodynamic matrix $[a_{ee}]$. This matrix is multiplied by the parameter DPMN = $2q/\beta$. DPMN is input via a PARAM card in the BULK DATA deck. DPMN is passed to KBAR through blank common from module EMG. The new EMG calling sequence allowing for the DPMN parameter is shown as follows:

```
EMG    EST,CSTM,MPT,DIT,GEOM2,/KELM,KDICT,MELM,MDICT,,/V,N,NOKGGX/ V,
       N,NOMGG/C,N,/C,N,/C,N,/C,Y,COUPMASS/C,Y,CPBAR/C,Y,CPROD/C,Y,
       CPQUAD1/C,Y,CPQUAD2/C,Y,CPTRIA1/C,Y,CPTRIA2/  C,Y,CPTUBE/C,Y,
       CPQDPLT/C,Y,CPTRPLT/C,Y,CPTRBSC/V,Y,DPMN $
```

The default value for DPMN, which is set in XMPLBD, is zero (0). This means if the PARAM card for DPMN is omitted, $[a_{ee}]$ will make no contribution in equation (14).

Subroutine SDR1A was modified to calculate the real part of $\{\phi\}_n e^{(\alpha + i\omega)t}$ where $\{\phi\}_n$ is the complex eigenvector generated by the module CEAD. To avoid entering the modified section of code each time SDR1A is called, a new parameter, IFLUT, was added to the DMAP calling sequence for module SDR1. The contents of IFLUT are passed through blank common from SDR1 to SDR1A. The default value for IFLUT, which is set in XMPLBD, is zero (0). When IFLUT = 0, the new code in SDR1A will not be executed. To set IFLUT = 1 and execute the new code in SDR1A, the following calling sequence for the SDR1 module is used:

```
SDR1    USET,PHIA,,,GØ,GM,KFS/PHIG,, BQG/1/*REIG*/1 $
```

The underlined parameter sets IFLUT to 1.

Once the changes were made to DBAR, KBAR, SDR1A, and XMPLBD, they were compiled and replaced the old DBAR, KBAR, SDR1A, and XMPLBD in the NASTRAN object library. Link 1, Link 3, Link 12, and Link 13 were relinked, creating a new executable NASTRAN. Although this procedure was done on a CDC computer, similar procedures will produce similar results on the IBM and UNIVAC computers.

To use this capability in NASTRAN, the DMAP sequence shown in Appendix A must be used. This sequence uses many of the new DMAP convenience features in Level 16 of NASTRAN. One of the features allows the REPT module to have a variable parameter. The variable parameter NLØØP is used for REPT in this DMAP sequence. NLØØP is input on a PARAM card in the BULK DATA deck. It sets the maximum number of iterations of the inner loop shown in figure 2. The only other input required to use this capability is the addition of another PARAM card in the BULK DATA deck. The parameter AMP corresponds to c and is used to specify the amplitude of vibration of this structure. This capability was added to an in-house version <u>only</u> and is <u>not</u> available in any standard NASTRAN level.

RESULTS AND DISCUSSION

The large deflection panel flutter analysis developed for use with NASTRAN has been applied to various panels. A typical BULK DATA deck for a simply supported panel at $\frac{c}{h} = 0.6$ and $\lambda = 600.0$ is given in Appendix B.

Convergence Study

Numerical results for the first two eigenvalues at $\lambda = 0$ and for the coalescence for a simply supported panel and a clamped panel are shown in Table 1. The exact results for eigenvalue coalescence are from reference 20. It is seen that an excellent approximation to the exact results is obtained with only eight elements.

The influence of large deflections on in-vacuo frequencies for a simply supported panel is given in Table 2. Analytical solutions using three different approaches from reference 21 are also given. Comparison of the NASTRAN results with the reference 21 methods show that the eight-element approximation gives very good results. Therefore, eight elements were used in modeling the panels in all the flutter results presented.

Simply Supported Panel and Effect of Aerodynamic Damping

Plots of the eigenvalues verses dynamic pressure for a simply supported panel at two different panel amplitudes $\frac{c}{h} = 0.0$ (linear theory) and 0.6, are shown in figure 4. The complete panel behavior is characterized by plotting the $(\alpha + i\omega)$ variation with increasing dynamic pressure λ, using equation (30) and figure 4, as shown in figure 5. For the case of negligible aerodynamic damping, $g_A \rightarrow 0$, instability does not set in until after the two undamped natural frequencies have merged. If some damping is present, the instability sets in at a somewhat higher value as indicated in figure 5. This occurs when $\alpha = 0$ in equation (30). By routine algebraic manipulation, this instability occurs at the value of λ when

$$g_A = \frac{\kappa_I}{\sqrt{\kappa_R}} \tag{32}$$

and the corresponding limit cycle frequency is

$$\frac{\omega}{\omega_o} = \sqrt{\kappa_R} \tag{33}$$

However, as discussed earlier, this instability is not catastrophic. The panel response does not grow indefinitely, but rather a limit cycle oscillation is developed with increasing amplitude as λ increases.

Boundary Support Effect

In figure 6, the panel amplitude of the limit cycle oscillation is given as a function of λ for various panel edge restraints. The most interesting result is that the limit cycle motions are different for hinged-clamped and clamped-hinged panels. This occurs because the aerodynamic matrices are different for the two support conditions, which leads to different deflection shapes for the panels as well as different geometrical stiffness matrices.

Effect of In-Plane Loading

Panel amplitude versus λ for several applied in-plane forces acting on a simply supported panel is shown in figure 7. The classical Euler buckling load for simply supported panels is $N_{cr} = -\pi^2 D/a^2$. The total membrane force is composed of the applied in-plane load N_{xo} and the membrane force N_x induced by large deflections of the panel. Figure 7 shows that the applied compressive in-plane force reduces the critical dynamic pressure. However, as the dynamic pressure is increased the panel amplitude increases, which induces tensile in-plane forces that counteract the applied compressive forces. This process continues until a flutter dynamic pressure is reached which corresponds to a given limit cycle amplitude.

CONCLUDING REMARKS

A large amplitude supersonic panel flutter capability has been developed for use with NASTRAN Level 16.0 by means of DMAP sequences and modifications to the code. An aerodynamic matrix for a two-dimensional plate element has been developed for NASTRAN by modifying subroutine KBAR. The iteration process has been implemented in NASTRAN through PARAM NLØØP in bulk data deck, modifications in subroutines DBAR, KBAR, and SDR1AZZ, and the DMAP sequences. Examples which include effects of aerodynamic damping, applied inplane forces and various support conditions have demonstrated the versatility of the method.

APPENDIX A

DMAP SEQUENCES

```
ID        NLPF,TWOD
APP       DMAP
BEGIN     $
XDMAP     GO,ERR=2,LIST
FILE      LAMA=APPEND/PHIA=APPEND $
GP1       GEOM1,GEOM2,/GPL,EQEXIN,GPDT,CSTM,BGPDT,SIL/V,N,LUSET/   V,N,
          NOGPDT $
SAVE      LUSET $
CHKPNT    GPL,EQEXIN,GPDT,CSTM,BGPDT,SIL $
GP2       GEOM2,EQEXIN/ECT $
CHKPNT    ECT $
PARAML    PCDB//C,N,PRES/C,N,/C,N,/C,N,/V,N,NOPCDB $
PURGE     PLTSETX,PLTPAR,GPSETS,ELSETS/NOPCDB $
COND      P1,NOPCDB $
PLTSET    PCDB,EQEXIN,ECT/PLTSETX,PLTPAR,GPSETS,ELSETS/V,N,NSIL/    V,N,
          JUMPPLOT=-1 $
SAVE      NSIL,JUMPPLOT $
PRTMSG    PLTSETX// $
PARAM     //C,N,MPY/V,N,PLTFLG/C,N,1/C,N,1 $
PARAM     //C,N,MPY/V,N,PFILE/C,N,0/C,N,0 $
COND      P1,JUMPPLOT $
PLOT      PLTPAR,GPSETS,ELSETS,CASECC,BGPDT,EQEXIN,SIL,,,,/PLOTX1/   V,N,
          NSIL/V,N,LUSET/V,N,JUMPPLOT/V,N,PLTFLG/V,N,PFILE $
SAVE      JUMPPLOT,PLTFLG,PFILE $
PRTMSG    PLOTX1// $
LABEL     P1 $
CHKPNT    PLTPAR,GPSETS,ELSETS $
GP3       GEOM3,EQEXIN,GEOM2/SLT,GPTT/V,N,NOGRAV $
CHKPNT    SLT,GPTT $
TA1       ECT,EPT,BGPDT,SIL,GPTT,CSTM/EST,GEI,GPECT,/V,N,LUSET/   V,N,
          NOSIMP/C,N,1/V,N,NOGENL/V,N,GENEL $
SAVE      NOSIMP,NOGENL,GENEL $
COND      ERROR1,NOSIMP $
PURGE     OGPST/GENEL $
CHKPNT    EST,GPECT,GEI,OGPST $
PARAM     //C,N,ADD/V,N,NOKGGX/C,N,1/C,N,0 $
PARAM     //C,N,ADD/V,N,NOMGG/C,N,1/C,N,0 $
EMG       EST,CSTM,MPT,DIT,GEOM2,/KELM,KDICT,MELM,MDICT,,/V,N,NOKGGX/ V,
          N,NOMGG/C,N,/C,N,/C,N,/C,Y,COUPMASS/C,Y,CPBAR/C,Y,CPROD/C,Y,
          CPQUAD1/C,Y,CPQUAD2/C,Y,CPTRIA1/C,Y,CPTRIA2/  C,Y,CPTUBE/C,Y,
          CPQDPLT/C,Y,CPTRPLT/C,Y,CPTRBSC/V,Y,DPMN $
SAVE      NOKGGX,NOMGG $
CHKPNT    KELM,KDICT,MELM,MDICT $
COND      JMPKGG,NOKGGX $
```

```
EMA       GPECT,KDICT,KELM/KGGX,GPST $
CHKPNT    KGGX,GPST $
LABEL     JMPKGG $
COND      ERROR5,NOMGG $
EMA       GPECT,MDICT,MELM/MGG,/C,N,-1/C,Y,WTMASS=1.0 $
CHKPNT    MGG $
COND      LBL1,GRDPNT $
GPWG      BGPDT,CSTM,EQEXIN,MGG/OGPWG/V,Y,GRDPNT/C,Y,WTMASS $
OFP       OGPWG,,,,,// $
LABEL     LBL1 $
EQUIV     KGGX,KGG/NOGENL $
CHKPNT    KGG $
COND      LBL11,NOGENL $
SMA3      GEI,KGGX/KGG/V,N,LUSET/V,N,NOGENL/V,N,NOSIMP $
CHKPNT    KGG $
LABEL     LBL11 $
PARAM     //C,N,MPY/V,N,NSKIP/C,N,0/C,N,0 $
GP4       CASECC,GEOM4,EQEXIN,SIL,GPDT,BGPDT,CSTM/RG,YS,USET,ASET/V,N,
          LUSET/V,N,MPCF1/V,N,MPCF2/V,N,SINGLE/V,N,OMIT/V,N,REACT/V,N,
          NSKIP/V,N,REPEAT/V,N,NOSET/V,N,NOL/V,N,NOA/C,Y,SUBID $
SAVE      MPCF1,MPCF2,SINGLE,OMIT,REACT,NSKIP,REPEAT,NOSET,NOL,NOA $
COND      ERROR6,NOL $
PARAM     //C,N,AND/V,N,NOSR/V,N,SINGLE/V,N,REACT $
PURGE     GM/MPCF1/GO,KOO,LOO,PO,UOOV,RUOV/OMIT/PS,KFS,KSS/SINGLE/  QG/
          NOSR $
CHKPNT    GM,RG,GO,KOO,LOO,PO,UOOV,RUOV,YS,PS,KFS,KSS,USET,ASET,QG $
COND      LBL4D,REACT $
JUMP      ERROR2 $
LABEL     LBL4D $
COND      LBL4,GENEL $
GPSP      GPL,GPST,USET,SIL/OGPST/V,N,NOGPST $
SAVE      NOGPST $
COND      LBL4,NOGPST $
OFP       OGPST,,,,,// $
LABEL     LBL4 $
EQUIV     KGG,KNN/MPCF1/MGG,MNN/MPCF1 $
CHKPNT    KNN,MNN $
COND      LBL2,MPCF2 $
MCE1      USET,RG/GM $
CHKPNT    GM $
MCE2      USET,GM,KGG,MGG,, /KNN,MNN,, $
CHKPNT    KNN,MNN $
LABEL     LBL2 $
EQUIV     KNN,KFF/SINGLE/MNN,MFF/SINGLE $
```

```
CHKPNT    KFF,MFF $
COND      LBL3,SINGLE $
SCE1      USET,KNN,MNN,,/KFF,KFS,KSS,MFF,, $
CHKPNT    KFS,KSS,KFF,MFF $
LABEL     LBL3 $
EQUIV     KFF,KAA/OMIT/MFF,MAA/OMIT $
CHKPNT    KAA,MAA $
COND      LBL5,OMIT $
SMP1      USET,KFF,,,/GO,KAA,KOO,LOO,UOO,,,, $
CHKPNT    GO,KAA,KOO,LOO,UOO $
SMP2      USET,GO,MFF/MAA $
CHKPNT    MAA $
LABEL     LBL5 $
RBMG2     KAA/LLL $
CHKPNT    LLL $
SSG1      SLT,BGPDT,CSTM,SIL,EST,MPT,GPTT,EDT,MGG,CASECC,DIT/PG/ V,N,
          LUSET/C,N,1 $
CHKPNT    PG $
EQUIV     PG,PL/NOSET $
CHKPNT    PL $
COND      LBL10,NOSET $
SSG2      USET,GM,YS,KFS,GO,,PG/,PO,PS,PL $
CHKPNT    PO,PS,PL $
LABEL     LBL10 $
SSG3      LLL,KAA,PL,LOO,KOO,PO/ULV,UOOV,RULV,RUOV/V,N,OMIT/V,Y,IRES=-1/
          C,N,1/V,N,EPSI $
SAVE      EPSI $
CHKPNT    ULV,UOOV,RULV,RUOV $
COND      LBL9,IRES $
MATGPR    GPL,USET,SIL,RULV//C,N,L $
MATGPR    GPL,USET,SIL,RUOV//C,N,O $
LABEL     LBL9 $
SDR1      USET,PG,ULV,UOOV,YS,GO,GM,PS,KFS,KSS,/UGV,PGG,QG/C,N,1/C,N,
          BKLO $
CHKPNT    UGV,QG,PGG $
SDR2      CASECC,CSTM,MPT,DIT,EQEXIN,SIL,GPTT,EDT,BGPDT,,QG,UGV,EST,,PGG/
          OPG1,OQG1,OUGV1,OES1,OEF1,PUGV1/C,N,BKLO $
PARAM     //C,N,MPY/V,N,CARDNO/C,N,0/C,N,0 $
OFP       OUGV1,OPG1,OQG1,OEF1,OES1,//V,N,CARDNO $
SAVE      CARDNO $
COND      P2,JUMPPLOT $
PLOT      PLTPAR,GPSETS,ELSETS,CASECC,BGPDT,EQEXIN,SIL,PUGV1,,GPECT,OES1/
          PLOTX2/V,N,NSIL/V,N,LUSET/V,N,JUMPPLOT/V,N,PLTFLG/V,N,PFILE $
SAVE      PFILE $
```

```
PRTMSG    PLOTX2// $
LABEL     P2 $
TA1       ECT,EPT,BGPDT,SIL,GPDT,CSTM/X1,X2,ECPT,GPCT/V,N,LUSET/  V,N,
          NOSIMP/C,N,0/V,N,NOGENL/V,N,GENEL $
DSMG1     CASECC,GPTT,SIL,EDT,UGV,CSTM,MPT,ECPT,GPCT,DIT/KDGG/  V,N,
          DSCOSET $
SAVE      DSCOSET $
CHKPNT    KDGG $
DPD       DYNAMICS,GPL,SIL,USET/GPLD,SILD,USETD,,,,,,,EED,EQDYN/V,N,
          LUSET/V,N,LUSETD/V,N,NOTFL/V,N,NODLT/V,N,NOPSDL/V,N,NOFRL/  V,
          N,NONLFT/V,N,NOTRL/V,N,NOEED/C,N,/V,N,NOUE $
SAVE      NOEED $
COND      ERROR3,NOEED $
CHKPNT    EED $
PARAM     //C,N,MPY/V,N,NEIGV/C,N,1/C,N,-1 $
LABEL     NLVIB $
ADD       KAA,/KTT/C,N,(-1.0,0.0)/C,N,(0.0,0.0) $
CHKPNT    KTT $
CEAD      KTT,,MAA,EED,CASECC/PHIA,LAMA,OEIGS/S,N,NEIGV $
OFP       OEIGS,LAMA//S,N,CARDNO $
COND      ERROR4,NEIGV $
SDR1      USET,,PHIA,,,GO,GM,,KFS/PHIG,,BQG/1/*REIG*/1 $
ADD       PHIG/PHIAMP/V,Y,AMP $
DSMG1     CASECC,,SIL,,PHIAMP,CSTM,MPT,ECPT,GPCT,DIT/KNGG/DSCOSET/1 $
CHKPNT    KNGG $
ADD5      KGG,KDGG,KNGG,, /KSGG $
CHKPNT    KSGG $
EQUIV     KSGG,KSNN/MPCF2/MGG,MSNN/MPCF2 $
CHKPNT    KSNN,MSNN $
COND      LBL2S,MPCF2 $
MCE2      USET,GM,KSGG,MGG/KSNN,MSNN $
CHKPNT    KSNN,MSNN $
LABEL     LBL2S $
EQUIV     KSNN,KSFF/SINGLE/MSNN,MSFF/SINGLE $
CHKPNT    KSFF,MSFF $
COND      LBL3S,SINGLE $
SCE1      USET,KSNN,MSNN/KSFF,KSFS,,MSFF $
CHKPNT    KSFF,KSFS,MSFF $
LABEL     LBL3S $
EQUIV     KSFF,KSAA/OMIT / MSFF,MSAA/OMIT $
CHKPNT    KSAA,MSAA $
COND      LBL5S,OMIT $
SMP1      USET,KSFF/GSO,KSAA,KSOO,LSOO,USOO $
SMP2      USET,GSO,MSFF/MSAA $
```

```
CHKPNT    KSAA,MSAA $
LABEL     LBL5S $
COPY      KSAA/KAA/IPARM=-1 $
COPY      MSAA/MAA/JPARM=-1 $
REPT      NLVIB,NLOOP $
SDR2      CASECC,CSTM,MPT,DIT,EQEXIN,SIL,,,BGPDT,LAMA,BQG,PHIG,EST,,/,
          OBQG1,OPHIG,OBES1,OBEF1,PPHIG/C,N,REIG $
OFP       CPHIG,CBQG1,CBEF1,CBES1,,//V,N,CARDNO $
SAVE      CARDNO $
COND      P3,JUMPPLOT $
PLOT      PLTPAR,GPSETS,ELSETS,CASECC,BGPDT,EQEXIN,SIL,,PPHIG,GPECT,
          OBES1/PLOTX3/V,N,NSIL/V,N,LUSET/V,N,JUMPPLOT/V,N,PLTFLG/V,N,
          PFILE $
SAVE      PFILE $
PRTMSG    PLOTX3// $
LABEL     P3 $
JUMP      FINIS $
LABEL     ERROR1 $
PRTPARM   //C,N,-1/C,N,NMDS $
LABEL     ERROR2 $
PRTPARM   //C,N,-2/C,N,NMDS $
LABEL     ERROR3 $
PRTPARM   //C,N,-3/C,N,NMDS $
LABEL     ERROR4 $
PRTPARM   //C,N,-4/C,N,NMDS $
LABEL     ERROR5 $
PRTPARM   //C,N,-5/C,N,NMDS $
LABEL     ERROR6 $
PRTPARM   //C,N,-6/C,N,NMDS $
LABEL     FINIS $
END       $
```

APPENDIX B

INPUT BULK DATA CARDS

```
$
$ GEOMETRY AND CONSTRAINTS
GRDSET                                                          246
GRID    1               0.0
GRID    2               0.125
GRID    3               0.25
GRID    4               0.375
GRID    5               0.50
GRID    6               0.625
GRID    7               0.75
GRID    8               0.875
GRID    9               1.0
GRID    20              0.0     10.0                            123456
SPC     1       1       13      0.0     9       3               0.0
$
$ STRUCTURAL AND AERODYNAMIC ELEMENTS
BAROR           15                      20                              2
CBAR    1               1       2
CBAR    2               2       3
CBAR    3               3       4
CBAR    4               4       5
CBAR    5               5       6
CBAR    6               6       7
CBAR    7               7       8
CBAR    8               8       9
MAT1*   25              1.0                                                     *MT1
*MT1    0.4367901341
PARAM   COUPMASS1
$ DPMN = 2.0*Q/(BETA)
$       WHERE Q = RHO*V**2/2.0, DYNAMIC PRESSURE
$             BETA = SQRT(MACH NO.**2 - 1.0)
PARAM   DPMN    600.0
PBAR*   15              25              2.289429        1.0             *PB1
*PB1    1.0
$
$ CONTROL DATA
EIGC    1       INV     MAX                                             +INV1
+INV1   41.0    -12.0   41.0    -14.0   1.00    1       1
$ AMP = AMPLITUDE/SQRT(I/A) = SQRT(12.0)*C/H = SQRT(12.0)*0.6 = 2.078461
$       WHERE I = AREA MOMENT OF INERTIA
$             A = AREA
PARAM   AMP     2.0784610.0
PARAM   NLOOP   3
$
$ APPLIED INPLANE LOADING
FORCE*  1               9                               9.86960440109   +FCE
+FCE    -1.0    0.0     0.0
ENDDATA
```

REFERENCES

1. Fung, Y. C.: On Two-Dimensional Panel Flutter, J. Aeronautical Sciences. Vol. 25, 1958, pp. 145-160.

2. Dugundji, J.: Theoretical Considerations of Panel Flutter at High Supersonic Mach Numbers. AIAA J., Vol. 4, 1966, pp. 1257-1266.

3. Dowell, E. H.: A Review of the Aeroelastic Stability of Plates and Shells. AIAA J., vol. 8, 1970, pp. 385-399.

4. Dowell, E. H.: Nonlinear Oscillations of a Fluttering Plate. AIAA J. Vol. 4, 1966, pp. 1267-1275.

5. Dowell, E. H. : Nonlinear Oscillations of a Fluttering Plate II. AIAA J., Vol. 5, 1967, pp. 1856-1862.

6. Eastep, F. E. and McIntosh, S. C.: The Analysis of Nonlinear Panel Flutter and Response under Random Excitation or Nonlinear Aerodynamic Loading. Proceedings AIAA/ASME 11th SDM Conference, Denver, Colo., April 1972, pp. 36-47.

7. Kuo, C. C., Morino, L. and Dugundji, J.: Perturbation and Harmonic Balance Methods for Nonlinear Panel Flutter. AIAA J., Vol 10, 1972, pp. 1479-1484.

8. Morino, L.: A Perturbation Method for Treating Nonlinear Panel Flutter Problems. AIAA J., Vol. 7, 1969, pp. 405-410.

9. Olson, M.S.: Finite Elements Applied to Panel Flutter. AIAA J. Vol. 5, 1967, pp. 2267-2270.

10. Kariappa and Somashekar, B.R.: Application of Matrix Displacement Methods in the Study of Panel Flutter. AIAA J., Vol. 7, 1969, pp. 50-53.

11. Olson, M.S.: Some Flutter Solutions Using Finite Elements. AIAA J., Vol. 8, 1970, pp. 747-752.

12. Kariappa, Somashekar, B. R. and Shah, C. G.: Discrete Element Approach to Flutter of Skew Panels with In-plane Forces under Yawed Supersonic Flow. AIAA J., Vol. 8, 1970, pp. 2017-2022.

13. Sander G., Bon C. and Geradin, M.: Finite Element Analysis of Supersonic Panel Flutter. Int. J. Numerical Methods in Engr., Vol. 7, 1973, pp. 379-394.

14. Rossettos, J. N. and Tong, P.: Finite-Element Analysis of Vibration and Flutter of Cantilever Anisotropic Plates. ASME Paper 74-WA/APM-15.

15. Bismarck-Nasr, M. N.: Finite Element Method Applied to the Supersonic Flutter of Circular Cylindrical Shells. Int. J. Numerical Methods in Engr., Vol. 10, 1976, pp. 423-435.

16. Mei, C.: Finite Element Displacement Method for Large Amplitude Free Flexural Vibrations of Beams and Plates. Int. J. Comp. & Stru., Vol. 3, 1973, pp. 163-174.

17. Mei, C. and Rogers, J. L., Jr.: NASTRAN Nonlinear Vibration Analysis of Beam and Frame Structures. NASA TM X-3278, 1975, pp. 259-284.

18. Rao, G. V., Raju, I. S. and Raju, K. K.: Nonlinear Vibrations of Beams Considering Shear Deformation and Rotatory Inertia. AIAA J., Vol. 14, 1976, pp. 685-687.

19. Bergan, P. G. and Clough, R. W.: Convergence Criteria for Iterative Processes. AIAA J., Vol. 10, 1972, pp. 1107-1108.

20. Olson, M. D.: On Applying Finite Elements to Panel Flutter. Aero. Rept. LR-476, National Research Council, Ottawa, Canada, March 1967.

21. Ray, J. D. and Bert, C. W.: Nonlinear Vibrations of a Beam with Pinned Ends. Trans. ASME, J. Engr. for Industry, Vol. 91, 1969, pp. 997-1004.

TABLE 1. IN VACUO EIGENVALUES AND COALESCENCE RESULTS FOR SIMPLY SUPPORTED AND CLAMPED PANELS

Simply Supported Panel

Number of Elements	In Vacuo κ_1	In Vacuo κ_2	Coalescence λ_{cr}	Coalescence κ_{cr}
2	98.1795	1920.00	398.536	1206.32
4	97.4597	1570.87	342.347	1043.47
8	97.4123	1559.35	343.280	1051.22
Exact (ref. 20)	97.4091	1558.55	343.3564	1051.797

Clamped Panel

Number of Elements	In Vacuo κ_1	In Vacuo κ_2	Coalescence λ_{cr}	Coalescence κ_{cr}
2	516.923	6720.00	922.388	3618.46
4	501.894	3874.23	636.437	2721.38
8	500.648	3808.34	636.586	2740.16
Exact (ref. 20)	500.564	3803.54	636.5691	2741.360

TABLE 2. EFFECT OF AMPLITUDE RATIO ON IN-VACUO FREQUENCY RATIOS $(\omega/\omega_o)_n$ FOR SIMPLY SUPPORTED PANEL

Amplitude $(\frac{c}{h})$	Mode n	Number of Elements 4	8	12	Theory (ref. 21) Assumed Space Mode	Assumed Time Mode	Galerkin
0.0	1	1.000	1.000	1.000	1.000	1.000	1.000
	2	1.004	1.000	1.000	1.000	-	-
0.2	1	1.038	1.039	1.040	1.056	1.032	1.048
	2	1.030	1.038	1.039	1.056	-	-
0.4	1	1.141	1.147	1.148	1.206	1.124	1.181
	2	1.106	1.141	1.146	1.206	-	-
0.6	1	1.292	1.304	1.306	1.411	1.262	1.375
	2	1.221	1.292	1.301	1.411	-	-
0.8	1	1.471	1.489	1.492	1.647	1.434	1.607
	2	1.367	1.471	1.484	1.647	-	-
1.0	1	1.667	1.690	1.693	1.902	1.627	1.863
	2	1.534	1.667	1.685	1.902	-	-
1.2	1	1.869	1.902	1.906	2.167	1.837	2.136
	2	1.716	1.870	1.895	2.167	-	-

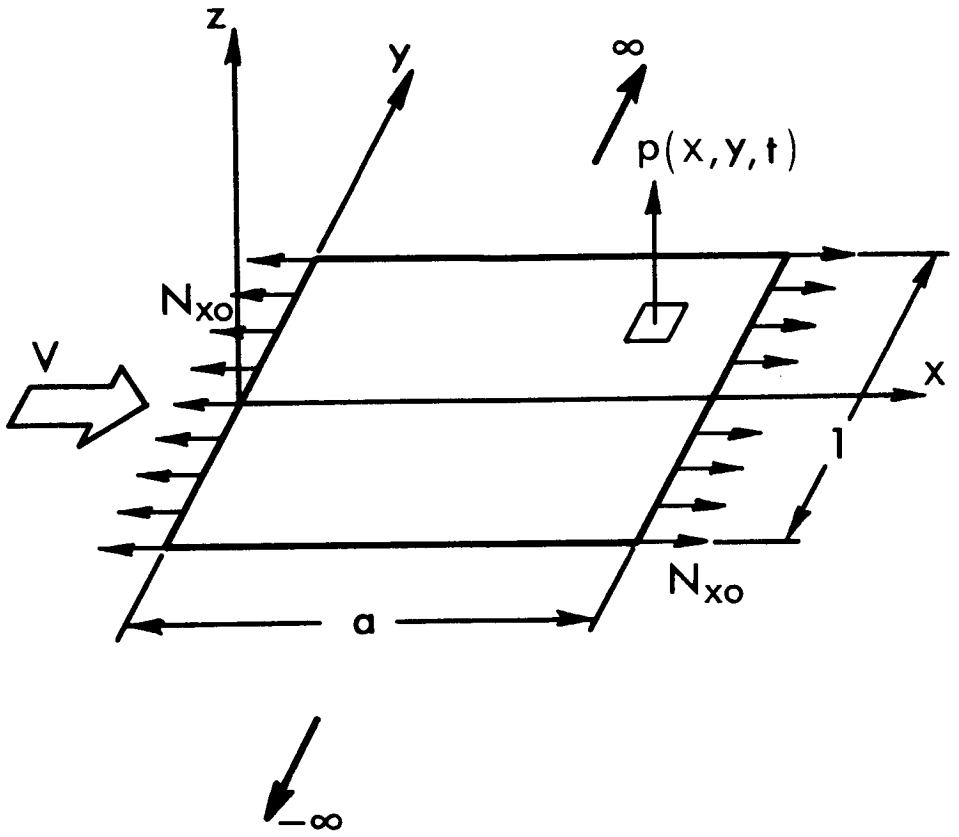

Figure 1. Panel geometry.

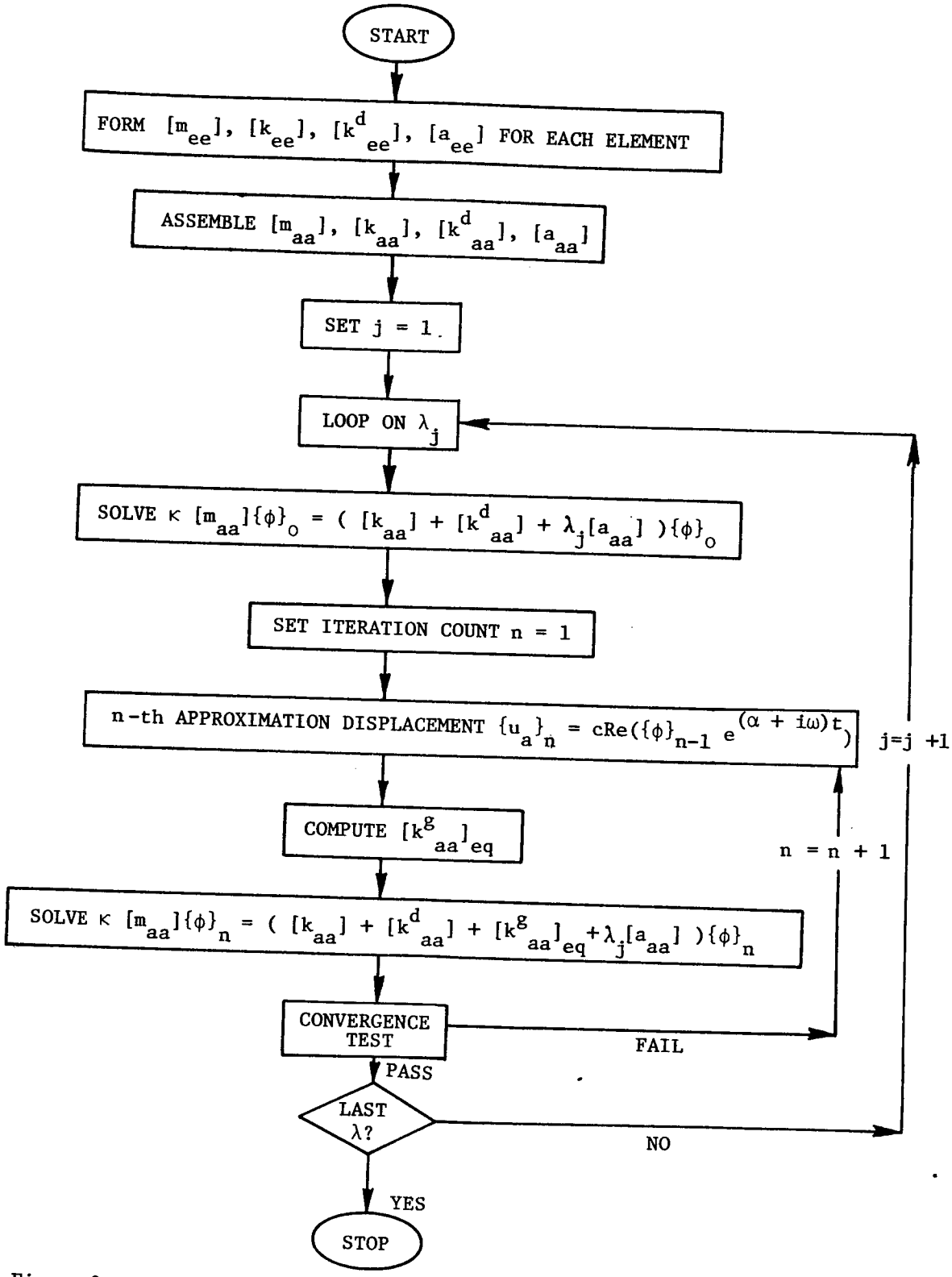

Figure 2. Simplified flow diagram for large deflection panel flutter analysis.

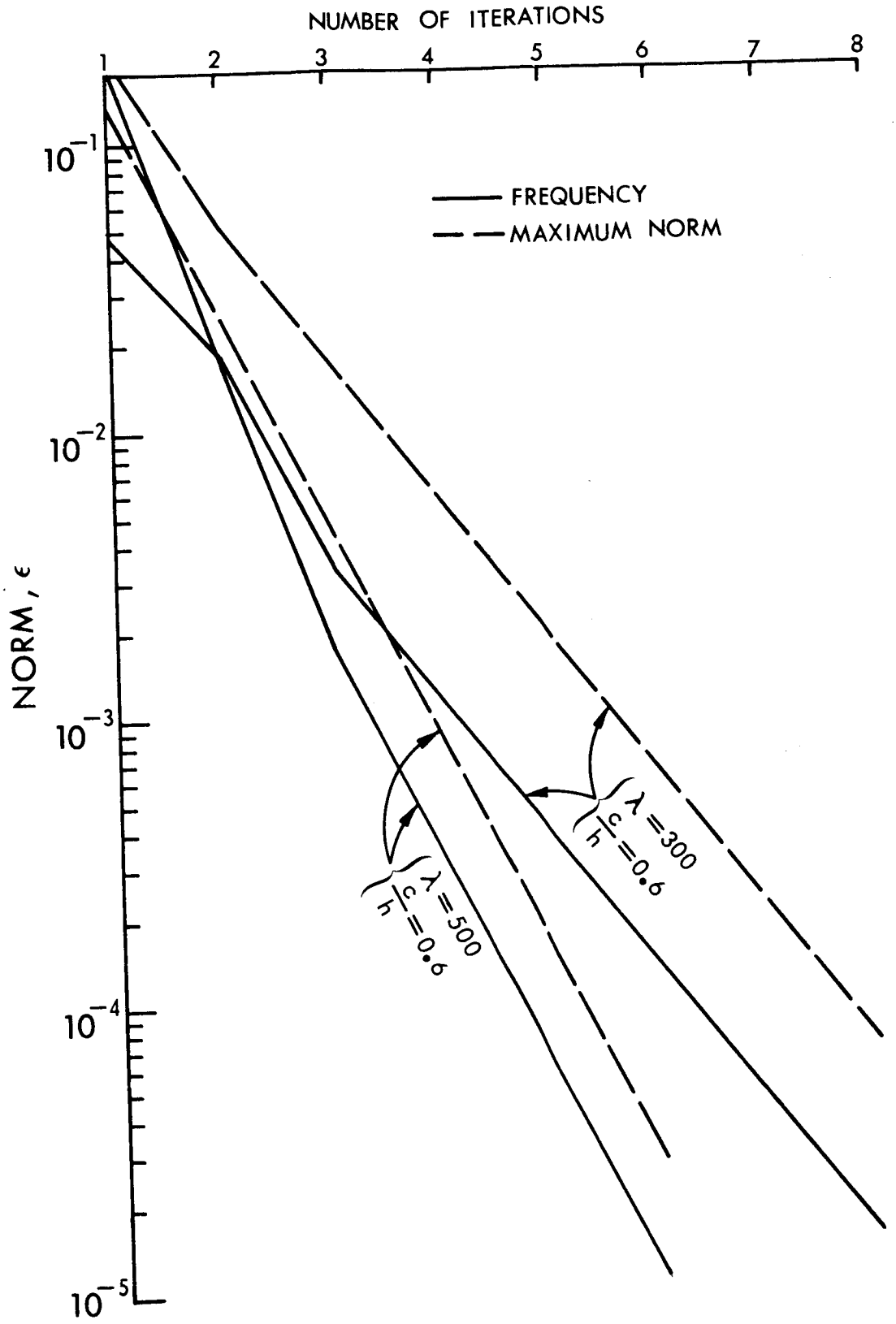

Figure 3. Convergence characteristics.

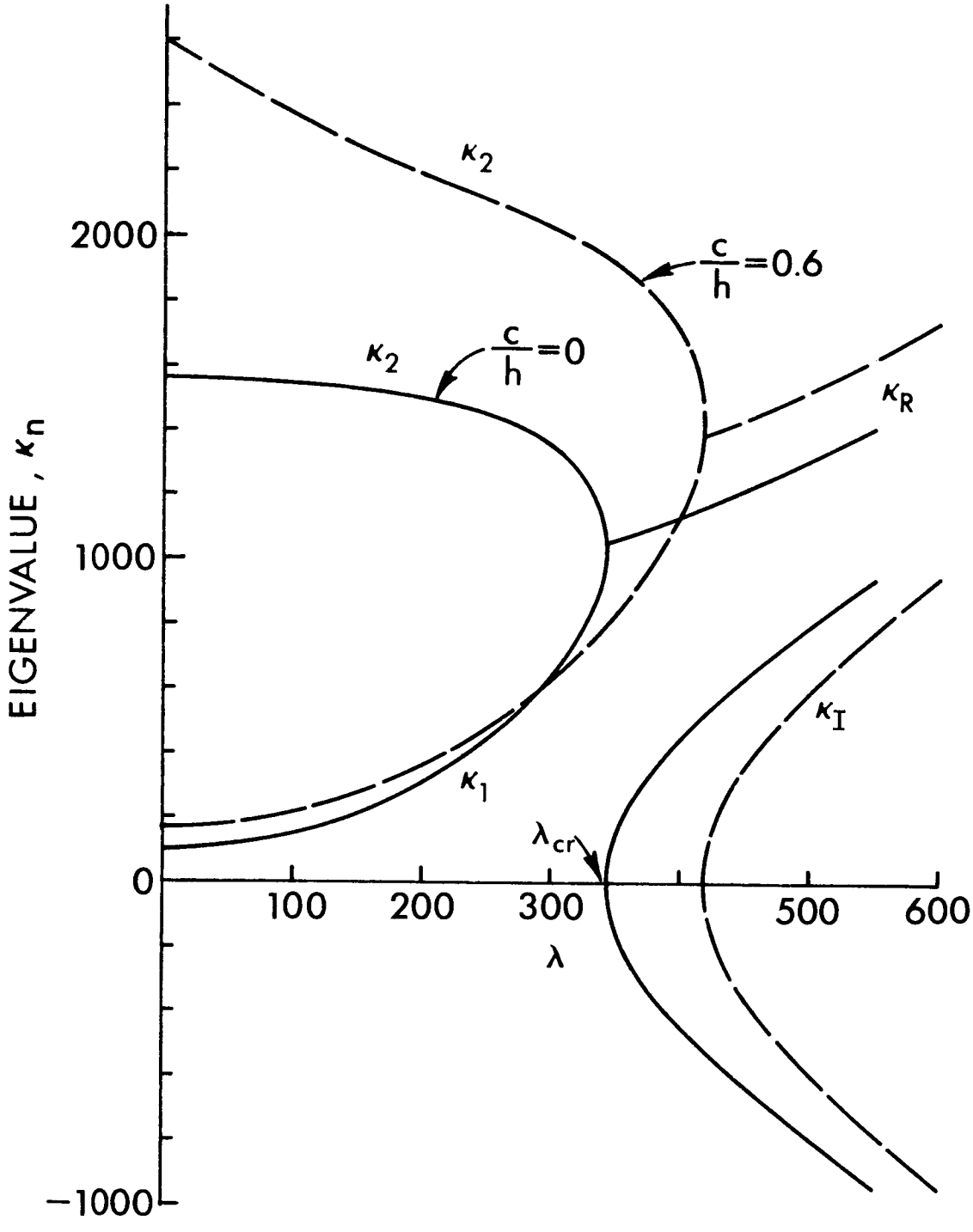

Figure 4. Variation of eigenvalues with dynamic pressure for simply supported panel ($N_{xo} = 0$).

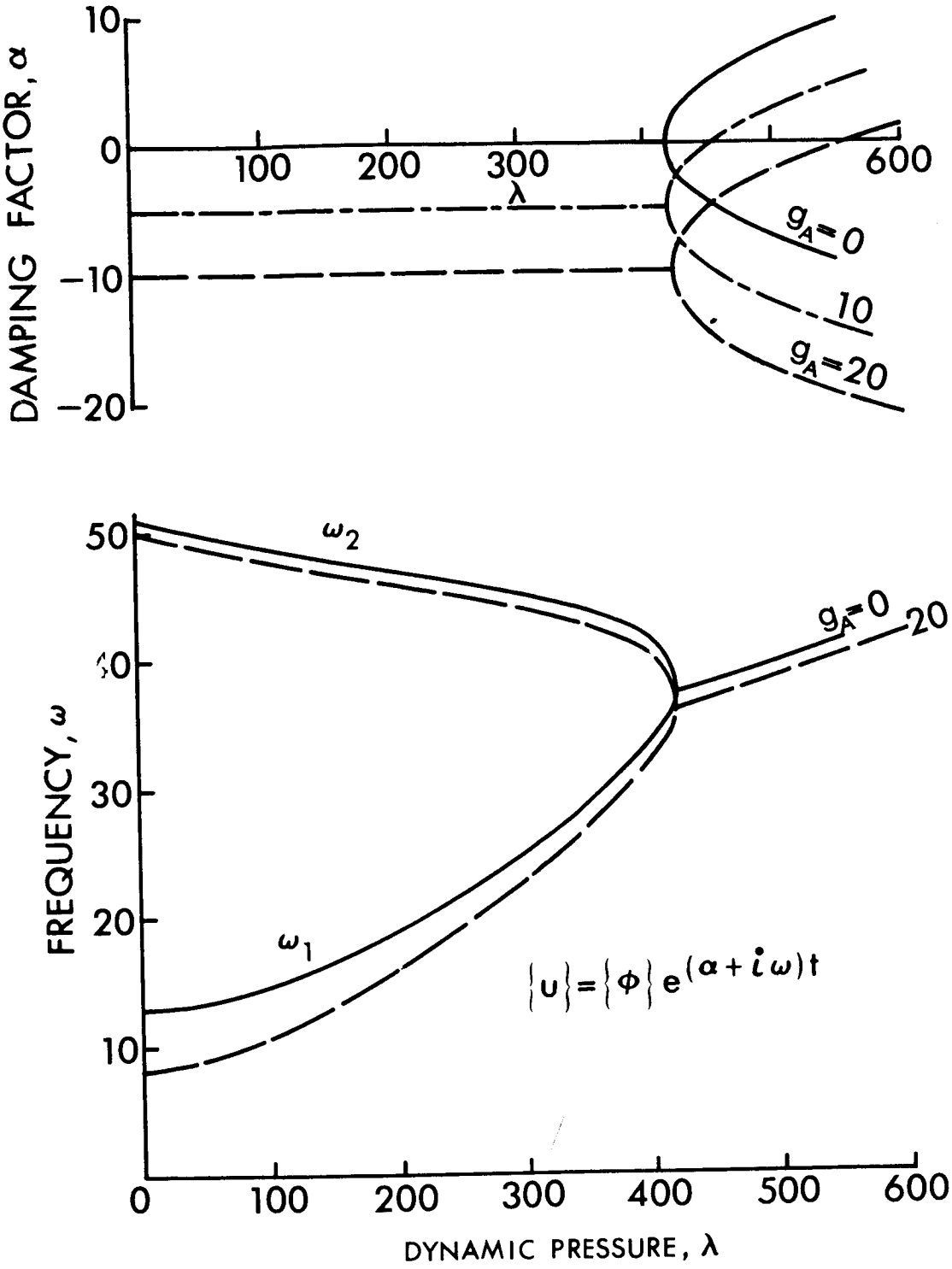

Figure 5. Typical plots of panel behavior and effect of aerodynamic damping (simply supported panel, $\frac{c}{h} = 0.6$ and $N_{xo} = 0$).

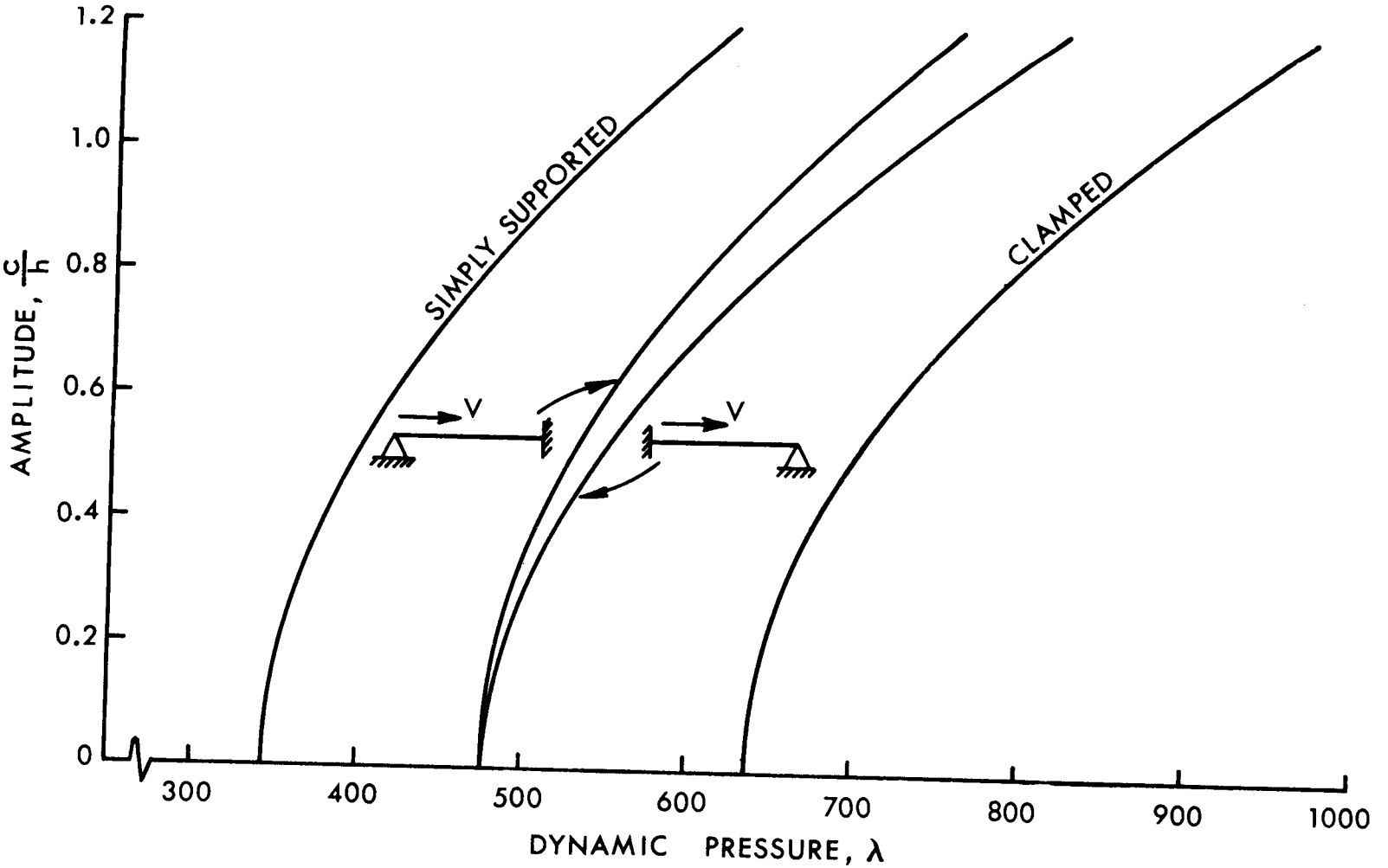

Figure 6. Limit cycle amplitude versus dynamic pressure for panels with various support conditions ($N_{xo} = g_A = 0$).

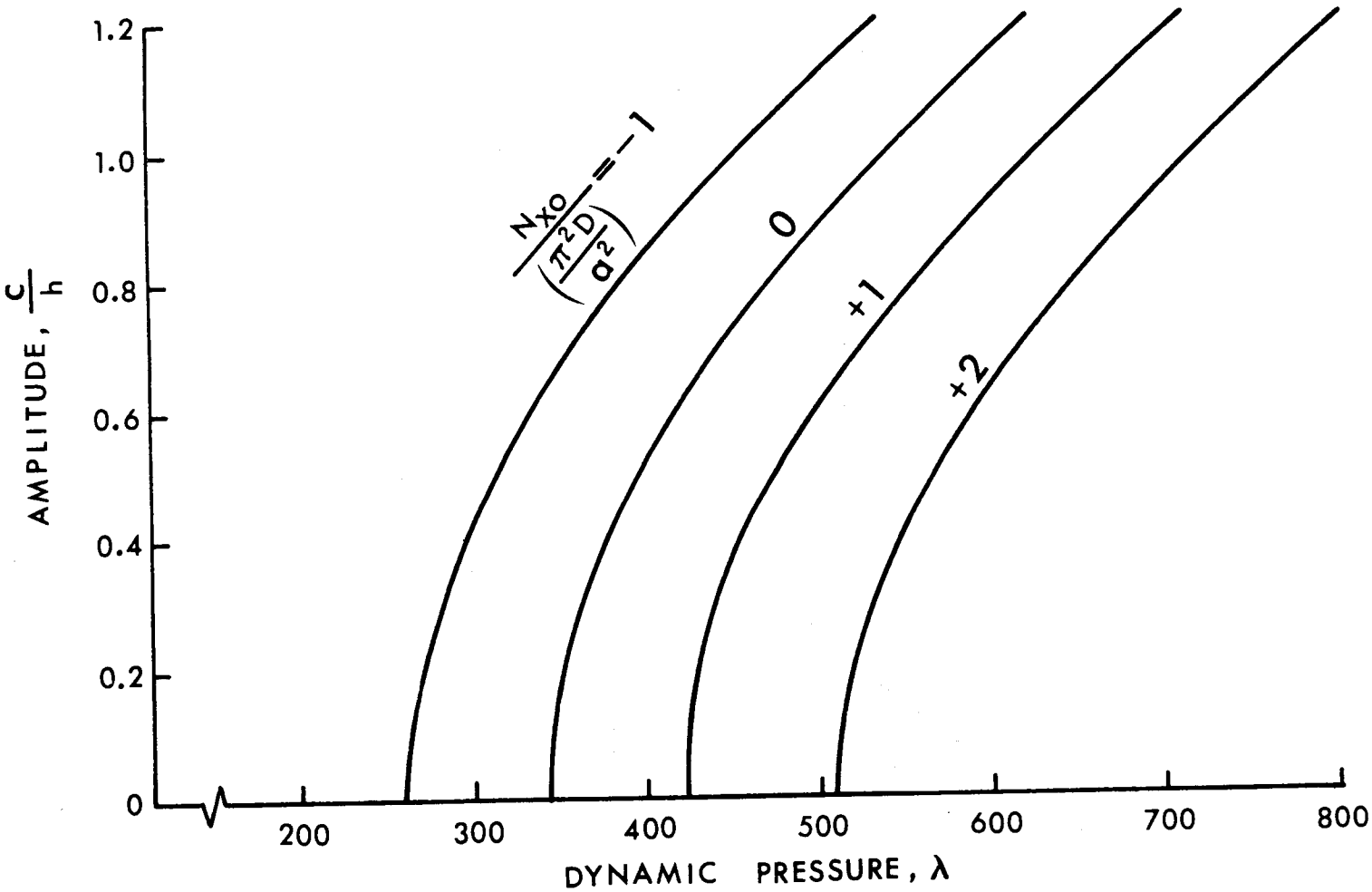

Figure 7. Limit cycle amplitude versus dynamic pressure for simply supported panel under different in-plane forces ($g_A = 0$).

THERMAL ANALYSES OF THE INTERNATIONAL ULTRAVIOLET EXPLORER (IUE) SCIENTIFIC INSTRUMENT USING THE NASTRAN THERMAL ANALYZER ($\bar{N}$TA) - A GENERAL PURPOSE SUMMARY

Clifton E. Jackson, Jr.
Goddard Space Flight Center

SUMMARY

The $\bar{N}$TA (reference 1) Level 15.5.2/3, was used to provide non-linear steady-state (NLSS) and non-linear transient (NLTR) thermal predictions for the International Ultraviolet Explorer (IUE) Scientific Instrument (SI)(reference 2). NASTRAN (references 3 and 4) structural models (reference 5) were used as the basis for the thermal models, which were produced by a straight-forward conversion procedure. The accuracy of this technique was subsequently demonstrated by a comparison of $\bar{N}$TA predicts with the results of a thermal-vacuum test of the IUE Engineering Test Unit (ETU) (reference 6). Completion of these tasks was aided by the use of $\bar{N}$TA pre-and-post-processors and by a significant amount of program modification to $\bar{N}$TA subroutines RMG and SSGHT.

INTRODUCTION

The NASTRAN program has quickly become a standard tool for the finite element structural analysis of large and/or complex structures. During this evolution it became apparent that the mathematical techniques employed in NASTRAN to solve structural analysis problems could be easily adapted to provide solutions to heat transfer problems (reference 7), with several major advantages accruing, in that:

(a) virtually the same finite element analytical model could be used for both cases;

(b) with the same analytical model being used for both structural and thermal analyses, thermal predictions could be

directly applied, with no error-inducing and/or time consuming interpolation, to the structural model to allow the calculation of thermally induced deformations.

An appealing concept, certainly, but concepts often run afoul of practical details and fail to ever be used effectively to produce the desired result of increased productivity. The intent of this paper is therefore basically to increase the steepness of the $\bar{N}$TA learning curve by describing in detail the actual techniques used in converting an existing NASTRAN structural model into an executable $\bar{N}$TA model. In support of this goal, information will be presented containing computer results, comparisons with test results, comments on effective analysis aids, and useful program coding modifications.

THE IUE SCIENTIFIC INSTRUMENT

Description

The IUE SI, as shown in Figure 1, consists of a Cassegrain telescope section and a spectrograph section, and as a whole is essentially an aluminum structure approximately 3 meters long and .7 meters in diameter. The prime purpose of this instrument is high resolution observation of stellar objects in the ultraviolet spectral region, and to this end tight optical tolerances of one arc-second resolution and less than one arc-second change in focus during a one-half hour observation were imposed. It was evident that the accurate optical performance analysis of this sensitive and complex system would require detailed structural and thermal models to provide the necessary predictions of optical component shifts due to thermally induced deformations. Given that detailed NASTRAN structural models of the telescope and the spectrograph already existed, the IUE SI clearly qualified as an ideal candidate for the first large-scale use of the $\bar{N}$TA for flight project support.*

The NASTRAN Structural Model

Figures 2 and 3 are $\bar{N}$TA plots of the major structure of the IUE telescope and spectrograph (plots of radiating elements were the most convenient to include here, but they are essentially

*The $\bar{N}$TA was previously used to support the OSO project (reference 8), but that effort was essentially intended to test the integrated analysis concept for debugging purposes.

direct overlays of the planar structural elements). In combination these models consisted of 3006 degrees of freedom (reference 5), approximately 550 GRID points and 900 structural elements, and would seemingly be very difficult to convert to thermal models due to their sheer size and complexity. This problem is specifically addressed in the next section, where it will be assumed that the reader is familiar with the basic organization of a NASTRAN problem, and is aware that the NASTRAN User's Manual (reference 3) and the $\bar{N}$TA Manuals (reference 1) may be consulted for detailed information on the implementation of any of the cited techniques.

GENERAL PURPOSE TECHNIQUE FOR THE CONVERSION OF A NASTRAN STRUCTURAL MODEL TO A $\bar{N}$TA THERMAL MODEL

The following Sections are a general purpose statement outlining the techniques used to convert the IUE NASTRAN model to a $\bar{N}$TA model.

Pre-modification

(1) Acquire a working understanding of the thermal design of the structure to be analyzed, with special attention being paid to areas with high power dissipations and/or crucial thermal contact couplings. It will often be the case that the structural model will be of insufficient detail in these areas, requiring additional modelling to be done.

This type of problem is too complex and non-general to be discussed in detail in this paper, as it falls into the category of engineering judgement;

(2) Obtain NASTRAN element and GRID point structure plots similar to those in Figures 2 and 3, along with a verbal description of the model including materials used and simplifying assumptions;

(3) Decide whether NLSS or NLTR results are required (linear problems may be solved by the same solution algorithms, or, for linear steady-state problems, a special algorithm is available). The conversion technique presented will initially produce a NLSS model, but the further changes required to produce a NLTR model will also be described.

Card Removal

Using a punched deck copy of the NASTRAN structural model:

(1) Remove the Executive and Case Control Decks;

(2) Remove all Bulk Data Deck cards except GRID, SPOINT, connection, property, coordinate, relevant $,GRDSET, BAROR, SEQGP, BEGIN BULK, and ENDDATA cards (the thermally acceptable connection cards are listed in the NTA Manual (reference 1);

(3) Remove any permanent constraints defined on GRID cards or on a GRDSET card.

This reduced structural model Bulk Data Deck is now ready for conversion to a NTA model.

NLSS Card Additions

Using the card deck generated in the previous section:

(1) Add Case Control and Executive Control Decks;

(2) If degree-of-freedom information is requested by a card-type, always use 1;

(3) Add MAT4, MATT4, MAT5, and/or MATT5 cards to define thermal conductivities (eg - W/m-°C) for each material type referenced by the property cards in the model;

(4) If any CELASi cards are present, examine them to determine, based on their location in the structure, what effective conductance (eg-W/°C) should be entered in field 3 of each card;

(5) List on an SPC1 card all GRID points which are to be held at fixed temperatures;

(6) If any GRID points are to be maintained at equal but unspecified temperatures, list them on one or more MPC cards (more complex temperature relationships may be defined if none of the GRID points involved are subject to non-linear effects);

(7) If any MPC, SPC, or permanent constraints were removed from the structural model, carefully examine the GRID points affected to verify that they are satisfactorily coupled into the thermal model;

(8) Define a temperature "guess vector" consisting of TEMP

cards and/or a TEMPD card. All GRID points in the model must have a guess temperature, and those GRIDs listed on an SPC1 card will be constrained to that temperature. In addition, to assure convergence, all guess temperatures should be no less than 80% of the final steady-state absolute temperature of the respective GRID points;

(9) Define a thermal load vector if heat is to be applied to any elements or GRID points;

(10) If radiative, convective, and/or contact heat exchange is to be allowed, CHBDY elements and supporting property and/or material cards must be added to define the active surfaces. In addition, if gray body radiative couplings are present, RADLST and RADMTX cards are required to, respectively, define the radiatively active CHBDY cards, and the area-times-view-factor coupling (eg-m^2) between the active CHBDY cards;

(11) Add four PARAM cards (EPSHT, MAXIT, TABS, and SIGMA) to define, respectively, the convergence criteria, the maximum number of iterations, the absolute temperature conversion factor (eg-273.15 for °C), and the Stefan-Boltzmann Constant.

This completes the basic Bulk Data Deck changes required to produce a NLSS NTA deck from a NASTRAN structural model.

Further NLTR Card Additions

The NLSS Card deck produced in the previous section may be converted to a transient form if the following changes are made:

(1) Minor modifications to the Executive and Case Control Decks are required;

(2) Proper thermal masses (eg-J/°C) must be applied to the GRID points in the model. This is done primarily through specifying a volume thermal mass (eg-J/m^3-°C) on the thermal material cards. Additional thermal mass may be applied through the use of CVISC and/or CDAMPi cards. The CHBDY card may also be used to provide thermal mass in conjunction with convection (½ of the thermal mass specified will be applied to the ambient point(s)). Note that structural mass has no relationship to thermal mass,* with the correct analogy equating viscosity or damping with thermal mass. Singular thermal mass matrices are allowed, but my experience has been that stability is somewhat impaired;

---

*Non-structural mass from the structural model will not supply any thermal mass.

(3) All thermal loads must be referenced via TLOAD1 and/or TLOAD2 card(s);

(4) An "initial condition" temperature set composed of TEMP cards and/or a TEMPD card must be supplied. The thermal "guess vector" used in the NLSS model should still be used, as it appears to improve the stability of problems with singular thermal mass matrices (for an oscillating solution, good results are obtained with a guess at approximately the average solution value);

(5) MPC's are unaffected, but SPC's may only be used to constrain GRID points to 0°. They must be replaced with the well-known "ground-and-load" system* which allows both fixed temperatures and fixed time/temperature histories to be specified;

(6) A TSTEP card must be added to specify the number of integration time steps, their length, and the frequency of output;

This completes the Bulk Data Deck changes required to convert a NLSS NTA model to a NLTR one.

IUE THERMAL PREDICTS vs TEST RESULTS

These procedures were followed to transform the structural models of the IUE telescope and spectrograph into a complete NLSS NTA model (reference 9). A comparison at representative points of the predicts generated by this model with the actual results of an ETU thermal vacuum test (reference 6) performed at the Goddard Space Flight Center is presented in Table 1, and is accompanied by the thermal predicts produced by the post-test updated model (reference 10). Agreement was in general excellent, with the major differences being traced to incorrect coating assumptions in the area of the secondary mirror and incorrect joint conduction assumptions at several points in the model.

ANALYSIS AIDS

In the course of using any program extensively, one slowly acquires a collection of especially effective or useful analysis aids or techniques which through lack of documentation and/or lack of general usage are not obvious to the new user. The following four items, all used in the IUE analyses, fall into this category and should prove useful to most NTA analysts.

---

*See Reference 1

The VIEW Program (references 11 and 12)

This program is designed to automatically produce the RADMTX and RADLST cards required to simulate diffuse radiative interchange, including shading, between CHBDY elements. As input, it requires primarily the same CHBDY, PHBDY, and GRID cards used in the NTA model, with one additional card type being used to specify mesh sizes and optional shading information. VIEW is currently operational on IBM 360-370 series computers (but could be converted to UNIVAC or CDC operation in roughly one month) and executes in as little as 110K decimal 8-bit bytes from an overlayed load module occupying 26 7294-byte tracks. VIEW was found to be vital to the IUE NTA analyses as it greatly simplified the required computation and correction of the large view factor matrices involved.

Modelling Multi-Layer Insulation (MLI)

A common problem in thermal modelling is how to account for MLI. If it is assumed that the heat loss through the MLI cannot simply be completely neglected, two methods are suggested:

(1) Effective emissivity. The NTA assumes that the information entered on the RADMTX cards is area-times-view-factor for gray bodies, rather than Script-AF data. Therefore the use of effective emissivity is approximately valid only when the CHBDY card using an effective emissivity sees only essentially black fixed temperature surfaces (such as the outside of the IUE Telescope looking at space). Also, of course, an effective absorbtivity would have to be specified to account for external inputs such as solar energy.

(2) Effective conductance per unit area. This is a more straight-forward technique, and requires that the analyst estimate the effective conductance through the MLI over a unit area (eg-W/m^2-°C) and assume that the CHBDY cards are on the outer layer of the MLI.* The emissivity and absorbtivity of the CHBDY cards would correspond to that of the outer surface of the MLI, and convection would be defined from the same CHBDY cards to the GRID points on the structure directly beneath the MLI, with the convective coefficient "h" corresponding to the effective conductance per unit area through the MLI (see Figure 4). This method is obviously much more flexible than the one previously described, as there are no constraints on the surroundings nor is there any need to calculate an effective absorbtivity. However, care must be taken to ensure that, for both NLSS and

*New GRID points must be defined for these elements.

NLTR runs, the thermal "guess vector" is appropriate for the GRID points associated with the CHBDYs on the MLI, or instabilities will result.

Solution and Transient Printer Plotting of Linear Equations

Early in the IUE analyses simple, linear parametric equations were developed relating the defocus of the telescope to factors such as axial and circumferential thermal gradients, changes in mirror temperatures, etc. It became apparent that these equations could be solved during a $\overline{\text{N}}$TA run by adding new GRID points whose values would be appropriately defined by MPCs. It would also be possible to use the $\overline{\text{N}}$TA printer-plotter, if the run were a transient, to plot the value of the GRID point which represented defocus as a function of time (see Figure 5*). This "on-line" analysis technique would obviously be applicable to all forms of linear equations and provides an excellent quick-look for the analyst faced with an otherwise difficult to peruse stack of $\overline{\text{N}}$TA output.

On-Line $\overline{\text{N}}$TA Post Processors

When a large $\overline{\text{N}}$TA model is to be run more than 10-15 times, a problem can develop with respect to actually examining the enormous volume of data which is generated. While transient plotting will help to some degree, an on-line post processor may be a better answer, as was found to be the case for the IUE analyses.

The method is quite simple, and involves requesting temperature, load, and constraint power output in punched as well as printed format (eg-OLOAD (PRINT, PUNCH) = ALL). The punched card images are sent to a direct-access storage unit instead of a card-puncher, and when the $\overline{\text{N}}$TA execution is complete, a user written FORTRAN program may be compiled and executed in-line to read the card images and print out neatly formatted summaries of the results for the job. Figure 6 shows the format of sample punched temperature, load, and constraint force cards, while Figure 7 shows an actual automatically and immediately generated summary report.

---

*A defocus/time plot from the $\overline{\text{N}}$TA OSO analyses (reference 8) is shown as it was the more reproducible of the plots available.

PROGRAM MODIFICATIONS

During the course of the IUE thermal analyses, it became obvious that several relatively minor improvements to the $\overline{N}$TA coding would allow a considerable increase in the program's efficiency, capability, and "useability." Since inclusion of the actual FORTRAN code changes would be too lengthy for this presentation, discussion will be limited to an outline of the use of the new features and the $\overline{N}$TA subroutines which were modified to implement them, with the understanding that more complete information can be obtained from either Mr. Clifton E. Jackson, Jr. or Mr. Reginald S. Mitchell, Code 720.2, Goddard Space Flight Center, Greenbelt, Maryland 20771.

Additional "Space Node" Flexibility

An option was supplied to allow elimination of the automatic assumption that any energy not accounted for in the RADMTX should be discarded (the so-called "space node" feature). The new option, if elected, would assume that energy not accounted for would be returned to the element from which it was radiated. Additional related features added included the capability to partition the RADMTX into "space node" and "non-space-node" portions, and a summation check to assure that the RADMTX does not in effect specify emissivities greater than 1.0. The addition of these features required modifications in subroutine RMG only.

Script-AF Input

The original $\overline{N}$TA required the use of an internal Script-AF generator in order to include radiative interchange, a fact that prevented the use of externally generated Script-AF matrices. A modification to subroutine RMG now optionally allows either symmetric or unsymmetric Script-AF matrices to be input to the NTA using the standard RADMTX and RADLST cards.

Symmetric Decomposition

When the full-scale NLSS model of the IUE experiment was first run, CPU and I/O solution times on the order of an hour were observed. An examination of the run logs for this problem indicated that large amounts of time were being spent in the unsymmetric decomposition of symmetric radiation and conductance matrices. It was determined that minor limitations on input (emissivities not equal to exactly 1.0, and uniform thermal guess

vectors for unconstrained GRID points if radiative interchange were included) would allow the use of symmetric decomposition in both cases. Modifications were made to subroutines RMG and SSGHT, an additional parameter was added, and run times were cut to less than 18 minutes CPU and I/0, with only round-off error changes in the answers produced. A similar conductance matrix decomposition feature was later added for transient runs, and it appears that it would be especially useful if time step sizes were changing frequently.

CONCLUDING REMARKS

The $\overline{\text{N}}$TA has been used to provide thermal analyses of the IUE SI using structural models as the analytical baseline. The verification of this technique via test has demonstrated the accuracy of the $\overline{\text{N}}$TA as a thermal analytical tool, and the analysis aids and program modifications listed will assist in making it a useful one.

REFERENCES

1. Lee, Hwa-Ping; Jackson, Clifton E., Jr.: NASTRAN Thermal Analyzer - Theory and Application Including a Guide to Modelling Engineering Problems (2 Volumes). NASA-Goddard Space Flight Center X-322-76-17, December, 1975.

2. System Design Report for the International Ultraviolet Explorer (IUE) - Volume I - Scientific Instrument. NASA-Goddard Space Flight Center, June, 1973.

3. MacNeal, R. H. (Editor): The NASTRAN Theoretical Manual. NASA SP-221, with Level 15.5 updates, December, 1972.

4. McCormick, C. W. (Editor): The NASTRAN User's Manual (Level 15). NASA SP-222(01), with Level 15.5 updates, June, 1972.

5. Case, William R.: Dynamic Substructure Analysis of the International Ultraviolet Explorer (IUE) Spacecraft. NASA TM X-3278, 1975, pp.221-248.

6. Seivold, A. L.: International Ultraviolet Explorer Engineering Test Unit - Final Report of the IUE-ETU Thermal Balance Test. NASA-Goddard Space Flight Center-Test and Evaluation Division Report #03169, December, 1975.

7. Mason, James B.: The Solution of Heat Transfer Problems by the Finite Element Method Using NASTRAN. NASA-Goddard Space Flight Center X-321-70-97, February, 1970.

8. Lee, Hwa-Ping; Jackson, Clifton E., Jr.: A Summary of the STOP Thermal Analysis of the OSO-I Colorado Experiment. NASA-Goddard Space Flight Center-Test and Evaluation Division Report #03064, April, 1974.

9. Jackson, Clifton E., Jr.: A Summary of the NASTRAN Thermal Analyses Performed on the IUE Scientific Instrument From 1-1-74 to 7-23-75. NASA-Goddard Space Flight Center X-322-75-306, August, 1975.

10. Jackson, Clifton E., Jr.: Verification of the NASTRAN Thermal Analyzer (NTA) Model of the IUE ETU Scientific Instrument. NASA-Goddard Space Flight Center, Test and Evaluation Division Memorandum to J. B. Mason, July 7, 1975.

11. Puccinelli, E. F.: View Factor Computer Program (Program VIEW) User's Manual. NASA-Goddard Space Flight Center X-324-73-272, July, 1973.

12. Jackson, Clifton E., Jr.: Programmer's Manual for VIEW-A Modification of the RAVFAC View Factor Program for Use With the NASTRAN Thermal Analyzer on IBM-360 Series Computers. NASA Goddard Space Flight Center X-322-73-120, March, 1973.

TABLE I - CORRELATION OF THE IUE TEST AND THE ANALYTICAL MODELS

Location	$\beta = 0^\circ$ (no sun on telescope)			$\beta = 90^\circ$ (sun angle perpendicular to telescope)		
	Test °C	Unverified model °C	Verified model °C	Test °C	Unverified model °C	Verified model °C
Secondary mirror baffle	-59 to -65	-50 to -51	-53 to -59	-52 to -58	-48 to -49	-47 to -53
Primary mirror baffle	-20 to -41	-23 to -42	-23 to -47	-14 to -34	-20 to -40	-18 to -41
Primary mirror	- .7 to 1.3	1.0	1.2	3.1 to 5.4	3.5 to 3.6	5.5
Focus drive mechanism	-40	-29	-38	-33	-28	-32
Secondary mirror	+13 to +18	-22	+13	16 to 21	-20	17
ACQ camera #1	+4 to +5	1.7	3.5	8 to 10	4	8
LWL camera #1	+6 to +9	2.2	4.1	11 to 13	5	8
SWL camera #1	+6 to +8	1.7	3.9	11 to 13	4	8
Fine error sensor sensor	+3 to +9	3	8	7 to 14	6	12
Fine error sensor electronics	+4 to +5	1	2	9	3	6
Acquisition deck	0 to +1	-2	-1.3	5 to 6	.5	3
Aperture deck	0	-1.0	- .7	4 to 5	1 to 2	3 to 4
Camera deck	3	1.5	1.7	7 to 8	4	6
Echelle deck	+3 to +4	.8	2.6	7 to 9	3 to 4	6 to 7
Collimator deck	+6	1.3	3.8	10	4	8
Sunshade	-98 to -112	-87 to -91	-95 to -106	-85 to -100	-76 to -86	-82 to -100
Tube	-20 to -64	-17 to -56	-18 to -60	-14 to -57	-14 to -55	-12 to -54
Strong ring	-16.8 to -17.8	-17.1 to -17.9	-17.3 to -18.4	-10.8 to -12.4	-13.1 to -14.3	-11.9 to -13
Spectrograph dust cover	-12 to +5	-7 to +2	-7 to +5	-7 to +9	-5 to +4	-2 to +8

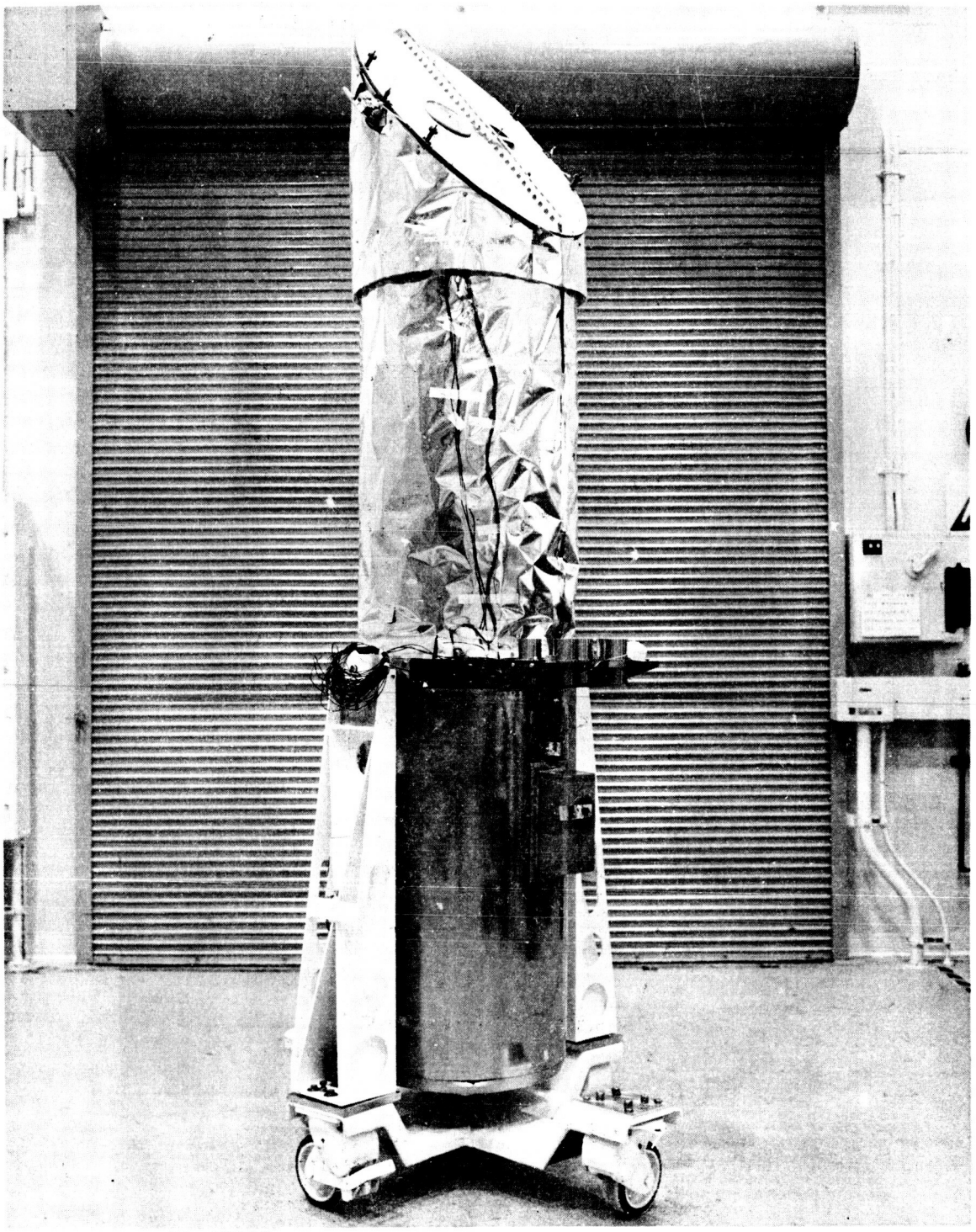

NASA G-75-05232

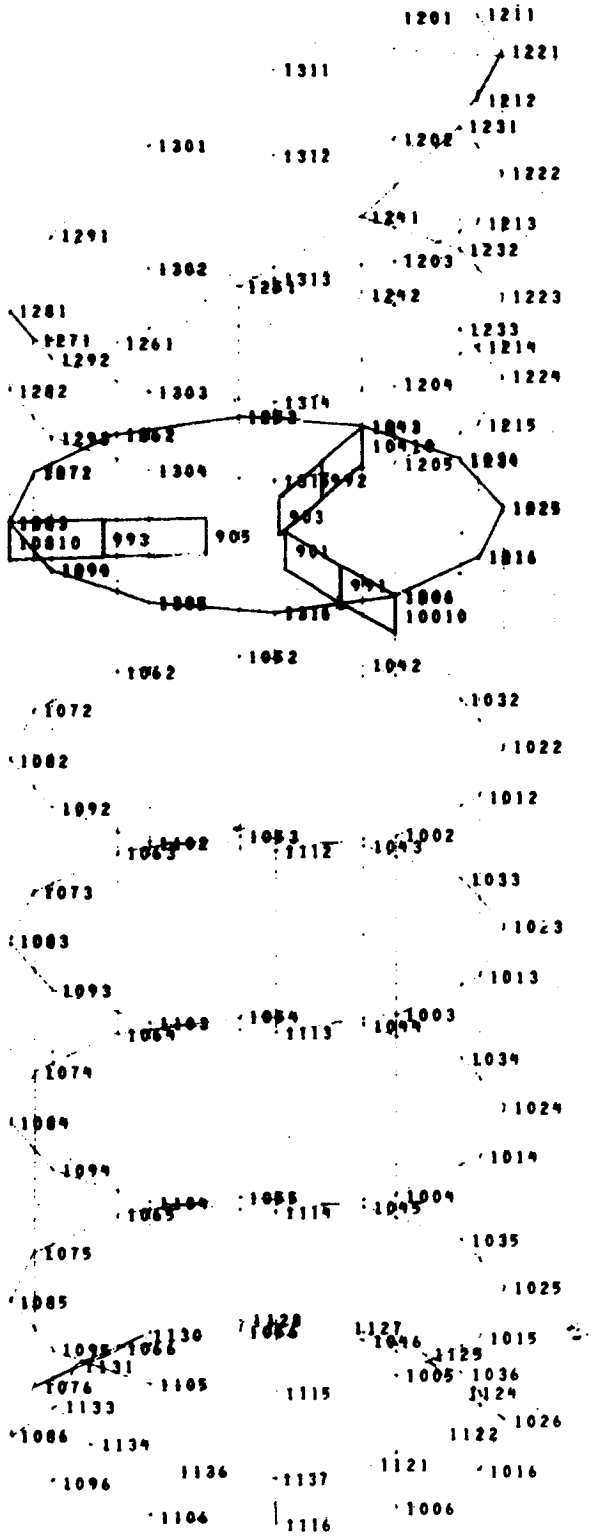

Figure 2. NTA Plot of the Major IUE Telescope Radiating Elements

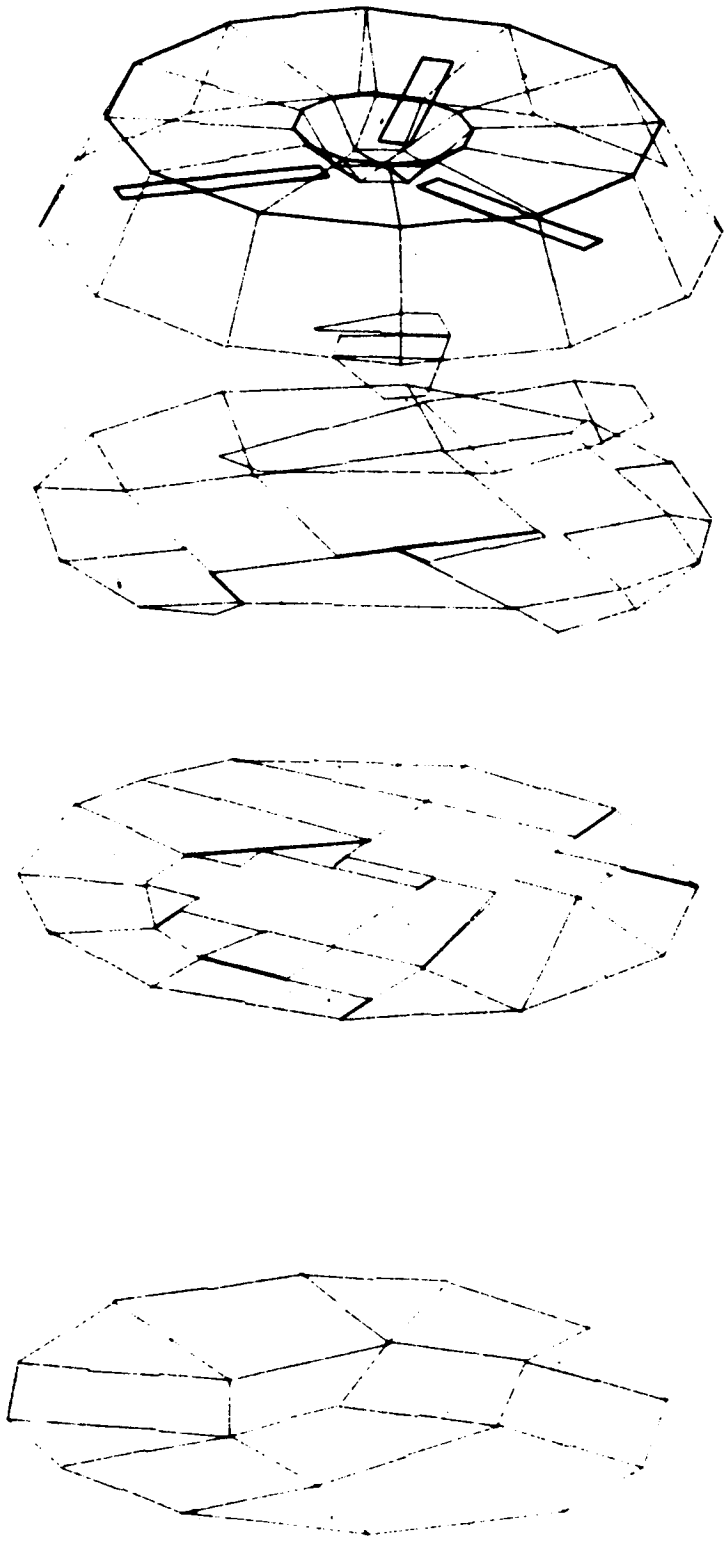

Figure 3. $\bar{N}$TA Plot of the Major IUE Spectrograph Deck's Radiating Elements

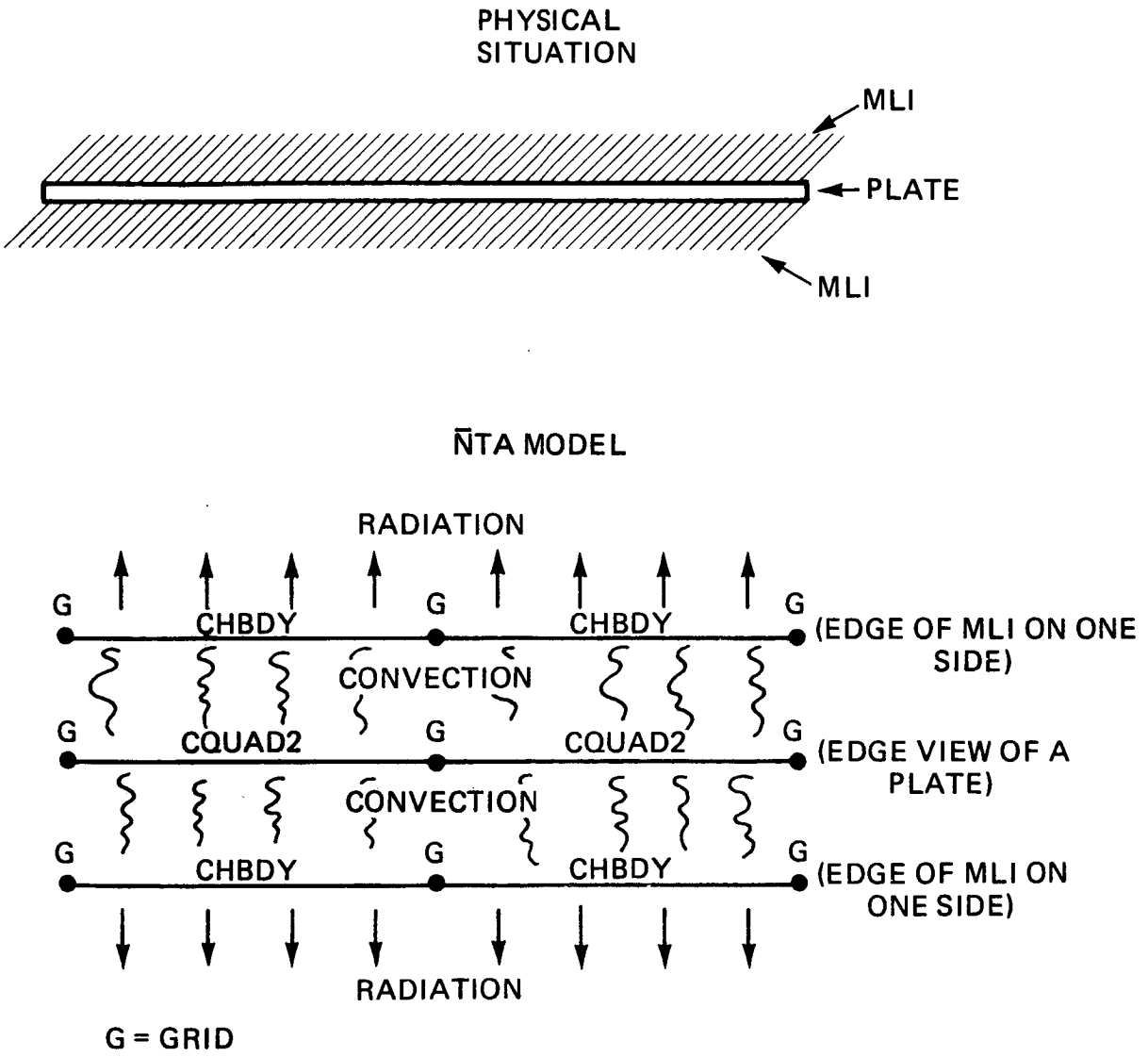

Figure 4. Outline of One Method of N̄TA MLI Modeling

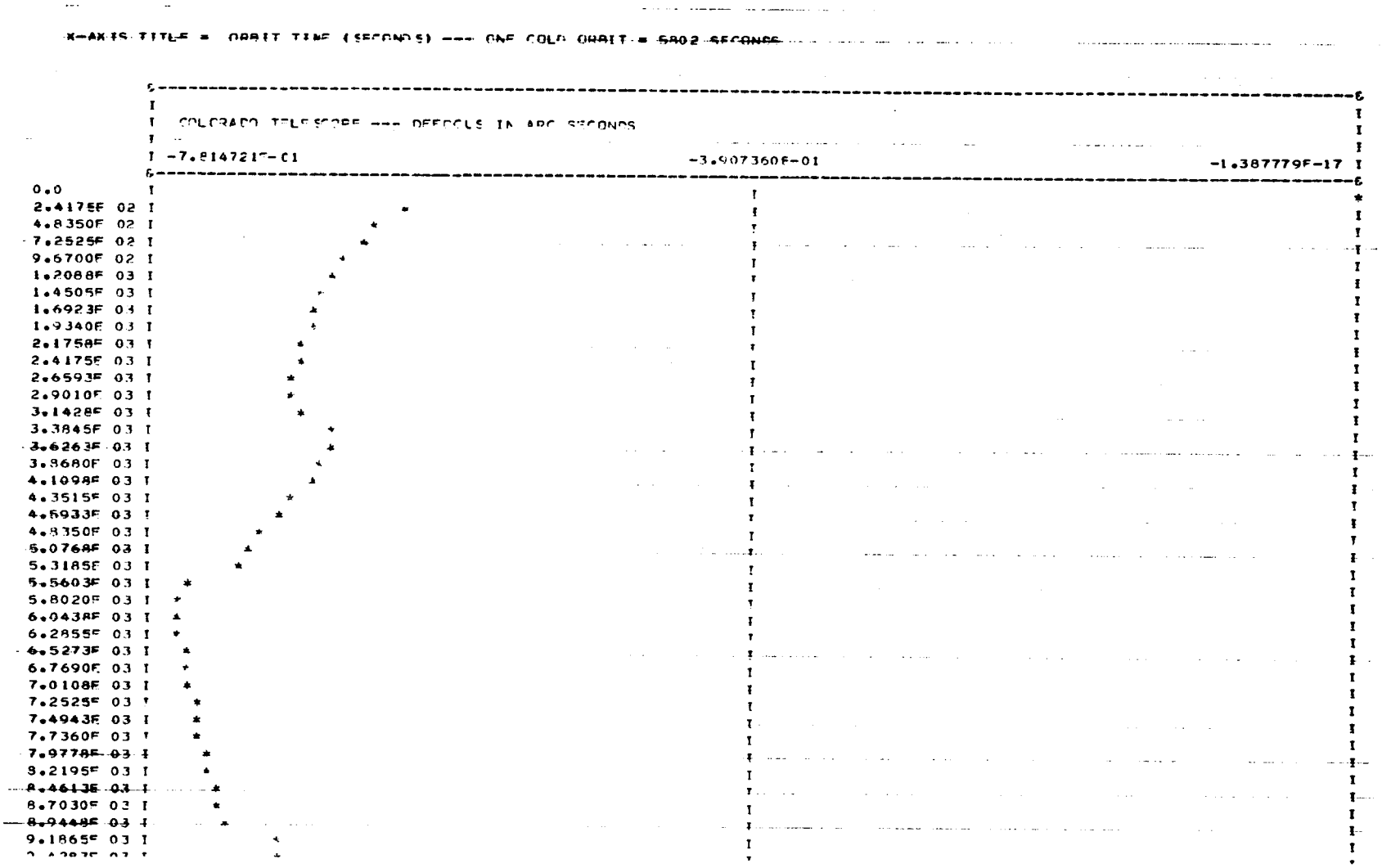

Figure 5. NTA Plot of Defocus (vs) Time for the OSO Telescope

```
TITLE    = IUE EXPERIMENT THERMAL MODEL --- 10/31/74
SUBTITLE = SPACECRAFT, PM AND SM, AND SPACE AS BOUNDARIES
LABEL    = TEST RUN OF THE COMBINATION PROCEDURE

DISPLACEMENTS
REAL OUTPUT
SUBCASE ID =          1
TEMP*                 1          607   -4.821902E 01
TEMP*                 1          608   -3.757886E 01
TEMP*                 1          609   -3.757886E 01

TITLE    = IUE EXPERIMENT THERMAL MODEL --- 10/31/74

SUBTITLE = SPACECRAFT, PM AND SM, AND SPACE AS BOUNDARIES

LABEL    = TEST RUN OF THE COMBINATION PROCEDURE

OLOADS
REAL OUTPUT
SUBCASE ID =          1
      611        S    1.099999E 00     0.0          0.0
-CONT-                 0.0              0.0          0.0
      612        S    8.200000E-01     0.0          0.0
-CONT-                 0.0              0.0          0.0
      613        S    8.200000E-01     0.0          0.0
-CONT-                 0.0              0.0          0.0
     1001        S    1.003368E-01     0.0          0.0
-CONT-                 0.0              0.0          0.0
     1002        S    1.760916E-01     0.0          0.0
-CONT-                 0.0              0.0          0.0
TITLE    = IUE EXPERIMENT THERMAL MODEL --- 10/31/74

SUBTITLE = SPACECRAFT, PM AND SM, AND SPACE AS BOUNDARIES

LABEL    = TEST RUN OF THE COMBINATION PROCEDURE

SPCF
REAL OUTPUT
SUBCASE ID =          1
     6000        S    2.920006E-04     0.0          0.0
-CONT-                 0.0              0.0          0.0
     8091        S   -1.870287E-02     0.0          0.0
-CONT-                 0.0              0.0          0.0
     8092        S   -1.703292E-02     0.0          0.0
-CONT-                 0.0              0.0          0.0
     8093        S   -2.009553E-02     0.0          0.0
-CONT-                 0.0              0.0          0.0
     8094        S   -1.684506E-02     0.0          0.0
-CONT-                 0.0              0.0          0.0
```

Figure 6. Partial IUE Punched Temperature, Thermal Load, and Constraint Force Output

SECONDARY MIRROR AREA

SECONDARY MIRROR=	9.6
SECONDARY MIRROR AXIAL DELTA T=	0.08
FOCUS DRIVE=	-17.3
INNER RING=	-50.7
CENTER OF VANE=	-53.3
OUTER RING=	-53.6
MAXIMUM DELTA T ON OUTER RING=	0.3
MINIMUM BAFFLE=	-50.4
MAXIMUM BAFFLE=	-47.2

PRIMARY MIRROR AREA

PRIMARY MIRROR =	3.8
MAX P.M. RADIAL DELTA T=	0.0560
AVERAGE TANGENT BAR=	3.3
STRONG RING=	-13.8
MAXIMUM DELTA T ON STRONG RING=	1.4
MINIMUM BAFFLE=	-41.3
MAXIMUM BAFFLE=	-18.3
MAIN BAFFLE SUPPORTS=	-14.9

GENERAL

MINIMUM SUNSHADE=	-100.3
MAXIMUM SUNSHADE=	-82.2
AVERAGE SUNSHADE=	-90.6
AVERAGE AXIAL TUBE DELTA T=	39.8
AVERAGE TUBE INCLUDING RINGS=	-32.7
AVERAGE TUBE EXCLUDING RINGS=	-36.8

POWER SUPPLIED

SECONDARY MIRROR=	2.74
PRIMARY MIRROR=	5.00
ISA =	0.00
S/C TO STRONG RING=	5.30
SOLAR INPUT=	4.09

SPECTROGRAPH TEMPERATURES

DUST COVER

THETA	TOP	MID	BOTTOM	BACK
0-120 DEG	-3.3	3.7	5.8	5.2
120-240 DEG	-5.8	2.8	5.5	
240-360 DEG	-2.5	3.6	5.7	
S/C ATTACH B= 0	12.0			
S/C ATTACH B=135	12.0			
S/C ATTACH B=225	12.0			

COMPONENTS

	LWL	SWL	FESS2	FESS1	ECHELLE
1	5.6	5.7	3.1	7.3	4.4
2	3.5	3.0			4.4

SPACECRAFT

0-120 DEG	14.0	14.0	17.0	5.0
120-240 DEG	14.0	5.0	8.0	
240-360 DEG	14.0	14.0	17.0	

DECKS

	APERTURE	ACQUISITION	CAMERA	ECHELLE	COLLIMATOR
AVERAGE TEMPERATURE =	0.8	1.6	2.4	4.7	6.0
MAXIMUM DELTA T =	0.1	7.4	1.5	0.3	0.1

SPECTROGRAPH POWERS

	LWL	SWL	FESS2	FESS1
1	4.48	4.48	0.00	2.50
2	0.00	0.00		

TOTAL SPECTROGRAPH=	11.46
SPACECRAFT TO DUST COVER=	9.97
DUMMY ELEMENT=	-0.21

TOTAL EXPERIMENT ENERGY SUMMARY

WATTS IN	WATTS OUT	PER CENT ERROR	WATTS TO SPACE
0.0	0.0	0.0	33.24

Figure 7. Sample Automatic Post-Processor Summary Report for the IUE SI

THE GSFC NASTRAN THERMAL ANALYZER NEW CAPABILITIES

Hwa-Ping Lee
NASA Goddard Space Flight Center

Robert L. Harder
The MacNeal-Schwendler Corporation

SUMMARY

An overview of four new analysis capabilities, which have been developed and integrated into the GSFC NASTRAN Thermal Analyzer, is given. To broaden the scope of applications, these new additions provide the $\bar{N}$TA users with the following capabilities of: (1) simulating a thermal louver as a means of the passive thermal control, (2) simulating a fluid loop for transporting energy as a means of the active thermal control, (3) condensing a large-sized finite-element model for an efficient transient thermal analysis, and (4) entering multiple boundary condition sets in a single submission for execution in steady-state thermal analyses.

INTRODUCTION

Four new capabilities have been recently developed and integrated into the GSFC NASTRAN Thermal Analyzer ($\bar{N}$TA), which is a finite-element based general-purpose heat transfer computer program in the NASTRAN system (refs. 1, 2, 3). The $\bar{N}$TA was originally designed to analyze a large and complex space-borne telescope optical sub-system (refs. 4, 5). The new additions have broadened the scope of engineering application of the $\bar{N}$TA from component level to system level, so that complete spacecraft, which would generally require passive and/or active thermal controls, can be treated. Also, the manipulative options relating to the operational efficiency of the computer program can become critical when large numbers of elements or grid points are employed in modeling rather than dealing with a problem of a small size. Specifically, the four new capabilities are:

(1) Temperature-dependent emissivity and absorptivity.

(2) One-dimensional thermo-fluid elements.

(3) The condensation of a finite-element thermal model including the non-linear radiative effect.

(4) The entry of multiple boundary condition sets in a single submission for execution.

The purpose of this paper is to provide NASTRAN users with an overview of these new capabilities. Definition, scope, features and limitation of each individual item are given. New elements needed to facilitate functional objectives are introduced. The use of these new elements together with the appropriate solution routines are described. Essential parts of program changes and new elements interfacing with different functional modules in the $\bar{N}$TA are outlined.

TEMPERATURE-DEPENDENT EMISSIVITY AND ABSORPTIVITY

In the Level 15.5 $\bar{N}$TA, the solution algorithm pertaining to the radiative exchanges is limited to the diffuse-gray case. The programming code is, therefore, sufficient to enter a single constant value for the emissivity, ϵ, and the absorptivity, α, of each surface. As a result, the radiation matrix (the module RMG) is symmetric. These program restrictions have been eliminated by this new capability which permits an independent specification of temperature-dependent emissivity $\epsilon(T)$ and absorptivity $\alpha(T)$. The application of this feature is for transient thermal analysis only. A notable engineering application is to simulate a thermal louver as a means of the passive thermal control.

To accommodate temperature-dependent emissivity and absorptivity through the boundary surface element, HBDY, the RMG module would have to be restructured. Such a rigorous approach would result in a prohibitively large effort, and excessively long computer run times would be required for the following reasons:

(1) The matrices which express the radiation properties are generated in the module RMG which is executed early in the program.

(2) If emissivity and absorptivity are temperature-dependent functions, it would be necessary to execute the RMG module and all subsequent modules up to and including the solution module, TRHT, for each time step.

(3) If radiative heat flow was requested in the output, it would be necessary to execute the data recovery modules after each time step, because $\bar{N}$TA does not have the ability to store the separate radiation flux matrices $[Q_{ge}]$ for each time step.

Although less flexible than the rigorous approach, an alternative has been adopted to employ the existing general nonlinear capability of NASTRAN (ref. 6). A nonlinear

element, NOLIN5*, has been newly introduced (ref. 7). It allows the emissivity and the absorptivity to be given independently as tabular functions of the radiating surface temperature.

NOLIN5 differs from other NASTRAN nonlinear load cards in that a large number of grid points may be involved. An area factor A_i is associated with each grid point. For the emitting surface, the convention is adopted that $A_i > 0$. The sum of the area factors of the grid points associated with the emitting surface is one; hence the average temperature T_{av}, of the emitting surface is

$$T_{av} = \sum_i A_i T_i \tag{1}$$

Other grid points, assigned to receive the radiation, are given area factors which are negative and are not included in the calculation of T_{av}. The emissivity $\epsilon(T_{av})$ is given as a tabular function of T_{av} by one of the TABLEDi data cards, as is the absorptivity $\alpha(T_{av})$. The rate at which the radiative heat is treated as a nonlinear load at point i is given by

$$N_i = -S\sigma A_i \epsilon(T_{av})\,(T_{av} + T_{abs})^4 \tag{2}$$

where S and A_i are data items and σ, the Stefan-Boltzmann constant, and T_{abs}, a datum temperature in an absolute scale, are rigid format parameters. The following changes have been made to the program:

IFP	New card NOLIN5.
DPD	Add NOLIN5 to subroutine DPD4.
TRHT	Add parameter TABS, SIGMA; add NOLIN5 to subroutine TRDID.
Rigid Format (SOL 9)	Add parameter to TRHT.

ONE-DIMENSIONAL THERMO-FLUID ELEMENTS

A simple but commonly used energy transporting means is the fluid loop consisting of a flowing fluid inside a tube, which may be made to contact a thermally conductive structure. New elements have been developed and added to the $\bar{N}$TA to allow the effect of an active thermal control to be included in a model.

*The names of actual $\bar{N}$TA cards are capitalized and underlined.

The tube to convey the flowing fluid is modeled using the existing TUBE element with modification that allows a tube of uniform wall thickness to have a constant bore and a linearly tapered geometry as well. The convective heat exchange between the fluid and the tube and any heat transferring from the tube to the surroundings are modeled using HBDY elements as shown in Figure 1. The HBDY element has been modified, as is reflected in the PHBDY data card, to accommodate the linear taper.

The developed thermo-fluid elements are available to both the cases of steady-state and transient thermal analyses. For steady-state analysis, a constant flow rate is specified by the user. A new fluid element FTUBE has been introduced. The unusual feature of this element is that it possesses an asymmetric conduction matrix which is characterized by the fluid phenomenon (ref. 8). This element has created a connection CFTUBE and a property PFTUBE data cards. Element routines are needed for IFP, SMA1, SMA2, SDR2, and OFP. This new fluid element can be used in the nonlinear steady-state solution routine, the rigid format APP HEAT, SOL 3.

For transient analysis, a table, TABLEDi, may be provided by the user with a time-dependent flow rate function. In addition to the FTUBE element, the fluid cylinder is also treated as a nonlinear load. A new nonlinear element NFTUBE has been introduced. Both methods can be used in the transient solution routine, the rigid format APP HEAT, SOL 9. These two approaches, the element method and the nonlinear load method, are equivalent and equally simple to apply as far as the user is concerned.

The following changes have been made to the program for this thermo-fluid capability:

IFP	Modify PTUBE, CHBDY; new CFTUBE, PFTUBE, NFTUBE.
GPTA1	New entries for block data.
SMA1, SMA2	FTUBE routine (asymmetric output); fix HBDY type "FTUBE".
SDR2	Compute convected power in FTUBE
OFP	Output SDR2 results.
DPD	Add NFTUBE to subroutine DPD4
TRHT	Add NFTUBE to subroutine TRD1D.

THE CONDENSATION OF A FINITE-ELEMENT THERMAL MODEL

Condensation is the reduction of the number of temperature variables (or the generalized degrees-of-freedom in the NASTRAN system) used for solution efficiency. The OMIT feature of NASTRAN was designed to provide the model condensation. This feature has been extended to the transient thermal analysis, using the rigid format APP HEAT, SOL 9, to include linear and nonlinear boundary conditions. It is accomplished through matrix transfer and partitioning. The computer code has been modified to allow for asymmetric matrix operations. As a result, the restriction used to limit "a grid point which is OMITted may not touch any nonlinear elements" has been removed.

This feature, however, is not available to the nonlinear steady-state thermal analysis. Since the possible increase of the computer run time expenditure due to the mathematical manipulations would not be justified by the saving that would be realized by a condensed model in the steady-state case.

The program changes made to accommodate this capability have been modifications of MCE2 and SMP1 for asymmetric operations.

THE ENTRY OF MULTIPLE BOUNDARY CONDITION SUBCASES IN ONE EXECUTION

The counterpart of this capability in NASTRAN has been known to its users as the SUBCASE, but this capability was not available to any of the three rigid formats in the $\bar{N}$TA. To loop through several subcases of distinct boundary condition sets is a very desirable feature, especially for a large-sized $\bar{N}$TA model, in which the types of input data card of a problem generally consist of the conduction elements (the connection and property data cards), the boundary surface elements, the material cards, the radiation matrix input cards (RADLST and RADMTX), and different thermal loading cards for specifying boundary conditions. Usually, thermal loadings need only a few cards to describe needed quantities and conditions in steady-state cases, while the rest of cards constitutes the major part of a bulky input deck. This feature has been developed and used to eliminate time-consuming repetitive submissions of bulky input data decks in succession with only changes pertaining to thermal loadings varied from case to case. This multiple entry feature is limited, however, to steady-state thermal analyses using the rigid formats of APP HEAT, SOL 1 and SOL 3. Specifically, a DMAP-ALTER has been added to handle the following loops for

(1) Only thermal loads are changed.

(2) The MPC and SPC constraints are changed.

(3) The boundary surface elements CHBDY are changed.

The required program changes for looping in this rigid format APP HEAT, SOL 3, are summarized as follows:

Write ALTER

Fix to IFP1, PARAML for ALTER.

The DMAP-ALTER packet is shown in Figure 2 for reference.

REFERENCES

1. Lee, H. P., and Mason, J. B.: NASTRAN Thermal Analyzer — A General Purpose Finite-Element Heat Transfer Computer Program. The 2nd NASTRAN User's Colloquium. NASA TMX-2637. Sept. 1972, pp. 443-454.

2. McCormick, C. W.: The NASTRAN User's Manual. NASA SP-222. Washington, D.C., Sept. 1970.

3. Lee, H. P.: NASTRAN Thermal Analyzer — Status, Experience and New Developments. The 4th NASTRAN User's Colloquium. NASA TMX-3278. Sept. 1975, pp. 523-528.

4. Lee, H. P.: Structural-Thermal-Optical-Program (STOP), Paper presented at NASA-GSFC 1970 Science and Technology Review, NASA-Goddard Space Flight Center, Jan. 13-14, 1971; also appears in: Significant Accomplishments in Technology: Goddard Space Flight Center, 1970. NASA SP-295. Washington, D.C., 1972, pp. 36-40.

5. Lee, H. P., and Jackson, C. E., Jr.: Using the NASTRAN Thermal Analyzer to Simulate a Flight Scientific Instrument Package. Proceedings of the 20th Annual Meeting of the Institute of Environmental Sciences, Apr. 1974, pp. 152-158.

6. MacNeal, R. H. (Editor): The NASTRAN Theoretical Manual. NASA SP-221, with Level 15·5 Updates. Washington, D.C., Dec. 1972.

7. Harder, R. L.: Functional Module Mathematical Specifications for the New Capabilities to be Added to the NASTRAN Thermal Analyzer. Report EC-346-1, (under the Contract NAS5-22560). The MacNeal-Schwendler Corporation, Oct. 1975.

8. Lee, H. P.: "On the One-Dimensional Thermo-Fluid Element." NASA-GSFC Test and Evaluation Division, Program STOP-Document, Greenbelt, Maryland, Jan. 1975.

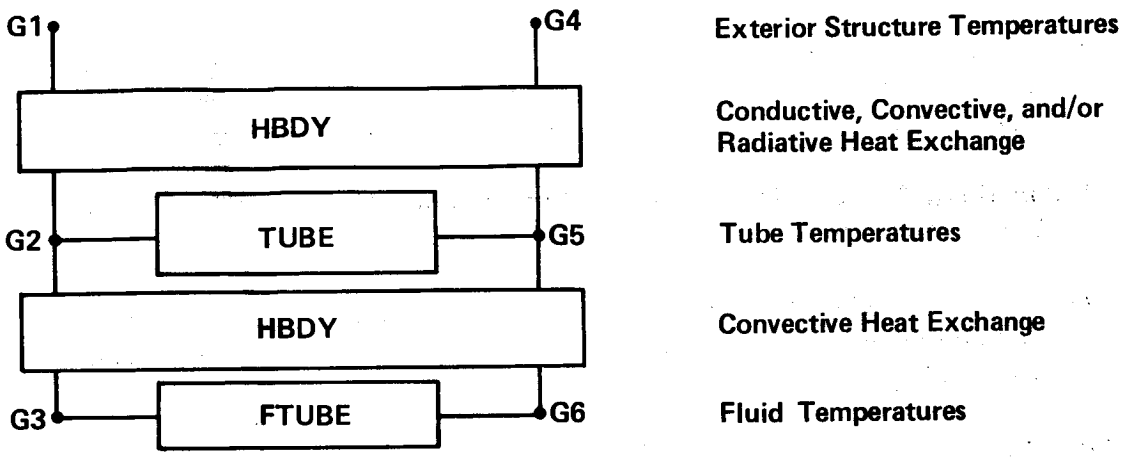

Figure 1. Combination of the $\bar{N}$TA elements to simulate thermo-fluid effects

```
$ THE DMAP-ALTER PACKET TO ALLOW BOUNDARY CONDITION SETS CHANGED IN RF-HEAT,3

$ TO ALLOW TEMP(MATERIAL) TO VARY FROM SUBCASE TO SUBCASE: ALTER 19
$ TO ALLOW SPC OR MPC TO VARY FROM SUBCASE TO SUBCASE: ALTER 31
$ TO ALLOW THERMAL LOAD TO VARY FROM SUBCASE TO SUBCASE: ALTER 58

ALTER 7,7
PLTHBDY  GEOM2,HECT,EPT,HSIL,HEQEXIN,HBGPDT/PECT,PSIL,PEQIN,PBGPDT/
         V,N,NHBDY/V,Y,MESH=NO $
SAVE NHBDY $
EQUIV    HECT,PECT,/NHBDY/HSIL,PSIL/NHBDY/HEQEXIN,PEQIN/NHBDY/HBGPDT,
         PBGPDT/NHBDY $
PLTSET   PCDB,PEQIN,PECT/HPLTSETX,HPLTPAR,HGPSETS,HELSETS/V,N,HNSIL/
         V,N,JUMPPLOT $
ALTER 13,13
PLOT     HPLTPAR,HGPSETS,HELSETS,CASECC,PBGPDT,PEQIN,PSIL,,,,/
         HPLOTX1/HNSIL/HLUSET/JUMPPLOT/V,N,HPLTFLG/V,N,HPFILE $
ALTER 19
SETVAL   //V,N,REPEATT/-1 $
LABEL LOOPTOP
CASE     CASECC,/CASEXX/TRAN/V,N,REPEATT/V,N,NOLOOP $
SAVE REPEATT,NOLOOP $
PARAML   CASEXX//DTI/1/8//V,N,TEMPMATE $
PARAM    //STSR/V,N,TEMPMATE/-10 $
ALTER 32,32
GP4    CASEXX,GEOM4,HEQEXIN,HSIL,HGPDT,,  /HRG,    ,HUSET,/HLUSET/
         V,N,HMPCF1/V,N,HMPCF2/V,N,HSINGLE/V,N,HOMIT/V,N,HREACT/
         0/0/V,N,HNOSET/V,N,HNOL/V,N,HNOA $
ALTER 33,33
SAVE HMPCF1,HMPCF2,HSINGLE,HOMIT,HREACT,HNOSET,HNOL,HNOA $
ALTER 37,37
CHKPNT   HGM,HPS,HKFS,HKSS,HUSET,HRG,HKNN,HRNN,HKSF,HRSN  $
ALTER 54
PARAM    //C,N,ADD/V,Y,KSYM/-1/0  $
ALTER 59,59
SSG1     HSLT,HBGPDT,HCSTM,HSIL,HEST,MPT,HGPTT,EDT,,CASEXX,DIT/HPG/
         HLUSET/1 $
ALTER 63,63
SSG2   HUSET,HGM,,,,,HPG/,,HPS,HPF $
ALTER 74,74
SDR2     CASEXX,HCSTM,MPT,DIT,HEQEXIN,,HGPTT,EDT,HBGPDP,HPG,HQG,
         HUGV,HEST,/HOPG1,HOQG1,HOUGV1,HOES1,HOEF1,HPUGV1/STATICS $
ALTER 81,81
PLTSET   PCDB,HEQEXIN,HECT/PSMES,DPLTPAR,DGPSETS,DELSETS/V,N,DSIL/
         V,N,DJ $
SAVE DSIL $
PLOT     DPLTPAR,DGPSETS,DELSETS,CASEXX,HBGPDP,HEQEXIN,HSIP,HPUGV1,,
         HECPT,HOES1/HPLOTX2/DSIL/HLUSEP/JUMPPLOT/V,N,HPLTFLG/
         V,N,HPFILE $
SAVE HPFILE $
ALTER 83
COND FINIS,REPEATT
REPT LOOPTOP,100
JUMP HERROR3 $

$ END OF DMAP-ALTER (53$48)
```

Figure 2. The DMAP-ALTER packet for the multiple boundary condition subcases in one execution.

REAL EIGENVALUE ANALYSIS IN NASTRAN

BY THE

TRIDIAGONAL REDUCTION (FEER) METHOD

Malcolm Newman and Paul F. Flanagan
Analytical Mechanics Associates, Inc.

and

James L. Rogers, Jr.
NASA Langley Research Center

SUMMARY

Implementation of the Tridiagonal Reduction method in Level 16 of NASTRAN for real eigenvalue extraction in structural vibration and buckling problems is described. The basic concepts underlying the method are summarized and special features, such as the computation of error bounds and default modes of operation are discussed. In addition, the new user information and error messages and optional diagnostic output relating to the Tridiagonal Reduction method are presented.

Some numerical results and initial experiences relating to usage in the NASTRAN environment are provided, including comparisons with other existing NASTRAN eigenvalue methods.

INTRODUCTION

The Tridiagonal Reduction or FEER method is based on an efficient algorithm which extracts eigensolutions in the neighborhood of a specified shift point in the eigenspectrum from a tridiagonal eigenvalue problem of highly reduced order. In essence, the size of the reduced problem is of the same order of magnitude as the number of desired roots, even when the fully discretized system possesses many thousand degrees of freedom. The computational scheme employed is basically a truncated version of the Lanczos Algorithm (ref. 1) as first proposed by Crandall (ref. 2), but its present level of performance derives from a series of improvements and numerical refinement which were started back in the late 1960's by Ojalvo and Newman (ref. 3) and subsequently developed into large-scale computational programs of general utility (refs. 4, 5, and 6).

The Tridiagonal Reduction method employs only a single, initial shift of eigenvalues and hence usually requires only one matrix decomposition. It consequently tends to be much more efficient than the inverse power method when many eigensolutions are required.

The version of the Tridiagonal Reduction method reported on here is the one implemented in Level 16 of NASTRAN for real eigenvalue extraction in structural vibration and buckling problems. The basic concepts underlying the method are summarized only briefly, since a more thorough exposition of the theoretical aspects are available in reference 7. The major emphasis of this paper is directed toward describing the features of this new capability in NASTRAN, outlining user procedures, and reporting on initial experiences relating to its usage in the NASTRAN environment.

PRELIMINARY OPERATIONS

The problem is to find a specified number of real eigenvalues, λ_a, and corresponding eigenvectors, $\{\phi\}$, for

$$[K - \lambda_a M]\{\phi\} = 0 \tag{1}$$

It is further required that these eigensolutions constitute a set lying closest to a specified point, λ_o, in the eigenspectrum.

The definitions of the eigenvalue, the matrices [K] and [M], and their mathematical properties, depend on the type of problem being solved. For real analysis, only two separate problem types need be considered: structural vibration and buckling problems. The matrix definitions and mathematical distinctions for these two cases are summarized in table I.

The essential differences between the two types of problems center around the properties of the [M] matrix, which is nonnegative for vibration mode problems, but indefinite for buckling problems, thereby permitting the existence of both positive and negative eigenvalues in the latter case. In addition, the stiffness matrix may be singular for vibration problems while it is always positive definite in buckling applications, which implies that the buckling analysis is performed on a kinematically stable structure.

Further, if the user requests vibration modes in the neighborhood of a specified frequency, ω_o, equation (1) can be written as

$$[\bar{K}]\{\phi\} = \lambda' \, [M_{aa}]\{\phi\} \tag{2}$$

where

$$[\bar{K}] = [K_{aa} - \omega_o^2 \, M_{aa}] \tag{3a}$$

and

$$\lambda' = \omega^2 - \omega_o^2 \tag{3b}$$

The resulting effective stiffness matrix, $[\bar{K}]$, is indefinite in this case, since it possesses both positive and negative eigenvalues. This requires that

a non-square root decomposition scheme be used in subsequent operations. However, $\omega_o = 0$ is taken as a default value, or it may be specified by the user. In this case, a specified number of natural frequencies starting with the lowest will be computed. In order to utilize a more efficient Cholesky decomposition of $[\bar{K}]$ under these conditions, a small negative shift $\lambda_o = -\alpha^2$ is used yielding

$$[\bar{K}] = [K_{aa} + \alpha^2 M_{aa}] \tag{4a}$$

and

$$\lambda' = \omega^2 + \alpha^2 \tag{4b}$$

The resulting effective stiffness matrix $[\bar{K}]$ is positive definite thereby allowing a square-root decomposition to be performed when the roots are computed in the neighborhood of zero. Since no shifting is performed in buckling problems, the effective stiffness matrix is $[\bar{K}] = [K_{aa}]$, which is always positive definite, again permitting the use of a Cholesky decomposition.

In any event, a decomposition or factoring of $[\bar{K}]$ is next performed:

$$[\bar{K}] = [L][d][L]^T \text{ (shifted vibration mode problems)} \tag{5a}$$

or

$$[\bar{K}] = [C][C]^T \text{ (buckling problems or vibration modes in the neighborhood of zero desired)} \tag{5b}$$

where $[L]$ and $[C]$ are lower triangular factors and $[d]$ is a diagonal matrix.

To facilitate computation of eigenvalues closest to the point of interest within the eigenspectrum, inverse forms of the eigenvalue problems are employed. The general form of the inverse problem may be written as

$$[B][X] = \Lambda[D][X] \tag{6}$$

where the above terms are defined in table II.

THE REDUCTION ALGORITHM

A reduction of the order of the above eigenvalue problem is effected through the transformation

$$\underset{n\times 1}{\{\bar{X}\}} = \underset{n\times m}{[V]} \underset{m\times 1}{\{y\}} \tag{7}$$

where $\{\bar{X}\}$ is an approximation of $\{X\}$, n is the order of the unreduced problem, and $m \leq n$. The transformation matrix is taken to be orthonormal to [D] so that

$$[V]^T [D][V] = [I] \tag{8}$$

From equations (6), (7), and (8) it is seen that

$$[A] \{y\} = \bar{\Lambda}\{y\} \tag{9}$$

where

$$\underset{mxm}{[A]} = [V]^T [B][V] \tag{10}$$

and $\bar{\Lambda}$ is an approximation of the eigenvalue, Λ.

Thus, equation (9) is an $m + n$ order eigenvalue problem where $m \leq n$. The essence of the reduction scheme lies in the choice of the transformation matrix, [V]. In the present case, the Lanczos algorithm is used to build up the [V] matrix, vector by vector, that is,

$$\underset{nxm}{[V]} = [\{v_1\}\{v_2\} \ . \ . \ .\{v_m\}] \tag{11}$$

such that the reduced mxm matrix [A] is tridiagonal and its eigenvalues accurately approximate the roots of the physical model closest to the specified point of interest in the eigenspectrum.

The theoretical recurrence formulas for generation of the columns of the [V] matrix are

$$\left.\begin{aligned} a_{i,i} &= \{v_i\}^T [B]\{v_i\} \\ \{\bar{v}_{i+1}\} &= [D]^{-1} [B]\{v_i\} - a_{i,i}\{v_i\} - d_i\{v_{i-1}\} \\ d_{i+1} &= [\{\bar{v}_{i+1}\}^T [D]\{\bar{v}_{i+1}\}]^{1/2} \end{aligned}\right\} i = 1,m \tag{12a}$$

$$\{v_{i+1}\} = \frac{1}{d_{i+1}} \{\bar{v}_{i+1}\}; \qquad i = 1, m - 1 \tag{12b}$$

where the sequence is initialized by choosing a random starting vector for $\{v_i\}$ and setting $d_i = 0$, $\{v_o\} = \{0\}$. In order to prevent numerical drift in the computations, each vector, $\{v_{i+1}\}$, is reorthogonalized to all previously computed $\{v\}$ - vectors before reentering equation (28a).

Again, the reader is referred to reference 7 for a more complete discussion of the underlying theoretical and numerical details.

The eigenvalues, $\bar{\Lambda}$, and eigenvectors, $\{y\}$ of equation (9) are extracted using a Q - R algorithm and eigenvector computational procedure similar to that employed in the Givens method. They are then converted to physical form as follows:

$$\bar{\lambda}_1 = -\frac{1}{\bar{\Lambda}_i} \text{ (buckling problems)} \tag{13a}$$

$$\bar{\omega}_i^{\,2} = \frac{1}{\bar{\Lambda}_i} - \alpha^2 \text{ (unshifted vibration mode problems)} \tag{13b}$$

$$\bar{\omega}_i^{\,2} = \frac{1}{\bar{\Lambda}_i} + \omega_o^{\,2} \text{ (shifted vibration mode problems)} \tag{13c}$$

$$\{\bar{\phi}_i\} = [C^{-1}]^T\,[V]\{y_i\} \text{ (buckling or unshifted vibration mode problems)} \tag{13d}$$

$$\{\bar{\phi}_i\} = [V]\{y_i\} \text{ (shifted vibration mode problems)} \tag{13e}$$

SIZE CRITERIA FOR THE REDUCED EIGENPROBLEM

The total number of eigensolutions is equal to the rank, r, of the [M] matrix. Thus, the size of the reduced problem, m, cannot be greater than r. If, in addition, f eigensolutions have previously been computed by NASTRAN (modes generated prior to a restart plus rigid body modes generated by using a SUPØRT card in the bulk data deck), these must be swept out of the problem by making all the $\{v\}$ vectors orthogonal to the previously computed eigenvectors. This implies that the maximum size of the reduced problem is further reduced to

$$\bar{r} = r - f \tag{14}$$

As a result of numerical experiments, it has been found that in cases where $m \ll \bar{r}$, a first grouping of more than m/2 eigenvalues closest to the shift point are in accurate agreement with the corresponding number of exact eigenvalues. The remaining reduced-system roots are spread across the remaining exact eigenspectrum.

In view of the above considerations, the order of the reduced problem solved by NASTRAN is

$$m = \min\,[(2\bar{q} + 10),\ \bar{r}] \tag{15a}$$

where

$$\bar{q} = q - f \tag{15b}$$

and q is the total number of eigenvalues requested by the user. The value "10" appearing in equation (15a) is somewhat conservative and was adopted to improve the accuracy of the user-requested eigenvectors, which tend to deteriorate more rapidly than the eigenvalues. However, if the user is not too concerned with the eigenvectors farthest removed from the shift point, he can reduce the problem size and decrease the run time by requesting a smaller value of q on the EIGR or EIGB bulk data card, with the assurance that in almost all cases, at least $\bar{q} + 5$ accurate eigenvalues will be computed by the Tridiagonal Reduction method.

ERROR BOUNDS ON THE COMPUTED EIGENVALUES

The maximum absolute relative errors in the computed physical eigenvalues (see ref. 7) are obtained from

$$\left|1 - \frac{\bar{\lambda}_{ai}}{\lambda_{ai}}\right| \leq \frac{\left|d_{m+1} \cdot y_{mi}\right|}{\left|\bar{\Lambda}_i \left(1 + \lambda_o \bar{\Lambda}_i\right)\right|}; \quad i = 1, m \tag{16}$$

where λ_{ai} is an exact system root, y_{mi} is the last element of the reduced-system eigenvector corresponding to $\bar{\lambda}_{ai}$ and λ_o is the shift point. Thus, it is seen that the eigenvalue errors are all proportional to d_{m+1}, which is the next off-diagonal term that would be generated, had the reduced tridiagonal matrix, [A], been increased from order m to order $m + 1$.

If the physical eigenvalue, $1/\bar{\Lambda}_i + \lambda_o$, corresponds to a rigid body mode, the above computation is invalid and therefore bypassed. A rigid body mode is assumed to occur whenever

$$\left|\frac{1}{\bar{\Lambda}_i} + \lambda_o\right| \leq 10^{-t/3} \tag{17}$$

where t is the number of decimal digits carried by the computer. In this case, the relative error is set to a flat zero.

The eigenvalues are processed in order of increasing distance from the center of range of interest, λ_o, to determine whether their associated error values meet an acceptable tolerance set by the user on the EIGR or EIGB bulk data card (the default value is 0.001/n percent. The first eigenvalue not meeting this tolerance test, as well as all subsequent eigenvalues farther removed from the center of interest, are considered to lack sufficient accuracy and are therefore rejected. Finally, acceptable eigenvalues obtained in the above manner are reordered in terms of increasing physical value for subsequent processing by NASTRAN.

NASTRAN USER'S INSTRUCTIONS

Figures 1 and 2 show modifications of the EIGR and EIGB cards in the NASTRAN bulk data deck which accommodate user implementation of the Tridiagonal Reduction method for real eigenvalue analysis. The modifications are constituted of additions to the standard user instructions and are underscored for ease in identification.

When the Tridiagonal Reduction method is invoked, the F2 or L2 parameter on these cards represents the maximum allowable value of the computed relative error in a physical eigenvalue. If this value is exceeded the associated eigensolution is not accepted for further processing by NASTRAN. A detailed list of the maximum relative errors in the computed eigenvalues can be obtained by requesting DIAG 16 in the NASTRAN Executive Control Deck.

USER MESSAGES AND OPTIONAL DIAGNOSTICS

Functional Module User Messages

The following is a description of the NASTRAN user messages which may be generated by NASTRAN during the execution of the Tridiagonal Reduction method and which are unique to this method. Explanatory information is provided following the text of each message and, in the case of a fatal message, corrective action is indicated. Refer to the NASTRAN Users' Manual, Section 6, for a complete listing of other system and user messages.

Fatal messages cause the termination of the execution following the printing of the message text. These messages will always appear at the end of the NASTRAN output. Warning and information messages will appear at various places in the output stream. Such messages convey only warnings or information to the user. Consequently, the execution continues in a normal manner following the printing of the message text.

Message List

2385*** USER WARNING MESSAGE 2385, DESIRED NUMBER ØF EIGENVALUES EXCEED THE EXISTING NUMBER, ALL EIGENSØLUTIØNS WILL BE SØUGHT.

The desired number of eigenvalues specified on the EIGR card (NEP) or the EIGR card (ND) exceeds the rank of the $[K^d_{aa}]$ or $[M_{aa}]$ matrix, which is the maximum number of existing eigenvalues.

2386*** USER FATAL MESSAGE 2386, STIFFNESS MATRIX SINGULARITY CANNØT BE REMØVED BY SHIFTING.

Check the specification of masses on CØNM1, CØNM2, CMASSi, material definition and element property cards to insure that the degrees of freedom in the analysis set are not all massless.

2387*** USER WARNING MESSAGE 2387, PRØBLEM SIZE REDUCED TØ **** DUE TØ ØRTHØGØNALITY DRIFT ØR NULL TRIAL VECTOR. ALL EXISTING MODES HAVE BEEN ØBTAINED. USE DIAG 16 TØ DETERMINE ERRØR BØUNDS.

The Tridiagonal Reduction method cannot generate a reduced problem size of the order prescribed in Section 10.6.2.3 of the Theoretical Manual. However, the desired number of accurate eigenvalues specified on the EIGB card (NEP) or the EIGR card (ND) may have been obtained. A detailed list of the computed error bounds can be obtained by requesting DIAG 16 in the EXECUTIVE CØNTRØL DECK.

2388*** USER WARNING MESSAGE 2388, USER SPECIFIED RANGE NØT USED FØR FEER BUCKLING, THE RØØTS ØF LØWEST MAGNITUDE ARE ØBTAINED.

The value of L1 specified on the EIGB card is ignored for buckling analysis by the Tridiagonal Reduction (FEER) method.

2389*** USER WARNING MESSAGE 2389, PRØBLEM SIZE REDUCED. NØ MØRE TRIAL VECTØRS CAN BE ØBTAINED.

The desired number of eigenvalues specified on the EIGB card (NEP) or the EIGR card (ND) exceeds the number that can be calculated by the Tridiagonal Reduction (FEER) method. Check whether the requested number of eigenvalues exceeds the rank of the $[K^d_{aa}]$ or $[M_{aa}]$ matrix, which equals the number of existing eigenvalues.

2390*** USER WARNING MESSAGE 2390, **** FEWER ACCURATE EIGENSØLUTIØNS THAN THE **** REQUESTED HAVE BEEN FOUND. USE DIAG 16 TØ DETERMINE ERRØR BØUNDS.

The number of eigenvalues passing the eigenvalue relative-error test is less than the number requested on the EIGB or EIGR card. The maximum allowable error is specified in field 5 on the above cards. A detailed list of the computed error bounds can be obtained by requesting DIAG 16 in the EXECUTIVE CØNTROL DECK. A checkpoint and restart should be employed to obtain additional accurate eigensolutions.

2391*** USER FATAL MESSAGE 2391, PRØGRAM LØGIC ERROR IN FEER.

An unexpected EØF or word count has been encountered.

2392*** USER INFØRMATIØN MESSAGE 2392, **** MØRE ACCURATE EIGENSØLUTIØNS THAN THE **** REQUESTED HAVE BEEN FOUND. USE DIAG 16 TØ DETERMINE ERRØR BØUNDS.

The number of eigenvalues passing the eigenvalue relative-error test is greater than the number requested on the EIGB or EIGR card. The maximum allowable error is specified in field 5 on

the above cards. A detailed list of the computed error bounds can be obtained by requesting DIAG 16 in the EXECUTIVE CØNTRØL DECK.

2393*** USER WARNING MESSAGE 2393, THE REDUCED-SYSTEM EIGENVECTØR CØRRESPØNDING TØ EIGENVALUE **** DØES NØT MEET CØNVERGENCE CRITERIØN. ABSØLUTE RELATIVE ERRØR BETWEEN SUCCESSIVE ITERATES IS ****.

The accuracy of the corresponding physical eigenvector is in doubt. Refer to the Eigenvalue Summary Table for the largest error in the generalized mass matrix.

The Eigenvalue Summary Table

The following summary of the eigenvalue analysis performed is automatically printed when rigid formats using the Tridiagonal Reduction (FEER) method are invoked:

1. The number of eigenvalues extracted.

2. Number of starting points used.

   This corresponds to the total number of random starting and restart vectors used by the FEER process.

3. Number of starting point moves.

   Not used in FEER (set equal to zero).

4. Number of triangular decompositions.

   Always equal to one, except for unshifted vibration problems (roots starting from the lowest requested). In this case, a maximum of three shifts and three decompositions are employed to remove possible stiffness matrix singularities.

5. Total number of vector iterations.

   The total number of reorthogonalizations of all the trial vectors employed.

6. Reason for termination.

   (0) Normal termination.

   (1) Fewer than the requested number of eigenvalues and eigenvectors have been extracted.

(3) The problem size has been reduced. However, the desired number of accurate eigensolutions specified on the EIGB or EIGR card may have been obtained. A detailed list of the computed error bounds can be obtained by requesting DIAG 16 in the EXECUTIVE CØNTRØL DECK.

7. Largest off-diagonal modal mass term and the number failing the mass orthogonality criterion.

Optional Diagnostic Output

The user can obtain special detailed information relating to the generation of the reduced problem size, the elements of the reduced tridiagonal matrix, computed error bounds, and other numerical tests by requesting DIAG 16 in the NASTRAN Executive Control Deck.

The meaning of this information is explained below in the order in which it appears in the DIAG 16 output.

ØRDER - The order of the unreduced problem (size of the $[K_{aa}]$ matrix)

MAX RANK - The maximum number of existing finite eigensolutions as initially detected by FEER

RED ØRDER - The order of the reduced eigenproblem which will be solved to obtain the number of accurate solutions requested by the user

ØRTH VCT - The number of previously computed accurate eigenvectors on the eigenvector file which were generated prior to a restart or by the NASTRAN rigid body mode generator

USER SHIFT - Used only in frequency problems. The user specified shift after conversion from cycles to radians - squared

INTERNAL SHIFT - Used only in frequency problems. A small positive value automatically computed to remove singularities if the user has specified a zero shift. Otherwise, the negative of the user shift

SINGULARITY CHECK - PASS: the shifted stiffness matrix is nonsingular
****: the number of internal shifts needed to remove stiffness matrix singularities

TRIDIAGØNAL ELEMENTS RØW j, **, ***, **** - Lists the computed tridiagonal elements of the reduced eigenmatrix:

j - Matrix row
** - Diagonal element
*** - Off-diagonal element
**** - First estimate of off-diagonal element in the next row

ØRTH ITER - The number of times a reorthogonalization of a trial vector has been performed

MAX PRØJ - The maximum projection of the above trial vector on the previously computed accurate trial vectors (prior to the current reorthogonalization)

NØRMAL FACT - The normalization factor for the reorthogonalized trial vector

ØPEN CØRE NØT USED *** FEER 3 - Open core not used by Subroutine FEER 3, in single-precision words

FEER QRW ELEMENT *, ITER **, ***, RATIO ****, PRØJ *****:

* - The internal eigenvalue number in the order of its extraction by FEER

** - The number of inverse power iterations performed to extract the associated eigenvector of the reduced system (this is not a physical eigenvector)

*** - If a multiple root has been detected, the number of times that the previous multiple-root, reduced-system eigenvectors have been projected out of the current multiple-root eigenvector before repeating the inverse power iterations

**** - The absolute ratio of maximum, reduced-system eigenvector elements for successive inverse power iterations

***** - The maximum projection of a current multiple-root eigenvector on previously computed eigenvectors for the same root

PHYSICAL EIGENVALUE *, **, THEØR ERRØR *** PERCENT, PASS OR FAIL:

* - The internal eigenvalue number in the order of its extraction by FEER

** - The associated physical eigenvalue (λ for buckling problems, ω^2 for frequency problems)

*** - Theoretical upper bound on the relative eigenvalue error, in percent

PASS - The computed error is less than or equal to the allowable specified on the EIGB or EIGR bulk data card (default is 0.001/n percent, where n is the total number of unconstrained degrees of freedom)

FAIL - The computed error is greater than the allowable and this mode is not accepted for further processing

ØPEN CØRE NØT USED *** FEER 4 - Open core not used by Subroutine FEER 4, in single precision words

FEER CØMPLETE *, **, ***, ****

*	- The remaining CPU time available following decomposition of the shifted stiffness matrix, in seconds (the total time is specified on the TIME card in the Executive Control Deck)
**	- The remaining CPU time, in seconds after completing Subroutine FEER 3
***	- The remaining CPU time, in seconds after completing Subroutine FEER 4
****	- The total operation count for FEER after decomposition of the shifted stiffness matrix. One operation is considered to be a multiplication or division followed by an addition

COMPARISON OF FEER WITH EXISTING NASTRAN EIGENVALUE METHODS

The AH1G helicopter three-dimensional built-up dynamic model was chosen for the comparison because it represented a moderately large, "real-world" problem. The order of the stiffness matrix was 1706, while its maximum rank was 1277. In addition, the average number of active columns (CAVG) per pivot row was 81. During the original analysis of the problem, the GIVENS method was used and 30 eigenvectors were found. Therefore, for comparison purposes, 30 eigenvalues were requested in runs 2-6 as shown in table III. The problem size for the GIVENS run, however, was reduced to 241 by using OMIT BULK DATA cards. A series of eight test cases were run. Each case was executed on a CDC 6600 computer in $164K_8$ core (except run 6 which used $230K_8$). The only changes made to the input deck were to the EIGR card. The first six eigenvalues found in each run were the rigid body modes. The timing results for these tests are shown in table III.

In runs 1-3 where OMIT cards were used, the obvious choice is the GIVENS method, since the other two methods require twice as much CPU time and get fewer eigenvalues. FEER reduced the problem order to 58, while the other two methods worked with an order of 241. The 30 eigenvalues found agreed exactly for all three methods, while the 30 eigenvectors from each method agreed to the fourth significant digit. The eigenvectors were all normalized to MAX by the EIGR card.

In runs 4-5 no OMIT cards were used and, therefore, the problem size (1706 degrees of freedom) was too large to use the GIVENS method. FEER showed a significant speed advantage over the INVERSE POWER method. In fact, the INVERSE POWER problem terminated after finding only 22 eigenvalues because of insufficient time to calculate another root and no eigenvectors were obtained. It is therefore reasonable to estimate that FEER (run 4) was at least twice as fast as the INVERSE POWER method (run 5). In each of these runs, since no OMIT

cards were used, no time was spent in modules SMP1 and SMP2. This reduced the total run time. FEER again reduced the problem order to 58, while INVERSE POWER worked on a problem size of 1706. The first 22 eigenvalues found in these two runs agreed to the fifth or sixth significant digit. No eigenvectors were printed for run 5 (INVERSE POWER), thus no comparison was made. The following list shows how the eigenvalues found in run 4 differ from the eigenvalues found in run 1.

Mode No.	Eigenvalues from FEER with no OMITS	Eigenvalues from GIVENS with OMITS
1	0.0	0.0
2	0.0	0.0
3	0.0	0.0
4	0.0	0.0
5	0.0	0.0
6	0.0	0.0
7	3.607787E+02	3.607830E+02
8	4.359254E+02	4.359756E+02
9	1.936684E+03	1.936968E+03
10	2.469448E+03	2.469903E+03
11	7.174892E+03	8.380196E+03
12	8.765565E+03	8.954930E+03
13	1.020949E+04	1.056439E+04
14	1.066561E+04	1.174620E+04
15	1.173722E+04	1.273280E+04
16	1.497434E+04	1.512035E+04
17	1.511484E+04	1.553434E+04
18	1.632569E+04	1.646955E+04
19	1.960200E+04	2.166074E+04
20	2.235550E+04	2.253426E+04
21	2.367533E+04	2.371600E+04
22	2.391382E+04	2.445306E+04
23	2.441746E+04	2.556377E+04
24	2.627131E+04	2.869502E+04
25	2.864655E+04	3.245894E+04
26	3.612023E+04	4.061178E+04
27	4.052112E+04	4.249005E+04
28	4.220211E+04	4.612667E+04
29	4.488473E+04	5.430758E+04
30	4.600289E+04	5.673561E+04

Significant differences can be seen between the two sets of eigenvalues beyond the fourth nonrigid body mode. Similar differences occurred for the eigenvectors. These results indicate that the engineer must seriously consider whether the savings in CPU time achieved by using the Guyan Reduction method (OMITS) are worth the price paid in loss of accuracy or, at best, doubtful accuracy in the results. Run 6 was an additional run using FEER with no OMIT cards, but with the storage increased from $164K_8$ to $230K_8$, to see if the increased core would decrease the run time for a problem of this size. This was not the case. Runs 2, 4, and 6 show that no matter which core size was

used or even whether or not OMIT cards were used, the CPU time in the READ module remains more or less constant.

A final pair of runs (7 and 8) were made to determine the effect of extracting only half (15) of the eigenvalues of the previous runs. For this case, FEER is 65 percent faster than INVERSE POWER and 32 percent faster than the total time for GIVENS with omits in run 1. In run 7, FEER used a reduced order of 30. INVERSE POWER method, however, missed six lower eigenvalues in the frequency range selected (0 to 500 cycles). Comparison of the eigenvectors to those in runs 4 and 5 reveal that the eigenvectors found by INVERSE POWER in run 8 agreed with the eigenvectors of both run 4 and run 5. The first 10 eigenvectors (including the six rigid body modes) found by FEER in run 7 agreed to significant digits with the first 10 eigenvectors found in run 4, after which the eigenvectors in run 7 deteoriated quickly.

CONCLUDING REMARKS

The GIVENS method, using the OMIT feature in NASTRAN, demonstrated the shortest run time for the problem considered but, as shown by the results, the approximations inherent in the Guyan Reduction scheme led to reduced accuracy in the eigensolutions. In fact, only four out of the 24 nonrigid body, eigenvalue modes computed in this manner were of good accuracy. Thus, if the problem contains more than just a few hundred mass degrees of freedom (thereby precluding the use of the GIVENS method without a Guyan Reduction), and the user does not wish to depend on a "judicious" choice of which of these degrees of freedom to omit, then the most reliable course is to omit none of them. In this case, FEER is the obvious choice over the INVERSE POWER method. This conclusion should be tempered somewhat by the fact that the FEER eigenvectors tend to deteriorate in accuracy as the computed modes become more remote from the shift point (center of the desired frequency range). However, it is not expected that this would seriously affect the accuracy of a dynamic response analysis in which there is limited frequency range for the dominant forcing functions.

It should be recognized that the above conclusions and run-time comparisons are only preliminary as of the time this report was written. As indicated by the operation count studies in reference 5, further numerical comparisons should show progressively increasing efficiency of FEER over the INVERSE POWER method as the problem size and matrix bandwidth increase.

REFERENCES

1. Lanczos, C.: An Iteration Method for the Solution of the Eigenvalue Problem of Linear Differential and Integral Operators. J. Res. Nat. Bur. Stand., Vol. 45, 1950, pp. 225-282.

2. Crandall, S. H.: Engineering Analysis. McGraw-Hill, New York, 1956, pp. 106-109.

3. Ojalvo, I. U.; and Newman, M.: Vibration Modes of Large Structures by an Automatic Matrix-Reduction Method. AIAA J., Vol. 8, No. 7, 1970, pp. 1234-1239.

4. Newman, M.; and Pipano, A.: Vibration Modes via Program NEWLAS. Chapter C - Program FEER (Fast Eigenvalue Extraction Routine). IAI TR 4842/6277, June 1971, pp. 7-16.

5. Newman, M.; and Pipano, A.: Fast Modal Extraction in NASTRAN via the FEER Computer Program. NASA TM X-2893, Sept. 1973, pp. 485-506.

6. Ojalvo, I. U.: ALARM - A Highly Efficient Eigenvalue Extraction Routine for Very Large Matrices. Shock and Vibration Digest, Vol. 7, No. 12, Dec. 1975.

7. Newman, M.; and Flanagan, P. F.: Eigenvalue Extraction in NASTRAN by the Tridiagonal Reduction (FEER) Method. NASA CR-2731, Aug. 1976.

TABLE I. PROBLEM FORMULATIONS

Problem type	Quantity	Definition	NASTRAN notation	Most general properties
Structural vibration modes	[K]	Stiffness matrix - analysis set	$[K_{aa}]$	Symmetric, nonnegative, semidefinite matrix
	[M]	Mass matrix - analysis set	$[M_{aa}]$	Same
	λ_a	Square of a circular natural frequency	ω^2	Positive
Buckling	[K]	Stiffness matrix - analysis set	$[K_{aa}]$	Symmetric, positive-definite matrix
	[M]	Differential stiffness matrix - analysis set	$[K^d_{aa}]$	Symmetric, indefinite matrix
	λ_a	Buckling load parameter	$-\lambda$	Positive or negative

TABLE II. INVERSE EIGENPROBLEM DEFINITIONS

	Problem type	[B]	[D]	{X}	Λ
1.	Shifted vibration modes	$[M_{aa}][L^{-1}]^T[d]^{-1}[L^{-1}][M_{aa}]$	$[M_{aa}]$	$\{\phi\}$	$\frac{1}{\omega^2 - \omega_o^2}$
2.	Unshifted vibration modes (in the neghborhood of zero frequency	$[C^{-1}][M_{aa}][C^{-1}]^T$	[I] (identity matrix)	$[C]^T\{\phi\}$	$\frac{1}{\omega^2 + \alpha^2}$
3.	Buckling modes	$[C^{-1}][K^d_{aa}][C^{-1}]^T$	[I]	$[C]^T\{\phi\}$	$-\frac{1}{\lambda}$

TABLE III. COMPARISON OF EIGENVALUE METHODS

Run	Method	OMITS	Number of eigenvalues found	Time in READ module (CPU sec)	Time in SMP1 and SMP2 modules (CPU sec)	Total time in READ, SMP1, and SMP2 modules (CPU sec)
1	GIVENS	Yes	241	495	669	1164
2	FEER	Yes	30	1809	669	2478
3	INVERSE POWER	Yes	30	1994	669	2663
4	FEER	No	30	1837	0	1837
5	INVERSE POWER	No	22	3118	0	3118
6	FEER	No	30	1817	0	1817
7	FEER	No	15	879	0	879
8	INVERSE POWER	No	15	1451	0	1451

Input Data Card EIGR

Description: Defines data needed to perform real eigenvalue analysis.

Format and Example:

EIGR	SID	METHØD	F1	F2	NE	ND	NZ	E	+abc
EIGR	13	DET	1.9	15.6	10	12	0	1.-3	ABC

+abc	NØRM	G	C						
+BC	PØINT	32	4						

Field	Content
SID	Set identification number (Unique integer > 0)
METHØD	Method of eigenvalue extraction, one of the BCD values "INV", "DET", "GIV", "FEER", "UINV", or "UDET".
	INV — Inverse power method, symmetric matrix operations.
	DET — Determinant method, symmetric matrix operations.
	GIV — Givens method of tridiagonalization.
	FEER — Tridiagonal reduction method, symmetric matrix operations.
	UINV — Inverse power method, unsymmetric matrix operations.
	UDET — Determinant method, unsymmetric matrix operations.
F1, F2	Frequency range of interest (Required for METHØD = "DET", "INV", "UDET", or "UINV") (Real ≥ 0.0; F1 < F2). Frequency range over which eigenvectors are desired for METHØD = "GIV". The frequency range is ignored if ND > 0, in which case the eigenvectors for the first ND positive roots are found. (Real F1 < F2). If METHØD = "FEER", F1 is the center of range of interest (Default is F1 = 0.0) (Real ≥ 0.0), and F2 is the acceptable relative error tolerance on frequency-squared, in percent (Default is .001/n where n is the order of the stiffness matrix) (Real > 0.0)
NE	Estimate of number of roots in range (Required for METHØD = "DET", "INV", "UDET", or "UINV", ignored for METHØD = "FEER") (Integer > 0)

Figure 1. Modifications to the EIGR bulk data card for the Tridiagonal Reduction method.

ND — Desired number of roots for METHØD = "DET", "INV", "UDET", or "UINV", (Default is 3 NE) (Integer > 0). Desired number of eigenvectors for METHØD = "GIV" (Default is zero) (Integer ≥ 0). Desired number of roots and eigenvectors for METHØD = "FEER" (Default is automatically calculated to extract at least one accurate mode) (Integer > 0)

NZ — Number of free body modes (Optional - used only if METHØD = "DET" or "UDET") (Integer ≥ 0)

E — Mass orthogonality test parameter (Default is 0.0 which means no test will be made) (Real ≥ 0.0).

NØRM — Method for normalizing eigenvectors, one of the BCD values "MASS", "MAX" or "PØINT"

MASS - Normalize to unit value of the generalized mass

MAX - Normalize to unit value of the largest component in the analysis set

PØINT - Normalize to unit value of the component defined in fields 3 and 4 - defaults to "MAX" if defined component is zero

G — Grid or scalar point identification number (Required if and only if NØRM = "PØINT") (Integer ≥ 0)

C — Component number (One of the integers 1-6) (Required if and only if NØRM = "PØINT" and G is a geometric grid point)

Remarks:

1. Real eigenvalue extraction data sets must be selected in the Case Control Deck (METHØD = SID) to be used by NASTRAN.

2. The units of F1 and F2 are cycles per unit time. If METHØD = "FEER", F2 represents the maximum upper bound, in percent, on $|\omega^2_{FEER}/\omega^2_{EXACT} - 1|$ for acceptance of a computed eigensolution.

3. The continuation card is required.

4. If METHØD = "GIV", all eigenvalues are found.

5. If METHØD = "GIV", the mass matrix for the analysis set must be positive definite. This means that all degrees of freedom, including rotations, must have mass properties. ØMIT cards may be used to remove massless degrees of freedom.

Figure 1. Continued.

6. A nonzero value of E in field 9 also modifies the convergence criteria. See Sections 10.3.6 and 10.4.4.2 of the Theoretical Manual for a discussion of convergence criteria.

7. If NØRM = "MAX," components that are not in the analysis set may have values larger than unit.

8. If NØRM = "PØINT," the selected component must be in the analysis set.

9. If METHØD = "GIV" and rigid body modes are present, F1 should be set to a small negative number rather than zero if the rigid body eigenvectors are desired.

10. The desired number of roots (ND) includes all roots previously found, such as rigid body modes determined with the use of the SUPØRT card, or the number of roots found on the previous run when restarting and APPENDing the eigenvector file.

Figure 1. Concluded.

BULK DATA DECK

Input Data Card EIGB Buckling Analysis Data

Description: Defines data needed to perform buckling analysis.

Format and Example:

1	2	3	4	5	6	7	8	9	10
EIGB	SID	METHØD	L1	L2	NEP	NDP	NDN	E	+abc
EIGB	13	DET	0.1	2.5	2	1	1	0.0	ABC

+abc	NØRM	G	C						
+BC	MAX								

Field	Contents
SID	Set identification number (Unique integer > 0)
METHØD	Method of eigenvalue extraction, one of the BCD values "INV", "DET", "FEER", "UINV", or "UDET" INV - Inverse power method, symmetric matrix operations DET - Determinant method, symmetric matrix operations FEER - Tridiagonal reduction method, symmetric matrix operations UINV - Inverse power method, unsymmetric matrix operations UDET - Determinant method, unsymmetric matrix operations
L1, L2	Eigenvalue range of interest (Real; L1 < L2 > 0.0) For METHØD = "FEER", L1 is ignored and L2 is the acceptable relative error tolerance on eigenvalues, in percent (Default is .001/n where n is the order of the stiffness matrix) (Real > 0.0)
NEP	Estimate of number of roots in positive range. Desired number of eigenvalues of smallest magnitude for METHØD = "FEER" (Default is automatically calculated to extract at lease one accurate mode) (Integer > 0)
NDP, NDN	Desired number of positive and negative roots (Default = 3 NEP) (Integer >0). Ignored for METHØD = "FEER"

Figure 2. Modifications to the EIGB bulk data card for the Tridiagonal Reduction method.

E	Convergence criteria (optional) (Real > 0.0)
NØRM	Method for normalizing eigenvectors, one of the BCD values "MAX" or "PØINT" MAX - Normalize to unit value of the largest component in the analysis set PØINT - Normalize to unit value of the component defined in fields 3 and 4 defaults to "MAX" if defined component is zero
G	Grid or scalar point identification number (Integer > 0) (Required if and only if NØRM = "PØINT")
C	Component number (One of the integers 1-6) (Required if and only if NØRM = "PØINT" and G is a geometric grid point)

Remarks

1. Buckling analysis root extraction data sets must be selected in the Case Control Deck (METHØD = SID) to be used by NASTRAN.

2. The quantities L1 and L2 are dimensionless and specify a range in which the eigenvalues are to be found. An eigenvalue is a factor by which the prebuckling state of stress (first subcase) is multiplied to produce buckling. If METHØD = "FEER", L1 is ignored and L2 represents the maximum upper bound, in percent, on $|\lambda_{FEER}/\lambda_{EXACT} - 1|$ for acceptance of a computed eigensolution.

3. The continuation card is required.

4. See Sections 10.3.6 and 10.4.2.2 of the Theoretical Manual for a discussion of convergence criteria.

5. If METHØD = "DET", L1 must be greater than or equal to 0.0.

6. If NØRM = "MAX", components that are not in the analysis set may have values larger than unity.

7. If NØRM = "PØINT", the selected component must be in the analysis set.

Figure 2. Concluded.

A COMPARISON OF THE TWO NASTRAN DIFFERENTIAL STIFFNESS TECHNIQUES

John R. McDonough
Computer Sciences Corporation

SUMMARY

NASTRAN contains two techniques to solve the differential stiffness problems. One is incorporated in a new static analysis rigid format and the other is contained in a new normal modes analysis rigid format. The purpose of this paper is to compare the two techniques relative to computational accuracy and time of execution on Level 16.0.

INTRODUCTION

Through Level 15.5, the Static Analysis with Differential Stiffness (Rigid Format 4) capability was based on a one-step process (Reference 1). This process was a static solution to obtain the linear stiffness matrix and internal element forces followed by an element differential stiffness computation. This procedure was based on the assumption that the internal force is a linear multiple of the applied load and that the applied load remains fixed in magnitude and direction, moving with its point of application. The user provided differential stiffness linear load factors. An iterative technique was introduced (Reference 2) and is now fully described in Reference 3.

The new approach to solve the differential stiffness problem is begun with the iteration of the displacements to compute the differential stiffness matrix K^d from

$$[K + K^d (u_i)] \{u_{i+1}\} = \{P\} \tag{1}$$

where u_i and u_{i+1} are the set of displacements at two successive iterations, K is a stiffness matrix, and P is a load vector. Rearranging terms, $[K^d (u_i)]$ is removed from the left hand side and is replaced with the term $[K^d (u_e)]$ to give

$$[K + K^d (u_e)] \{u_{i+1}\} = \{P\} + [K^d (u_e) - K^d (u_i)] \{u_i\} \tag{2}$$

or

$$(K + K^d (u_e)] \{u_{i+1}\} = \{P\} + [K^d (u_e - u_i)] \{u_i\} \tag{3}$$

where u_e is an estimate initially equal to the linear elastic solution. With this technique the internal loads may change due to differential stiffness effects so that the solution is not linearly related to the applied load. Thus equation (3) treats the change in differential stiffness as a load correction.

Three PARAMeters are provided to control the iterative process. The first, BETAD, limits the number of load corrections before adjusting the differential stiffness. The second, NT, limits the cummulative number of iterations. Thus load correction iterations can be performed up to the limit BETAD, at which time the differential stiffness is adjusted, and then more load correction iterations are performed and an adjustment is made to a new differential stiffness until NT is exhausted. The third, EPSIØ, is a convergence criteria which terminates the process when successive iterations of the differential stiffness are sufficiently small. Convergence occurs when ε_i < EPSIØ where

$$\varepsilon_i = \frac{|\{u_{i+1}\}^T \{P_{i+1} - P_i\}|}{|\{u_{i+1}\}^T \{P_i\}|} \tag{4}$$

The user either relies on the default values of BETAD=4, NT=10, and EPSIØ=1.0×10^{-5} or prescribes values through a PARAM bulk data card.

Figure 1 is a simplified flow diagram of the procedure. The requirements of the rigid format are that two subcases be used to define the static output requests and the differential stiffness requests. Loads and constraints are defined above the subcase level and plot requests are last in the Case Control Deck.

A new normal Normal Modes Analysis with Differential Stiffness (Rigid Format 13) capability was described (Reference 2) which combines static, differential stiffness, and normal modes analyses.

Presently, this technique is based on the original differential stiffness approach (Reference 1), but is limited to one loop (or load factor) through the Rigid Format.

Figure 2 is a simplified flow diagram of this process. The rigid format is utilized via three subcases. The first pertains to the static analysis where the load is defined, the second prescribes one load factor for differential stiffness, and the third contains a method for a real eigenvalue analysis. Individual output requests can be made at the subcase level and plot requests are last in the Case Control deck.

TEST CASE

The test case used is the standard NASTRAN Demonstration Problem for Rigid Format 4. The structure is a hanging cable acted upon by its own weight, which is an equilibrium position, assumes the shape of a catenary. The original shape of the cable is circular. The final shape of the cable is readily predictable from equations developed in Reference 5.

The coordinates of a point (x,y) on the catenary are defined by

$$x = \frac{H}{w} \sinh^{-1} \left(\frac{ws}{H}\right) \quad , \tag{5}$$

and

$$y = \frac{H}{w} \left[\left(1 + \left(\frac{ws}{H}\right)^2\right)^{1/2} - 1\right] \quad , \tag{6}$$

where H is the tension at the bottom of the catenary, w is the weight per unit length of the cable, and s is the distance along the curve.

The original demonstration problem is in English units and are converted to the Newton-meter system for this discussion. The input data decks are shown in Tables 1 through 5. Notice the alter for Rigid Format 13 necessary to allow multiple load coefficients and plots for the original differential stiffness technique.

RESULTS

Tables 6 and 7 show the deflection results obtained by the two techniques compared to the theoretical expectations. The results computed by Rigid Format 4 were obtained in four iterations when the convergence criteria changed from 4.5×10^{-5} to 4.3×10^{-6}. On the CDC 6600, Functional Module, DSCHK, which performs differential stiffness computations in Rigid Format 4, spent about 2 cpu seconds. Functional Module DSMG1 (used four times) consumed approximately 5 cpu seconds. The results shown for Rigid Format 13 were those obtained after the first load coefficient. (Successive coefficients produced deteriorating answers.) Using Rigid Format 13, Functional Module, DSMG1, used 1.25 cpu seconds and Functional Module, DSMG2, used about one-third of a second.

Figure 3 shows the graphical results of this test.

CONCLUSIONS

For a simple structural element case that can be readily verified, there is no appreciable difference in the results computed. In fact, Rigid Format 13, when using only one differential stiffness coefficient, actually computes the nonlinear solution faster than the Rigid Format 4 counterpart. Thus, the two differential stiffness techniques available in NASTRAN can be utilized equally well depending upon the user's preference.

REFERENCES

1. The NASTRAN Theoretical Manual, NASA SP-221(01), December, 1972, Section 7.1.

2. McDonough, John R., "A Survey of NASTRAN Improvements Since Level 15.5", NASTRAN Users' Experiences, NASA TM X-3278, September, 1975, pp. 11-22.

3. The NASTRAN Theoretical Manual, NASA SP-221(03), March, 1976, Section 7.1.

4. The NASTRAN Demonstration Problem Manual, NASA SP-224(03), March, 1976, Section 4.

5. Spiegel, Murray R., Applied Differential Equations, Prentice-Hall, Inc., 1958, pp. 105-108.

Table 1. Executive Control Deck for Rigid Format 4.

```
ID        DIFFSTIF,RF4
APP       DISPLACEMENT
SOL       4,0
TIME      10
CEND
```

Table 2. Executive Control Deck for Rigid Format 13.

```
ID        DIFFSTIF,RF13
$ REQUIRED ALTER TO CORRECT AN ERROR IN THE RIGID FORMAT
ALTER 29 $
PARAM    //C,N,ADD/V,N,NOMGG/C,N,1/C,N,0 $
$ ALTERS TO CHANGE THE RIGID FORMAT FOR MULTIPLE D. S. FACTORS
ALTER   139 $
JUMP    DSLOOP $
LABEL    DSLOOP $
ALTER    155 $
COND    LBL8D,REPEATD $
REPT    DSLOOP,10 $
PARAM    //C,N,NOT/V,N,TEST/V,N,REPEAT $
LABEL    LBL8D $
ALTER    158, 174 $
ALTER    176, 176 $
PLOT      PLTPAR,GPSETS,ELSETS,CASECC,BGPDT,EQEXIN,SIL,,PUBGV1,GPECT,
          DESB1/PLOTX3/V,N,NSIL/V,N,LUSET/V,N,JUMPPLOT/V,N,PLTFLG/
          V,N,PFILE $
ALTER    187, 188 $
ENDALTER $
APP       DISPLACEMENT
SOL       13,0
TIME      10
CEND
```

Table 3. Case Control Deck for Rigid Format 4.

```
TITLE = DIFFERENTIAL STIFFNESS ANALYSIS FOR A HANGING CABLE
SUBTITLE = RIGID FORMAT 4 SOLUTION
LABEL = INITIAL SHAPE IS A CIRCLE, FINAL SHAPE IS A CATENARY
LOAD = 32
SPC = 2
DISPLACEMENT = ALL
SPCFORCE = ALL
STRESS = ALL
FORCE = ALL
OLOAD = ALL
SUBCASE 1
LABEL = LINEAR SOLUTION
SUBCASE 2
LABEL = NONLINEAR SOLUTION
BEGIN BULK
```

Table 4. Case Control Deck for Rigid Format 13.

```
TITLE = DIFFERENTIAL STIFFNESS ANALYSIS FOR A HANGING CABLE
SUBTITLE = RIGID FORMAT 13 SOLUTION
LABEL = INITIAL SHAPE IS A CIRCLE, FINAL SHAPE IS A CATENARY
SPC = 2
DISPLACEMENT = ALL
SPCFORCE = ALL
STRESS = ALL
FORCE = ALL
SUBCASE 1
LABEL = LINEAR SOLUTION
LOAD = 32
OLOAD = ALL
SUBCASE 2
LABEL = NONLINEAR SOLUTION
DSCOEFFICIENT = 50
BEGIN BULK
```

Table 5. Bulk Data Deck

```
$ GEOMETRY IN CYLINDRICAL SYSTEM MEASURED IN METERS
$
CORD2C  10      0       0.0     0.0     0.0     0.0     0.0     1.0     +COORD
+COORD  1.0     0.0     0.0
GRID    10              3.048   0.0                                     TOP
GRID    11              3.048   10.0
GRID    12              3.048   20.0
GRID    13              3.048   30.0
GRID    14              3.048   40.0
GRID    15              3.048   50.0
GRID    16              3.048   60.0
GRID    17              3.048   70.0
GRID    18              3.048   80.0
GRID    19              3.048   90.0                                    BOTTOM
$
$ CONNECTIONS VIA BARS
$
BAROR                                   -1.2    1.0     0.0     1
CBAR    10      10      10      11                                      TOP
CBAR    11      10      11      12
CBAR    12      10      12      13
CBAR    13      10      13      14
CBAR    14      10      14      15
CBAR    15      10      15      16
CBAR    16      10      16      17
CBAR    17      10      17      18
CBAR    18      10      18      19                                      BOTTOM
$
$ GRAVITY LOAD FOR NEWTON-METER SYSTEM
$
GRAV    32      0       9.8     0.0     1.0     0.0
$
$ CONSTRAINTS
GRDSET                                          0       345
SPC     2       10      12      0.0     19      1       0.0
$
$ MATERIAL AND PROPERTY DEFINITIONS
$
MAT1    1       2.63+7          .3      1.78-2
PBAR    10      1       9.29-3  6.87-6  6.87-6
$
$ DIFFERENTIAL STIFFNESS PARAMETERS FOR RF4
$
PARAM   BETAD   8                                                       RF4
PARAM   EPSIO   1.0-5                                                   RF4
PARAM   NT      18                                                      RF4
$
$ DIFFERENTIAL STIFFNESS COEFFICIENTS FOR RF13
$
DSFACT  50      1.0     2.0     3.0     4.0     5.0                     RF13
$
ENDDATA
```

Table 6. Horizontal Deflections

Grid Point	s	Ux - Horizontal		
		Theory	NASTRAN RF4	NASTRAN RF13
11 (10°)	4.25	-0.1480	-0.1445	-0.1441
13 (30°)	3.19	-0.2452	-0.2337	-0.2325
15 (50°)	2.12	-0.1577	-0.1406	-0.1394
17 (70°)	1.06	-0.0338	-0.0267	-0.0264
19 (90°)	0.0	0.0	0.0	0.0

Table 7. Vertical Deflections

Grid Point	s	Uy - Vertical		
		Theory	NASTRAN RF4	NASTRAN RF13
11 (10°)	4.25	-0.00341	-0.01245	-0.01241
13 (30°)	3.19	-0.00696	-0.03865	-0.03432
15 (50°)	2.12	0.000914	0.04478	0.09006
17 (70°)	1.06	0.1737	0.2430	0.2418
19 (90°)	0.0	0.2846	0.3707	0.3679

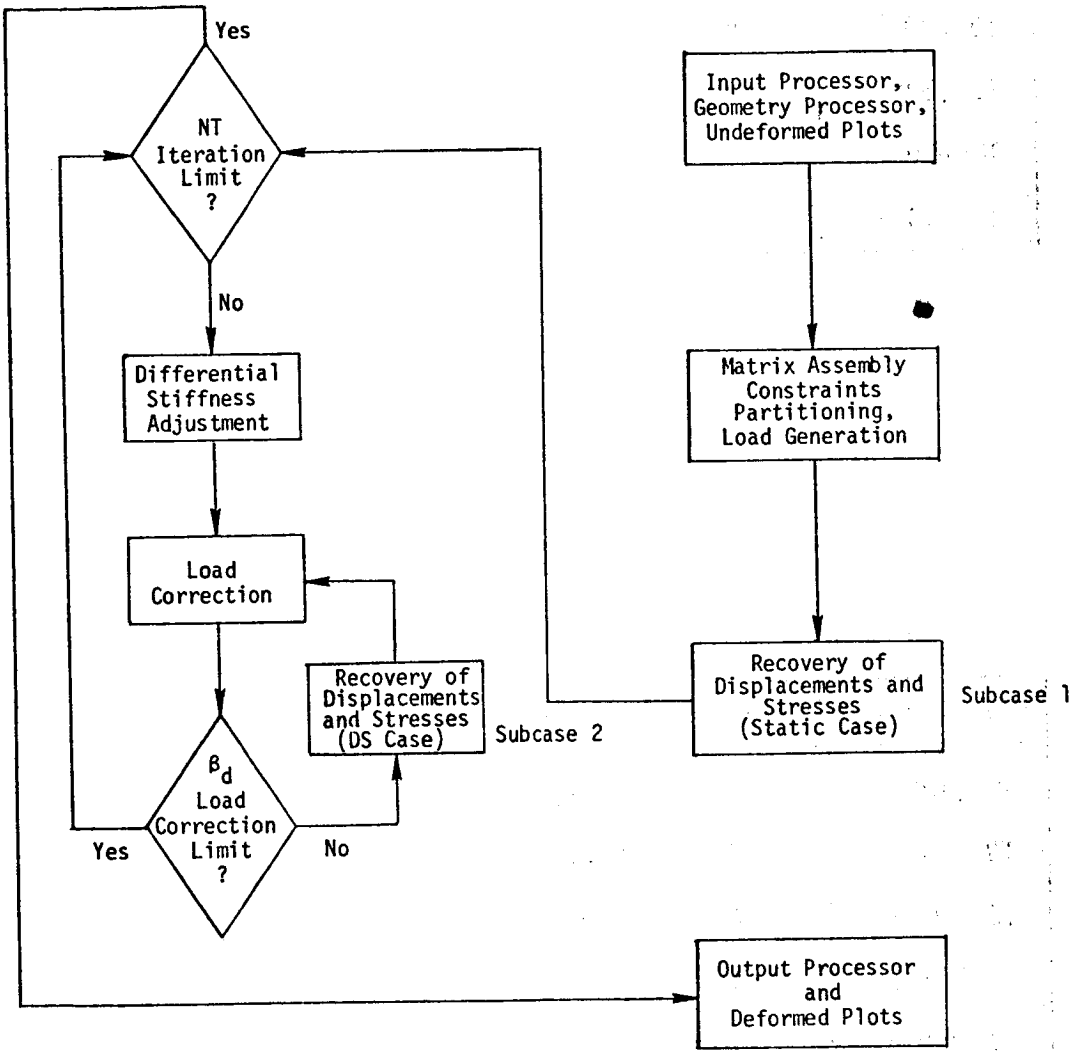

Figure 1. Simplified flow diagram of Rigid Format 4 procedure.

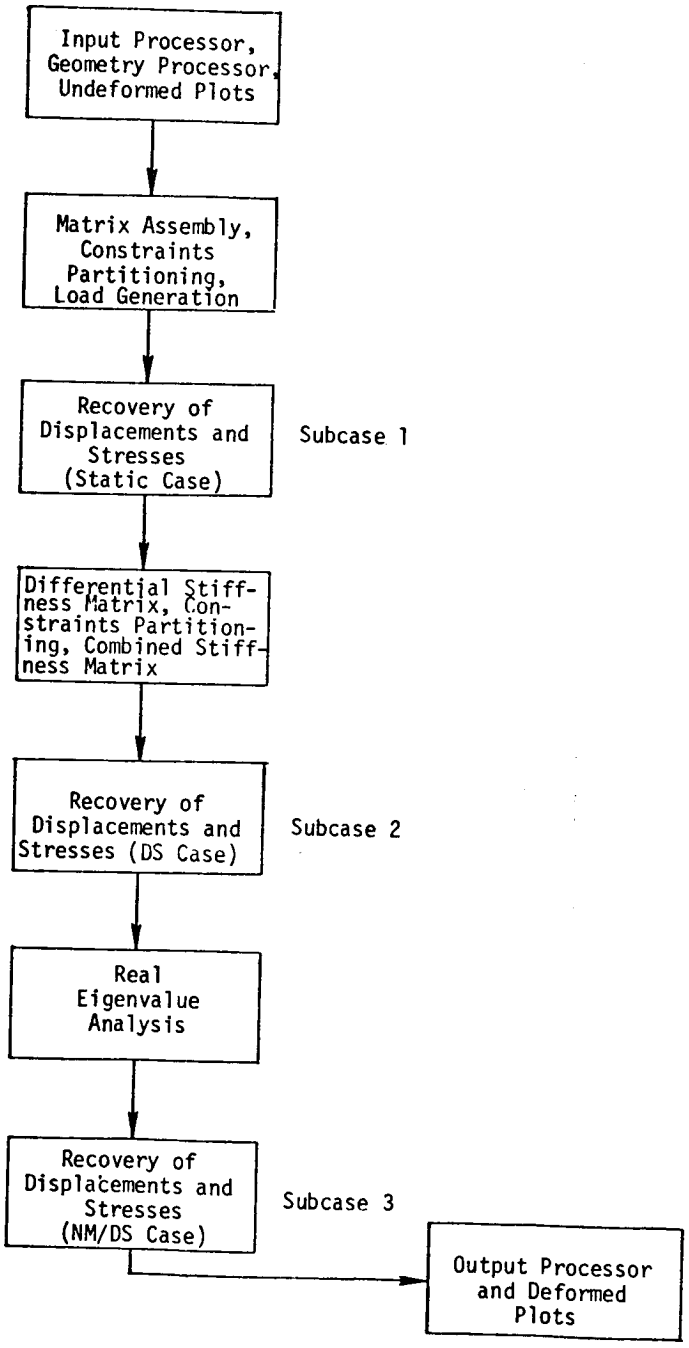

Figure 2. Simplified flow diagram of Rigid Format 13 procedure.

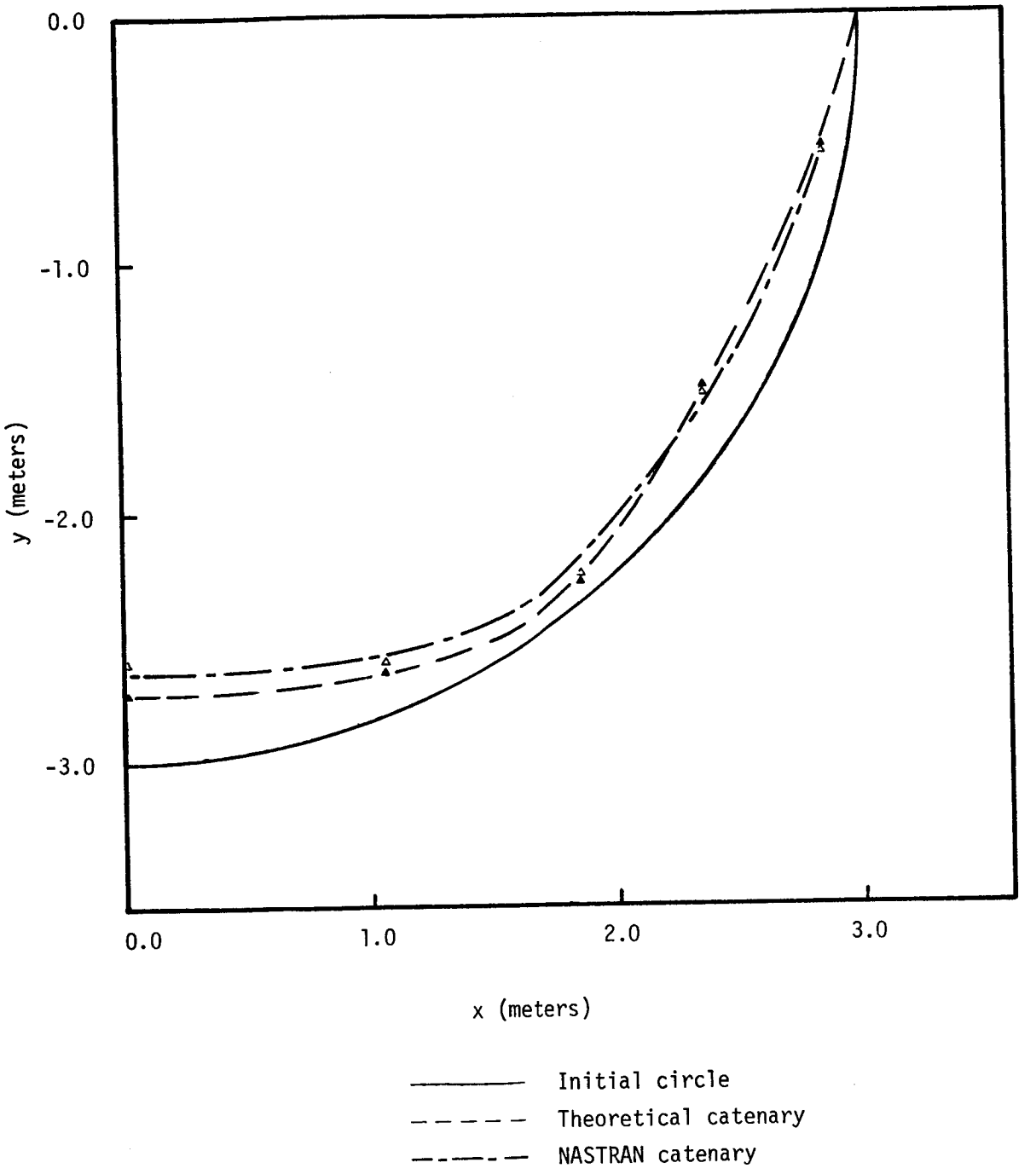

Figure 3. Hanging Cable Test.

DEFORMATIONS OF THICK TWO-MATERIAL CYLINDER UNDER AXIALLY VARYING RADIAL PRESSURE

Yakub A. Patel
Sargent & Lundy

SUMMARY

Stresses and deformations in thick, short, composite cylinder subjected to axially varying radial pressure are studied. Effect of slippage at the interface is examined. In the NASTRAN finite element model, multipoint constraint feature is utilized. Results are compared with theoretical analysis and SAP-IV computer code. Results from NASTRAN computer code are in good agreement with the analytical solutions. Results suggest a considerable influence of interfacial slippage on the axial bending stresses in the cylinder.

INTRODUCTION

The analysis of composite (multilayered) cylinders and other axisymmetric bodies with shrink (or press) fit forms an extremely useful class of problem in the design of pressure vessels and various machine components. For example, Figure 1 illustrates a special slipping pipe anchor (Ref. 1) consisting of the clamped (or press fit) support. Figure 2 illustrates a typical bar drawing die composed of an outer hardened steel cylinder press fitted on the inner carbide insert. The loading, in both cases, on the inside surface of the cylinder is variable axial pressure dependent on the seismic motions (Fig. 1) and percentage reductions (Fig. 2) respectively. This paper attempts to present the problem in a generalized way and indicates, in quantitative terms, the effect of interfacial slippage on the various stress components.

SYMBOLS

E Young's modulus of elasticity, MPa

ν Poisson's ratio (Note: Suffix 1 refers to inner cylinder and 2 refers to outer cylinder)

u_r Radial displacements, cm.

u_z Axial displacements, cm.

L Length of the cylinder, cm.

Z	Axial coordinate
y,r	Radial coordinate
P	Internal pressure, MPa
k	Scale factor for pressure
σ_{zz}	Axial bending stress, MPa
$\sigma_{\theta\theta}$	Hoop stress, MPa
σ_{rr}	Radial stress, MPa
a	Inside radius, cm.
b	Interface radius, cm.
c	Outside radius, cm.

$$A_1 = (a^2b^2)/(b^2-a^2)$$

$$A_2 = b^2c^2/(c^2-b^2)$$

$$B_1 = (b^2+a^2)/(b^2-a^2)$$

$$B_2 = c^2+b^2/(c^2-b^2)$$

$$C_1 = A_1/2(1-\nu_1)$$

$$N_1 = B_1/(1+\nu_1)16$$

$$M_1 = (a^2+b^2)N_1 + \frac{A_1C_1}{a^2}\ln\frac{b}{a}$$

M_c = Residual moment for inner cylinder

$$\alpha_1 = \frac{1+\nu_1}{E_1}\left[-\frac{1}{2}\left(\frac{1-\nu_1}{1+\nu_1}\right)B_1b-\frac{A_1}{b}\right]$$

$$\alpha_2 = \frac{1+\nu_1}{E_1}\left[-\frac{1}{2}\left(\frac{1-\nu_1}{1+\nu_1}\right)b\right]$$

$$\alpha_5 = \frac{1+\nu_2}{E_2}\left[-\frac{1}{2}\left(\frac{1-\nu_2}{1+\nu_2}\right)B_2b-\frac{A_2}{b}\right]$$

$$\alpha_6 = \frac{1+\nu_2}{E_2}\left[-\frac{1}{2}\left(\frac{1-\nu_2}{1+\nu_2}\right)b\right]$$

ANALYTICAL MODELS

Figure 3 shows the NASTRAN (Ref. 2) finite element model of the composite cylinder. The inner cylinder is of carbide and the outer cylinder is of steel. The model consists of 210 nodes and 168 axisymmetric trapezoidal ring (CTRAPRG) elements. Dimensions and material properties are typical of a bar drawing die used in actual steel drawing process.

The loading consists of an axially varying radial pressure defined by the equation $P = k(Lz - z^2)$. This pressure was input as discrete load on the inside surface using the 'FORCE' card of NASTRAN.

Nodes 91 through 120 are nodes along the interface of the carbide and steel. This interface needs special consideration in the finite element model. In practice, the case is shrinkfitted on the carbide insert, and a large amount of compressive preloading is generated in the relatively brittle carbide insert. This compressive preloading reduces the probability of cracking of the insert during operation.

Since there is no welding (or permanent connection) along the interface, during nonuniform loading, slippage will occur along the mating surfaces. At the interface, compatibility of the radial displacement provides:

$$u_r \Big)_{carbide} = u_r \Big)_{steel} \quad \text{for} \quad 0 \leq Z \leq L$$

The axial displacement could vary depending on the amount of slippage. Thus

$$u_z \Big)_{carbide} \neq u_z \Big)_{steel}$$

NASTRAN (Ref. 3) has a very useful option available through the MPC command. It defines the multipoint constraint of the form:

$\sum_j A_j u_j = 0$ where A_j's are the real coefficients and u_j are the nodal displacements.

Using this option, the present analysis was carried out on NASTRAN level 15.5 through the UCC 1108 System.

Figure 4 shows the finite element model for the SAP-IV computer code (Ref. 4). This model is similar to the NASTRAN model - however, no slippage can be allowed along the interface. Due to this, the compatibility of deformation along the interface does not represent the actual deformation mode.

THEORETICAL ANALYSIS

A theoretical analysis of this problem is carried out by the author*. In this analysis, the governing equations of three dimension elasticity are

*Being published as a separate paper.

satisfied on the curved surfaces using the series approach of Lee (Ref. 3). The residual elasticity problem is then solved to partially satisfy the boundary conditions on the ends of the cylinder. The compatibility of displacements along the interface is included in such a manner that axial slip is allowed during deformation. The resultant stress components derived are as follows:

$$\sigma_{zz}\Big|_{carbide} = (-2k_1 + 2k)\left[4N_1 r^2 + (C_1 - 2M_1) + 2C_1 \ln \frac{r}{a}\right]$$

$$- \frac{(2k_1 - 2k)}{8(1+\nu_1)}\left[2r^2 - (a^2 + b^2)\right] + \frac{12}{(b-a)^3}\left(\frac{a+b}{2} - r\right)M_c$$

$$\sigma_{\theta\theta} = (k_1 - k)(Lz - z^2)\left[-\frac{B_1}{2} - \frac{A_1}{r^2}\right] - \frac{1}{2}\left[(k_1 + k)(Lz - z^2)\right]$$

$$+\nu_1\left\{(-2k_1 + 2k)\left[3N_1 r^2 + (C_1 - M_1)(M_1 - a^2 N_1)\frac{a^2}{r^2} + C_1 \ln \frac{r}{a}\right]\right.$$

$$\left. - \frac{2k_1 + 2k}{16(1+\nu_1)}\left[3r^2 - (a^2 + b^2) - \frac{a^2 b^2}{r^2}\right]\right\} + \frac{u_c}{r} E_1 + \nu_1 \sigma_{zz}^{R}$$

$$\sigma_{rr} = \left[(k_1 - k)(Lz - z^2)\right]\left[-\frac{B_1}{2} + \frac{A_1}{r^2}\right] - \frac{1}{2}\left[(k_1 + k)(Lz - z^2)\right]$$

$$+\nu_1\left\{(-2k_1 + 2k)\left[N_1 r^2 - M_1 + (M_1 - a^2 N_1)\frac{a^2}{r^2}\right.\right.$$

$$\left.\left. + C_1 \ln \frac{r}{a}\right] - \frac{2k_1 + 2k}{16(1+\nu_1)}\left[r^2 - (a^2 + b^2) + \frac{a^2 b^2}{r^2}\right]\right\}$$

where: $$k_1 = \frac{k(\alpha_1 - \alpha_2)}{\alpha_1 + \alpha_2 + \alpha_5 - \alpha_6}$$

RESULTS AND DISCUSSIONS

Fig. 5 shows the variation of axial stresses (σ_{zz}) at r = a,b along the length of the inner cylinder. The axial stresses reach their maximum value at the center of the cylinder and the variation is symmetrical about Z = L/2 due to the symmetry of the loading. The results from the NASTRAN model are in good agreement with the analytical solution. Further, it may be noted that the results are in better agreement on the inside surface than the outside surface of inner cylinder - the maximum deviations are 2.8% and 8% respectively. This is due to the fact that the inner surface is farther away from the slipping interface thereby less sensitive to the boundary effects.

Variations of the hoop stresses (Figure 6), radial stresses (Fig. 7) and deflections (Fig. 8-9) also indicate good agreement between the analysis and NASTRAN model. At the interface, in Fig. 7, the radial stresses on the outside surface of carbide and inner surface of steel are identical from the analytical solution. In Figure 9, the length is twice the value given in Fig. 3 while the remaining dimensions are the same as Fig. 3.

The effect of slippage at the interface, in quantitative terms, is demonstrated by the values of stresses from SAP IV, NASTRAN and the analytical solution (Table 1). As is indicated by this table, the effect is more pronounced in the values of σ_{zz} - since the slippage makes the bending process more symmetrical.

CONCLUDING REMARKS

The stresses and deformations in composite cylinder subjected to axially varying radial pressure are examined using the NASTRAN finite element models. The MPC feature of NASTRAN is very useful in simulating accurately the slipping interface between carbide and steel. Results from the NASTRAN finite element models and the analytical solutions are found to be in good agreement.

TABLE 1

Stresses in Carbide (Inner) Cylinder (Units: MPa)

Description	Analytical Solution	NASTRAN F.E. Model	SAP IV F.E. Model
At radius = 5.08 cm.			
σ_{zz}	-124.6	-121.0	-136.2
$\sigma_{\theta\theta}$	362.3	366.2	355.0
σ_{rr}	-223.4	-221.8	-220.6
At radius = 6.99 cm.			
σ_{zz}	110.93	102.0	26.2 (Regular) 87.5 (Modified*)
$\sigma_{\theta\theta}$	279.7	275.2	279.2
σ_{rr}	-69.9	-74.4	-72.4

(*Modified using, in steel at interface, one layer of a material having low modulus of elasticity in z direction)

REFERENCES

1. Patel, Y. A.; Cho, F. L.; Dimopoulos, A. P.: Slipping Pipe Anchor - A Novel Design for Piping in High Seismic Intensity Zones - ASME Paper 75-PVP-58, ASME Conf. on Pressure Vessels and Piping, June 1975.

2. C. W. McCormick (Edit.) - The NASTRAN User's Manual - NASA SP-222(01) - National Aeronautics and Space Administration, June 1972.

3. Lee, C. W.: A Theory of Thick Walled Cylinder Under Axisymmetric Loading - Proceedings of the Fourth U. S. National Congress of Applied Mechanics, (ASME) N.Y., 1962, p. 662.

4. Bath, K. J.; Wilson, E. L. and Peterson, F. E.: SAP-IV - A Structural Analysis Program for Static and Dynamic Response of Linear Systems. EERC Report 73-11, University of Calif., Berkeley, June 1973.

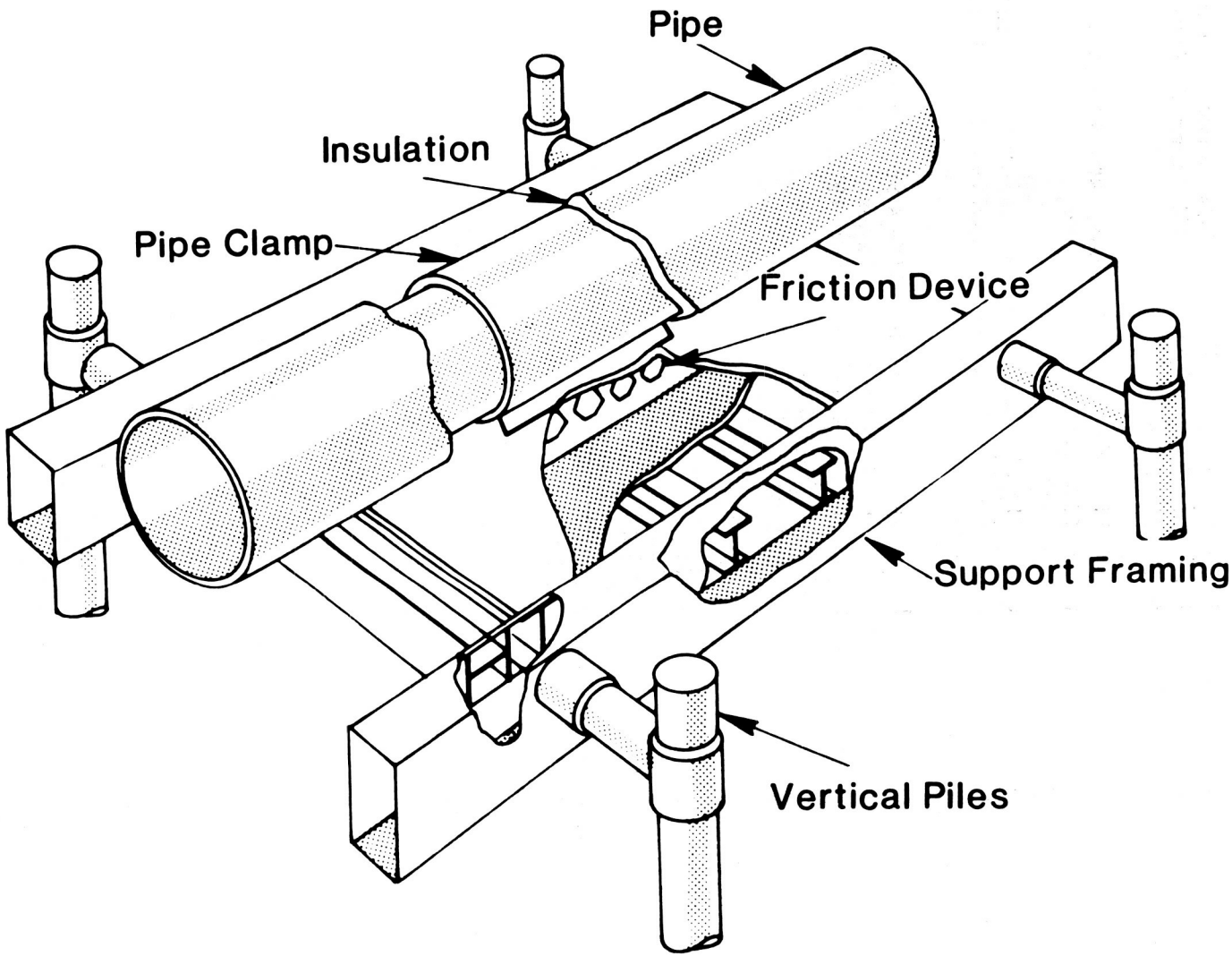

Fig. 1 Slipping pipe anchor.

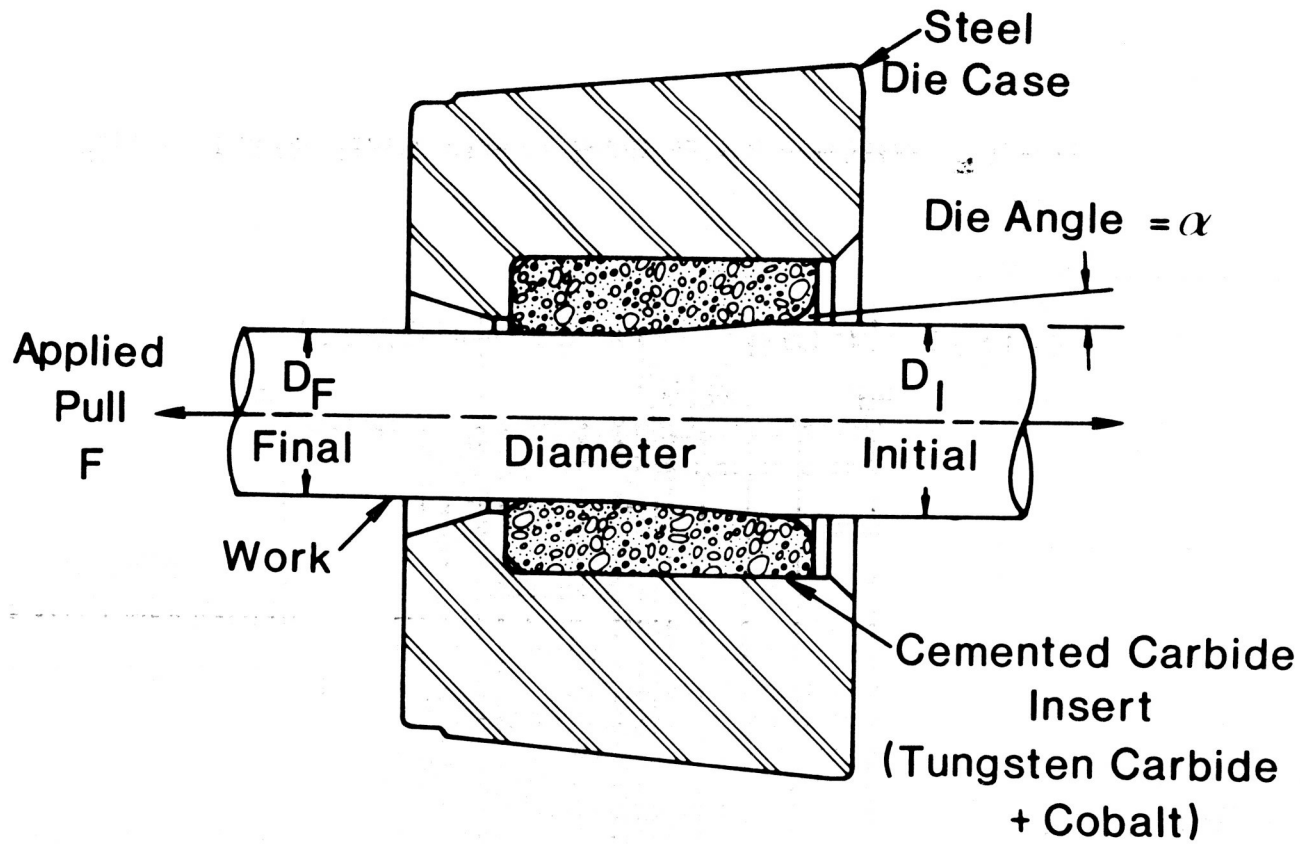

Fig. 2 Section of a typical draw die and workpiece.

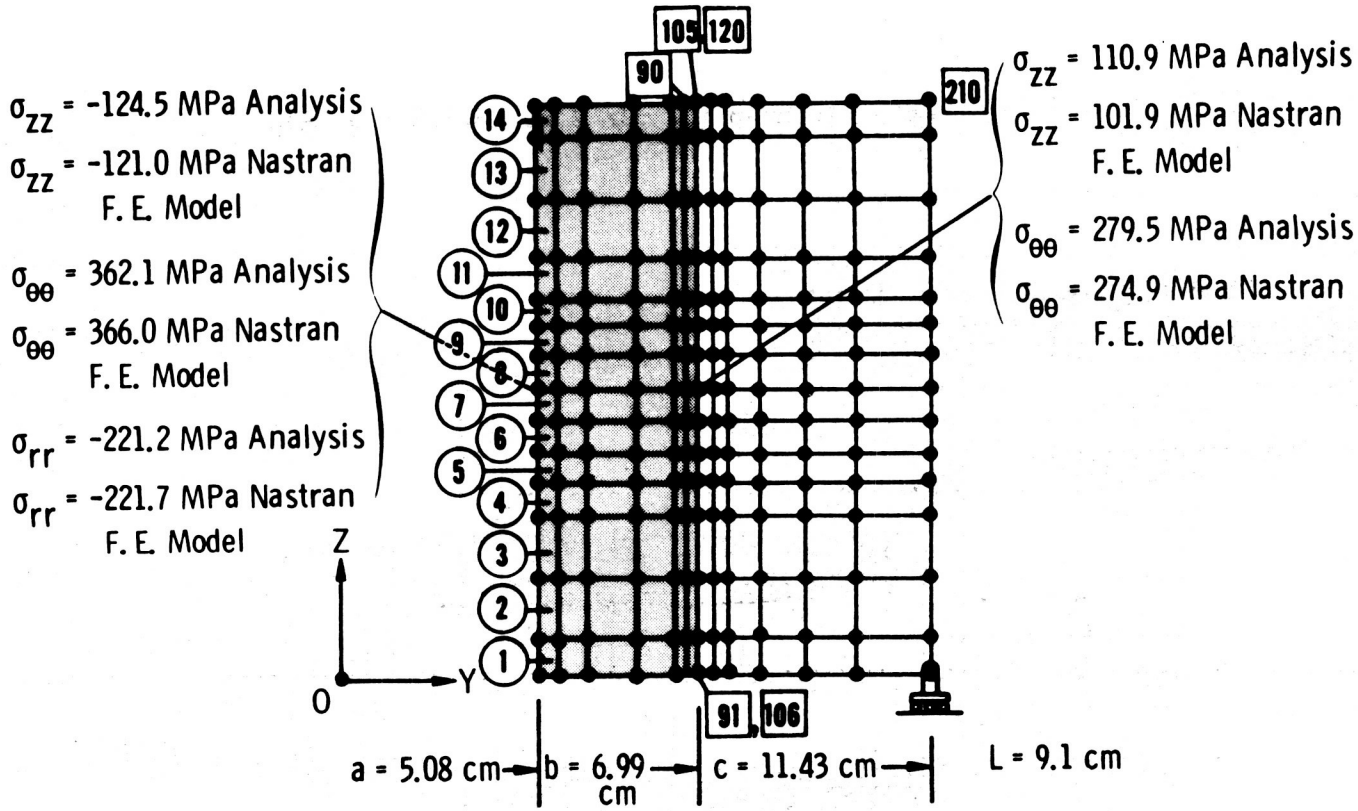

Fig. 3 Nastran finite element model of the composite cylinder.

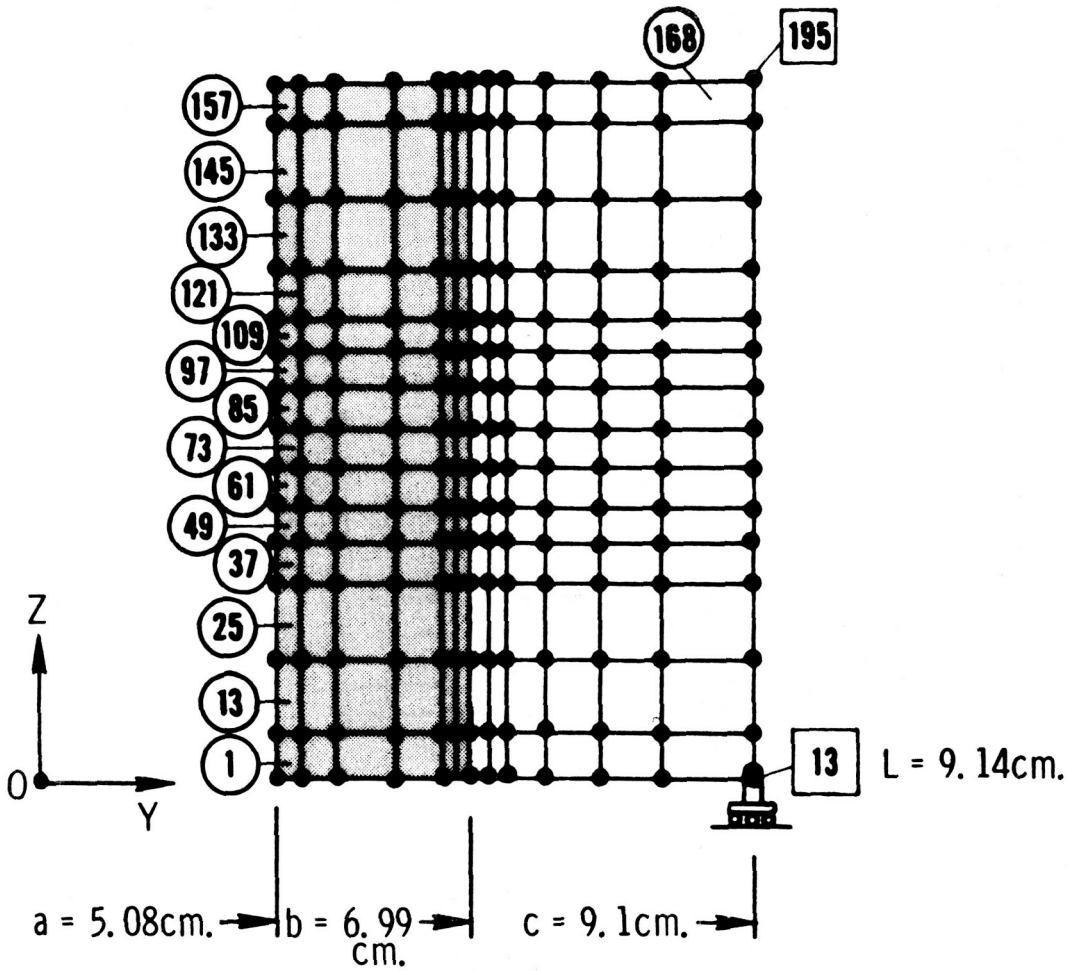

Fig. 4 SAP IV finite element model of the composite cylinder.

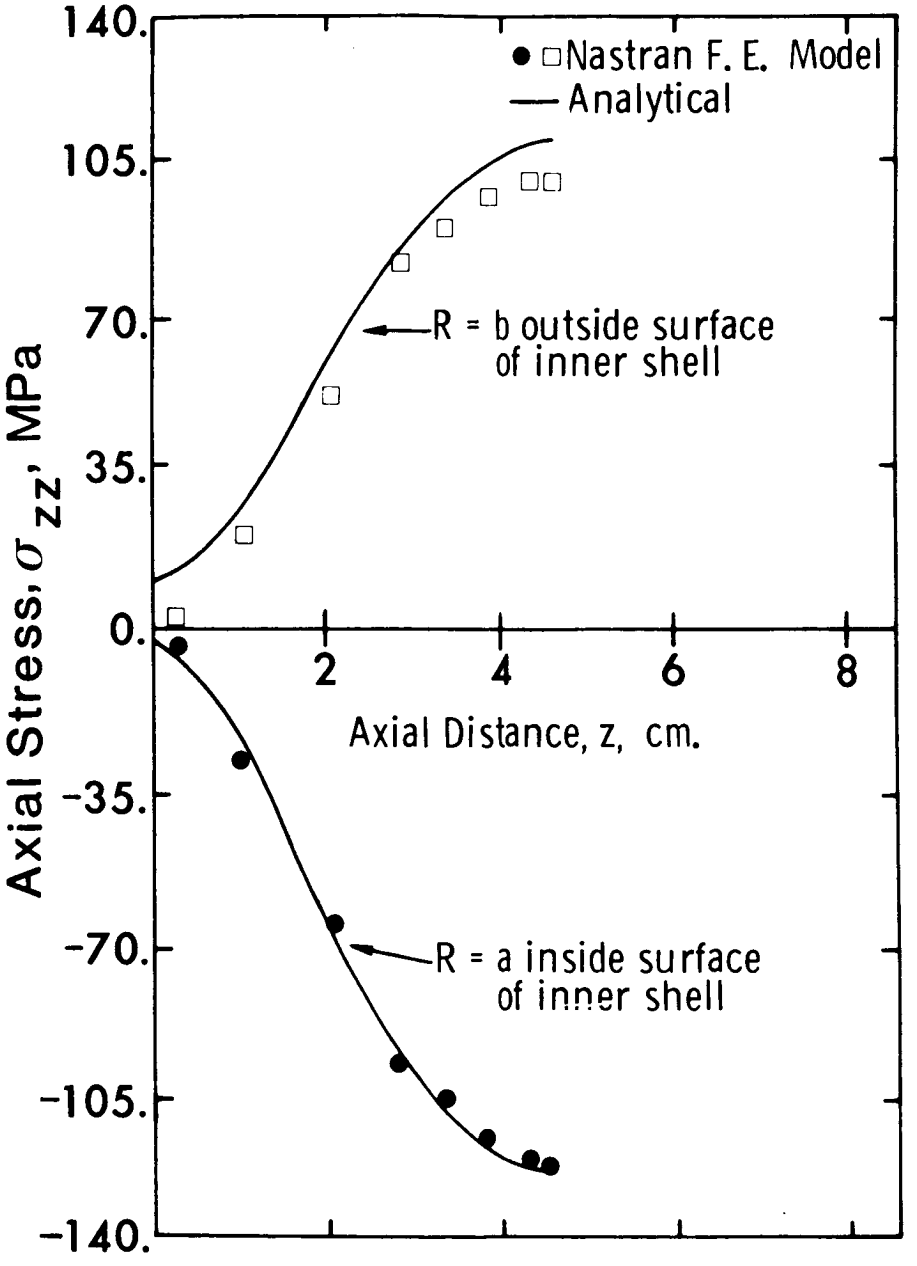

Fig. 5 Variation of axial stresses.

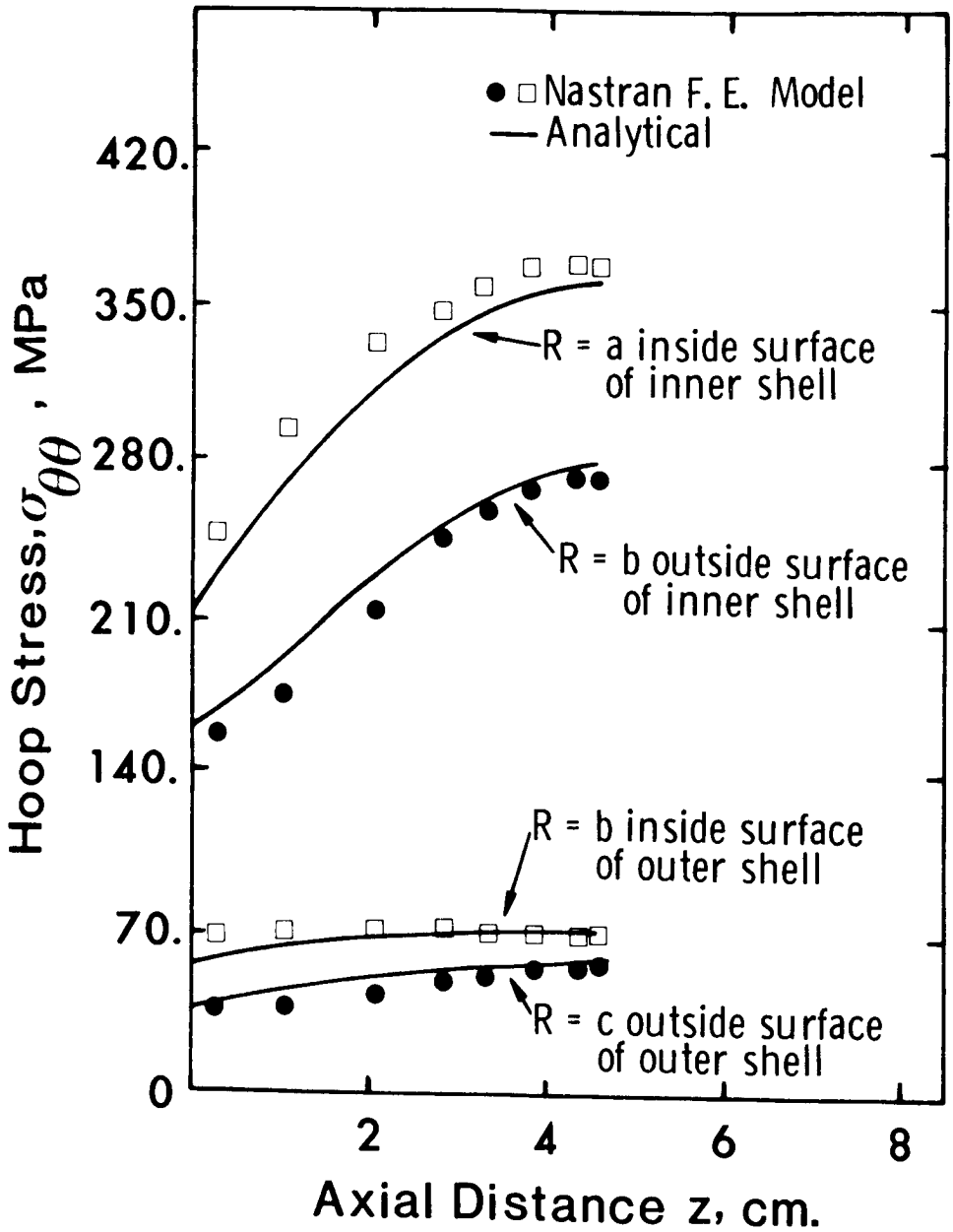

Fig. 6 Variation of hoop stresses with axial distance.

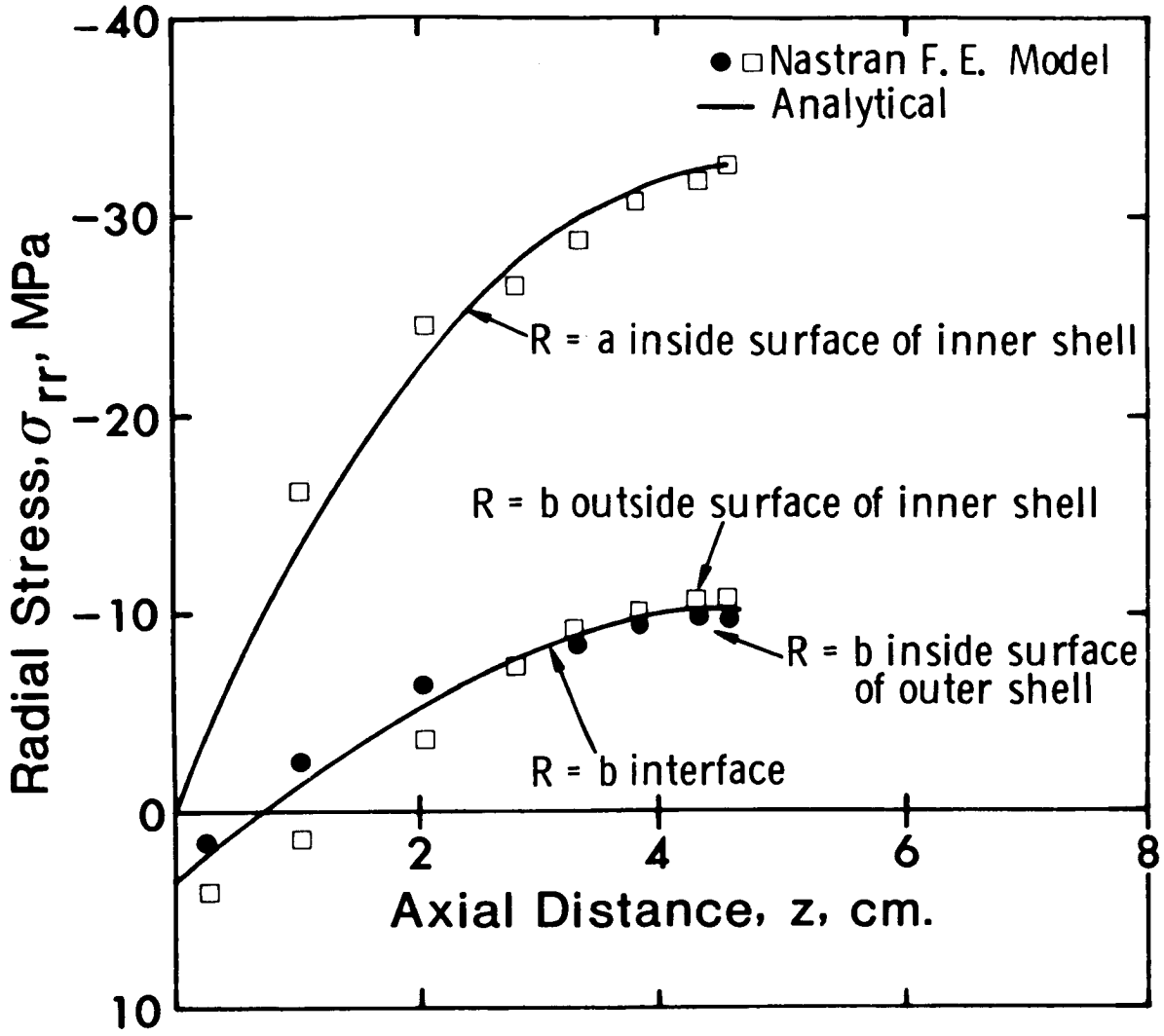

Fig. 7 Variation of radial stresses with axial distance.

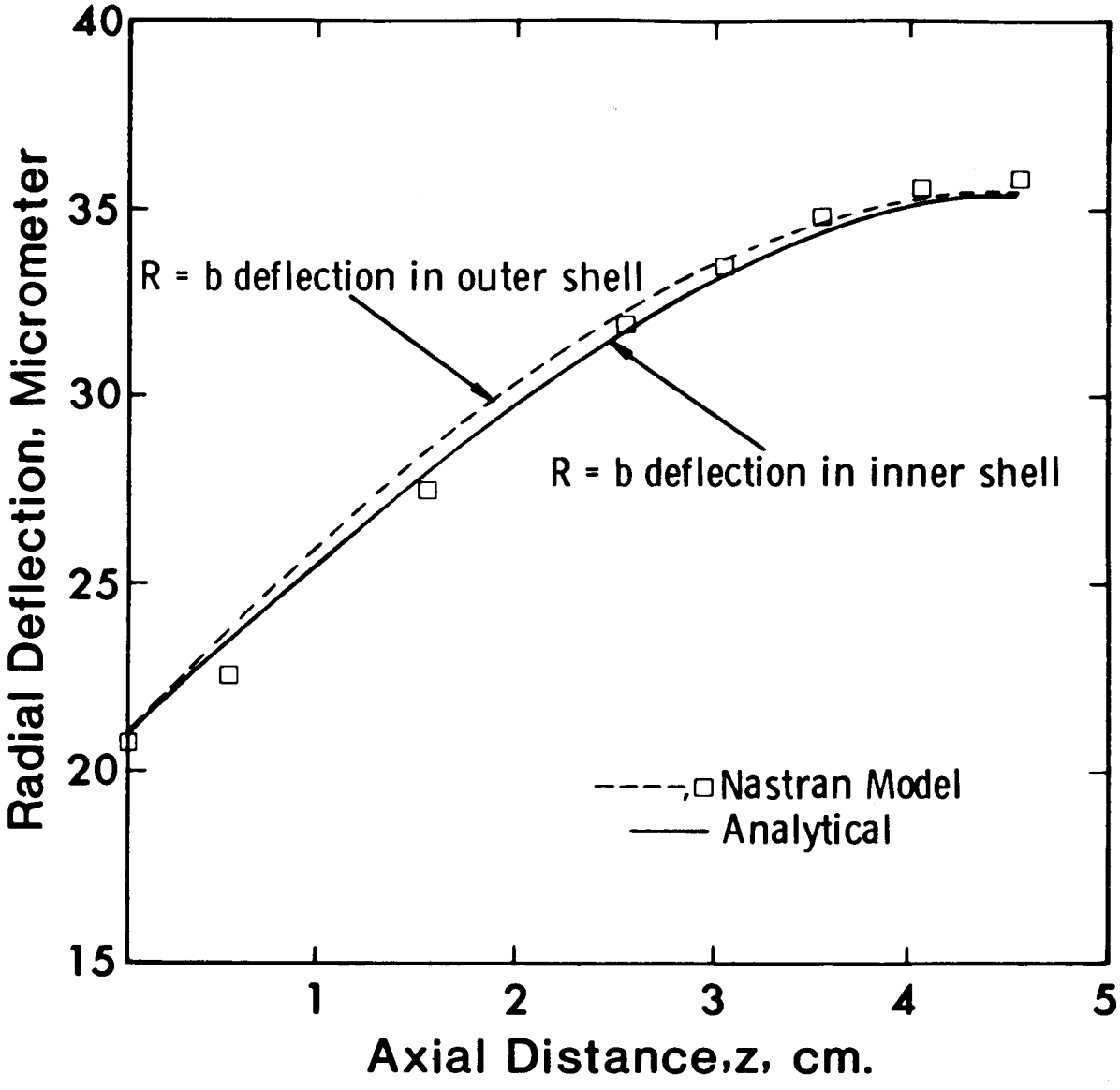

Fig. 8 Variation of radial deflections with axial distance z.

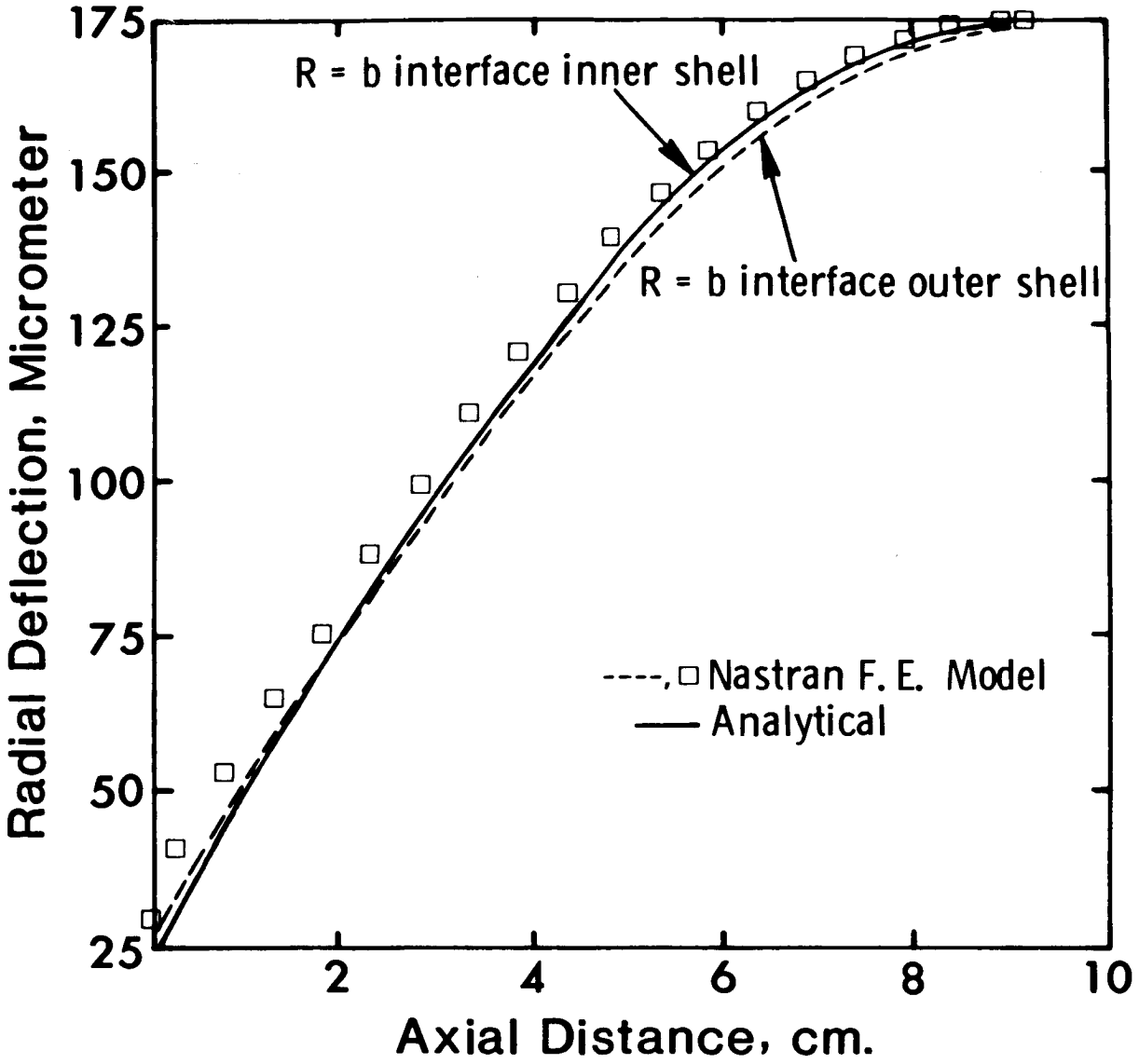

Fig. 9 Variation of radial deflection.

A NUMERICALLY EFFICIENT FINITE ELEMENT HYDROELASTIC ANALYSIS*

Robert N. Coppolino**
The Aerospace Corporation

SUMMARY

A finite element hydroelastic analysis formulation is developed on the basis of Toupin's complementary variational principle. Emphasis is placed on the special case of an incompressible fluid model which is applicable to propellant tank hydroelastic analysis. A concise fluid inertia representation results from the assumption of incompressibility and the hydroelastic equations reduce to a simplified form associated with the structure alone. The efficiency of the incompressible hydroelastic formulation is enhanced for both fluid and structure by introduction of harmonic reduction as an alternative to Guyan reduction. The theoretical developments are impelemented in the NASTRAN Program and the technique is verified and demonstrated as an efficient and accurate approach with a series of illustrative problems including the 1/8-scale Space Shuttle external tank.

INTRODUCTION

The increasing complexity of launch vehicle configurations, particularly in the case of the Space Shuttle, recently has stimulated considerable interest in the dynamic behavior of liquid-filled tanks. The prevention of coupled structure-propulsion instability (pogo), for example, requires very complete and accurate mathematical models for the calculation of propellant tank hydroelastic modes (ref. 1) in the frequency range of concern (2-50 Hz for the Space Shuttle).

Various fluid modeling techniques for hydroelastic analysis (refs. 2-7) have been mechanized for digital computation. These techniques range from finite element and finite difference techniques to approximate analytical approaches taking advantage of the properties of the fluid velocity potential and the consequences of Green's theorem. Most hydroelastic analysis methods, however, are limited to special geometric configurations. Furthermore, although theoretically rigorous, most contain deficiencies in computational economy and/or numerical accuracy.

---

*Work performed at Grumman Aerospace Corporation under Contracts NAS1-10635-21 and POM3WXMZ-483002 for NASA Langley Research Center and Rockwell International Space Division, respectively.

**Member Technical Staff, Vehicle Engineering Division

In particular, the hydroelastic analysis technique used in NASTRAN (ref. 7) is deficient in computational economy. This technique employs a large unsymmetrical eigenvalue problem formulated in terms of mixed fluid pressure and structural displacement generalized coordinates. In this formulation, the fluid coefficient matrices, derived by a Galerkin-type approach, are interpreted according to a structural analogy. The resulting fluid pseudo-mass and pseudo-stiffness matrices are recognized herein as flexibility and inverse mass (inertance) matrices, respectively, on the basis of Toupin's complementary variational principle (ref. 8). This revised interpretation is central to the formulation of the hydroelastic problem presented here. Although the effort in the present work was initially directed towards alleviation of difficulties encountered in the NASTRAN hydroelastic analysis, it has been found that Toupin's principle provides fundamental physical insight for a variational approach to hydroelasticity and it provides a rigorous basis for the development of fluid finite elements.

A derivation of fluid matrix equations on the basis of Toupin's principle, and manipulation of the interacting structure equations to a form consistent with the complementary principle, ultimately results in a symmetric kinetic formulation for compressible hydroelasticity. A detailed development of the compressible formulation is not presented in this paper. The special case of incompressible hydroelasticity is of primary interest as it is particularly applicable in the study of propellant tank dynamics.

In the special case of incompressibility, the interior fluid pressure fluctuations are algebraically dependent on surface pressure fluctuations. Although this property is illustrated from the viewpoint of a matrix approach, it is well known as a consequence of the application of Green's theorem to a continuum potential description. Moreover, the surface pressure fluctuations are algebraically related to the fluid accelerations normal to the bounding surface, and this is equivalent to a statement of the "surface flux" boundary condition. In addition, it is recognized on physical as well as mathematical grounds that there exists an overspecification in the surface pressure/acceleration relationships which implicitly defines a compatibility condition. In very simple terms the condition which requires that under uniform pressure the fluid will not move manifests itself as a necessary singularity in the fluid inertance matrix. Upon elimination of the surface pressure singularity by introduction of pressure deviation dynamic variables, a concise fluid mass matrix is formed in terms of bounding-surface displacements alone; this matrix is simply added to the structural mass matrix, resulting in a symmetric kinematic set of hydroelastic dynamic equations. This description represents a drastic reduction in system variables.

It is noted in this paper that the sequencing of kinematic reduction operations (e.g., Guyan, etc.) on fluid and structure is crucial to the economy of the analysis approach. In addition, a matrix harmonic reduction scheme is introduced as an efficient alternative to Guyan reduction for geometrically, but not necessarily structurally, axisymmetric configurations to further reduce the number of system variables.

A series of illustrative problems is presented to demonstrate the present incompressible hydroelastic analysis, which has been implemented in

NASTRAN. In particular the problems illustrate the use of harmonic reduction, and the accuracy and efficiency of the hydroelastic formulation in general, by comparison with exact analytical and available test results. Moreover, computation times for the standard NASTRAN and the present hydroelastic analysis techniques are compared.

SYMBOLS

A	generalized area matrix
B	fluid bulk modulus
C	flexibility matrix
C_f, C_s	fluid, structural flexibility matrix
E	structural elastic modulus
F_s	internal structural generalized force
G	matrix defined in equation (29b)
I	identity matrix
K	stiffness matrix
K_s, K_s^*	structural stiffness matrix, constrained structural stiffness matrix [eq. (32d)]
L	inertance matrix
L_f, L_s	fluid, structural inertance matrix
M_f	fluid mass matrix
M_s, M_s^*	structural mass matrix, constrained structural mass matrix [eq. (32c)]
M_θ, M_z	cylindrical-shell bending-moment resultants [eq. (40a)]
N_θ, N_z	cylindrical-shell membrane-stress resultants [eq. (40a)]
P, P'	pressure, pressure deviation array
R	hemisphere or cylindrical shell radius
S	surface area
T_c, U_c	complementary kinetic, potential energy function

T_{sd}, T_h	reduction transformation [eq. (34)], harmonic transformation [eq. (36)]
U	displacement array
V	volume
δW_c	complementary virtual work function
h	shell thickness
ℓ	cylindrical shell axial dimension
m, n	meridional, circumferential wave index
$\hat{n}$	surface outward normal unit vector
p	pressure
p_o	static pressurization level (gage)
$p_o(r_i, z_i)$, $p_K(r_i, z_i)$, $p_K^*(r_i, z_i)$	harmonic distribution pressure amplitudes [eq. (37)]
r	radial coordinate in cylindrical reference frame
t	time
$u, \vec{u}$	displacement, displacement vector
u^*	surface displacement
z	axial coordinate in cylindrical reference frame
Γ	matrix defined in equation (28c)
Ω	nondimensional frequency
α	stiffness constant for hemisphere [eq. (38)]
ν	Poisson's ratio
ρ_f, ρ_s	fluid, structural density
ω	circular frequency

Operators

$d(\ )$	total differential
$\nabla\cdot(\ )$	divergence
$\nabla(\ )$	gradient
$\partial(\ )$	partial derivative
$\delta(\ )$	variation
$(\ )$	total impulse $\int_{-\infty}^{t}(\ )\,dt$
$(\dot{\ })$	time derivative, $d(\ )/dt$

Subscripts

i, j, k	denote elements of a matrix or vector

Abbreviations

DOF	degrees of freedom
CPU	central processing unit

THEORETICAL DEVELOPMENT

The class of problems considered here consists of the interaction of irrotational, inviscid, compressible fluids with flexible structures for which both fluid and structural motions are assumed small compared to overall dimensions. The approach used to describe the dynamics of the fluid is a finite element technique which utilizes energy expressions based on Toupin's principle (ref. 8). A detailed derivation of Toupin's principle and a complementary form of Hamilton's principle are presented in reference 9 as consequences of a postulated complementary D'Alembert principle.

The equation of motion of a fluid particle is

$$\ddot{\vec{u}} = -\frac{1}{\rho_f}\nabla p \tag{1}$$

and the constitutive relationship for an inviscid, compressible fluid is

$$p = -B\nabla\cdot\vec{u} \tag{2}$$

where $\nabla \cdot \vec{u}$ represents the dilatational strain. In order to obtain a fluid velocity expression, equation (1) is integrated to yield

$$\dot{\vec{u}} = -\frac{1}{\rho_f}\nabla\hat{p} \tag{3}$$

where $\hat{p}$ is the pressure impulse

$$\hat{p} = \int_{-\infty}^{t} p\,dt \quad \text{or} \quad \dot{\hat{p}} = p \tag{4}$$

Complementary kinetic and strain energy (T_c and U_c, respectively) may now be expressed in terms of impulsive pressure (the complementary dynamic variable) as

$$T_c = \frac{1}{2}\int_V \frac{1}{\rho_f}(\nabla\hat{p} \cdot \nabla\hat{p})\,dV \tag{5a}$$

$$U_c = \frac{1}{2}\int_V \frac{1}{B}(\dot{\hat{p}})^2\,dV \tag{5b}$$

The motion dependent and impulse dependent energy expressions are generally not equivalent; they are equivalent, however, for linear systems (ref. 10). The complementary virtual work performed by boundary surface displacements, $\vec{u}^*$, is

$$\delta W_c = \int_S \delta\hat{p}\,(\dot{\vec{u}}^* \cdot \hat{n})\,dS \tag{6}$$

The concept of complementary virtual work (ref. 10) may be viewed as a consequence of a complementary D'Alembert principle (ref. 9).

The above energy expressions substituted into the complementary form of Hamilton's principle

$$\delta\int_{t_o}^{t_1}(T_c - U_c)\,dt + \int_{t_o}^{t_1}\delta W_c\,dt = 0 \tag{7}$$

ultimately yields, after use of Green's theorem and integration by parts, integrated expressions corresponding to the wave equation and natural boundary conditions.

The complementary formulation is presently applied, however, as an approximate analysis tool. Consider an approximation of a fluid pressure (impulse) state expressed as a linear function of a finite set of generalized impulses. Let us also require that any such approximation contains spatially uniform pressure as a state describable by the chosen generalized impulses; this is analogous to the requirement in kinematic finite element analysis that assumed displacement states must contain rigid-body motions. The fluid complementary kinetic and strain energies resulting from the assumed pressure impulse states are therefore the quadratic functions

$$T_c = \frac{1}{2} \sum_i \sum_j L_{ij} \hat{p}_i \hat{p}_j \tag{8a}$$

$$U_c = \frac{1}{2} \sum_i \sum_j C_{ij} \dot{\hat{p}}_i \dot{\hat{p}}_j \tag{8b}$$

with the elements of the symmetric inertance matrix L and flexibility matrix C defined as

$$L_{ij} = \frac{\partial^2 T_c}{\partial \hat{p}_i \partial \hat{p}_j}, \quad C_{ij} = \frac{\partial^2 U_c}{\partial \dot{\hat{p}}_i \partial \dot{\hat{p}}_j} \tag{9a,b}$$

The L_{ij} are proportional to $1/\rho_f$ and the C_{ij} are proportional to $1/B$. The complementary virtual work is expressed as

$$\delta W_c = \sum_i \int_s \left[\frac{\partial \hat{p}}{\partial \hat{p}_i} \dot{\vec{u}}^* \cdot \hat{n} \right] dS \, \delta \hat{p}_i \tag{10}$$

For the special case in which the surface displacements are physically discretized, the complementary virtual work may be expressed as

$$\delta W_c = \sum_k \sum_i A_{ik} \dot{u}_k^* \, \delta \hat{p}_i \tag{11a}$$

with an element of the generalized area matrix A defined as

$$A_{ik} = \int_{S_k} \left(\frac{\partial \hat{p}}{\partial \hat{p}_i} \right) \left[\frac{\partial \dot{\bar{u}}^*}{\partial \dot{u}_k} \cdot \hat{n} \right] dS \tag{11b}$$

Substitution of equations (8) and (11) into equation (7), with the appropriate integrations by parts, results in the complementary Euler-Lagrange equations

$$\sum_j (L_{ij}\hat{p}_j + C_{ij}\ddot{\hat{p}}_j) = - \sum_k A_{ik}\dot{u}_k^* \tag{12}$$

By taking the time derivative of this expression noting equation (4), the Euler-Lagrange equations become

$$\sum_j (L_{ij}p_j + C_{ij}\ddot{p}_j) = - \sum_k A_{ik}\ddot{u}_k^* \tag{13}$$

This is the form of the fluid dynamic finite element equations for individual elements and stacked systems of elements. In the case of a stacked system of elements, the matrix A represents only bounding surface generalized areas and u_k^* represents discrete surface displacements. The pressures p_j comprise the set of boundary surface and internal pressures; therefore the matrix A is rectangular.

The above set of fluid equations is derived for NASTRAN (ref. 7) by a Galerkin-type approach which "constructs" a minimal principle. In this latter approach, the matrix expressions are interpreted according to a mathematical analogy and physical insight is lost; that is, L_{ij} is mathematically analogous to kinematic stiffness, C_{ij} is analogous to kinematic mass and the right-hand side is analogous to a kinematic generalized force vector.

A Symmetric Kinetic Formulation for Compressible Hydroelasticity

In the general case of compressible fluid/structure interaction, the fluid is described in terms of the complementary form

$$L_f P + C_f \ddot{P} = - A^T \ddot{U} \tag{14a}$$

and the structure under fluid pressure excitation is described in the standard kinematic form

$$M_s \ddot{U} + K_s U = AP \tag{14b}$$

Direct coupling of the above set in terms of the mixed pressure and structural displacement variables [as in the standard NASTRAN formulation (eq. (7))] results in an unsymmetric eigenvalue problem.

A symmetric formulation can be derived by the complementary principle or by an equivalent manipulation of the structural dynamic equations to the complementary form. If the latter approach is taken, internal structural generalized forces, F_s, are related to the structural displacements, U, according to

$$K_s U = F_s \tag{15}$$

Suppose that K_s represents a stiffness matrix of an interacting supported structure such that rigid body deflections do not occur; the transformation to internal forces is defined as

$$U = K_s^{-1} F_s \tag{16}$$

Incorporation of this transformation into the hydroelastic equation set, equation (14), yields the symmetric set of hydroelastic equations in terms of force-type variables.

$$\left[\begin{array}{c|c} C_f & 0 \\ \hline 0 & C_s \end{array}\right] \left\{\begin{array}{c} \ddot{P} \\ \hline \ddot{F}_s \end{array}\right\} + \left[\begin{array}{c|c} L_f + A^T L_s A & -A^T L_s \\ \hline -L_s A & L_s \end{array}\right] \left\{\begin{array}{c} P \\ \hline F_s \end{array}\right\} = \left\{\begin{array}{c} 0 \\ \hline 0 \end{array}\right\} \tag{17}$$

with the structural inertance and compliance matrices defined, respectively, as

$$L_s = M_s^{-1}, \quad C_s = K_s^{-1} \tag{18}$$

The formulation presented here provides a symmetric kinetic formulation for inviscid, compressible fluid hydroelastic problems for which efficient eigenvalue analysis techniques are applicable. Further discussion of the compressible formulation is not presently warranted since the class of problems of interest is limited to incompressible fluids interacting with flexible structures. The alternate simplified kinematic formulation to be derived below is appropriate for this case.

In the special case for which fluid compressibility is negligible ($C_f \sim 0$) the complementary fluid dynamic equations, equation (14a), reduce to a set of algebraic equations relating fluid pressures and boundary-surface accelerations. One is strongly motivated to utilize this quality to solve for the pressures in terms of surface accelerations--and ultimately obtain a kinematic formulation which is identical in form to a standard set of structural dynamic equations.

Two fundamental properties of the fluid are recognized as consequences of the simplifying assumption of fluid incompressibility. These properties are necessarily inherent in both the continuum and the present matrix finite element descriptions. The first property requires that for an incompressible fluid the interior pressures are related to the surface pressures in a purely geometric sense; from the continuum viewpoint, this is a consequence of Green's theorem applied to an incompressible fluid. The second property requires that the net flux (or normal flow) out of the fluid volume is zero. This latter property amounts to a statement of constraint on flow normal to the bounding surface, and simultaneously it is recognized as a compatibility constraint on surface pressures. A simple physical statement of this second property is that, under the uniform surface pressure (impulse) state, the fluid surface will not deform and consequently, the fluid volume will not move. This point is illustrated mathematically by noting that in the uniform pressure state the pressure gradient, ∇p, is null throughout the fluid volume; hence the complementary kinetic energy, equation (5a), is null.

The complementary fluid matrix equation set for the special case of an incompressible fluid [see equation (14a) for $C_f = 0$] in a conveniently partitioned form is expressed as

$$\begin{bmatrix} L_{ff} & L_{fs} & L_{fi} \\ L_{sf} & L_{ss} & L_{si} \\ L_{if} & L_{is} & L_{ii} \end{bmatrix} \begin{Bmatrix} P_f \\ P_s \\ P_i \end{Bmatrix} = - \begin{bmatrix} A_{ff}^T & A_{sf}^T \\ A_{fs}^T & A_{ss}^T \\ 0 & 0 \end{bmatrix} \begin{Bmatrix} \ddot{U}_f \\ \ddot{U}_s \end{Bmatrix} \tag{19}$$

The pressure partitions, P_f, P_s and P_i correspond to a single surface reference pressure or free-surface pressure set, the complement of the total surface pressure set, and the internal fluid pressure set, respectively; the displacement partitions U_f and U_s correspond to a single surface reference displacement or free surface displacement set and the complement of the total surface displacement set, respectively. The structural dynamic equation set with applied fluid pressure loading is, in partitioned form

$$\begin{bmatrix} M_{ff} & M_{fs} \\ M_{sf} & M_{ss} \end{bmatrix} \begin{Bmatrix} \ddot{U}_f \\ \ddot{U}_s \end{Bmatrix} + \begin{bmatrix} K_{ff} & K_{fs} \\ K_{sf} & K_{ss} \end{bmatrix} \begin{Bmatrix} U_f \\ U_s \end{Bmatrix} = \begin{bmatrix} A_{ff} & A_{fs} & 0 \\ A_{sf} & A_{ss} & 0 \end{bmatrix} \begin{Bmatrix} P_f \\ P_s \\ P_i \end{Bmatrix} \tag{20}$$

where the structural mass and stiffness matrices are expressed in partitioned form in accordance with the surface reference displacement set and the complement of the total surface displacement set, respectively. If the reference subsets of pressure, P_f, and displacement, U_f, should correspond to a free fluid surface rather than a structural interface, then the structural mass partitions M_{ff}, M_{sf}, M_{fs} would be null. In addition, the stiffness partitions K_{ff}, K_{fs}, K_{sf} would correspond to contributions due to the surface gravitational potential and possibly ullage pressure fluctuation. In many cases the free surface and ullage stiffness are negligible relative to the structural stiffness, K_{ss}, and may therefore be neglected. The development of the incompressible hydroelastic equations presented below treats the most general case implied in equation (20), with the above special cases illustrated at the completion of the derivation.

From equation (19), the internal pressures are related to the surface pressures by

$$P_i = - L_{ii}^{-1} [L_{if} L_{is}] \begin{Bmatrix} P_f \\ P_s \end{Bmatrix} \tag{21}$$

and the reduced fluid dynamic equation set, in terms of surface quantities only, is

$$\begin{bmatrix} L'_{ff} & L'_{fs} \\ L'_{sf} & L'_{ss} \end{bmatrix} \begin{Bmatrix} P_f \\ P_s \end{Bmatrix} = - \begin{bmatrix} A_{ff}^T & A_{sf}^T \\ A_{fs}^T & A_{ss}^T \end{bmatrix} \begin{Bmatrix} \ddot{U}_f \\ \ddot{U}_s \end{Bmatrix} \tag{22a}$$

with

$$\begin{bmatrix} L'_{ff} & L'_{fs} \\ L'_{sf} & L'_{ss} \end{bmatrix} = \begin{bmatrix} L_{ff} & L_{fs} \\ L_{sf} & L_{ss} \end{bmatrix} - \begin{bmatrix} L_{fi} \\ L_{si} \end{bmatrix} L_{ii}^{-1} [L_{if} L_{is}] \tag{22b}$$

The reduced inertance matrix is singular since an incompressible fluid under uniform pressure does not deform. This singularity is assured in the individual finite element inertance matrices by the use of admissible pressure distributions; it is a necessary condition for compatibility.

For a fluid represented by discrete surface pressures the normalized uniform pressure state is

$$\left\{\begin{array}{c} P_f \\ \hline P_s \end{array}\right\} = \left\{\begin{array}{c} 1 \\ \hline 1 \\ \vdots \\ 1 \end{array}\right\} \tag{23}$$

Under such loading the surface normal accelerations must be null and the necessary property of the reduced inertance matrix is

$$\sum_j L'_{ij} = 0 \tag{24}$$

The uniform pressure singularity pertains as well to the full pressure set with the members of P_i also unity; the reduction to the surface pressure set is made in this derivation mainly to illustrate the first basic property, of geometric dependence of internal pressure. For axisymmetric fluid elements with generalized pressure variables corresponding to amplitudes of circumferential harmonics, this discussion pertains to the zeroth harmonic, only, which contains the uniform pressure singularity. The singularity is removable by introduction of the concept of pressure deviation in which the deviations from the reference uniform pressure state of value, P_f, are

$$P'_{s_i} = P_{s_i} - P_f \tag{25}$$

Thus the relationship between pressures and pressure deviations may be expressed by the transformation

$$\left\{\begin{array}{c} P_f \\ \hline P_s \end{array}\right\} = \left[\begin{array}{c|ccc} 1 & & & \\ \hline 1 & 1 & & \\ \vdots & & \ddots & \\ 1 & & & 1 \end{array}\right] \left\{\begin{array}{c} P_f \\ \hline P'_s \end{array}\right\} \tag{26}$$

when P_f represents a single discrete reference pressure. If P_f represents a pressure subset comprised of all free surface pressures (to be nulled in the case of negligible surface gravitational potential and ullage pressure strain energy), the constraint relationship is somewhat different; consideration of this latter case, however, is reserved for a later part of the present discussion.

Application of the above transformation on the reduced fluid equation set in equation (22), noting equation (24), yields

$$L'_{fs} P'_s = - A^T_{ff} \ddot{U}_f - A^T_{sf} \ddot{U}_s \tag{27a}$$

$$L'_{ss} P'_s = - A^T_{fs} \ddot{U}_f - A^T_{ss} \ddot{U}_s \tag{27b}$$

Suppose now that the displacement U_f is directed normal to the reference surface; the area coupling partitions A^T_{fs} and A^T_{sf} are therefore null, simplifying the above expressions. It should be noted that this restriction is made for clarity of the present development and the more general case is derivable with some additional algebraic complication. Solution for the pressure deviations in equation (27b) and substitution of the result in equation (27a) yields the pressure deviation recovery relationship and the displacement recovery relationship, respectively.

$$P'_s = - L'^{-1}_{ss} A^T_{ss} \ddot{U}_s \tag{28a}$$

$$\begin{Bmatrix} U_f \\ U_s \end{Bmatrix} = \begin{bmatrix} \Gamma \\ I \end{bmatrix} \begin{Bmatrix} U_s \end{Bmatrix} \tag{28b}$$

with

$$\Gamma = A^{-T}_{ff} L'_{fs} L'^{-1}_{ss} A^T_{ss} \tag{28c}$$

The latter result is equivalent to imposing a kinematic constraint on outward normal surface flow (incompressibility)

$$\begin{Bmatrix} 0 \\ A^T_{ss} U_s \end{Bmatrix} = \begin{bmatrix} I & G \\ 0 & I \end{bmatrix} \begin{Bmatrix} A^T_{ff} U_f \\ A^T_{ss} U_s \end{Bmatrix} \tag{29a}$$

where

$$G = - L'_{fs} L'^{-1}_{ss} \tag{29b}$$

the companion pressure (compatibility) constraint expression is

$$\begin{Bmatrix} P_f \\ P_s \end{Bmatrix} = \begin{bmatrix} I & 0 \\ G^T & I \end{bmatrix} \begin{Bmatrix} P_f \\ P_s' \end{Bmatrix} \tag{30}$$

Physically the matrix G must consist of a row matrix with unit entries when P_f represents a single reference pressure. It is noted now that the use of an identity matrix in equation (28) and equation (30), implying that P_f and U_f may comprise pressure and acceleration subsets rather than individual quantities, is deliberate; the case in which a free surface pressure subset is null is therefore covered by the subsequent development.

Substitution of equations (29) and (30) into equation (22a) yields

$$\begin{bmatrix} L_{ff}' - L_{fs}' L_{ss}'^{-1} L_{sf}' & 0 \\ 0 & L_{ss}' \end{bmatrix} \begin{Bmatrix} P_f \\ P_s' \end{Bmatrix} = \begin{Bmatrix} 0 \\ A_{ss}^T \ddot{U}_s \end{Bmatrix} \tag{31a}$$

The lower partition merely represents the result already obtained in equation (27b). The upper partition may be interpreted in two ways which consists of (1) the general case in which a single reference pressure, P_f, is chosen to express the uniform pressure state and (2) the special case in which a set of free surface pressures, P_f, must be zero. For the first general case, the singularity condition is expressed as

$$L_{ff}' - L_{fs}' L_{ss}'^{-1} L_{sf} = 0 \tag{31b}$$

The constraints presented in equations (29) and (30) are now applied to the structural dynamic equation set equation (20), noting equations (28) and (31), resulting in the symmetric kinematic equation set

$$(M_s^* + M_f) \ddot{U}_s + K_s^* U_s = 0 \tag{32a}$$

where the fluid mass matrix is

$$M_f = A_{ss} L_{ss}'^{-1} A_{ss}^T \tag{32b}$$

and the constrained structural mass and stiffness matrices are

$$M_s^* = \Gamma^T M_{ff} \Gamma + \Gamma^T M_{fs} + M_{sf} \Gamma + M_{ss} \tag{32c}$$

and

$$K_s^* = \Gamma^T K_{ff} \Gamma + \Gamma^T K_{fs} + K_{sf} \Gamma + K_{ss} \tag{32d}$$

Complete displacement recovery is obtained through equation (28b) and pressure deviation recovery is obtained through equation (28a). Surface pressure recovery is achieved by combining the upper partition equation set in equation (20) with equation (28b); thus the surface pressure recovery equation set consists of

$$P_f = A_{ff}^{-1} (M_{ff} \Gamma + M_{fs}) \ddot{U}_s + A_{ff}^{-1} (K_{ff} \Gamma + K_{fs}) U_s \tag{33}$$

and equations (28a) and (30).

The symmetric kinematic formulation developed above is useful in hydroelastic analyses for which either a fluid free surface is not present or free surface gravitational potential and/or ullage stiffness is significant. In most practical analyses involving tanks partially filled with fluid, the free surface strain energy is insignificant relative to the structural energy. In such cases low frequency slosh dynamics is approximated with rigid structure and flexible structure/fluid interaction dynamics is approximated with zero free surface pressure. In the latter case, the reference pressure set, P_f, consists of all free surface pressures (set to zero) and the reference surface displacement set U_f consists of all free surface displacements. It is noted again as in the opening of this section that when a free surface is present M_{ff} and M_{fs} are null; and when surface strain energy is insignificant, K_{ff} and K_{fs} are null.

DISPLACEMENT SET REDUCTION FOR THE HYDROELASTIC PROBLEM

General Considerations

For typical launch vehicle propellant tank models, the structural grid displacement set, U_s, may be fairly large (in excess of 1000 degrees of freedom) and the fluid mass matrix, equation (32b), is typically full. Reduction to a much smaller dynamic set of variables is therefore very desirable for computational economy in free vibration analysis. The fullness of the mass matrix is peculiar to the hydroelastic problem and therefore special care must be taken in the reduction process.

Consider the reduction transformation

$$U_s = T_{sd} U_d \tag{34}$$

formed by static condensation of the stiffness matrix (Guyan reduction) or by some other process. Application of this transformation to the hydroelastic equation set, equation (32), with the constituent matrices explicitly defined yields the expressions for reduced mass and stiffness matrices. The most critical operations with respect to computational economy are those used in formation of the reduced fluid mass matrix

$$(M_f)_{reduced} = (T_{sd}^T A_{ss}) L_{ss}^{-1} (A_{ss}^T T_{sd}) \tag{35}$$

If the fluid mass matrix in the structural grid set, equation (32b), is explicitly formed, a symmetric reduction process with T_{sd} may be quite time consuming and expensive due to the fullness of the original mass matrix. However, by first forming the reduced generalized area matrix $A_{ss}^T T_{sd}$ as implied above in equation (35), the large, full fluid mass matrix need not be explicitly formed; the reduced mass matrix is calculated only, resulting in substantial computational economy.

Harmonic Reduction of Geometrically Axisymmetric Structures

The general category of structures of interest in propellant tank hydroelastic analysis consists of configurations which possess, for the most part, geometrically axisymmetric fluid cavities. The tank structure may have a variety of structural asymmetries such as circumferential thickness variation in both shell and rings, discrete longitudinal stiffeners and asymmetric supports. The finite element description of such a structure typically must have a fine and fairly uniform nodal mesh distribution for adequate description of the structural behavior. The use of Guyan reduction in such cases (when the grid-set displacement degrees of freedom are on the order of thousands) may be inefficient and result in an inaccurate dynamic description when extreme coordinate reduction is used. An alternative scheme, which expresses the circumferential displacement distribution in terms of a chosen set of harmonics (harmonic reduction), alleviates the difficulties encountered with Guyan reduction. This is especially true when only a few harmonic shapes appear sufficient to describe the anticipated dynamic behavior of interest.

Harmonic reduction of a discrete structural grid is accomplished by use of the geometric transformation (see ref. 9 for details)

$$U_s = T_h U_h \tag{36}$$

where U_s corresponds to the physical grid degrees of freedom to be transformed, and U_h corresponds to the harmonic degrees of freedom (plus any discrete degrees of freedom not transformed). The transformation or constraint matrix T_h is composed of the appropriate sinusoidal functions evaluated at the discrete variable locations. It should be noted that discrete displacements expressed in terms of cylindrical or spherical reference frames are most convenient for this procedure. For a typical shell structure with JxK grid points such that there are J meridional rows and K circumferential points in a row, the grid set has typically 6 x JxK degrees of freedom and the matrix semibandwidths are 6xK (assuming K < J). Application of the harmonic transformation as a reduction scheme, where the number of harmonics N is much less than K, results in a U_h set of 6 x JxN generalized coordinates with matrix semibandwidths of 6xN. If $N \ll K$ harmonic reduction represents a radical reduction in the number of degrees of freedom as well as matrix bandwidth. Further reduction of the system description is possible by a small Guyan reduction made by choosing the generalized rotation degrees of freedom and tangential degrees of freedom as members of the omitted set of displacements. In such a case the analysis set consists of JxN degrees of freedom. This represents a radical reduction in degrees of freedom by a factor of (N/6K), without a costly large matrix decomposition typical of Guyan reduction.

NUMERICAL STUDIES

The new incompressible hydroelastic formulation and harmonic reduction have been implemented in NASTRAN and verified and demonstrated on a number of problems. The problems fall into two categories, namely, analytical verification problems for which exact solutions are known, and demonstration problems for which experimental data are available. The 1/8-scale Space Shuttle external tank is included in the second category. The fluid idealizations utilized in the hydroelastic problems are based on existing elements of revolution in NASTRAN.

The present hydroelastic analysis employs NASTRAN structural as well as fluid elements and provides for a description of dynamics of axisymmetrically configured fluids in terms of circumferential harmonic pressure distributions. The distribution of pressure is typically

$$p(r_i, \theta_i, z_i) = p_o(r_i, z_i) + \sum_{k=1}^{N} \left\{ p_k(r_i, z_i) \cos k\,\theta_i + p_k^*(r_i, z_i) \sin k\,\theta_i \right\} \tag{37}$$

The fluid containing structure is described in terms of discrete physical displacements so that the structural representation is not limited to structurally axisymmetric containers. Coupling of harmonic pressure distributions with discrete structural displacements in this formulation is not strictly consistent; moreover, in many cases it is inefficient. When a structure described in terms of discrete displacements is coupled with a fluid described in terms of circumferential harmonics, inconsistencies may arise if too few pressure harmonics are utilized; structural deformation shapes associated with higher harmonics not included in the fluid representation will reflect a lack of fluid inertia loading. Alternatively, when the discrete structural grid is too coarse to accurately describe the highest harmonic pressure distributions, large errors in the mode shapes associated with higher harmonics will be present. A consistent grid representation is realized by use of harmonic reduction when the number of structural harmonics coincides with the number of fluid pressure harmonics. This provides additional motivation for the use of harmonic reduction which is peculiar to use of the NASTRAN fluid elements. When harmonic reduction is not utilized, special care must be taken to utilize fluid harmonic and discrete structural descriptions of equivalent complexity.

Analytical Verification Problems

Spherical Cap. Harmonic reduction was first demonstrated on a spherical cap structure of uniform thickness to radius ratio, $h/R = 0.05$. The base of the cap, 60 degrees from the pole, is taken as rigidly fixed. The material properties are: elastic modulus $E = 10^7$, a Poisson's ratio $\nu = 0.3$, and mass density $\rho_s = 0.05$.

A nodal grid, consisting of 20 circumferential divisions in a semicircle and 10 meridional divisions, was chosen resulting in a structural model with 1266 DOF (degrees of freedom). Three circumferential harmonics (0, 1, 2) were chosen for harmonic reduction. The apex node was left in terms of rectangular coordinates since the polar degrees of freedom have no meaning at this node. After application of the fixed-base boundary condition and symmetric kinematic constraints at the pole, and a small Guyan reduction, an analysis set of 72 outward-normal and meridional generalized harmonic displacements resulted. At this point, all natural frequencies and the first 15 modes were calculated. Circumferential harmonics were uncoupled because of the axisymmetry in shell thickness.

The results of the above approach were compared to results based on various Guyan reduction strategies and to "exact" results based on the STARS-II program (ref. 11). A comparison of computed natural frequencies (table I) indicate that the overall accuracy of the 72-DOF harmonic reduction representation is better than the 190-DOF Guyan reduction representation. The computation time associated with eigenvalue analysis of the harmonic analysis set is much less than that associated with the Guyan reduction analysis set. Central processing unit (CPU) times were 238 and 531 seconds, for the harmonic and Guyan reduction representations, respectively. This is

attributed to elimination of a large-scale matrix decomposition, characteristic of Guyan reduction, and to the fact that much fewer degrees of freedom are required for comparable accuracy (e.g., harmonic 72-DOF for 5% accuracy versus Guyan 190-DOF for 12% accuracy.

Fluid-Filled Hemisphere. The first problem for hydroelastic verification consists of an open hemispherical container filled with fluid. The container is massless and follows the artificial structural law

$$p = \alpha u_r \tag{38}$$

where u_r is the local radial displacement; the exact free-vibration solution is known (ref. 12). The finite element model of the fluid and container is illustrated in figure 1. A diagonal structural stiffness matrix with entries

$$K_{ii} = \alpha A_i \tag{39}$$

results from the artificial structural law in which A_i is the area associated with the "ith" radial degree of freedom. The fluid model is expressed in terms of the circumferential pressure harmonics n = 0, 2, 4 and the structural surface and free surface grids are reduced by harmonic reduction accordingly. The fluid mass matrix is expressed in terms of a 21-DOF analysis set of structural radial displacements at seven meridional locations.

A comparison of exact and finite element nondimensional natural frequencies is presented in table II and comparisons of selected modal displacement distributions are presented in figure 2. The finite element results are in very good agreement with the exact solution, with the level of accuracy decreasing with modal complexity as expected.

Fluid-Filled Cylinder. Another hydroelastic verification problem consists of the fluid-filled, circular cylindrical shell illustrated in figure 3. The shell structure is taken as one with bending as well as membrane stiffness. The geometric properties of the shell consist of a cylinder with length/radius ratio $(\ell/R) = 2$ and a thickness/radius ratio $(h/R) = 0.01$. In addition, the ratio of fluid to structure density $(\rho_f/\rho_s) = 1/3$ and the structural material Poisson ratio $(\nu) = 0.3$. An exact hydroelastic modal solution is known for an infinitely long cylinder (refs. 13, 14) which holds for the present problem when the structure is subjected to the boundary conditions

$$u_r = M_\theta = N_\theta = N_z = 0 \text{ (shear diaphragm for } z = \ell,\ r = R) \tag{40a}$$

$$p = 0 \text{ (free surface) for } z = \ell,\ r \le R \tag{40b}$$

$$\frac{\partial u_r}{\partial z} = u_z = \frac{\partial M_z}{\partial z} = N_z = 0 \text{ (symmetry) for } z = 0,\ r = R \tag{40c}$$

$$u_z = 0 \text{ (fixed bottom) for } z = 0,\ r \leq R \tag{40d}$$

The finite element models of the quarter shell ($-0 \leq z \leq \ell$, $0 \leq \theta \leq 90$ deg) and fluid were constructed taking advantage of symmetry. The structural grid for the quarter shell consists of 726 DOF (11 meridional nodal rows, 11 circumferential nodal columns) and the fluid grid consists of 165 DOF (55 nodes of rotation, circumferential harmonics n = 0,2,4). A 30-DOF set was obtained using (1) a harmonic transformation retaining harmonics n = 0,2,4, (2) the application of single-point constraints to enforce boundary conditions, and (3) a small Guyan reduction retaining only radial displacements.

All 30 natural frequencies and 25 mode shapes with and without the fluid included were calculated. Frequency spectra for the empty and fluid-filled shells are presented in figure 4, illustrating generally excellent comparison between finite element and exact results in both cases.

A characteristic of the present formulation, which is as significant as numerical accuracy, is computational economy. On the IBM 370/165 computer the total solution time for the empty cylinder was about 2 CPU minutes; for the fluid-filled cylinder an additional CPU minute was required to form the fluid mass and pressure recovery matrices.

Comparisons with Experimental Data

Liquid-Filled Cylinders Under Static Pressurization. A detailed experimental study of the dynamics of structurally axisymmetric and asymmetric circular cylinders under various water fill and static pressurization conditions has been conducted at NASA Langley Research Center by Mr. Robert Herr. Data resulting from these tests (unpublished) are quite complete and provide an excellent basis for analysis/test correlation studies. The test articles are aluminum cylinders with mean radius of 25.4 cm (10 in.) and height of 50.8 cm (20 in.). The cylinder walls are welded at the top and bottom to heavy aluminum plates. The axisymmetric test article has a cylinder wall thickness of 0.081 cm (0.032 in.) and the asymmetric test article has a wall thickness variation around the circumference of 0.051-0.102 cm (0.020-0.040 in.) according to the equation

$$\frac{h}{h_{max.}} = 0.75 + 0.25 \cos \theta \tag{41}$$

A structural model for the half-cylinder (0 deg $\leq \theta \leq 180$ deg) taking advantage of the single axis of symmetry was assembled with sufficiently fine grid to simulate the circumferential harmonic shapes up to n = 15, which were known a priori from the experimental results to dominate in the lowest frequency modes. The structural grid set consists of 2046 DOF resulting from 11 axial grid rows and 31 circumferential grid columns all evenly distributed. The fluid representation chosen at the half-filled condition is illustrated in figure 5. The 480-DOF (pressures) fluid model results from the 30 fluid-grid locations of revolution expressed in terms of the circumferential harmonics n = 0 to 15, with a sufficiently fine grid near the structural wall to simulate the sharp pressure gradients occurring in the higher harmonics. Since modes with significant harmonic content up to n = 15 were of interest, harmonic reduction was not utilized here; computational economy would not be improved by the harmonic transformation and thus only a Guyan reduction was utilized.

A series of cases including symmetric and asymmetric cylinders in the half-filled and empty configurations were studied. In addition, the effects of static pressurization were included by use of differential stiffness capability in NASTRAN.

The first cases studied pertained to the cylinder of uniform thickness. The empty cylinder was first considered with an assumed axial plane of symmetry at z = 25.4 cm such that only m = 1, 3, 5 modes would be calculated. The grid set of 1116 DOF, consisting of nodes below z = 25.4 cm, was reduced by Guyan reduction to an analysis set of 276 radial DOF with the lower end completely fixed (clamped). The unpressurized and pressurized shell frequency spectra of m = 1, $n \geq 4$ modes are illustrated in figure 6 along with the test results. The calculated frequency spectrum was higher than the experimental frequency spectrum for both unpressurized and pressurized conditions. A series of modifications of the structural model to reconcile the differences in results were considered. It was finally concluded that axial flexibility idealized as an axially free condition in the cylinder/plate weld, provided the proper correction. Incorporation of the relaxed boundary conditions

$$u_r = \frac{\partial u_r}{\partial z} = N_z = 0 \qquad \text{for } z = 0,\ 50.8 \text{ cm} \tag{42}$$

resulted in extremely accurate frequency spectra for the empty cylinder as illustrated in figure 6.

The half-filled condition was then considered. The cylinder structure in this case does not have a dynamic plane of symmetry at z = 25.4 cm; the lower portion ($z \leq 25.4$ cm) is loaded by fluid structural inertia whereas the upper portion ($z > 25.4$ cm) is loaded only by the structural inertia. This provides motivation for Guyan reduction with all degrees of freedom at and above z = 25.4 cm omitted (not including the supported degrees of freedom). A Guyan reduction on the structure and fluid was then performed resulting in an analysis set consisting of 248 radial DOF consistent with the fluid mass matrix. Hydroelastic modes, based on the clamped and modified-clamped

end conditions [eq. (40)], were then calculated. The $m = 1$, $n \geq 4$ modal frequency spectra, illustrated in figure 6, show that the representation with the relaxed end conditions is quite accurate, as concluded in the empty case.

The unsymmetric cylinder structural model consists of the same grid set as in the case of the axisymmetric cylinder, and the Guyan reduction discussed above was utilized. The hydroelastic study of this cylinder was limited to the half-filled condition with the "realistic" edge condition applied. The $m = 1$ mode shapes illustrated in figure 7 are in very good agreement with the unpressurized and pressurized test results, as are the modal frequencies.

Computation times for the cylinder study were moderate since harmonic reduction, which was not appropriate, was not utilized. In all cases considered, all 248 eigenvalues and 25 eigenvectors were calculated. Computation time for the empty axisymmetric cylinder was 509 CPU sec. Preparation of fluid matrix data required 97 CPU sec and computation of hydroelastic modes required 1,193 CPU sec. The increased CPU time required in this case is predominantly due to the increased structural grid set size of the fluid-filled cases; the increase in Guyan reduction time for systems of equivalent matrix bandwidth is proportional to the increase in grid set degrees of freedom. Computation times for the unsymmetric cylinder were similar to those required for the axisymmetric cylinder.

The 1/8-Scale Space Shuttle External Tank. An investigation of the dynamics of a 1/8-scale Space Shuttle external tank in a free-free supported condition is in progress at NASA Langley Research Center. The 1/8-scale external tank consists of two separate propellant tanks connected by a cylindrical section. Although the fluid/structure interface is axisymmetric, the tank structure contains thickness and stiffener asymmetries. The finite element hydroelastic model for half the structure, taking advantage of the single axis of symmetry, is described in detail in references 9 and 15. It consists of a grid set of 348 pressure DOF and 2058 structural DOF (and 768 harmonic structural DOF to be used in harmonic reduction). The structural grid deformed in the fundamental bending mode is illustrated in figure 8. Harmonics $n = 0, 1, 2, 3$ were chosen to describe asymmetric dynamics with the pitch plane taken as an axis of symmetry. The analysis set of displacements resulting from a combination of harmonic and Guyan reductions consists of 128 harmonic DOF associated with outward normal motion of the tank wall.

Three conditions have been studied consisting of nearly full, intermediate and empty propellant fill conditions. For each of the fill conditions, 128 natural frequencies and 25 mode shapes and modal pressure distributions were calculated with very good computational efficiency. About 20 CPU minutes per liquid level on the IBM 370/165 computer was required to perform the entire analysis including matrix assembly, reduction and modal analysis. In previous attempts to study the dynamics of the same finite element representation with the standard unsymmetric NASTRAN hydroelastic analysis, computation times were about 52 CPU minutes for only one natural frequency and mode shape from a 412-DOF analysis set (ref. 15).

Excellent agreement between analysis and experimental frequencies occurred in the first axial mode but poor agreement occurred in the bending modes. A thorough investigation of the fluid model revealed good consistency in the idealization. As a result, the source of the discrepancy is believed to be in the finite element representation of the structure which was constructed prior to the present work.

CONCLUDING REMARKS

Symmetric finite element matrix formulations for compressible and incompressible hydroelasticity have been developed on the basis of Toupin's complementary formulation of classical mechanics. The incompressible formulation applicable in propellant tank hydroelastic analysis has been implemented in NASTRAN to replace an inefficient unsymmetric matrix formulation. The new technique which utilizes existing fluid and structural finite elements has been verified and demonstrated to be accurate and efficient.

The fluid representation in the incompressible case reduces to a symmetric fluid mass matrix described in terms of surface deformation only upon recognition of a singularity in the fluid inertance matrix. The singularity describes a physically necessary compatibility condition in that it assures that the incompressible idealization will not move under uniform pressure. Moreover, the singularity defines a kinematic constraint which is applied to the structural idealization when the fluid is completely bounded by a structural interface and when free surface ullage and/or gravitational stiffness are significant. The fluid mass matrix is added directly to the structural mass matrix, forming a symmetric set of hydroelastic equations in terms of structural displacements. Modal hydroelastic analysis is performed with the same efficiency as in the case of a non-fluid-filled structure, since no additional degrees of freedom are required for the fluid (other than free surface displacements when necessary).

The efficiency of the new hydroelastic analysis technique has been enhanced for both fluid and structure by introduction of harmonic reduction, applicable to geometrically axisymmetric structures, as an alternative to Guyan reduction. When the number of harmonics utilized is much less than the number of discrete nodes about a circumference, overall matrix size and bandwidth are significantly reduced.

The formulation has been verified by comparison with exact analytical results for a fluid-filled hemispherical container and a fluid-filled circular cylindrical shell. In all cases, excellent correlation was exhibited as well as very good computational efficiency. In addition, the analysis/test correlation study on symmetric and unsymmetric circular cylindrical shells under various fluid-fill conditions is considered very good.

Analysis/test discrepancies on the 1/8-scale external tank model for the space shuttle have not yet been resolved. The efficiency of the current analysis, however, is very encouraging based upon comparison of

computation times between the present and the standard unsymmetric NASTRAN hydroelastic formulations.

The more general kinetic formulation which includes fluid compressibility has yet to be investigated in detail and applied. Typical applications include underwater explosion and acoustic analysis in general. In addition, a set of polyhedral complementary fluid finite elements should be incorporated to allow for modeling of general fluid configurations.

REFERENCES

1. Prevention of Coupled Structure-Propulsion Instability (POGO). NASA SP-8055, Oct. 1970.

2. Pinson, L. D. and Brown, C. G.: A Finite Element Method for Non-axisymmetric Vibrations of Pressurized Shells of Revolution Partially Filled with Liquid. AIAA Paper No. 73-399, Mar. 1973.

3. Feng, G. C. and Jones, C. E.: Dynamics of a Flexible Bulkhead and Contained Fluid. Lockheed Missiles and Space Co., Huntsville Res. and Eng. Center, Final Report LMSC-HREC TR D306476, May 1973.

4. Palmer, J. H. and Asher, G. W.: Calculation of Axisymmetric Longitudinal Modes for Fluid-Elastic Tank-Ullage Gas Systems and Comparison with Model Test Results. AIAA Symposium on Structural Dynamics and Aeroelasticity, Aug. 30-Sept. 1, 1965, pp. 189-193.

5. Guyan, R. J.: Study on Dynamics of an Ellipsoidal Bulkhead Containing Fluid. Rockwell International, Space Div., Tech. Summary Report SD71-183, Sept. 1971.

6. Goldman, R. L.: Longitudinal Vibration Analysis of Partially Filled Ellipsoidal Tanks by Finite Differences. RIAS Tech. Report No. TR70-6C, Aug. 1970.

7. MacNeal, R. H. (Ed.): The NASTRAN Theoretical Manual - Addendum: Chapter 16, Interaction of Structures and Fluids. NASA SP-211, Apr. 1, 1972.

8. Toupin, R. A.: A Variational Principle for the Mesh-Type Analysis of a Mechanical System. J. Appl. Mech., June 1952, pp. 151-152.

9. Coppolino, R. N.: A Numerically Efficient Finite Element Hydroelastic Analysis. Vol. I: NASA CR-2662, Apr. 1976, Vol. II: NASA CR-132684, Nov. 1974.

10. Crandall, S. N., et al: Dynamics of Mechanical and Electromechanical Systems. McGraw-Hill Book Co., 1968.

11. Svalbonas, V. and Ogilvie, P.: Numerical Analysis of Stiffened Shells of Revolution. NASA CR-2273, Sept. 1973.

12. Coppolino, R.N.: Exact Hydroelastic Solution for an Ideal Fluid in a Hemispherical Container. J. Spacecraft and Rockets, vol. 10, no. 9, Sept. 1973, pp. 612-613.

13.. Abramson, H.N. (Ed.): The Dynamic Behavior of Liquids in Moving Containers. NASA SP-106, 1966, pp. 321-338.

14. Leissa, A.W.: Vibration of Shells. NASA SP-288, 1973, pp. 62-64, 248-265.

15. Bernstein, M., et al: Development of Technology for Fluid-Structure Interaction Modeling of a 1/8-Scale Dynamic Model of the Shuttle External Tank (ET). NASA CR-132549, Aug. 1974.

TABLE I. - 60-DEG SPHERICAL CAP - COMPARISON OF MODAL FREQUENCIES

Mode		"Exact"	Harm. Red. (72 DOF)	Guyan Red. (190 DOF)
m	n	Ω_{exact}	Error*	Error
1	0	637	0.015	0.029
2		697	0.004	0.020
3		720	0.016	0.051
4		760	0.023	-----
5		820	0.028	-----
1	1	611	0.008	0.047
2		687	0.012	0.037
3		715	0.015	0.045
4		738	0.029	0.074
5		810	0.0	-----
1	2	684	0.023	0.067
2		711	0.029	0.075
3		742	0.027	0.084
4		765	0.060	-----
5		831	0.036	-----
1	3	694	-----	0.088
2		714	-----	0.103

*Error = $\frac{\Omega}{\Omega_{exact}} - 1$

TABLE II. - FLUID IN A HEMISPHERICAL CONTAINER NATURAL FREQUENCY COMPARISONS

m	Ω_{exact}*	Error**		
		n=1	n=2	n=4
1	1	0		
3	1.732	-0.02	0.089	
5	2.236	-0.02	0.059	0.032
7	2.646	-0.065	0.026	0.020
9	3.	-0.042	-0.003	-0.052
11	3.317	-0.103	-0.014	-0.038
13	3.606	-0.168	0.071	-0.073

*$\Omega_{exact} = \sqrt{m}$ m, ODD > n (see Ref. 12 for details)

**Error = $\frac{\Omega}{\Omega_{exact}} - 1$

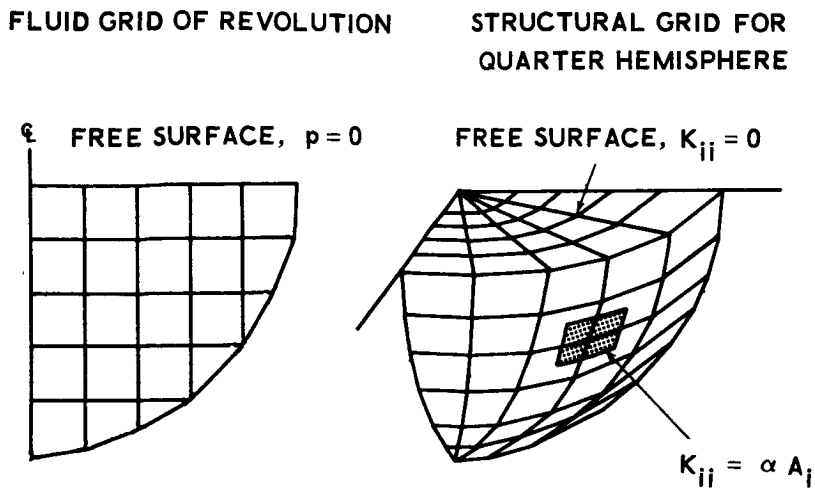

FIGURE 1. - FLUID AND HEMISPHERICAL CONTAINER MODEL

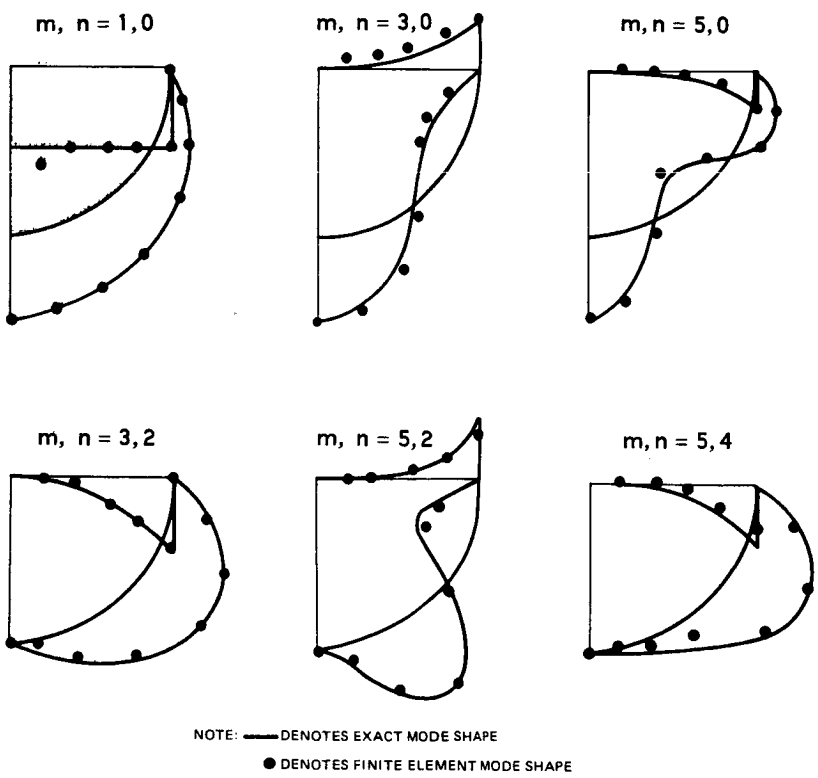

FIGURE 2. - HEMISPHERE HYDROELASTIC MODE SHAPES

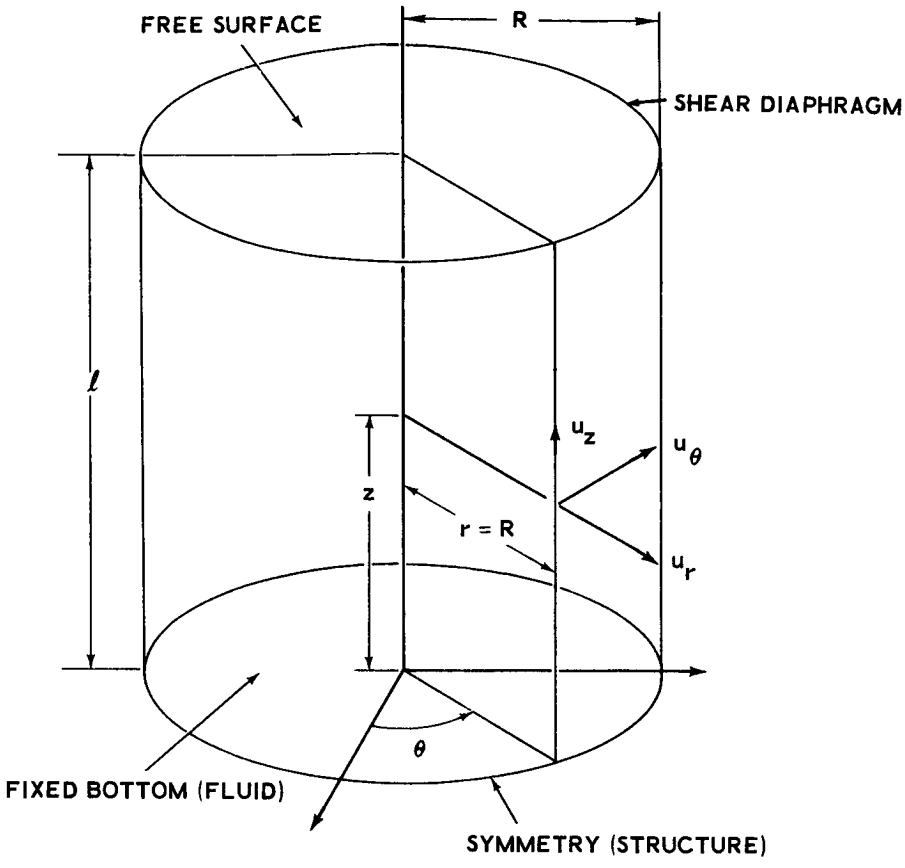

FIGURE 3. - FLUID-FILLED CIRCULAR CYLINDRICAL SHELL

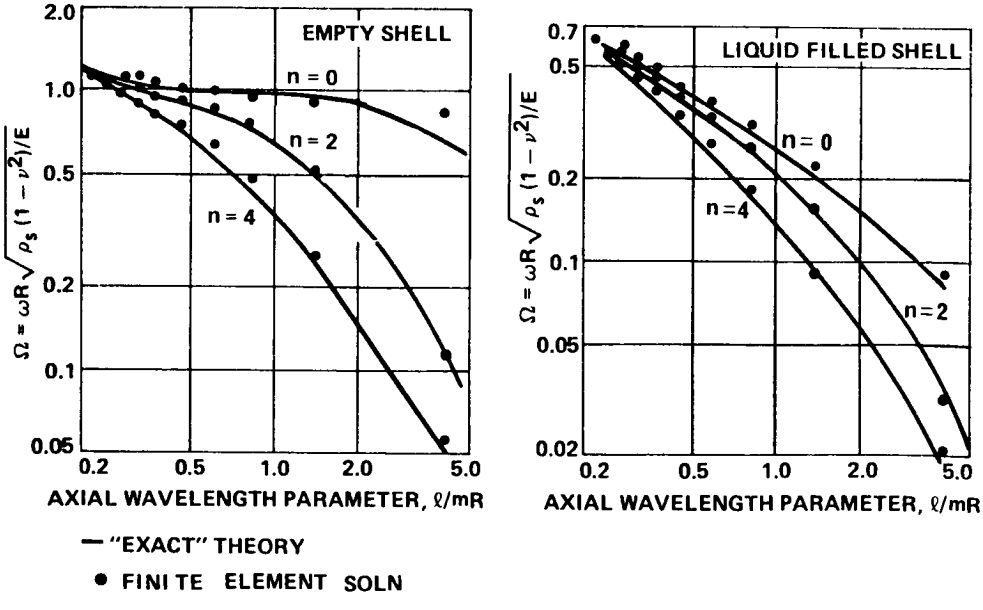

FIGURE 4. - CIRCULAR CYLINDRICAL SHELL FREQUENCY SPECTRA

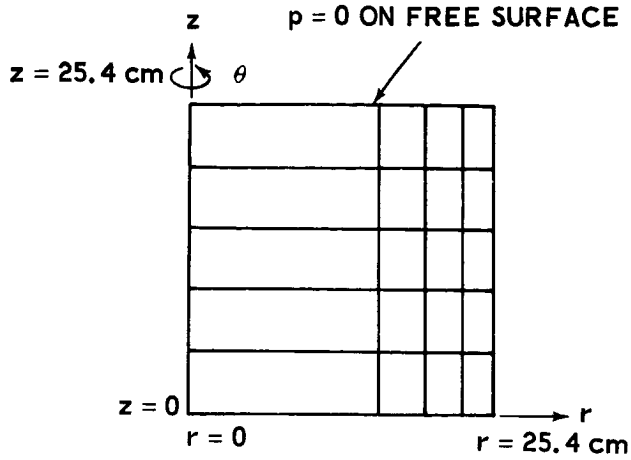

FIGURE 5. - HALF-FILLED CYLINDER FLUID IDEALIZATION

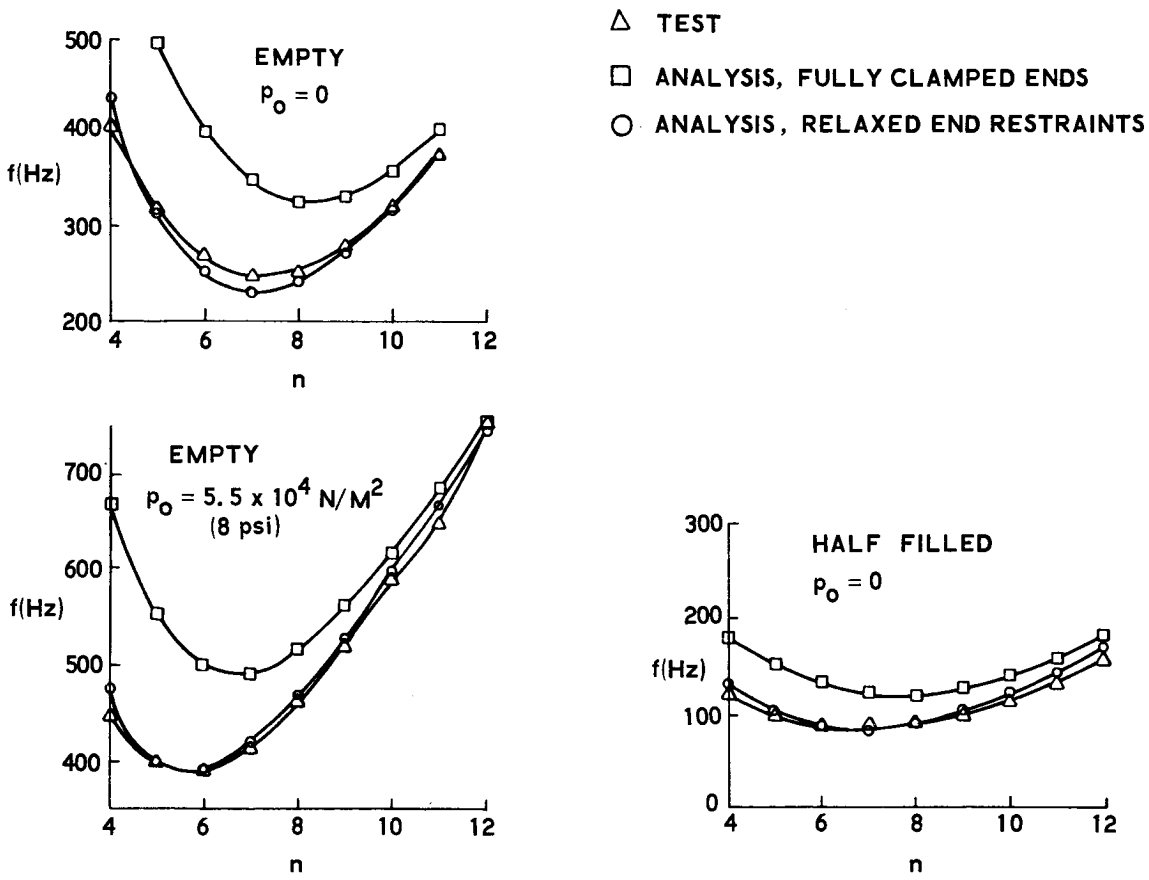

FIGURE 6. - AXISYMMETRIC CYLINDER FREQUENCY SPECTRA (m = 1 MODES)

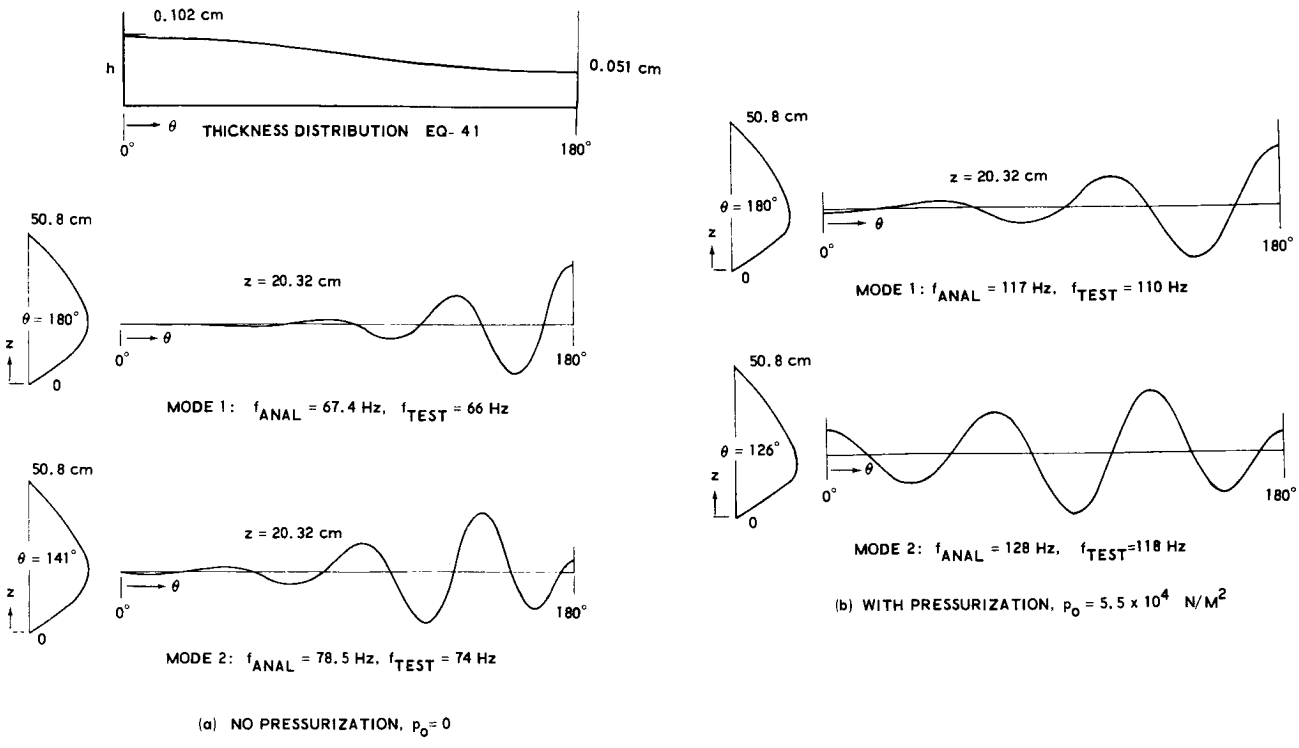

FIGURE 7. - UNSYMMETRIC CYLINDER HYDROELASTIC MODES

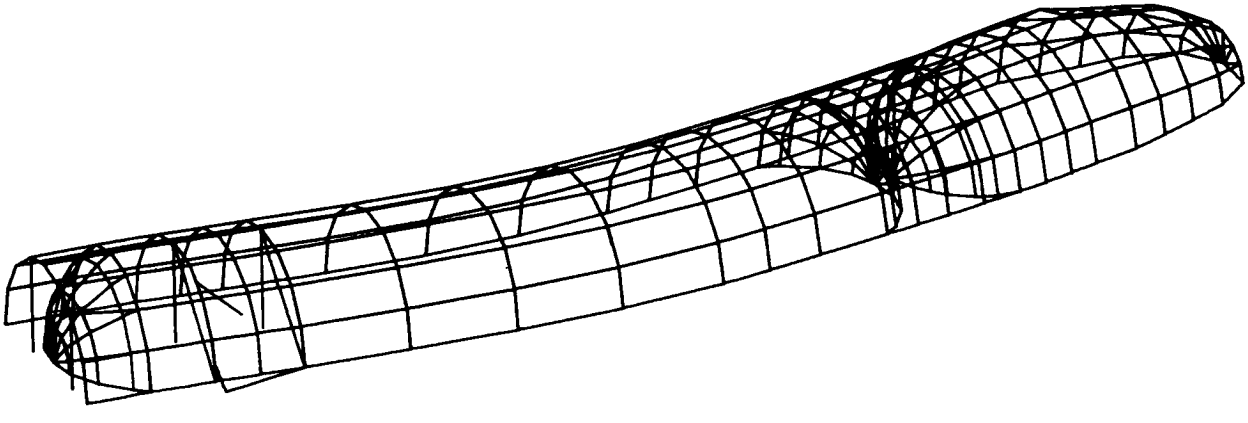

FIGURE 8. - 1/8-SCALE SPACE SHUTTLE EXTERNAL TANK FUNDAMENTAL HYDROELASTIC BENDING MODE

A NASTRAN IMPLEMENTATION OF THE DOUBLY ASYMPTOTIC APPROXIMATION FOR UNDERWATER SHOCK RESPONSE*

Gordon C. Everstine
David W. Taylor Naval Ship Research and Development Center

SUMMARY

A detailed description is given of how the decoupling approximation known as the doubly asymptotic approximation (DAA) can be implemented with NASTRAN to solve shock problems for submerged structures. The general approach involves locating the nonsymmetric terms (which couple structural and fluid variables) on the right-hand side of the equations. This approach results in coefficient matrices of acceptable bandwidth but degrades numerical stability, requiring a smaller time step size than would otherwise be used. It is also shown how the structure's added (virtual) mass matrix, a necessary ingredient to DAA, can be calculated with NASTRAN. The version of NASTRAN used is NASA's standard level 16 with one program modification, velocity-dependent nonlinear loads, for which the FORTRAN changes are listed.

STATEMENT OF THE PROBLEM

The general class of problems known as fluid-structure interaction problems includes the special case of determining the shock response of submerged structures. This is of particular interest to naval engineers concerned with the dynamic structural response of submarines (including the hull, appendages, and internal equipment).

Consider the idealized situation consisting of a ring-stiffened cylindrical shell with flat end caps which is deeply submerged in water, initially at rest, and subjected to the shock of a distant underwater explosion (fig. 1). The general problem is to compute the time-dependent elastic structural response of the cylinder. We will further simplify the problem with the following assumptions:

1. The shock wavefront in the vicinity of the cylinder is planar, a reasonable assumption whenever the source of the shock is located far away.

2. The time history of the free-field incident pressure is a step function. This assumption can be made without loss in generality since the

* Sponsored in part by the joint DNA/Navy program in "Advanced Submarine Shock Survivability in Underwater Nuclear Attack."

structural response to an arbitrary time variation of the pressure history can be easily obtained by a convolution integral involving the step response. (See Appendix D.)

3. The shock wave hits the cylinder from the side rather than from the end or from some more general oblique direction. This assumption results primarily in simplifying the data deck which describes the problem. Removing the restriction presents no conceptual difficulty.

BACKGROUND

In either the absence or the presence of the surrounding water, the structure can be modeled with finite elements in the usual way: with plate or shell elements for the unstiffened cylinder, and with beam elements for the ring stiffeners.

The fluid is generally treated as an acoustic medium (e.g., see ref. 1): a compressible, inviscid fluid which undergoes only small amplitude motion and whose pressure p satisfies the wave equation

$$\nabla^2 p = \ddot{p}/c^2 \tag{1}$$

where dots indicate time differentiation and c is the speed of sound. At an interface between the fluid and a solid

$$\frac{\partial p}{\partial n} = -\rho\, \ddot{u}_n \tag{2}$$

where n is the unit outward normal from the solid at the interface, ρ is the fluid mass density, and u_n is the outward normal component of displacement of the interface.

In principle, the fluid part of the problem can be handled by modeling a portion of the fluid with finite elements (refs. 2, 3). In reference 3, for example, the analogy was drawn between the scalar wave equation (1) and the elasticity equations so that a standard structural analysis computer program like NASTRAN (refs. 4, 5) can be used to solve problems involving the wave equation, Poisson's equation, or Laplace's equation. For finite fluid regions such an approach presents no significant problems. However, for structures submerged in infinite fluids, the analyst is faced with the additional problem of truncating the fluid and applying a radiation condition at the artificial boundary in order to absorb outgoing waves. Even if a reasonable radiation condition could be formulated, the cost of explicit fluid modeling could be prohibitive.

An attractive alternative to such modeling is provided by approximations (refs. 6, 7) which uncouple the structural response from the fluid response in the sense that the fluid pressure at the fluid-structure interface is determined (approximately) from a knowledge of only the interface motion. Although

several such decoupling approximations have been formulated, one which is currently attracting attention is the doubly asymptotic approximation (DAA) of Geers (ref. 6). This paper shows how the DAA scheme can be cast in a form which can be conveniently solved by NASTRAN. The version of NASTRAN used is NASA's standard level 16 with one program modification: velocity-dependent nonlinear loads. The less efficient earlier version of NASTRAN, level 15, can also be used, although at greater computer expense. The addition of velocity-dependent nonlinear load capability is convenient, but not crucial, for the NASTRAN implementation of DAA.

THE DOUBLY ASYMPTOTIC APPROXIMATION (DAA)

A submerged structure subjected to an underwater shock wave experiences, at any given time t, a total dynamic pressure p which can be considered to comprise two components: an incident pressure p_i which would occur if no obstacle (the structure) were present, and a scattered pressure p_s which is the difference between the total pressure and the incident pressure. Thus,

$$p = p_i + p_s \tag{3}$$

The scattered pressure p_s is sometimes further decomposed as

$$p_s = p_{rs} + p_r \tag{4}$$

where p_{rs} is the scattered pressure which would result if the structure were rigid and stationary and p_r, the radiated pressure, is the remainder. Of the three components of pressure, only p_r depends on the structural motion, whereas both p_i and p_{rs} can be computed as if the structure were rigid and stationary.

For the submerged ring-stiffened cylinder of interest (fig. 1), the plane wave incident pressure p_i is taken to be a step function (with wavefront moving to the left):

$$p_i(x,t) = p_0 H(x - x_0 + ct) \tag{5}$$

where H is the dimensionless Heaviside unit step function (zero for negative argument and unity for positive argument), x_0-ct is the location of the wavefront at time t, c is the speed of sound, and p_0 is a constant.

The scattered pressure p_s, which depends on the structural motion and hence cannot be precomputed as a function of time, is determined by the doubly asymptotic approximation (DAA) (ref. 6) from

$$\dot{p}_s + \rho c M_a^{-1} A p_s = \rho c \ddot{\bar{u}}_s \tag{6}$$

where p_s is the vector of unknown scattered pressures at the wet grid points of

the structure, M_a is the (full) added mass matrix for the structure (see Appendix A), ρ and c are the fluid mass density and sound speed, respectively, A is a diagonal area matrix converting grid point pressures to grid point forces, and $\ddot{\bar{u}}_s$ is the vector of scattered wave particle accelerations normal to the structure's surface. The bar is used to distinguish this vector from the complete acceleration vector $\ddot{u}_s$, which involves all structural degrees of freedom rather than just the normal components at wet points. Surface normals are taken as positive going into the fluid.

Surface normal accelerations, like pressures, are decomposed into incident and scattered components; hence,

$$\ddot{\bar{u}}_s = \ddot{\bar{u}} - \ddot{\bar{u}}_i \tag{7}$$

where $\ddot{\bar{u}}$ is the vector of total normal accelerations at the wet grid points, and $\ddot{\bar{u}}_i$ is the vector of normal components (positive into the fluid) of incident fluid particle accelerations.

Equation (6) was designated "doubly asymptotic" because it exhibits the correct asymptotic behavior at both the low and high frequency limits: at the low frequency limit (which normally corresponds to late time behavior for transient situations), the first term of (6) is dominated by the second term, and (6) reduces to

$$F_s = A p_s = M_a \ddot{\bar{u}}_s \tag{8}$$

in which the fluid loading is due to added (virtual) mass effects alone. At the high frequency limit (early time behavior), the first term of (6) dominates the second term, and (6) reduces to

$$p_s = \rho c \dot{\bar{u}}_s \tag{9}$$

which is the usual radiation damping relation. Equations (8) and (9) are referred to individually as the virtual mass and plane wave approximations, respectively.

In general, the DAA, equation (6), yields better results than either of the special cases, equations (8) or (9). Huang (ref. 8) compared a DAA solution to an exact solution for a spherical shell and found that the DAA solution had slightly faster oscillations and stronger damping. Nevertheless, the DAA provides a good compromise between cost and accuracy for underwater shock problems.

DAA WITH NASTRAN

The differential equation of motion for the ring-stiffened cylinder of interest (fig. 1) is

$$M\ddot{u} + Ku = -\bar{A}p = -\bar{A}(p_i + p_s) \tag{10}$$

where u is the vector of unknown displacements at the grid points, M and K are the structure's finite element mass and stiffness matrices, respectively, p is the vector (of dimension equal to the number of wet grid points) of fluid pressures at the wet grid points, and $\bar{A}$ is an area matrix converting pressures to forces. $\bar{A}$ is not square (and hence not diagonal) because the vectors u and p are of different dimension. $\bar{A}$ contains non-zeros (equal to the area contributions) only at the intersections of rows corresponding to wet structural degrees of freedom with the columns of associated pressure variables. Thus, each row and column of $\bar{A}$ has at most one non-zero entry. $\bar{A}$ reduces to A if the zero rows are deleted and if the wet structural degrees of freedom are sequenced in the same order as the corresponding fluid pressure degrees of freedom. The area matrices defined here are "lumped" rather than "consistent". To switch to consistent loading, one need only change the area matrices A and $\bar{A}$.

In equation (10), the total dynamic fluid pressure p is decomposed into incident and scattered pressures given by equations (5) and (6), respectively. Since (6) is a differential equation, the complete problem involves solving (10) and (6) simultaneously, where the right-hand side of (6) is replaced by its equivalent from equation (7).

The incident fluid particle normal acceleration vector $\ddot{\bar{u}}_i$ is computed as follows: In general, the ratio of the pressure to the volume strain defines the bulk modulus k. Since $k = \rho c^2$ for the acoustic fluid, we have, for a plane wave,

$$p = -k\frac{\partial u_x}{\partial x} = -\rho c^2 \frac{\partial u_x}{\partial x} \tag{11}$$

In particular, for the incident component,

$$p_i = -\rho c^2 \frac{\partial u_{xi}}{\partial x} \tag{12}$$

From (5) and (12), it follows that

$$p_i = -\rho c \dot{u}_{xi} \tag{13}$$

where $\dot{u}_{xi}$ is the x-component of incident fluid particle velocity. The normal component of incident particle velocity $\dot{\bar{u}}_i$ is

$$\dot{\bar{u}}_i = \dot{u}_{ix} \cos\theta \tag{14}$$

Hence

$$p_i \cos\theta = -\rho c \dot{\bar{u}}_i \tag{15}$$

Because p_i as given by (5) is a step function, the $\ddot{\bar{u}}_i$ needed on the right-hand side of (6) is a Dirac delta. This problem can be avoided by defining a new variable q such that

$$\dot{q} = p_s \tag{16}$$

and time integrating equation (6). Equations (10) and (6) then become

$$\begin{aligned} M\ddot{u} + Ku &= -\bar{A}p_i - \bar{A}\dot{q} \\ A\dot{q} + \rho c A M_a^{-1} A q &= \rho c \bar{A}^T \dot{u} + A p_i \cos\theta \end{aligned} \tag{17}$$

where the second of equations (17) has also been multiplied by the area matrix A to symmetrize the coefficient matrices, and

$$A\dot{\bar{u}} = \bar{A}^T \dot{u} \tag{18}$$

In matrix format, these equations are

$$\begin{bmatrix} M & \\ & 0 \end{bmatrix} \begin{Bmatrix} \ddot{u} \\ \ddot{q} \end{Bmatrix} + \begin{bmatrix} 0 & \\ & A \end{bmatrix} \begin{Bmatrix} \dot{u} \\ \dot{q} \end{Bmatrix} + \begin{bmatrix} K & \\ & \rho c A M_a^{-1} A \end{bmatrix} \begin{Bmatrix} u \\ q \end{Bmatrix} = \begin{Bmatrix} -\bar{A}p_i - \bar{A}\dot{q} \\ \rho c \bar{A}^T \dot{u} + A p_i \cos\theta \end{Bmatrix} \tag{19}$$

which is the form of the equations which NASTRAN uses.

It is interesting to observe that the new variable q defined by equation (16) is, in essence, the (scattered) velocity potential, since for an acoustic fluid the velocity potential ϕ is related to the pressure p by (ref. 9)

$$p = -\rho\dot{\phi} \tag{20}$$

Thus, as a consequence of trying to avoid the numerical problem of a Dirac delta, the fundamental unknown for the fluid is switched from the pressure to the velocity potential, thus returning to the established convention of fluid dynamicists.

In equation (19), the unknowns u and q are defined using GRID cards. For the variables q, only one degree of freedom per point is retained. The usual finite element modeling of the structure yields M and K. The damping matrix is created by attaching dashpots (CDAMPi) between each interface fluid point and ground. The fluid matrix $\rho c A M_a^{-1} A$ can be assembled either by supplying it directly (on DMIG or DMI cards) or by letting NASTRAN compute it using an explicit finite element model of a portion of the fluid region. In Appendix A, it is shown that

$$\rho c A M_a^{-1} A = c H \tag{21}$$

where H is the fluid stiffness matrix condensed to the wet degrees of freedom. This condensation (using OMIT cards) is not necessary for the calculation but may result in a faster integration. The multiplicative constant c in the term cH, equation (21), can be automatically incorporated by setting the shear modulus on the MAT1 card equal to c rather than unity.

The right-hand side of (19) consists of both time-dependent and velocity-dependent loads, which are supplied using TLOAD1 and NOLIN1 cards, respectively. (See Appendix C.) The input of the incident pressure is particularly simple since it is a step function. The input data can be further simplified by using the DELAY card to indicate that the incident wavefront (which is traveling at speed c) does not reach all points at the same time.

In equation (19), M and A are diagonal matrices, and K and H are positive definite and symmetric. K is also large and banded. H can be either large and banded, or small and full, depending on whether a static condensation (with OMIT's) is applied to it.

The unknowns in equation (19) are arranged so that the structural and fluid variables are uncoupled on the left-hand side, the only coupling occurring on the right. Thus the grid points should be sequenced to maintain the indicated partitioning and to give both K and H the smallest possible matrix wavefront (refs. 10, 11).

The time step size needed to achieve numerical stability when the velocity-dependent terms are on the right was found to be about 1/10 of the transit time (the time required for a wave to travel one radius of the cylinder at speed c).

ALTERNATIVE DAA APPROACHES

Since the velocity-dependent loads in equation (19) are linear, they can be moved to the left-hand side and incorporated in the damping matrix. Symmetry (but not positive definiteness) is then retained by dividing the second equation in (19) by $-\rho c$. Since this formulation causes fluid-structural coupling on the left, the unknowns have to be sequenced taking into account this new connectivity. This approach is practical only if the fluid stiffness matrix $\bar{H}$ is not condensed but left large and banded, so that the overall system can be made banded. Otherwise, the added mass matrix coupling causes non-zeros far off the matrix diagonals.

The principal advantage in placing the velocity-dependent terms on the left is numerical stability, so that a larger integration time step can be used. With those terms on the right, as in equation (19), the matrix bandwidth (and hence wavefront) is smaller, and the user has the option of condensing the fluid "stiffness" matrix $c\bar{H}$ into the smaller, but full, matrix $\rho c A M_a^{-1} A$.

Another possible way to formulate the DAA is to make use of the decomposition of scattered pressure p_s into rigid body scattered and radiated components (eq. (4)). Since only the radiation pressure p_r depends on structural motion, the rigid body scattered pressure p_{rs} can be precomputed and combined with the incident pressure p_i. In that case, the DAA (eq. (6)) must supply only p_r, which satisfies

$$\dot{p}_r + \rho c M_a^{-1} A p_r = \rho c \ddot{\bar{u}}_r \tag{22}$$

where the normal component of fluid particle acceleration at the fluid-solid interface is decomposed into

$$\ddot{\bar{u}} = \ddot{\bar{u}}_i + \ddot{\bar{u}}_{rs} + \ddot{\bar{u}}_r \tag{23}$$

For rigid stationary structures, equation (23) simplifies to

$$\ddot{\bar{u}}_i + \ddot{\bar{u}}_{rs} = 0 \tag{24}$$

at the interface, so that, in general,

$$\ddot{\bar{u}} = \ddot{\bar{u}}_r \tag{25}$$

at the interface. Thus, (22) is equivalent to

$$\dot{p}_r + \rho c M_a^{-1} A p_r = \rho c \ddot{\bar{u}} \tag{26}$$

The advantage of this general approach is that the rigid body scattered pressure p_{rs} can be computed in advance to whatever accuracy one wants, so that the only approximation remaining involves the radiation pressure p_r. The disadvantage, however, is that the pre-calculation (a nontrivial one) has to be done at all. The decision of whether to use equation (6) or (26) also depends on the relative sizes of p_{rs} and p_r, since if p_{rs} were small it would not make sense to compute it accurately. Unfortunately, the relative sizes are problem-dependent and hard to estimate.

EXPLICIT FINITE ELEMENT FLUID MODELING

The problem of computing the linear shock response of submerged structures can, in principle, be solved by explicit finite element modeling of a portion of the fluid volume. The purpose of this section is to formulate the problem sufficiently so that it can be solved by NASTRAN once the user has picked a suitable radiation condition to apply at the outer fluid boundary.

The total dynamic fluid pressure satisfies the wave equation (1) in the field. This pressure can be decomposed into the sum of incident and scattered pressures, p_i and p_s, as in equation (3). Since p_i is defined to satisfy (1),

p_s must also satisfy the wave equation (1). At a fluid-solid interface, the boundary condition (2) becomes

$$\frac{\partial p_s}{\partial n} = - \frac{\partial p_i}{\partial n} - \rho \ddot{\bar{u}} \tag{27}$$

where, for the finite cylinder of figure 1 subjected to a plane wave incident pressure, equation (5), we have

$$\frac{\partial p_i}{\partial n} = \underset{\sim}{\nabla} p_i \cdot \underset{\sim}{n} = \frac{\partial p_i}{\partial x} \cos \theta \tag{28}$$

and

$$\frac{\partial p_i}{\partial x} = \frac{1}{c} \dot{p}_i \tag{29}$$

Thus, from (27),

$$\frac{\partial p_s}{\partial n} = - \frac{1}{c} \dot{p}_i \cos \theta - \rho \ddot{\bar{u}} \tag{30}$$

The above Neumann boundary condition is equivalent to specifying a "load" on each interface pressure variable p_s equal to

$$A\left(\frac{1}{c}\dot{p}_i \cos \theta + \rho \ddot{\bar{u}}\right) \tag{31}$$

where A is the area associated with the interface point, so that the resulting finite element equations take the form (ref. 3)

$$\begin{bmatrix} M & \\ & cQ \end{bmatrix} \begin{Bmatrix} \ddot{u} \\ \ddot{q} \end{Bmatrix} + \begin{bmatrix} K & \\ & c\bar{H} \end{bmatrix} \begin{Bmatrix} u \\ q \end{Bmatrix} = \begin{Bmatrix} -\hat{A} p_i - \hat{A} \dot{q} \\ \tilde{A} p_i \cos \theta + \rho c \hat{A}^T \dot{u} \end{Bmatrix} \tag{32}$$

where here q, defined as in equation (16), includes all fluid points, not just interface points. The area matrices also have to be redefined slightly to reflect the change in dimension of the vector q. The above formulation is consistent with the definitions of fluid inertia Q and stiffness $\bar{H}$ given in Appendix A, which differ from the definitions of ref. 3 by a constant factor ρc^2.

Equation (32) is complete except for a radiation condition on the pressure variable q. Once the user decides what radiation condition to use, it can be incorporated into the matrix equation (32).

It is interesting to observe the similarity between the explicit finite element formulation, equation (32), and that which arises from the doubly asymptotic approximation, equation (19). The right-hand sides and the overall stiffness matrices are the same in both cases. In (32), the overall mass

matrix now includes the fluid inertia, which NASTRAN computes whenever the user supplies a non-zero mass density, in this case equal numerically to 1/c. The damping matrix in (19) also appears in (32) if a radiation condition involving dashpots is used, although in (32) the dashpots connect the outer boundary points, rather than the interface pressure points, to ground.

Another approach using explicit fluid modeling was recently described by Newton and Atchison (ref. 12), who elected to use the full fluid pressure p (rather than p_s) as the fundamental pressure unknown. In that case, the time-dependent part of the right-hand side of the equations of motion is replaced by a non-zero initial condition on p and $\dot{p}$ throughout the fluid region.

The main impediments to solving the shock problem by these approaches are the potentially high cost of modeling a three-dimensional region of fluid and the difficulty in determining the radiation condition. For one-dimensional problems, the correct radiation condition merely involves attaching grounded dashpots to the outer fluid boundary (ref. 2). However, for general three-dimensional situations, the mathematically exact radiation condition is a more complicated relation (which cannot be modeled using only masses, springs, and dashpots) coupling all pressure variables at the outer boundary (ref. 13). Since the implementation of such a condition is impractical, the analyst must resort to approximate radiation conditions which will not absorb 100% of outgoing waves. It is for reasons like these that decoupling approximations such as DAA are being used.

REFERENCES

1. Geers, T.L.: "Transient Response Analysis of Submerged Structures," Finite Element Analysis of Transient Nonlinear Structural Behavior, AMD-Vol. 14, edited by T. Belytschko, J.R. Osias, and P.V. Marcal, The American Society of Mechanical Engineers, New York, 1975, pp. 59-84.

2. Zienkiewicz, O.C., and Newton, R.E.: "Coupled Vibrations of a Structure Submerged in a Compressible Fluid," Proc. Int. Symp. on Finite Element Techniques, Stuttgart, 1969.

3. Everstine, G.C., Schroeder, E.A., and Marcus, M.S.: "The Dynamic Analysis of Submerged Structures," NASTRAN: Users' Experiences, NASA TM X-3278, Sept. 1975, pp. 419-429.

4. "The NASTRAN Theoretical Manual," NASA SP-221(03), Washington, D.C., March 1976.

5. "The NASTRAN User's Manual," NASA SP-222(03), Washington, D.C., March 1976.

6. Geers, T.L.: "Residual Potential and Approximate Methods for Three-Dimensional Fluid-Structure Interactions Problems," J. Acoust. Soc. Amer., vol. 49, no. 5 (part 2), 1971, pp. 1505-1510.

7. Clark, A.V., Jr.: "A Study of Fluid-Structure Interaction and Decoupling Approximations," Naval Research Laboratory Report 7590, Washington, D.C., December 1973.

8. Huang, H.: "A Qualitative Appraisal of the Doubly Asymptotic Approximation for Transient Analysis of Submerged Structures by Weak Shock Waves," NRL Memorandum Report 3135, Naval Research Laboratory, Washington, D.C., Sept. 1975.

9. Newton, R.E.: "Finite Element Analysis of Two-Dimensional Added Mass and Damping," chap. 11 in Finite Elements in Fluids, vol. 1, ed. by R.H. Gallagher, J.T. Oden, C. Taylor, and O.C. Zienkiewicz, John Wiley and Sons, Ltd., London, 1975, pp. 219-232.

10. Everstine, G.C.: "The BANDIT Computer Program for the Reduction of Matrix Bandwidth for NASTRAN." NSRDC Report 3827, Naval Ship Research and Development Center, Bethesda, Md., March 1972.

11. Everstine, G.C.: "Recent Improvements to BANDIT," NASTRAN: Users' Experiences, NASA TM X-3278, September 1975, pp. 511-521.

12. Newton, R.E., and Atchison, D.L.: "Response of a Ring-Stiffened Cylinder to an Acoustic Blast Wave," Second International Symposium on Finite Element Methods in Flow Problems, S. Margherita Ligure, Italy, June 1976, pp. 701-713.

13. Zarda, P.R.: "A Finite Element-Analytical Method for Modeling a Structure in an Infinite Fluid," NASTRAN: Users' Experiences, NASA TM X-3428, October 1976.

14. Protter, M.H., and Weinberger, H.F. : Maximum Principles in Differential Equations, Prentice-Hall, Inc., Englewood Cliffs, N.J., 1967.

15. Khabbaz, G.R.: "Dynamic Behavior of Liquids in Elastic Tanks," AIAA Journal, vol. 9, no. 10, October 1971, pp. 1985-1990.

16. Gallagher, R.H.: Finite Element Analysis Fundamentals, Prentice-Hall, Inc., Englewood Cliffs, N.J., 1975.

17. Streeter, V.L.: Fluid Dynamics, McGraw-Hill Book Company, Inc., New York, 1948.

18. Przemieniecki, J.S.: Theory of Matrix Structural Analysis, McGraw-Hill Book Company, Inc., New York, 1968.

19. Glockner, P.G.: "Symmetry in Structural Mechanics," J. Struct. Div., Proc. ASME, vol. 99, no. ST1, Jan. 1973, pp. 71-89.

20. Joseph, J.A., editor: "MSC/NASTRAN Application Manual for CDC 6000 Series," MSR-32, The MacNeal-Schwendler Corporation, Los Angeles, Calif., 1975; also, pub. no. 86616700, Control Data Corporation, Data Services Publications, Minneapolis, Minn., 1975.

21. Hildebrand, F.B.: Advanced Calculus for Applications, Prentice-Hall, Inc., Englewood Cliffs, N.J., 1963.

APPENDIX A - ADDED MASS MATRICES

Consider an elastic structure submerged in a finite acoustic fluid, whose pressure p satisfies the wave equation

$$\nabla^2 p = \ddot{p}/c^2 \tag{A1}$$

where c is the speed of sound in the fluid. If both structure and fluid are modeled with finite elements, the resulting matrix equations take the general form (refs. 2, 3)

$$\begin{bmatrix} M & 0 \\ -\rho\hat{A}^T & Q \end{bmatrix} \begin{Bmatrix} \ddot{u} \\ \ddot{p} \end{Bmatrix} + \begin{bmatrix} K & \hat{A} \\ 0 & \bar{H} \end{bmatrix} \begin{Bmatrix} u \\ p \end{Bmatrix} = \begin{Bmatrix} f \\ 0 \end{Bmatrix} \tag{A2}$$

where M and K are the usual structural mass and stiffness matrices, Q and $\bar{H}$ are the inertia and "stiffness"matrices for the fluid, $\hat{A}$ is the area matrix converting pressure to force at the fluid-structure interface nodes, and ρ is the fluid's mass density.

In equation (A2), $\bar{H}$ can be assembled from standard 3-D elasticity finite elements (ref. 3) if only the x-component of displacement at each point is retained (to represent the scalar quantity p) and Hooke's law is specified as

$$\begin{Bmatrix} \sigma_{xx} \\ \sigma_{yy} \\ \sigma_{zz} \\ \sigma_{xy} \\ \sigma_{yz} \\ \sigma_{xz} \end{Bmatrix} = \begin{bmatrix} 1 & -1 & -1 & & & \\ -1 & 1 & -1 & & & \\ -1 & -1 & 1 & & & \\ & & & 1 & & \\ & & & & 1 & \\ & & & & & 1 \end{bmatrix} \begin{Bmatrix} \varepsilon_{xx} \\ \varepsilon_{yy} \\ \varepsilon_{zz} \\ \gamma_{xy} \\ \gamma_{yz} \\ \gamma_{xz} \end{Bmatrix} \tag{A3}$$

In terms of the usual engineering constants, equation (A3) is equivalent (numerically) to choosing the shear modulus G and Young's modulus E as

$$G = 1$$

$$E = \alpha G, \ \alpha >> 1$$

whose α must be large enough so that $\alpha+1$ is indistinguishable (numerically) from α. On most computers, $\alpha = 10^{20}$ suffices. Equation (A4) applies only in three dimensions. In two dimensions (plane stress), the corresponding constants are

$$G = 1$$
$$E = \beta G, \ \beta << 1 \tag{A5}$$

where β should not be so small that $1+\beta$ is indistinguishable (numerically) from unity. On most computers, $\beta = 10^{-4}$ suffices.

Equation (A5) also applies to axisymmetric problems formulated in cylindrical coordinates with axisymmetric elements such as NASTRAN's CTRAPRG. However in this case only the z-component of displacement can be used to represent pressure, in contrast to Cartesian coordinates in which any of the three translation components can be used.

In equation (A2), Q can be assembled from standard elasticity finite elements (ref. 3) if the mass density assigned to the material is numerically equal to $1/c^2$.

For an incompressible fluid, $c \to \infty$ (or the frequency $\omega \to 0$) and the wave equation (A1) reduces to Laplace's equation

$$\nabla^2 p = 0 \tag{A6}$$

Also, $Q = 0$, so that p can be eliminated from (A2) to yield

$$(M + \rho \hat{A} \bar{H}^{-1} \hat{A}^T) \ddot{u} + K u = f \tag{A7}$$

thus defining the added mass matrix

$$\bar{M}_a = \rho \hat{A} \bar{H}^{-1} \hat{A}^T \tag{A8}$$

for the submerged structure.

We observe that the area matrix $\hat{A}$ is non-square since the vectors u and p are of different dimension. In addition, $\hat{A}$ is such that each row or column has but one non-zero entry. This entry is the area assigned to a particular node and located at the row corresponding to the nodal outward normal displacement and column corresponding to the associated pressure variable. Thus, since $\hat{A}$ involves only the interface variables, the fluid stiffness matrix $\bar{H}$ in equation (A8) can be reduced by static condensation (Guyan reduction) prior to performing the matrix product in (A8). If the condensed stiffness matrix is denoted H, then the corresponding added mass matrix is

$$M_a = \rho A H^{-1} A \tag{A9}$$

where A is the diagonal area matrix and M_a involves only wet degrees of freedom rather than all structural degrees of freedom as in $\overline{M}_a$.

A physical interpretation of a particular ij entry in M_a or $\overline{M}_a$ is that it is the normal fluid force induced at point i (on the fluid-structure interface) due to a unit normal acceleration at interface point j, with all other points held fixed. Thus, it is clear that M_a is a fully populated matrix. Since the interface boundary condition is

$$\frac{\partial p}{\partial n} = -\rho \ddot{u}_n \tag{A10}$$

the specification of acceleration at the interface is equivalent to a Neumann boundary condition. Hence, the calculation of the added mass matrix is mathematically equivalent to solving Laplace's equation (A6) in the fluid region with Neumann boundary conditions. For uniqueness, p must be specified somewhere.

This Neumann problem is also equivalent to a steady-state heat conduction problem in which one seeks the temperatures at all mesh points (on the fluid-solid interface) due to a unit heat source at each such point in turn. The matrix $\overline{H}$ in equation (A8) is exactly the heat conduction "stiffness" matrix computed by finite element heat transfer computer programs if the thermal conductivity is specified as unity.

Since, in heat conduction problems, the extreme temperatures must occur on the boundary, and uneven temperature distributions can be maintained only by supplying heat at the warmest point on the boundary and removing heat from the coolest point (ref. 14), it follows that the individual elements of the added mass matrix are always positive.

Thus far, this discussion of added mass matrices has assumed the fluid region to be finite. Of more interest in naval applications is the infinite region. In this case one can define and model a finite region of fluid whose outer boundary (where p=0) is "sufficiently far" from the structure. The major problem facing the analyst is deciding where to locate this outer boundary. For a given problem, one approach to insure that the outer boundary is distant enough is to compute the added mass matrix M_a (condensed to include only wet degrees of freedom) with two different locations of the outer boundary and look for convergence of the dominant terms in the matrix.

The calculation of added mass matrices for structures submerged in infinite fluids would be more appealing if it did not involve the explicit modeling of a portion of the fluid. Since the problem to be solved is a Neumann problem in the infinite region surrounding the structure, it can also be formulated in terms of simple sources distributed over the fluid-solid interface (ref. 15). For economy, the source density distribution is usually assumed constant over each surface element. Consequently all matrices (including the added mass matrix) refer to element centroids rather than to the finite element grid points. One possible approach for transforming an added mass matrix from element to grid point values is as follows: For simplicity assume a rectangular mesh of surface elements (fig. 2), where a typical element

(number 4) is shown connecting grid points 5, 6, 15, and 16. The simplest relationship between the central and nodal displacements is the arithmetic average

$$\hat{u}_4 = (u_5 + u_6 + u_{15} + u_{16})/4 \tag{A11}$$

A more complicated relation taking into account the element shape function can also be written. The complete transformation involving all elements is of the form

$$\hat{u} = \Gamma u \tag{A12}$$

where $\hat{u}$ is the displacement vector for the element centroids, u is the displacement vector for the grid points, and Γ is the transformation matrix. The added mass matrix can then be computed from

$$M_a = \Gamma^T \hat{M}_a \Gamma \tag{A13}$$

which is the usual transformation relationship for finite element matrices (ref. 16). In equation (A13), $\hat{M}_a$ is the added mass matrix referred to centroidal coordinates. The transformation (A13) may result in converting $\hat{M}_a$, which is non-singular, into a singular matrix M_a.

Virtual Mass

It is of interest to relate the added mass matrix (as used here) to the added mass (virtual mass) defined by hydrodynamicists (e.g., ref. 17). Virtual mass is a scalar quantity defined and computed for rigid structures oscillating in a specific rigid body motion, e.g., heave of a ship hull form. Since the added mass matrix is general enough to allow arbitrary elastic structural motion, virtual mass is merely a special case.

Recall that a physical interpretation of the added mass matrix is that a particular ij entry is the normal fluid force at point i due to a unit normal acceleration at j, with all other points held fixed. In computing virtual mass, the acceleration at all points is specified, and the component of force in a particular direction is desired. For example, if ϕ is a vector describing the amplitude of the desired rigid body motion, the virtual mass m in the same direction is

$$m = \phi^T M_a \phi \tag{A14}$$

where M_a is the added mass matrix and each component of ϕ is equal to the cosine of the angle between the surface normal at a point and the direction of motion (assuming unit amplitude motion). Equation (A14) is identical in form to the definition of generalized mass for vibration mode shapes (ref. 18).

In general, there exist six rigid body modes (three translations and three rotations), each of which induces six components of force. Thus (A14) can be

generalized to define a 6x6 rigid body virtual mass matrix m whose ij entry is

$$m_{ij} = \phi_i^T M_a \phi_j \tag{A15}$$

where ϕ_j is the vector specifying the rigid body acceleration and ϕ_i is the vector describing the direction of the generalized force induced.

APPENDIX B - USE OF STRUCTURAL SYMMETRY

In general, it is economically advantageous to exploit as much structural symmetry as possible when performing a structural analysis. This exploitation is possible whenever the structure, in the absence of loads, possesses geometrical and structural symmetry (ref. 19). Since time-dependent nonsymmetric loads can always be decomposed into the sum of symmetric and anti-symmetric parts, the overall problem can be decomposed in the same way. The purpose of this appendix is to summarize how this decomposition works for the class of wave problems arising in computing submerged shock response.

Consider the cylinder cross-section shown in figure 3 with a typical point number 1 and its image point number 2. The applied loads at the two points can be arbitrary functions of time.

The cylinder possesses numerous planes of symmetry, including the xz- and yz-planes. Thus, only one-fourth of the circumference has to be modeled. (In this particular case, the structure is axisymmetric and thus can be modeled using axisymmetric elements with nonsymmetric loading.) The indicated loading is symmetric with respect to the xz-plane and nonsymmetric with respect to yz. Since the problem is linear, the loading can be decomposed as shown in figure 3. with

$$\begin{aligned} F_s(t) &= (F_1(t) + F_2(t))/2 \\ F_a(t) &= (F_1(t) - F_2(t))/2 \end{aligned} \tag{B1}$$

where the decomposition results in one problem which is symmetric with respect to the yz-plane and another problem which is anti-symmetric with respect to yz. For each component part, it suffices to model but one quadrant (fig. 3) and apply the appropriate boundary conditions (either symmetric or anti-symmetric) for all points in the symmetry planes.

For structural grid points (whose fundamental unknown is displacement) lying in a plane of symmetry, the boundary conditions are that the points can suffer no translation out of the plane of symmetry and no rotation about in-plane lines. The anti-symmetry boundary conditions are that the complementary degrees of freedom are constrained. For example, in figure 3, all points lying in the yz-plane must satisfy

$$u_x = \theta_y = \theta_z = 0 \quad \text{for symmetry}$$

$$u_y = u_z = \theta_x = 0 \quad \text{for anti-symmetry} \tag{B2}$$

where θ denotes rotations.

For fluid grid points (whose fundamental unknown is pressure) lying in a plane of symmetry or anti-symmetry, the boundary conditions are

$$\frac{\partial p}{\partial n} = 0 \quad \text{for symmetry}$$

$$p = 0 \quad \text{for anti-symmetry} \tag{B3}$$

In finite element analysis, the above symmetry condition on p is a natural boundary condition and thus automatically satisfied if the unknown p is left free.

These conditions on fluid pressure grid points are applicable for any pressure points lying in a plane of symmetry or anti-symmetry, including those occurring in an explicit modeling of the fluid volume for the purpose of computing added mass matrices; i.e., the added mass matrix also has to exhibit the proper symmetry.

APPENDIX C - VELOCITY-DEPENDENT NONLINEAR LOADS

The finite element formulation derived to implement the doubly asymptotic approximation (DAA) with NASTRAN involves loads which, at each time step, depend explicitly on the current structural motion rather than on time. The standard versions of NASTRAN (levels 15 and 16) currently allow displacement-dependent loads but provide no convenient way to specify loads which depend on velocity or acceleration. (The implementation of such loads with a combination of transfer function (TF) and nonlinear load (NOLINi) cards is not only inconvenient but also results in nonsymmetric matrices.)

NASTRAN can be easily modified to allow the user to apply velocity- and acceleration-dependent loads using the NOLINi cards now used only for displacement-dependent loads. This appendix summarizes the FORTRAN changes to NASTRAN (level 16) needed to implement such loads.

The approach taken is compatible with that used in MSC/NASTRAN (ref. 20), in which the user indicates velocity dependence by adding 10 to the displacement component number CJ or CK on the NOLINi card. This modification is extended here to allow acceleration dependence, which is indicated by adding 20 to CJ or CK. Acceleration dependence as implemented here, however, is <u>not</u> fully general, since it does not allow a change in the time step size. The velocity dependence is fully general.

The finite difference formulas used to compute velocity and acceleration at the nth time step are

$$\dot{u}_n = (u_n - u_{n-1})/\Delta t \tag{C1}$$

$$\ddot{u}_n = (u_n - 2u_{n-1} + u_{n-2})/\Delta t^2 \tag{C2}$$

where u_n is the displacement vector at the nth time step and Δt is the time step size.

The listing of the FORTRAN changes to NASTRAN (level 16) appears in figure 4, in which the format of CDC's UPDATE utility is used. These modifications were adapted from similar changes made to NASTRAN's level 15 by Messrs. James M. McKee and Myles M. Hurwitz of the David W. Taylor Naval Ship Research and Development Center.

APPENDIX D - RESPONSE TO ARBITRARY TIME-DEPENDENT LOADING BY CONVOLUTION

When the linear shock response of large complex structures is to be computed with NASTRAN, it is often preferable to compute first the response to a step function, because (1) input data preparation for NASTRAN is simplified considerably, and (2) the response for any arbitrary time-dependent loading can be easily computed later by a convolution (superposition) integral (e.g., ref. 21), the formulas for which are summarized here.

Consider the general equation

$$L\,w(x,t) = f(t) \tag{D1}$$

where L is a linear differential operator, w is some response variable (e.g., displacement, velocity, stress, etc.), and the forcing function f is considered here to represent the incident free-field pressure which arises in underwater shock problems.

If $w_s(x,t)$ is the response to a unit step function, then

$$\begin{aligned} w(x,t) &= f(0)w_s(x,t) + \int_0^t f'(\tau)w_s(x,t-\tau)d\tau \\ &= f(t)w_s(x,0) + \int_0^t f(\tau)w_s'(x,t-\tau)d\tau \end{aligned} \tag{D2}$$

where we define

$$w_s'(x,t) \equiv \frac{\partial}{\partial t} w_s(x,t) \tag{D3}$$

Either of the quadrature formulas (D2) can be used to compute the response to an arbitrary forcing function f(t). Since the two relations give different results numerically, the convolution can be computed both ways and averaged. For our work, a short computer program was written to compute w, given tabulated values of f and w_s for non-uniform spacing of the abscissas.

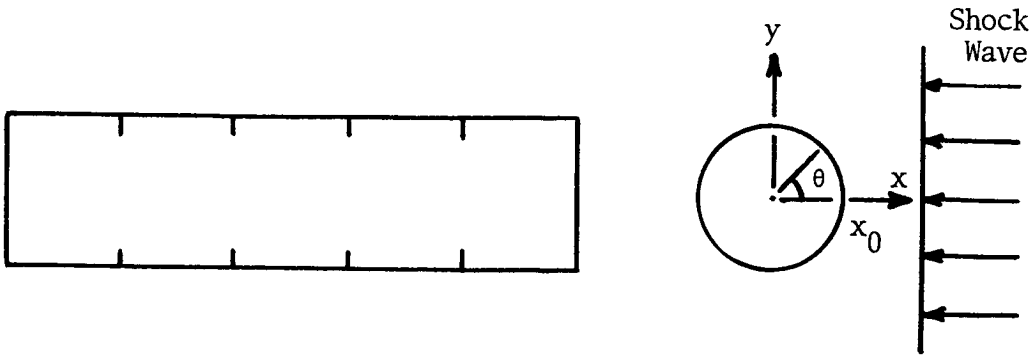

Figure 1. - Ring-Stiffened Cylindrical Shell
Subjected to Plane Wave Shock

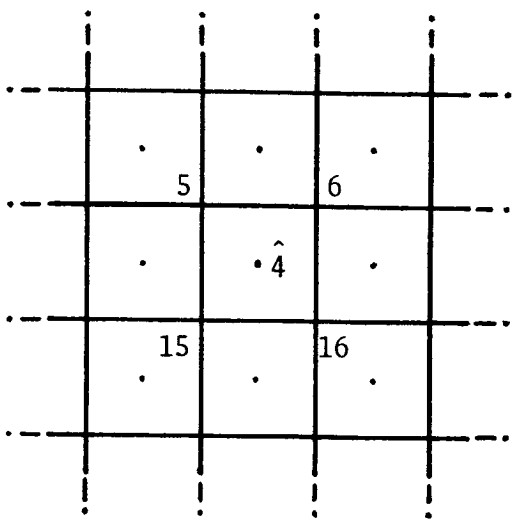

Figure 2. - Rectangular Mesh of Surface Elements
for Added Mass Matrix Transformation

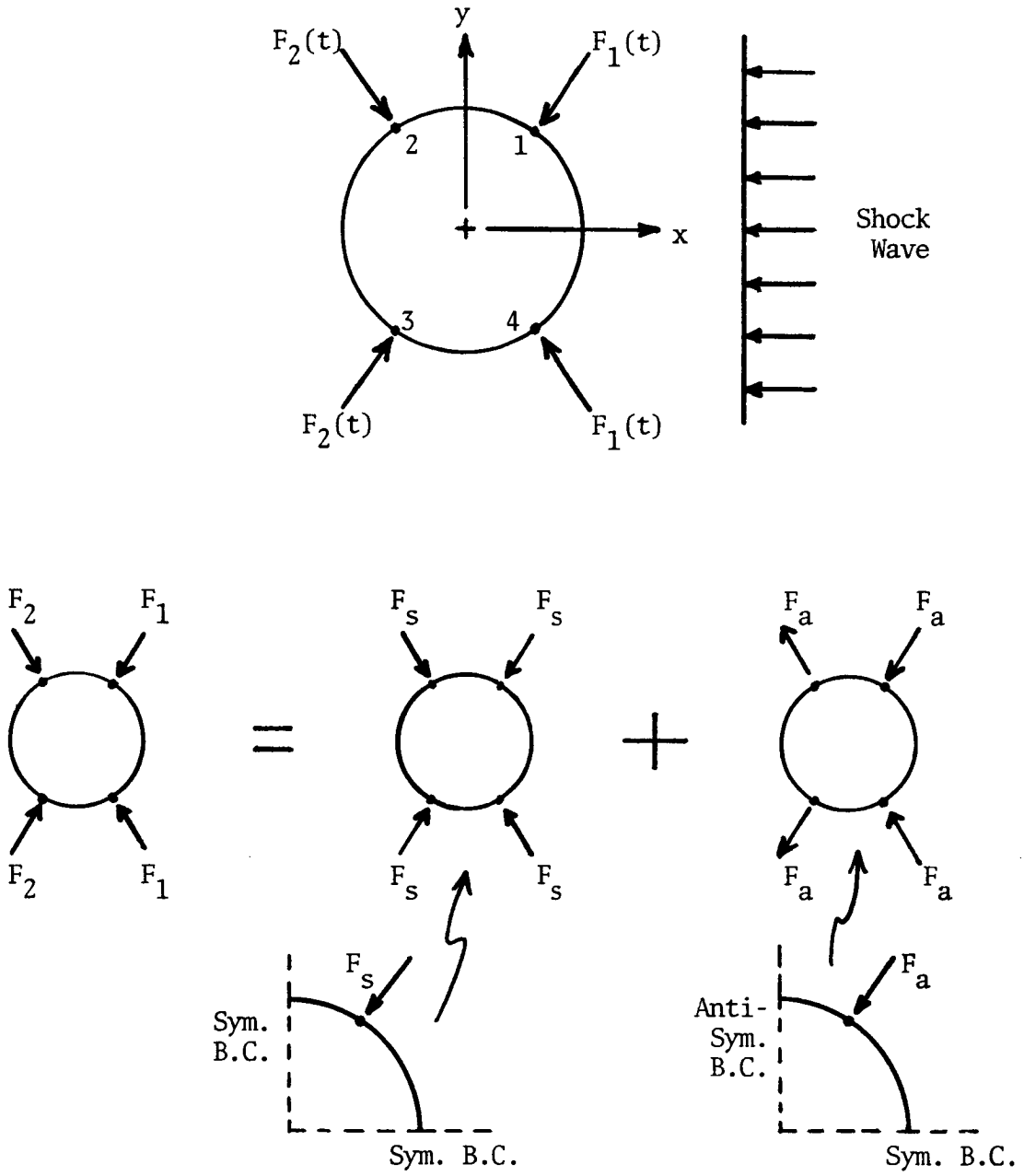

Figure 3. - The Superposition of Symmetric and Anti-Symmetric Solutions for Time-Dependent Problems with Nonsymmetric Loading

```
*IDENT EE042976
*COMPILE DPD4,IFS1P,TRD1C,TRD1D
*DELETE DPD4.70,DPD4.78
C
C    VELOCITY- OR ACCELERATION-DEPENDENT NL LOAD
C
C     LOOK FOR COMPONENTS .GT. 6 FOR INDEPENDENT DOF AND PACK WITH
C                 NOLIN CARD TYPE
C     VELOCITY (OR ACCELERATION) IS INDICATED BY ADDING 10 (OR 20) TO
C                    COMPONENT
C
      IUDOT=0
      IF(BUF(6).LE.6) GO TO 1341
      IUDOT=(BUF(6)/10) * 10
      BUF(6)=BUF(6)-IUDOT
 1341 IF(II.NE.2) GO TO 1345
      IF(BUF(8).LE.6) GO TO 1345
      IGET=(BUF(8)/10) * 10
      BUF(8)=BUF(8)-IGET
      IUDOT=IUDOT+10*IGET
*DELETE DPD4.87
      BUF(2) = II + IUDOT
*DELETE DPD4.163,DPD4.164
      IGET= BUF(1) - (BUF(1)/10) * 10
      IF(IGET.NE.2.AND.KK.EQ.8) GO TO 1396
*DELETE IFS1P.243
      IF( (M(6)/10) .GT.2) GO TO 8
      IF( (M(6)- (M(6)/10) * 10) .GT.6) GO TO 8
*DELETE IFS1P.250
      IF( (M(8)/10) .GT.2) GO TO 8
      IF( (M(8)- (M(8)/10) * 10) .GT.6) GO TO 8
*INSERT TRD1C.20
     2     ,IU3
*INSERT TRD1D.13
     3    ,IU1,DELTAT,IU3
C    IN NL LOAD CALCULATION, IU IS LATEST U, IU1 IS ONE BACK, AND
C                    IU3 IS TWO BACK
*DELETE TRD1D.125
      IGET=IZ(L)-(IZ(L)/10) * 10
      IF(IGET.NE.1) GO TO 110
*INSERT TRD1D.181
C
C     VELOCITY- AND ACCELERATION-DEPENDENT NL LOADS
C
C     STRIP VELOCITY OR ACCEL FLAGS FROM NOLIN CARD TYPE AND COMPUTE
C           VEL OR ACCEL FOR FLAGGED COMPONENTS . . . .
C        UDOT = (U(N)-U(N-1))/DELTAT
C        UDOTDOT= (U(N) - 2 * U(N-1) + U(N-2))/DELTAT**2
C
C*********************************************************************
C
C     NOTE - - -      ACCELERATION-DEPENDENT NL LOADS DO NOT WORK IF A
C                     CHANGE IN TIME STEP SIZE OCCURS.
C
C*********************************************************************
      H=1.0/DELTA T
      HH=H*H
*DELETE TRD1D.185,TRD1D.186
      MM=IU1+IZ(I+2)
      MMM=IU3+IZ(I+2)
      JFLG=IZ(I)/100
      IFLG=(IZ(I)-JFLG*100)/10
      L=IZ(I)-JFLG*100-IFLG*10
      IFLG=IFLG+1
      JFLG=JFLG+1
      GO TO (192,193,194), IFLG
C  DISPLACEMENT-DEPENDENT
  192 X=Z(M)
      GO TO 196
C  VELOCITY-DEPENDENT
  193 X=(Z(M)-Z(MM))*H
      GO TO 196
C  ACCELERATION-DEPENDENT
  194 X=0.
      IF(ICOUNT.GT.1)
     -X=(Z(M)-2.*Z(MM)+Z(MMM))*HH
  196 CONTINUE
*DELETE TRD1D.197
      MM=IU1+IZ(I+4)
      MMM=IU3+IZ(I+4)
      GO TO (212,213,214), JFLG
C  DISPLACEMENT-DEPENDENT
  212 FX=X*Z(M)
      GO TO 240
C  VELOCITY-DEPENDENT
  213 FX=X*(Z(M)-Z(MM))*H
      GO TO 240
C  ACCELERATION-DEPENDENT
  214 FX=0.
      IF(ILOOP.GT.1.OR.ICOUNT.GT.1)
     -FX=X*(Z(M)-2.*Z(MM)+Z(MMM))*HH
```

Figure 4. - Listing of FORTRAN Changes to NASTRAN Level 16 for Velocity- and Acceleration-Dependent Nonlinear Loads

A SUMMARY OF NASTRAN FLUID/STRUCTURE INTERACTION CAPABILITIES

By Anthony J. Kalinowski and Jayant S. Patel

Naval Underwater Systems Center

SUMMARY

A summary of fluid/structure interaction capabilities for the NASTRAN computer program is presented. The paper concentrates on indirect applications of the program towards solving this class of problem; for completeness and comparitive purposes, direct usage of NASTRAN will be briefly discussed. The solution technology addresses both steady state and transient dynamic response problems.

INTRODUCTION

A substantial amount of activity is in progress in the general area of applying the NASTRAN computer program to fluid/structure interaction problems. The class of problems under consideration is limited to linear elastic structures in contact with a fluid. The fluid constitutive equation is represented by an acoustical type small deformation relation wherein pressure is proportional to the divergence of the displacement field (per cent change in elemental volume). The time domain character of the problems treated are either transient (usually incident step pressure waves with an exponential decay wave form) or steady state (acoustical induced response resulting from a harmonic train of incident or radiating pressure waves).

The direct use of NASTRAN to solve problems in the category described above is documented in the NASTRAN program manuals, therefore the paper will only briefly mention direct usage for completeness and comparitive purposes. Instead, the paper concentrates on nonstandard fluid/structure applications of NASTRAN that range anywhere from employing the program directly (through an analogy argument) to using the program capability indirectly (in conjunction with auxiliary post-processing programs).

Special attention is given to the case where an elastic structure is completely submerged in a limitless fluid domain. Five methods are presented for handling the modeling problem of having to represent an infinite fluid region with only a finite number of elements. Methodology is covered that enables one to either eliminate the need for any fluid elements at all (through the proper handling of the fluid/structure interface) or requires one to only model a tractable finite number of fluid elements. Two of the five methods cover transient problems and the remaining ones are for steady state problems. Exact versus finite element solutions are presented for most of the methods covered in the paper.

STEADY STATE-UNCOUPLED FLUID FIELD

This class of problems treats the case where a totally submerged elastic structure is interacting with an infinite fluid domain. The structure is represented by finite elements whereas fluid field is represented by a continuum. This category of problem is not handled by any of the rigid formats currently in NASTRAN. A special post-processing program called FIST (reference 4) was written that will accept basic mode shape information directly from the NASTRAN rigid format output tape. FIST is designed to process this information into the desired solution for the complete fluid/structure interaction response.

The method centers about the process of obtaining a relation between the fluid/structure interface fluid pressure and the interface normal velocity. Once this relationship is determined, the uncoupling process unfolds. The starting point for formulations of this type (references 6-9) is the Helmholtz integral, reference 5, where for any point, x, on the closed submerged surface, S, which interfaces with the fluid, the total pressure p(x) on the surface is related to the normal velocity, w, on the surface by the integral relation

$$p(\bar{x}) = p^{i}(\bar{x}) - 2\int_S p(\bar{y}) \frac{\partial G(\bar{x},\bar{y})}{\partial n(\bar{y})} dS(\bar{y}) + 2i\omega\rho\int_S w(\bar{y})G(\bar{x},\bar{y})dS(\bar{y}) \qquad (4)$$

where $\bar{y}$ is a dummy variable for any position $\bar{x} \in S$, ρ the mass density of the fluid and G is the free space Green's function given by

$$G(\bar{x},\bar{y}) = \frac{\exp(-i\omega|\bar{x}-\bar{y}|/c)}{4\pi|\bar{x}-\bar{y}|} \qquad (5)$$

The development to follow in this subsection on harmonic analysis follows reference 2 (modified for incident pressure by the method given in reference 3) for the first part of this subsection on a direct solution to the problem and follows reference 4 for the modal solution to the problem. The partial derivative of G with respect to $n(\bar{y})$ denotes the rate of change of G in the direction normal to the surface at point $\bar{y}$, and $|\bar{x}-\bar{y}|$ denotes the distance between the $\bar{x}$ and $\bar{y}$ points.

The next step is to obtain a discrete version of equation (4) which is accomplished by representing the surface pressure and normal velocity in terms of a linear combination of scalar basis functions ψ_i defined as

$$p(\bar{x}) = \sum_{n=1}^{N} p_n \psi_n(\bar{x}) \qquad (6)$$

$$w(\bar{x}) = \sum_{n=1}^{N} w_n \psi_n(\bar{x})$$

where N denotes the number of surface grid points in contact with the fluid. For example, reference 4 has used a cubic spacial distribution con-

sistent with the finite element displacement fields for the neighboring structural elements. This is in contrast to reference 10 which employs a piecewise constant distribution of pressure over the interface zones of the structure or to reference 11 which employs a quadratic distribution. Employing a higher order basis function has the advantage that the same solution accuracy can be achieved with a coarser interface mesh. This fact ultimately results in a cost-effective computer program that should run more efficiently, while maintaining the same accuracy, when employing the higher order distribution basis functions.

Upon substituting equations (6) into equation (4) and evaluating equation 4 over a discrete set of points (x_j, j = 1, 2, J) corresponding to the fluid structure interface node points, one obtains

$$[L]\{P\} = [R]\{W^I\} + \{P^i\} \tag{7}$$

where [L] and [R] are JxJ matrices and $\{P^i\}$ is a known Jx1 column vector, and {P} is a column vector of discrete pressure values $p(\bar{x})$; these matrices result from the evaluation of equation (4).

Assuming for the moment that the driving frequency, ω, is not at (or very near) certain characteristic wave numbers of the fluid field enclosing the structure, equation (7) can be solved for {P}, thus

$$\{P\} = [Z(\omega)]\{W\} + [L]^{-1}\{P^i\} \tag{8}$$

where $[Z(\omega)] \equiv [L]^{-1}[R]$.

Reference 13 has presented a method for arriving at equation (8) even in situations where ω is at or near one of the characteristic cavity resonance frequencies.* Briefly stated, the improved method consists of determining the unique surface pressure, $p(\bar{x})$, that simultaneously satisfied the surface Helmholtz integral equation (4) and the interior Helmholtz integral reference 14. The interior Helmholtz integral is a relation similar to the form of equation (4) except it relates the fact that the fluid pressure for <u>all</u> points in the region of space occupied by the structure is zero. Enforcing this interior Helmholtz integral over a judiciously selected set of M interior points leads to a matrix analogous to equation (7) in the form

$$[L^1]\{P\} = [R^1]\{W\} \tag{9}$$

Thus, equations (7) and (9) result in a set of (J+M) equations for the J unknowns {P}. Solving the overdetermined set of equations specified by equations (7) and (9) in a least square sense leads to an equation in the same form as equation (8) except that $Z(\omega)$ is determined in a more involved manner.

Next, by employing the principal of virtual work, the total surface pressures can be related to a set of consistent interaction nodal forces, {F}, thus

$$\{F\} = [C^I]\{P\} \tag{10}$$

* This is sometimes referred to as the cavity resonance problem.

For harmonic steady state problems, the continuous velocity, $w(t)$, and displacement, $u(t)$, amplitudes are related by $w(t) = i\omega u(t)$. Making use of this relation in conjunction with the surface geometry relating normal components of motion into the Cartesian components employed in equation (1) results in the expression

$$\{W\} = i\omega[S]\{U\} \tag{11}$$

Thus, combining equations (10), (8), and (11) leads to

$$\{F\} = [T]\{U\} + [C^I][L]^{-1}\{P^i\} \tag{12}$$

where $[T] \equiv i\omega[C^I][Z][S]$ is typically a fully populated matrix that relates the interaction forces to the boundary displacement field.

For steady state harmonic motion, all response qualities are proportional to $\exp(+i\omega t)$. Thus, $\{U\} = \{U\}^\circ \exp(i\omega t)$, $\{F\} = \{F\}^\circ \exp(i\omega t)$ and $\{F_E\} = \{F_E\}^\circ \exp(i\omega t)$ and the corresponding equation of motion for the structure (equation (1)) becomes

$$\left(-\omega^2[M] + i\omega[C] + [K]\right)\{U\}^\circ = -\{F\}^\circ + \{F_E\}^\circ \tag{13}$$

where $e^{i\omega t}$ has been canceled out on both sides of the equation. Thus, substituting equation (12) into equation (13) results in the relation

$$[V]\{U\}^\circ = \{F_A\}^\circ \tag{14}$$

where $[V] \equiv -\omega^2[M] + i\omega[C] + [K] + [T]$ and $\{F_A\}^\circ = \{F_E\}^\circ - [C^I][L]^{-1}\{P^i\}$.

It is to be noted that equation (13) contains matrices that are the size of the entire structure whereas the matrix size in equation (12) is only a size corresponding to the nodes in contact with the fluid. Thus, when substituting equation (12) into equation (13), allowances must be made in filling out the [T] and product matrix $[C^I][L]^{-1}$ with zeros in the appropriate place to account for the matrix size mismatch.

Formally, one may now state the solution to the interaction problem as finding the inverse of the highly populated [V] matrix. Thus,

$$\{U\}^\circ = [V]^{-1}\{F_A\}^\circ \tag{15}$$

Once $\{U\}^\circ$ is determined all other response quantities can be routinely computed. Substituting the solution $\{U\}^\circ$ into equation (6) and equation (11) and then equation (11) into equation (8) provides the total pressure, $\{P\}$, at the interface. Then substituting the surface pressure and surface velocity into the exterior form of the Helmholtz integral, reference 3, the pressure in any far field point in the media can easily be computed. Premultiplying the surface motion, $\{U\}^\circ$, by the individual (unassembled) stiffness matrix for each element produces the individual structural nodal forces which in turn can be converted to element stresses.

For large size problems, the nonsymmetry and highly populated form of the complex [V] matrix makes its inversion somewhat of a problem when [V] is large. In some situations, [V] is ill-conditioned for certain frequency ranges due to the presence of large size [K] terms in the [V] expression in comparison to the rest of the terms comprising [V]. To get around these problems, an alternate modal analysis approach is sometimes taken, references 4 and 15.

For the modal approach, let $[\phi]$ be the NxM matrix of M undamped, in vacuo modes of the structural vibrations having N degrees of freedom, thus

$$[\phi] = [\{\psi_1\},\{\psi_2\}, \ . \ . \ .\{\psi_M\}] \tag{16}$$

where $\{\psi_m(\bar{x})\}$ is the mth mode column vector which is normalized to the MxM unit identity matrix [I] such that

$$[\phi]^T[M][\phi] = [I] \tag{17}$$

The modes $[\phi]$ have the property that

$$[\phi]^T[K][\phi] = [\lambda] \tag{18}$$

where $[\lambda]$ is a MxM diagonal eigenvalue matrix whose non-zero elements are the squares of the natural frequencies (rad/sec) of the structure. The displacement field can be expressed in terms of the modes by the relation

$$\{U\}^\circ = [\phi]\{Q\}^\circ \tag{19}$$

Next, upon substituting equation (19) into equation (14) and premultiplying the result by $[\phi]^T$, one obtains

$$[\phi]^T[V][\phi]\{Q\}^\circ = [\phi]^T\{F_A\}^\circ \tag{20}$$

which can be rewritten in short notation as

$$[\bar{V}]\{Q\}^\circ = \{F_G\}^\circ \tag{21}$$

where $[\bar{V}] \equiv -\omega^2[I] + [\lambda] + [\phi]^T\Big(i\omega[C] + [T]\Big)[\phi]$ (22)

and $\{F_G\}^\circ \equiv [\phi]^T\{F_A\}^\circ$ (23)

Generally, the MxM $[\bar{V}]$ matrix is complex, nonsymmetric and only under special situations is the $[\bar{V}]$ matrix fully diagonal (note only the first two contributions to equation (22) are diagonal). When $[\bar{V}]$ is fully diagonal, its inversion is trivial, however, the general case must usually be considered where one is faced with the inversion of the $[\bar{V}]$ matrix in order to solve the system of equations defined by equation (21). Formally, then, the solution to the fluid structure interaction problem can be written as

$$\{Q\}^\circ = [\bar{V}]^{-1}\{F_G\}^\circ \tag{24}$$

where we have traded having to invert a NxN [V] matrix in the direct approach for having to invert MxM $[\bar{V}]$ matrix in the modal approach. Strictly speaking, there is one mode shape for each degree of freedom, consequently, if M is set equal to N, one is right back where one started in being faced with the inversion of a NxN complex matrix. However, one can usually judiciously relate the important modes of vibrations based on certain symmetries of loading or based on the customary omission of the higher modes of vibration. After the selection process, one is usually left with a $[\bar{V}]$ matrix that is substantially smaller in size than the original [V] matrix encountered in the direct approach.

The previous development is for a general shaped submerged structure. In the special case where the body has an axis of revolution, it is possible to use a Fourier series decomposition in the angular variable of a cylindrical coordinate system centered about the axis of revolution. Thus, one can describe an arbitrary pressure (or velocity) distribution through the relations

$$
\begin{aligned}
p(\bar{x},\theta) &= \sum_{n=0}^{\infty} p_n(\bar{x})\mathrm{Cos}n\theta + \sum_{n=1}^{\infty} \tilde{p}(\bar{x})\mathrm{Sin}n\theta \\
w(\bar{x},\theta) &= \sum_{n=0}^{\infty} w_n(\bar{x})\mathrm{Cos}n\theta + \sum_{n=1}^{\infty} \tilde{w}_n(\bar{x})\mathrm{Sin}n\theta
\end{aligned}
\tag{25}
$$

Applying such an expansion to the development just presented for the general three-dimensional case results in problem formulation analogous to equation (14) or to equation (21). The main difference is that the coefficient matrix [V(n)] in equation (15) (or corresponding $[\bar{V}(n)]$ matrix in equation (21)) is now a function of the wave number n corresponding to the expansions in equation (25). Consequently, solving the full three-dimensional problem is equivalent to solving a sequence of n = 1, 2, . . $\bar{N}$ smaller sets of linear equations (i.e equations (14) or (21)). The phrase "smaller sets of linear equations" is used since the elimination of the third spacial dimension (through the introduction of the Fourier expansion) substantially reduces the size of the coefficient matrix [V]. From a computational point of view, it is usually more efficient to solve, say, six ($\bar{N}$=6) two-dimensional size problems than one large three-dimensional one. The details of setting up the actual [V(n)] array, for cubic polynomial displacement fields, is presented in more detail in reference 4. Consequently, it will not be repeated here.

The interface of this solution technique with the NASTRAN computer program can be made in one of two ways where the selected approach depends on whether the direct or modal solution technique is used to solve the problem. In the case of the modal formulation, a computer program called FIST (Fluids Interacting with STructures) has been written which directly accepts, as input from NASTRAN, the structural mode shapes for the in vacuo normal modes or mass and stiffness matrices. With the addition of a few simple alter cards in the NASTRAN run stream, the modes are written on tape from NASTRAN using the module OUTPUT 2. For example, in rigid format 3, adding the cards

```
ALTER 84
OUTPUT2 KAA,MAA,,,//C,N,1/C,N,0 $
ALTER 94
OUTPUT2 PHIA,MI,,,//C,N,1/C,N,0 $
ALTER 96
OUTPUT2 PHIG,,,,//C,N,1/C,N,0 $
ENDALTER
```

in the EXECUTIVE control deck is all that is needed to have the information needed by FIST to solve the fluid/structure interaction problem. The current version of FIST is currently limited to axisymmetric structures subject to non-axisymmetric loadings.

In the case of the direct formulation, FIST has an option which permits one to solve the system of linear complex simultaneous equations (14). However, the current version is limited to a 40 x 40 nonsymmetric, fully populated matrix. In situations where the [V] matrix is large, the NASTRAN mathematical solution routines can be utilized to solve the problem at hand. The frequency response rigid format number 8 solves the following problem

$$\Big[[M]\omega^2 + i\omega[B] + [K]\Big]\{X\} = \{P\} \tag{26}$$

for the displacement amplitude $\{X\}$, where the multiplying matrix on $\{X\}$ can be, in general, nonsymmetric and complex. The complex loading vector, $\{P\}$, can be introduced into NASTRAN through the RLØAD1 bulk data card and the [M], [B], and [K] arrays need not be computed by NASTRAN but rather can be directly inserted, element by element, through a DMIG card. Since no structure is given to NASTRAN directly, all the [M], [B] and [K] matrices are zero, except for the direct input components (denoted by $[M^2_{dd}]$, $[B^2_{dd}]$, and $[K^2_{dd}]$ in the NASTRAN theoretical manual, pg. 9.3-7). The [M] and [B] arrays are zero by virtue of not defining them in any way. Thus, there remains the $[K^2_{dd}]$ array which is read in (in complex form) via the DMIG card. NASTRAN will proceed in the usual manner for the direct frequency response solution and compute the $\{X\}$ solution which, of course, corresponds to the desired result $\{U\}^\circ$ (i.e. equation (15)).

By employing alter instructions, one who is familiar with DMAP can most likely perform the desired operations in a more direct fashion. The advantage of the dummy stiffness application method is that is can all be done within the current fixed format of the program.

As an illustration of the solution technique, consider the situation where a steel submerged thin wall spherical shell is harmonically driven by a point concentrated force. The shell has a radius of 2.54 cm, wall thickness of 0.127 cm and a nondimensional driving frequency of KA = 0.4 ($K \equiv \omega/c$ where ω is the driving frequency in rad/sec and c is dilatational wave speed in the water). The exact solution to this problem is shown in figure 1 by the solid line (reference 12) and is processed using the first 50 axisymmetric modes of a thin sphere. The fine dashed line corresponds to a FIST solution to the problem (employing a cubic distribution pressure variation) which uses the direct solution approach (equation (15)) with the sphere subdivided into eight segments. The coarse dashed line corresponds to a modal solution (equation (24))

that employs three mode shapes and an eighteen segment subdivision. Both FIST solutions employ too coarse of a mesh to predict an accurate response near the point load. Agreement away from the point load is seen to be very good.

STEADY STATE-COUPLED FLUID FIELD

Again, the case of a totally submerged elastic structure is treated, except that in this case the structure as well as the fluid is modeled with finite elements. The first approach, of the two presented in this subsection, is the situation where displacement (or "mock") fluid elements is employed in the problem formulation, references 17, 18. In this situation, we start with the three-dimensional elasticity equations

$$\rho \frac{\partial^2 u_i}{\partial t^2} = \frac{\partial \sigma_{ij}}{\partial x_j} \qquad i = 1,2,3 \tag{27}$$

with $\sigma_{ij} = \lambda\delta_{ij} \dfrac{\partial u_k}{\partial x_k} + \mu\left[\dfrac{\partial u_i}{\partial x_j} + \dfrac{\partial u_j}{\partial x_i}\right]$ (δ_{ij} is the Kronecker delta) (27a)

We start by letting the Lamé constant $\mu \to 0$; the Lamé constant $\lambda \to k$; and noting that the reduced equation (27a) now implies that

$$\sigma_{11} = \sigma_{22} = \sigma_{33} \tag{28}$$

and $\sigma_{12} = \sigma_{31} = \sigma_{32} = \sigma_{21} = \sigma_{13} = \sigma_{23} = 0$.

Finally, upon defining $P \equiv -\sigma_{11} = -\sigma_{22} = -\sigma_{33}$, it is seen that the reduced equations (27) and (27a) represent the same field equations as those defined by equations (2, 2a).

Consequently, any solid elements in NASTRAN that are built from working with equations (27, 27a) can be converted into mock fluid elements by appropriately refining the constants in the elasticity stress-strain law

$$\{\sigma\} = [G]\{\varepsilon\}$$

For three-dimensional type elements like brick and ring elements, the array of elastic constants for an isotropic material can be written as

$$[G] = \begin{bmatrix} (\lambda+2\mu) & \lambda & \lambda & 0 & 0 & 0 \\ \lambda & (\lambda+2\mu) & \lambda & 0 & 0 & 0 \\ \lambda & \lambda & (\lambda+2\mu) & 0 & 0 & 0 \\ 0 & 0 & 0 & \mu & 0 & 0 \\ 0 & 0 & 0 & 0 & \mu & 0 \\ 0 & 0 & 0 & 0 & 0 & \mu \end{bmatrix} \tag{29}$$

Similarly, for two-dimensional solid elements, like membrane elements, the array of elastic constants (corresponding to $\{\sigma_{xx}, \sigma_{yy}, \sigma_{xy}\}$ can be written as

$$[G] = \begin{bmatrix} G_{11} & G_{12} & G_{13} \\ G_{21} & G_{22} & G_{23} \\ G_{31} & G_{32} & G_{33} \end{bmatrix} \tag{30}$$

For the NASTRAN program installation of the mock elements for 2-D membrane solid elements is achieved through a MAT2 card wherein

$$G_{11} = G_{12} = G_{21} = G_{22} = k \equiv \text{fluid bulk modulus}$$

and the remaining $G_{13} = G_{23} = G_{31} = G_{32} = G_{33} = 0.0$.

For employing three-dimensional mock elements, the situation would be straightforward if the [G] matrix were allowed to be input in a general form like the two-dimensional case; or, if the stress-strain matrix were written in terms of Lamé constants rather than in terms of the more common modulus of elasticity, E, and Poisson's ratio, ν. For the latter case, one need only set $\mu = 0$ and $\lambda = k$ and the desired mock element could be formed. In actuality, the NASTRAN [G] array accepts input in the form* of E and ν and internal to the program, the elements of the [G] array are defined as follows

$$G_{11} = G_{22} = G_{33} = E(1-\nu)/[(1-2\nu)(1+\nu)]$$

$$G_{12} = G_{21} = G_{13} = G_{31} = G_{23} = G_{32} = E\nu/[(1-2\nu)(1+\nu)] \tag{31}$$

$$G_{44} = G_{55} = G_{66} = .5E/(1+\nu)$$

The problem can be resolved by rewriting a small portion of the Fortran coding that fills out the material constants array in the desired form.

An alternate procedure is to adjust the values of E, ν (or G) on a MAT1 card so that $\lambda = k$ and $\mu = 0$. Setting $G = 0$ (note that $\mu \equiv G$) and solving for the E required to be consistent with the proper fluid bulk modulus, k, will not work because the NASTRAN coding tries to form ν by dividing G (see footnote) and dividing by zero will not be handled properly by the computer.

---

* The shear modulus, G, can be given in place of E (or ν) in which case the E or ν is computed internally from $E = 2G(1+\nu)$ (or $\nu = \frac{E}{2G} - 1$).

One way to resolve the problem is to relax the strict equalities for the mock element that $\lambda = k$ and $\mu = 0$ but rather enforce them only approximately such that $\lambda \approx k$ and $\mu \approx 0$ (i.e. so long as $\lambda >>> \mu$). By setting

$$\nu = 0.49999$$

and

$$E = \frac{k(1-2\nu)(1+\nu)}{\nu} \equiv k/16{,}664.44 \tag{31a}$$

on the MAT1 cards, NASTRAN will internally generate a set of G_{ij} constants that will adequately represent (but not be exactly equal to) the desired exact values. As an illustration, consider water that has a bulk modulus of k = 316,000 psi (2.18×10^9 N/m^2). Thus, for $\mu = 0$, typical proper values of the [G] array would correspond to

$$G_{11} = 316{,}000, \; G_{12} = 316{,}000, \text{ and } G_{44} = 0.0.$$

Applying the suggested approximate approach via equations (31a), NASTRAN invokes equations (31); thus would internally compute the typical [G] array elements as

$$G_{11} = 316{,}050 \qquad G_{12} = 316{,}037 \qquad G_{44} = 6.32$$

which should be sufficiently close to produce fluid response results of the same degree of accuracy had the exact [G] entries been used.

Pressure distribution information is obtained by examining the stress output from NASTRAN. The fluid pressure is obtained by reversing the sign of the normal stress output (since all the normal components are equal for mock elements, the user can select any normal component).

The boundary between the fluid and solid is handled by only forcing the normal component of fluid displacement to be equal to the normal displacement of the interfacing solid. This can be easily done through the introduction of a double node in conjunction with a MPC constraint. The boundary at infinity is handled analogous to the approach used in solids for earthquake problems (reference 19) and later in fluid applications (references 17, 18). This is accomplished by placing the fluid boundary not at infinity, but at a finite distance that is far enough so that interaction waves radiating from the submerged structure will satisfy (or nearly satisfy) the boundary condition

$$p = \rho c \dot{u}_n \tag{32}$$

where ρ is the fluid mass density, c is the fluid sound speed and $\dot{u}_n$ is the velocity normal to the outer boundary. This condition is true for plane waves and asymptomatically true for cylindrical and spherical waves. The finite element form of equation (32) is given by

$$\{F_b\} = [C_b]\{\dot{U}\} \tag{33}$$

where $[C_b]$ is a diagonal matrix with zero diagonal values for non-outer boundary points and a value of $\rho c \Delta A_i$ for normal outer boundary degrees-of-freedom where ΔA_i is the pressure-to-force conversion term and corresponds to a segment area $_i$ at the boundary node. In NASTRAN, the boundary dash pots are applied with CDAMP1 cards.

A rough guideline is needed for determining how far the fluid boundary should be placed in order for the plane wave approximation, equation (32), to be valid. A steady state solution can be constructed from some distribution of point sources around the structure fluid boundary. For a 3-D problem, a single source will approach (within 98.6%) a plane wave pressure velocity relationship (like equation (32)) after moving one wave length away from the source. The percentage quoted refers to the fact that complex impedance ($z = p/\dot{u}_n$ is $.986\rho c$. Moving away 1 1/2 wave lengths, this percentage becomes 99.4%. Thus, we are suggesting that the single source decay information can be used to judge the distance to place the absorbing boundary. For 2-D problems, a line source emitting cylindrical waves will approach a plane wave boundary condition to within 99.2% for one wave length away and to within 99.7% for 1 1/2 wave lengths away. Thus, it is suggested to place the boundary a distance $\tilde{D}$ away from the structure where

$$\tilde{D} = \alpha\tilde{\lambda} \tag{34}$$

and α is a proportionality constant (e.g. 1.5 for a 99.4% correct plane wave assumption) related to the degree of the plane wave boundary condition assumption, and $\tilde{\lambda}$ is the wave length of the steady state driving frequency in water (i.e. $\tilde{\lambda} = 2\pi c/\omega$).

Next, one must consider the size elements to use so that the elements of the mesh do not artificially "ring" at their natural frequencies. To avoid ringing, there exists a minimum element length, Δ_L, that is related to some fraction, β, of the wave lenght of the driving frequency in the fluid, thus

$$\Delta L = \beta\tilde{\lambda} \tag{35}$$

The value of β will depend on the type of elements being used. For example, if one employs CQDMEM elements of the NASTRAN program, $\beta \approx 1/6$ to avoid mesh ringing. Modeling the region from the fluid structure interface out to the mathematical cut in the fluid boundary would result in $\tilde{n}$ elements of length Δ_L, thus

$$\tilde{n} = \frac{\tilde{D}}{\Delta L} \tag{36}$$

Substituting equations (34) and (35) into equation (36) results in the expression

$$\tilde{n} = \frac{\alpha}{\beta}$$

which is independent of the driving frequency $\tilde{\omega}$. Thus, employing typical values of $\alpha = 1.5$ and $\beta = 1/6$ into equation (36) shows, for example, that regardless of the driving frequency magnitude, it is possible to model the fluid field with

as few as 9 elements in the direction normal to the surface. In cases where the surface structure elements are coarse, more elements would be needed to blend in the fine surface elements into the coarser field elements.

For radiation type problems (i.e. a structure vibrating and transmitting outgoing waves), one can handle the infinite boundary problem by placing the dash pots around the outer boundary. For scattering type problems where a submerged structure is subject to an incident wave input, the handling of the infinite boundary problem is more complicated in that both the incident wave driving force and the boundary dash pots both appear on the boundary. The manner in which this class problem is handled is discussed in reference 17 and will not be repeated here.

As a demonstration problem consider the two-dimensional problem of an infinitely long cylindrical inclusion imbedded in an acoustical fluid medium. The inclusion is subjected to an incident harmonic plane wave (this is classified as a scattering problem). A sketch of the full model and corresponding finite element sketch is illustrated in figure 2. Constant strain CQDMEM elements are used to construct the model for both the solid and mock fluid elements. Two solutions (for two different inclusion types) are presented in the form of a comparison between an exact and corresponding finite element response. In either case, the exact solution (references 20, 21) is represented by the solid curve and the dots are the corresponding finite element solution. The solution response is given, in non-dimensional form, as the ratio between the total pressure to the incident free field amplitude. The parameters in the upper right corner of the figure denote a set of non-dimensional parameters that characterize the physical parameters of the problem and have the corresponding definitions

$$KA = \text{non-dimensional driving frequency} = \frac{\omega \cdot \text{inclusion radius}}{\text{fluid wave speed}}$$

$$\bar{R} = \frac{\text{radial coordinate}}{\text{inclusion radius}}$$

$$\bar{D} = \frac{\text{fluid dilatational wave speed}}{\text{inclusion dilatational wave speed}}$$

$$\bar{C} = \frac{\text{inclusion dilatational wave speed}}{\text{inclusion shear wave speed}}$$

$$\bar{\rho} = \frac{\text{fluid mass density}}{\text{inclusion mass density}}$$

The response shown in figure 3 corresponds to a vacuous inclusion and the response in figure 4 to an elastic aluminum inclusion. Except for the 0° and 180° (back and front) data points on the aluminum cylinder, the response results agreement was good. Response comparison for other radii (both closer and further away from the results presented) gave equally good results. The mesh size used was pushing the limit regarding the size needed to avoid ringing. It is felt that a finer mesh would have improved the results in the 0° or 180° data points for the aluminum solutions.

Reference 22 presents another completely different approach to solving steady state problems with NASTRAN. In this approach the submerged structure is surrounded with a sphere shaped region of finite elements. The proper boundary condition for handling the infinite fluid domain beyond the bounding sphere surface is treated with an eigenvalue expansion approach. The details are presented in reference 22 (paper in this colloquium), therefore will not be repeated here.

TRANSIENT-UNCOUPLED FLUID FIELD

This class of problem treats a totally submerged structure subject to dynamic loading usually in the form of an incident pressure wave. Reference 23 presents an application of the NASTRAN program towards solving transient fluid/structure interaction problems with the DAA (doubly asymptotic approximation) method. This method involves imposing an analytical decoupling relation (in differential equation form) describing the relationship between the pressure at the interface and the corresponding interface motion. The decoupling approximation eliminates the need for modeling the fluid field with finite elements. A brief outline of the method is presented in reference 23. A more detailed discussion of the implimentation into NASTRAN is presented as a paper in this colloquium (reference 24), therefore the reader is referred to that paper for more details.

TRANSIENT-COUPLED FLUID FIELD

The class of problem considered here is the same as the previous transient category except in this case the fluid is modeled as part of the finite element network. The first NASTRAN application in this category considers the case where pressure type fluid elements are used to model the fluid field. These types of elements are different from the displacement type elements discussed earlier in that there is only one degree of freedom per node (namely pressure); this is in constrast* to one, two or three degrees of freedom per node for mock fluid elements which have displacements as the basic unknowns. The implementation of this method into NASTRAN requires one to dummy the construction of the stiffness and mass matrices of a conventional displacement type finite element so that only one displacement component is active (the remaining ones are zero); and further, the remaining nonzero component plays the role of pressure. The proper units are handled through redefining the elements of the [G] stress-strain matrix. This approach to solving fluid/structure interaction problems with NASTRAN was first introduced in the 4th NASTRAN User's Colloquium (reference 23). The complete details of the implementation of the method is presented in the current 5th NASTRAN User's Colloquium (reference 24).

The second application of NASTRAN (employing the coupled fluid field approach) is that of using the mock fluid elements. These displacement type elements were already discussed in the previous secion on harmonic analysis. The method of implementing them via the stress-strain matrix [G] is done in

---

* The actual number depends on whether one is solving a one, two, or three-dimensional problem.

exactly the same manner as for the transient type problems as well. Transient problems using mock elements are solved using rigid format number 9. The infinite fluid boundary problem can be handled by temporal truncation. This is the most straightforward approach and is readily adaptable to both the pressure or mock element type transient solutions. In construction of the finite element mesh, one models the fluid surrounding the solid cutout to, say, 2 structure lengths. For scattering or radiation type problems, one can take advantage of the fact that the continuous equations are hyperbolic in nature. Thus for, say, a radiation problem, the solution will be such that the response in front of a radiating wave is zero, thus the problem does not know a boundary to the mesh even exists until the radiating wave actually gets there (due to the discretization of the problem, the governing equations do not exactly behave like hyperbolic equations, but the idea of traveling waves are still roughly approximated by the governing discretized differential equations). Thus, the solution to the problem can be obtained in the same manner as a finite boundary case, except that the solution response must be truncated at the time when the radiated wave reaches the mesh boundary.

Scattering problems can be treated in a similar manner. The free-field incident wave solution starts the problem, i.e. the initial conditions for the problem solution are obtained by setting the response field, behind the incident wave, equal to the free-field solution. The equations of motion are integrated in time in the usual manner but must be truncated when scattered waves off the structure reach the finite fluid mesh boundary.

One-dimensional wave propagation examples using mock elements in NASTRAN are presented in reference 17*. A solution employing mock elements for a three-dimensional problem is shown in figure 5. The problem corresponds to a plane step wave traveling through a solid elastic homogeneous medium and interacting with a spherical cavity filled with fluid. At the time these runs were made, a level of NASTRAN capable of solving axis of revolution solid strcutures subject to nonsymmetric loading was not yet available, consequently, a program (reference 25) other than NASTRAN was used to generate the result shown in figure 6. The program uses a harmonic decomposition in the angular coordinate of a cylindrical coordinate system to reduce the full three-dimensional problem to that of solving a set of smaller two-dimensional ones (with the harmonic wave number as a parameter in each two-dimensional subproblem). The full three-dimensional response is obtained by superposition over the angular harmonics (usually 5 terms are adequate). The response shown in figure 6 is the pressure at the center of the fluid sphere for both the exact solution (reference 26) and the corresponding finite element solution. For reference, the pressure in the free field (negative of the average normal stress in the solid) is also shown. Transient finite element solutions of this type tend to ring about the true solution. The frequency of the ringing is associated with the highest natural frequency of the mesh. Reference 27 discusses this point in detail and provides a digital filtering technique for eliminating some of the ringing problem.

---

* In reference 17, there are several sign errors that should be pointed out to avoid confusion with the development presented here; namely, on page 74 of reference 17, replace k with -k in equation (3), replace -k with +k on the third line from bottom and , finally, replace -k with +k at the bottom of page 75.

For completeness, a brief discussion of the direct application of the NASTRAN computer program for solving fluid/structure interaction problems is presented next. The NASTRAN program has built-in pressure type elements (called CFLUID1 elements) and are described through RINGFL, PRESPT and FREEPT type fluid nodes. The elements are designed to operate in contained tanks that may have either rigid or elastic walls. These special elements have the following restrictions:

1. The user may not apply loads, constraints, sequencing or omitted coordinate directly on the fluid nodes involved. Instead, the user supplies information related to the boundaries and NASTRAN internally generates the correct constraints, sequencing, and matrix terms.

2. The input data to NASTRAN may include all of the existing operations except the axisymmetric structural element data (e.g., axisymmetric shell elements cannot be used).

3. The fluid must lie within the walls of an open or closed tank.

4. The first 6 rigid formats of NASTRAN may not be used in conjunction with these elements. NASTRAN assumes the walls of the container are rigid for these first 6 rigid formats but allows elasticity for the remaining 6 (fortunately direct frequency and direct transient response are included in the remaining 6).

5. No means are provided for the direct input of applied loads on the fluid. Loading must come through the motion of the walls.

The list of constraints that are placed on the usage of these elements rather severely limits the range of application, particularly in the case where unbounded fluid regions are of interest. Even within these constraints (reference 28), however, some rather interesting applications to acoustic noise problems associated with automobiles have been found.

Another unique feature that the NASTRAN program has is the ability to treat the free surface problem and include gravity terms into the fluid equations of motion.

CONCLUSIONS

The latest version of the NASTRAN computer program, as of this writing, does not handle a very large class of fluid/structure interaction problems via the direct rigid format application of the program. This paper presents a variety of nonstandard usage of the program to broaden the scope of problem application in the area of fluid/structure interaction. The implementation of the techniques presented here varies from one extreme of requiring the user to only make slight modifications to the standard problem input of NASTRAN-to-another extreme of requiring a substantially sized auxiliary support computer program to handle pre- and/or post-processing of the input and output data. The implementation of these methods depends, to some degree, upon the ingenuity of the user. Hopefully, future versions of NASTRAN will have more automatic procedures for solving problems of the type addressed in this paper.

REFERENCES

1. Morse, P. M., Vibration and Sound, McGraw-Hill, New York, 1948.

2. Smith, R. R., Hunt, J. T., and Barach, D., "Finite Element Analysis of Acoustically Radiating Structures with Application to Sonar Transducers," Journal of the Acoustical Society of America, 54, 1973, pp. 1277-1288.

3. Hunt, J. T., Knittel, M. R., Nichols, C. S., and Barach, D., "Finite Element Approach to Acoustic Scattering from Elastic Structures," Journal of the Acoustical Society of America, 57, July 1973, pp. 287-299.

4. Patel, J. S., "Fluids Interacting with Structures," NUSC TM No. EM-51, Naval Underwater Systems Center, 1975.

5. Baker, B. B. and Copson, E. T., The Mathematical Theory of Huygens Principle, Clarendon Press, Oxford, England, 1950.

6. Chen, L. H. and Schweikert, D. G., "Sound Radiation from an Arbitrary Body," Journal of the Acoustical Society of America, Vol. 35, Oct 1963, pp. 1616-1632.

7. Copley, L. G., "Integral Equation Method for Radiation from Vibrating Bodies," Journal of the Acoustical Society of America, Vol. 41, July 1966, pp. 807-815.

8. Schenck, H. A., "Improved Integral Formulation for Acoustic Radiation Problems," Journal of the Acoustical Society of America, Vol. 44, Jan 1968, pp. 41-58.

9. Chertock, G., "Sound Radiation from Vibrating Surfaces," Journal of the Acoustical Society of America, Vol. 36, July 1964, pp. 1305-1313.

10. Henderson, F. M., "Radiation Impedance Calculations with the X-WAVE Computer Program," Naval Ship Research and Development Center, Report No. 4033, March 1973.

11. Engblem, J. J. and Nelson, R. B., "Consistent Formulation of Sound Radiation from Arbitrary Structures," Journal of Applied Mechanics, Transactions of the ASME, June 1975, pp. 295, 300.

12. Hayak, S., "Vibration of a Spherical Shell in an Acoustic Medium," Journal of the Acoustical Society of America, Vol. 40, No. 2, 1966, pp. 342-348.

13. Schenck, H. A., "Improved Integral Formulation for Acoustic Radiation Problems," Journal of the Acoustical Society of America, Vol. 44, pp. 41-58.

14. Kupradze, V. C., "Fundamental Problems in the Mathematical Theory of Diffraction," translated by C. D. Benster (NBS Report No. 2008, Oct 1952).

15. Chakrabarti, P. and Chopru, A. K., Earthquake Engineering and Structural Dynamics, Vol. 2, 1973, pp. 143-160.

16. Junger, M. C., "Normal Modes of Submerged Plates and Shells," Fluid Solid Interaction, The American Society of Mechanical Engineers, 1967, pp. 79-119.

17. Kalinowski, A. J., "Proceedings of the Fifth Navy/NASTRAN Colloquium," Navy/NASTRAN System Office Report No. CMD-32-74, Sept 1974.

18. Kalinowski, A. J., "Fluid/Structure Interactions," Shock and Vibration Computer Programs Reviews and Summaries, edited by W. Pilkey and B. Pilkey, The Shock and Vibration Information Center, 1975.

19. Lysmer, T. and Kuhlemeyer, R. L., "Finite Dynamic Model for Infinite Media," Journal of Engineering Mechanics Division, ASCE, Vol. 95, Aug 1969, pp. 859-877.

20. Faran, J. J., "Sound Scattering by Solid Cylinders and Spheres," Journal of the Acoustical Society of America, Vol. 23, 1951, pp. 405,418.

21. Pao, Y. and Mow, C. C., Diffraction of Elastic Waves and Dynamic Stress Concentration, The Rand Corporation, 1971.

22. Zarda, P. R., "Analytical Methods for Modeling Structures in an Infinite Fluid," 5th NASTRAN Users Colloquium, 1976.

23. Everstine, G. C., Schroeder, E. M., and Maran, M. S., "The Dynamic Analysis of Submerged Strcutures," 4th NASTRAN Users Colloquium, Langley Research Center (NASA TM X-3278), Sept 1975.

24. Everstine, G. C., "NASTRAN Implimentation of the Doubly Asymptotic Approximation for Underwater Shock Response," 5th NASTRAN Colloquium, 1976.

25. Welch, E. et al, Three-Dimensional Structures/Media Interaction, IIT Research Institute Report to Shock Physics Directorate Headquarters, Defense Atomic Support Agency, Contract DASA 01-69-C-0028, Feb 1970.

26. Mion, F. C. and Mow, C. C., The Effect of Stress-Wave Diffraction in Stress Measurements and a Concept for An Omnidirectional Dynamic Stress Gage, (KM-5860-PR) Rand Corporation, Jan 1969.

27. Holmes, N. and Belytschko, T., "Postprocessing of Finite Element Transient Response Calculations by Digital Filters," Computers and Structures, Vol. 6, No. 3, 1976.

28. Wolf, J. A. Jr., and Nefske, D. J., "NASTRAN Modeling and Analysis of Rigid and Flexible Walled Acoustic Cavities," 4th NASTRAN User's Colloquium, Langley Research Center, Sept 1975.

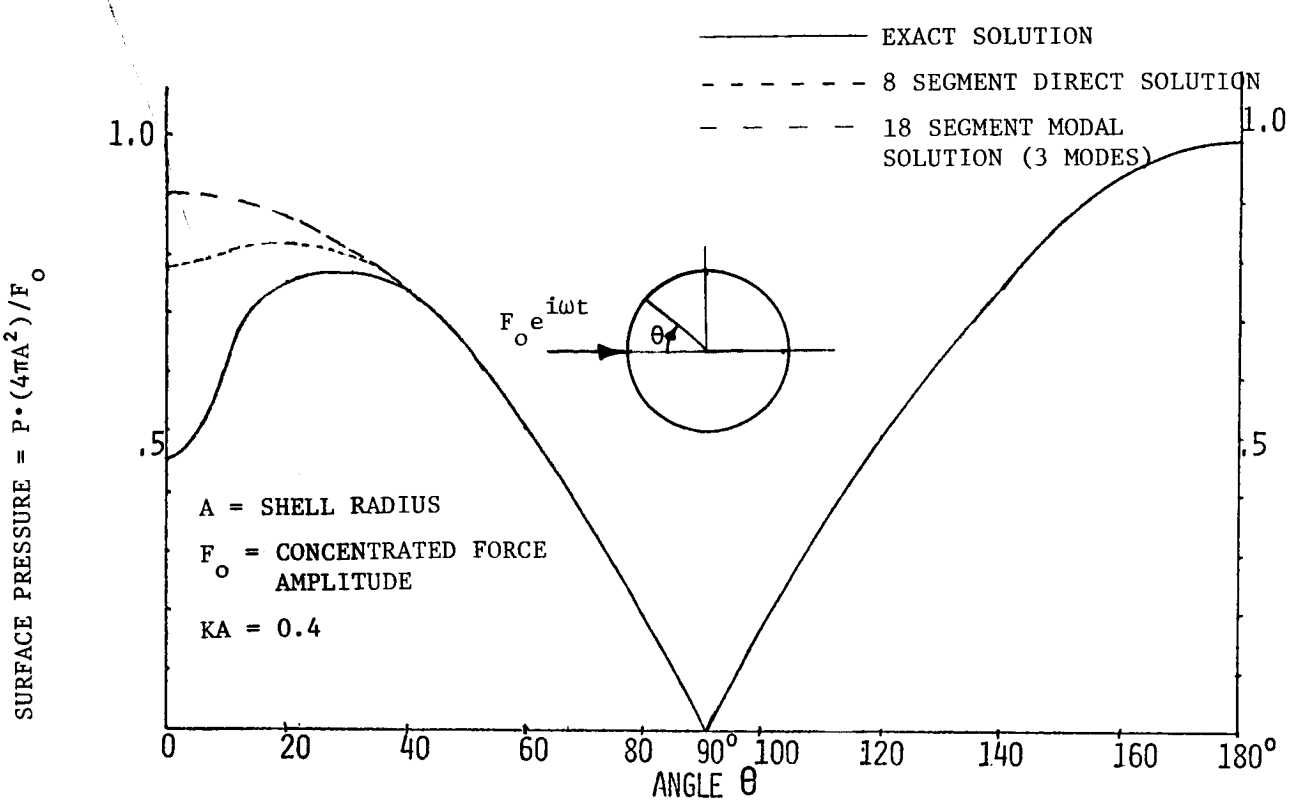

Figure 1. - Surface Pressure on a Point Loaded Thin Wall Sphere

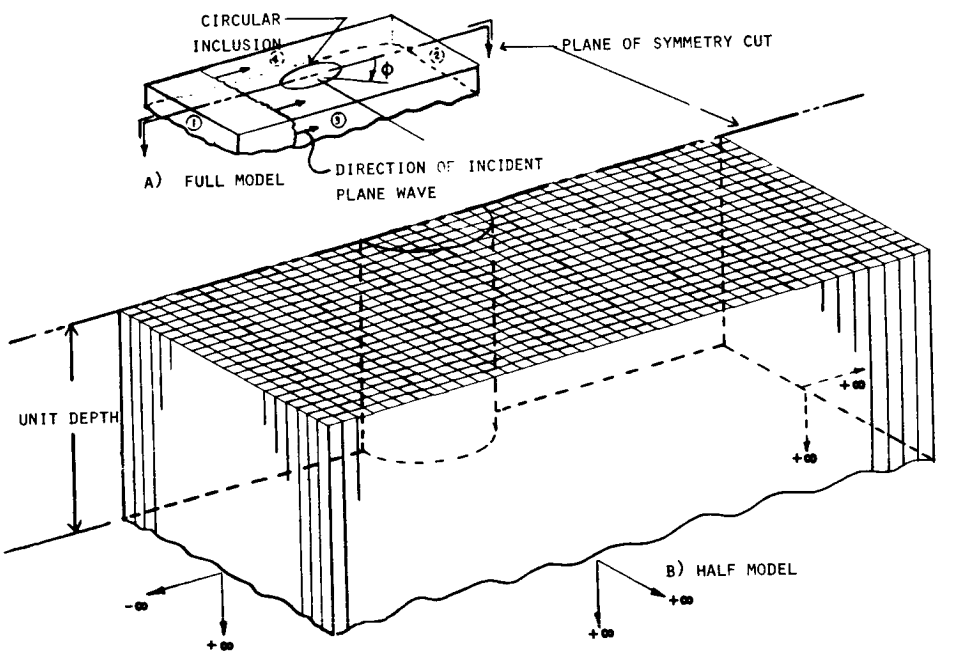

Figure 2. - Finite Element Mesh for Cylindrical Inclusions

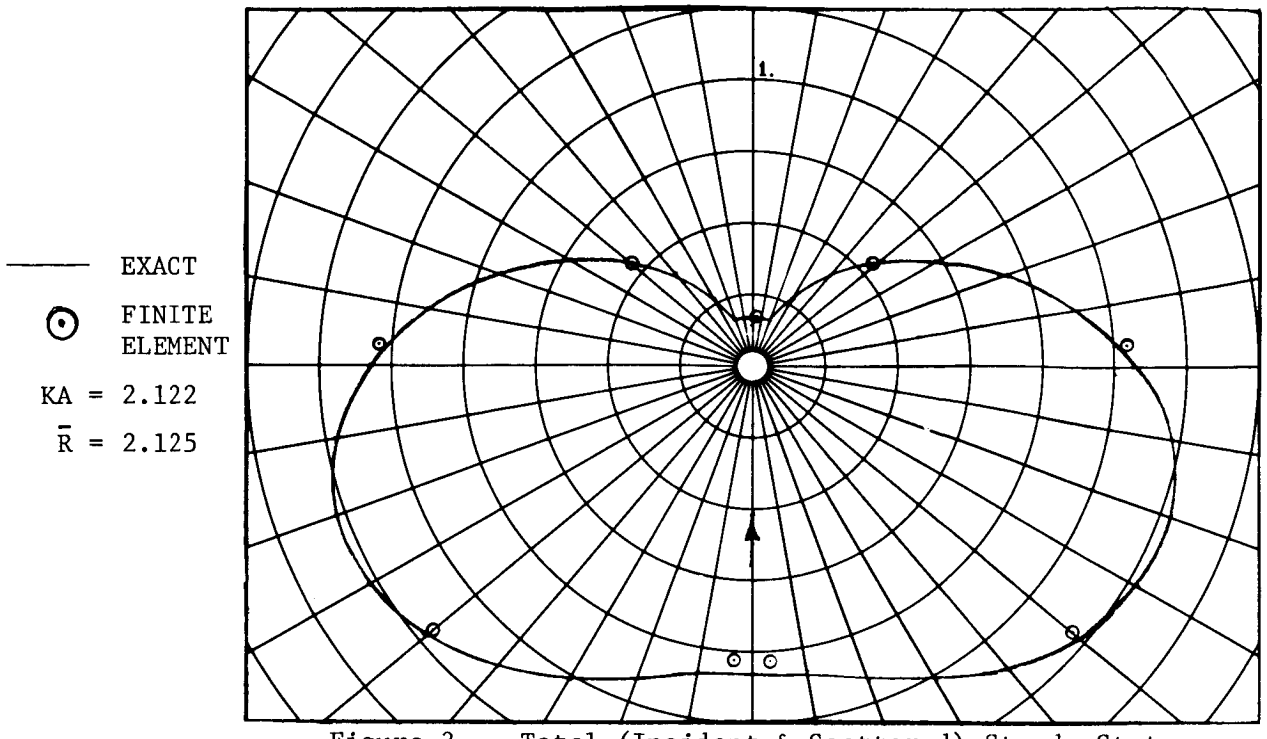

Figure 3. - Total (Incident & Scattered) Steady State Pressure Response of a Cylindrical Void in Water

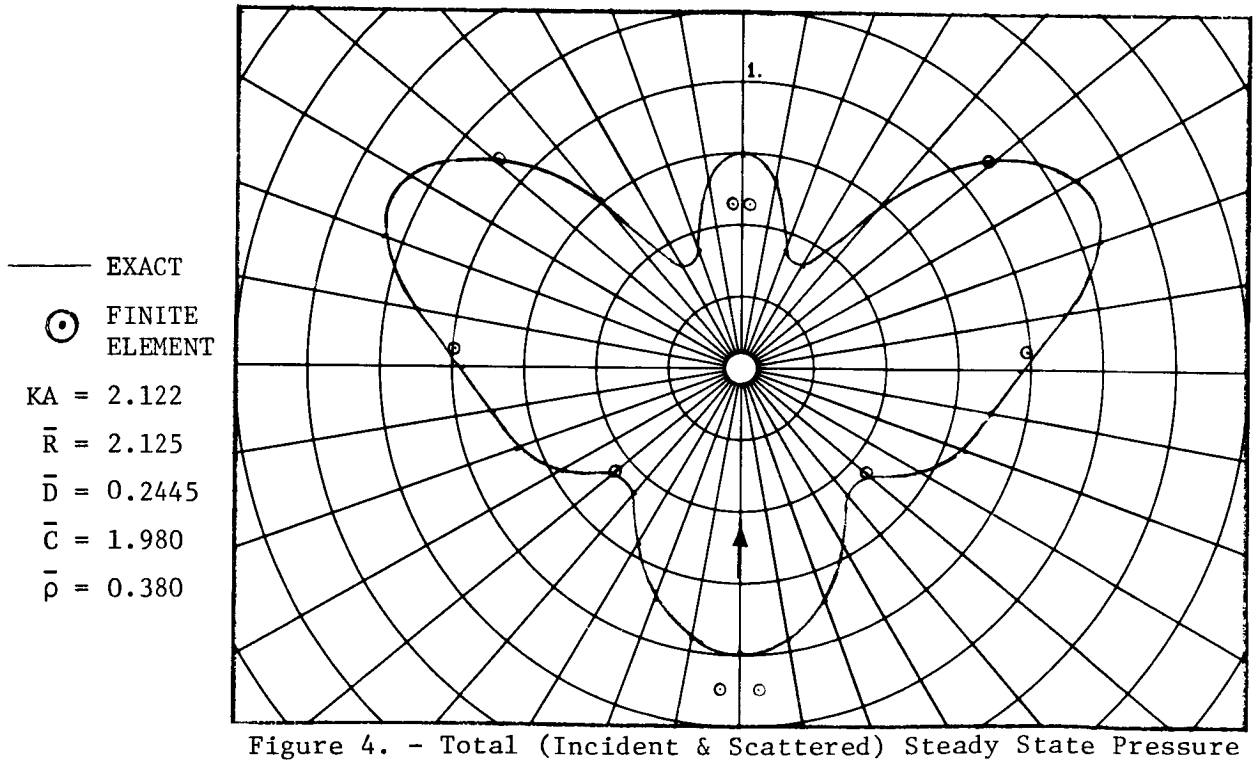

Figure 4. - Total (Incident & Scattered) Steady State Pressure Response of a Solid Elastic Aluminum Cylindrical Inclusion In Water

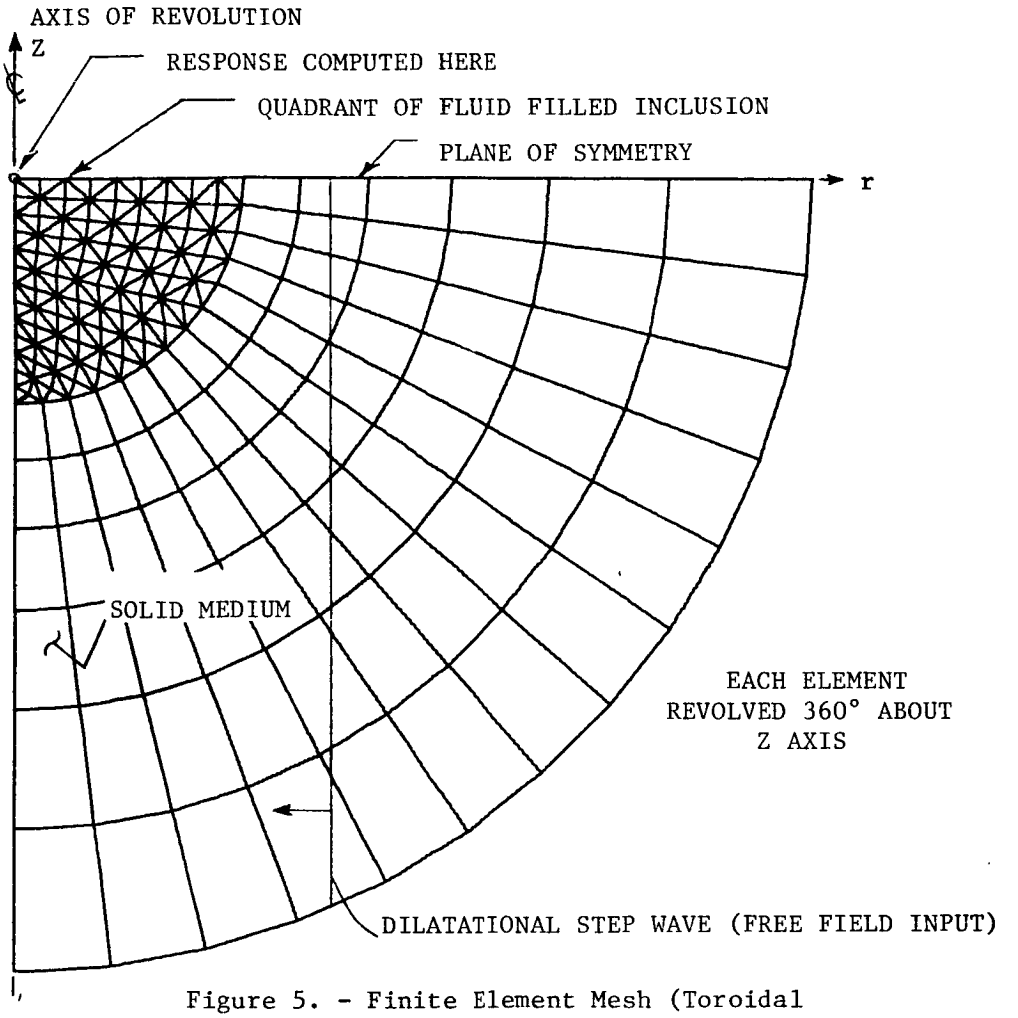

Figure 5. - Finite Element Mesh (Toroidal Element Construction)

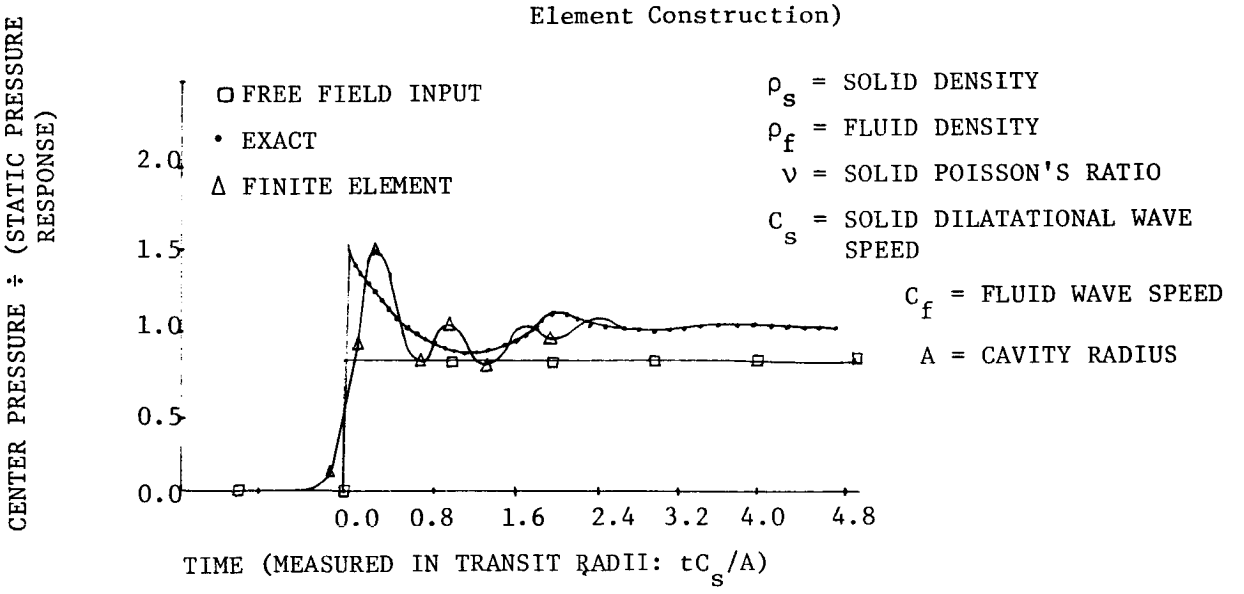

Figure 6. - Pressure Transient Response at Fluid Cavity Center ($\rho_s/\rho_f = 1$; $C_s/C_f = 1$; $\nu = 1/4$)

A FINITE ELEMENT-ANALYTICAL METHOD FOR MODELING A STRUCTURE IN AN INFINITE FLUID

P. Richard Zarda
David W. Taylor Naval Ship Research and Development Center

SUMMARY

A method is described from which the interaction of an elastic structure with an infinite acoustic fluid can be determined. The displacements of the structure and the pressure field of the immediate surrounding fluid are modeled by finite elements, and the remaining pressure field of the infinite fluid region is given by an analytical expression. This method yields a frequency dependent boundary condition for the outer fluid boundary when applied to the frequency response of an elastic beam in contact with an acoustic fluid. The frequency response of the beam is determined using NASTRAN, and compares favorably (1-2% error) to the exact solution which is also presented. The effect of the fluid on the response of the structure at low and high frequencies is due to added mass and damping characteristics, respectively.

INTRODUCTION

The interaction of an acoustic fluid with an elastic solid has received considerable attention in the literature. Some areas of investigation in the frequency domain include underwater vibrations, vibrations of liquids in elastic containers, and the evaluation of the near and far pressure field of an acoustical fluid surrounding a sinusoidally excited elastic structure. A finite element modeling of the combined problem was formulated by Zienkiewicz and Newton (ref. 1). Their finite element modeling of the displacements of a structure and the pressure field of a finite acoustical fluid leads to a system of unsymmetric linear equations to be solved.

Problems involving a finite domain can at least conceptually (and usually practically) be modeled using finite elements (see ref. 2, for example), but those problems involving an infinite fluid domain must necessarily be modeled with only a finite portion of the fluid if the finite element method is to be used. The appropriate boundary condition at the truncated fluid boundary is often in doubt. Zienkiewicz and Newton (ref. 1) suggest a system of dashpots at this outer fluid boundary, but it will be shown that this is the proper boundary condition only in the high frequency limit. This paper formulates the the boundary condition that should be applied at this outer boundary, and shows how this condition is incorporated into the finite element method. To this end, the fluid is divided into a region immediately surrounding the structure (which is to be modeled by finite elements) and an infinite region. Within the

infinite region a series expansion is chosen for the pressure, the coefficients of which are unknowns of the problem. Hunt et al (ref. 3) have a similar model, except the pressure field in the infinite region is given by the surface Helmholtz integral equation. In any case, the expression for the pressure field in the infinite region identically satisfies the governing wave equation and the proper boundary conditions at infinity.

A variational principle, presented specifically for a beam with one face in an acoustical fluid, suggests the proper coupling not only between the structure and the fluid but also between the finite and infinite fluid regions. If a coordinate surface is chosen as the outer fluid boundary, orthogonality relationships of the series expansion may be used to satisfy continuity of the pressure field at this boundary. This orthogonality allows the coefficients of the series expansion to be eliminated as unknowns from the problem, and results in an additional stiffness matrix for the nodal pressures on the outer boundary. This matrix is full, symmetric, and frequency-dependent, and is implemented in NASTRAN by direct matrix input.

This method is applied specifically to the frequency response of a simply supported beam with one face in contact with an infinite acoustical fluid (2-D problem). The exact solution for the frequency response of the beam is presented, and the finite element results compare favorably with the exact solution. It is also shown that at low frequencies the effect of the fluid on the structure is an added mass, while at high frequencies it is a damping. Moreover, the far field pressure in the infinite region can be determined from the series expansion once the nodal pressures at the outer fluid boundary are known.

While this method is applied for a 2-D frequency response, it can be generalized to the response of a 3-D elastic structure in an infinite acoustic fluid. The outer surface of the fluid must be a coordinate surface of a space in which the wave equation is separable since the orthogonality of the series expansion on this surface is used. Once again, the structure and the portion of the fluid between the structure and this coordinate surface are modeled by finite elements. Unfortunately, the additional stiffness matrix couples all the pressure nodes at the outer boundary, and, in general, is frequency dependent. If the frequency is specified, the additional stiffness matrix is known, although in general it could increase the bandwidth of the problem. On the other hand, for determining the submerged natural frequencies of structures an iterative procedure is necessary since the natural frequency is unknown.

A VARIATIONAL PRINCIPLE

It is convenient in applying the finite element method to have a variational principle on which the discretized finite element model can be based. Such principles involving the displacements of an elastic structure can be found in references 4 and 5; similar principles for fluid mechanics problems are presented by Olson in reference 6. Gladwell (refs. 7, 8, 9) presents variational theorems for the acoustic fluid for both pressure and displacement

formulations. For the coupled structural-fluid problem, a suitable variational formulation can be found by properly combining those for an elastic structure and an acoustic fluid. Such a principle is a reliable basis and guide for numerically solving a fluid-structure problem using finite elements. Moreover, with the fluid divided into a finite region (modeled by finite elements) and an infinite region (fluid described by an analytical expression), the variational formulation will necessarily point to the proper coupling of each.

Finite Fluid Region

A simply supported beam is shown in figure 1 which has one side in contact with a finite acoustic fluid and subjected to a sinusoidal load per unit length of $w(x)e^{i\Omega t}$. The deflection of the beam in the y-direction, $u(x)e^{i\Omega t}$, satisfies the differential equation

$$EI \frac{d^4u}{dx^4} - m\Omega^2 u = - p(x,0)h + w(x) \tag{1}$$

where E is the modulus of elasticity of the beam, I is the moment of inertia, m is the mass per unit of length of the beam, and h is the depth of the beam in the z-direction. The pressure $p(x,y)e^{i\Omega t}$ of the fluid region A satisfies the wave equation

$$\frac{\partial^2 p}{\partial x^2} + \frac{\partial^2 p}{\partial y^2} = \frac{1}{c^2}\frac{\partial^2 p}{\partial t^2} = - \frac{\Omega^2}{c^2} p \tag{2}$$

where c is the speed of sound in the fluid. It is also assumed that

$$\frac{\partial p}{\partial n} = 0 \quad \text{on } S \tag{3}$$

where S, shown in figure 1, is the boundary of A excluding the beam's surface. On the surface of the beam, it is also necessary to enforce (see refs. 1, 2) the condition, which comes from conservation of momentum, that

$$\frac{\partial p}{\partial y} = - \rho \ddot{u} = \rho \Omega^2 u \quad \text{on } y = 0 \tag{4}$$

where ρ is the density of the fluid.

It is possible to formulate a mixed variational principle that will incorporate both equations (1) and (2) and the appropriate boundary conditions for each. Consider the functional F(u,p) given by

$$F(u,p) = \frac{1}{2}\int_0^{\ell} EI\left(\frac{d^2u}{dx^2}\right)^2 dx - \frac{1}{2}m\Omega^2 \int_0^{\ell} u^2 dx + \int_0^{\ell} p(x,0)h\,u\,dx$$
$$- \int_0^{\ell} w(x)u\,dx + \frac{1}{2\rho\Omega^2}\int_A \left[\left(\frac{\partial p}{\partial x}\right)^2 + \left(\frac{\partial p}{\partial y}\right)^2\right]hdA - \frac{1}{2\rho c^2}\int_A p^2 hdA \tag{5}$$

The first two terms are the strain energy and kinetic energy of the beam, respectively. The next two terms are minus the work done by the pressure and forcing function on the beam, and the last two terms represent the kinetic and potential energies of the fluid, respectively. The functional F is a function of both the structural displacements u and the fluid pressure p. If independent variations of F are taken with respect to u and p, it follows that

$$\delta F(u,p) = \int_0^{\ell}\left[EI\frac{d^4u}{dx^4} - m\Omega^2 u + ph - w(x)\right]\delta u\,dx$$
$$- \int_A \left[\frac{1}{\rho\Omega^2}\left(\frac{\partial^2 p}{\partial x^2} + \frac{\partial^2 p}{\partial y^2}\right) + \frac{p}{\rho c^2}\right]\delta p\,hdA + EI\frac{d^2u}{dx^2}\delta u'\Big|_0^{\ell} \tag{6}$$
$$- EI\frac{d^3u}{dx^3}\delta u\Big|_0^{\ell} + \frac{1}{\rho\Omega^2}\int_S \frac{\partial p}{\partial n}\delta p\,hds + \int_0^{\ell}\left[-\frac{1}{\rho\Omega^2}\frac{\partial p}{\partial y} + u\right]\delta p\,h\,dx$$

If u and p are found such that

$$\delta F(u,p) = 0 \tag{7}$$

with any trial function u satisfying

$$u(0) = u(\ell) = 0 \tag{8}$$

then it can be seen from equation (6) that u and p necessarily satisfy equations (1) and (2) and the boundary conditions given by equations (3) and (4).

Coupling of the Infinite Fluid

If the region of the fluid is infinite, as shown in figure 2, the fluid is subdivided: the finite element description of the pressure in the fluid is used in a finite region A_1 surrounding the structure, and an analytical expression (which identically satisfies the wave equation) is used in the remaining infinite region A_2. In order to properly couple the two solutions, the pressure field must be continuous and consistent with the variational principle. The functional F(u,p) in equation (5) now contains two additional terms which are the same as the last two terms but integrated over the remaining infinite region. The analytical expression for p in this region satisfies the proper boundary conditions at infinity (Somerfeld radiation condition). Variations of

F taken with respect to u and p in both regions give

$$\delta F(u,p) = \int_0^{\ell} \left[EI \frac{d^2u}{dx^4} - m\Omega^2 u + ph - w(x) \right] \delta u \, dx + \frac{1}{\rho\Omega^2} \int_S \frac{\partial p}{\partial n} \delta p \, h \, ds$$

$$+ EI \frac{d^2u}{dx^2} \delta u' \Big|_0^{\ell} - EI \frac{d^3u}{dx^3} \delta u \Big|_0^{\ell} + \int_0^{\ell} \left[\frac{1}{\rho\Omega^2} \frac{\partial p}{\partial n} + u \right] \delta p \, dx$$

$$- \int_{A_1} \frac{1}{\rho\Omega^2} \left(\frac{\partial^2 p}{\partial x^2} + \frac{\partial^2 p}{\partial y^2} + \frac{p}{\rho c^2} \right) \delta p \, h dA_1 + \frac{1}{\rho\Omega^2} \int_s \frac{\partial p}{\partial n_1} \delta p \, h \, ds \tag{9}$$

$$- \int_{A_2} \frac{1}{\rho\Omega^2} \left(\frac{\partial^2 p}{\partial x^2} + \frac{\partial^2 p}{\partial y^2} + \frac{p}{\rho c^2} \right) \delta p \, h dA_2 + \frac{1}{\rho\Omega^2} \int_s \frac{\partial p}{\partial n_2} \delta p \, h \, ds$$

where s is the boundary between the finite and infinite fluid regions. With the analytical function p identically satisfying the wave equation, the coefficient of δp in the next to last term is identically zero. Hence, only the term

$$I = \frac{1}{\rho\Omega^2} \int_s \frac{\partial p}{\partial n_s} \delta p \, h \, ds \tag{10}$$

which is the loading of the infinite region on the finite must be included. In the integral I, p is given by an analytical expression which must match the finite element nodal approximation on the fluid-fluid interface. Assume the analytical expression for p is given by an expansion

$$p = \sum_{n=1}^{N} A_n f_n(x,y) \tag{11}$$

where the A_n's are undetermined coefficients and the functions $f_n(x,y)$ identically satisfy the wave equation. Equation (11), together with the finite element description of the pressure at the interface and the continuity of the pressure field, will permit the integral in equation (10) to be evaluated. The continuity of the pressure field can be easily obtained by choosing an outer boundary on which the orthogonality of the functions $f_n(x,y)$ can be used. The evaluation of equation (11) will be carried out specifically for the frequency response of a beam in an infinite fluid.

FINITE ELEMENT FORMULATION

Beam and Neighboring Fluid

The finite element method approximates the displacements u of the beam by

$$u = \sum_i N_i^S u_i \tag{12}$$

where u_i is a generalized nodal displacement, and N_i^S is a shape function for the displacements of the beam. Similarly, the pressure field in the fluid is approximated by

$$p = \sum_i N_i^F p_i \tag{13}$$

where p_i is a nodal pressure. Substituting these approximations into equation (6) and interpreting equation (7) to mean that partial derivatives with respect to nodal displacements and pressures should equal zero, the following set of equations is determined:

$$\begin{bmatrix} K & L \\ 0 & \frac{1}{\rho\Omega^2}H \end{bmatrix} \begin{Bmatrix} u \\ p \end{Bmatrix} - \Omega^2 \begin{bmatrix} M & 0 \\ -\frac{1}{\Omega^2}L^T & \frac{1}{\rho c^2\Omega^2}Q \end{bmatrix} \begin{Bmatrix} u \\ p \end{Bmatrix} = \begin{Bmatrix} f \\ 0 \end{Bmatrix} \tag{14}$$

where

$$K_{ij} = \int_0^\ell EI \frac{d^2N_i^S}{dx^2} \frac{d^2N_j^S}{dx^2} dx \tag{15}$$

$$M_{ij} = m \int_0^\ell N_i^S N_j^S dx \tag{16}$$

$$f_i = \int_0^\ell w(x) N_i^S dx \tag{17}$$

$$L_{ij} = \int_0^\ell N_i^S N_j \, h dx \tag{18}$$

$$H_{ij} = \int_A \left[\frac{\partial N_i^F}{\partial x} \frac{\partial N_j^F}{\partial x} + \frac{\partial N_i^F}{\partial y} \frac{\partial N_j^F}{\partial y} \right] h dA \tag{19}$$

$$Q_{ij} = \int_A N_i^F N_j^F h dA \tag{20}$$

Multiplying the second set of equations by $(\rho c\Omega)^2$ gives

$$\begin{bmatrix} K & L \\ 0 & \rho c^2 H \end{bmatrix} \begin{Bmatrix} u \\ p \end{Bmatrix} - \Omega^2 \begin{bmatrix} M & 0 \\ -(\rho c)^2 L^T & \rho Q \end{bmatrix} \begin{Bmatrix} u \\ p \end{Bmatrix} = \begin{Bmatrix} f \\ 0 \end{Bmatrix} \tag{21}$$

This form is the same as that derived by Zienkiewicz and Newton (ref. 1), but equations (21) are based on a variational principle. The set of equations (11)

can be generated by NASTRAN as outlined in reference 2, although matrices L and L^T are inputted directly by DMIG cards.

For more complicated geometries and structures, the form of equation (21) is unchanged. While the variational principle and the finite element formulation were given specifically for the elastic beam-acoustic fluid problem, they can be easily generalized to account for an elastic structure bounded by an acoustic fluid.

Infinite Fluid Coupling Matrix

The loading of the infinite fluid on the finite portion is found by computing the integral

$$I = \frac{1}{\rho\Omega^2} \int_s \frac{\partial p}{\partial n_2} \delta p \, h \, ds \tag{22}$$

over the outer fluid face (see eq. (10)). This integral is to be discretized and then added to the set of equations (14). At the fluid-fluid interface the pressure is given by

$$p = \sum_{i=1}^{M} N_i p_i \tag{23}$$

where N_i is the shape function for the pressure in the fluid evaluated at the fluid-fluid interface, p_i is a nodal pressure on the face, and M is the number of pressure nodes at the fluid-fluid interface. The δp in equation (22) is equal to the partial of p with respect to p_i (which is equal to N_i from equation (23)). Then the term

$$\frac{1}{\rho\Omega^2} \int_s \frac{\partial p}{\partial n_2} N_i \, h \, ds \tag{24}$$

is added to the p_i equation of equations (14).

Consider the frequency response of a beam with one side immersed in an infinite acoustic fluid, as shown in figure 3. Both the displacements of the beam and the pressure field of the neighboring acoustic fluid are modeled by finite elements. The pressure field in the fluid for y>b must be bounded and satisfy

$$\frac{\partial^2 p}{\partial x^2} + \frac{\partial^2 p}{\partial y^2} = -\left(\frac{\Omega}{c}\right)^2 p \tag{25}$$

with the boundary condition that

$$p = 0 \quad \text{at} \quad x = 0 \quad \text{and} \quad x = \ell \tag{26}$$

and the condition that only waves outgoing from the structure are allowed.

Separation of variables leads to the following expression for p:

$$p = \sum_{n=1}^{N} A_n \sin\left(\frac{n\pi x}{\ell}\right) e^{-\alpha_n y} \tag{27}$$

with

$$\alpha_n^2 = \left(\frac{n\pi}{\ell}\right)^2 - \left(\frac{\Omega}{c}\right)^2 \tag{28}$$

The N arbitrary coefficients A_n are yet to be determined, and α_n may be either real or imaginary depending on n and Ω.

The integral in equation (22) can now be evaluated. From equation (27),

$$\frac{\partial p}{\partial n_2} = - \frac{\partial p}{\partial y}\bigg|_{y=b} = \sum_{n=1}^{N} A_n \sin\left(\frac{n\pi x}{\ell}\right) \alpha_n e^{-\alpha_n b} \tag{29}$$

Substituting equation (29) into the expression (24), the following matrix expression is added to the left-hand side of equations (14):

$$\frac{1}{\rho\Omega^2} [G]\{A\} \tag{30}$$

where {A} is a vector of the N coefficients A_j and [G] is an MxN matrix given by

$$G_{ij} = \int_0^{\ell} N_i \sin\left(\frac{j\pi x}{\ell}\right) \alpha_j e^{-\alpha_j b} dx \tag{31}$$

The number of unknowns in equation (14) has been increased by N, the number of A_j coefficients. An additional set of equations to make the set complete is found by requiring the pressure to be continuous; that is, equation (23) must match equation (27) evaluated at the interface y=b:

$$\sum_{i=1}^{M} N_i p_i = \sum_{n=1}^{N} A_n \sin\left(\frac{n\pi x}{\ell}\right) e^{-\alpha_n b} \tag{32}$$

Multiplying both sides by

$$\sin\left(\frac{k\pi x}{\ell}\right)$$

and integrating from 0 to ℓ with the orthogonality condition that

$$\int_0^{\ell} \sin\left(\frac{n\pi x}{\ell}\right) \sin\left(\frac{k\pi x}{\ell}\right) dx = \begin{cases} 0 & n \neq k \\ \frac{\ell}{2} & n = k \end{cases} \tag{33}$$

gives

$$\{A\} = [R]\{p\} \tag{34}$$

where [R] is an NxM matrix and is given by

$$R_{ij} = \frac{2\,e^{\alpha_i b}}{\ell} \int_0^{\ell} N_j \sin\left(\frac{i\pi x}{\ell}\right) dx \tag{35}$$

The additional N equations from equation (34) form a complete set with equations (14) and (30). Alternatively, equation (34) can be used to eliminate the series coefficients A_j from the expression (30) in favor of the nodal pressures of the fluid-fluid interface. Thus,

$$\frac{1}{\rho\Omega^2}[G]\{A\} = \frac{1}{\rho\Omega^2}[G][R]\{p\}$$

Define

$$[H'] = [G][R] \tag{36}$$

with matrices [G] and [R] given by equations (31) and (35). The effect of the infinite fluid on the finite is to add to the fluid stiffness matrix [H] of equations (14) the matrix [H']. [H'] is an MxM symmetric matrix which may be complex. It is full, frequency-dependent and couples just the nodes at the outer fluid boundary.

If $\Omega \to 0$ or equivalently $c \to \infty$, the effect of the infinite fluid on the finite fluid is one of stiffness. From equation (28),

$$\alpha_j \to \frac{j\pi}{\ell} \quad \text{as} \quad \Omega \to 0 \tag{37}$$

and

$$G_{ij} \to a_j e^{-\alpha_j b} F_{ij} \tag{38}$$

where

$$F_{ij} = \int_0^{\ell} N_i \sin\left(\frac{j\pi x}{\ell}\right) dx \tag{39}$$

The matrix [F] does not depend on the frequency Ω. Similarly,

$$R_{ij} \to \frac{2\,e^{\alpha_i b}}{\ell} F_{ij} \quad \text{as} \quad \Omega \to 0 \tag{40}$$

Then matrix [H'] = [G][R] is given by

$$H'_{ij} = \sum_{k=1}^{N} G_{ik} R_{kj} \tag{41}$$

Substituting equations (37), (38), and (40) into equation (41) gives

$$H'_{ij} = \frac{2\pi}{\ell^2} \sum_{k=1}^{N} k F_{ik} F_{jk} \tag{42}$$

where [H'] is a constant matrix (independent of frequency) and is added directly to the stiffness matrix [H] of the fluid. If the outer finite element boundary is chosen to be the surface of the beam, then the matrices [H] and [Q] of equation (14) are zero. Then the second set of equations (14) can be written, with the matrix H' now included, as

$$\frac{1}{\rho\Omega^2}[H']\{p\} + [L^T]\{u\} = 0$$

This gives

$$\{p\} = -\rho\Omega^2[H']^{-1}[L^T]\{u\}$$

Substitution of this equation into the first set of equations (14) gives the following added mass matrix:

$$[M'] = \rho[L][H']^{-1}[L^T] \tag{43}$$

Matrix [M'] is symmetric and full and shows that the effect of the fluid on the structure is added mass.

When $\Omega \to \infty$ or $c \to 0$, the effect of the infinite fluid on the finite is a pure damping. For, from equation (28),

$$\alpha_j \to \frac{\Omega}{c} i$$

where i is $\sqrt{-1}$. Then

$$H'_{rs} = \frac{2}{\ell}\frac{\Omega}{c} i \sum_{k=1}^{N} F_{rk} F_{sk} \tag{44}$$

[H'] is a pure imaginary matrix, linear in Ω, which is to be added to the stiffness matrix [H] in equation (14). Then rewriting equation (14) in the form of equation (21) gives

$$\begin{bmatrix} K & L \\ 0 & \rho c^2 H \end{bmatrix}\begin{Bmatrix} u \\ p \end{Bmatrix} + i\Omega\begin{bmatrix} 0 & 0 \\ 0 & \rho c B \end{bmatrix}\begin{Bmatrix} u \\ p \end{Bmatrix} - \Omega^2\begin{bmatrix} M & 0 \\ -(\rho c)^2 L^T & \rho Q \end{bmatrix}\begin{Bmatrix} u \\ p \end{Bmatrix} = \begin{Bmatrix} f \\ 0 \end{Bmatrix} \tag{45}$$

where [B] is an MxM damping matrix and an element of matrix [B] is given by

$$B_{rs} = \frac{2}{\ell} \sum_{k=1}^{N} F_{rk} F_{rs} \tag{46}$$

The coefficient F_{ij}, defined in equation (39), is equal to $(\ell/2)$ times the jth Fourier sine coefficient of the shape function N_i. Hence the sum of terms on the right-hand side of equation (46) is the dot product of the Fourier coefficients of the function N_r with N_s. It can be shown that this dot product is equal to $(2/\ell)$ times the inner product of the shape function N_r with N_s over the length of the beam. Thus,

$$B_{rs} = \frac{2}{\ell} \sum_{k=1}^{N} F_{rk} F_{sk} = \int_0^{\ell} N_r N_s \, dx \tag{47}$$

This term is identical to the one suggested by Zienkiewicz and Newton (ref. 1), which is a boundary condition derived by assuming that the pressure in the fluid takes the form of a plane wave. The boundary condition is to be applied at a boundary which has been placed "far enough" from the structure and is the proper boundary condition only in the high frequency limit.

If the outer fluid boundary is reduced to that of the beam, then both matrices [H] and [Q] in equation (45) are zero. Solving the second set of equations (45) for {p} in terms of {u} gives

$$\{p\} = \rho c(\Omega i)[B]^{-1}[L^T]\{u\} \tag{48}$$

Substituting this equation into the first set gives

$$[K]\{u\} + (\Omega i)\rho c L[B]^{-1}[L^T]\{u\} - \Omega^2[M]\{u\} = \{f\} \tag{49}$$

Then the matrix

$$\rho c[L][B]^{-1}[L^T]$$

is a damping matrix, which means that the effect of the fluid on the structure at high frequencies (or small c) is damping.

EXACT SOLUTION - FREQUENCY RESPONSE OF BEAM

The differential equation of motion for the elastic beam shown in figure 3 subjected to a uniform load varying sinusoidally in time is

$$EI \frac{\partial^4 u}{\partial x^4} + m \frac{\partial^2 u}{\partial t^2} + p(x,0,t)h = w_0 e^{i\Omega t} \tag{50}$$

where p(x,y,t) is the acoustical pressure which must satisfy the wave equation

$$\frac{\partial^2 p}{\partial x^2} + \frac{\partial^2 p}{\partial y^2} = \frac{1}{c^2} \frac{\partial^2 p}{\partial t^2} \tag{51}$$

A solution for u of the form

$$u(x,t) = \sum_{n=1}^{\infty} A_n \sin(\frac{n\pi x}{\ell}) e^{i\Omega t} \tag{52}$$

is chosen, where the A_n's are undetermined coefficients of $\sin \frac{n\pi x}{\ell}$, which are the out-of-fluid eigenvectors for the simply supported beam. Equation (51) is solved using separation of variables. The pressure field is bounded and the boundary condition at x=0 and x=ℓ is that p=0. Allowing only outgoing waves from the beam leads to the following equation for p:

$$p = \sum_{n=1}^{\infty} C_n \sin(\frac{n\pi x}{\ell}) e^{-\alpha_n y} e^{i\Omega t} \tag{53}$$

where

$$\alpha_n^2 = (\frac{n\pi}{\ell})^2 - (\frac{\Omega}{c})^2$$

The C_n's are undetermined coefficients to be found by properly coupling the fluid and the structure. At the fluid-structure interface, one requires (see, for example, ref. 2)

$$\frac{\partial p}{\partial n} = -\rho \ddot{u}_n \quad \text{at} \quad y = 0 \tag{54}$$

Since the fluid and structural modes are uncoupled for this problem, equation (54) yields

$$C_n = -\frac{\rho\Omega^2}{\alpha_n} A_n \tag{55}$$

Substituting equation (55) into equation (53), and the expressions for u and p into equation (50), gives

$$\sum_{n=1}^{\infty} \left\{ -(m+\frac{\rho h}{\alpha_n})\Omega^2 + EI(\frac{n\pi}{\ell})^4 \right\} A_n \sin(\frac{n\pi x}{\ell}) e^{i\Omega t} = w_0 e^{i\Omega t} \tag{56}$$

with

$$\alpha_n^2 = (\frac{n\pi}{\ell})^2 - (\frac{\Omega}{c})^2$$

When both sides are multiplied by $\sin(\frac{k\pi x}{\ell})$ and integrated from 0 to ℓ to take advantage of orthogonality relationships, the solution is

$$u(x,t) = \sum_{n=1,3,\ldots}^{\infty} A_n \sin \frac{n\pi x}{\ell} e^{i\Omega t} \tag{57}$$

$$p(x,y,t) = \sum_{n=1,3,\ldots}^{\infty} - \frac{\rho\Omega^2}{\alpha_n} A_n \sin\frac{n\pi x}{\ell} e^{-\alpha_n y} e^{i\Omega t} \tag{58}$$

with

$$A_n = \frac{4w_0}{n\pi\{-\Omega^2(m+\frac{\rho h}{\alpha_n}) + EI(\frac{n\pi}{\ell})^4} \tag{59}$$

and

$$\alpha_n^2 = (\frac{n\pi}{\ell})^2 - (\frac{\Omega}{c})^2 \tag{60}$$

In general α_n may be real or imaginary depending on the driving frequency Ω. If

$$\Omega \leq \frac{\pi c}{\ell}$$

then for all n, α_n is real. In this case the pressure and displacement are real and in phase and no radiation occurs. If $\Omega > (\pi c/\ell)$, then for some n, α_n becomes imaginary. In this case, both u and p are complex and out of phase and hence radiation may occur.

Peaks in the frequency response will occur at the in-fluid natural frequencies of the beam. Although the in-fluid and in-air mode shape of the beam are unchanged in this particular problem, the natural frequency of the beam does change. The in-fluid natural frequencies are found by setting the term in brackets in equation (56) equal to zero and solving for Ω. The solution always gives $\Omega_n < (n\pi c/\ell)$, which means that the in-fluid modal shapes of the beam do not radiate.

RESULTS

Computations were carried out by NASTRAN using the finite element-analytical method previously described. A typical grid is that shown in figure 3, where CBAR elements were used to model the beam and 2-D isoparametric elements (with quadratic approximation for the pressure) were chosen to model the fluid. The usual double numbering of grid points at the fluid-structure interface is necessary with this formulation (this procedure is outlined in ref. 2), and the nodal pressures and displacements of the interface are coupled through matrix [L] of equation (14). This matrix is entered into NASTRAN by DMIG cards. The frequency dependent matrix [H'] defined in equation (36), which models the effect of the infinite fluid on the finite, is also inputted into NASTRAN by DMIG cards. The results shown in figures 4 through 8 are for the following values: h = 2.54 cm (1 inch), ℓ = 50.8 cm (20 in.), c = 1.460 km/sec (5.748×10^4 in/sec), E = 206.8 GPa (3×10^7 psi), I = 3.468 cm^4 (.08333 in^4), m = 7.827 g/cm^3 (7.324×10^{-4} lb-sec^2/in^4), ρ = 1.029 g/cm^3 (9.633×10^{-5} lb-sec^2/in^4), w_0 = 1.751 N/cm (1 lb/in). The solid line in each of these figures is

the exact solution given by equations (57) through (60). The finite element solution is shown at specific plotted points.

Figure 4 is a plot of the magnitude of the pressure at the center of the beam versus the driving frequency Ω. The pressure peaks at approximately 1062 rad/sec and 11350 rad/sec, which are the in-fluid natural frequencies of the beam for modes n = 1 and n = 3 (these values can be determined by solving equation (56) for Ω with $w_0 = 0$). There is a discontinuity in the slope of the curve for $\Omega \approx 9029$ radians/sec, which is the frequency at which radiation occurs ($\Omega = \pi c/\ell = 9029$ rad/sec). For frequencies greater than $\pi c/\ell$, energy is being carried away by the outgoing pressure waves and the beam is said to radiate. In this case net work is done by the forcing function.

Figures 5 and 6 are plots of the magnitude of the beam's displacement at its center as a function of the driving frequency Ω. In figure 6 the displacement shows the discontinuity in slope that the pressure exhibits when the beam begins to radiate. As Ω goes through $\pi c/\ell$, the displacement of the beam increases corresponding to the reduction in pressure.

The variations of the phase angles of the pressure and displacement with frequency are shown in figures 7 and 8, respectively. For $\Omega \leq \pi c/\ell$ (9029 rad/sec), the displacement is in phase (or 180° out of phase) with the driving force and no work is done. For $\Omega > \pi c/\ell$, the displacement is out of phase with the driving frequency and radiation occurs. The only exception to this condition occurs when Ω approaches a natural frequency. The mode shape for that frequency dominates, and, since the in-fluid mode shapes of the beam do not radiate, the phase angle of the displacement is in phase (or 180° out of phase) with the driving force.

Figures 4-8 show that the finite element solution obtained through NASTRAN was reliable in modeling the elastic beam in the infinite acoustical fluid. The errors of the results shown were 1-2% for the grid shown in figure 3. The same accuracy was also obtained at a few frequencies in which the outer fluid boundary was chosen to be that of the beam (that is, b=0). In these cases, matrix [H'] (defined in eq. (36)) corresponds to the nodal pressures at the fluid-structure interface.

For the limiting case of $\Omega \to 0$, the effect of the fluid on the structure is an added mass; this effect is approximated within the finite element method by modeling the structure with NASTRAN and adding to the mass matrix generated by NASTRAN the additional mass matrix [M'] given by equation (43). The natural frequencies and mode shapes of this computation agreed favorably (less than 1% error) with those from the exact solution. The exact solution is determined from equation (56) by solving for Ω with $w_0 = 0$ and $c \to \infty$.

CONCLUSIONS

The boundary condition at the truncated fluid boundary of an infinite acoustical fluid is, in general, frequency dependent. For a finite element formulation this condition leads to a stiffness matrix [H'] which is added to

the stiffness matrix of the fluid. [H'] is a full, symmetric, complex, frequency dependent matrix which couples the infinite region to the finite region and involves only the outer boundary nodes. If the driving frequency is specified (in the case of frequency response), the coupling matrix [H'] can be inputted into NASTRAN by DMIG cards. The computation of eigenvalues and eigenvectors, on the other hand, would necessarily involve an iteration scheme since the frequency of the mode shape is not known.

Although only the portion of the fluid immediately surrounding the structure is modeled by finite elements, the infinite fluid region is effectively modeled through the coupling matrix [H']. Moreover, the far field pressure can be determined once the outer boundary pressures are computed. This pressure is given by equation (27) with the series coefficients {A} determined from equation (34). If a finite portion of the fluid is modeled without including the boundary condition matrix [H'], then the fluid region is actually a finite domain. Not only is it impossible to determine the far field pressure but also some of the eigenvalues and eigenvectors found can be shown to be associated with the finite problem. These additional modal values do not appear if [H'] is included.

This type of finite element-analytical solution, presented here for a two-dimensional problem, can be readily generalized to a three-dimensional problem of modeling an elastic structure in an infinite acoustic medium. In this case the outer fluid boundary would be a sphere, and the pressure field would be given by an expansion of spherical harmonics. The frequency dependent matrix could be generated in NASTRAN by program modifications and would be accessed through DMAP alters. Unfortunately, because of the full coupling of all the outer boundary nodes, the increase in the bandwidth for a three-dimensional problem might make the computer cost prohibitive.

REFERENCES

1. Zienkiewicz, O.C., and Newton, R.E.: "Coupled Vibrations of a Structure Submerged in a Compressible Fluid," Proc. Int. Symp. on Finite Element Techniques, Stuttgart, 1969.

2. Everstine, G.C., Schroeder, E.A., and Marcus, M.S.: "The Dynamic Analysis of Submerged Structures," NASTRAN: Users' Experiences, NASA TM X-3278, Sept. 1975, pp. 419-429.

3. Hunt, John T., Knittel, Max R., and Barach, Don: "Finite Element Approach to Acoustic Radiation from Elastic Structures," J. Acoust. Soc. Am., vol. 55, no. 2, Feb. 1974.

4. Zienkiewicz, O.C.: The Finite Element Method in Structural and Continuum Mechanics, McGraw-Hill Book Company, Inc., 1970.

5. Gallagher, R.H.: Finite Element Analysis Fundamentals, Prentice-Hall, Inc., Englewood Cliffs, N.J., 1975.

6. Olson, M.D.: "Variational-Finite Element Methods for Two-Dimensional and Axisymmetric Navier-Stokes Equations," Finite Elements in Fluids, Gallagher et al, editors, vol. 1, Wiley, 1975, pp. 57-72.

7. Gladwell, E.M.L.: "A Variational Formulation of Damped Acousto-Structural Vibration Problems," J. Sound Vib., 4(2), (1966), pp. 172-186.

8. Gladwell, E.M.L., and Zimmerman, E.: "On Energy and Complementary Energy Formulations of Acoustic and Structural Vibration Problems," J. Sound Vib., 3(3), (1966), pp. 233-241.

9. Gladwell, E.M.L., and Mason, V.: "Variational Finite Element Calculation of the Acoustical Response of a Rectangulan Panel," J. Sound Vib., 14(1), (1971), pp. 115-135.

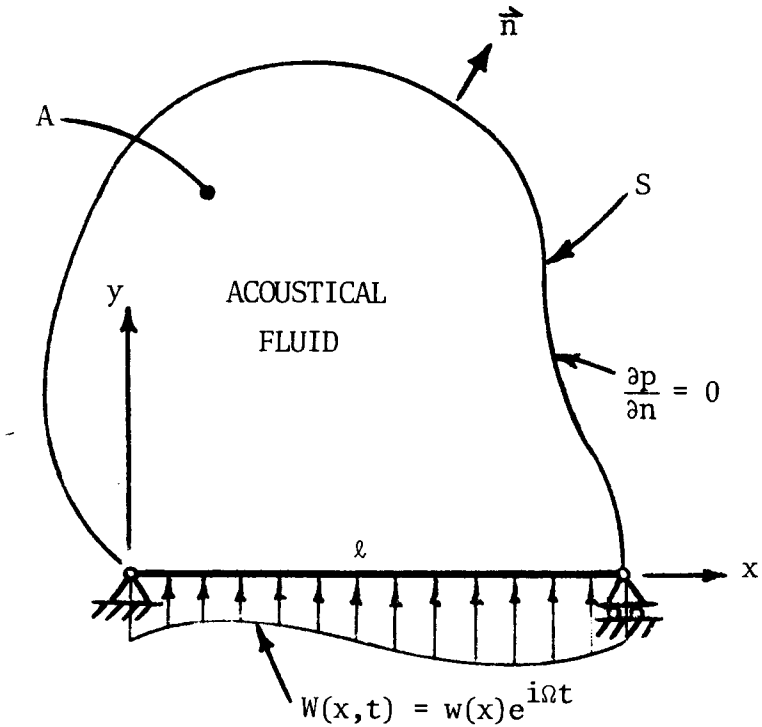

Figure 1. Sinusoidally Loaded Beam with One Side Immersed in a Finite Acoustical Fluid.

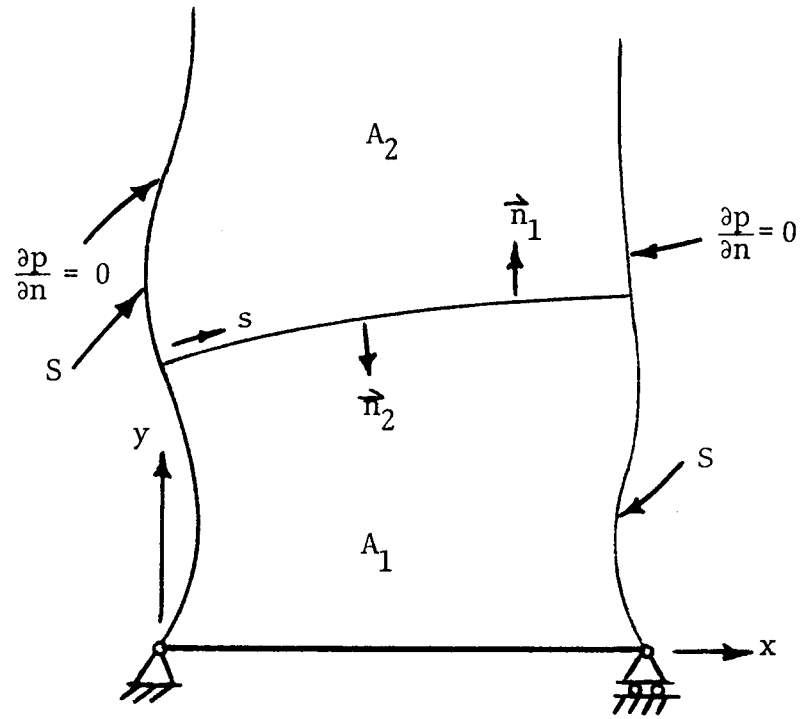

Figure 2. Fluid Region Divided into Finite Region A_1 and Infinite Region A_2.

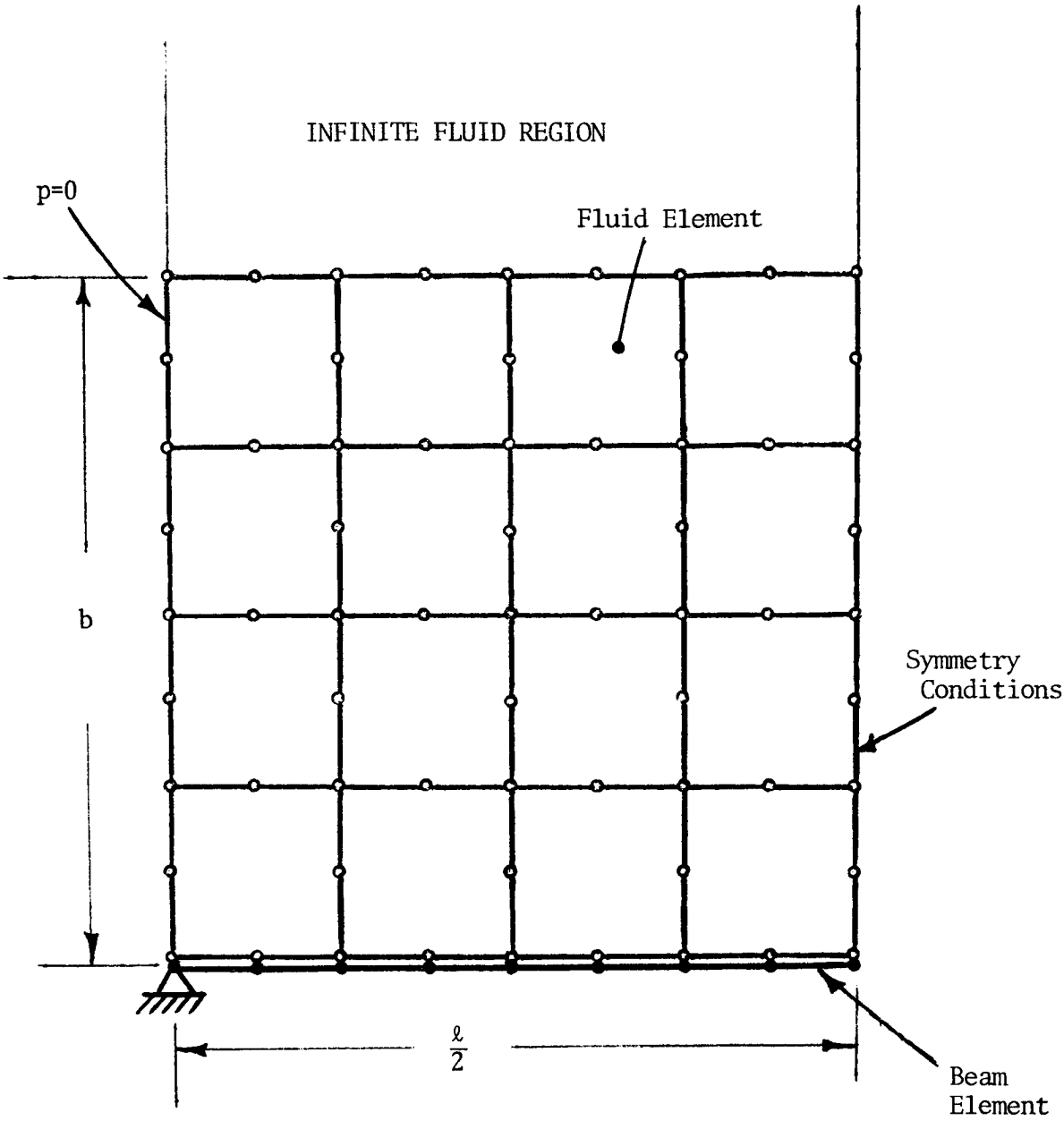

Figure 3. Finite Element Grid Showing Both the Fluid and Beam Elements. Nodal Pressures of the Fluid and Nodal Displacements of the Structure are the Unknowns.

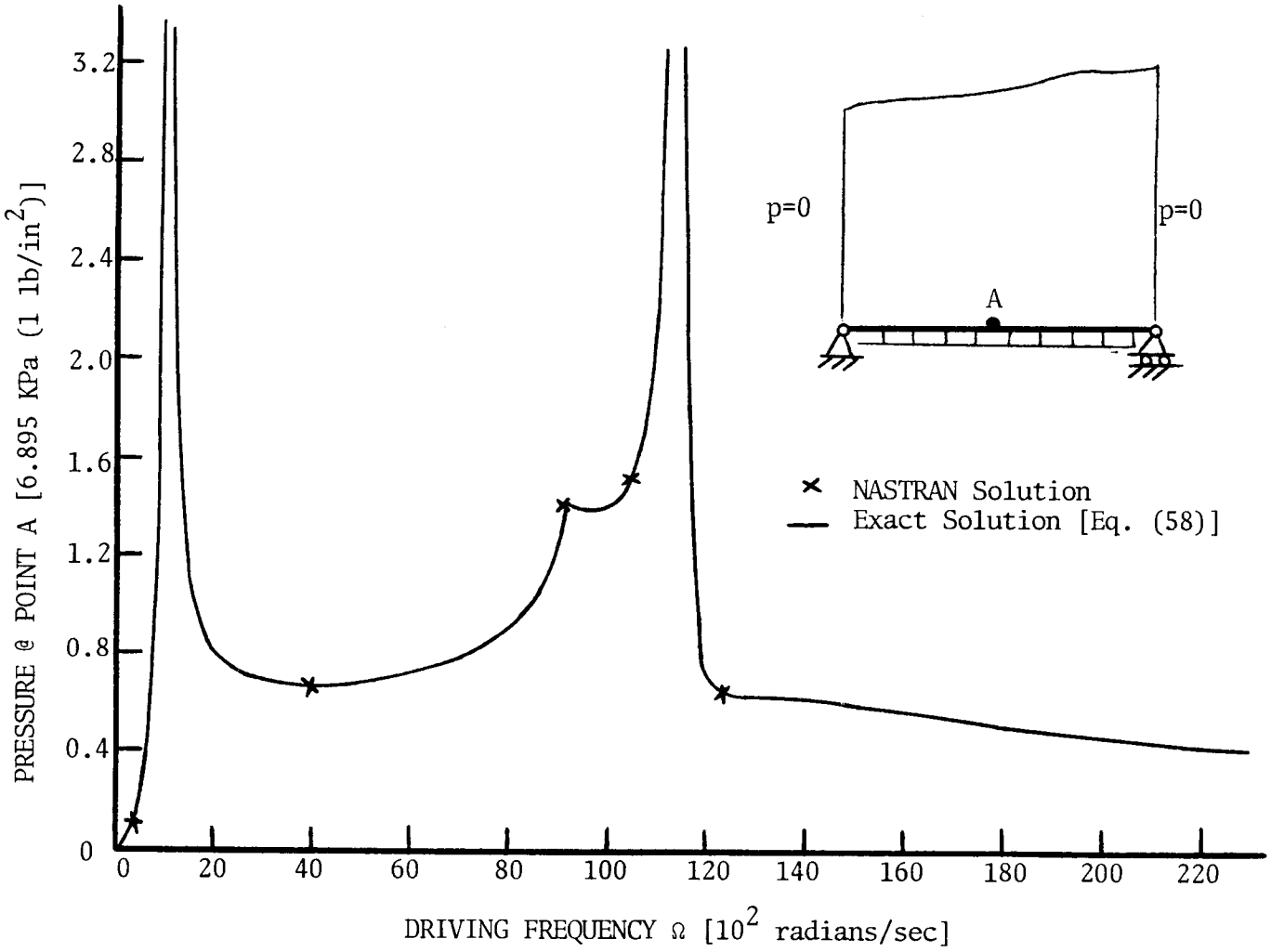

Figure 4. Magnitude of the Acoustical Pressure at Point A (Center of Beam) as a Function of the Driving Frequency. Peaks Occur at the In-Fluid Natural Frequencies Given by Equation (56).

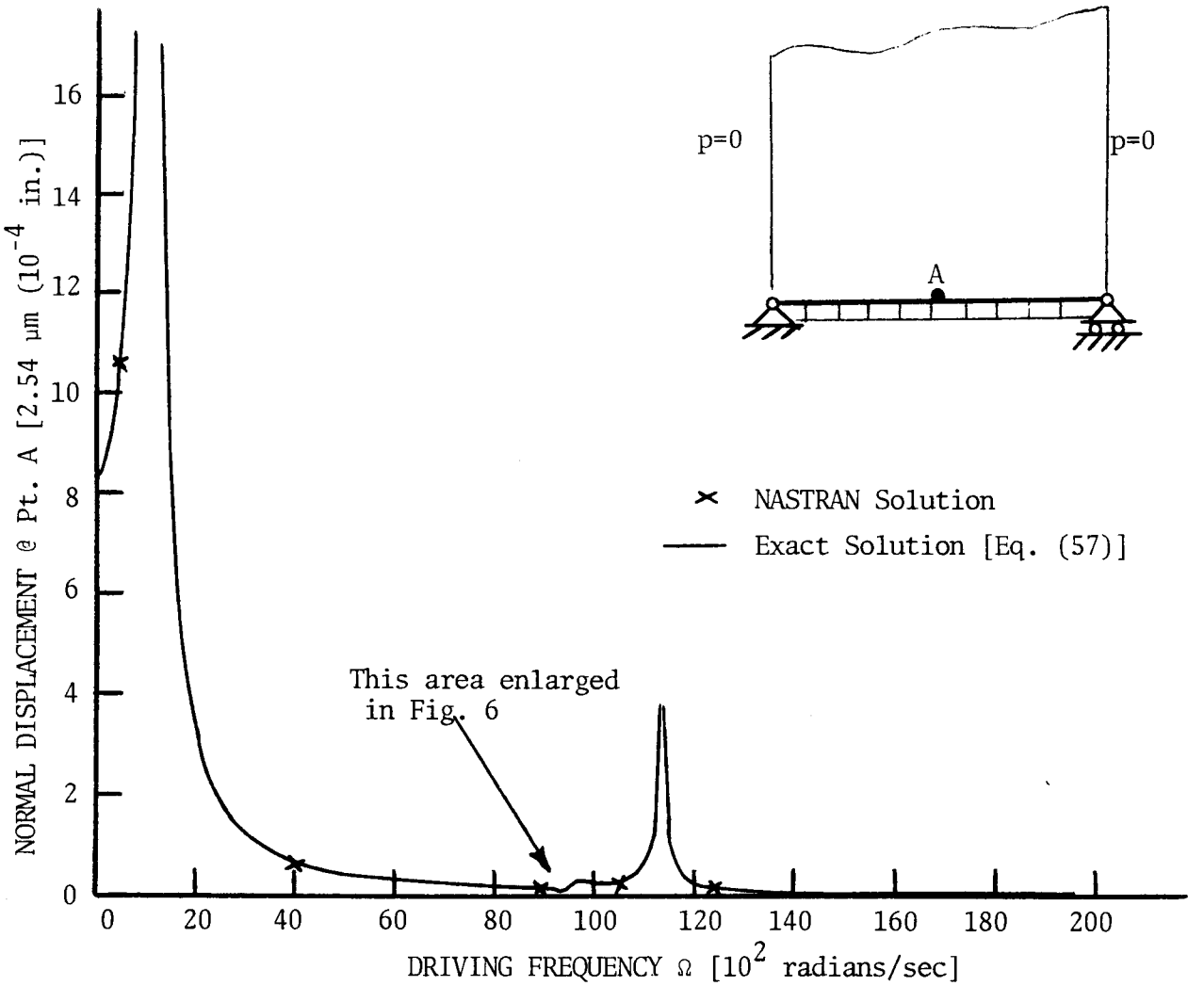

Figure 5. Magnitude of the Normal Displacement of the Center Beam Point (Point A) as a Function of the Driving Frequency. Peaks Occur at the Natural Frequencies Given by Equation (56).

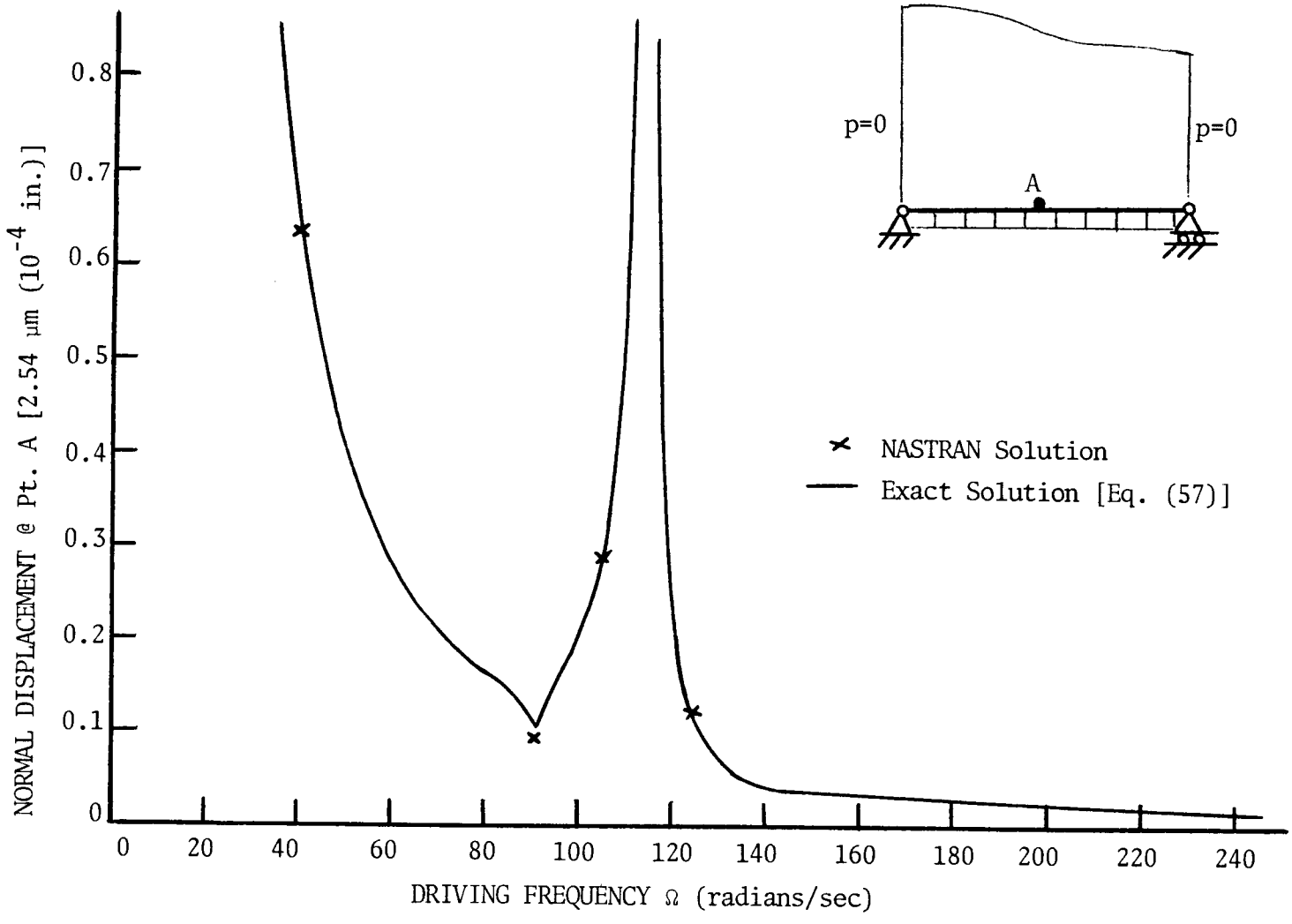

Figure 6. Magnitude of the Normal Displacement of the Center Beam Point (Pt. A) as a Function of the Driving Frequency. Peaks Occur at the Natural Frequencies Given by Equation (56).

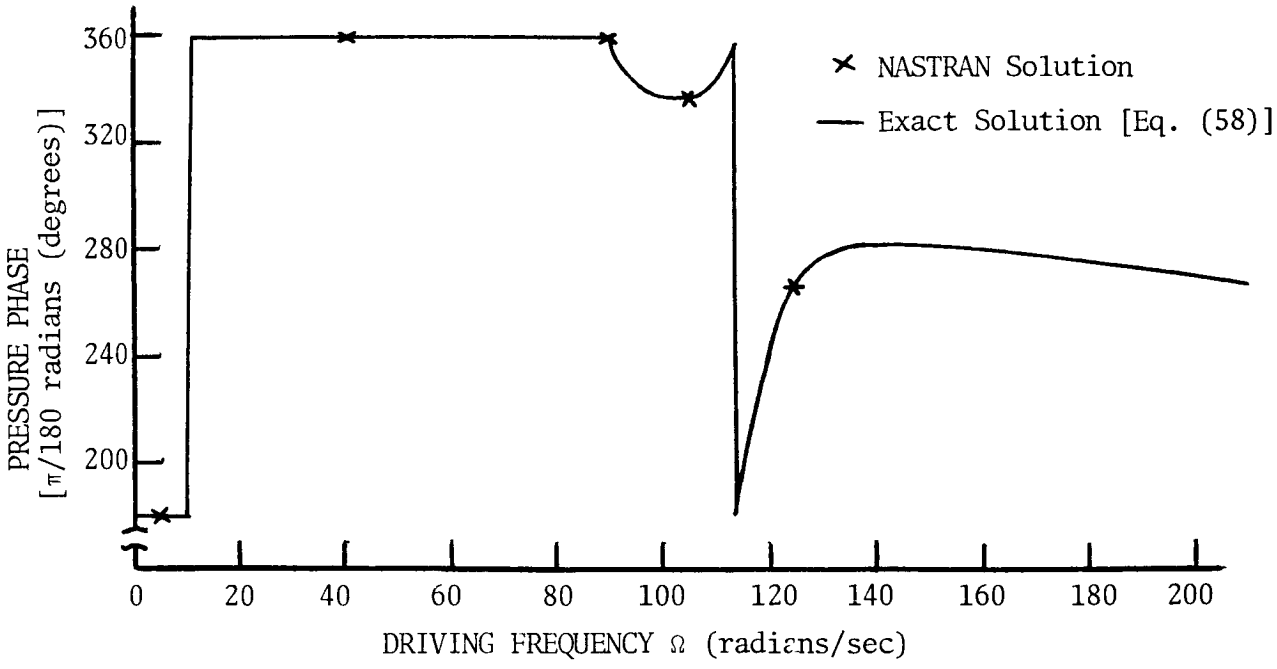

Figure 7. Phase Angle of the Acoustical Pressure at the Center of the Beam as a Function of the Driving Frequency Ω.

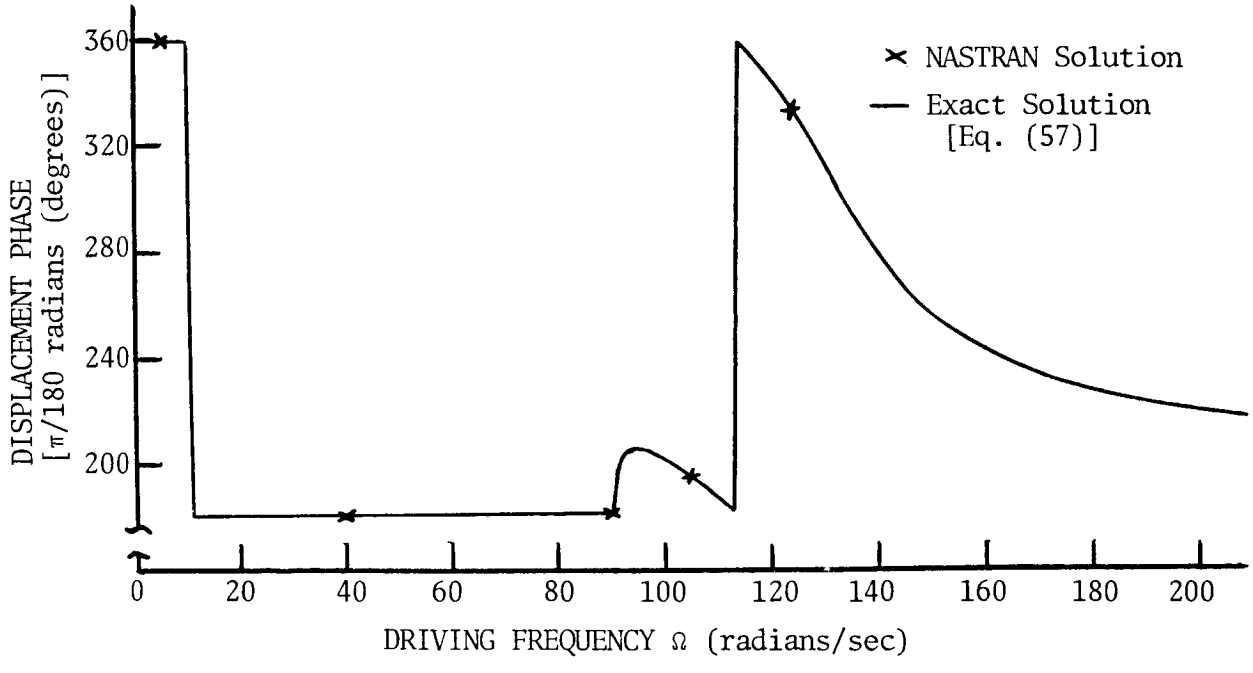

Figure 8. Phase Angle of the Normal Displacement of the Center Beam Point as a Function of the Driving Frequency Ω.

DEVELOPMENT, DOCUMENTATION AND CORRELATION OF A NASTRAN VIBRATION MODEL OF THE AH-1G HELICOPTER AIRFRAME

J. D. Cronkhite
Bell Helicopter Textron

SUMMARY

The results of two contracted efforts[1] directed towards evaluating NASTRAN for vibration analysis of the helicopter airframe are presented. The first effort involved development of a NASTRAN model of the AH-1G helicopter airframe and comprehensive documentation of the model so that government personnel could clearly see the techniques and assumptions used in the modeling as well as utilize the model for their own in-house analyses. The next effort was to assess the validity of the NASTRAN model by comparisons with static and vibration tests. In general, the comparisons show good agreement between the NASTRAN results and experimental results. Some problems that were encountered are discussed.

INTRODUCTION

Before the availability of large finite element computer programs, the dynamic behavior of the helicopter airframe was approximated with simple beam analyses. Although not very accurate, these analyses were relatively easy to document and explain to government personnel monitoring a contractor's work. After the development of NASTRAN, and other similar programs, more accurate and representative analyses could be performed. However, before NASTRAN can be executed the helicopter airframe must be represented as a three-dimensional finite element model. This involves modeling assumptions in the idealization of the actual structure as well as generation of a large amount of input data required to describe the structure model. Without clear documentation of these analyses or compatible finite element

---

[1]Work described in this paper was done under U. S. Army Armament Command (ARMCOM) Contract No. DAAF03-73-C-0122 (July 1973 to April 1974) and NASA Contract No. NAS1-13801 (February 1975 to December 1976).

programs, it would be a difficult task for government monitors to check and utilize these analyses. NASTRAN promised to solve this problem by providing adequate analysis capability to satisfy contractors' needs. Also, it was inexpensive, widely used, and available on a variety of computers used at most contractor and government facilities.

A program was initiated by the Army to evaluate NASTRAN as a workable tool for satisfying the needs of industry and the government as well as to develop a useful helicopter airframe model at the same time. The first part of the program was to develop a NASTRAN model of the AH-1G helicopter that would represent the low frequency (below 30 Hertz) vibration characteristics of the airframe. In addition, clear and complete documentation was required so that government personnel could independently make changes to the model and use it for in-house analyses, in particular, response to automatic weapon firing and rotor vibration. Following development and documentation of the NASTRAN model, correlation with static and vibration tests was to be done to assess the validity of the model. Static load deflection testing of the AH-1G fuselage, wings, tailboom and vertical fin was to be used to verify the stiffness modeling and sinusoidal vibration testing, to verify the dynamic characteristics (including both stiffness and mass effects) of the NASTRAN model. The results of this program are discussed in the paper.

DEVELOPMENT AND DOCUMENTATION OF THE NASTRAN MODEL

Description of the Model

The NASTRAN model was developed to represent the low frequency (below 30 Hertz) vibration response of the AH-1G helicopter airframe. This is the frequency range of interest for airframe vibration response at predominant main rotor excitation frequencies and response to recoil when firing large caliber, turret-mounted guns from the nose of the helicopter. The mathematical model is a linear elastic representation of the airframe structure with items such as the gun turret, fuel, main and tail rotors and crew modeled as lumped masses. A structure plot of the NASTRAN model developed during the contract is shown in figure 1.

The idealized model is described in detail in reference 1. A brief description of the model is discussed below.

- The fuselage and wing structures are built-up idealizations using primarily rods and shear panels in the bending sections.

- The tailboom is modeled as an elastic line using bar elements. This was done since the tailboom structure

is a semimonocoque structure that can be accurately represented using section properties. In addition, changing the stiffnesses of a few bars to reflect different amounts of effective skin is easier for the NASTRAN user than if it were a built-up model with numerous rod and shear panel elements. The variation in the bar element stiffnesses for various maneuver conditions is tabulated in the documentation report. Most of the other areas of the airframe structure are of sandwich construction where the skins are assumed fully effective.

- The main rotor pylon is idealized as an elastic line using bar elements with scalar springs used to represent the elastomeric isolation mounts at the pylon attachments to the fuselage. MPC's are used to tie the transmission case to the mounts. The landing gear, engine mounting, elevator, vertical tail and tail rotor mast are modeled using bars, rods and MPC's.

- Most of the several thousand weight items in the helicopter are distributed automatically to the grid points of the NASTRAN model by a preprocessing program shown schematically in figure 2. Large weight items and useful weights are distributed separately by the modeler.

- After idealizing the structure into a stiffness model and distributing the weights to grid points, Guyan reduction is used to reduce the number of degrees of freedom to an acceptable analysis size (about 250 degrees of freedom) for the Givens eigenvalue solution.

It was decided that the NASTRAN modeling would involve no special analysis such as DMAPing or require special elements or options such as rigid elements that are available in the MacNeal-Schwendler (MSC) version of NASTRAN but are not available to the public version. This was done so that the NASTRAN input data deck could be used directly at Army and NASA facilities equipped with different computers and public version of NASTRAN, level 15. The model was delivered to the Army in January 1974 and has been run on the CDC 6600 machine at NASA Langley and the IBM 360/65 computer at AVSCOM, St. Louis. This was to show that a model developed by a contractor could be delivered to and used by the contracting Army agency that may have a different computer. In addition, the NASTRAN model has been used for in-house weapon system analyses by ARMCOM.

Documentation

Very detailed documentation of the NASTRAN model was provided to the Army in the contract final report, reference 1. One of the

objectives of the documentation was to thoroughly explain the dynamic modeling of the airframe structure to someone in the Army who had a basic understanding of the NASTRAN program. The documentation was also to provide adequate information so that the model could be used independently by the Army and modified for in-house analyses. The government personnel involved felt that these objectives were met.

Some features of the documentation provided to the Army are briefly discussed below:

- The unsorted input data deck itself is well commented and systematically arranged to enable someone familiar with NASTRAN to use the model or modify it with minimum need for reference to the documentation report.

- Modeling philosophy, techniques, and assumptions are discussed in the documentation report.

- The stiffness modeling is described in detail by drawings and sketches organized in a manner similar to the design drawings for the helicopter but depicting the finite element model rather than the actual structure. The model description is broken down into Final Assembly, Major Assembly, Subassembly, and Detail sketches. Structural element descriptions, constraints and omitted degrees of freedom are tabulated and explained on the Detail sketches. Subassemblies of the fuselage major assembly, as well as a typical detail sketch, are shown in figure 3.

- Weights distributed automatically by a preprocessing program and weights distributed separately are discussed.

- A structural element and grid point index serves as a cross reference to locate where an element or grid point is described in the report.

- Finally, a rigid format 3, Normal Modes, sample run is included in the report.

CORRELATION

The correlation effort was directed towards assessing the validity of the NASTRAN model in light of the assumptions made, i.e., an elastic structural model aimed at representing airframe vibration below 30 Hertz. Both stiffness and mass modeling are involved in the modeling. It is desirable, but not possible, to correlate each separately. Stiffness modeling can be correlated directly with static load-deflection test data, but mass modeling

can be correlated only indirectly with shake test data which contains both stiffness and mass effects. If correlation is good between analytical and test results for both static and dynamic tests, both stiffness and mass modeling will be judged as good. If static test correlation is good and dynamic test correlation is bad, then the error should be in the mass modeling.

Three sets of tests were conducted in the correlation effort:

1. Static fuselage load-deflection tests done at the Rock Island Arsenal,

2. Static tailboom load-deflection tests done at Bell,

3. Airframe vibration tests done at Bell, but under another contract, Army Contract DAAJ02-C-0105.

The test procedure and results are covered in detail in references 2, 3 and 4, respectively. A summary of test results and details of the correlation with NASTRAN is included in reference 5.

STATIC TESTING

Fuselage

Fuselage static testing was done to determine the stiffnesses of the fuselage and wing structures. The test setup is shown in figure 4. Five separate loadings were applied; vertical, lateral and torsion loadings applied to the fuselage and beamwise (vertical) and torsion loadings applied to the wings. For ease of mounting, the fuselage was placed nose up in the fixture and cantilever supported at the aft end. Loads were applied to the nose of the fuselage and at the wing tips.

Deflection data was recorded electrically using linear variable differential transformers (LVDT's). Data was automatically reduced into load versus deflection curves for each measurement location along the fuselage or wing.

When compared to the test results, NASTRAN was consistently about 15% stiffer than the experimental data for all fuselage and wing tests. A typical comparison is shown in figure 5 for the fuselage lateral test. It so happened that the lateral test had to be rerun because of some problems with mislocated instrumentation, but for this test, dial indicators were used rather than LVDT's. The dial indicator data showed somewhat stiffer results than the LVDT data and agreed better with the NASTRAN results. This is shown in figure 5.

Because of the discrepancy in the measurements it was not felt that it was necessary to try to modify the model to agree better with the test results. If the fuselage stiffness was 15% high as indicated with the LVDT measurements, it should be reflected later in the vibration test results. The airframe natural frequencies from the NASTRAN analysis should be about 7% higher than test for modes controlled by the fuselage stiffness.

Tailboom

Tailboom static testing was done to determine the stiffnesses of the tailboom and vertical fin structures. The tailboom was cantilever supported at the forward end where it attaches to the fuselage and loads were applied separately at the aft end. Six loadings were applied; vertical, lateral and torsion loadings applied at the end of the tailboom and lateral, torsion and chordwise loadings applied at the top of the fin. Deflections were measured using dial indicators except at the support end of the tailboom where electrical measurements were used to record base motions.

Comparisons of the test results with the NASTRAN model using fully effective skin showed very good agreement. A comparison for the tailboom vertical loading condition is shown in figure 6. Conventional methods for calculating effective skin used by stress analysts give results that are much too soft. Experimental work needs to be done to quantify the actual amounts of effective skin for panels under compressive loading. Using the experimental results, analytical methods can be evaluated for calculating effective skin more accurately. Accurate panel stiffness representation can be very important in predicting the vibration characteristics of the airframe structure.

VIBRATION TEST CORRELATION

The test setup is shown in figure 7. The helicopter was supported by a soft (bungee) suspension system so that the free vibration modes of the airframe would not be affected. Sinusoidal excitation was applied separately at five locations; vertically, laterally and longitudinally at the main rotor hub and vertically and laterally at the tail. A sinusoidal forcing function was applied while sweeping frequency from 0 to 30 Hertz.

For correlation with the NASTRAN model, exciting at the tail was preferred to the hub excitation since the force is applied directly to the airframe structure. When exciting at the main rotor hub, the force is applied through the dynamically complex pylon isolation system and is expected to give questionable

results. The emphasis in this study was to correlate the vibration characteristics of the basic airframe structure.

The data acquisition and reduction procedures are shown in figure 8. Accelerometers measuring response along the airframe feed signals to the on-site data system which is used for monitoring the test and as a check on the off-site results. Response versus frequency plots obtained through the off-site data reduction procedure were used for comparison with the NASTRAN results.

The frequency response information was the basis for the comparison between test and NASTRAN. Overall amplitudes, frequency placement of peak responses (resonances) and general curve shape for response versus frequency data are compared. In addition, forced response mode shapes are compared at response peaks. NASTRAN results were generated using rigid format 11, Modal Frequency Response, to simulate the vibration test.

Effects of Damping

Structural damping is difficult if not impossible to predict analytically. The amount of modal damping used in the NASTRAN analysis was two percent of critical. This was based on past experience with vibration tests of airframe strcutures and some studies on the effects of varying damping on the NASTRAN frequency response characteristics.

Damping was varied to see the effects on the shape of the frequency response curves. Values of 0%, 2%, 5% and linear (0% at 0 Hertz to 6% at 30 Hertz) damping were used. Frequency response results using no damping and 2% damping are compared in figure 9. It appears that some small amount of damping should be used in the analysis to smooth out the response of insignificant modes which results in a curve shape more representative of the actual structure.

In design studies, damping should be varied to see the effects on frequency response characteristics. It is sometimes assumed that using a <u>lower</u> value of damping for the analysis is conservative, that is, a <u>higher</u> vibration response would be predicted than would be expected on the actual structure. This is true near resonance, but in the low response frequency ranges (anti-resonances) this would not be true, that is, the response predicted by lower damping would be lower than expected on the actual structure. This is shown in figure 10 where NASTRAN response is compared to test for values of 2% and 5% modal damping.

Low response areas or 'valleys' of the frequency response curve are very important in the helicopter airframe design because it is desired to locate these valleys at rotor excitation

frequencies to minimize vibration. For the Bell two-bladed rotor used on the AH-1G helicopter, the predominant excitation frequency is twice the rotor rpm (two-per-rev).

Frequency Response

Typical frequency response comparisons of test data with NASTRAN are shown in figure 11. Comments on the comparisons follows:

- Overall magnitude and shape of the response curves agree well especially through 20 Hertz.

- In the 20 to 30 Hertz range, experimental responses at locations that are a considerable distance from the excitation point, such as the pilot seat, tend to drop off indicating some attenuation through the intervening structure. The damping present in the modes in this frequency range also looks considerably higher than the 2% damping used in the NASTRAN analysis. For example, the fuselage torsion/wing yaw mode, indicated on the lateral response curve in figure 11, shows very high peak response near resonance on the NASTRAN curve but there is little peaking on the test curve.

- Peaks agree well through 20 to 25 Hertz except for the second lateral bending mode where NASTRAN is shown to be about 7% lower than test (this is the opposite of what might be expected from the fuselage static test results).

- A comparison of natural frequencies that could be identified from the frequency response results are tabulated below:

Vertical Tail Excitation

Mode	Test	NASTRAN
Fore-and-Aft Pylon	3.9	3.0
First Vertical Bending	8.0	8.0
Fuselage Torsion	15.5	15.7
Second Vertical Bending	18.0	17.5

Lateral Tail Excitation

Mode	Test	NASTRAN
First Lateral Bending	7.1	7.1
Fuselage Torsion	15.5	15.7
Second Lateral Bending	18.9	17.5
Third Lateral Bending	24.4	25.8

- Generally, the tail excitation results agreed well. There was a problem with the hub excitation due to an undesired suspension system or hub fixture mode strongly affecting the test responses.

A comparison of forced response mode shapes at resonance is shown in figure 12. The NASTRAN first vertical bending mode agrees well in frequency and response magnitude with test. The pylon mode frequency from test is considerably higher than NASTRAN (3.9 Hertz compared to 3.0 Hertz). This is probably due to pendulum stiffening of the pylon when suspended from the hub. This would occur in flight also since the helicopter is suspended at the hub by the main rotor. The response of the pylon mode from test is about one fourth of the NASTRAN response. This indicates much higher damping of the pylon mode than the 2% used in the NASTRAN analysis. These effects observed in the pylon dynamics (pendulum stiffening and high damping) should be incorporated in the NASTRAN model.

CONCLUSIONS

Development and Documentation

1. It was shown that a rather complex NASTRAN vibration model could be developed by a contractor at his facility and delivered to the Army, to be run on their computer and independently used by them for in-house analysis.

2. The Guyan reduction procedure used to reduce the number of degrees to an acceptable size before using the Givens method was found to be a major difficulty in dynamic modeling. It is also difficult to document and explain why each degree of freedom was omitted. An eigenvalue method such as FEER (reference 6) should be incorporated into NASTRAN that eliminates the need for the Guyan reduction.

3. There were some incompatibilities between the MSC version of NASTRAN that is used at Bell and level 15.1 of the public version which was being used by the Army. The incompatibility that caused the chief problem was that no rigid elements are available in the public version and MPC's or stiff bars had to be used. In addition, for normal modes analysis, MSC NASTRAN was found to be about 2.5 times faster than level 15.1, but this may not be true in level 16.0.

Correlation

1. When comparing NASTRAN to the fuselage static test results, analysis was consistently about 15% stiffer than experiment. However, one of the test conditions was repeated using a different method of measurement and deflections agreed much better with NASTRAN. The vibration testing did not indicate that the NASTRAN model was stiffer than the actual airframe structure.

2. NASTRAN agreed very well with the tailboom static test results. Fully effective skin on the tailboom panels was used in the analysis. Conventional stress analysis procedures for determining effective skin do not agree with this. Better procedures for determining the effective skin should be developed to determine the stiffness of sheet metal panels under compression load for use in dynamic analyses.

3. Comments on the results of the vibration test comparisons sons are the following:

   - Damping is difficult to quantify in analysis. A value of 2% modal damping was used for NASTRAN comparison with test. In a helicopter design analysis, damping should be varied to see the effect on the frequency response characteristics, especially in the low response valleys where it is desired to locate excitation frequencies.

   - Frequency response characteristics (magnitude levels, resonance locations, curve shape) agreed well through 20 Hertz when comparing excitation at the tail of the airframe. Above 20 Hertz, test results generally showed more damping than the NASTRAN analysis and indicated attenuation by the structure for locations well removed from the excitation point.

   - Pendulum stiffening and high values of damping of the pylon modes were indicated by test and should be reflected in the NASTRAN model.

REFERENCES

1. Cronkhite, J. D., Berry, V. L., and Brunken, J. E.: A NASTRAN Vibration Model of the AH-1G Helicopter Airframe, U. S. Army Armament Command Report No. R-TR-74-045, Research Directorate, Gen. Thomas J. Rodman Laboratory, Rock Island Arsenal, Rock Island, Illinois, June 1974.

2. Frericks, D. E., et. al.: Measurement of the Static Influence Coefficients of the AH-1G Cobra Fuselage, U. S. Army Armament Command Report No. R-TR-76-005, February 1976.

3. Slack, J. R.: Static Load Deflection Test of Tailboom Installation for AH-1G Helicopter, Bell Helicopter Textron Report No. 299-095-003, Bell Helicopter Textron, Fort Worth, Texas, December 1975.

4. White, J. A.: Model AH-1G Airframe and Control System Ground Vibration Test Results, Bell Helicopter Textron Report No. 299-099-819, February 1976.

5. Cronkhite, J. D. and Berry, V. L.: Correlation of AH-1G Airframe Test Data with a NASTRAN Mathematical Model, Bell Helicopter Textron Report No. 699-099-016, February 1966.

6. Newman, M. and Pipano, A.: Fast Modal Extraction in NASTRAN Via the FEER Computer Program, NASA TM X-2893 NASTRAN: User's Experiences, September 1973, pp 485-506.

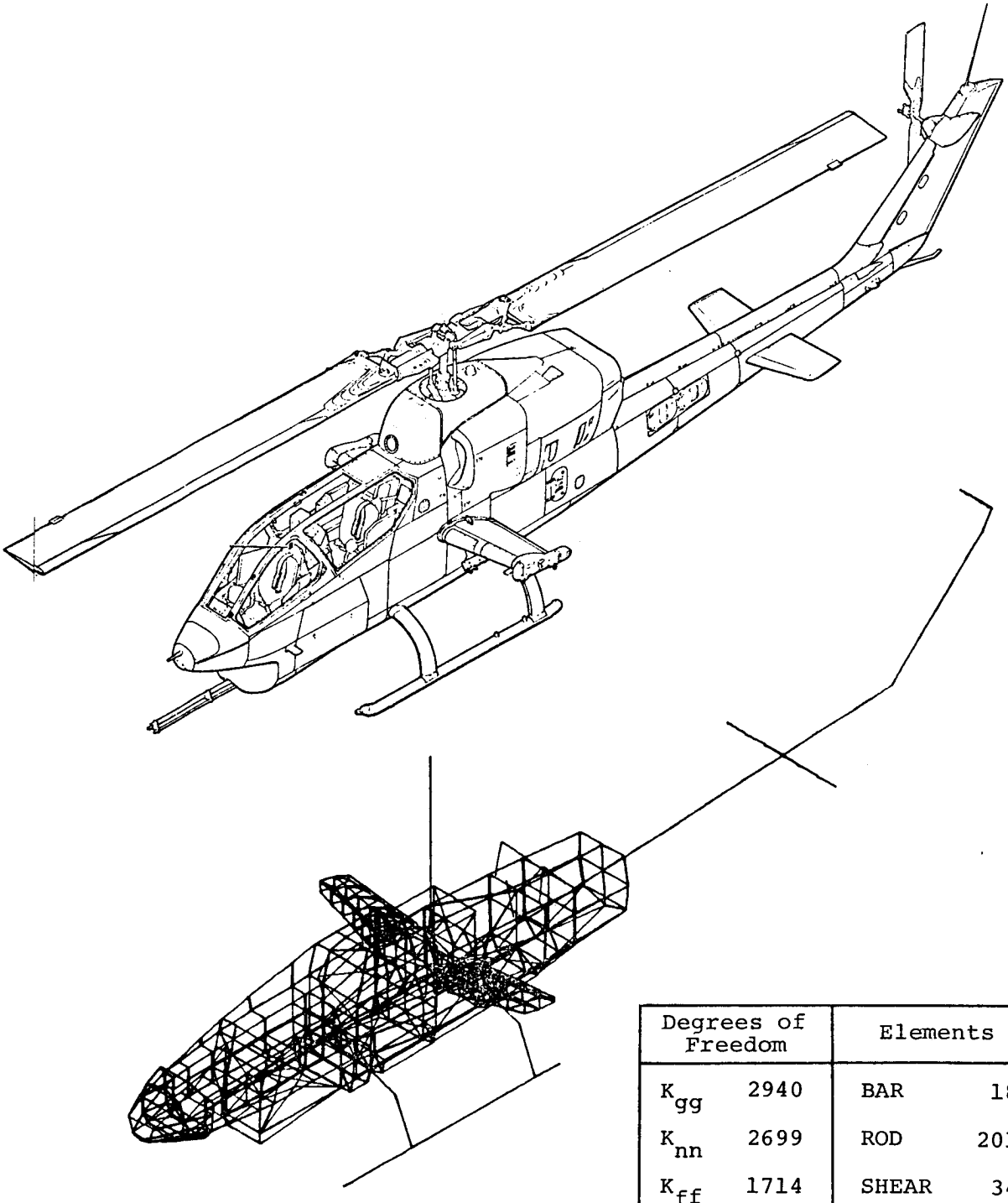

Degrees of Freedom		Elements	
K_{gg}	2940	BAR	184
K_{nn}	2699	ROD	2013
K_{ff}	1714	SHEAR	340
K_{aa}	241	QDMEN	160
K_{ll}	235	TRMEM	243

Figure 1. NASTRAN Model of the AH-1G Helicopter Airframe.

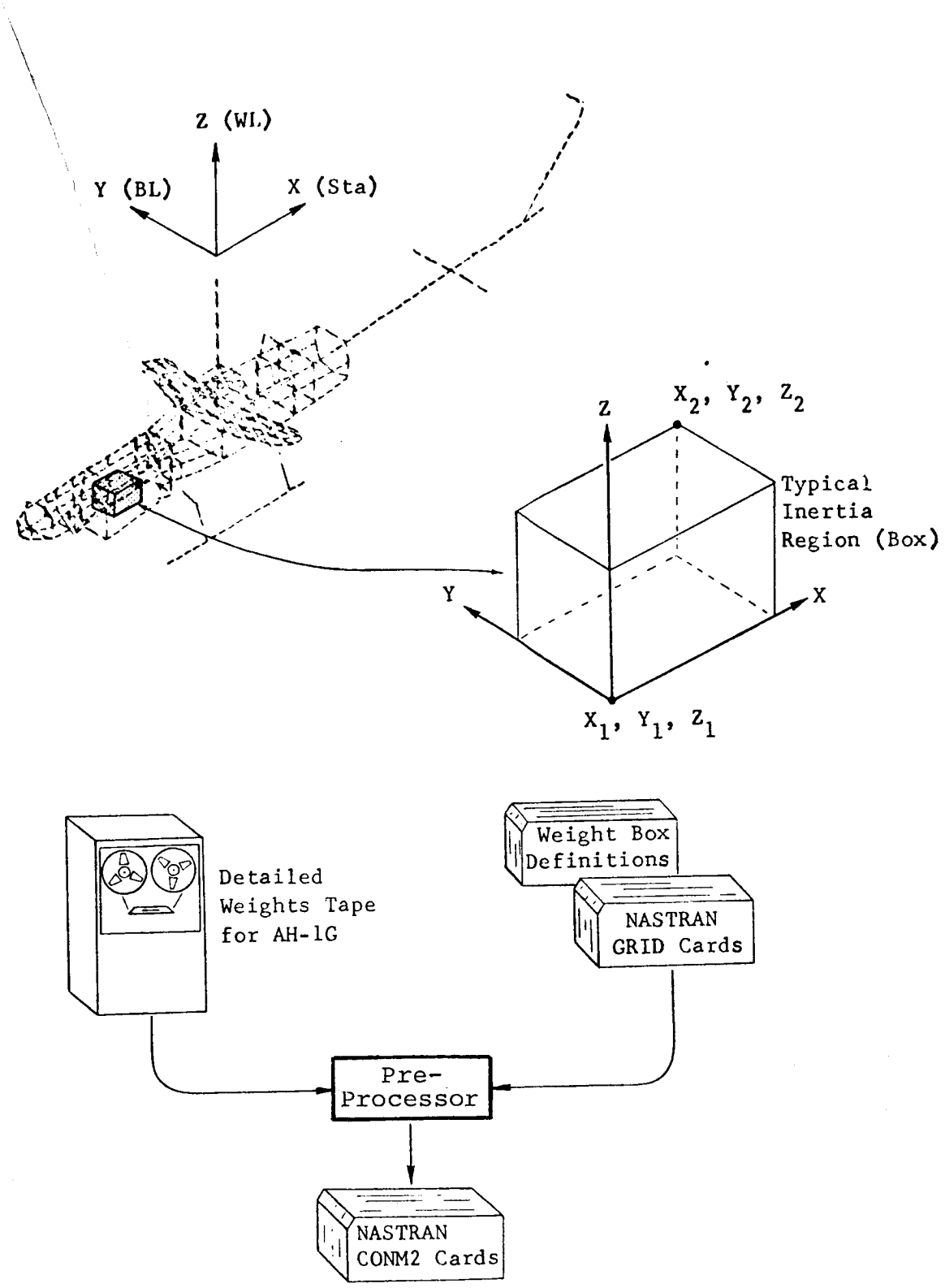

Figure 2. Automatic Weight Distribution Pre-Processor.

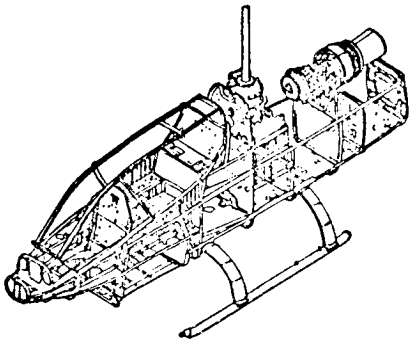

Actual Structure
for Reference

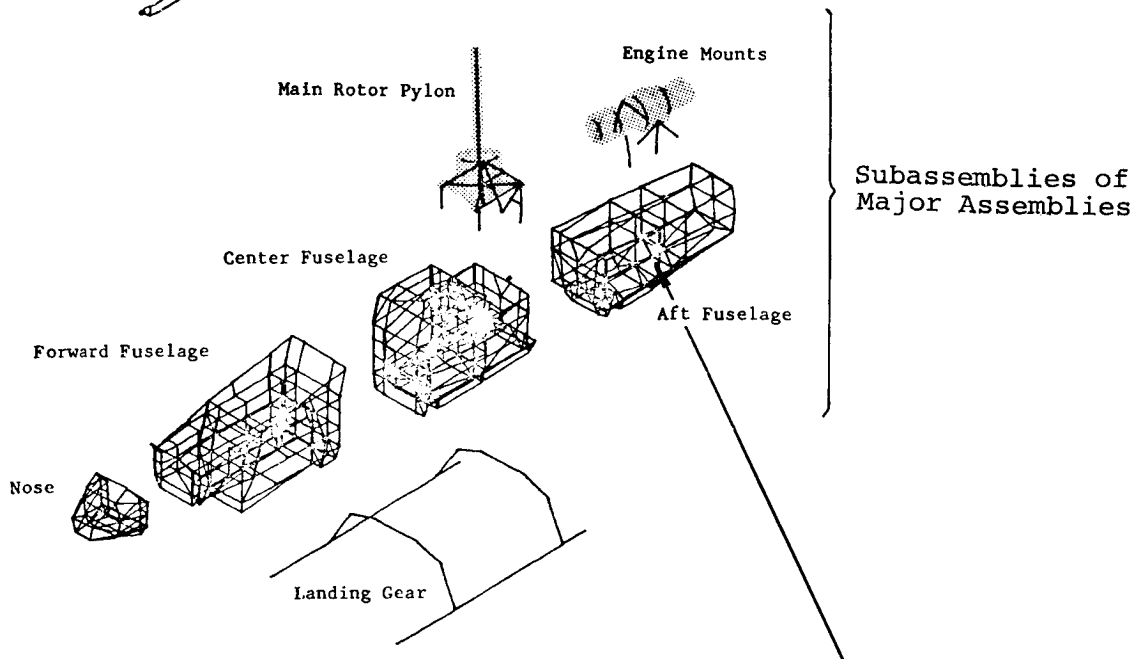

Bulkhead Detail

NOTE: Each element shown in the sketch could represent several NASTRAN elements. Element descriptions and grid point constraints and omits are listed with each detail.

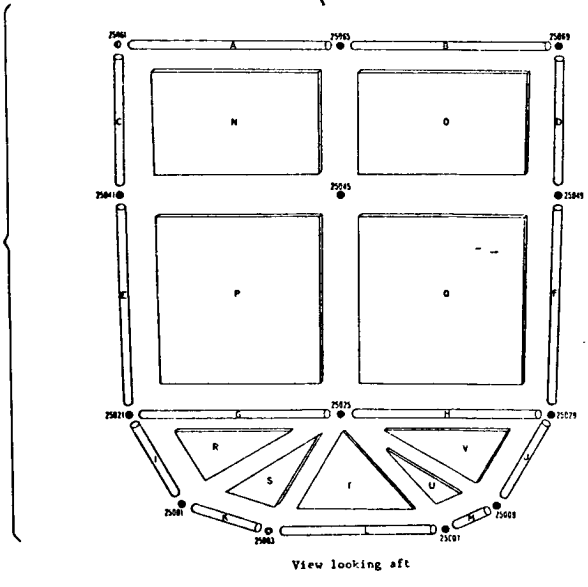

Figure 3. Typical Sketches Used in the Description of the NASTRAN Model.

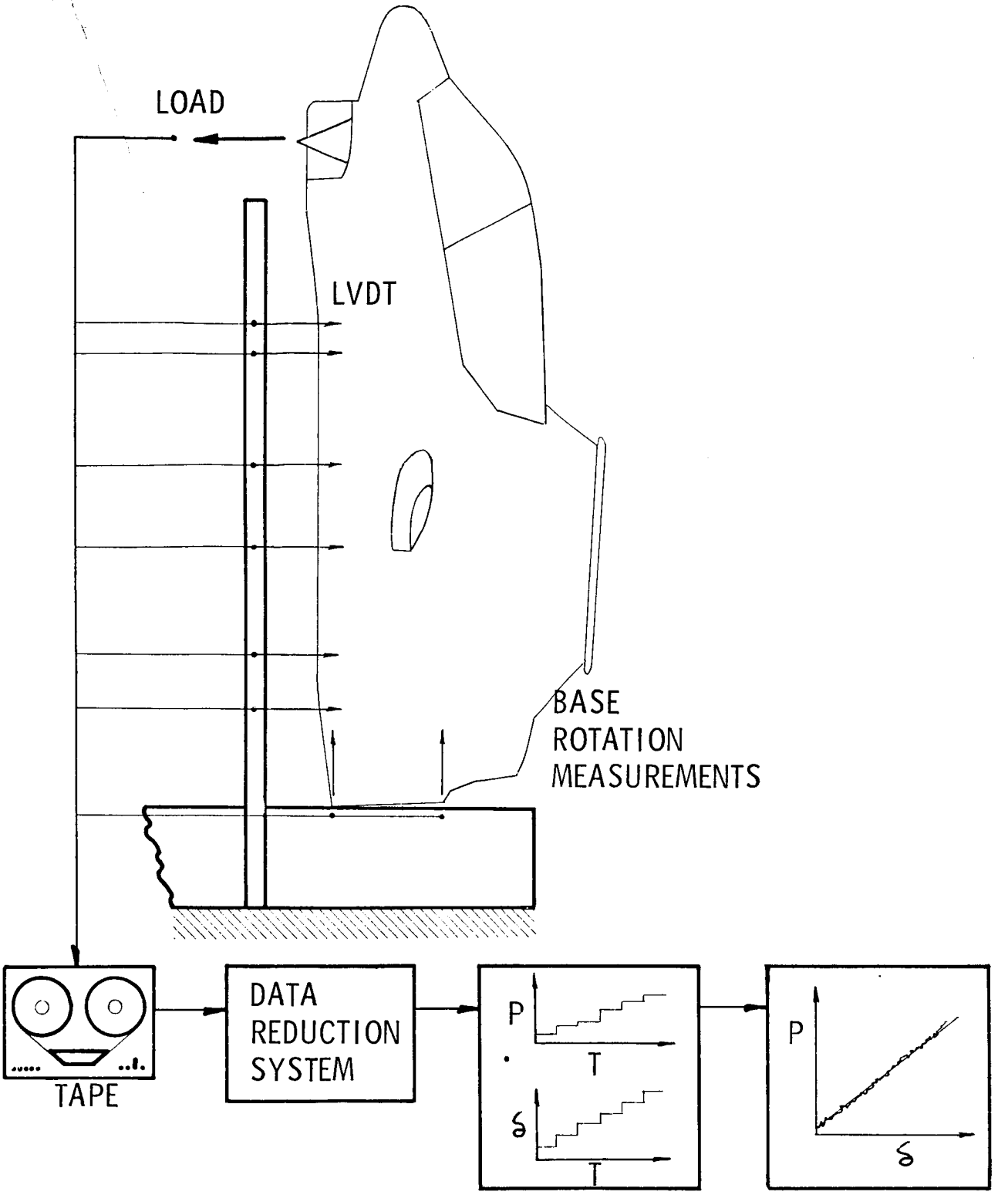

Figure 4. Fuselage Static Test Setup.

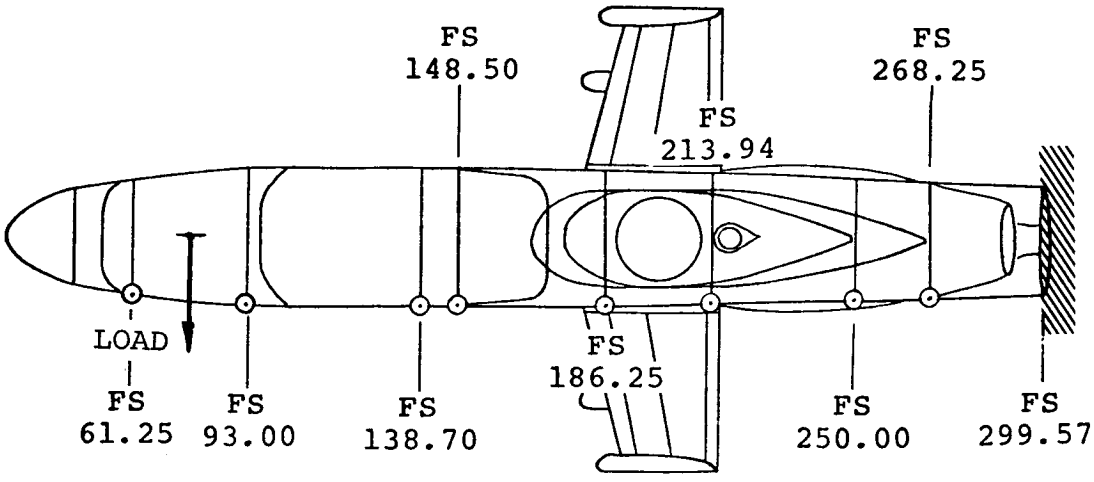

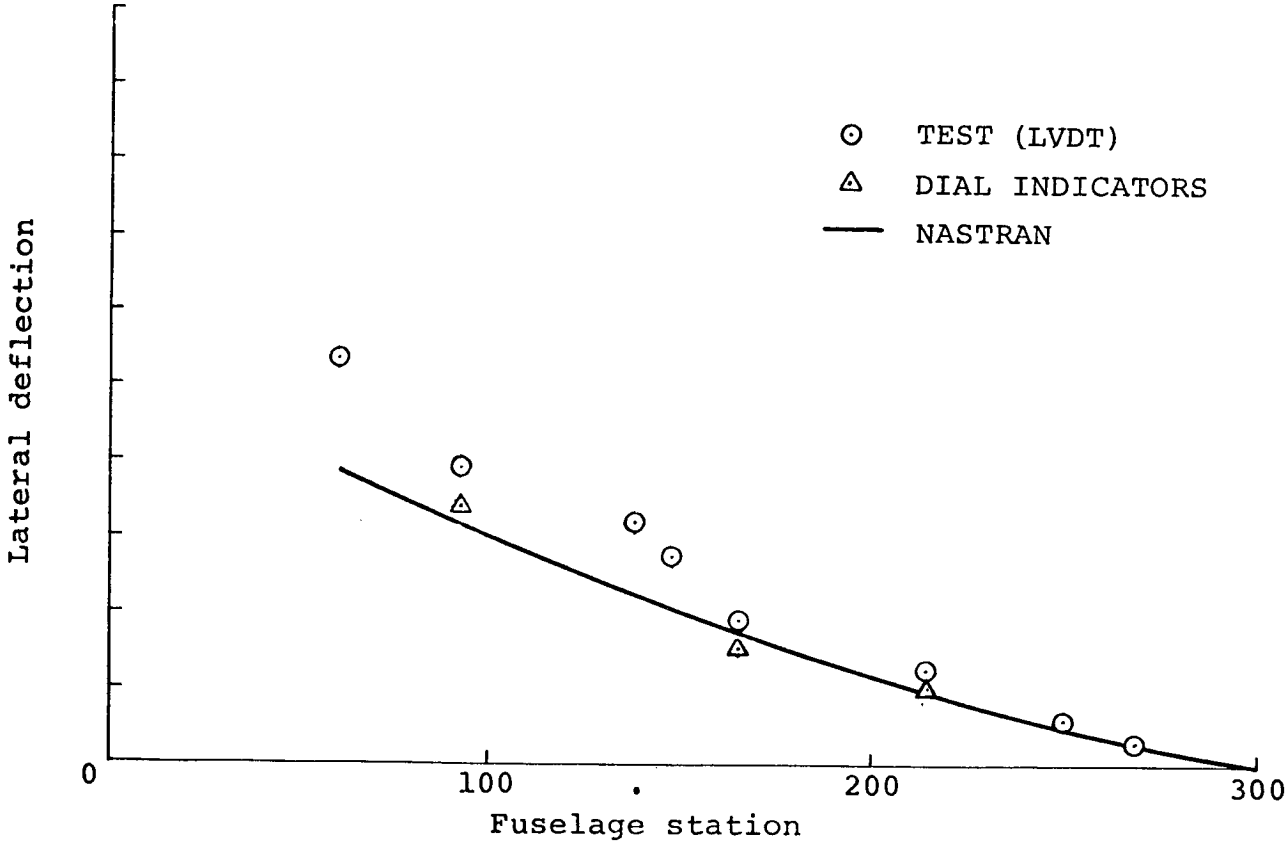

Figure 5. Fuselage Lateral Load-Deflection Comparison.

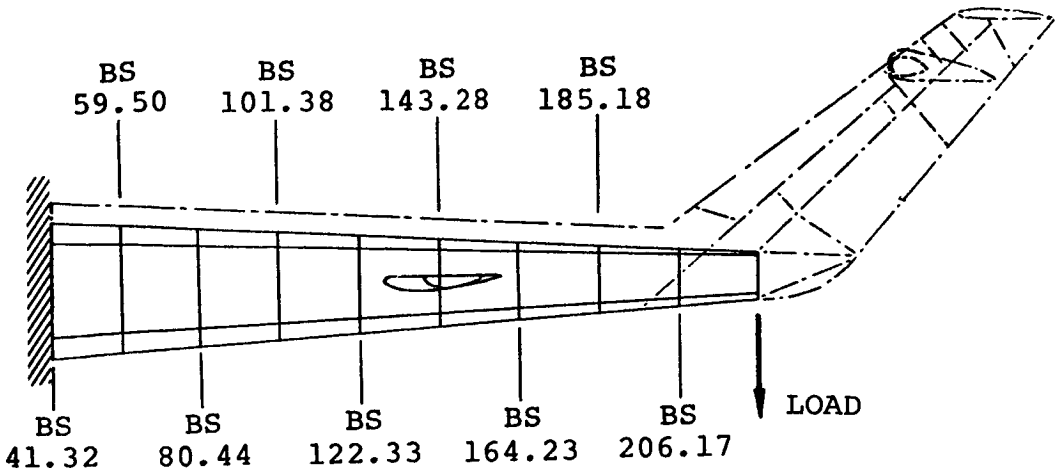

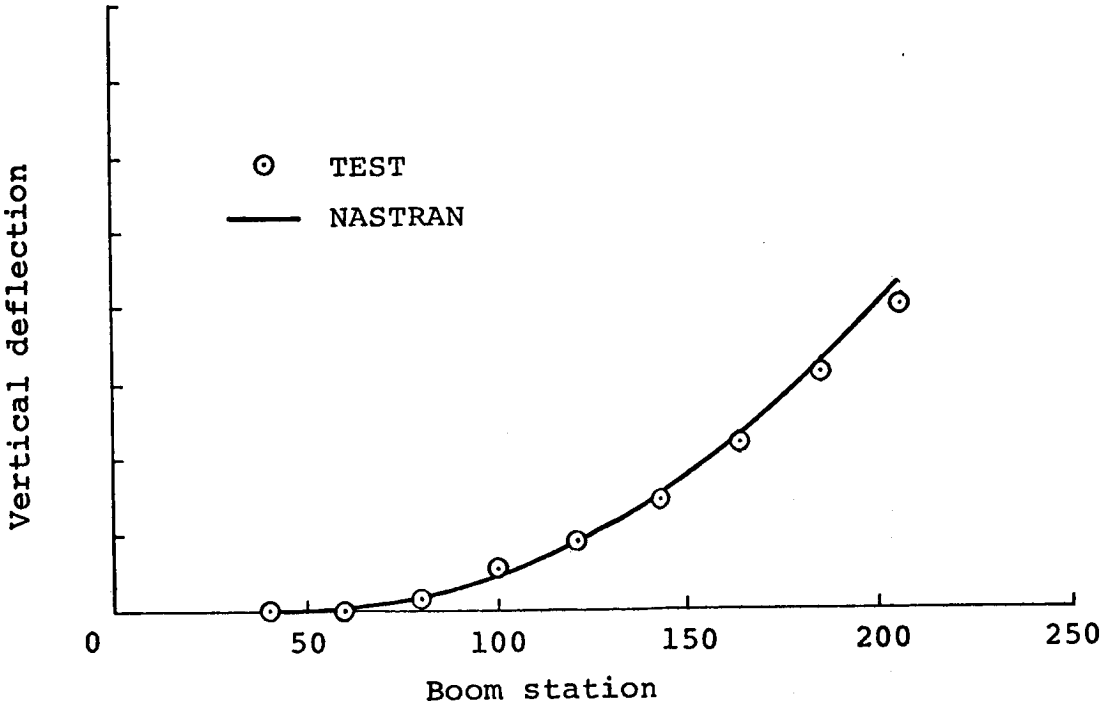

Figure 6. Tailboom Vertical Load-Deflection Comparison.

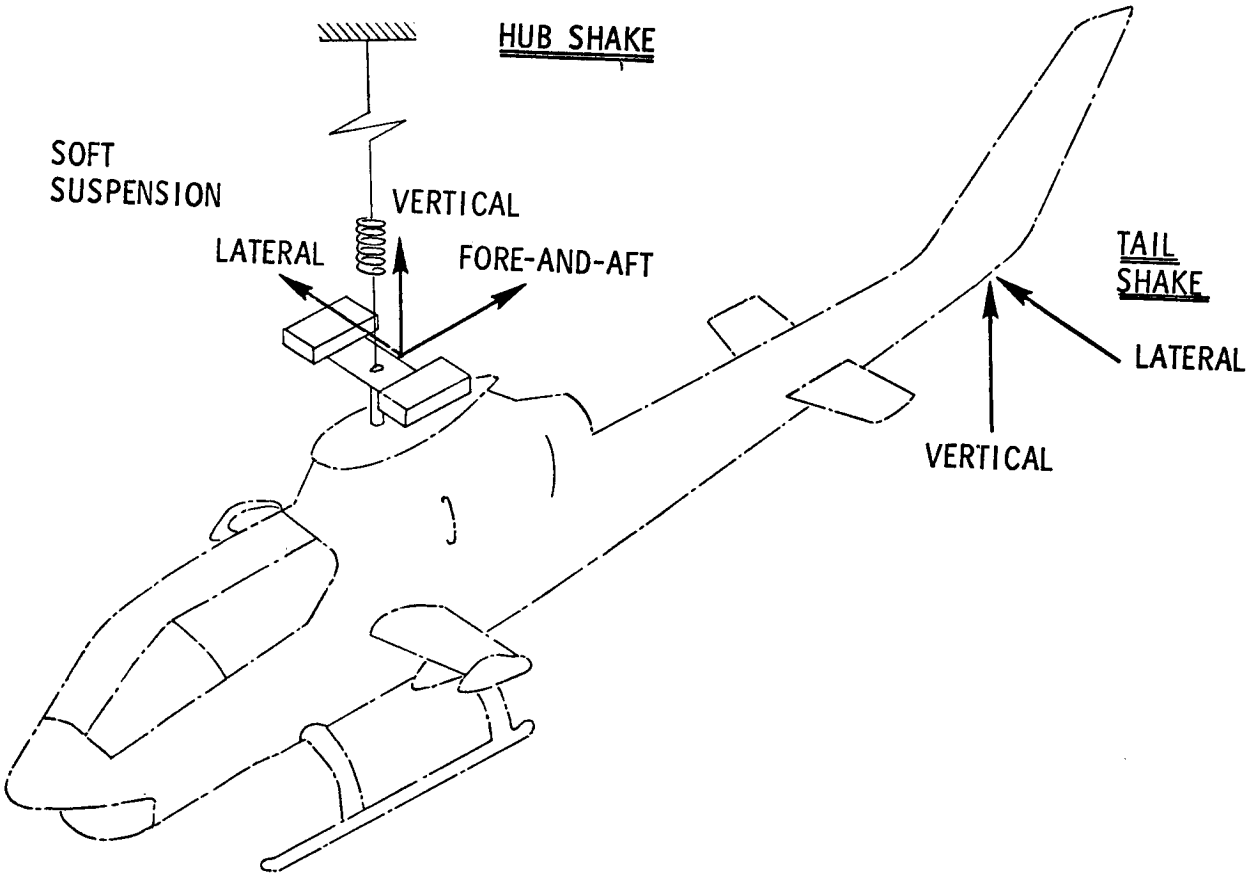

Figure 7. Airframe Sinusoidal Vibration Test Setup.

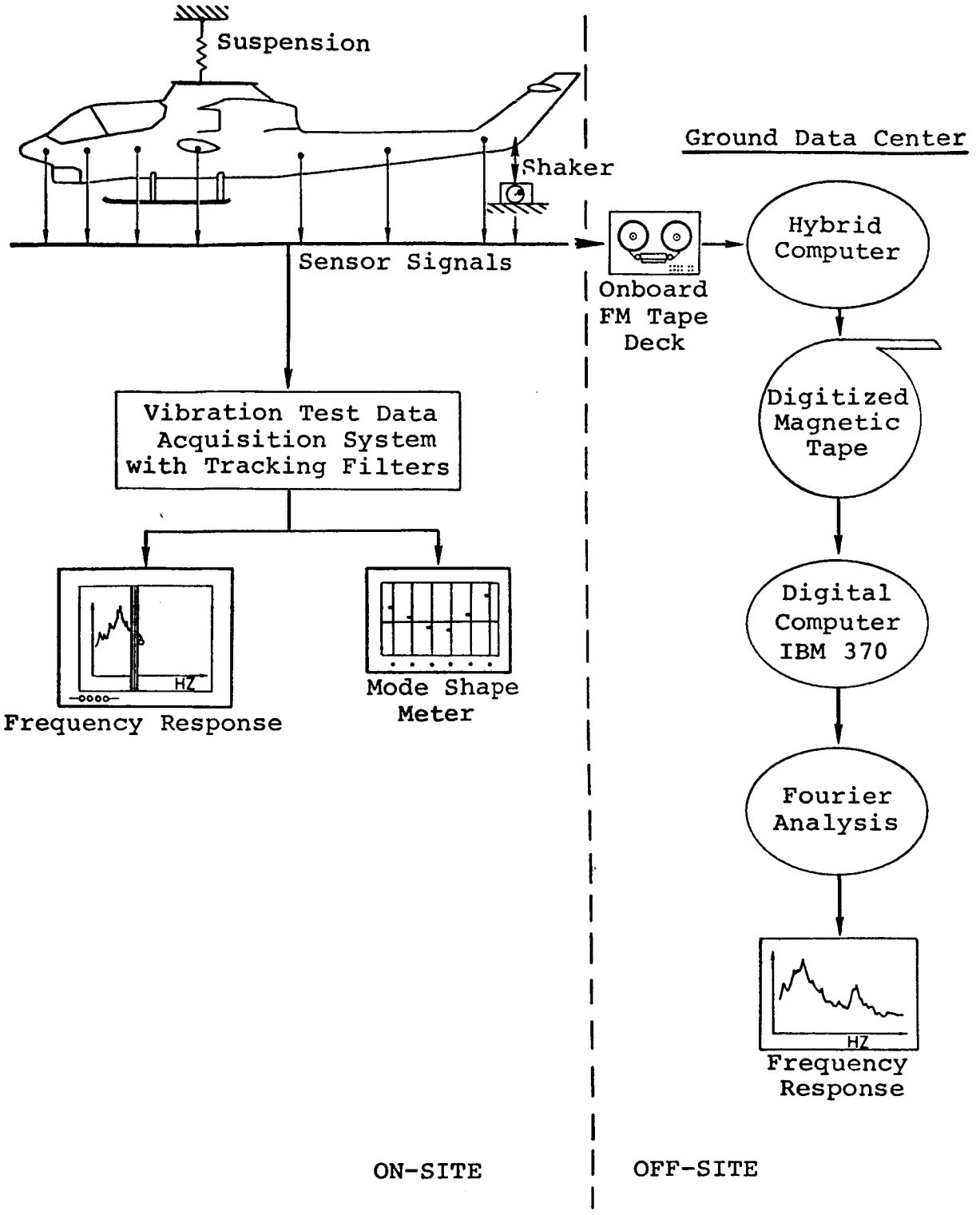

Figure 8. Shake Test Data Reduction Flow Chart.

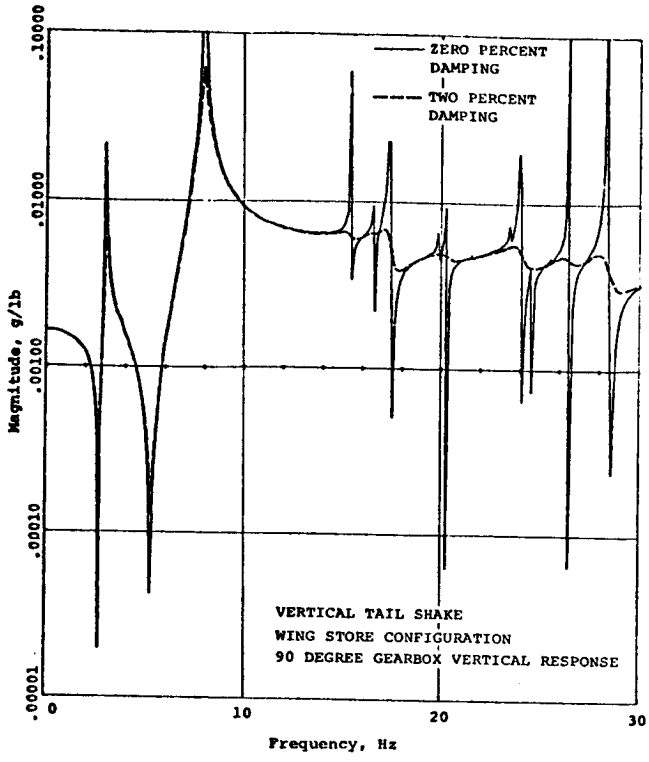

Figure 9. Effect of Damping on Removing Responses of Insignificant Modes.

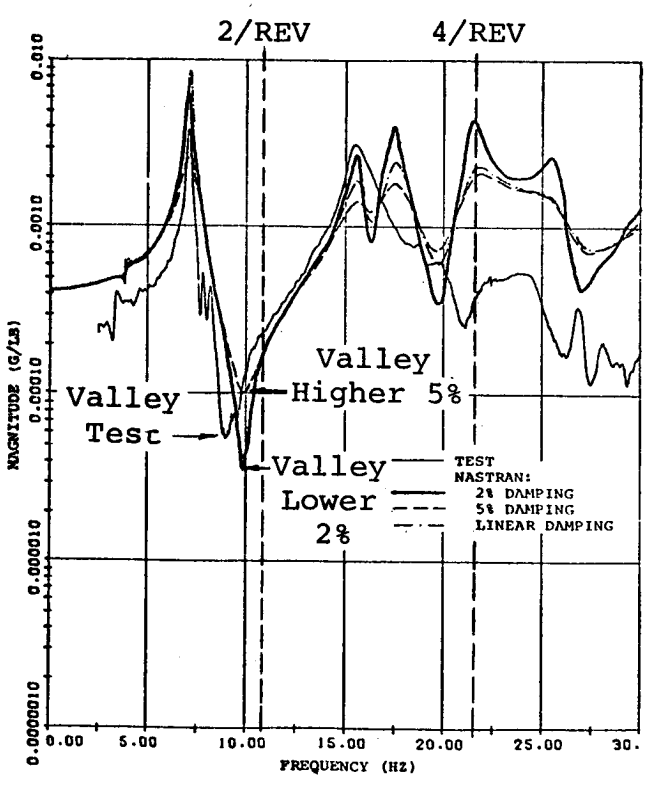

 Figure 10. Effect of Damping on Response Valleys.

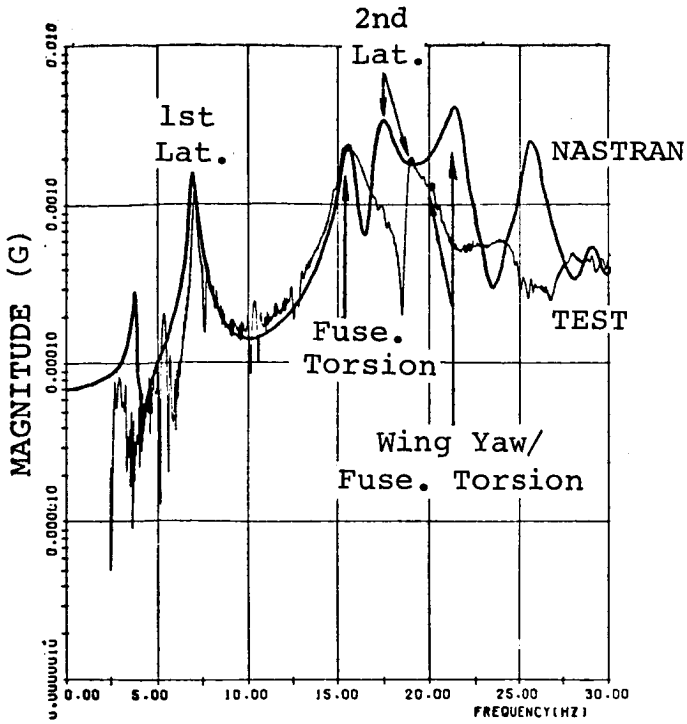

Pilot Seat Lateral Response to Tail Lateral Excitation.

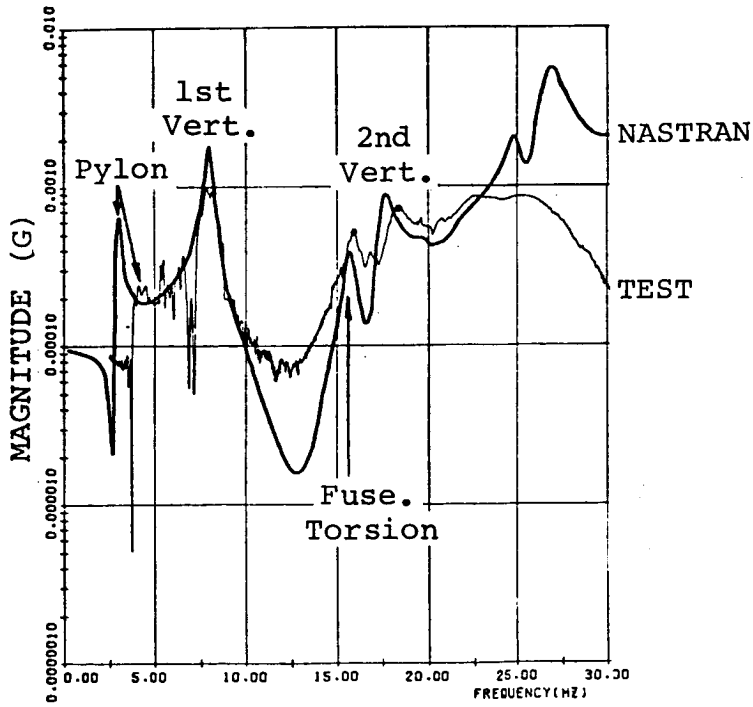

Pilot Seat Vertical Response to Tail Vertical Excitation.

Figure 11. Comparison of Frequency Response Results.

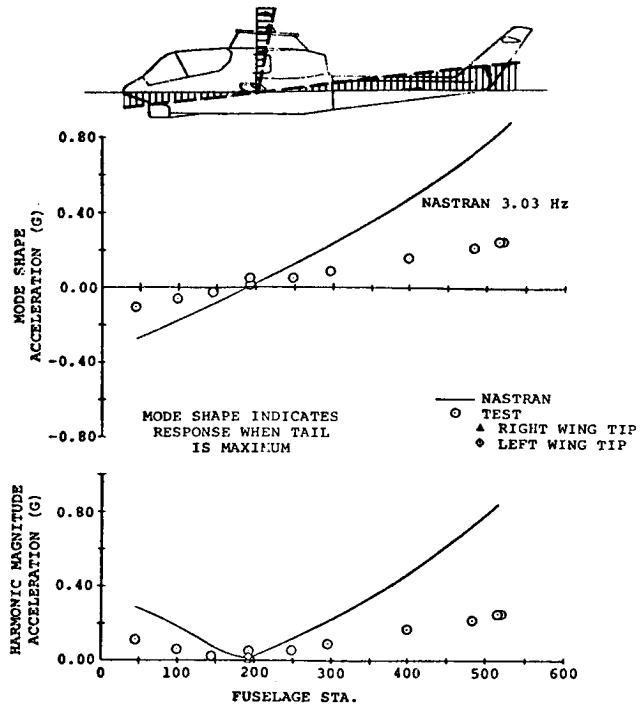

MAIN ROTOR PYLON FORE-AND-AFT ROCKING MODE

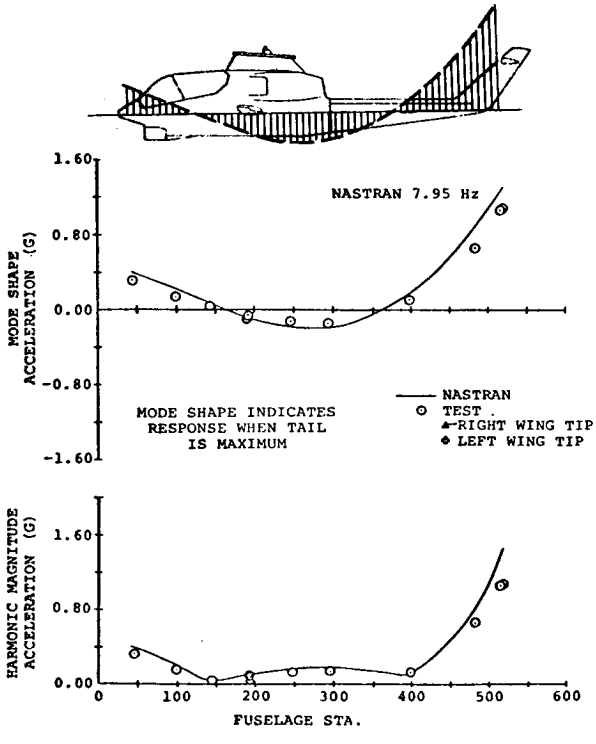

FIRST FUSELAGE VERTICAL BENDING MODE

Figure 12. Comparison of Forced Response Mode Shapes.

APPLICATION OF NASTRAN TO LARGE SPACE STRUCTURES

T. Balderes, J. Zalesak, V. DyReyes
and E. Lee

Grumman Aerospace Corporation

SUMMARY

The application of NASTRAN to design studies of two very large-area lightweight structures is described. The first is the Satellite Solar Power Station, which would help meet the energy needs of the future, while the second is a deployable three hundred meter diameter antenna. A brief discussion of the operation of the SSPS is given, followed by a description of the structure. The use of the NASTRAN program for static, vibration and thermal analysis is illustrated and some results are given. Next, the deployable antenna is discussed and the use of NASTRAN for static analysis, buckling analysis and vibration analysis is detailed.

INTRODUCTION

The space programs of the future will involve the operation of very large structures in space. Current studies (References 1,2,4) are involved with various aspects of these projects, from assessing what type of space station would best serve as a prototype, to considerations of orbital construction techniques. A feature common to these investigations, is the large area structures involved. In fact a recent conference (Reference 3) sponsored by the Office of Aeronautics and Space Technology of NASA identified the principal driver in tomorrow's space technology as large area space structures. This paper describes the application of the NASTRAN program to this technology. The analysis of large space structures using the NASTRAN program is described. The first is the Satellite Solar Power Station which would help meet the energy needs of the future, and the second is a deployable 300 m (1,000 ft.) diameter antenna.

DISCUSSION

A. Solar Satellite Power Station

The Solar Satellite Power Station represents one of the energy sources of the future. Its feasibility, in terms of cost and needed technology, are being evaluated by Grumman in continuing studies that began five years ago. It has definite advantages over other alternatives such as ground based solar systems, nuclear fusion, and tapping the remaining coal deposits. Large energy storage systems are not required since operation is continuous, the necessary technology exists, and it represents an environmentally clean source. Moreover, initial economic studies indicate that power from an SSPS would be cost competitive with projected coal derived power.

The current SSPS design (Figure 1) consists of two large rectangular, solar panels, each measuring 6.5 km (4 miles) long by 4.7 km (2.9 miles) wide by 200 meters deep, interconnected by a single large mast. Solar reflectors consisting of lightweight plastic mirrors are arranged to concentrate solar energy onto the solar cells, effectively doubling the energy they receive (Figure 2). The electrical energy produced by the solar cells is transmitted in the form of d.c. power via a bus structure to the microwave antenna located between the two rectangular solar panels. The microwave antenna is .83 km (.52 miles) in diameter. The microwave beam is transmitted to earth where it is reconverted into electric power by an antenna-rectifier array and then fed into the power grid. The system under study would provide 5,000 megawatts of power at the receiving station, roughly enough to power a city the size of New York.

This entire concept requires the design of a large area lightweight structure that can not only support the solar cell blankets, concentrator mirrors, transmission bus system and antenna for the various loadings, but one that can be controlled in space.

A further constraint on the structure is that it be assembled or manufactured in space. This constraint becomes more obvious when the size and weight of the SSPS are considered. First, the structure is too large to be assembled in existing buildings (note that the vertical assembly building can be set between the truss structures that support the solar reflector panels). Second, handling on the ground would crush the lightweight structures. It has been determined that lifting a beam (made for a large space structure) longer than 18 m would exceed its allowable loading. Furthermore, estimates of the weight of the SSPS range as high as 18×10^6 Kg (40

million pounds). Noting that the Shuttle Orbiter's payload is 30. x 10^3 Kg (65,000 pounds), it becomes evident that a Heavy Lift Launch Vehicle that can carry 180. x 10^3 Kg (400,000 lbs.) will be needed. Moreover, to minimize the number of flights, manufacturing would be done in space, thus maximizing launch density. The concept of manufacturing in space has been under investigation and is being further studied under a current contract (Ref. 2). By using spools of material, structural elements would be made up with triangular cross-sections and then built up into complete beams, which would serve as truss members. The actual construction would be carried out using fabrication modules, as shown in Figures 3, 4 and 5. After the SSPS is completely assembled in low earth orbit, it would be transported to its final geosynchronous orbit with the use of a solar-electric propulsion system, as depicted in Figure 6.

The first operational SSPS could be built beginning in 1990 and would deliver power by the year 2000. Smaller systems (1 Mw) to demonstrate the concept and perform tests on the manufacturing techniques are being planned for the 1985-87 period.

The objective of this study was to perform structural and dynamic analyses of the SSPS structure for the purposes of:

- o providing elastic characteristics (natural frequencies, and mode shapes) of the structure for use in an analytical investigation of the elastic coupling between the SSPS attitude control system and the spacecraft's structural modes;

- o determining deflections and internal member loads for the various flight loading conditions in order to verify operational and structural integrity.

Figure 7 shows the general structural arrangement of the SSPS vehicle. The main structural framework for each of the two solar panels consists of a large diameter (80m) coaxial mast transmission bus, transverse power busses and nonconductive support structure. Shear loads are transmitted by prestressed tension-only wires. Structural continuity between the two solar arrays is supplied by the mast and dielectric structure running outboard of the antenna. The entire structure is aluminum alloy except for the carry-through structure surrounding the microwave antenna, which must have microwave transparency, and is glass/epoxy with quartz wire tension braces.

The structure of each solar array consists of 20 longitudinal (x-direction) truss girders inclined at 30 degrees from the x-z plane. Each truss girder consists of 20 meter deep members with shear stiffness provided by cross bracing cables. The mast is also considered part of the primary structure and is included in the analysis. The primary chordwise members are located at x = 630 m , x = 2109 m, x = 3588 m, x = 5607 m and x = 6546 m. These are made up of 20 m girders of various lengths. The lower members of the chordwise trusses are conductors that tie to the main bus and are considered to be structurally effective.

Each primary member (20m) consists of three 1-meter truss girder cap members held together by 1-meter truss girders spaced at 40m with cross bracing cables. The 1-meter truss girder is the basic structural member and is made up of three vee section caps braced every 3 meters. The mass breakdown for the SSPS is given in Table I.

The finite element model used in the NASTRAN analysis is shown in Figures 8, 9 and 10. An isometric view of the model is shown in Figure 8, while the top chord, bottom chord, concentrator wire bracing and the structure between top and bottom chords are shown in Figures 9 and 10. One half of the entire structure was modeled, with symmetric and antisymmetric boundary conditions applied. The symmetric model had 1,364 degrees of freedom and the antisymmetric had 1,342.

Using the above model, free vibration modes of the structure were obtained employing Rigid Format 3 and the Inverse power method. The two lowest symmetric and antisymmetric modes are shown in Figures 11 through 14.

The lowest mode is a symmetric bending mode with a frequency of 5.26 cycles/hour and would be excited by symmetric thruster forces such as those used in transport from low earth orbit to geosynchronous orbit. The second symmetric mode has a frequency of 14.14 cycles/hour and involves torsional motion. This is the lowest mode excited by the roll (rotation about x axis) control thrusters in their present configuration. The lowest antisymmetric mode involves torsional motion and has a frequency of 9.36 cycles/hour. The second antisymmetric mode is a bending mode (15.6 cycles/hour) which would be excited by the pitch (rotation about y axis) control thrusters.

In order to perform the transient response analysis, the number of degrees of freedom was reduced by employing the Guyan reduction technique. The symmetric model was reduced to 174 degrees of freedom and the antisymmetric to 162. A comparison of the model data revealed that the first 15 frequencies agreed to within 10% and the lowest 4 frequencies to within 3%. The NASTRAN

program, however, was not used for the frequency and transient response because of problems with Rigid Format 11 in level 15.5. The FRRD module would not execute, and it was found that for problems using multipoint constraints an overlay problem existed. Although the problem was eventually corrected, the project schedule did not allow the use of NASTRAN. Alternate in-house programs were used.

Transient response analyses were carried out for control forces and transport forces (transport from LEO to geosynchronous orbit). The response analysis due to attitude control and station keeping yielded deflections and maximum member loads that are well within the allowables. Thrust forces related to 90, 150 and 365 day transit from LEO to gyosynchronous orbit indicated that the bending moments were within the allowables for the 365 day trip.

The SSPS is exposed simultaneously to solar heating and to electrical heating in the electrical transmission buses which are structural members. A thermal stress analysis was performed to determine if the distortions are severe enough to degrade the efficiency and to determine the thermal stresses in the structure. Two thermal conditions were considered. Electrical heating in the mast (resulting in a 150°C rise in temperature) while the SSPS is in the earth's shadow; electrical heating in the mast when the SSPS is exposed to the sun. Deflections due to these two thermal conditions are shown in Figure 15. The maximum deflection for both cases occurs at the tip of the mast and is 50m for the first case and 21m for the second. Both of these represent less than 1° slopes which is the limit specified on distorations to assure sufficient sunlight impinging on the solar cells so that cell efficiency is not degraded. Maximum loads in the structure for these two conditions were within allowables, except for some cable loads (providing shear ties in trusses) which had high compressive loads. Providing alternate load paths or sufficient preloading of the cables must be considered.

B. 300 Meter (1,000 ft.) Diameter Deployable Antenna

The second large structure, designed to operate in space, where NASTRAN was the analytical tool applied is the 300m diameter deployable antenna. The antenna would operate in an earth orbit and would be subjected to gravity gradient, solar pressure, control loads and temperature distributions. The configuration of the structure is shown in Figure 16. The structure consists of 72 rim members (each 13m (43') long) connected end to end to form the 300 meter diameter rim. The rim is supported by two sets of 36 cables (under tension) the forestays and backstays, connecting to alternate points on the rim. A gore structure, supporting antenna elements, is positioned in the plane of the rim and is also under tension. The upper systems module is

placed at the end of the mast which is 750 meters (2,500 ft.) from the plane of the rim. The rim elements consist of 13.3 cm ($5\frac{1}{4}$ in.) diameter tubes of graphite epoxy with a thickness of .038 cm (.015 in.). The forestays and backstays are unidirectional graphite epoxy tapes, the former being 2.54 cm (1.0 in.) wide and .03 cm (.012 in.) thick and the latter 1.9 cm (.75 in.) wide and .005 cm (.002 in.) thick. The mast structure, shown in Figure 17a is a graphite epoxy truss structure using three cap members, transverse support members and diagonal ties. The gore is made up of 72 triangular sectors, two of which are shown in Figure 17b, constructed of perforated aluminum sheet.

The entire structure is designed so that it can be packaged in the Space Shuttle Orbiter for transport to low earth orbit. There it would be deployed and transported to a geostationary orbit. The deployment procedure for a similar antenna is depicted in Figure 18. In the packaged configuration, the mast is collapsed, and the rim members are lined up axially one next to the other around the canister containing the mast. The rim elements are hinged, the top to the rim member to the left and the bottom to the rim member on the right. After the mast has extended, the rim members begin to deploy, moving outward radially from the mast and rotating about the center of their lengths. In the process the circle formed around the mast by the inclined rim members gets larger. In the deployed position each rim member is horizontal and has rotated 90° about a radial line outward from the mast. The NASTRAN analysis helped to establish guidelines for the design of the structure, which was required to hold stringent dimensional tolerances. The following analyses were performed using NASTRAN: static analysis with pretension loads; buckling analysis and vibration analysis.

The finite element model is shown in Figures 19 and 20. The rim and mast were modeled with bar elements, the forestays and backstays with rod elements and the gore sectors with membrane triangles.

The static analysis involved determining the deflections and member loads of the structure due to the operational pretension loads in the stays and gore. For all the static analysis, the structure was supported in a statically determinate fashion and Rigid Format 1 was used. The stays were pretensioned by applying a load of 89.09 N (20.0316) in the z direction at node 146 (see Figure 19), while the gore was pretensioned by applying inward radial loads of 23.6 N (5.32 lb.) at the apex of each triangular sector. The resulting member loads and deflections are given in Table II. Note that points on the rim to which forestays are attached have different deflections from points to which backstays are attached due to the different loads in the forestays and backstays. Deflections and members loads in the prestressed structure due to, in one case a broken forestay, and in the second case a broken

backstay were also obtained. Since the structure is not symmetric about the gore plane, a broken frontstay and a broken backstay will have different effects. Member loads for both cases did not change appreciably from their values under nominal prestress conditions. The resulting deflections of points on the rim in the radial and axial directions, are shown in Figures 21 and 22. Note that the distortions are very local being confined to a maximum of eight neighboring node points on the rim.

Under the action of the pretension loads, the rim experiences a compressive load of 413.7 N (93 lbs.), and hence may be subject to an instability condition. This was investigated by employing Rigid Format 5 to obtain the buckling loads of the structure. The mode shape corresponding to the lowest buckling load (1089.8 N (245 lbs.) compression in the rim) is shown in Figure 23. For this mode the structure behaves as a series of beams with length equal to twice the length of a single rim member supported at the center by a spring (and nct as a ring on a continuous elastic foundation).

The vibration analysis of the antenna was carried out to obtain the free-free modes which would then be used in a subsequent analysis to determine the structural response due to control forces. The finite element model was the same as that used for the static analysis. The mass of the structure was lumped at the nodes. The mass of the gore material in the plane of the rim (thin disk) was distributed by lumping 50% of its mass at the nodes of the rim, and the remaining 50% on the mast node (thus preserving the mass moments of inertia). Some of the lower modes are shown in Figures 24 and 25. Note that the lowest modes involve bending of the mast, while higher modes involve bending of the rim.

CONCLUSIONS

The application of NASTRAN to the analysis of two very large-area lightweight space structures has been described. The broad capability and large capacity of the NASTRAN program make it well suited for the analysis tasks required in the design studies. Static, buckling and free vibration analyses were carried out without any problems. Difficulties were, however, encountered in running Rigid Format 11 (Frequency response analysis) and an alternate program was used. The results of the analysis indicated the feasibility of the designs and helped pinpoint problem areas requiring design modifications.

From an overall viewpoint, the NASTRAN program is one of the major structural analysis tools at Grumman and is used on many other projects. On the average, it represents 30% of computer time used for structural analysis with additional usage (approximately 1/3 to 1/2 of the above computer time) attributed to dynamic analysis. Its broad applicability will insure its use on future work, it must however be maintained and updated on a continuing basis.

REFERENCES

1. Space Station Systems Analysis Study; Grumman Contract No. NAS-8-31993.

2. Orbital Construction Demonstration Study; Grumman Contract No. NAS-9-14916

3. OAST Summer Workshop Proceedings; Structures and Dynamics Panel; Aug. 3-16, 1975, Conducted at Madison College, Harrisonburg, Va.

4. Second interim report, space-based solar power conversion delivery systems study; vol 2 Engr Analysis of Orbital Systems; in support of contract No. NAS 8-31308 to NASA/MSFC.

TABLE I

SSPS MASS DISTRIBUTION

ITEM	MASS	
	Kg x 10^6	lb. x 10^6
SOLAR CELL BLANKETS	7.82	17.25
SOLAR CONCENTRATORS	1.23	2.71
NONCONDUCTING STRUCTURE	2.33	5.14
CONDUCTING BUSSES	.27	.59
MAST	.62	1.37
MICROWAVE ANTENNA	5.55	12.23
ROTARY JOINT	.17	.37
CONTROL SYSTEM	.036	.08
TOTAL	18.02	39.74

TABLE II

MEMBER LOADS & DEFLECTIONS DUE TO

PRETENSION LOADS IN DEPLOYABLE ANTENNA

LOADS IN MEMBERS		
Rim - axial compression -	416.8 N	(93.7 lbs.)
Forestays - axial tension -	22.24 N	(5.0 lbs.)
Backstays - axial tension -	4.804 N	(1.08 lbs.)
Gore - average σ_{rr} -	620 kPa	(90 psi)

DEFLECTIONS	Δr		Δz	
Points on Rim to which forestays are attached	-.386 cm	-.152 in.	-6.63 cm	-2.61 in.
Points on Rim to which backstays are attached	-.335 cm	-.132 in.	-7.08 cm	-2.79 in.

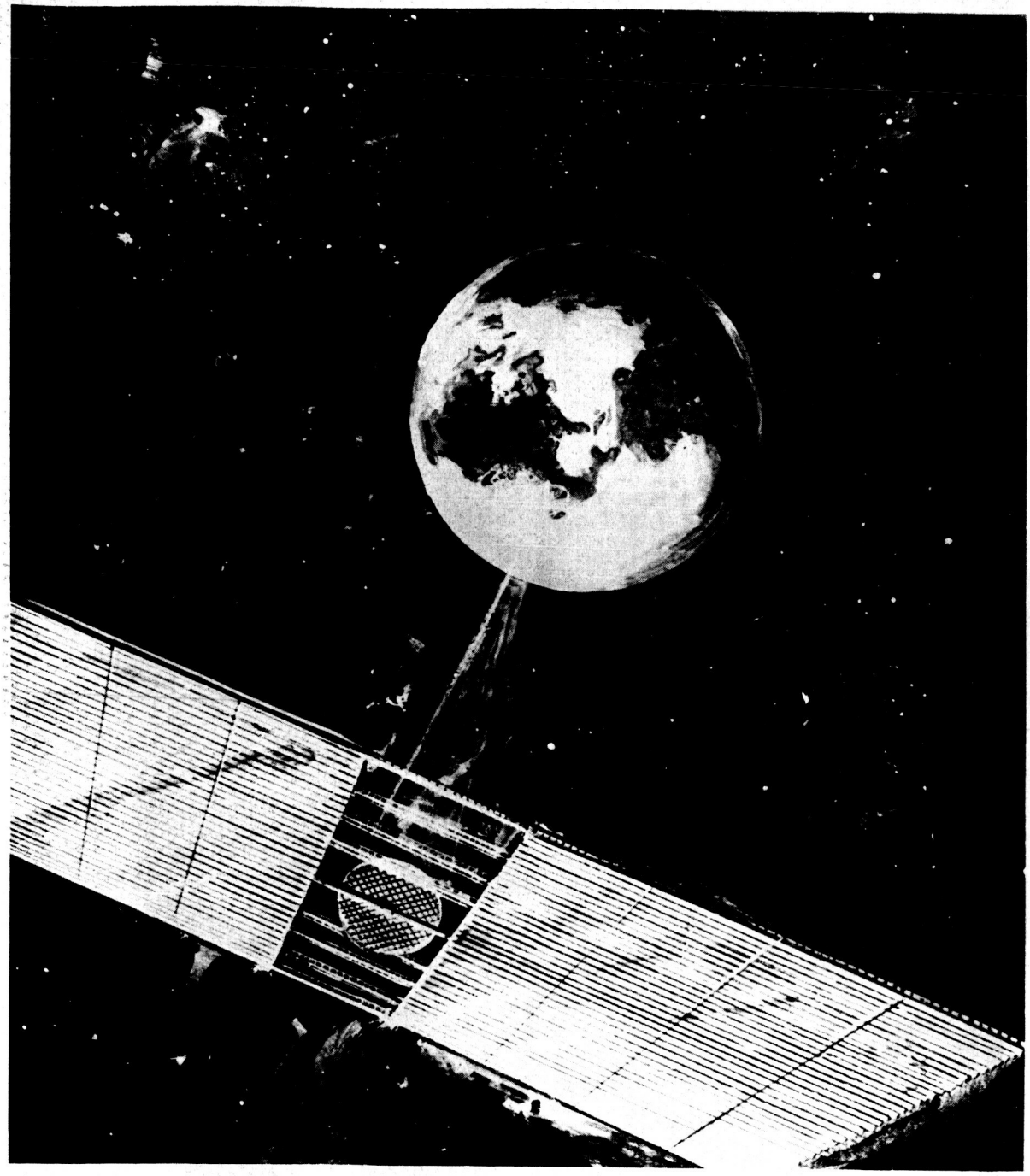

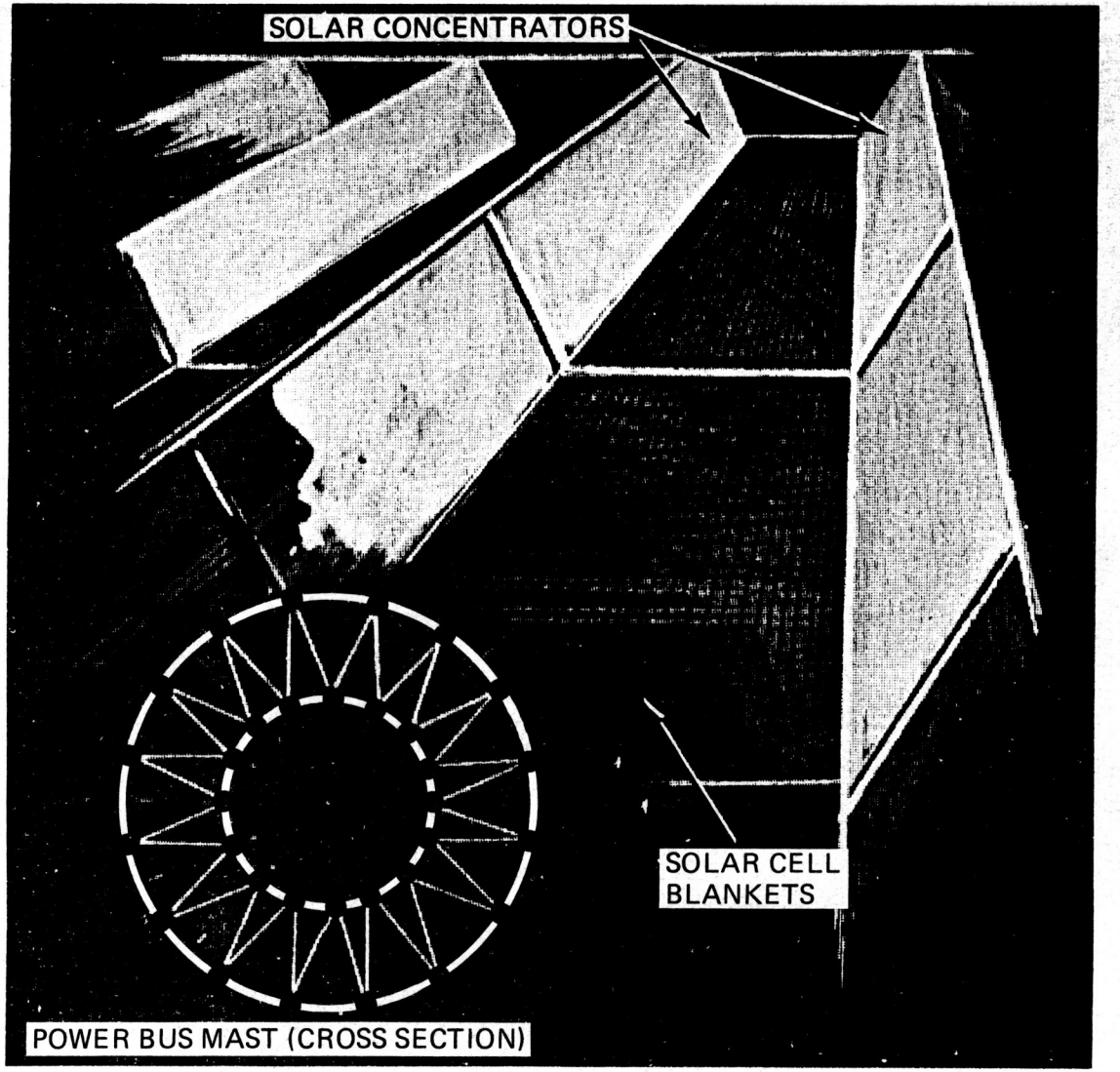

Fig. 2 Solar Panel Detail

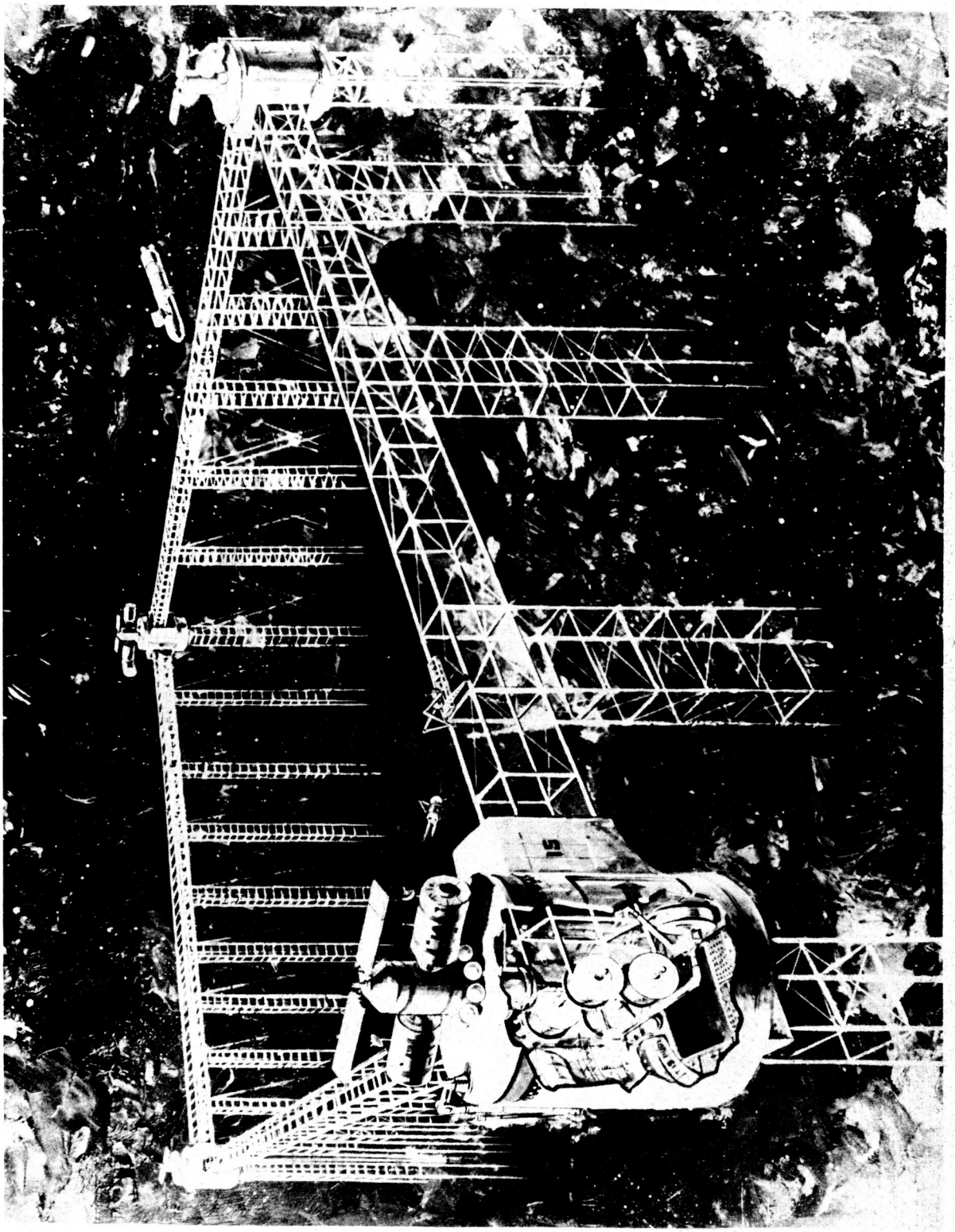

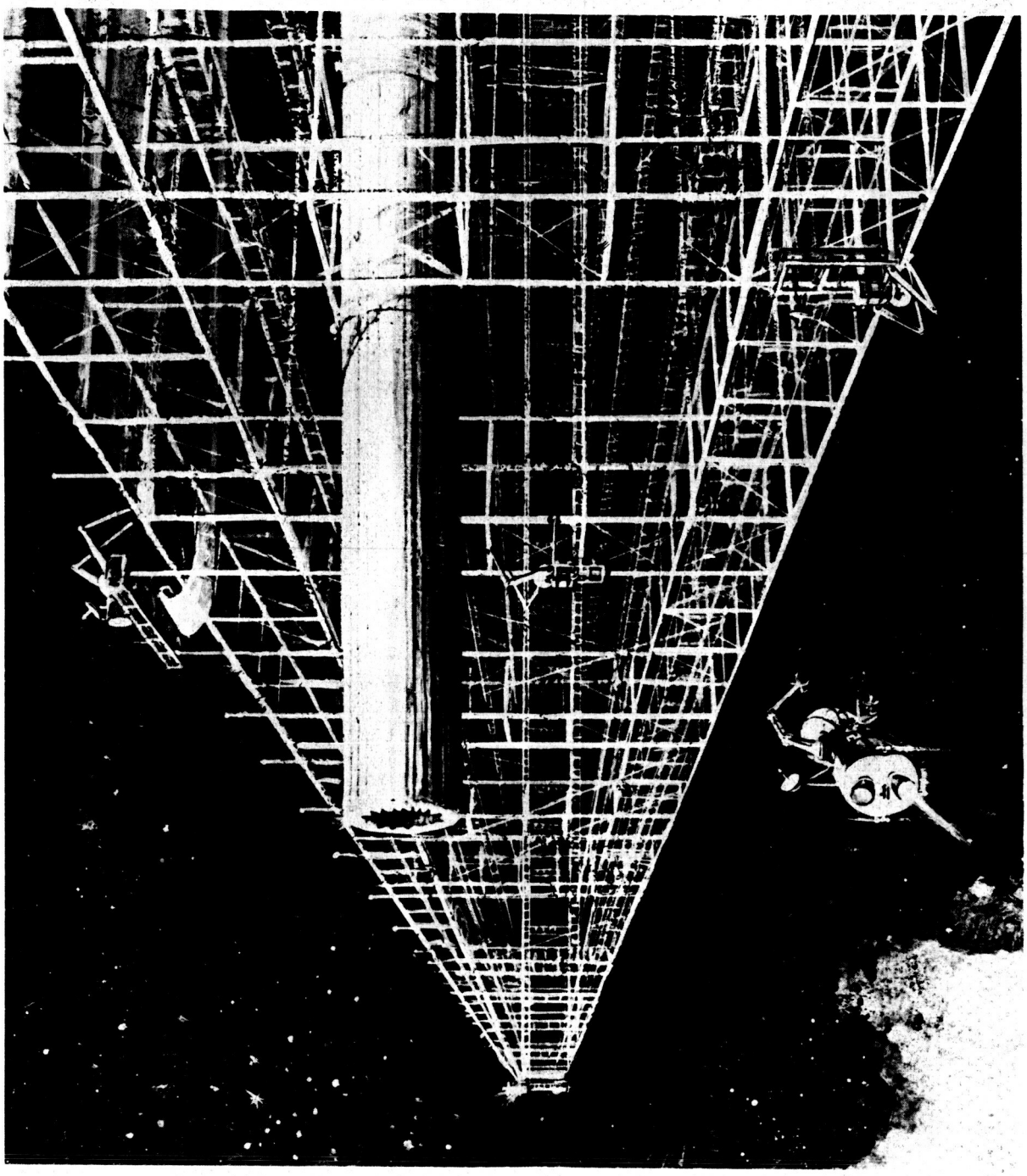

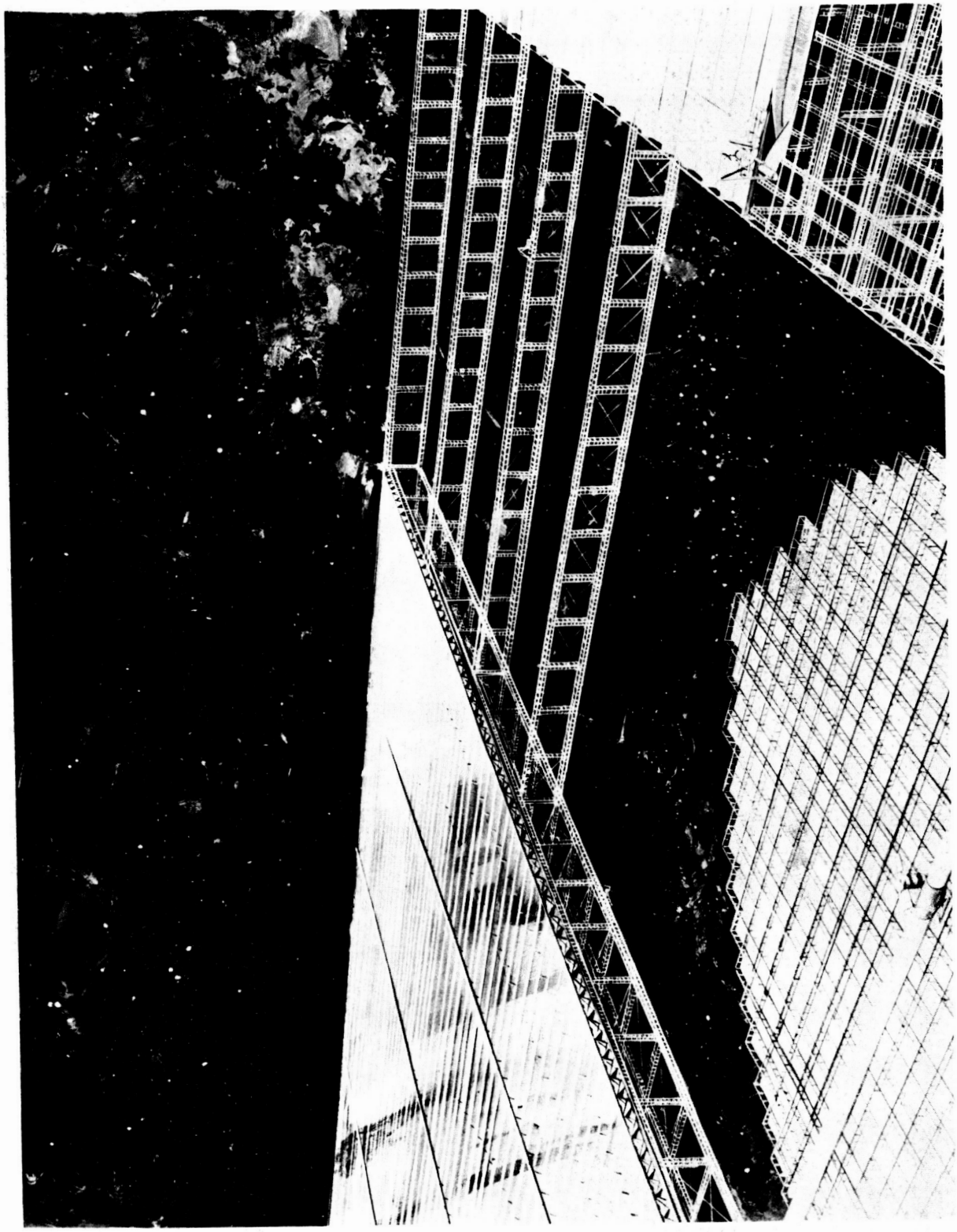

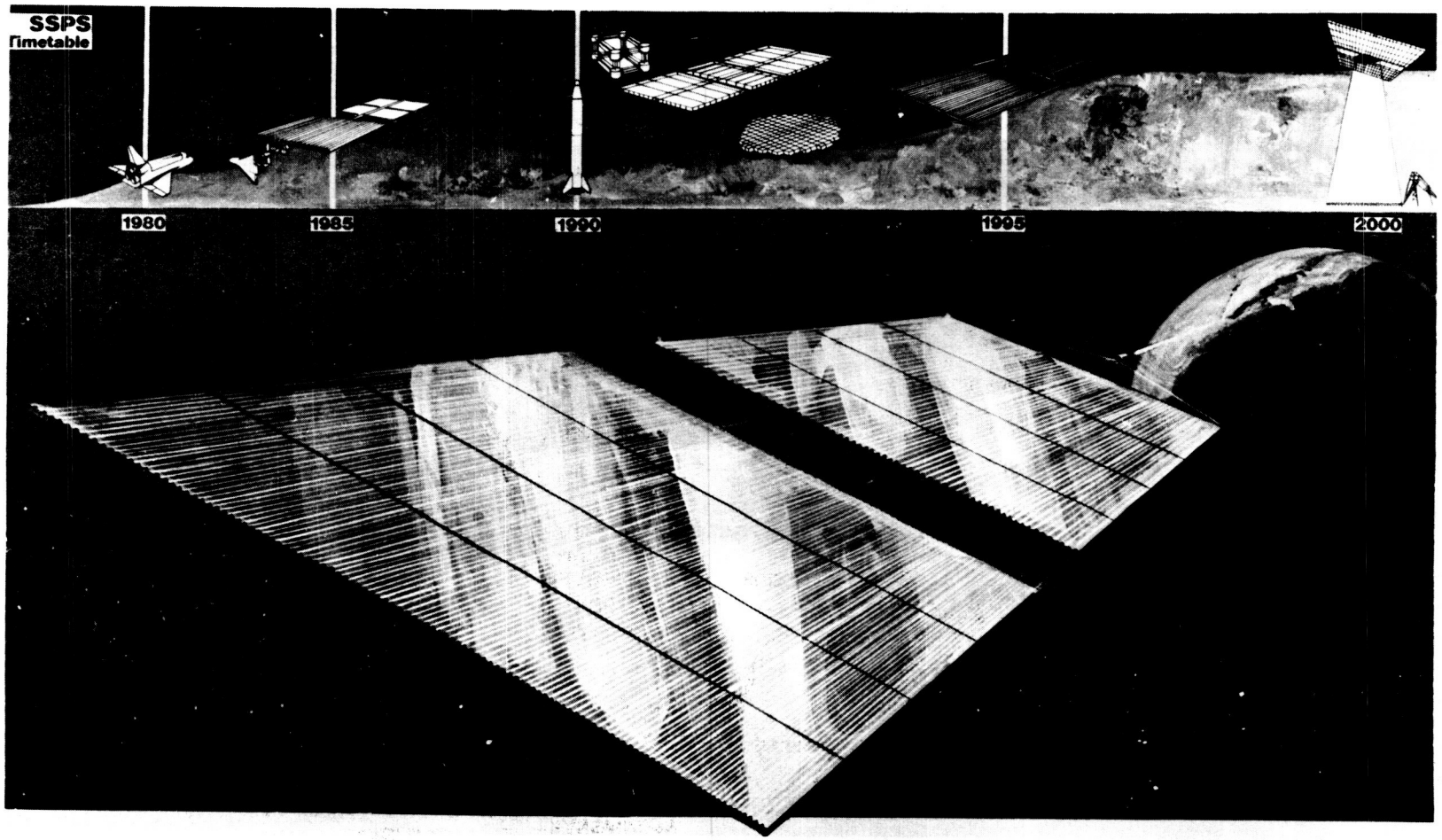

Fig. 6 Transport of SSPS From LEO to Geosynchronous Orbit

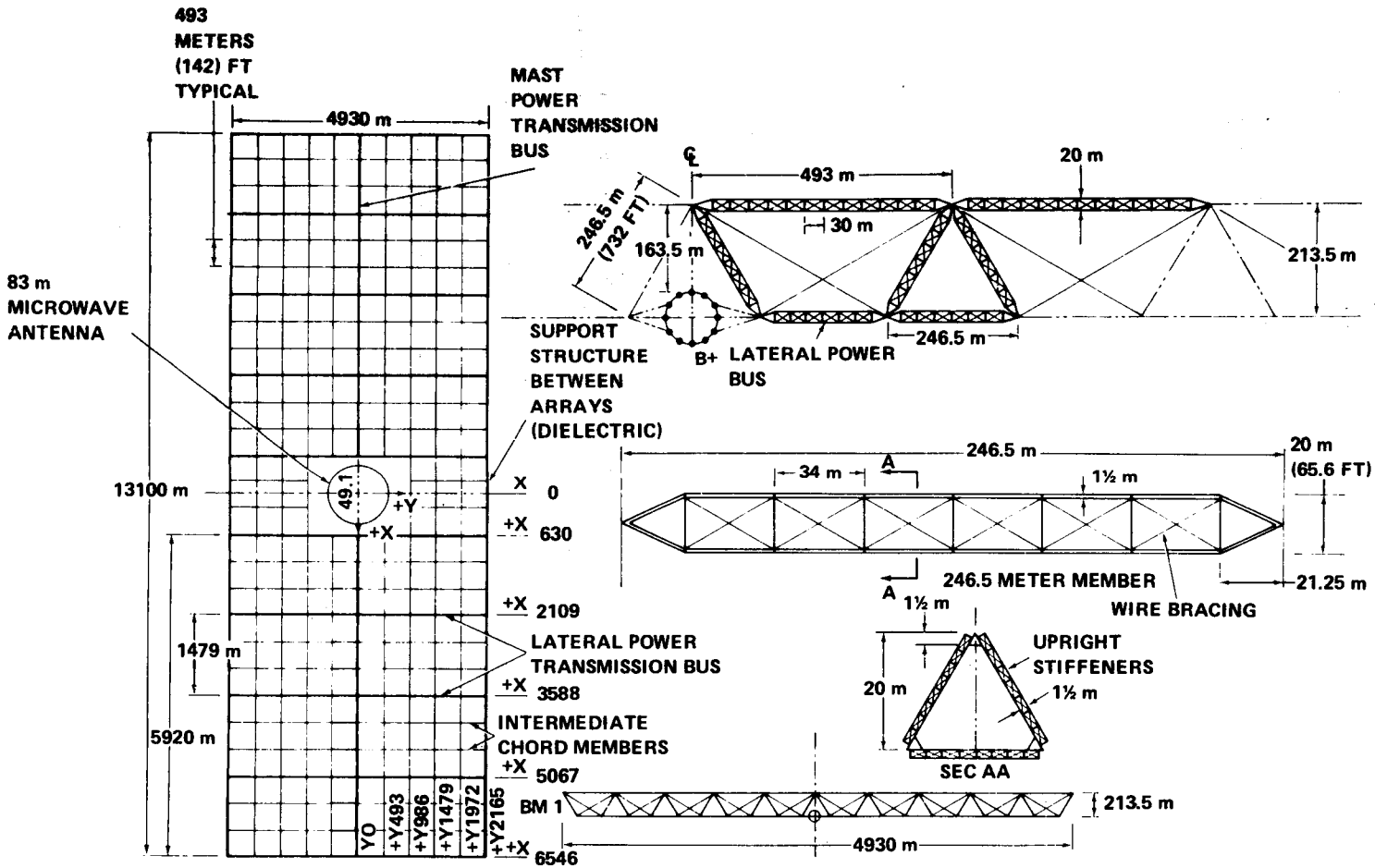

Fig. 7 SSPS Structural Arrangement

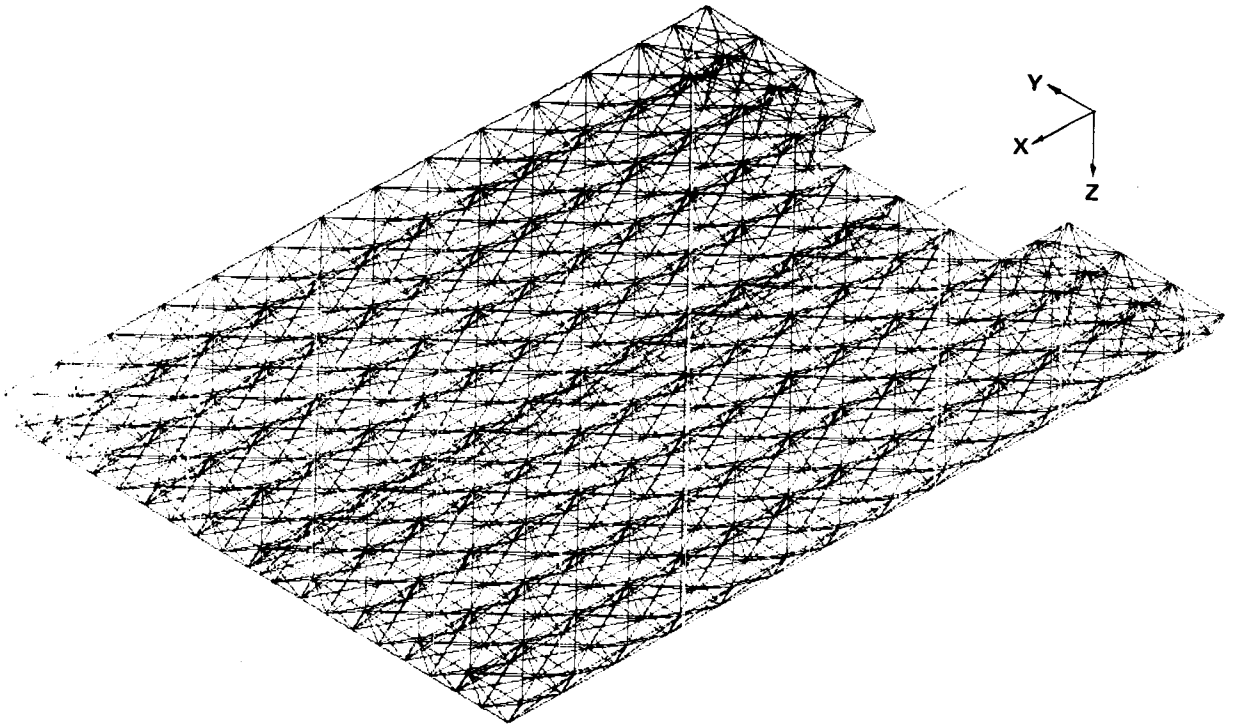

- HALF STRUCTURE CONSISTS OF 1127 MEMBERS AND 462 NODES
- SATELLITE WEIGHT DISTRIBUTED AS LUMPED MASSES AT NODE POINTS
- TENSION-ONLY WIRES REPLACED BY TENSION/COMPRESSION STRUTS
- PROPRETIES

WT = 18.02×10^6 KG (39.74×10^6 LB)

$X_{CG} = 0$

$Y_{CG} = 0$

Z_{CG} = 261.6M (858.3 FT)

$I_X = 2.445 \times 10^{13}$ KG-M^2 (1.803×10^{13} SLUG-FT^2)

$I_Y = 1.883 \times 10^{14}$ KG-M^2 (1.389×10^{14} SLUG-FT^2)

$I_Z = 2.118 \times 10^{13}$ KG-M^2 (1.5652×10^{14} SLUG-FT^2)

Fig. 8 Finite Element Model

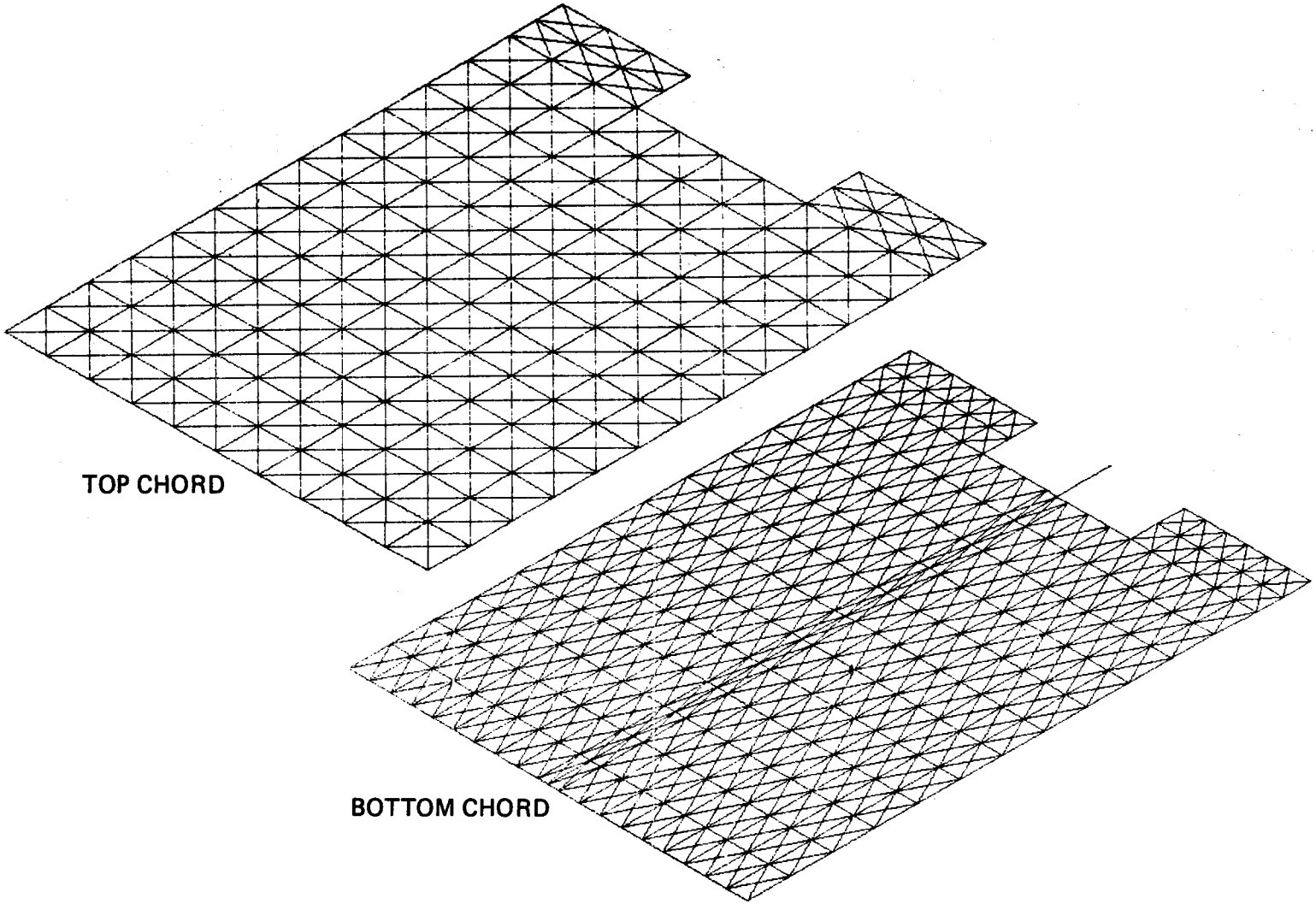

Fig. 9 Finite Element Model

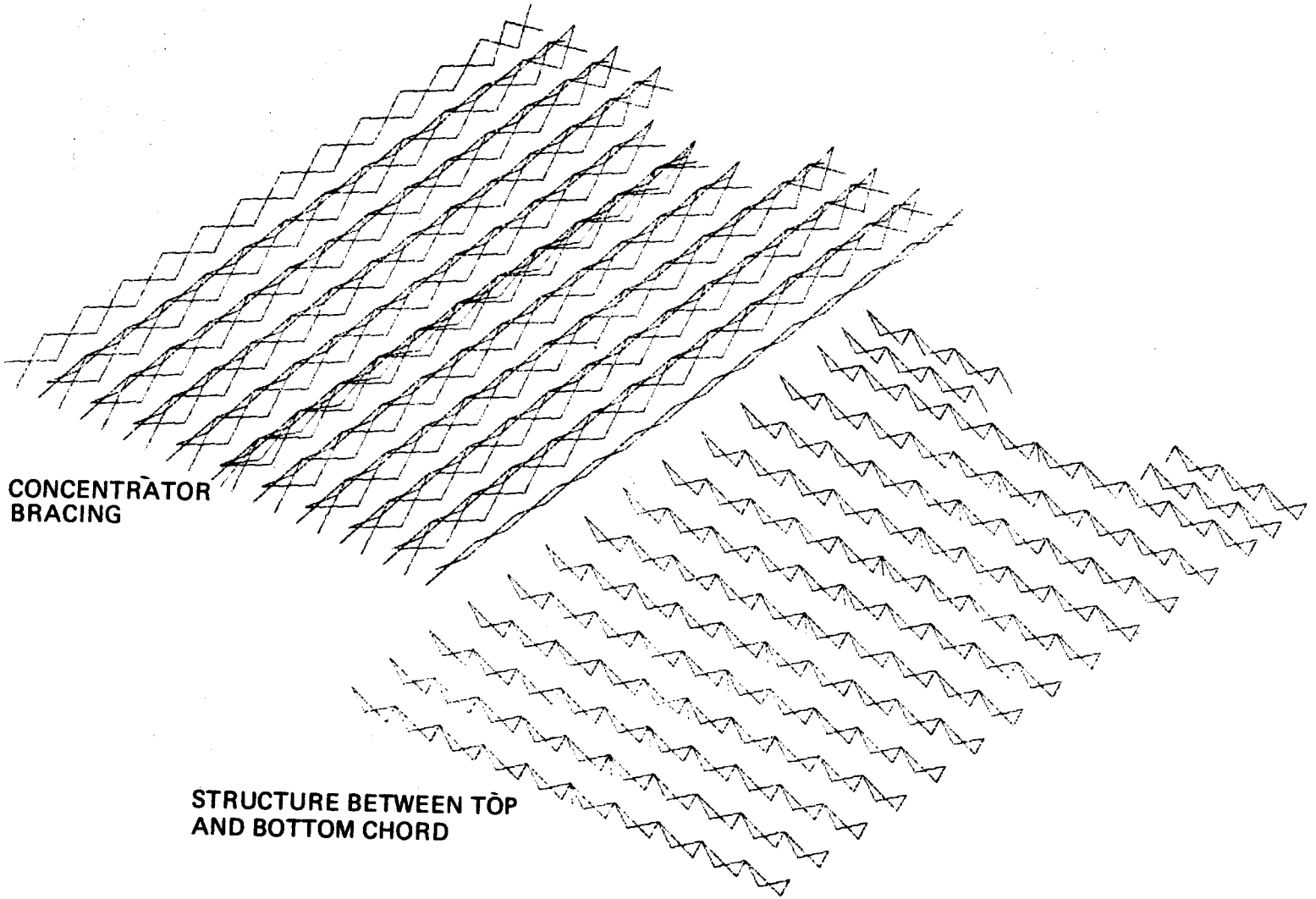

Fig. 10 Finite Element Model

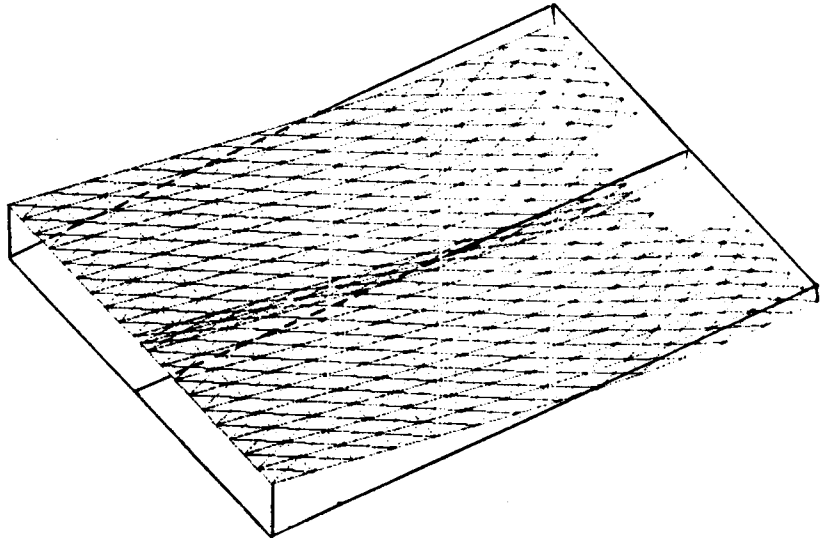

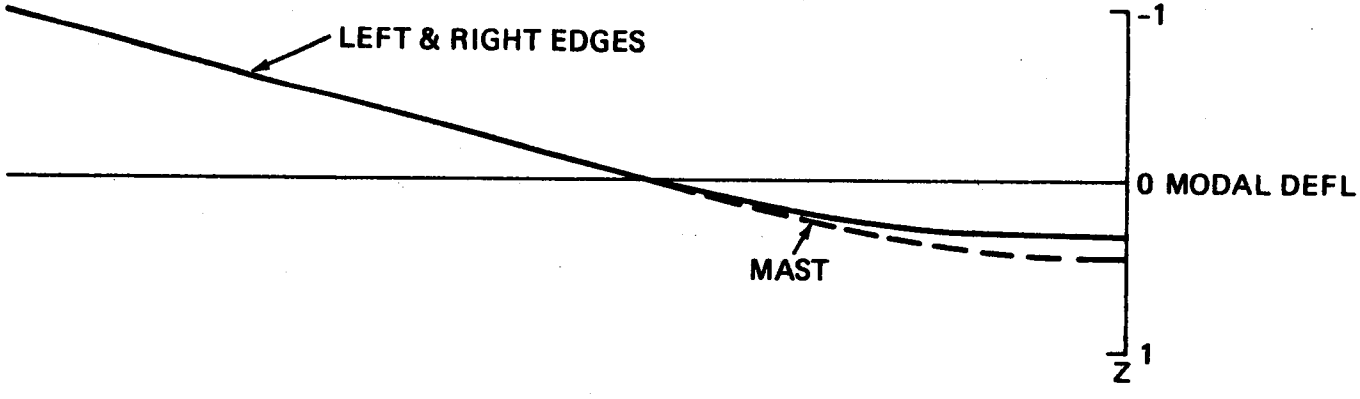

Fig. 11 SSPS Symmetric Mode - First Bending, Frequency = 5.26 C/Hr

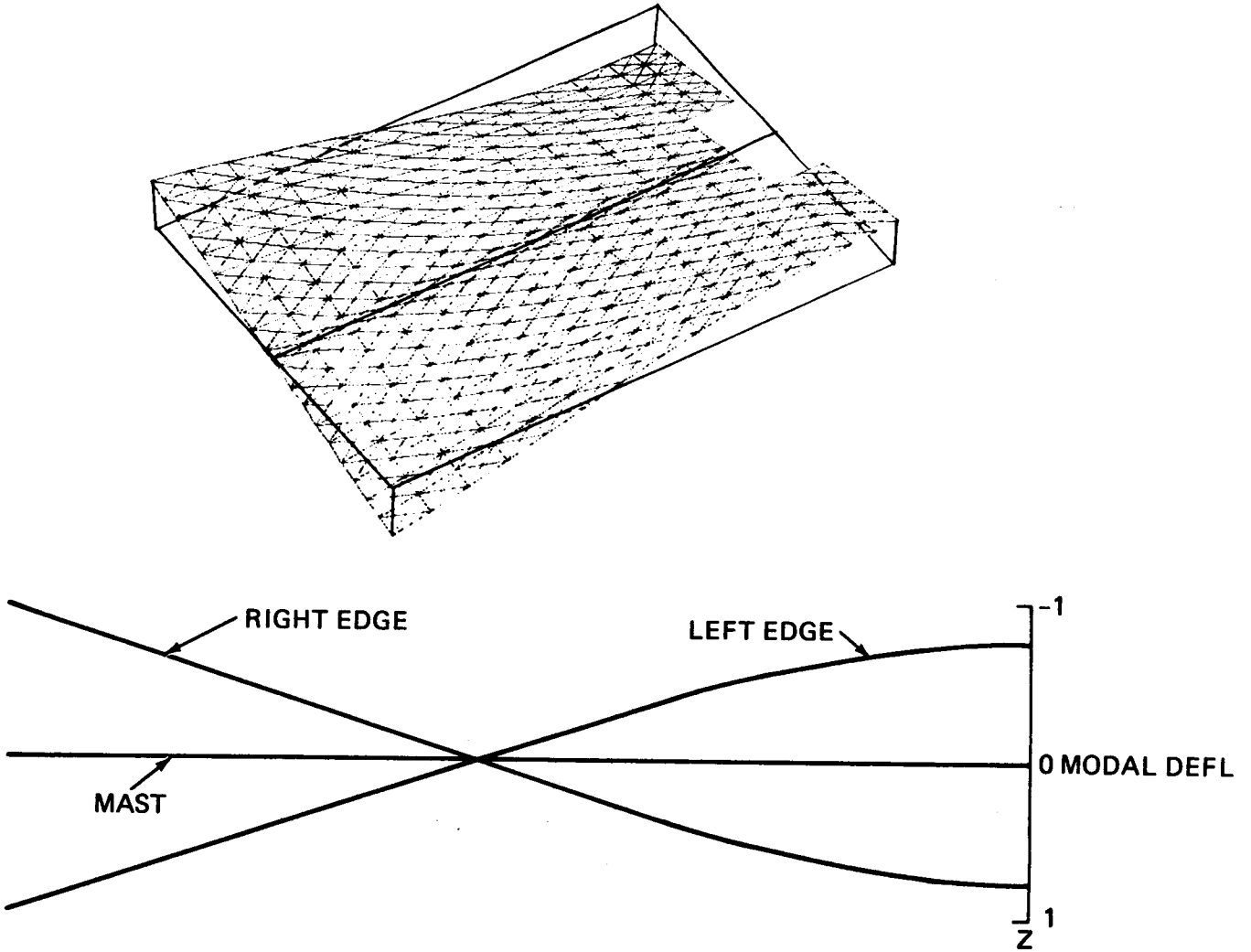

Fig. 12 SSPS Symmetric Mode - First Torsion, Frequency = 14.14 C/Hr

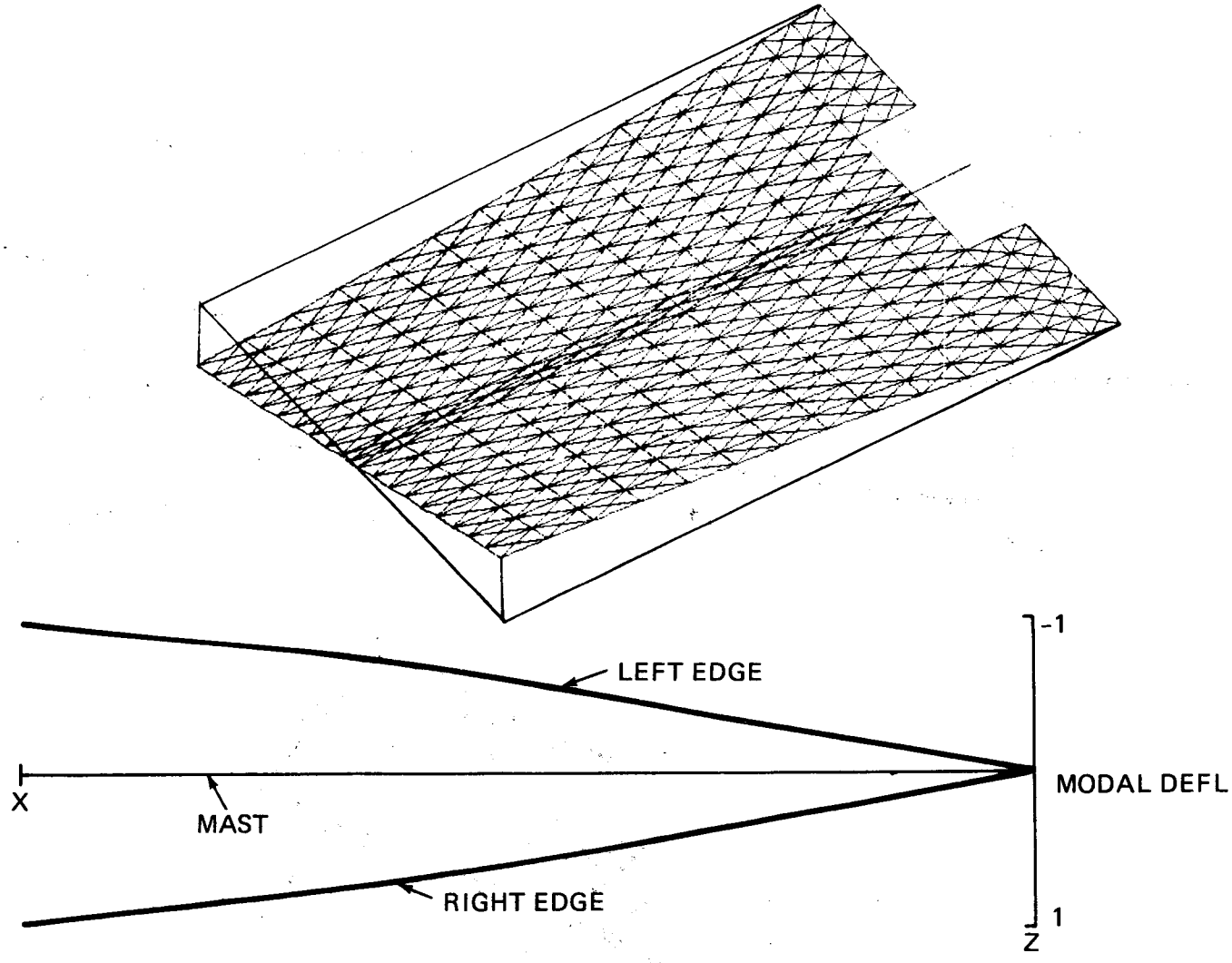

Fig. 13 SSPS Antisymmetric Mode - First Torsion, Frequency = 9.36 C/Hr

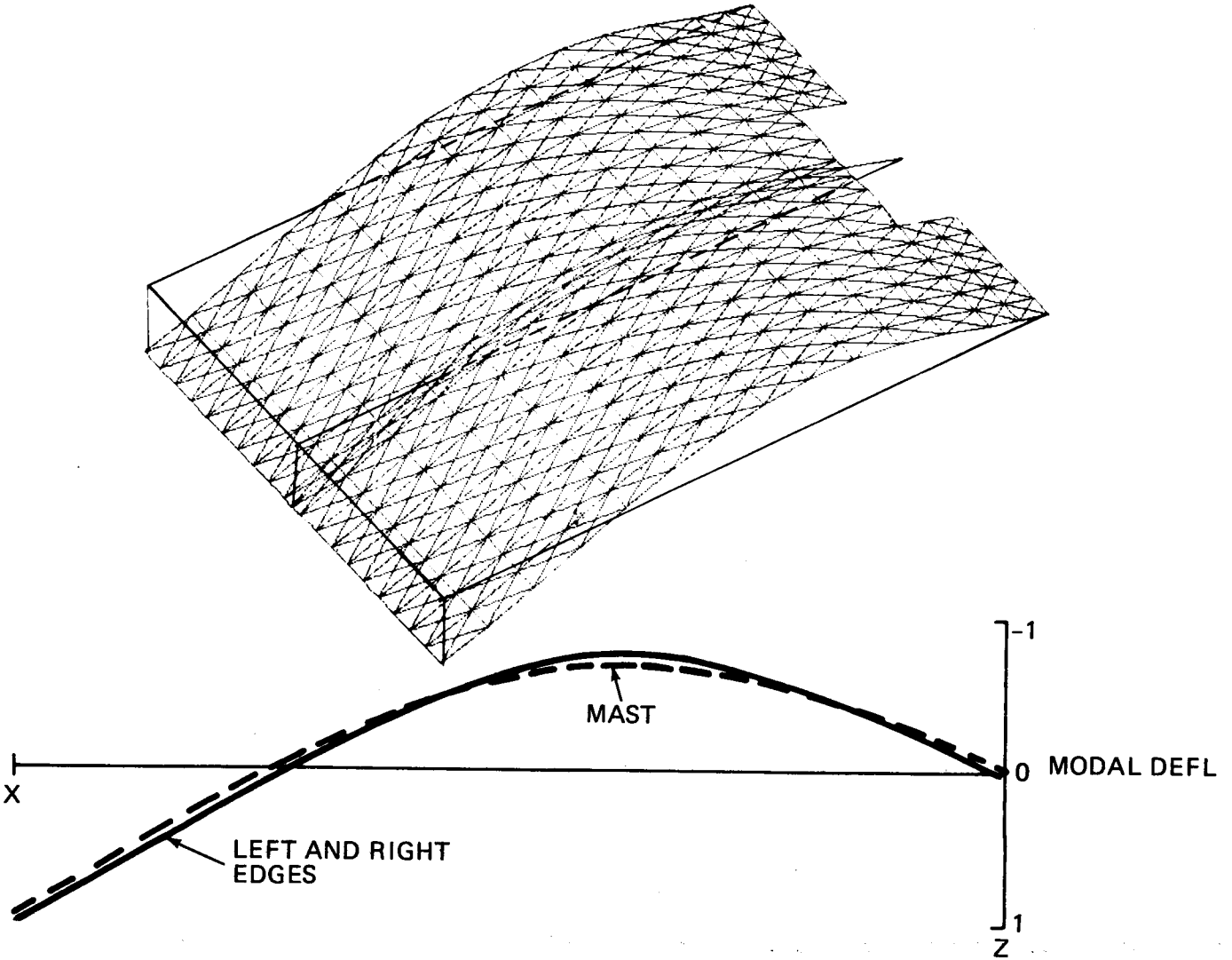

Fig. 14 SSPS Antisymmetric Mode - First Bending, Frequency = 15.65 C/Hr

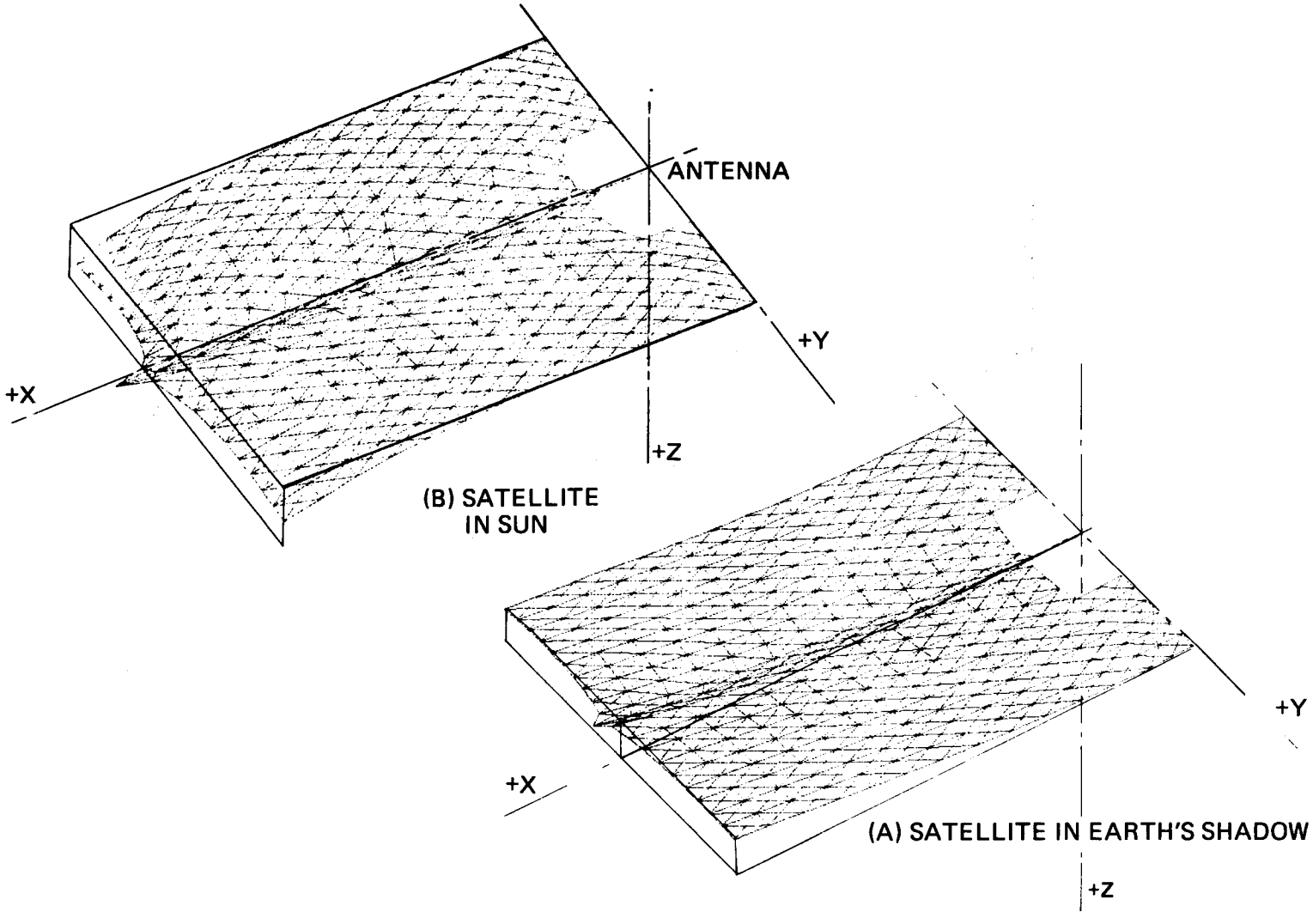

Fig. 15 Deflections Due to Thermal Conditions

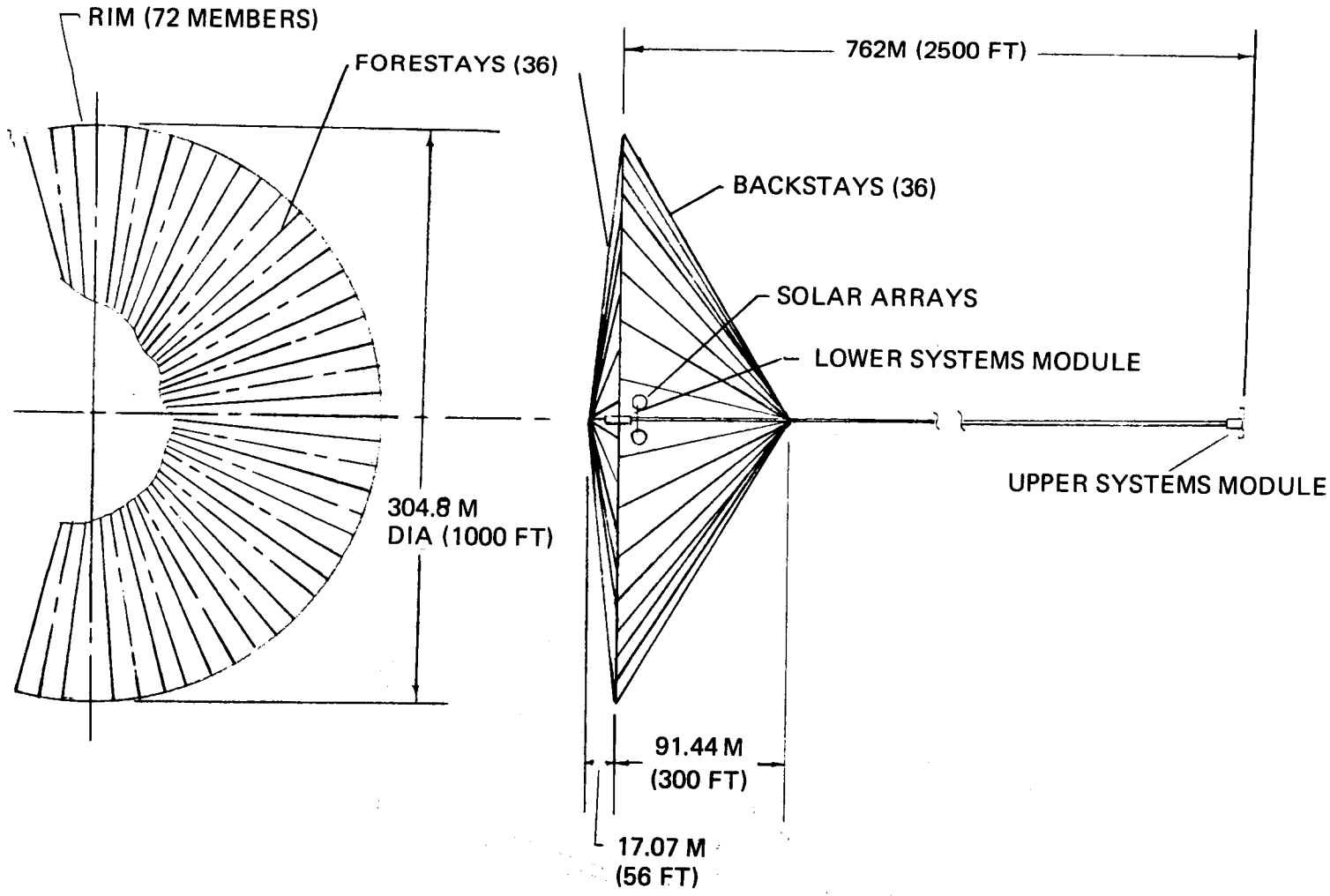

Fig. 16 Configuration of 300M (1000 FT.) Diameter Deployable Antenna

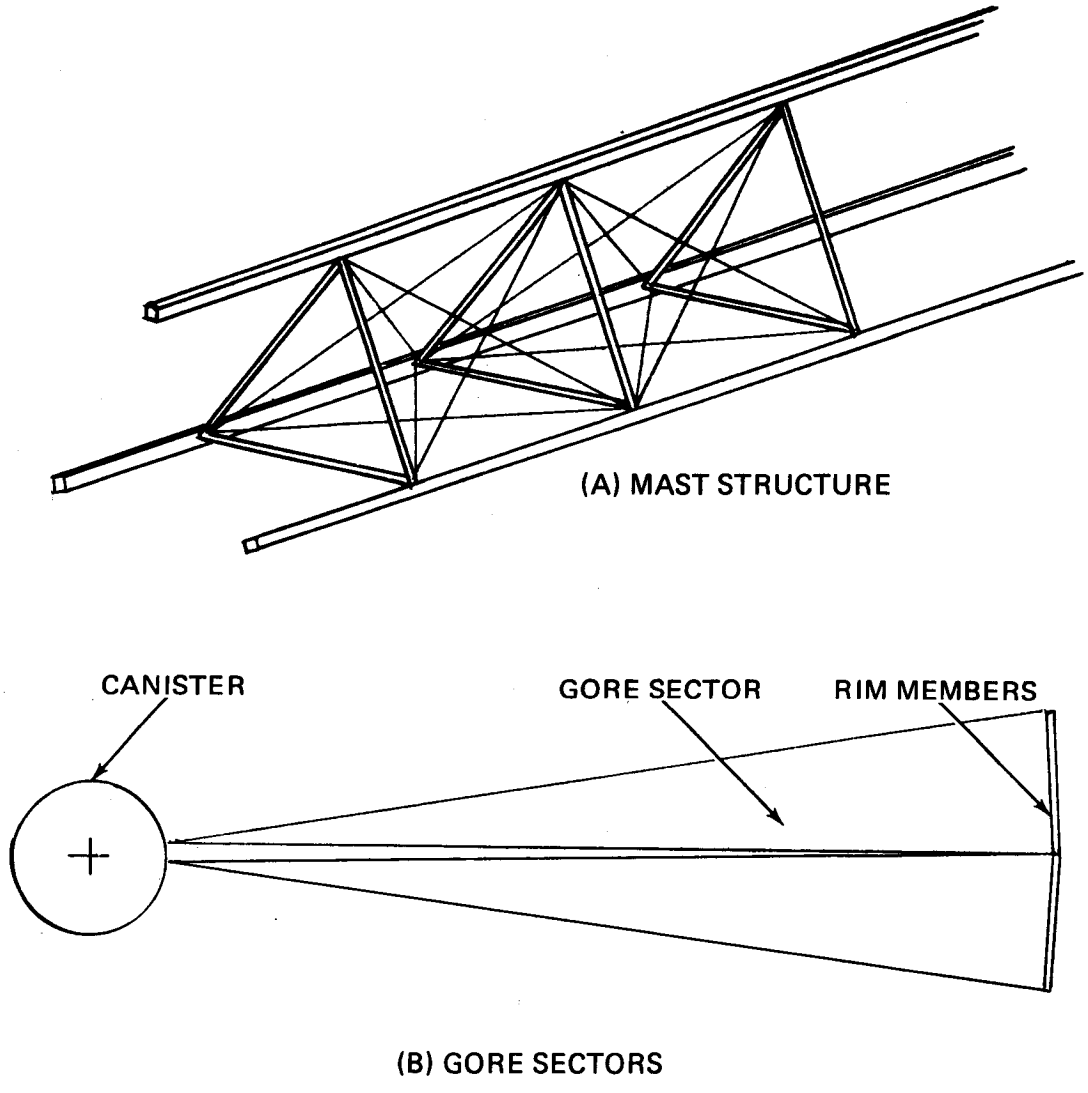

Fig. 17 Structural Components of Antenna

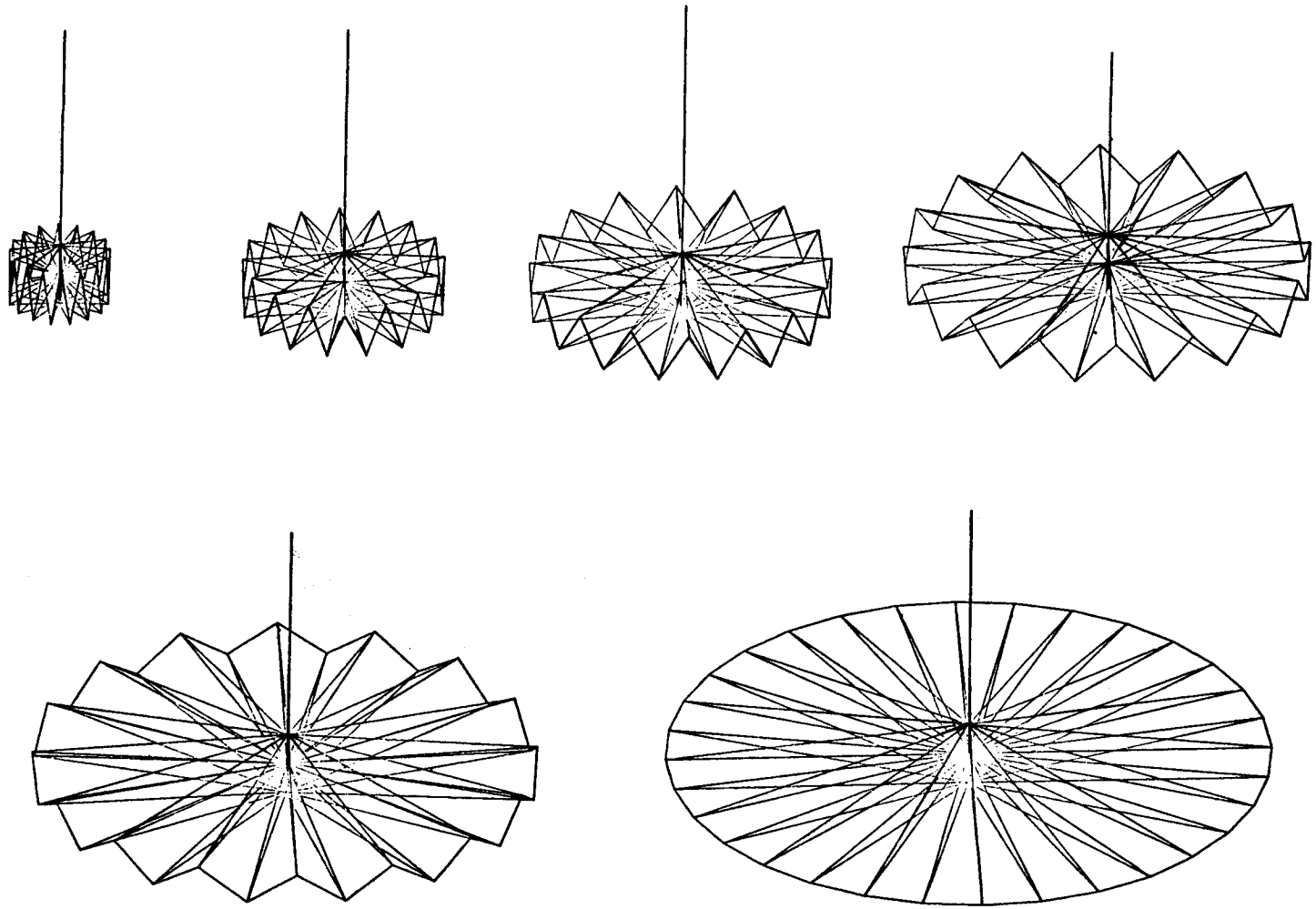

Fig. 18 Antenna Deployment Procedure

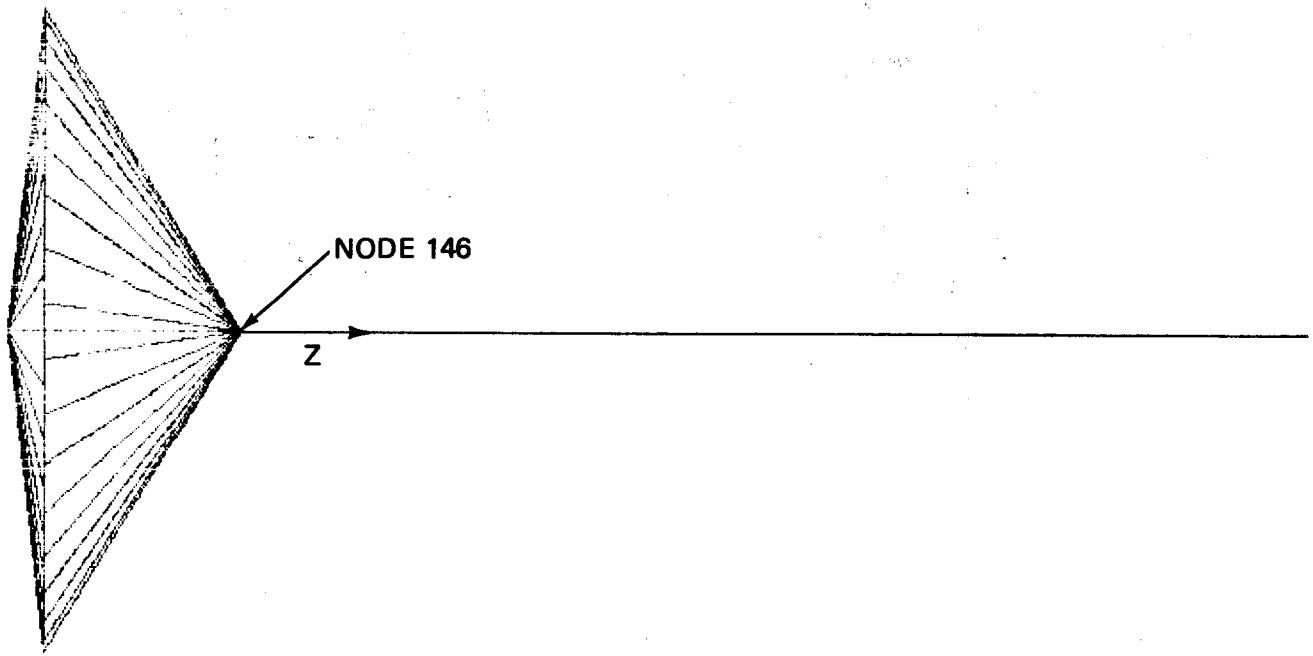

Fig. 19 Finite Element Model

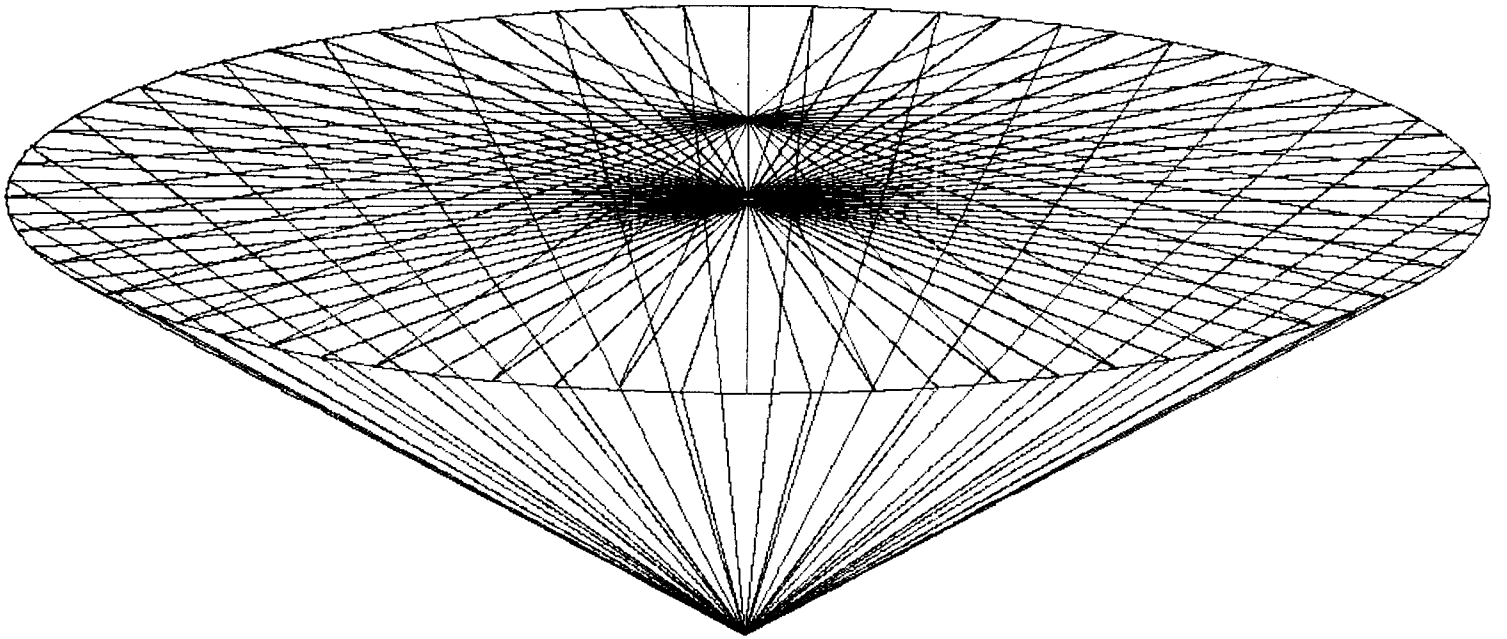

Fig. 20 Finite Element Model

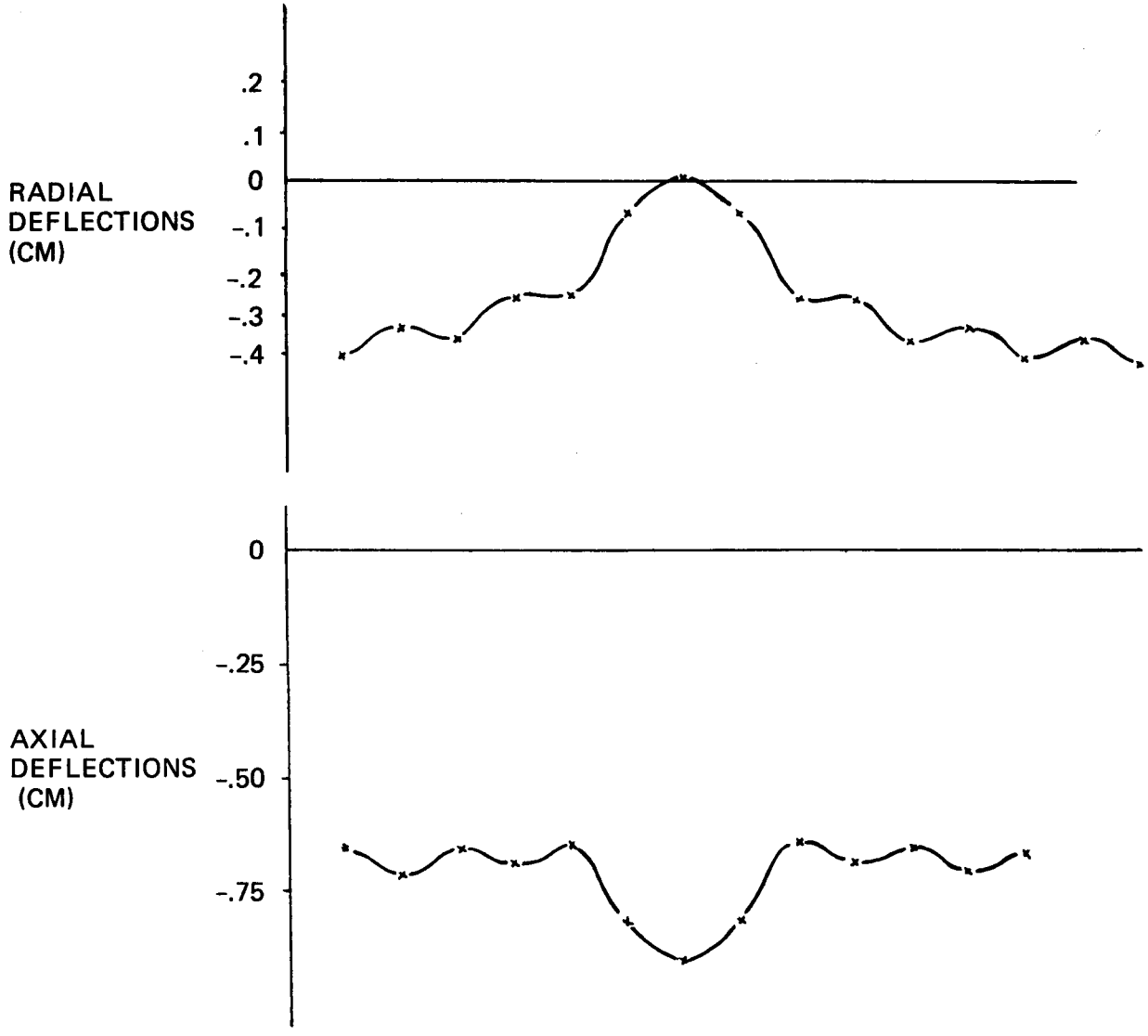

Fig. 21 Deployable Antenna Deflections with Forestay Removed

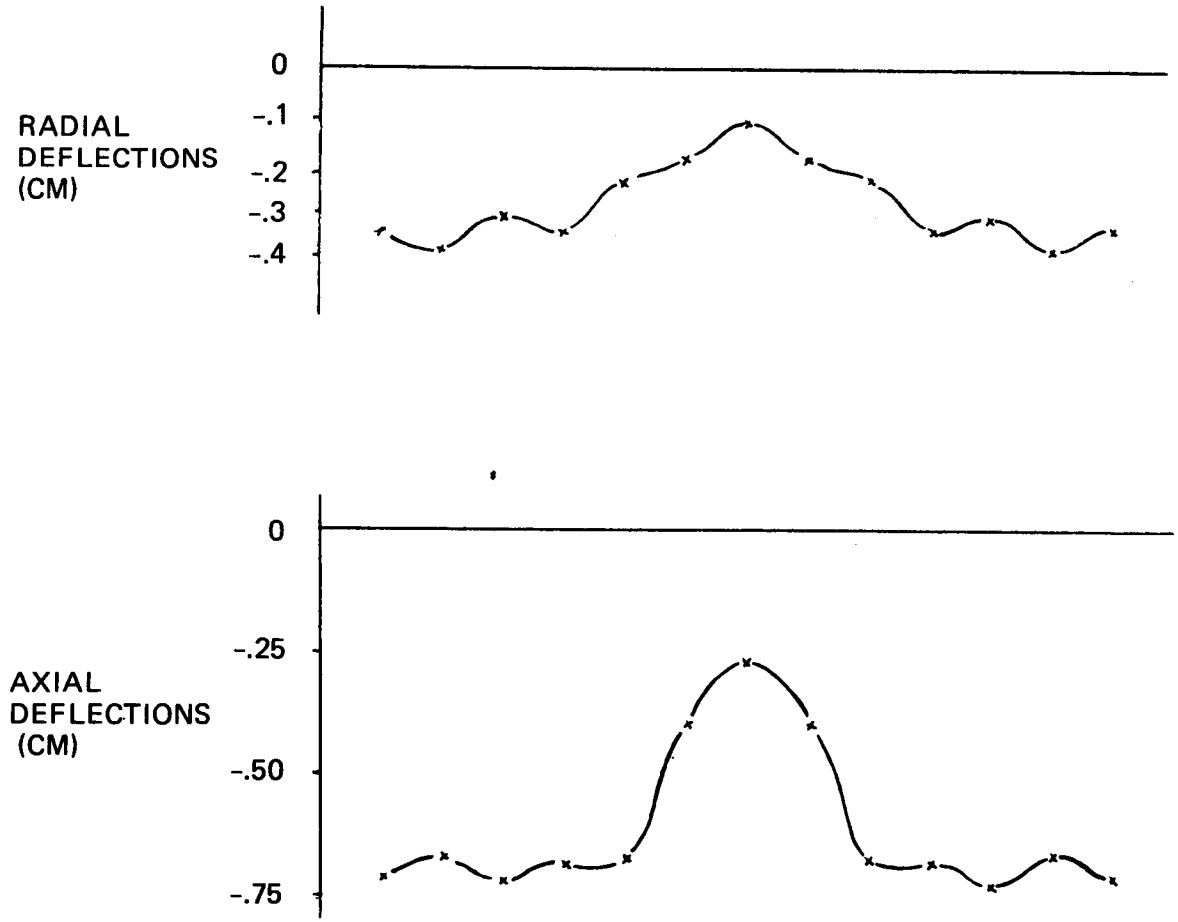

Fig. 22 Deployable Antenna Deflections with Backstay Removed

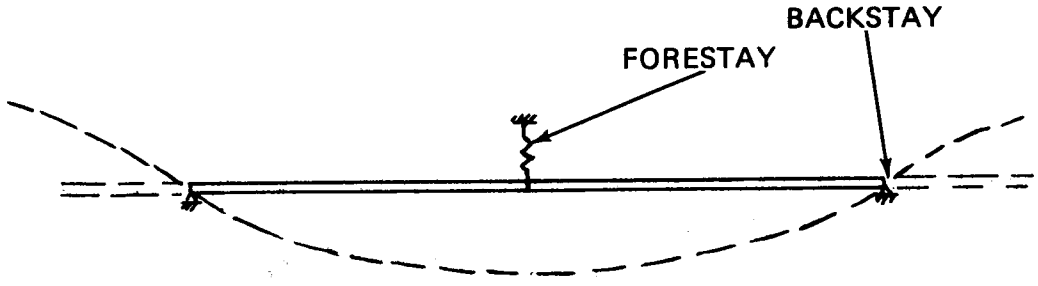

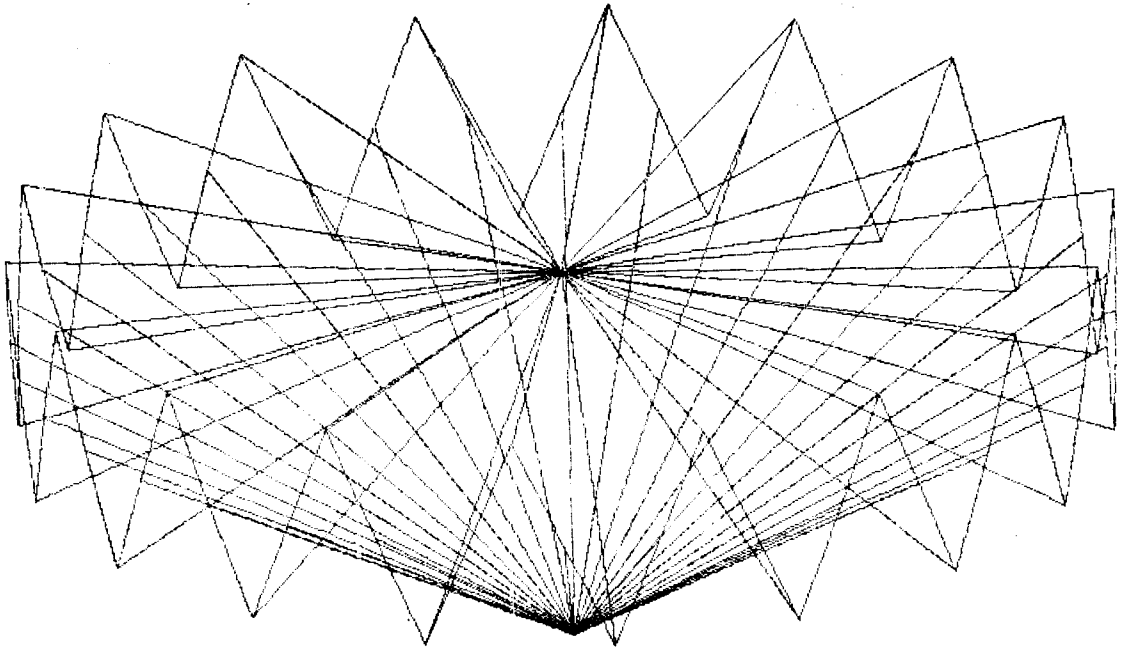

Fig. 23 Buckling Mode Shape of Antenna

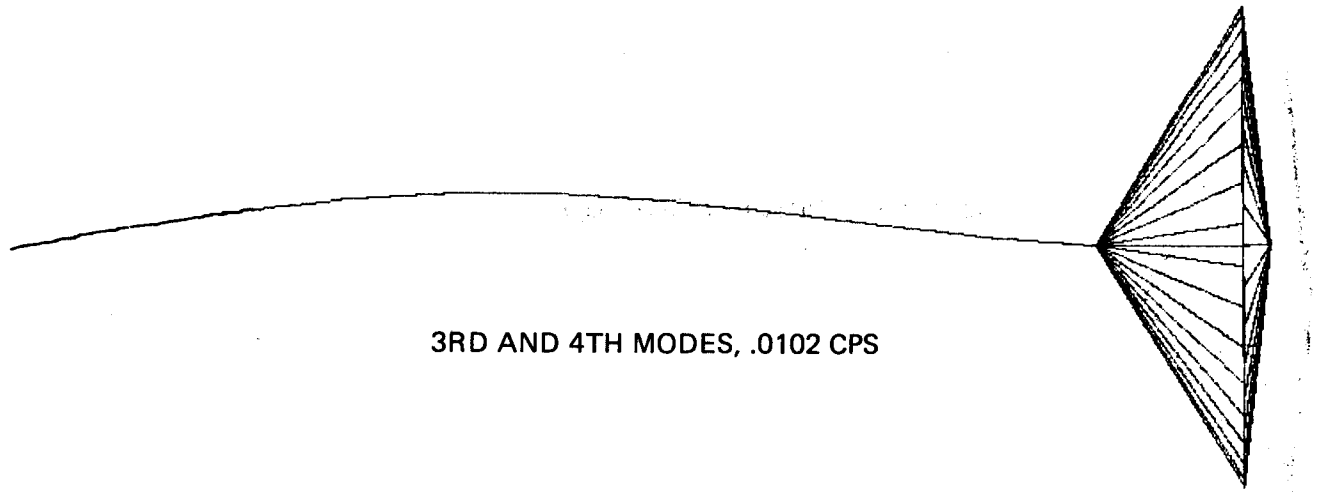

3RD AND 4TH MODES, .0102 CPS

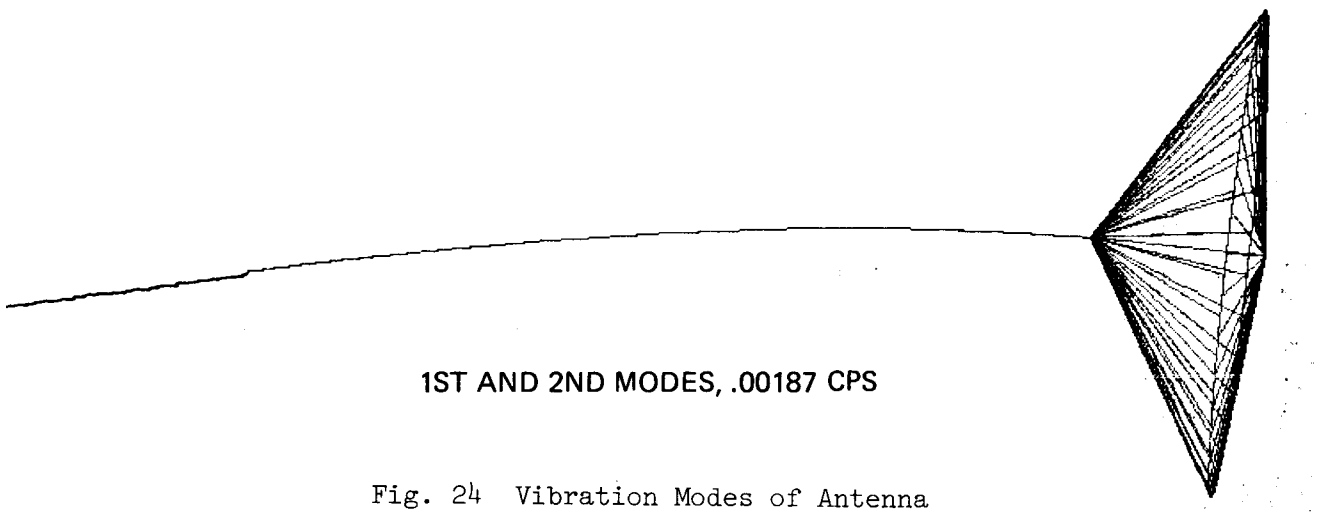

1ST AND 2ND MODES, .00187 CPS

Fig. 24 Vibration Modes of Antenna

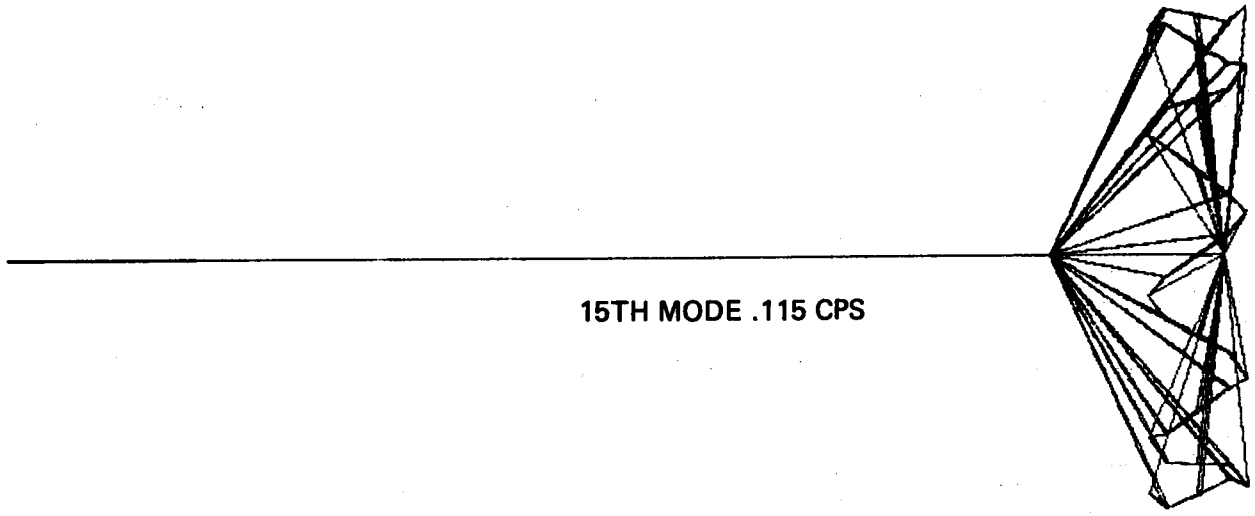

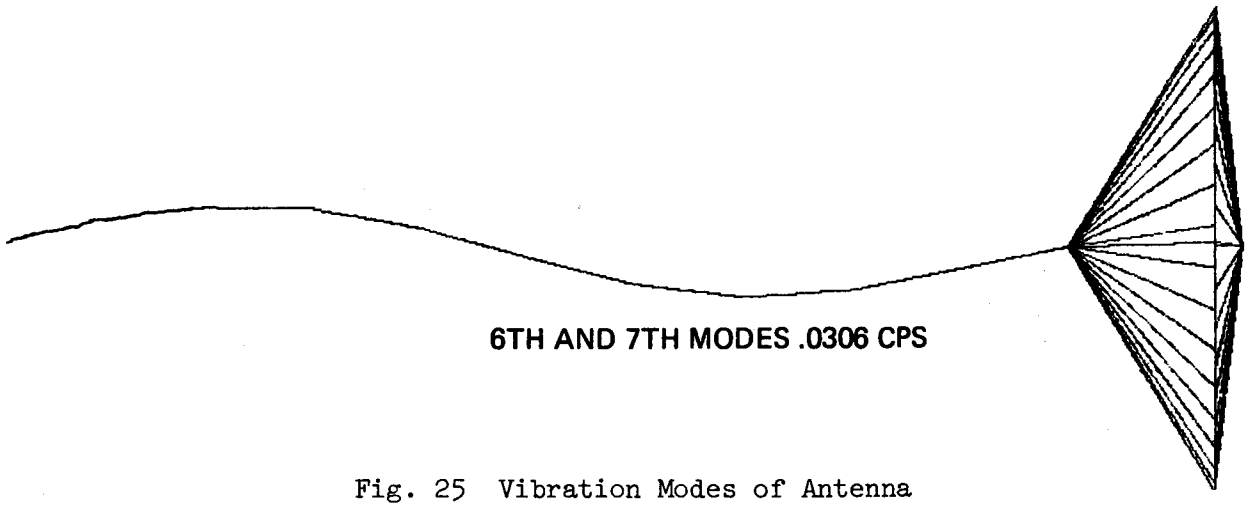

Fig. 25 Vibration Modes of Antenna

ANALYSIS OF THE LEARJET 35/36 WING AND CORRELATION WITH EXPERIMENTAL RESULTS

Mike H. Abla and Robert R. Boroughs
Gates Learjet Corporation

Everett L. Cook
Wichita State University

SUMMARY

Two NASTRAN models of the Gates Learjet Corporation Model 35/36 Wing have been developed. This paper describes the models and discusses the problems encountered in their development. A skin buckling analysis used for the ultimate loading conditions is presented. A discussion of the static tests and the correlation of the static test with the NASTRAN results and the results of a supplementary semimonocoque beam analysis are also included.

INTRODUCTION

The purpose of the investigation described herein is to develop an accurate finite element model of the Gates Learjet Corporation (GLC) Model 35/36 wing. This wing is an 8-spar wet wing with large external fuel tanks at the tips (fig. 1). It is continuous from tip to tip with all loads transferred to the fuselage through four fittings on each side. It is a derivative of previous GLC wings, with the most noticeable difference being the wing tip extensions. There are also internal structural modifications which were incorporated to accommodate the increased gross weight of the Model 35/36.

An in-house finite element program, based on reference 1, was used during the design and certification testing of the wing. This program has severe time and space limitations; therefore, the decision was made to acquire and implement NASTRAN. The prior experience with modeling the wing, plus the extensive experimental dtat available from the static tests, resulted in the decision to develop a new wing model to demonstrate the capabilities of NASTRAN.

SYMBOLS

Values are given in both SI and U.S. Customary Units. The measurements and calculations were made in U.S. Customary Units.

b	width of a skin panel, cm (in.)
b'	reduced width of a skin panel, cm (in.)
C	constant = b'/2b
E	Young's modulus, N/M^2 (psi)

$F_{c_{cr}}$	buckling stress of a skin panel, N/m^2 (psi)
F_{st}	allowable stress of a spar cap, N/m^2 (psi)
f	local stress in a skin panel, N/m^2 (psi)
f_{st}	actual stress in a spar cap, N/m^2 (psi)
P	total load carried by one-half of a skin panel, N (lb)
t	actual thickness of a skin panel, cm (in.)
t_e	effective thickness of a skin panel, cm (in.)
w	effective width of skin acting with a spar cap at failure, cm (in.)
x	distance from centerline of spar cap to point where local stress is measured, cm (in.)

NASTRAN MODELS

Two NASTRAN models were generated and analyzed. The first model, called the Demonstration Model, has a relatively coarse grid pattern and was used to gain experience with NASTRAN at a reasonable cost. It was not expected that the results obtained from this model would be satisfactory for comparison with the experimental data. The final model, called the Refined Model, is a much more accurate model of the wing. Some of the results of the analysis of the Refined Model are subsequently compared with the experimental data.

The wing structure is symmetrical with respect to the centerline of the airplane; therefore, only the left wing is modeled.

The Demonstration Model

The grid points for the primary wing structure were selected at the spar cap-rib cap intersections (fig. 2). Except for Spar 6, the spars are continuous from tip-to-tip, although there are changes in sweep angles at some of the ribs. Spar 6 only extends from the landing gear rib outboard. The ribs are continuous from the front to the rear spar and are parallel to the airplane centerline, except for the fuselage attach rib which does not extend through the wheel well. This rib is also not straight in order that the attachment fittings may be properly aligned with the fuselage fittings. Thus, the primary structure is defined by 126 grid points. The leading edge, which extends from the landing gear rib to the tip, is defined by four rows of grid points forward of Spar 1; and a simulated tip tank is defined by an additional ten grid points. Therefore, this model has a total of 160 grid points.

The skins from the centerline of the airplane to the wing tip extension rib are machine sculptured. The upper skin tapers, while the lower skin is of constant thickness. The leading edge and the skins on the wing extension are standard aluminum sheet. The NASTRAN element used to model the skins and the leading edge is the QDMEM1 isoparametric quadrilateral membrane. This element was chosen because it does not overestimate the stiffness as much as the other two quadrilateral membranes (ref. 2). There are no skin elements in the wheel well region on either surface; although on the actual wing, the upper wheel well cutout only extends outboard to the fuselage attach rib.

The spars are a combination of formed channels and built-up channels and I-sections, with most of the formed sections in the outboard wing and most of the built-up sections inboard. The spar webs are modeled with SHEAR elements and the spar caps with ROD elements. The cap areas include not only the actual cap areas, but also the areas of the lands in the sculptured skin and the effective area of the spar webs. The ribs are also modeled with SHEAR's for the webs and ROD's for the caps. The only other internal structure in this model, the vertical stiffeners on the spars, are modeled with ROD's.

Since loads were applied to the tip tank during the static test, a simulated tip tank is included in the model. A series of nodes along the centerline of the tank are connected together by very stiff BAR elements. These nodes are then connected to the outboard ends of the spars with a series of ROD elements.

All of the grid points, except those on the tip tank, are constrained against rotation. The only other constraints are at the root rib and at the fuselage attach rib. Due to the symmetry of both the structure and the loadings, all of the grid points at the centerline of the airplane are constrained in the spanwise direction. They are free, however, to translate in the other two coordinate directions. The fuselage fittings on the fuselage attach rib extend upward from the upper surface at Spars 2, 5, 7 and 8. Due to the complexity of these fittings and their matching fittings on the fuselage, no attempt was made to model them; so the constraints are applied at the corresponding upper surface grid points. The main fitting at Spar 5 is assumed to be constrained in the vertical and chordwise directions, while the others are constrained only in the vertical direction.

The Refined Model

All of the grid points in the Demonstration Model are included in the Refined Model. Chordwise rows of grid points were added between the ribs to form approximately square skin panels (fig. 3). Figure 4 shows the details of a typical spanwise section between two ribs. Additional grid points were also added in order to be able to model the diagonal redistribution stringers that transfer the loads from Spar 6 to Spars 5 and 7 just outboard of the wheel well cutouts. This resulted in a total of 538 grid points for the model.

The first version of the Refined Model had the same basic elements as the Demonstration Model: QDMEM1's for the skins, SHEAR's for the spar and rib webs and ROD's for the spar and rib caps and spar stiffners. However, problems developed with the QDMEM1 skin elements. Since all of the ribs outboard of the fuselage attach rib are parallel, the skin elements are very nearly trapezoids, and in the wing tip extension are very nearly parallelograms. This geometry apparently caused a near-singularity in the generation of the element stiffness and/or stress matrices, because the calculated stresses for some of the elements were obviously erroneous. It has been shown (refs. 2 and 3) that singularities do occur when a general gradrilateral approaches a more regular shape, such as a trapezoid or parallelogram. NSMO was contacted regarding the problem. They were able to duplicate our results on the IBM version of NASTRAN, but not on the CDC version, and found that the problem could be eliminated by rotating the node numbering sequence 90 degrees (ref. 4). Rather than reordering the nodes, it was decided to model all of the quadrilateral membranes with QDMEM2 elements, and no further problems have been encountered.

The most important new members included in the Refined Model are the splice plates and the stringers between the spars. In addition to the diagonal redistribution stringers, there are spanwise stringers between the spar caps throughout the inboard portion of the wing. To avoid adding more grid points, ROD elements were added in parallel with the spar cap elements to effectively add the stringer areas to the spar cap areas. Another problem associated with these stringers is due to the fact that their main function is to increase the buckling stresses of the skin panels, so they are not continuous across all of the ribs. This causes stress concentrations in the skins at these ribs that are difficult to reproduce in the finite element analysis. This effect is approximately accounted for by reducing the stringer areas near their ends. The splice plates at the wing root were handled in essentially the same way as the stringers; QDMEM2 elements were added in parallel with the appropriate skin elements. The addition of the redistribution stringers necessitated the use of some TRMEM elements in the upper and lower skins (fig. 3). It was also necessary to introduce dummy ROD elements to support the upper skin over the wheel well.

Another important consideration in the Refined Model are the access doors in the lower skin. These doors cover cutouts that are used during the assembly of the wing and later provide access to the fuel tanks and the control systems. To provide easy access and interchangeability, the doors are attached by means of screws and nut plates through medium tolerance holes. As a result, they are not fully effective, and a study of the strain gage data revealed that their effectiveness is different in tension and compression. The values selected for the final analyses were 35 percent effectiveness for tension and 72 percent for compression. These values were used to calculate the effective thickness of the skin elements affected.

The initial limit load analyses after the skin elements were changed to QDMEM2's produced acceptable results outboard of the landing gear rib, but not inboard. Both skins are extensively sculptured in the inboard region, plus the lower skin has several small cutouts. Therefore, an integration scheme was used

to redefine the effective skin thicknesses. This resulted in a marked improvement in the calculated deflections and stresses, but more work needs to be done to accurately model this complex region of the structure.

The constraints are the same for both the Demonstration and Refined Models. The tip tank models are also the same, although figure 3 shows a new, more accurate tip tank model that is being developed.

LOADS AND THE STATIC TEST

The primary purpose of the analysis reported here is to provide a comparison of the NASTRAN results with the static test results. Therefore the loads used with the NASTRAN data were derived from the static test loads.

Eight symmetric loading conditions were included in the static test program. These include fuel tank integrity tests and fail safe tests as well as strength tests. Three of these loading conditions were selected for the NASTRAN analysis: limit positive bending, ultimate positive bending and ultimate negative bending.

The test article was a complete airplane, with the loads applied to the wing and tip tank and reacted by the fuselage. Hydraulic actuators were used to apply the loads, through whiffle tree systems, to tension patches on the wing and straps riveted to the tip tanks. Figures 5 and 6 show the test set-up for positive and negative bending, respectively.

The tension patch loads were "beamed" to the grid points at the adjacent ribs. Grid points were located at the load points on the tip tank, so no transfer of load was required. The loads are identical for both the Demonstration and Refined Models.

Two hundred channels of strain gage and deflection transducer data were recorded for each test. Originally, there were 114 strain gages on the outer surface of the left wing and 9 gages on the spar caps in the wing. They were arranged in both spanwise and chordwise rows so that an excellent picture of the strain distribution was obtained. Several gages were destroyed in a local failure during an early test, but these gages were replaced by corresponding gages on the right wing. Of course, there were other gage failures prior to the destruction test, but there was still sufficient data for a good comparison with the ultimate positive bending NASTRAN analysis.

BUCKLING ANALYSIS

In the usual wing strength analysis, there are two primary criteria: there shall be no detrimental permanent set at limit loads, and the structure shall not fail at ultimate loads. The limit load strength analysis is generally

limited to showing that any skin panels that buckle do so elastically, rather than plastically. For the ultimate load analysis, the major concern is the calculation of the allowable bending moments at the critical cross sections, so they can be compared with the actual bending moments. Since the compression skins are usually buckled at failure, it is customary to replace the buckled skin with effective widths of skin acting with the compression stringers. The effective width is given by the equation (refs. 5 and 6):

$$w = 1.7t\sqrt{\frac{E}{F_{st}}} \tag{1}$$

The purpose of this analysis, however, was not to predict the failing loads; but to compare analytical and experimental deflections and stresses at specified loads. Therefore, a method was needed for calculating the effective skin at stresses between the skin buckling stress and the spar cap buckling stress. Figure 7 shows the assumed post-buckling stress distribution. The stress adjacent to the spar cap is a cosine distribution and is given by

$$f = \frac{f_{st} + F_{c_{cr}}}{2} + \frac{f_{st} - F_{c_{cr}}}{2} \cos \frac{2\pi x}{b'} \quad \left(0 \le x \le \frac{b'}{2}\right) \tag{2}$$

while the stress in the center of the panel is

$$f = F_{c_{cr}} \quad \left(\frac{b'}{2} \le x \le \frac{b}{2}\right) \tag{3}$$

The total load represented by this stress distribution is the area under the curve times the thickness, or

$$P = \left[\frac{b}{2} F_{c_{cr}} + \frac{b'}{2} \left(\frac{f_{st} - F_{c_{cr}}}{2}\right)\right] t \tag{4}$$

The distance b'/2 is determined by requiring that in the limiting case of $f_{st} = F_{st}$, the total load be equal to

$$P = \frac{w}{2} F_{st}\, t \tag{5}$$

Equating equations (4) and (5) gives

$$\frac{b'}{2} = \frac{w\,F_{st} - b\,F_{c_{cr}}}{F_{st} - F_{c_{cr}}} \tag{6}$$

For a finite element analysis with membrane elements for the skins, it is more convenient to use an effective thickness, instead of an effective width. This thickness can be defined by requiring the total load at the specified stringer stress to be

$$P = \frac{b}{2}\,f_{st}\,t_e \tag{7}$$

Then by equating equations (4) and (7)

$$\frac{t_e}{t} = C + (1 - C)\,\frac{F_{c_{cr}}}{f_{st}} \tag{8}$$

Note that since $t_e/t = 1$ when $f_{st} = F_{c_{cr}}$ and $b'/2$ was defined to give the standard effective width at failure, equation (8) provides an approximate method of interpolating between the limiting cases of skin buckling and stringer failure. At stresses below the buckling stress, the skin is assumed to be fully effective.

There were a few buckled skin panels at limit positive bending, but a buckling analysis was not performed for this loading condition. In fact, the primary reason for including limit positive bending was to obtain good analytical-experimental correlation prior to incorporating the buckling analysis. There was extensive buckling for the other two loading conditions, however; and reasonable correlation could not be achieved without including this nonlinear effect. Because of the nonlinearities, an iterative procedure was required. The stresses were first calculated, and punched, assuming that the skins were fully effective. A special program was then used to determine which panels were buckled and to calculate, and punch, effective skin thicknesses for these panels. This procedure was repeated, usually 4 or 5 iterations were necessary, until convergency was obtained.

There are two parameters in equations (1), (6) and (8) that must be specified: the spar cap allowable, F_{st}, and the skin buckling stress $F_{c_{cr}}$. In all cases the spar cap allowable was taken as the crippling stress, since the spar caps are stabilized against column buckling by the skin and spar webs. The skin buckling stresses were more of a problem. After considerable

experimentation, the panels inboard of the landing gear rib were assumed to be fully clamped, while those in the outboard wing were assumed to have edge conditions intermediate between clamped and simply supported.

SEMIMONOCOQUE BEAM ANALYSIS

The NASTRAN analysis was supplemented by a semimonocoque beam analysis for the ultimate positive bending condition. The analysis was performed using a program, SEMOBEAM, based on the displacement method (ref. 7). The spanwise stations at which the spar cap stresses were calculated corresponded to the NASTRAN grid point locations, except at the fuselage attach rib. Here, a dummy rib, parallel to the other ribs, was used.

The spar cap areas and web thicknesses used in the NASTRAN analysis are the average values in the bay between grid point lines. For the semimonocoque beam analysis these values were assumed to be those at the inboard end of the bay, i.e., at the inboard station. Since both the spar cap areas and the thicknesses generally increase from tip to root, this assumption will give slightly conservative results.

Several other modifications of the NASTRAN model were required for the SEMOBEAM model. These include:

1. Adding the axial load carrying capability of the skins to the spar cap areas. Since the thickness of any buckled panels had already been reduced in the NASTRAN model, all skins were assumed to be fully effective.

2. Adding dummy web elements in the wheel well region. Since the semimonocoque beam analysis used is valid only for beams with closed cells, the upper and lower skins and the web in Spar 6 were assumed to have a thickness of 0.001 inch.

3. Allocating the areas of the diagonal redistribution members to the adjacant spar caps.

4. Reducing the spar cap areas of Spar 6 at, and outboard of, the wheel well cutout to approximately account for shear lag effects. The areas of the leading edge stringers were also modified at, and outboard of, their inboard ends for the same reason.

The last three of the modifications described above are all in the root region of the wing where the results of the semimonocoque beam analysis are not expected to be accurate.

COMPARISON OF RESULTS

The correlation between the analytical and experimental results is good for all three loading conditions, with the best correlation being for the limit positive bending condition. The correlation is generally better outboard of the landing gear rib for all three loading conditions.

Sample plots from the ultimate positive bending analysis are shown in figures 8 to 11. Figure 8 shows the deflection of the front spar versus wing station. Although there were deflection scales on the inboard wing, they were not read above limit load; so that the only data shown is from the deflection transducers at the centerline and near the tips. The calculated deflections at the wing tips are somewhat less than the experimental values, as would be expected, because the finite element model is stiffer than the actual structure.

Figure 9 shows the strains in the upper skin approximately midway between Spars 4 and 5, where Spar 5 is the spar just forward of the wheel well. Strains are plotted, instead of stresses, because all of the experimental data is from axial strain gages, so that the Poisson's ratio effects are unknown. Thus, it is much more accurate to convert the calculated stresses to strains. The correlation for gages 90, 25, 140 and 143 is very good. Gages 135 and 147 are both on buckled panels, so they are not expected to show good correlation. Gage 22 shows an example of the stress concentration in the skin due to a stringer discontinuity across the landing gear rib.

Figures 10 and 11 show the upper and lower spar cap strains in Spars 3 and 5, respectively. In addition to the NASTRAN and experimental strains, the results of the SEMOBEAM analysis are shown in these figures. The NASTRAN/experimental correlation is good, with the calculated strains being generally conservative. Note that where there are two experimental values at a wing station, they represent back-to-back gages. The agreement between the NASTRAN and SEMOBEAM results is good outboard of the landing gear rib, but gets poorer as the root is approached.

CONCLUSIONS

The objective of the investigation is essentially accomplished. The Refined Model is considered to be an accurate finite element model of the GLC Model 35/36 wing; however, additional improvements are being made.

The complexity of this wing, particularly the sculptured skin and the access doors, created severe modeling problems. The availability of excellent strain gage data helped solve these problems and provided valuable modeling experience for future applications. The experimental data was also used as a guide in determining the edge conditions of the skin panels for the buckling analysis.

The only major NASTRAN related problem was the failure of the QDMEM1 element. Both the stresses and the deflections would probably have been more accurately calculated if this element could have been used for the skins.

It was not expected that the agreement between the finite element and semimonocoque beam analyses would be as good as they are in the outboard wing. These results indicate the semimonocoque beam analysis, coupled with the buckling analysis, would be adequate for design. This would allow a more detailed finite element model of the inboard wing.

REFERENCES

1. Abla, M.H.: Structural Analysis of Substructures Using Component Direct Stiffness Synthesis. M.S. Thesis, Wichita State University, February 1969.

2. Adelman, H.M.; Walz, J.E.; and Rogers, J.L.: An Isoparametric Quadrilateral Membrane Element for NASTRAN. NASTRAN: Users' Experiences, NASA TM X-2637, 1972, pp. 315 - 336.

3. Radovanov, M.N.: Quadrilateral Plate in Plane Stress. M.S. Thesis, Wichita State University, May 1970.

4. NASTRAN NEWSLETTER, Number 10 - August 22, 1975.

5. Bruhn, E.F.: Analysis and Design of Flight Vehicle Structures. Tri-State Offset, 1973 (pp. C7.10-11).

6. Peery, D.J.: Aircraft Structures, McGraw-Hill, 1950 (pp. 371 - 375).

7. Cook, E.L.: Semimonocoque Beam Analysis - A Displacement Formulation. SAE Paper 740385, April 1974.

FIGURE 1. LEARJET MODEL 35/36 AIRCRAFT

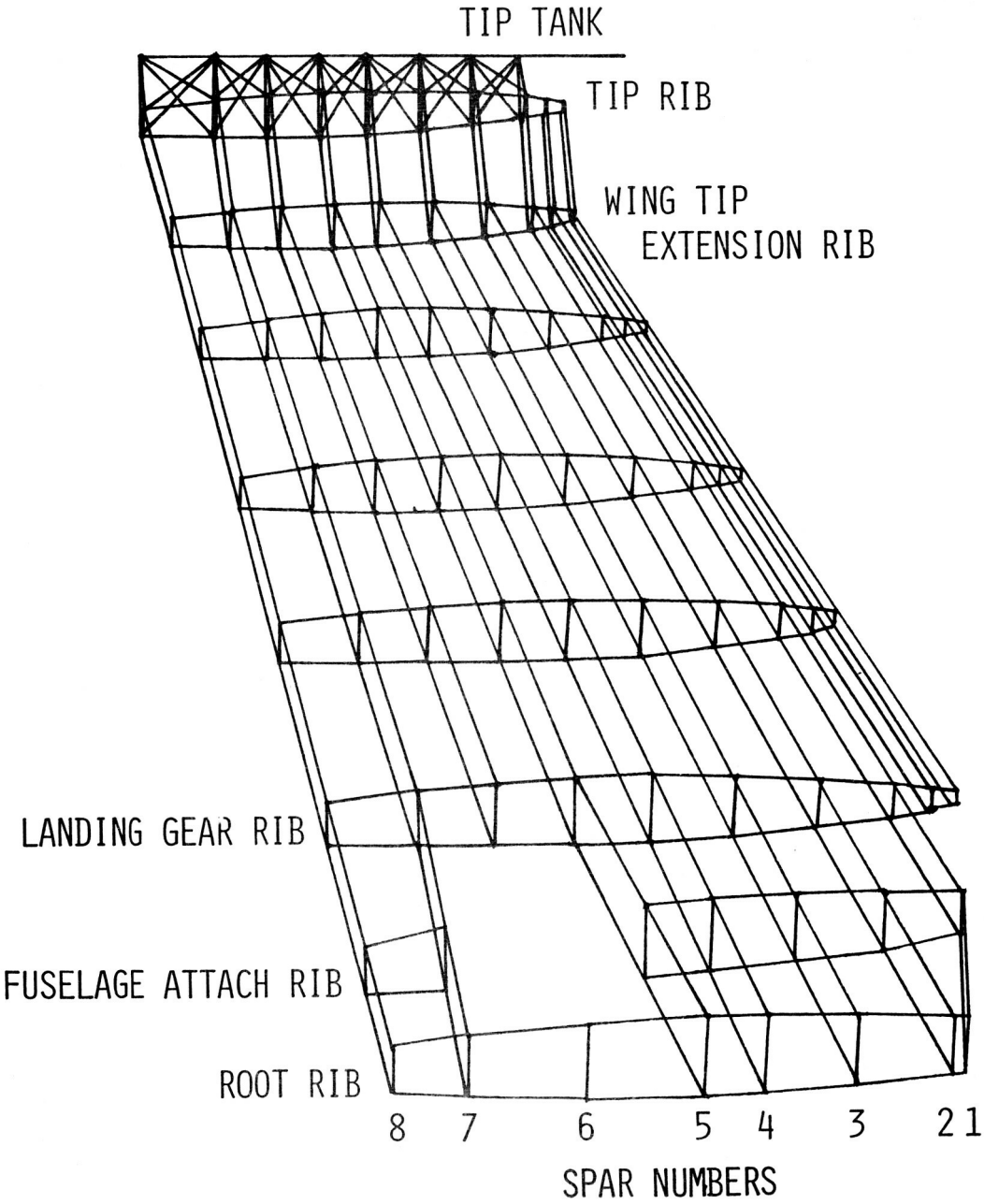

FIGURE 2. DEMONSTRATION MODEL

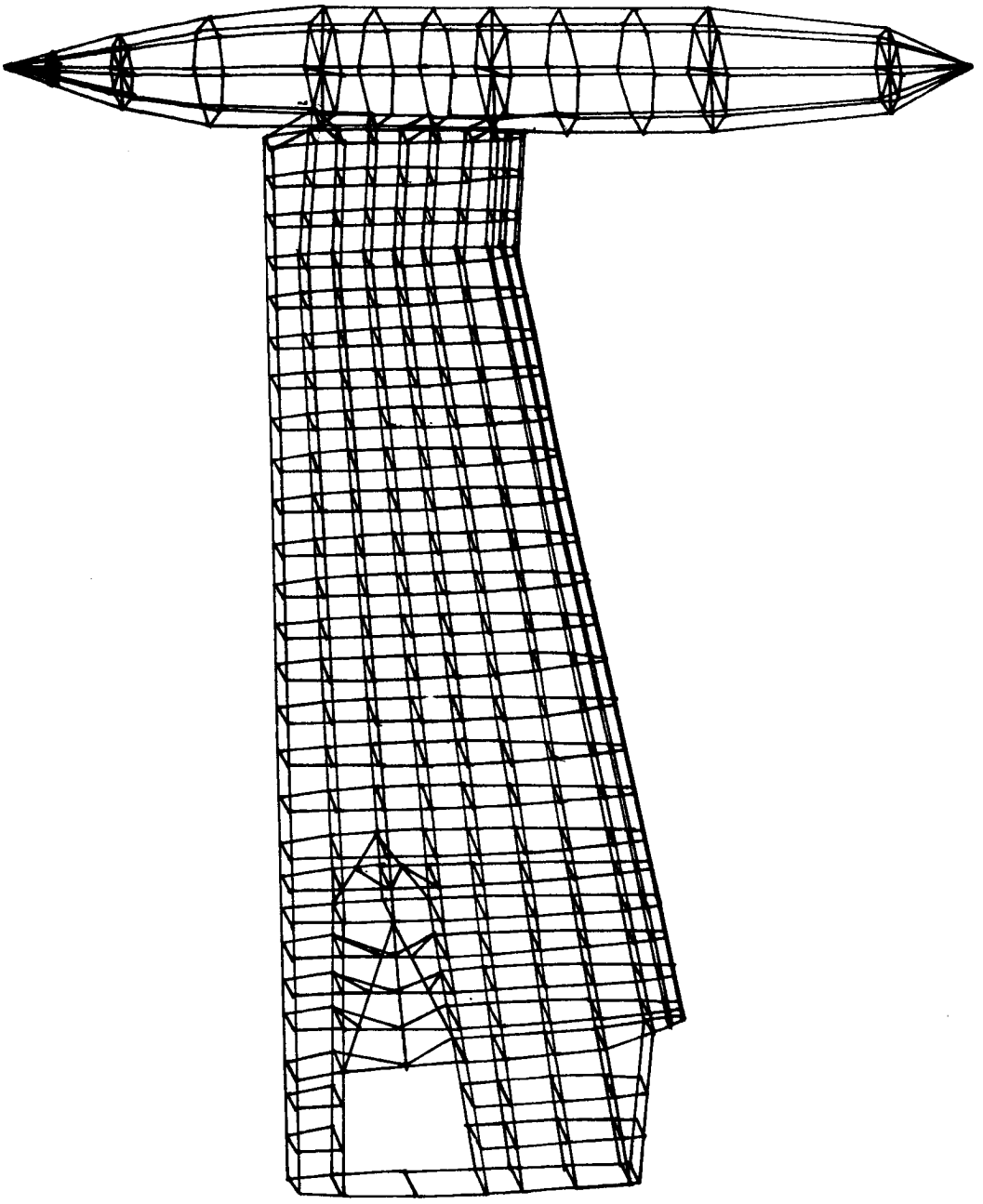

FIGURE 3. REFINED MODEL

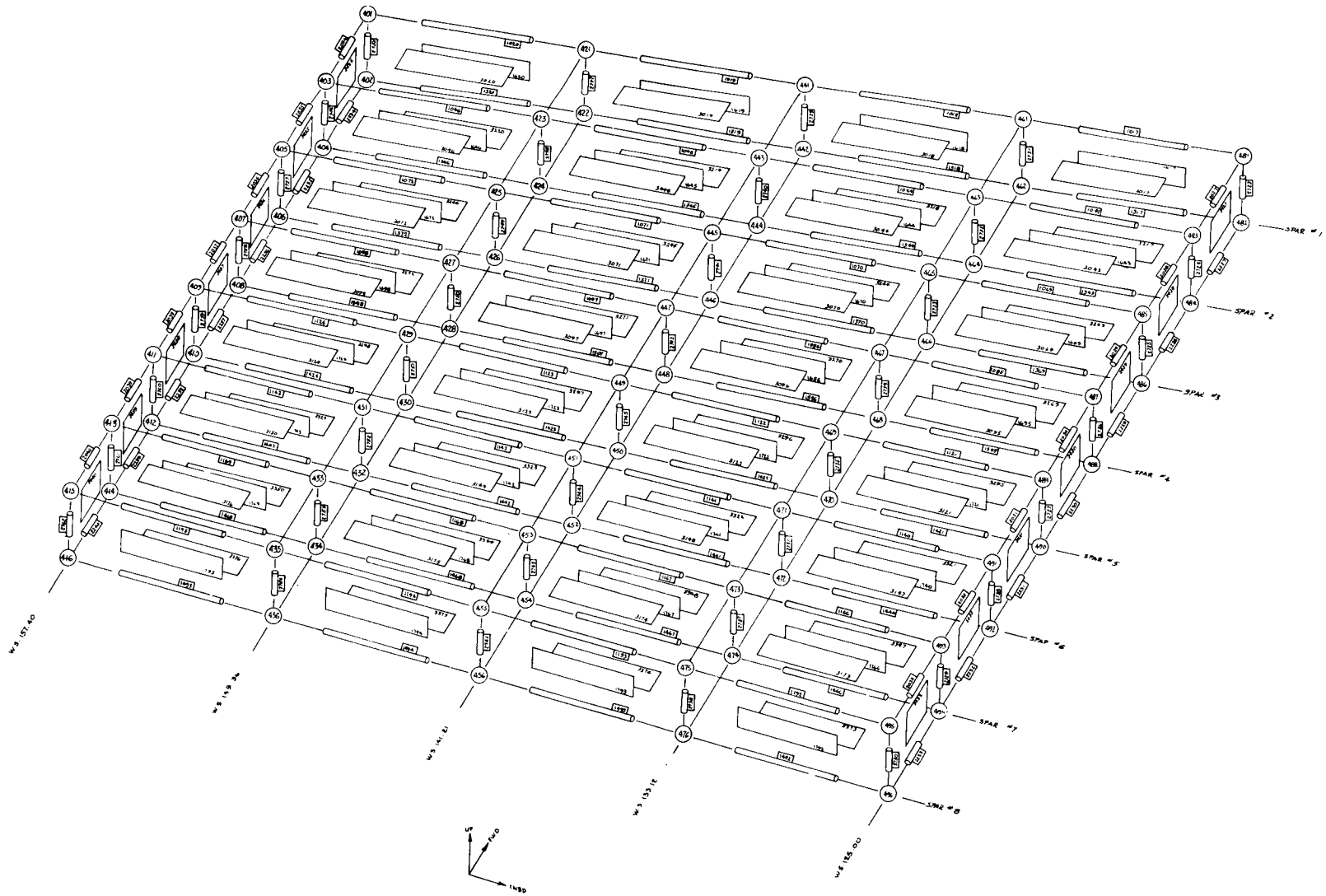

FIGURE 4. DETAILS OF THE REFINED MODEL

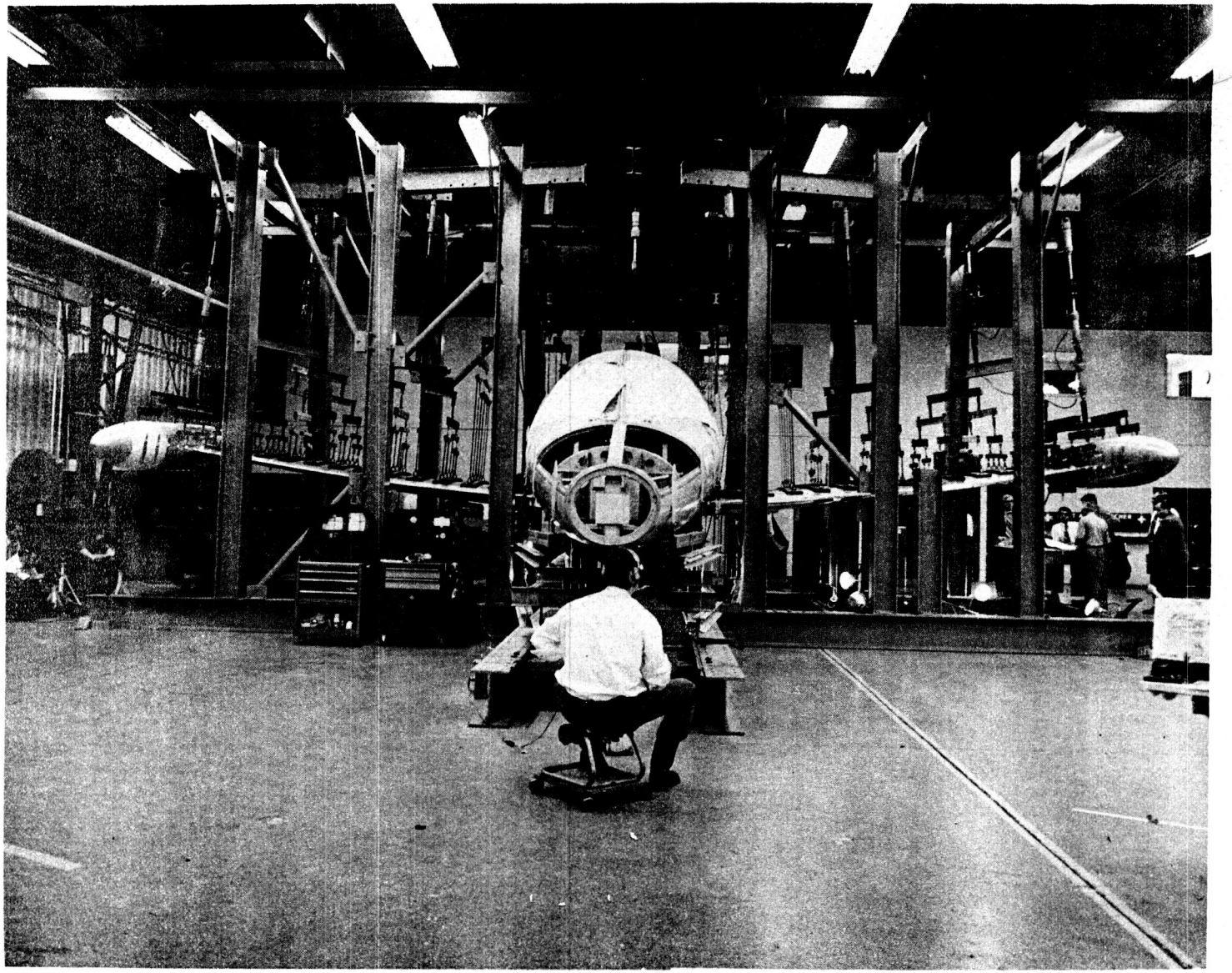

FIGURE 5. POSITIVE BENDING

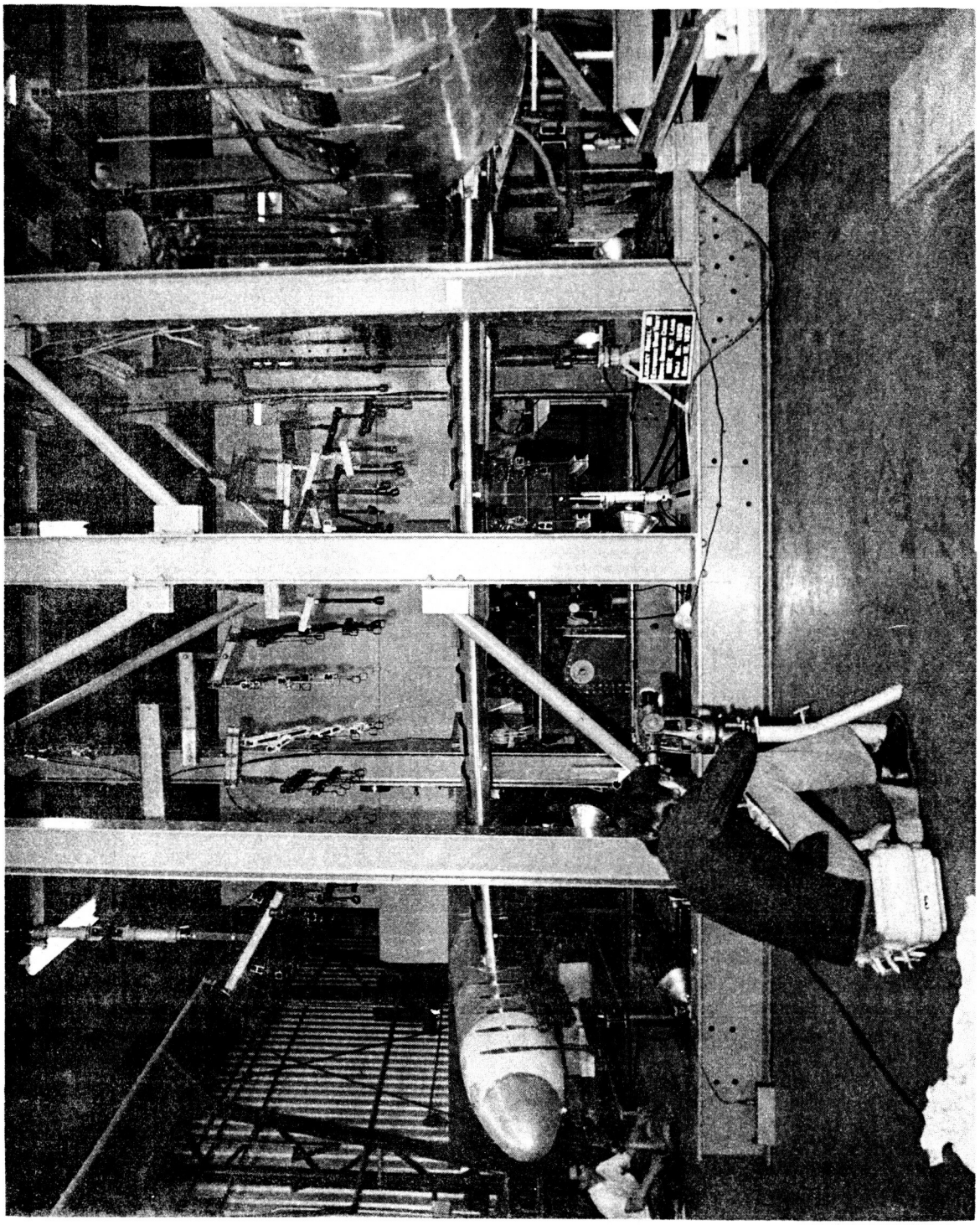

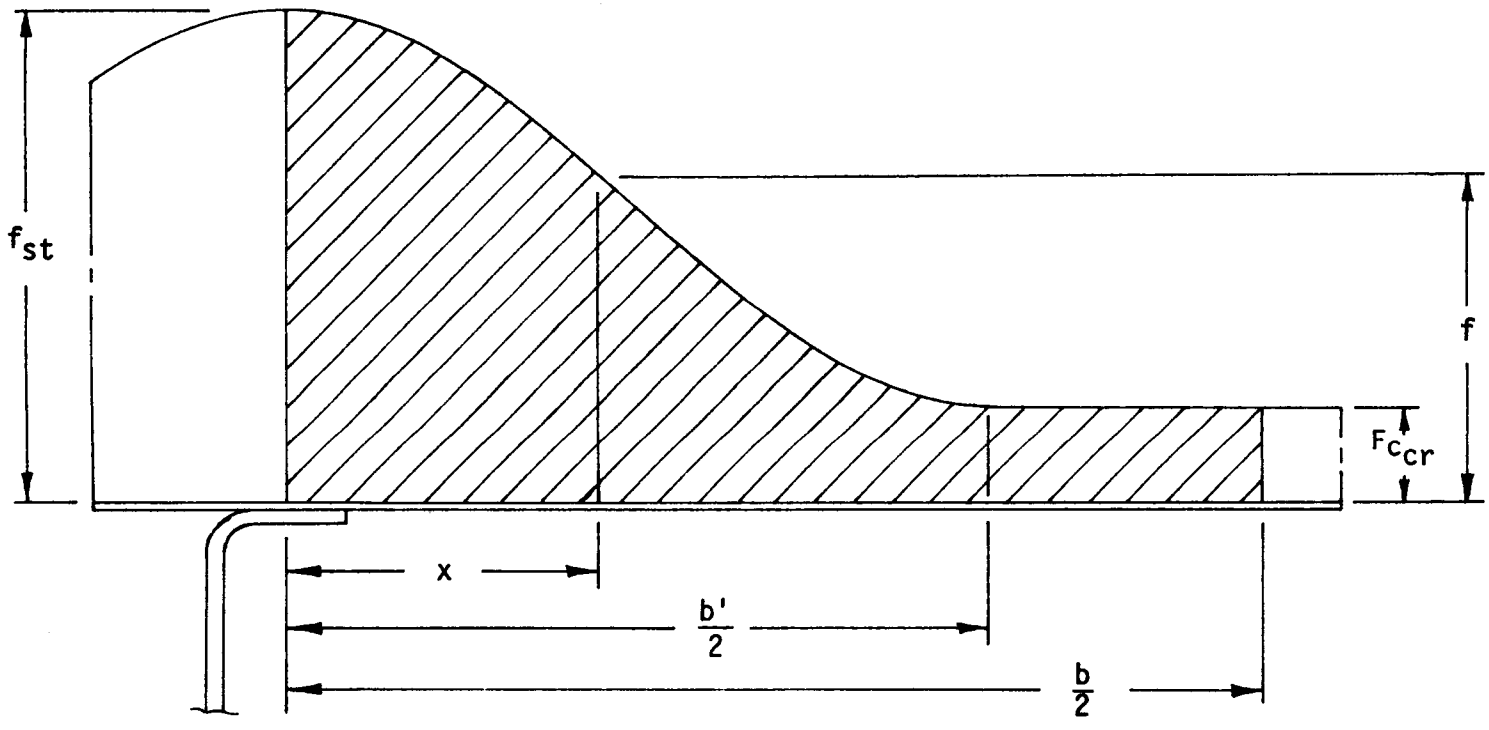

FIGURE 7. BUCKLED SKIN STRESS DISTRIBUTION

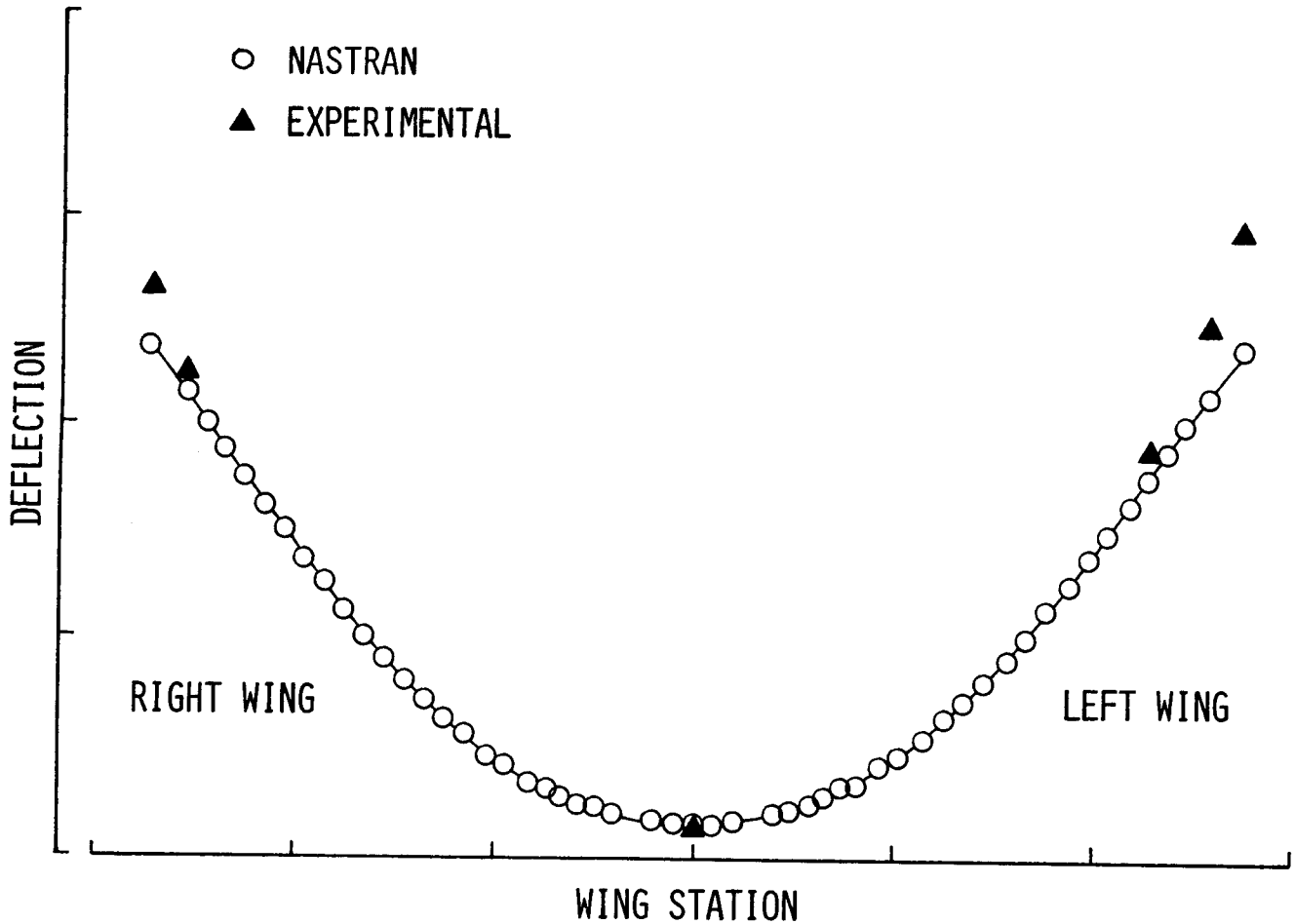

FIGURE 8. DEFLECTION OF SPAR 1 AT ULTIMATE POSITIVE BENDING

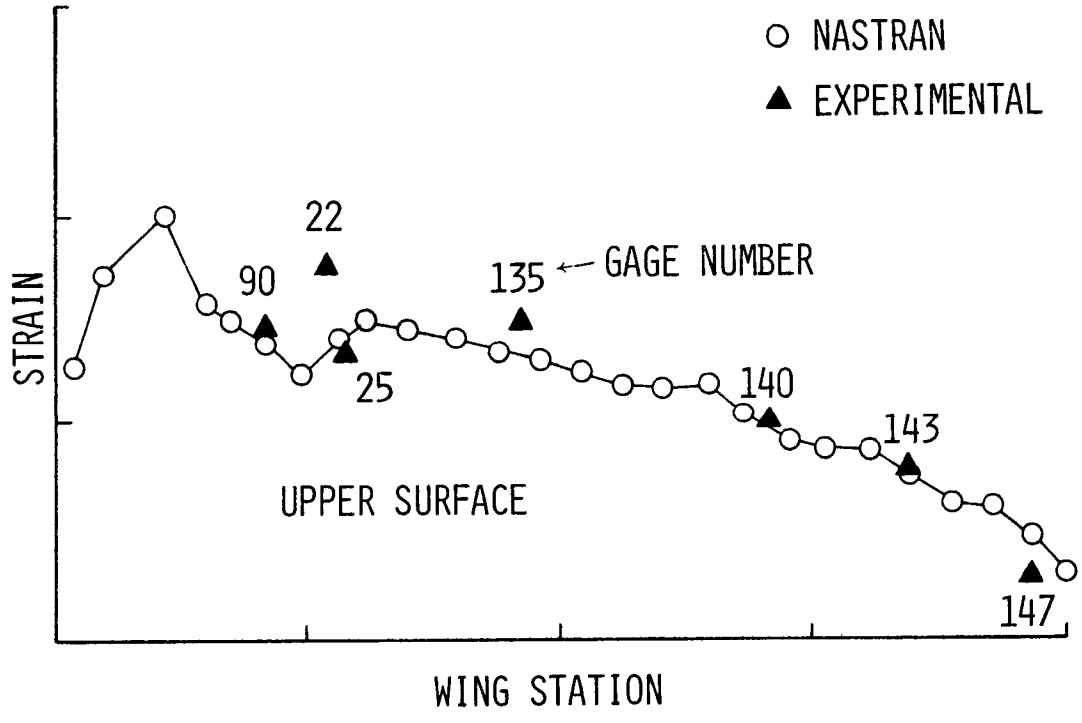

FIGURE 9. STRAINS BETWEEN SPARS 4 & 5 AT ULTIMATE POSITIVE BENDING

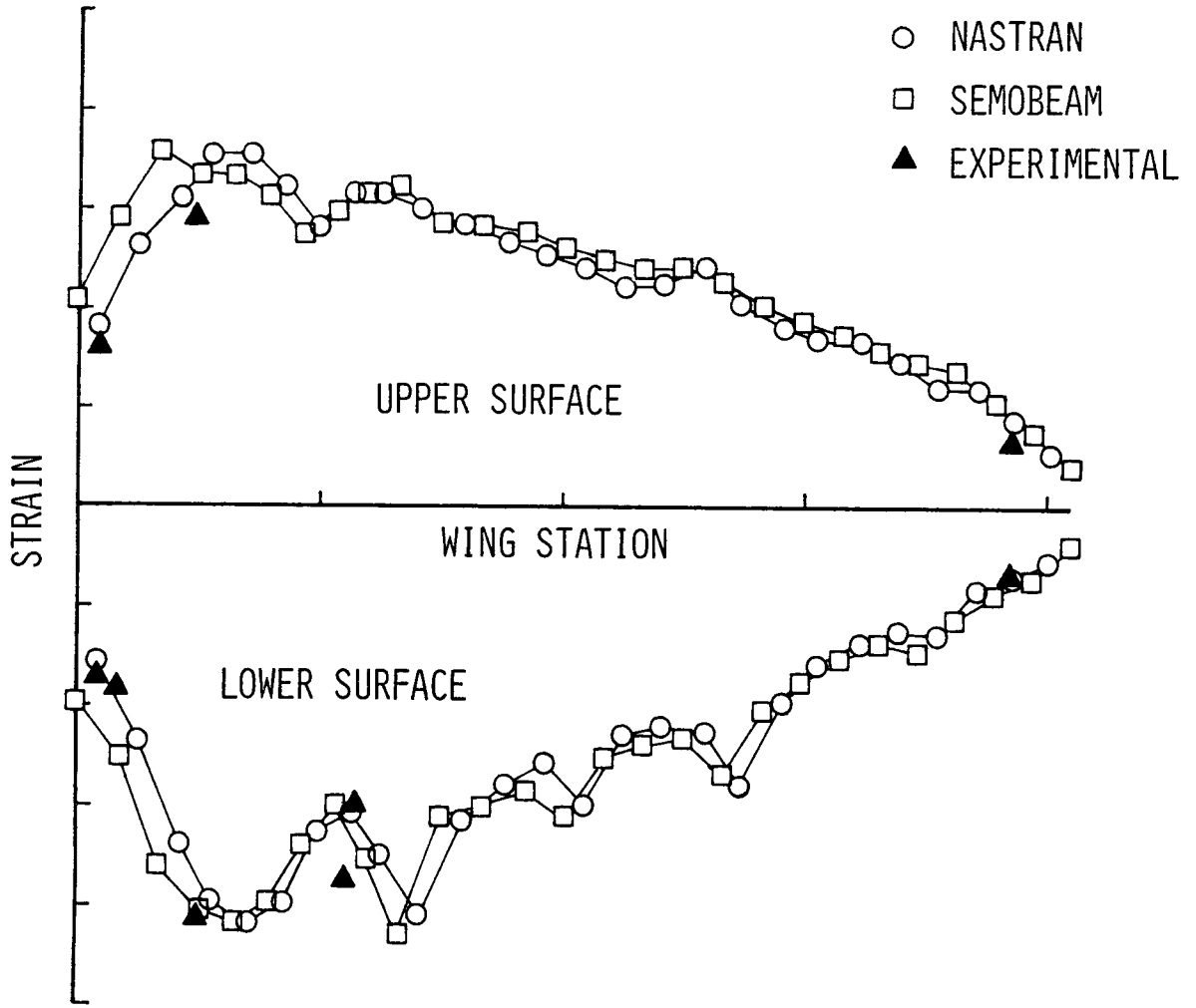

FIGURE 10. SPAR CAP STRAINS IN SPAR 3 AT ULTIMATE POSITIVE BENDING

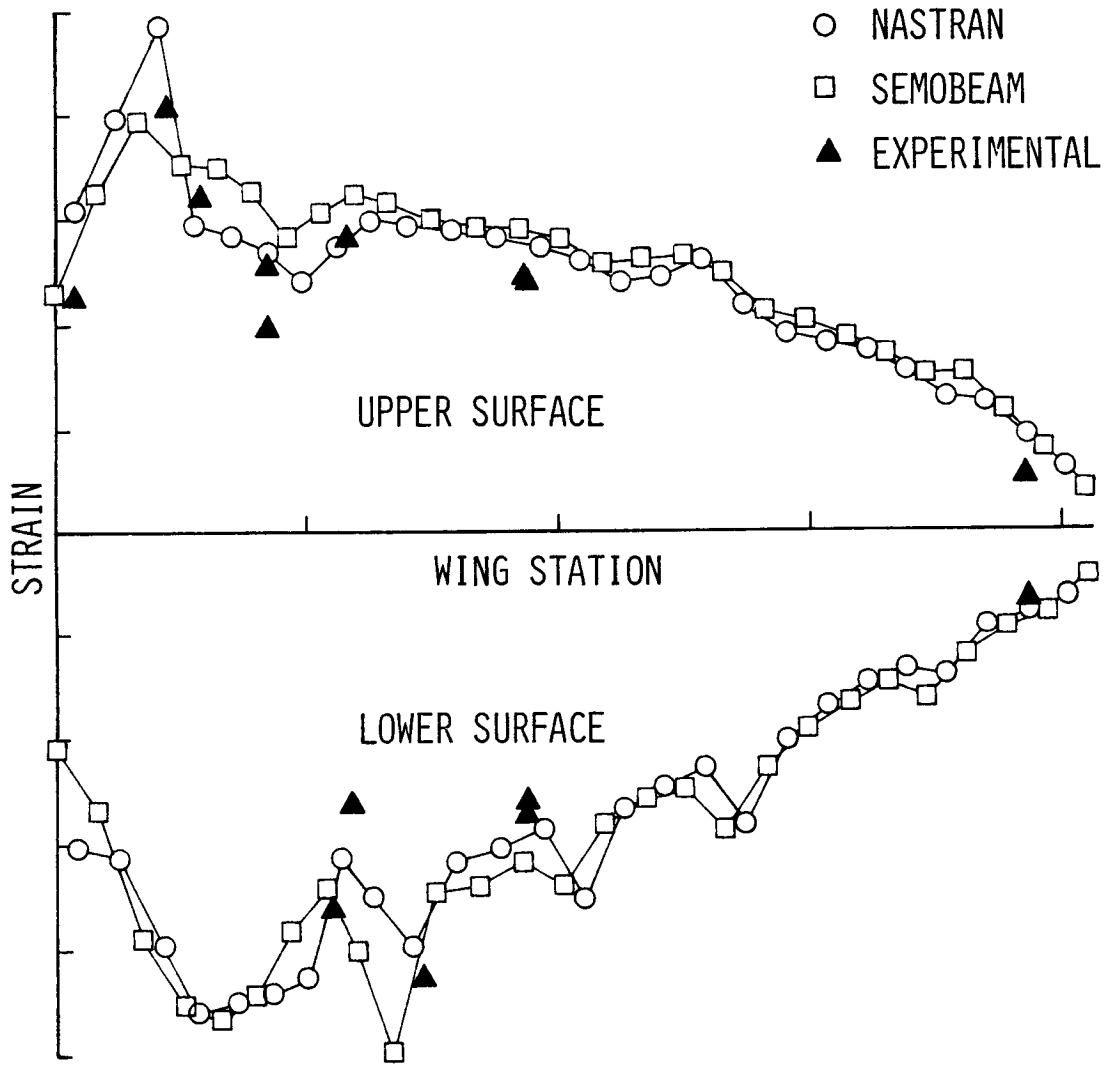

FIGURE 11. SPAR CAP STRAINS IN SPAR 5 AT ULTIMATE POSITIVE BENDING

THERMAL AND STRUCTURAL ANALYSIS OF HELICOPTER TRANSMISSION HOUSINGS USING NASTRAN*

R. W. Howells and J. J. Sciarra
Boeing Vertol Company

G. Shek Ng
USAAMRDL, Eustis Directorate

SUMMARY

The application of NASTRAN to improve the design of helicopter transmission housings is described. A finite element model of the complete forward rotor transmission housing for the Boeing Vertol CH-47C helicopter has been used to study thermal distortion and stress, stress and deflection due to static and dynamic loads, load paths, and design optimization by the control of structural energy distribution. The analytical results are being correlated with test data and used to reduce weight and to improve strength, service life, failsafety, and reliability. The techniques presented, although applied herein to helicopter transmissions, are sufficiently general to be applicable to any power transmission system.

INTRODUCTION

Improved power-to-weight ratio capability, extended service life, improved reliability/maintainability, better survivability/vulnerability, reduced vibration/noise, and lower cost are among the continually escalating design requirements imposed upon helicopter transmissions. To meet this array of goals substantial research has been devoted to investigating and improving individual transmission components such as gears, bearings, and lubrication systems. In contrast, housings have not received the attention necessary to fully define and optimize their functional requirements and a gap in transmission technology has existed in this area.

*This work has been performed under U. S. Army contracts DAAJ02-75-C-0053 and DAAJ02-74-C-0040, U. S. Army Air Mobility Research and Development Laboratory, Eustis Directorate, Fort Eustis, Virginia.

The functions of a helicopter transmission housing are to transmit rotor loads to the airframe, to support the gears and bearings, and to contain the lubricant. These housings are generally designed to have high strength margins and hence seldom exhibit gross structural failures. However, since the housing provides structural support to the internal components, its characteristics significantly affect overall transmission performance and life in terms of internal bearing capacity, gear capacity, fretting, misalignments, and load maldistributions. Housing deflections under load have been identified as a cause of accelerated wear and surface deterioration of gears, bearings, splines, retention hardware, and interface connections and joints. Reduction in the magnitude of these housing deflections by structural optimization and the use of advanced materials will prolong the life and improve the performance of transmission components.

During the past few years a variety of computer studies have been conducted at Boeing Vertol to evaluate the feasibility of applying finite element methods to the design of transmission systems. NASTRAN has been found to be extremely versatile and has been used to study many facets of transmission design and operation. The thrust of the current effort at Boeing Vertol is concentrated in two areas - dynamic analysis aimed at vibration/noise reduction, which was covered in reference 1, and thermal/static structural analyses of the housing which are discussed herein.

FINITE ELEMENT MODEL

Housing Model

The finite element model of the transmission housing used for this work is shown in figure 1. The geometric grid points for the model were defined from design drawings and by cross-checking on an actual housing. CQUAD2 (Quadrilateral) and CTRIA2 (Triangular) homogeneous plate (membrane and bending) elements were used to connect the grid points and build the NASTRAN structural model. A Boeing Vertol preprocessor program (SAIL II - Structural Analyses Input Language) for the automatic generation of grid point coordinates and structural element connections was used. This preprocessor allows the user to take advantage of any pattern which occurs in the data by providing techniques for describing algorithms to generate blocks of data. The extensive computer generated plotting capability of NASTRAN was used to debug the structural model.

For ease of identification the housing was subdivided into several regions and the grid points in each region were labeled with a specific, but arbitrary, series of numbers. Although these grid point numbers act only as labels, they effect the bandwidth of the stiffness and mass matrices. In order to minimize the matrix bandwidth for most efficient running of NASTRAN, the BANDIT computer program (reference 2) was used to automatically renumber and assign internal sequence numbers to the grid points. The output from BANDIT is a set of SEQGP cards which is then included in the NASTRAN bulk data deck and which relates the original external grid numbers to the new internal numbers. A summary of the important model parameters is provided in figure 2. A more thorough description of the model was presented in reference 1.

Internal Components

For the dynamic analysis of the housing (reference 1) the internal components were included only in the sense that the dynamic forces generated by them were applied to excite the housing. The additional structural constraints imposed upon the housing when subjected to static load conditions must also be considered. Since only the gross effect on the housing was desired, these components were represented by simple beam models.

For the thermal analysis the internal components were not included. The bearing outer races, which are the housing/internal component interface, are press-fit into the housing. Elevated temperatures cause the magnesium case to expand away from the steel outer races and may result in a "floating" fit at operating temperatures. This has happened during testing and it was necessary to key the outer races to prevent rotation permitted by increased clearances caused by thermal expansion. This condition, plus bearing internal tolerances, precludes the transmittal into the housing of thermally induced radially outward loads. Furthermore, the bearing races cannot impose radial restraint upon the housing expansion. Thus, no representation of the internal components in the radial direction is necessary. Since axial thermal growth of the internal components is absorbed by reduction of gear backlash, no axial loads are induced unless the temperature exceeds that necessary to reduce the backlash to zero. In such a situation the housing loads would be of little interest since the gears would distress and fail.

For the static stress analysis, only the resistance of the outer races to radially inward forces on the housing is significant. The races do not resist outward forces on the housing. NASTRAN has no capability for a beam which acts only in compression. Thus, a beam model of a bearing race will also act to impose unwanted restraint on the housing directed radially inward. This could be circumvented by first analyzing only the housing model and thereby

defining the housing/bearing interfaces with inward deflections. A beam model could then be inserted at these points to resist the radially inward forces and the analysis could be re-run.

TRANSMISSION HOUSING DESIGN REQUIREMENTS

To provide an understanding of the configuration, functional requirements, and design criteria for a helicopter transmission, a brief description is included. A contemporary helicopter main transmission housing is generally composed of three main parts with essentially separate functions: the upper cover, ring gear and case. This configuration is demonstrated by the CH-47C forward rotor transmission in figure 1.

The upper cover supports the rotor shaft and provides lugs for mounting the transmission to the airframe. The rotor system loads are transmitted through the upper cover into the airframe. The upper cover design criteria include ultimate, fatigue, and crash load conditions. The case contains and supports the main bevel gears and may also include a tail rotor or sync shaft drive, lube pump, or accessory drives. The transmission may also have a separate sump for containment of the lubricant, as does the CH-47C, or it may use an integrally closed lower portion of the case for this purpose. The gear case design criteria include strength and stiffness for gear mounting and fatigue loads in certain areas. The stationary ring gear, which connects the upper cover and case, contains the planetary gear system. The ring gear must provide adequate strength to react the planetary gear loads and support the case and must also provide sufficient stiffness to maintain planet/ring gear tooth alignment. The entire housing also performs the functions of sealing in the lubricant, providing passages for lubricant delivery, protecting critical transmission components and dissipating heat. Figure 3 shows the transmission case in detail since much of the work herein is concentrated upon analysis of the case.

A critical requirement of a helicopter transmission is proper alignment of each gear-mesh and bearing, which requires dimensional stability of the housing at bearing mounting locations. Predicted improvement in load capacity due to advances in gear and bearing technology may be offset in practice by poor load distribution resulting from misalignment caused by the deflection of mounting surfaces within the housing.

Analytical evaluation of the load capacity of gears involves assumptions regarding the nature of the tooth contact for the specific gear mountings under load. A uniform stress distribution across the tooth and rigid mounting are typically assumed. Unless

these assumptions are relatively accurate, actual stresses may vary considerably from the calculated values (figure 4) resulting in a service life reduction. The detrimental effect of misalignment on gear teeth has been documented by the American Gear Manufacturers Association (reference 3). Gear tooth bending and surface contact stresses are proportional to factors which evaluate the effects of non-uniform load distribution. These load distribution factors are in turn dependent upon items including gear mesh misalignment due to housing distortion caused by loads and thermal variations. Cases of gear failure can be attributed to uneven load distribution caused by misalignment, which can result in tooth pitting and scuffing. Gear mesh misalignment is also important from the aspect of vibration/noise generation (figure 5).

Present bearing life equations also assume that the bearing is rigidly supported, operates under no misalignment, and operates under a constant and uniform load. In helicopter applications, both the above assumptions are not true and therefore calculated lives are not precise. Experience to date has been associated with reduced bearing lives due to indeterminable system stiffness and early bearing failures have resulted from shaft misalignment (edge loading) and non-uniform housing support (local hard spots).

Although present methods of transmission analysis include complex computer programs, the capability to evaluate the effect on life of structural shape and flexibility is very limited. Since the full benefits of advancements achieved in component technology cannot be realized until the housing is optimized, analytical methods must be developed to permit evaluation of design parameters, allow trade-studies, and provide guidance to designers. Special consideration must be given to the uniform rigid support of critical components, since reduced shaft and housing deflection will result in better performance and life of gears, bearings, and other components.

To continue to improve transmission analysis capability and to design for improved performance, a detailed understanding of the structural and thermal aspects of the transmission housing must be developed. Because of the many functions performed by a transmission housing and its complex geometry, analysis is difficult and previously the designer had little guidance for selection of the design with best structural efficiency. The objective of the work being conducted at Boeing Vertol is to develop and demonstrate a comprehensive finite element technique with the capability for analyzing and designing transmission housings. NASTRAN fulfills this need by providing a multipurpose standardized source for static, thermal, and dynamic analysis as well as possessing the capability and flexibility for analyzing conventional cast metal housings, advanced composites, or fabricated structures. The work encompasses the study of thermal distortion and stress, stress and deflection due to static and dynamic loads, load path definition, dynamic response, and the

control of structural energy distribution. The results are being used to optimize strength and weight, and to assess operational housing life, failsafety, and reliability. The investigation of the housing structural characteristics has been categorized under two broad headings - thermal analyses and stress analyses. Each of these is discussed below.

THERMAL ANALYSES

When two bevel gears are properly mounted, their cone centers are coincident (at room temperature). The gears, shafts, and bearings are made of steel, but the housing and bearing cartridges are generally made of a lighter material such as magnesium. Due to the different thermal coefficients and the varying temperatures existing within the transmission, differential thermal expansion causes the relative positions of mating bevel gears to change. The cone centers therefore may no longer be coincident at operating temperature and the contact pattern and stress distribution across the gear teeth will change. This is one example of the importance of temperature effects in regard to transmission design. Figure 6 indicates the overall scheme of the thermal analysis which will enable the design team to define the thermally induced distortions and stresses in a transmission housing.

Uniform Temperature Study

As part of a thermal investigation, uniform temperature distributions were applied analytically to the housing model to represent current operating (71°C), projected operating (177°C), and loss-of-lubricant emergency operating (371°C), temperatures. The thermally induced deformations and growth are indicated in the computer generated plots of figure 7. For validation of the NASTRAN thermal model, the housing was experimentally heated to several temperatures in the range of 71-204°C, and selected dimensions of the housing were measured before and after heating. Figure 8 shows the housing in the oven and a typical measuring instrument used. This dimensional data at normal and elevated temperatures experimentally determined the thermal distortion and growth of the transmission case.

The experimental data obtained is plotted in figure 9 as the change in linear dimensions versus temperature. Also shown in the figure are the theoretical changes in the dimensions predicted both by the NASTRAN thermal analysis and by a simple linear thermal expansion calculation. The agreement of the data and both analyses

confirms the validity of the model and provides confidence in the model for predicting deformations of the housing.

Thermal Mapping Study

A complete thermal map of an operating CH-47C forward rotor transmission at various torque loads and inlet oil temperatures was determined in a previous experimental program conducted by Boeing Vertol (reference 4). This program provided considerable insight into the thermodynamics of an operating transmission. Figure 10 is a cut-away diagram of the specimen transmission showing typical temperature measurements. Measurements between selected points on the transmission housing were made at room temperature and also at various operating remperatures. The results indicated that significant thermal growth had occurred.

To further investigate the effects of temperature upon a transmission housing, thermal map data similar to figure 10 for oil-out temperatures of 85°C, 141°C, and 204°C at 100% torque were applied to the housing model, and NASTRAN Rigid Format 1 static analysis was used to calculate the thermal distortions and stresses. For each case clearances, dimensional stability of critical housing points, and misalignment effects were evaluated.

The computer generated plot in figure 11 shows the regions of the housing where it interfaces with the bearings. The vectors plotted indicate the displacements at each grid point due to the applied temperature distribution from reference 4 for 85°C oil-out temperature. First consider the pinion shaft. By evaluating the distortion of the bearing interface at each end of the shaft individually and then evaluating the relative distortion between the shaft ends, the thermally induced misalignment of the pinion shaft was calculated. By comparing the relative misalignment between the pinion and gear shafts, the overall effect of temperature upon the gear mesh alignment was assessed.

A NASTRAN post-processor computer program was written which uses the grid point displacement and geometry data to calculate these induced misalignments. This program indicates that the induced slopes of the pinion and bevel/sun shaft are .0003 and .0004, respectively. Also, the displacements at the pinion and bevel gear pitch diameter are .015cm and .018cm, respectively. These displacements are shown schematically in figure 12.

At the 204°C condition, the pinion and sun/bevel gear shaft slopes are .0007 and .0009, respectively; the displacements at the pitch diameter are .033cm and .038cm, respectively. Depending upon the type of shaft support bearings, shaft slopes of these magnitudes can be detrimental to bearing performance. Similarly, the displacements at the gear mesh point must be further evaluated

to determine the effect on gear performance. A summary of the housing thermal distortions and also thermal stresses is included in table I.

Although thermal mapping tests determine the thermal conditions of an existing transmission, the design of a new transmission requires this information prior to manufacture. In order to determine thermal distortions/stresses for a new or conceptual transmission housing, it is necessary to calculate the heat generated by the gear meshes and bearings which are the forcing functions for the thermal model. The analysis of gear/bearing heat generation is a goal of the work being conducted currently. It is necessary input to a realistic conceptual modeling procedure. Approximate methods may be used rather than completely rigorous analyses.

STRESS ANALYSES

Using the finite element housing model, a variety of static and dynamic analyses have been conducted to predict structural deformation and stress distributions. By applying loads representative of the operating transmission to the model, stress distributions throughout the housing have been calculated. The static and dynamic stresses thus calculated, when superimposed upon the thermal stress distribution, provide an accurate overall picture of both the steady-state and time dependent (fatigue producing) stresses occurring in the housing of an operating transmission. From this combined stress distribution, the structural load paths can be identified, and the structural portions of the housing segregated from the non-structural portions. Furthermore, methods for structural optimization using strain energy have been used to define wall thickness and geometry changes. Figure 13 depicts the stress analysis scheme.

Various maneuver conditions, such as symmetric dive and pull-out (nose-up pitching), yawing, and recovery from rolling pull-out, have been analyzed. Resulting forces imposed upon the housing due to rotor loads, steady-state gear loads, and inertia loads have been considered. Rotor hub loads and gear loads were converted to forces acting at the shaft support bearings and applied to the housing at the bearing support locations. The inertia loads were applied uniformly throughout the housing. After running a NASTRAN Rigid Format 1 analysis, the post-processor mentioned in the previous section was used to calculate the deflections. In order to establish a baseline for comparison of the rigidity of magnesium and advanced material housings, the deflections were also calculated for a steel housing. The deflections due to the ultimate load condition for both the magnesium and steel housings are shown schematically in figure 14 and are summarized for comparison in

table II. Also shown in table II are some typical maximum stresses calculated by NASTRAN for various load conditions.

CONCLUDING REMARKS

A transmission is a complex system wherein all components interact and influence each other; hence, a unified analysis is necessary to optimize the components for the unique operating environment of a specified transmission system. The housing structural analysis using NASTRAN described herein represents a significant step toward this goal. Based on the Thermal/Static/Dynamic analyses accomplished to date, it is apparent that NASTRAN can be applied to transmission design. In fact, there is no other comprehensive analytical tool. Application of these methods during the design phase may return substantial benefits over the life of a transmission.

The ability of NASTRAN to accurately predict thermal distortions of a transmission housing has been verified by correlation of test data. The heat transfer/thermal stress capability of NASTRAN has been utilized for a lubrication/cooling analysis.

When analyzing the housing structure, the effect of the internal components (i.e. gears, bearings, shafts) must be considered. Hence, it may be necessary to model these components either in detail or in a simplified manner. Furthermore, in some instances such as a thermal growth analysis it may be possible to ignore the internal components because of different coefficients of thermal expansion.

More significant application of a structural load path analysis can probably be made to advanced transmission concepts employing fabricated housings, composite materials and other advanced concepts which will permit greater design flexibility. For example, major load paths could be selectively reinforced while the thickness of non-load carrying regions of the housing wall could be reduced to the minimum necessary for containment of the lubricant. NASTRAN can handle composite materials by using a 6 x 6 material property matrix along with an orienting angle for each element to define the direction of the input properties.

By evaluating the displacements of the housing model grid points at the bearing/housing interfaces, the shaft slopes and displacements at the gear mesh have been determined. Although the magnitude of these displacements is appreciable, further evaluation is needed to establish the effect on life and performance.

REFERENCES

1. Howells, R. W., and Sciarra, J. J., FINITE ELEMENT ANALYSIS USING NASTRAN APPLIED TO TRANSMISSION VIBRATION/NOISE REDUCTION, NASA TMX-3278, September 1975.

2. Everstine, G., BANDIT - A COMPUTER PROGRAM TO RENUMBER NASTRAN GRID POINTS FOR REDUCED BANDWIDTH, Naval Ship Research and Development Center Technical Note AML-6-70, February 1970.

3. American Gear Manufacturers Association Standard 210.02.

4. Tocci, R. C., Lemanski, A. J., and Ayoub, N. J., TRANSMISSION THERMAL MAPPING, USAAMRDL TR 73-24, May 1973.

TABLE I. THERMAL DISTORTION AND THERMAL STRESS SUMMARY

THERMAL LOAD CONDITION	SHAFT SLOPE		MESH DISPLACEMENT - cm (in)	
	PINION	GEAR	PINION	GEAR
85°C (185°F) Thermal Map	.0003	.0004	.015 (.006)	.018 (.007)
204°C (400°F) Thermal Map	.0007	.0009	.033 (.013)	.038 (.015)

THERMAL LOAD CONDITION	HOUSING THERMAL STRESSES - kPa (PSI)	
	MAXIMUM	NOMINAL RANGE
85°C (185°F) Thermal Map	22060 (3200)	1380 - 17240 (200 - 2500)
Uniform Temperature 71°C (160°F)	13790 (2000)	690 - 4140 (100 - 600)

TABLE II. DEFLECTION AND STRESS SUMMARY

LOAD CONDITION	SHAFT SLOPE		MESH DISPLACEMENT - cm (in)	
	PINION	GEAR	PINION	GEAR
ULTIMATE				
Magnesium	.0017	.0005	.0429 (.0169)	.0091 (.0036)
Steel	.0004	.0001	.0094 (.0037)	.0018 (.0007)
STEADY FLIGHT (1-g)				
Magnesium	.0006	.0002	.0147 (.0058)	.0030 (.0012)
Steel	.0001	.0000	.0033 (.0013)	.0005 (.0002)

LOAD CONDITION	TYPICAL MAGNESIUM HOUSING STRESS - kPa (PSI)
ULTIMATE	±103425 to ±172375 (±15000 to ±25000)
STEADY FLIGHT (1-g)	±20685 (±3000)
YAWING MANEUVER	±137900 (±20000)
RECOVERY FROM ROLLING PULLOUT	±34475 (±5000)

CH-47 FORWARD TRANSMISSION

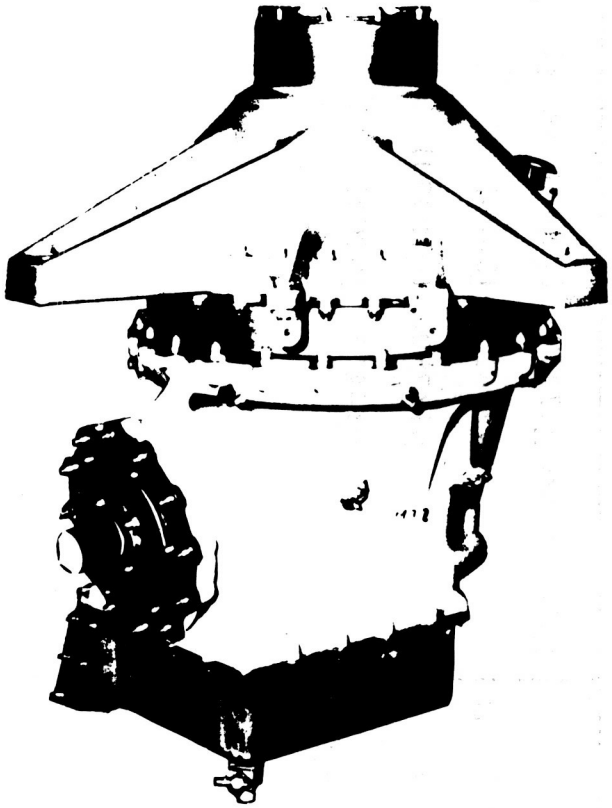

2684 kW (3600 HP) Rating

TRANSMISSION HOUSING MODEL

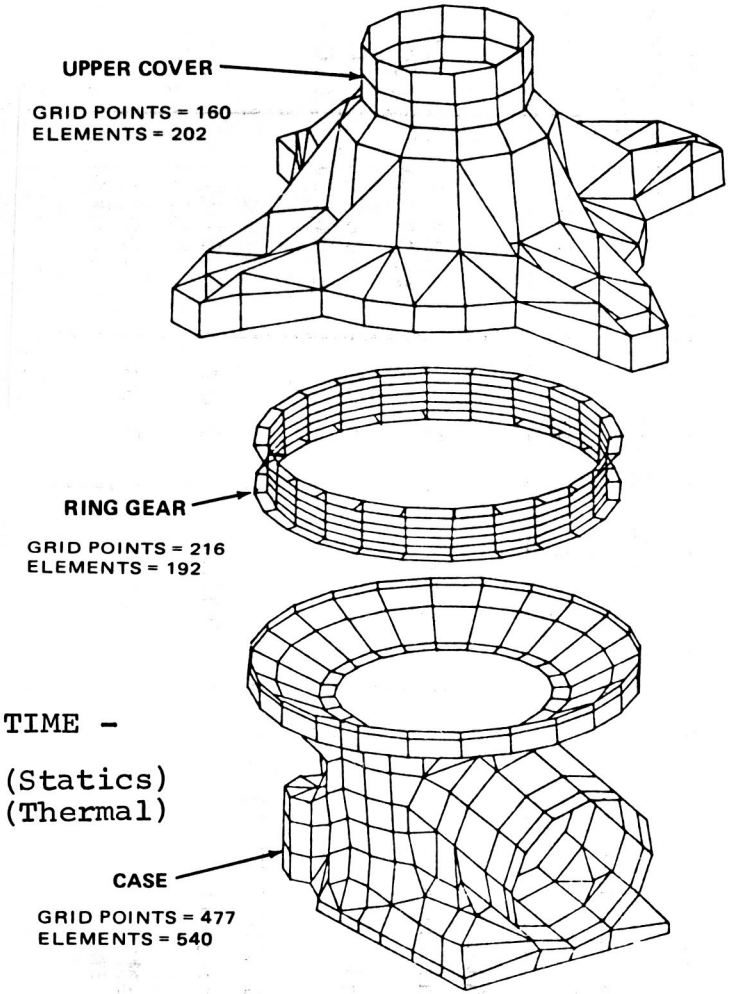

CPU TIME -

.66 HR (Statics)
.05 HR (Thermal)

Figure 1. Boeing Vertol CH-47 Helicopter Forward Rotor Transmission Housing and Computer Generated Plot of NASTRAN Model.

MODEL PARAMETERS

	NUMBER GRID POINTS	NUMBER ELEMENTS	NUMBER DEGREES OF FREEDOM				BANDWIDTH			CPU TIME (HOURS)*
			TOTAL	SPC	OMIT	RETAINED	FULL	REDUCED	ACTIVE COLUMNS	
Upper Cover	160	202	960	184	614	162	34	162	0	
Ring Gear	216	192	1296	216	828	252	-	252	0	
Case	477	540	2862	529	2024	309	61	309	0	.66 Statics .05 Thermal
TOTAL	853	934								

*RIGID FORMAT 1 ON IBM 370

COMPARISON OF CALCULATED AND ACTUAL WEIGHTS*

	MODEL	HARDWARE	DIFFERENCE
Sump	3.7 kg (8.2 lb)	5.5 kg (12.2 lb)	**
Case	25.1 kg (55.4 lb)	24.6 kg (54.2 lb)	+ 2.2%
Ring Gear	34.9 kg (77.0 lb)	34.9 kg (77.0 lb)	0% (Lumped Masses for Teeth)
Upper Cover	62.8 kg (138.5 lb)	64.1 kg (141.4 lb)	- 2.0%

*(Case weight based on AZ91C cast magnesium alloy, density 1.799g/cc (.065 lb/in^3); upper cover weight based on 2014-T6 forged aluminum, density 2.796g/cc (.101 lb/in^3), both per MIL-HDBK-5B 1 September 71.)

**Model excludes internal passageways.

Figure 2. Summary of CH-47 Forward Transmission Housing NASTRAN Model.

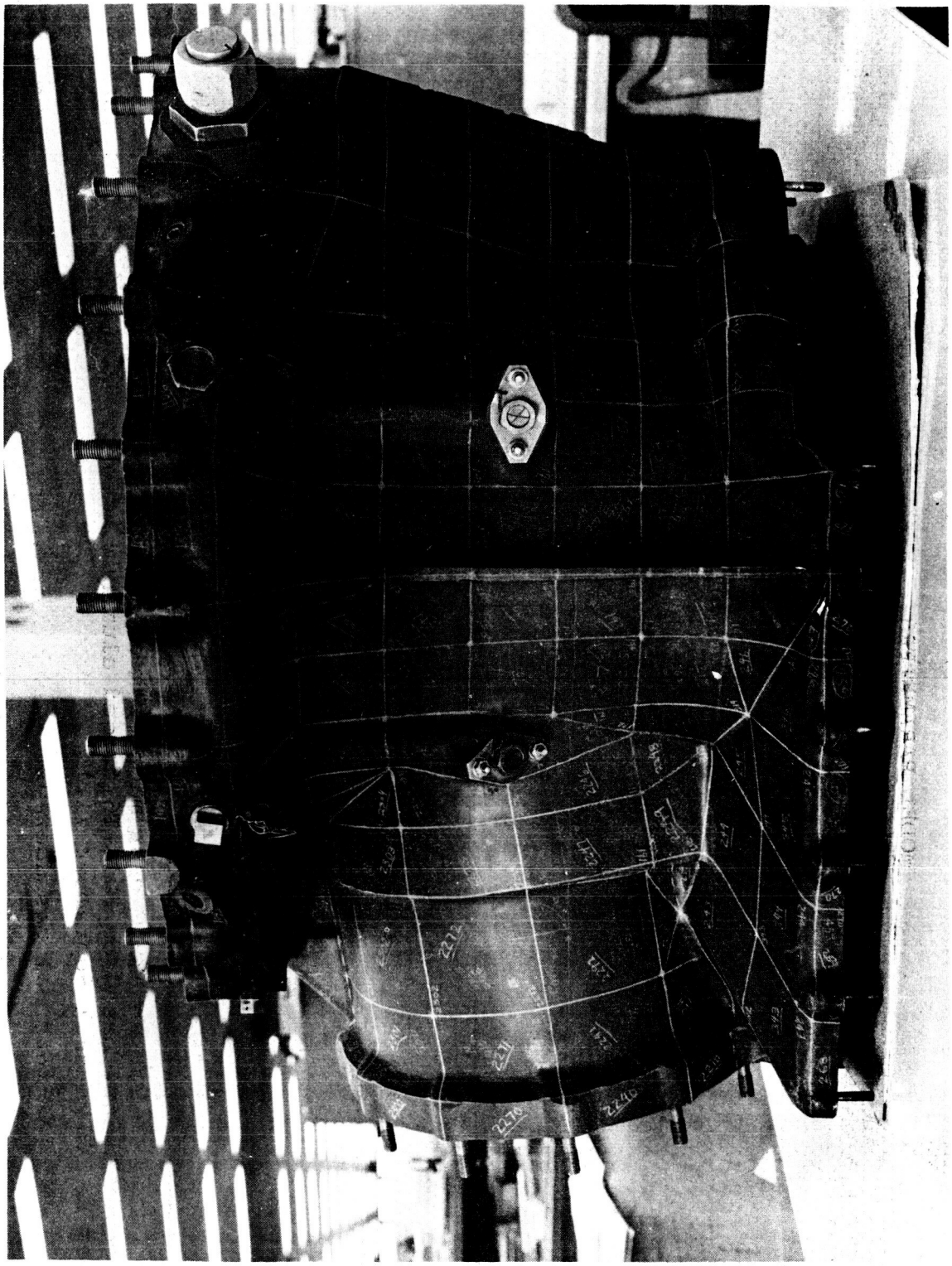

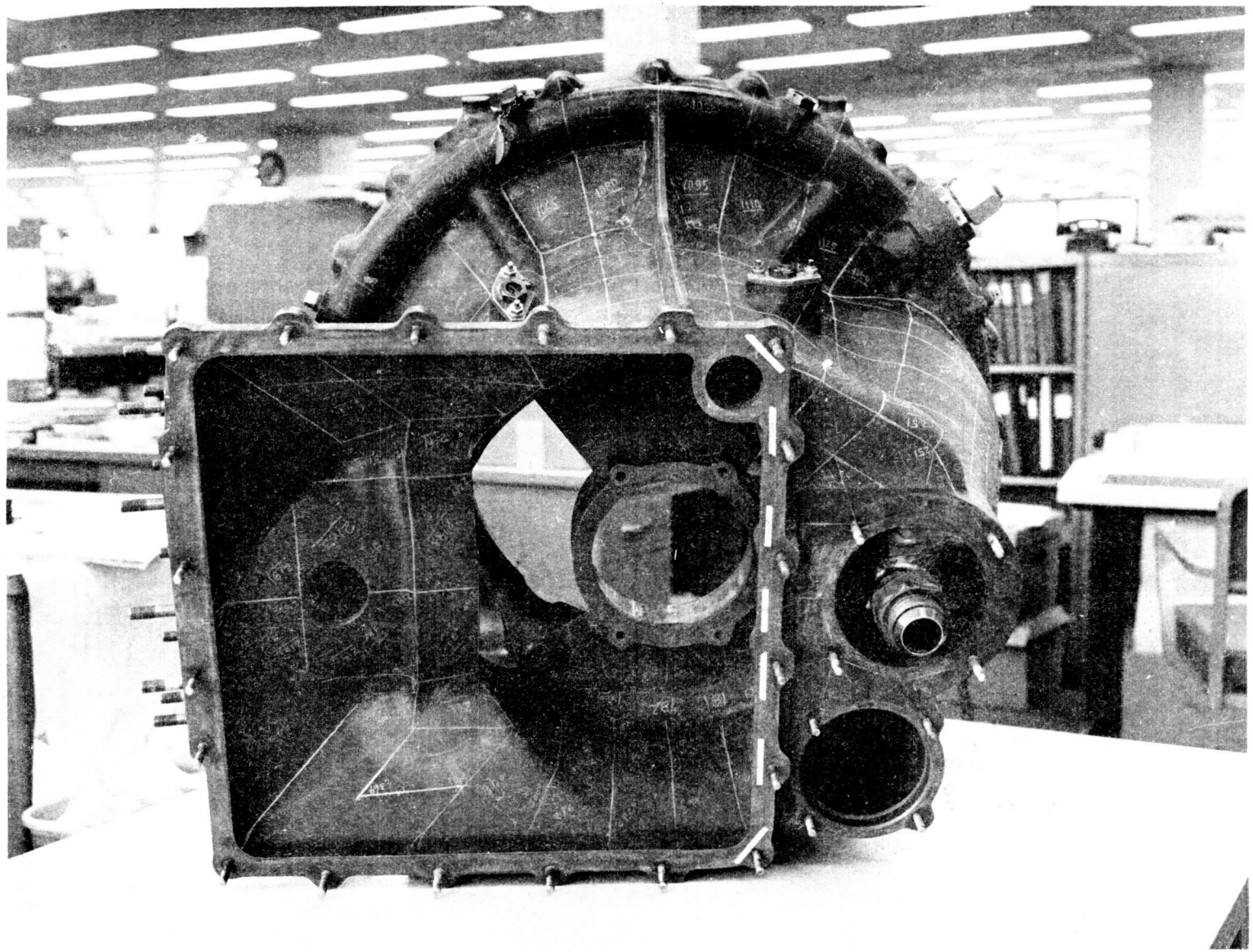

Figure 3b. CH-47C Forward Transmission Lower Housing (Bevel Gear Case).

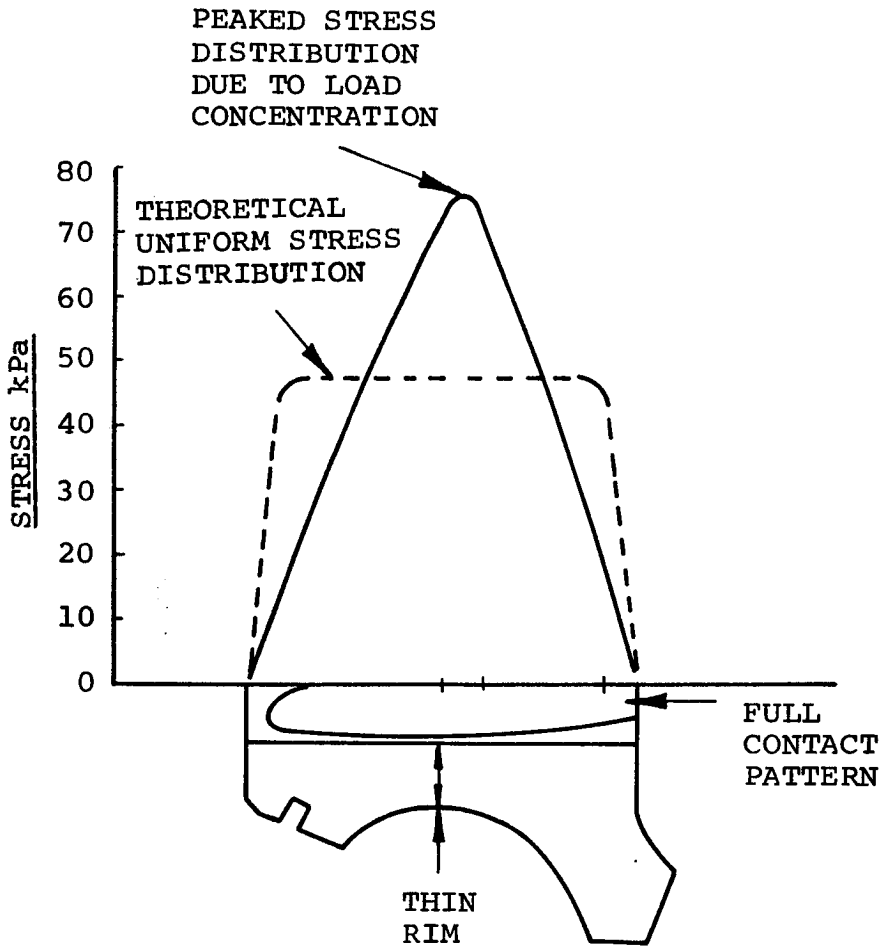

Figure 4. Typical Measured and Theoretical Stresses in Bevel Gears.

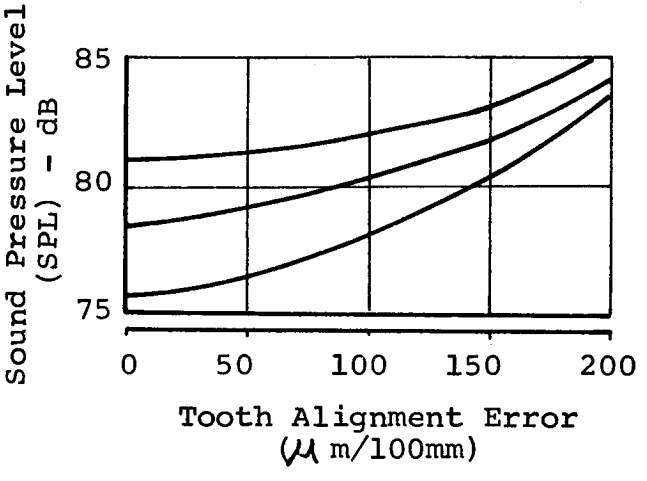

Figure 5. Typical Influence of Tooth Alignment Error on Gear Noise.

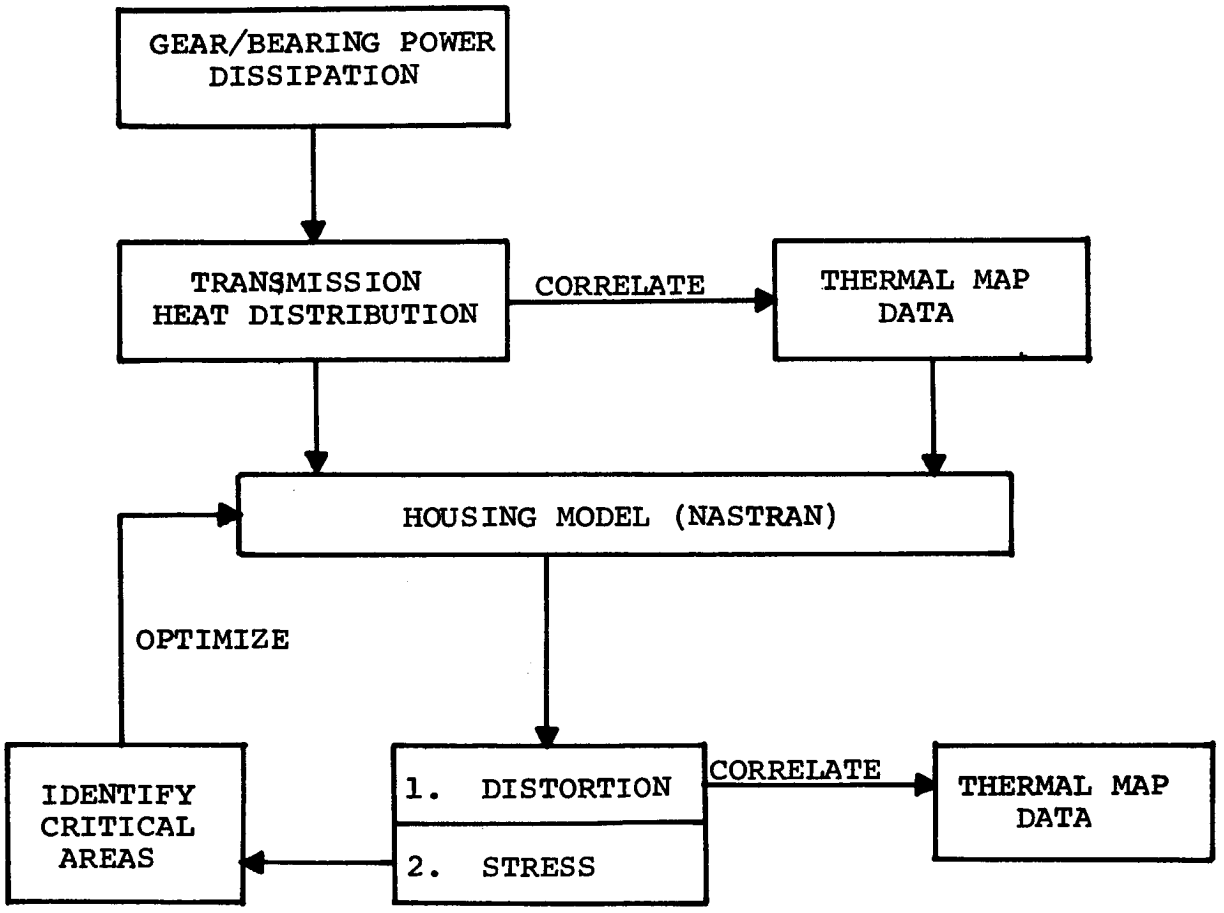

Figure 6. Flow Diagram of NASTRAN Thermal Analysis.

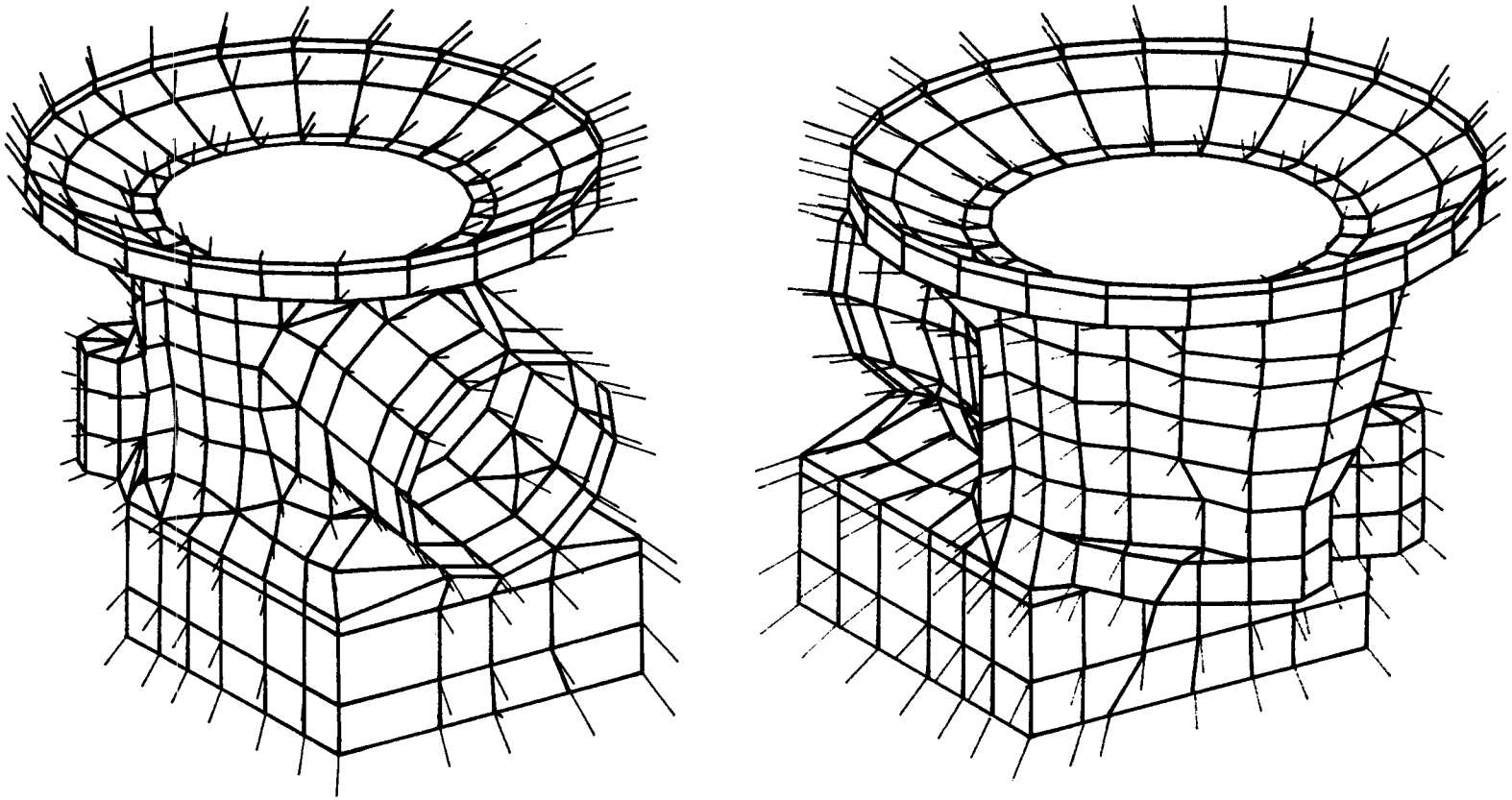

NOTE: VECTORS INDICATE DISPLACEMENTS.

SUBCASE	TEMPERATURE	MAXIMUM DEFORMATION
1	71°C (160°F)	0.0612 cm (0.0241 in)
2	177°C (350°F)	0.1839 cm (0.0724 in)
3	371°C (700°F)	0.4100 cm (0.1614 in)

Figure 7. CH-47 Forward Transmission Case Uniform Temperature Analysis, Static Deformation Due to Elevated Temperatures.

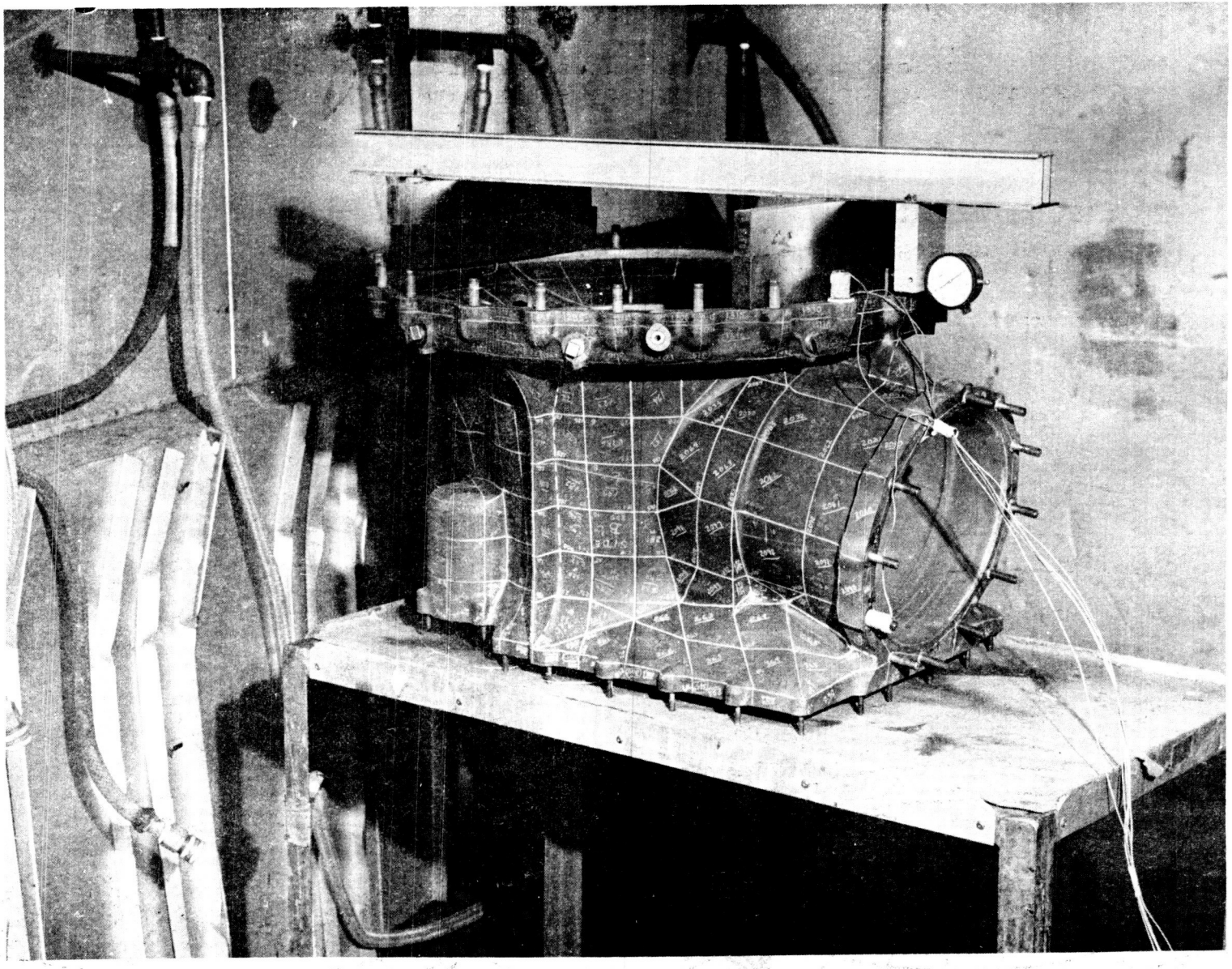

Figure 8. Measurement Procedure — Bar Type Dial Indicator Gage.

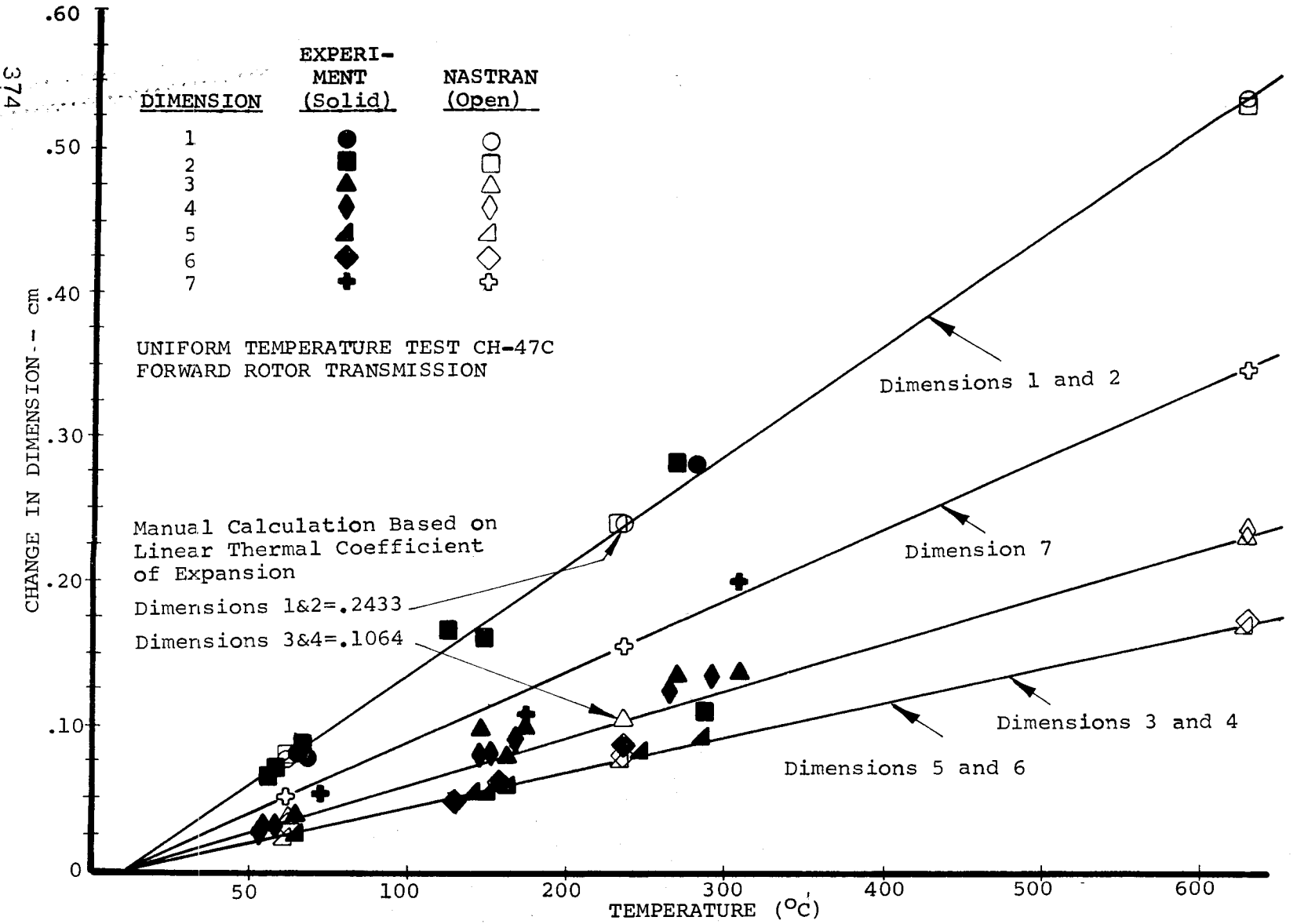

Figure 9. Transmission Housing Dimensional Changes as a Function of Temperature.

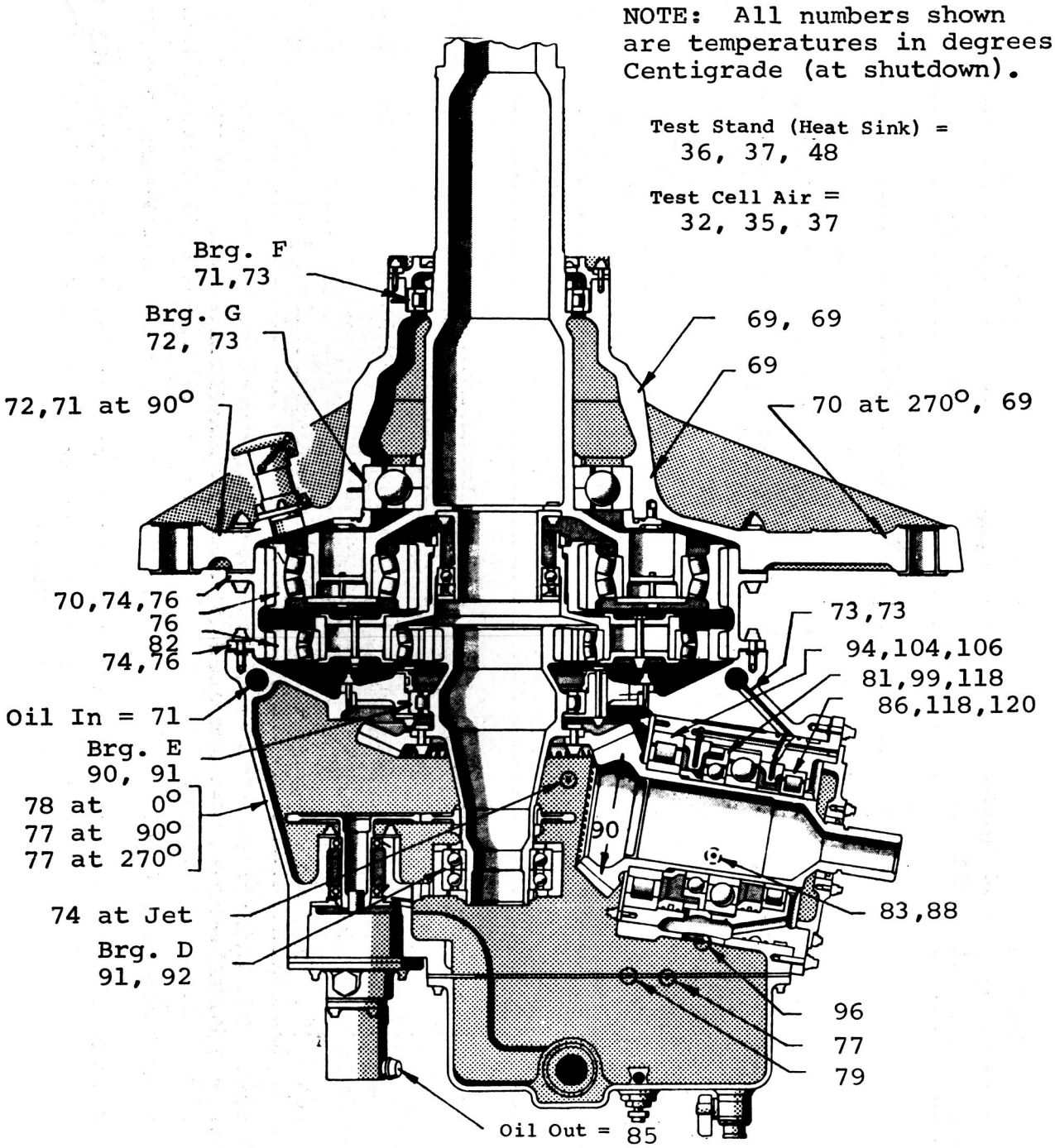

Figure 10. Typical Thermal Map of CH-47C Forward Transmission - 85°C (185°F) Oil-Out Temperature.

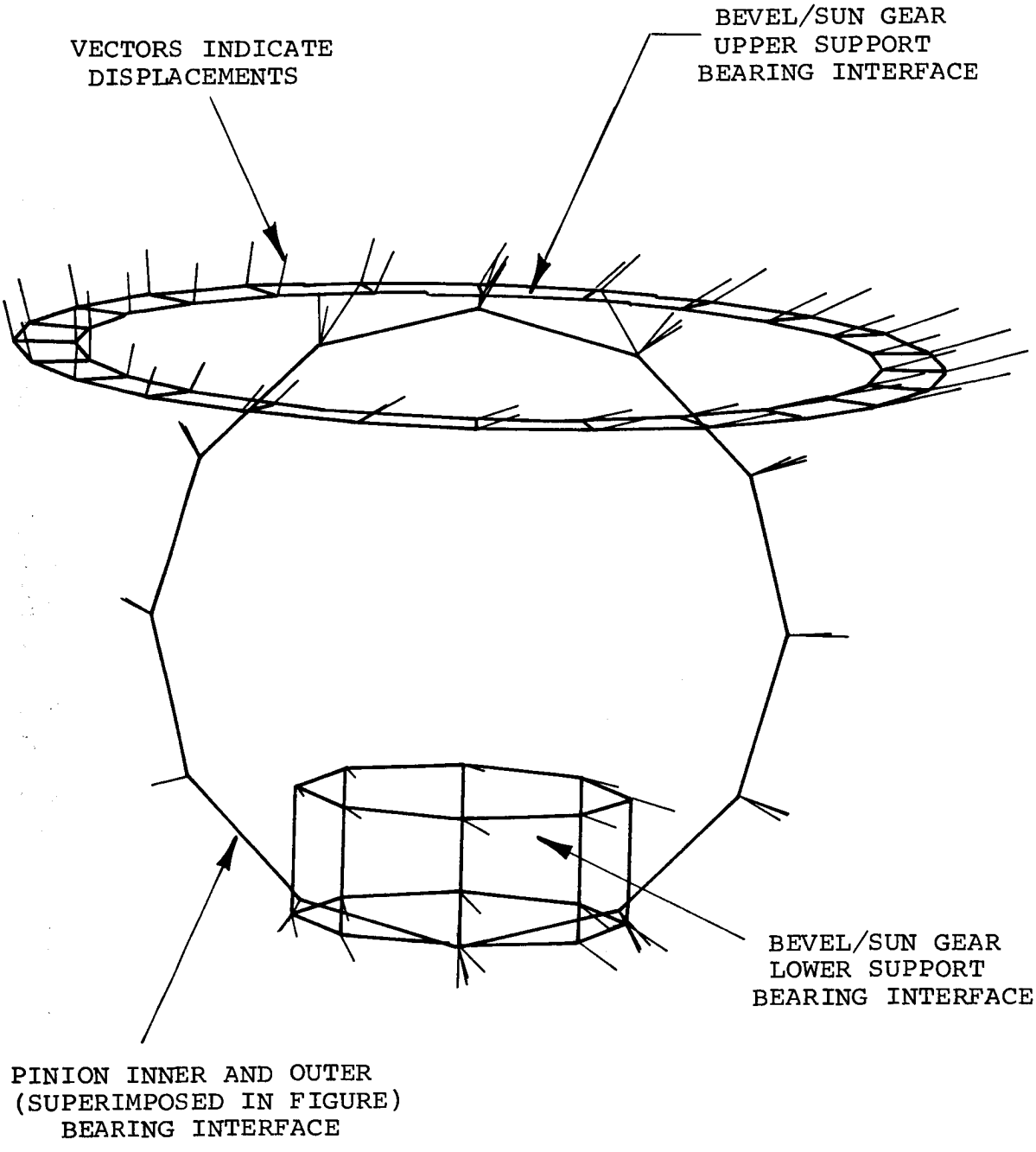

Figure 11. Induced Displacements at Housing/Bearing Interfaces Due to Temperature - Thermal Map Data for 85°C (185°F) Oil-Out.

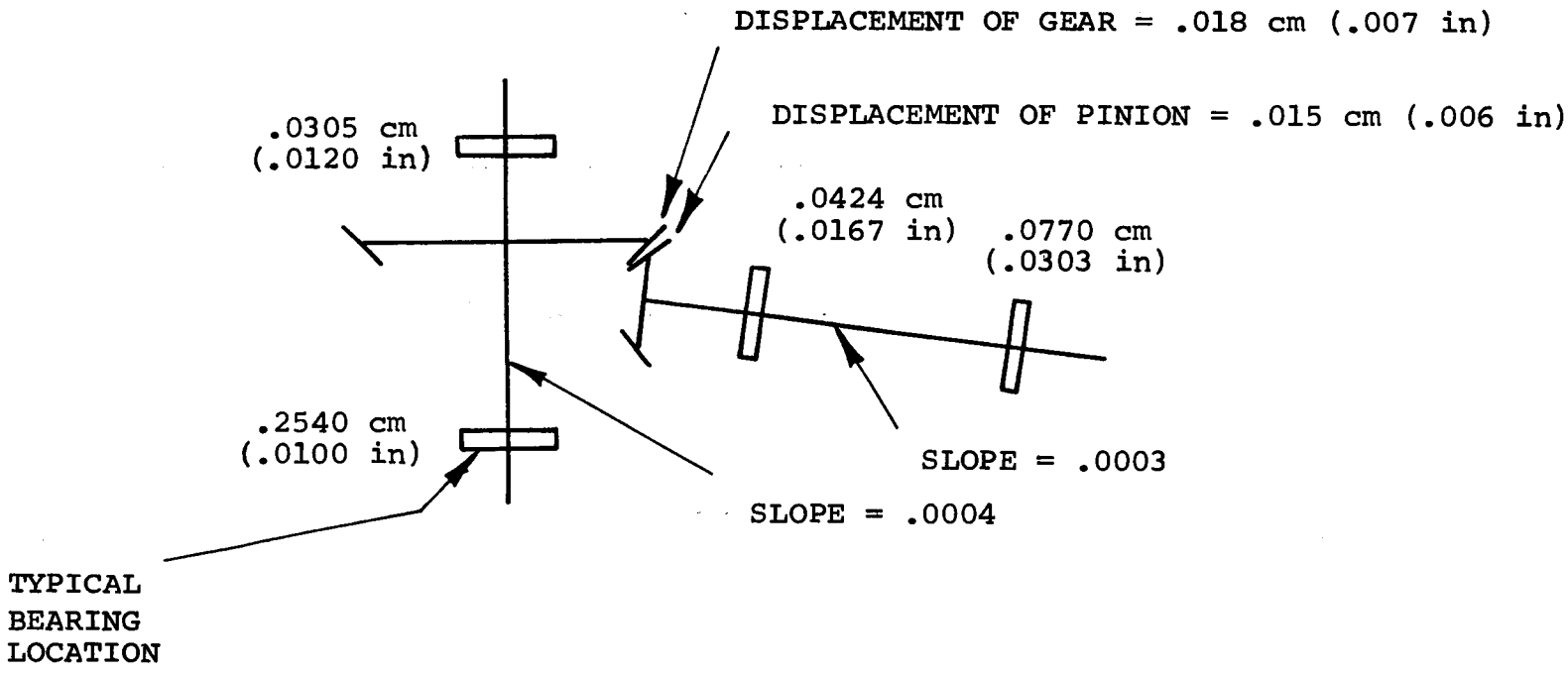

Figure 12. Displacement of Internal Components Due to Thermal Loads - Thermal Map Data 85°C (185°F).

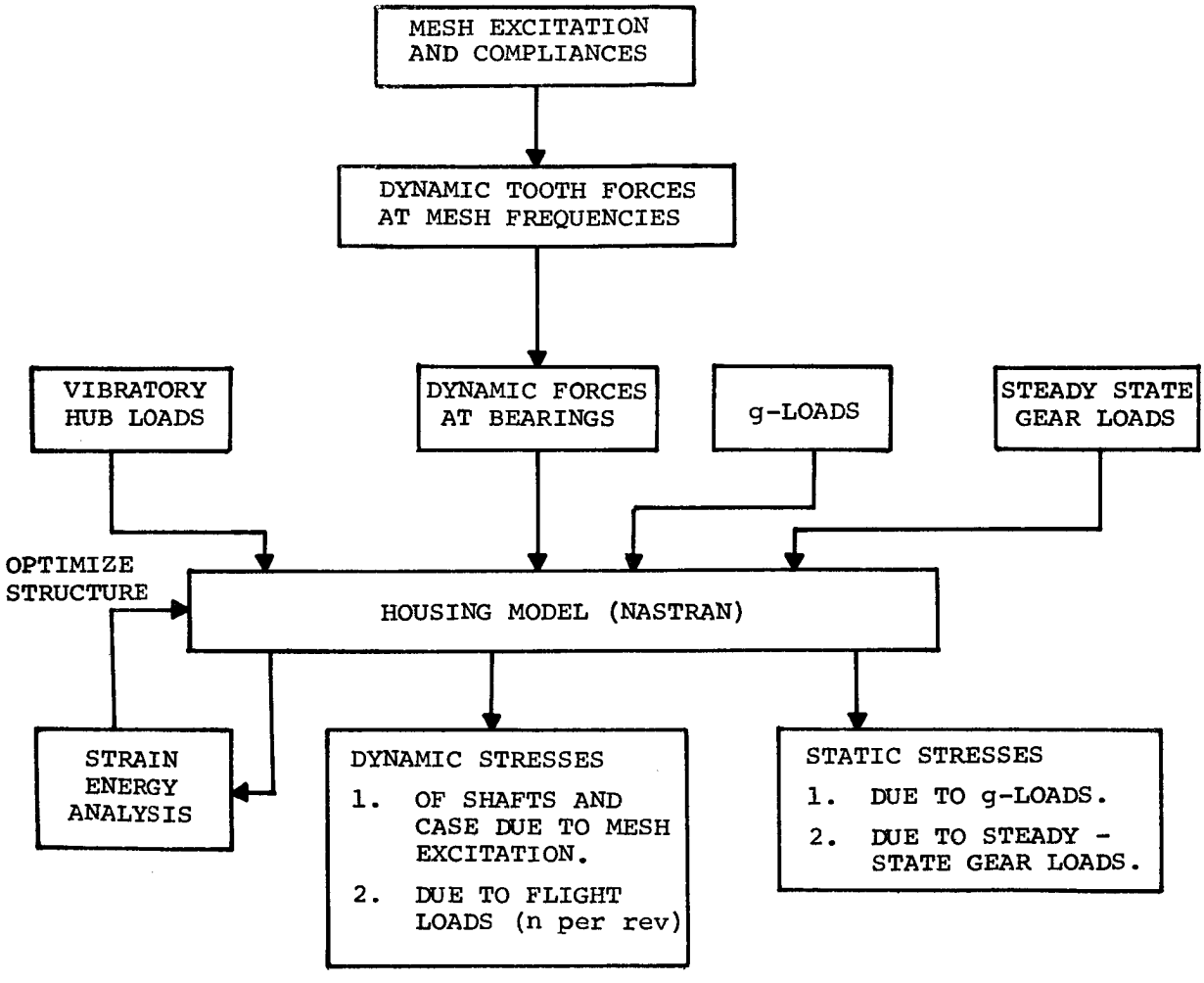

Figure 13. Flow Diagram of NASTRAN Stress Analysis.

MAGNESIUM CASE (Figure 14a)

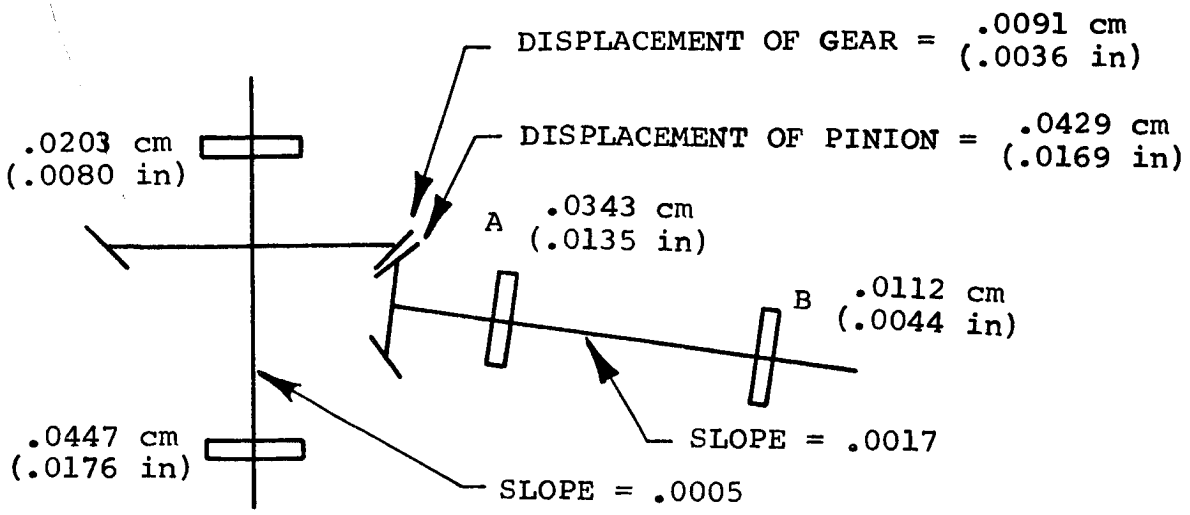

STEEL CASE (Figure 14b)

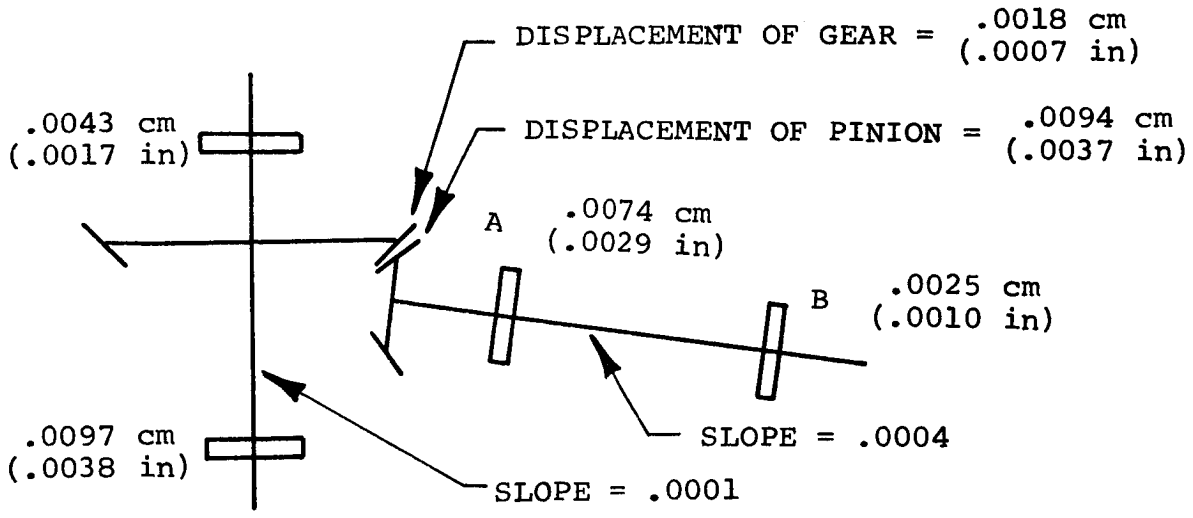

Figure 14. Displacement of Internal Components Due to Ultimate Load Condition.

NASTRAN AS AN ANALYTICAL RESEARCH TOOL FOR COMPOSITE MECHANICS AND COMPOSITE STRUCTURES

C. C. Chamis, J. H. Sinclair, and T. L. Sullivan
Lewis Research Center

ABSTRACT

Selected examples are described in which NASTRAN is used as an analysis research tool for composite mechanics and for composite structural components. The examples were selected to illustrate the importance of using NASTRAN as an analysis tool in this rapidly advancing field. The results obtained demonstrate rather convincingly the versatility and effectiveness of NASTRAN in such applications.

INTRODUCTION

This paper describes selected examples in which NASTRAN was used as an analysis tool for composite mechanics and for composite structural components. Typical examples for composite mechanics include: stress analysis of the load transfer region of off-axis (with respect to fiber direction) composite specimens, the vibration response of specimens with defects, the effects of in-plane and out-of-plane (plane of specimen) eccentricities on test results, the stress variation in the load transfer region of thin composite tubular specimens, the stress distribution in the near and far field regions of a composite cantilevered plate subjected to a concentrated load, and the determination of the bending modulus in composite specimens with non-uniform thickness. The examples for composite structures include: stress analysis of composite blades for aircraft turbine engines, and stress and vibration analysis of a composite thin shell airfoil section.

The description of each example includes: the objective of the study, a brief background of its genesis, a schematic of the geometry, the finite element representation (number of grid points, number and type of elements, computer running times), typical results in graphical and/or tabular form, and comparisons with measured data when available.

OFF-AXIS COMPOSITE TENSILE SPECIMENS

The objective of using NASTRAN in this study was to predict the stress state near the end tabs and at mid length of off-axis composite specimens tested in tension. The results were subsequently used for comparisons with measured data and for identifying possible out-of-plane eccentricities that might be present during testing.

The geometry and instrumentation of the specimen is shown in figure 1. This specimen was made from high modulus graphite-fiber epoxy resin composite (Modnor I/epoxy (MOD I/E)). The laminate configuration of the specimen con-

sisted of 8-plies $[0_8]$, all oriented in the same direction. The specimen thickness was about .057 inch and it was loaded at 30° to the fiber direction.

The NASTRAN model is shown in figure 2. The NASTRAN model consisted of 657 nodes and 576 quadralateral plate (CQUAD2) elements which included the tapered portion of the reinforcing end tabs. Note that the finite element representation includes two groups of elements. At each end, the elements are 0.0625 in. long; these represent the tapered portion of the reinforcing tabs and the first quarter inch segment of the test section which is the site of the top strain gages. The remaining elements of the representation are 0.125 inch in length. All elements for this model are 0.0625 wide. The element size was made small enough to study the zones where the strain gages were located on the actual specimen. The material properties required for NASTRAN were generated using the composite mechanics code (ref. 1). Typical CPU (central processing unit) time was 18 minutes for the UNIVAC 1110.

Axial strains across the width of the 30° off-axis specimen as determined by NASTRAN are shown in figure 3 along with the measured fracture strains. Midlength measured strains at fracture ranged from 0.365 to 0.380 percent while those at the tab end were 0.395 and 0.424 percent. The NASTRAN analysis axial strains across the specimen midlength were between 0.374 and 0.426 percent and those at the tab-end were between 0.353 and 0.447 percent. A glance of figure 3 shows that NASTRAN predicted strains are a little higher than the measured strains at the specimen midlength and lower than the measured strains near the specimen end. Although not shown in figure 3, NASTRAN strain predictions for a section of the specimen lying midway between the tab-end and specimen midlength were between the two curves, as would be expected. The discrepancy between the strains measured at midlength and tab-end of the specimens are not accounted for by the NASTRAN analysis.

This leads to the conclusion that the discrepancy is probably produced by possible out-of-plane load eccentricities which were investigated and are described in the next section. The important point to be noted is the use of NASTRAN in identifying possible test difficulties.

OUT-OF-PLANE ECCENTRICITIES IN COMPOSITE OFF-AXIS SPECIMENS

The objective of using NASTRAN in this study was to assess whether possible out-of-plane of the specimen eccentricities such as bending or twisting could produce part or all of the discrepancy described in the previous section.

The geometry of the specimen and the NASTRAN model are the same as described in the previous section (figs. 1 and 2, respectively). For this study, the specimen was first loaded with an out-of-plane (plane of specimen) bending moment and then with a twisting moment at one end of the specimen. The ends of the specimen were constrained to lie in the same plane for the out-of-plane bending case. The center line of the specimen was constrained to lie in the same plane for the twisting case.

The out-of-plane bending effects predicted by NASTRAN on axial strain for the 30° off-axis specimen subjected to a 100 inch-pound bending moment are

shown in figure 4. Those for torsion are shown in figure 5 (100 in.-lb twisting moment).

At specimen midlength, the twisting effects are very small, figure 5, but near the grip they are important and are of opposite signs on the two edges of the specimen. The out-of-plane bending effects shown in figure 4 are moderate but all in the same direction at specimen midlength. Near the tab they are of the opposite sign and are much larger at one edge of the specimen than at the other. The combined effect of twisting and out-of-plane bending near the tab end of the tensile specimen could be sizeable and data provided by a strain gage at such a location could be erroneously interpreted.

The important conclusion from the previous discussion is: out-of-plane eccentricities of tensile specimens could give rise to very large strains near the end tabs of the specimen. This may be a cause of the frequent failure of this type specimen near the tab. It is significant to note that to have arrived at the same interpretation through the use of strain gages would have required a large number of strain gages which would have been impractical. Therefore, the effectiveness of using NASTRAN in this study as a research tool is obvious.

VIBRATION OF COMPOSITE SPECIMENS WITH DEFECTS

The objective of using NASTRAN in this study was to predict the effects of defects in composite specimens on the free vibration modes of these specimens. For this purpose, the vibration modes of composite specimens with progressively larger through-the-thickness defects were determined.

The specimen geometry is shown in figure 6. The specimen analyzed was assumed to be made from Thornell 75/Epoxy (T75/E)$[\pm 45, 90, 90, 0, 0]_s$ composite. The defects considered were slits 1/4, 1/2, and 3/4 of the specimen width, in length, respectively, and 1/4 inch wide.

The NASTRAN model is shown in figure 7. The model consists of 297 nodes and 256 CQUAD2 elements. The through-the-thickness defect was simulated by removing elements 124 and 125 for the 1/4, 123 to 126 for the 1/2, and 122 to 127 for the 3/4 size defect, respectively. The material properties required for NASTRAN were obtained from the composite mechanics computer code (ref. 1). Typical CPU times were 17 minutes in the UNIVAC 1110.

Free vibrational frequencies were calculated for an undamaged specimen and for a specimen with defects at midlength which spanned 1/4, 1/2, and 3/4 of the width of the specimen by removing the connection cards for the appropriate elements. Table I shows the frequencies for the first four modes for each condition. The frequencies are lowered by the defect. Table II shows the percent reduction in specimen area resulting from the defects of the three sizes as well as the relative changes in the corresponding frequencies. A defect spanning one-fourth of the specimen width which removes 0.78 percent of the bulk of the material in the specimen reduces the vibrational frequency by no more than 1.2 percent in the case of the first four modes. This would represent a very large crack in an actual component, which leads to the conclusion that it would take a large defect or imperfection to affect the integrated stiffness and mass of

the component. Also the vibration frequencies are not very sensitive to small defects in composite structures. Figure 8 shows the fourth mode shapes for an undamaged composite specimen and the 1/2 size defect (1.56 percent of the specimen area). The mode shapes are almost identical and the frequency drop due to this large defect is less than 3.0 percent.

The important conclusion from this study is that the vibration frequency measurement used as an NDE procedure for evaluating a composite structure with defects of the type investigated is not likely to prove a practical procedure. This example illustrates the use of NASTRAN as a research analysis tool for assessing the practicality of such NDE procedures.

TRANSITION REGION STRESSES IN TUBULAR COMPOSITE SPECIMENS

The objective of using NASTRAN in this study was to predict the stress state near the grip area (transition region) in thin composite tubular specimens. The predicted stress state was used to (1) compare it with measured data and (2) more importantly, evolve grip designs which minimize the stress in the transition region. Thin tubular specimens are important in studying failure and failure mechanisms of composites subjected to controlled combinations of multiaxial loading, references 2 and 3.

Numerous grip failures were occurring in tests of tubular unidirectional composite test specimens. The specimens were potted into metal grips with an epoxy resin as shown in figure 9. One of these specimens was instrumented with strain gages in the grip transition region so that predicted results using NASTRAN could be compared with measured data. The geometry of the specimen which was used in the NASTRAN stress analysis is shown in figure 10. The composite material used in the analysis was MOD I/E with a laminate configuration of $[0_8]$. The material properties required for use in NASTRAN were determined from data provided by the material supplier.

A schematic of the NASTRAN model is shown in figure 11. The model consisted of 576 nodes and 552 CQUAD2 elements, 24 around the circumference and 23 along the length. These elements were used to model the tube wall and the potting material. The elements representing the potting material were normal to those for the tube wall. Typical computer CPU times were 21 minutes in the UNIVAC 1106.

Figure 12 compares the experimental and predicted results. The good agreement between the predicted results and the experimental data gave confidence in the NASTRAN model. It was then used to determine the effect on grip transition stresses of different grip designs and potting material properties. With the aid of this model it is possible to identify grip designs with reduced transition stresses and, thereby, evolve a more practical grip design.

BENDING MODULUS OF COMPOSITE ANGLEPLIED LAMINATES WITH SOME THICKNESS VARIATION

The objective of using NASTRAN in this study was to identify an effective

means for determining the bending modulus of specimens from composite angleplied laminates with variations in thickness. The bending modulus and the usual elastic modulus, measured in a tensile test, are different for angleplied laminates in general.

The material was MOD I/E and was in the form of tensile specimens with end tabs already in place and the thickness of the test section varied by as much as 7 percent. For cantilever bending, stiffness is related to fundamental frequency by the following expression:

$$E = 3.2\, f_1^2 \frac{\bar{m}L^4}{I} \tag{1}$$

where E is the bending modulus, f_1 is the fundamental frequency, $\bar{m}$ is the mass per unit length, L is the length of the cantilever, and I is the moment of inertia.

The fundamental frequency was determined experimentally. To relate this frequency to bending modulus, the specimen was modeled for NASTRAN taking into account the thickness variation and the end tab. Assuming that the bending modulus was constant along the length of the specimen, the modulus was determined from the relationship

$$E_e = E_N \left(\frac{f_e}{f_N}\right)^2 \tag{2}$$

where E_e is the effective bending modulus, E_N is a trial bending modulus used in the NASTRAN model, f_e is the experimentally determined fundamental bending frequency, and f_N is the fundamental frequency obtained from the NASTRAN model. Schematics of the tensile specimen and the NASTRAN model are shown in figure 13. Bending moduli determined from the above procedure for four quasi-isotropic angleplied laminates with different laminate configurations are shown in table III. This example illustrates the versatility of NASTRAN.

HIGH VELOCITY IMPACT COMPOSITE CANTILEVER SPECIMENS

The objective of the NASTRAN stress analysis of this specimen was to determine high stress regions and stress types under point load. The information obtained was used to: (1) guide the selection of sites for placing strain gages to measure the high velocity impact response of composite centilevers and (2) to help interpret some of the high velocity impact data generated in reference 4 under contract to NASA LeRC.

A photograph of an impacted specimen reported in reference 4 is shown in figure 14. The geometry of the specimen is depicted in figure 15. The NASTRAN model is shown in figure 16. The NASTRAN model consisted of 333 nodes and 288 CQUAD2 elements. Typical CPU times were about 4.5 minutes in the UNIVAC 1110. The specimen, for which results will be presented, was made from intraply hybrid composite with the following constituents: 75-percent type AS graphite fiber-epoxy resin composite (AS/E) and 25-percent S-glass - epoxy resin com-

posite (S-Gl/E). The laminate configuration for the specimen was $[\pm 40, 0, 10, 0, -10]_2$ which is representative of composite blade airfoil laminate configurations to minimize residual stresses. The material properties required for use in NASTRAN were generated using the composite mechanics code, ref. 1.

Predicted stresses on the back surface of the composite specimen due to a unit point load at the impact point are shown in stress contour plots as follows (refer to fig. 16 for directions): spanwise stress (σ_x) in figure 17(a), chordwise stress (σ_y) in figure 17(b), and in-plane shear stress (σ_{xy}) in figure 17(c). The important points to be observed from these stress contour plots are:

1. High spanwise stresses at the support near the specimen center, figure 17(a)
2. High chordwise stresses near the specimen center, in-board from the impact point, figure 17(b)
3. High in-plane shear stresses at the specimen edges near the support, figure 17(c)

The important conclusion from the above observations is that high stress regions for these types of specimens are readily identified using NASTRAN. Strain gages should be placed at these regions for obtaining optimum information. It is also important to note that the estimated maximum impact force built up during these tests is about 1000 pounds for 700 feet per second projectile velocity within 50 microseconds from initial contact (ref. 5). This magnitude of impact force will produce high tensile chordwise stresses in the back surface of the specimen near the impact point, figure 17(b), which, in turn, will produce splitting and delaminations at this region. This is consistent with the test result exhibited in figure 14.

HIGH-TIP-SPEED COMPOSITE FAN BLADE

The original objective of this investigation was to develop a computerized capability which couples NASTRAN with composite mechanics for the structural and stress analysis of composite fan blades for aircraft engines. A description of this capability and results obtained therefrom have been reported previously in references 6, 7, and 8. Herein, predicted stresses at design loads are compared with fracture stresses in tensile specimens cut from the critically stressed region in the composite blade. The design loads include aerodynamic pressure and temperature, and centrifugal forces resulting from 2200 feet per second tip speed with a mean tip radius of 16.4 inches (ref. 6).

A photograph of the fabricated composite blade is shown in figure 18. The blade is twisted, cambered, and tapered (both spanwise and chordwise). The blade was made from high-tensile-strength graphite fiber in Kerimid polyimide matrix (HTS/K601). The blade consisted (blade laminate configuration) of 73 plies at its thickest portion 30-percent of which were oriented at $\pm 40^\circ$ to the radial direction at the surface (shell plies) and 70-percent were oriented at 0° to the radial direction at the center (core plies). This type of laminate configuration is usually called shell/core. In addition, the blade had $\pm 20^\circ$ transition plies between the $\pm 40^\circ$ shell plies and the 0° core plies, and also $\pm 70^\circ$ plies near the tip for increased flutter resistance. For additional de-

tailed description see references 6 and 8.

The NASTRAN model of the composite blade is shown in figure 19. The model consisted of 299 nodes and 531 triangular plate (CTRIA2) elements. Typical CPU times were 11.5 minutes in the UNIVAC 1106. The average stresses predicted by NASTRAN for the design load are shown in a contour plot in figure 20. Stresses from the high stress region points A, B, and C in figure 20 are tabulated in table IV. Also shown in this table are the material fracture stresses measured using tensile specimens cut from the same region from fabricated blades (in situ material fracture stresses). As can be seen in table IV, the predicted stresses on the pressure surface are higher than the fracture stress. As a point of interest, some of these blades failed below or at design load during spin tests.

The important conclusion from the previous discussion is that NASTRAN coupled with composite mechanics can be used to predict fracture stress in structural components with complex geometry in anisotropic heterogeneous materials. The significant point to be emphasized here is that predicted stresses must be compared with in situ material fracture stresses for reliable assessment of the design.

FIBER COMPOSITE THIN SHELL AIRFOIL

The objective of this study was to select on a preliminary design basis a laminate configuration for NACA 64A010 type airfoils for wind tunnel wing simulation studies. The design load conditions were: (1) dynamic pressure typical for this type of airfoil, (2) first mode natural frequency of 60 Hz or greater, and (3) a maximum weight of 20 pounds. The margin of safety on stresses due to dynamic pressure was about 5, to account for possible fatigue, and on the first mode frequency was about 1.5.

The geometry of the airfoil section is shown in figure 21. Note the airfoil is a thin shell so that the weight is kept to a minimum. The composite material selected was graphite/epoxy (AS/E) 32 plies (0.005 in./ply) for a laminate thickness of 0.160 inch. The laminate configuration was $[(\pm 45)_2, 90_2, 0_{10}]_s$. The density of the composite is about 0.054 pound per inch^3 resulting in an airfoil weight of 18 pounds which is 2 pounds less than the design requirement. The NASTRAN model is shown in figure 22 (a-suction surface and b-pressure surface) and consisted of 130 nodes and 120 CQUAD2 elements. The material properties required for use in NASTRAN were generated using the composite mechanics code (ref. 1). Typical CPU time for the UNIVAC 1110 was: 7 minutes for the static case and 15 minutes for the first 10 vibration modes.

NASTRAN predicted spanwise stresses on the suction surface are shown in stress contour plots in figure 23(a), and for the pressure surface in figure 23(b). The maximum bending stress predicted by NASTRAN was about 7 ksi in the spanwise direction near the 1/3 chord point at midspan. The corresponding fracture stress measured in laboratory specimens with the same laminate configuration was 128 ksi which is much more than five times the design load stress of 7 ksi. Analogous comparisons were found for the other stresses.

The first eight vibration modes predicted by NASTRAN are tabulated in ta-

ble V where the predominant vibration mode shape is also identified. The first predicted mode is 90 Hz which is 1.5 times the minimum design requirement of 60 Hz. An interesting result from the vibration analysis is the second mode which is an accordion type mode shape.

It is important to note that the laminate configuration described above was arrived at after two NASTRAN analysis cycles. This laminate configuration is not claimed to be optimum. Nevertheless, the example illustrates convincingly the effectiveness of NASTRAN as an analysis tool in the preliminary designs of composite airfoils.

SUMMARY OF RESULTS AND CONCLUSIONS

The major results and conclusions of this investigation are as follows:

1. Out-of-plane eccentricities such as bending and twisting give rise to very large strains near the tab ends of off-axis composite tensile specimens and thereby initiate fracture at these locations.
2. Vibration frequency measurements for evaluating the presence and/or effects of small defects (about 2 percent by volume) in composites may not prove practical.
3. Grip and/or end attachments can be designed to minimize transitional region strains due to load transfer in thin composite tubes using NASTRAN with plate elements.
4. Effective bending moduli of composites with variable thickness can be determined using NASTRAN in conjunction with suitable frequency measurement experiments.
5. NASTRAN can be used to help establish an effective plan for instrumenting high-velocity-impact composite specimens.
6. Stresses predicted using NASTRAN must be compared with in-situ material fracture stresses for reliable assessment of the design.
7. The number of iteration analysis cycles in sizing airfoil-type composite components may be kept to as small as two with judicious use of NASTRAN.
8. The results of the various analyses described in this summary paper demonstrate rather convincingly the versatility and effectiveness of NASTRAN as an analysis research tool in the rapidly advancing methodology associated with composite mechanics and composite structural components.

REFERENCES

1. Chamis, Christo C.: Computer Code for the Analysis of Multilayered Fiber-Composites: User's Manual. NASA TN D-7013, 1971.

2. Sullivan, T. L.; and Chamis, C. C.: Some Important Aspects in Testing High-Modulus Fiber Composite Tubes Designed for Multiaxial Loading. NASA TM X-68045, 1972.

3. Chamis, C. C.; and Sullivan, T. L.: Combined-Load Stress-Strain Relationships for Advanced Fiber Composites. NASA TM X-71825, 1976.

4. Pike, R. A.; and Novak, R. C.: Design, Fabrication and Tests of Multi-Fiber Laminates. (R75-911730-15, United Aircraft Corp.; NAS3-17778), NASA CR-134763, 1975.

5. Friedrich, L. A.; and Preston, J. L., Jr.: Impact Resistance of Fiber Composite Blades Used in Aircraft Turbine Engines. (PWA-TM-4727, Pratt and Whitney Aircraft; NAS3-15568), NASA CR-134502, 1973.

6. Chamis, C. C.; and Lynch, J. E.: High-Tip-Speed Fiber Composite Fan Blades: Vibration and Stress Analysis. NASA TM X-71589, 1974.

7. Chamis, C. C.; and Minich, M. D.: Structural Response of a Fiber Composite Compressor Fan Blade Airfoil. NASA TM X-71623, 1975.

8. Chamis, C. C.: Vibration Characteristics of Composite Fan Blades and Comparison with Measured Data. 17th Conference on Structures, Structural Dynamics, and Materials. Am. Inst. Aeron. Astron., Inc., 1976, pp. 98-104.

TABLE I. - FREE VIBRATION FREQUENCIES OF GRAPHITE/EPOXY (THORNEL 75/epoxy $[\pm 45, 90_2, 0_2]_s$) COMPOSITE LAMINATE WITH DEFECTS

Defect ratio $\left(\frac{a}{w}\right)$	Frequency (Hz) for Mode			
	1	2	3	4
0	1385.9	3907.0	5453.9	7819.4
1/4	1368.9	3906.6	5399.3	7763.4
1/2	1321.5	3903.5	5345.0	7589.1
3/4	1215.8	3895.1	5282.4	7261.9

a = defect width
w = specimen width

TABLE II. - CHANGE IN FREE VIBRATION FREQUENCIES CAUSED BY DEFECTS (THORNEL 75/EPOXY $[\pm 45, 90_2, 0_2]_s$)

Length of defect $\left(\frac{a}{w}\right)$	Defect area (percent of total area)	Percent change in frequency for mode shown			
		1	2	3	4
1/4	0.781	-1.2	-0.01	-1.0	-0.7
1/2	1.56	-4.6	-0.09	2.0	-2.9
3/4	2.34	-12.3	-0.3	3.1	-7.1

a = defect width
w = spedimen width

TABLE III. - SUMMARY OF BENDING MODULI OF QUASI-ISOTROPIC COMPOSITES FROM GRAPHITE/EPOXY (MODMOR I/ERLA 4617)

Layup	Outer fiber direction	Bending modulus* (10^6 psi)
$(0, \pm 60)_s$	0 90	21.2 3.4
$(0, \pm 45, 90)_s$	0 90	16.4 3.4
$(0, \pm 30, \pm 60, 90)_s$	0 90	17.6 3.0
$(0, \pm 22.5, \pm 45, \pm 67.5, 90)_s$	0 90	17.2 2.8

*Average of two tests.

TABLE IV. - COMPARISON OF COMPUTED AND FRACTURE STRESSES AT REGION OF MAXIMUM AVERAGE COMPOSITE STRESS AT DESIGN LOAD

Blade point schematic	Surface stresses, ksi	
	Computed	Fracture[a]
A(S.S.)[b] (P.S.)	-7.86 67.1	52.3 - 65.4
B(S.S.) (P.S.)	-6.18 64.16	
C(S.S.) (P.S.)	-4.75 66.0	

[a]Measured in tensile specimens cut from fabricated blade.

[b]For location of these points, see fig. 20; S.S. denotes suction surface; P.S. denotes pressure surface.

TABLE V. - NASTRAN VIBRATION RESULTS FOR A FIBER

COMPOSITE THIN SHELL AIRFOIL

Mode number	Frequency, Hz	Predominant mode shape
1	90	First spanwise bending (ISB)
2	118	Accordian type
3	135	Coupled torsion-bending (TB)
4	157	Coupled spanwise-chordwise bending
5	181	First torsion (1T)
6	187	Second torsion (2T)
7	229	Third torsion (3T)
8	245	Second chordwise bending (2CB)

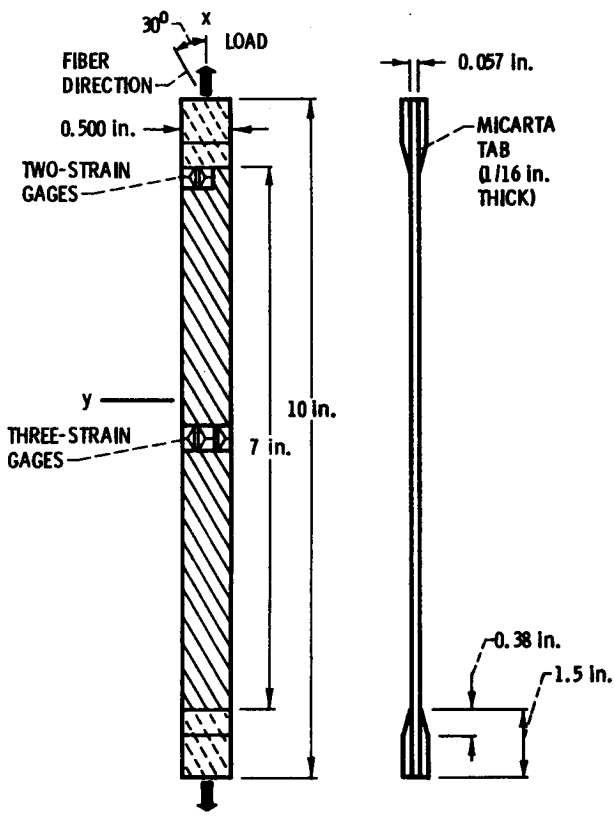

Figure 1. - Specimen geometry and instrumentation of off-axis specimen ($[0_8]$MOD I/E).

Figure 2. - NASTRAN model of off-axis specimen (657 nodes; 576 CQUAD2 elements).

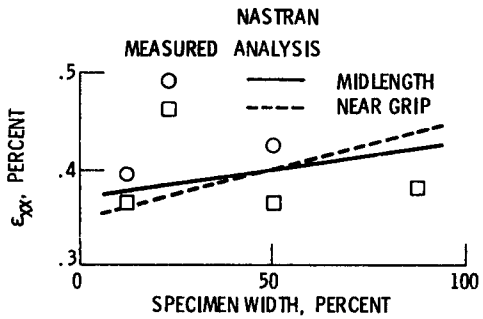

Figure 3. - Axial strain variation across 30^0 off-axis tensile specimen of graphite/epoxy composite (MOD I/E $[0_8]$).

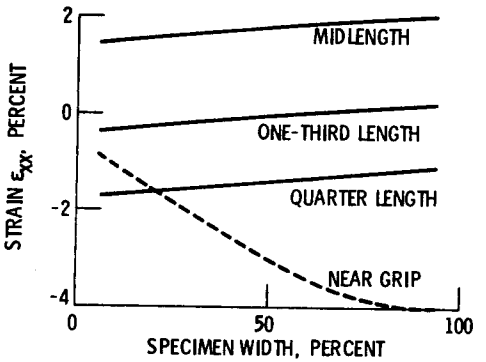

Figure 4. - Out-of-plane bending effects on axial strain of the 30^0 off-axis specimen (100 in.-lb bending moment).

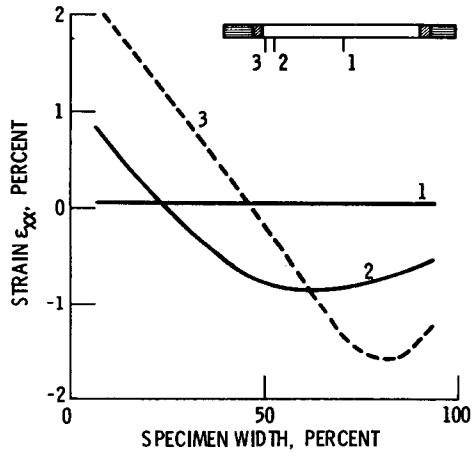

Figure 5. - Twisting effects on axial strain of the 30^0 off-axis specimen (100 in.-lb torque).

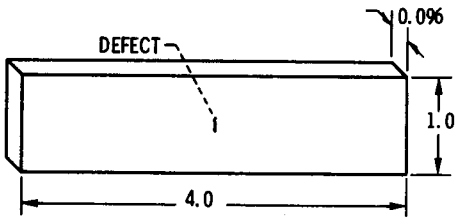

Figure 6. - Schematic of specimen with defects (T-75/PR288 [45, -45, 90, 90, 0, 0]$_s$, all dimensions are in inches).

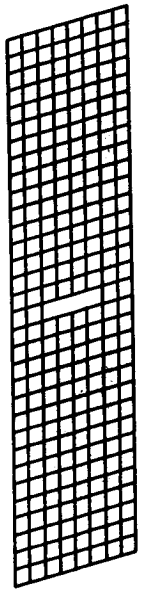

Figure 7. - NASTRAN model for composite specimens with defects; (297 nodes; 256 elements).

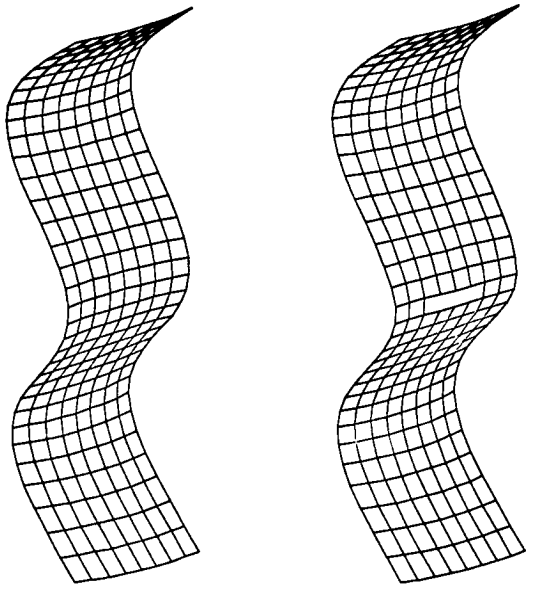

(a) NO DEFECT FREQUENCY: 7819 Hz.

(b) WITH DEFECT (a/w = 1/2) FREQUENCY: 7589 Hz.

Figure 8. - Fourth free vibration mode shape of composite specimen with and without defect.

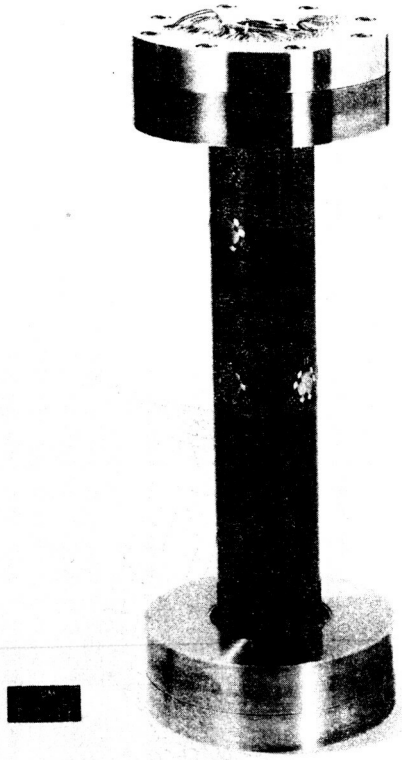

Figure 9. - Photograph of instrumented tube mounted in grips, (MOD I/E, $[0_8]$).

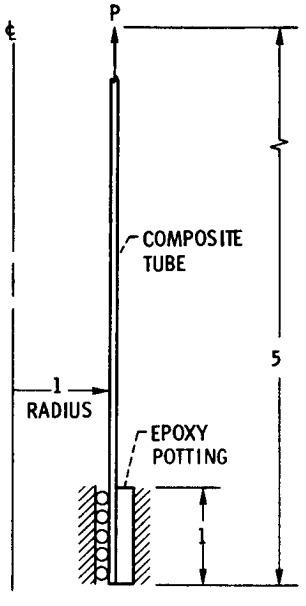

Figure 10. - Schematic of thin composite tubular specimen. (All dimensions are in inches.)

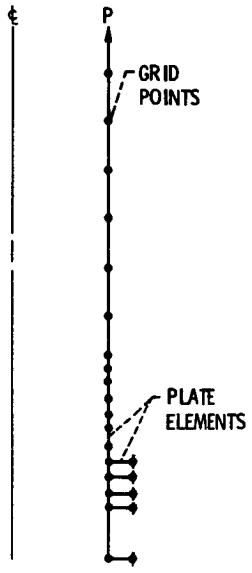

Figure 11. - Schematic of NASTRAN model (Quadrilateral plate elements).

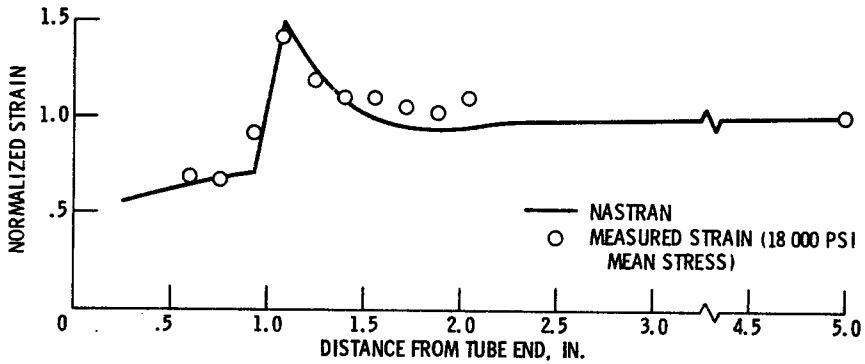

Figure 12. - Comparison of predicted and measured strains for a unidirectional composite tube.

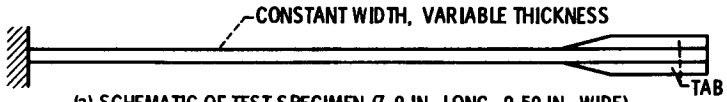

(a) SCHEMATIC OF TEST SPECIMEN (7.0 IN. LONG, 0.50 IN. WIDE).

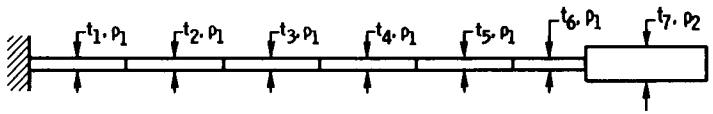

(b) SCHEMATIC OF NASTRAN MODEL (BAR ELEMENTS).

Figure 13. - Geometry and NASTRAN model for a composite angleplied laminate (t = thickness, ρ = density).

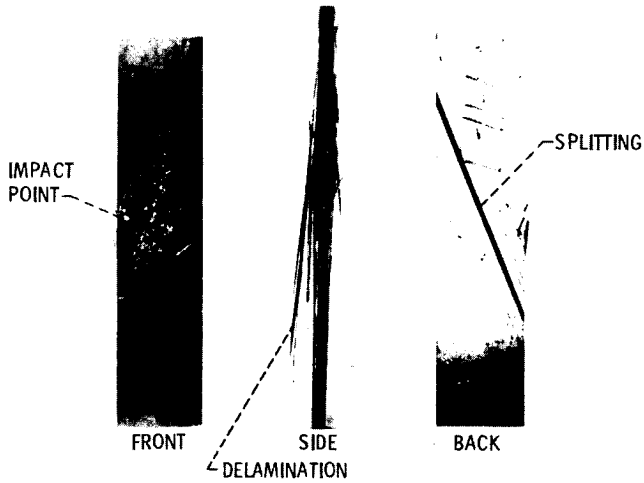

Figure 14. - Typical composite cantilever specimen after high velocity impact test (ref. 4).

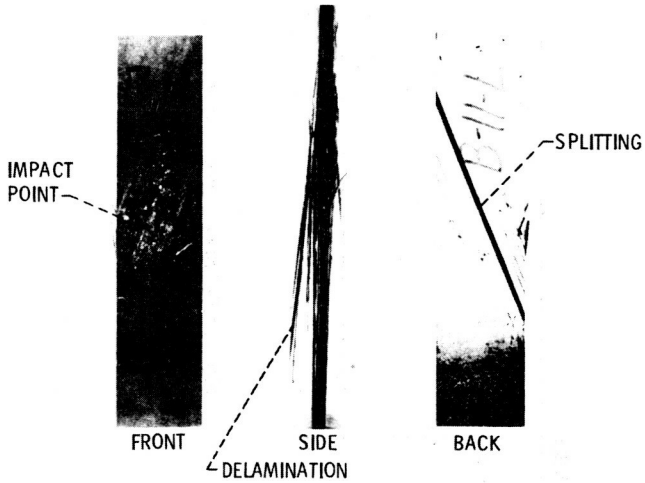

Figure 14. - Typical composite cantilever specimen after high velocity impact test (ref. 4).

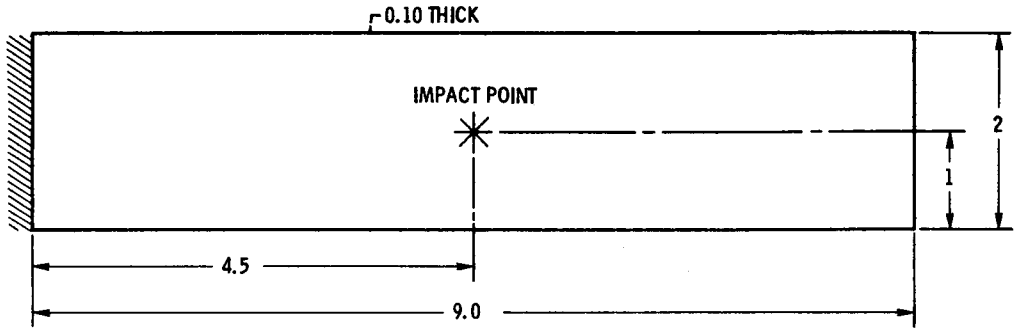

Figure 15. - Geometry of composite cantilever specimen for high velocity impact studies. (Dimensions are in inches.)

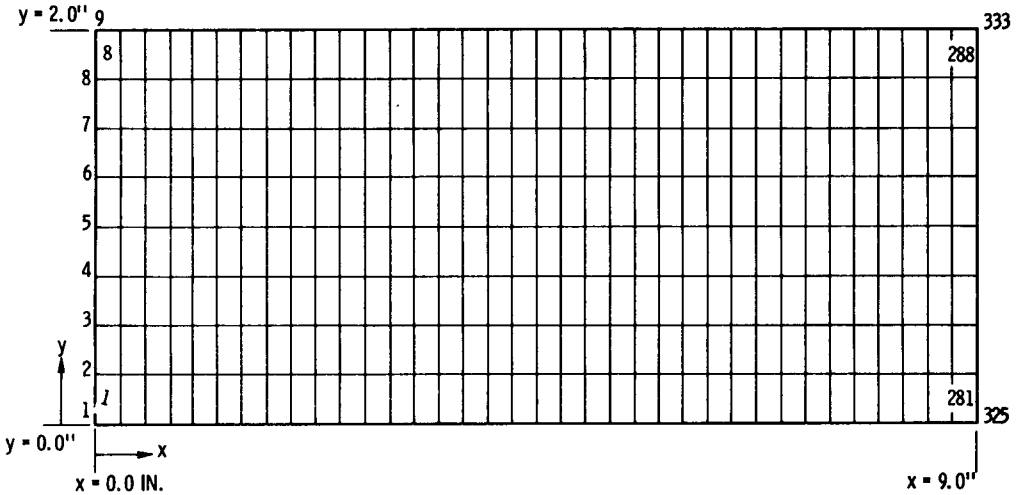

Figure 16. - NASTRAN model of the composite cantilever impact specimen (333 nodes; 288 CQUAD2 elements).

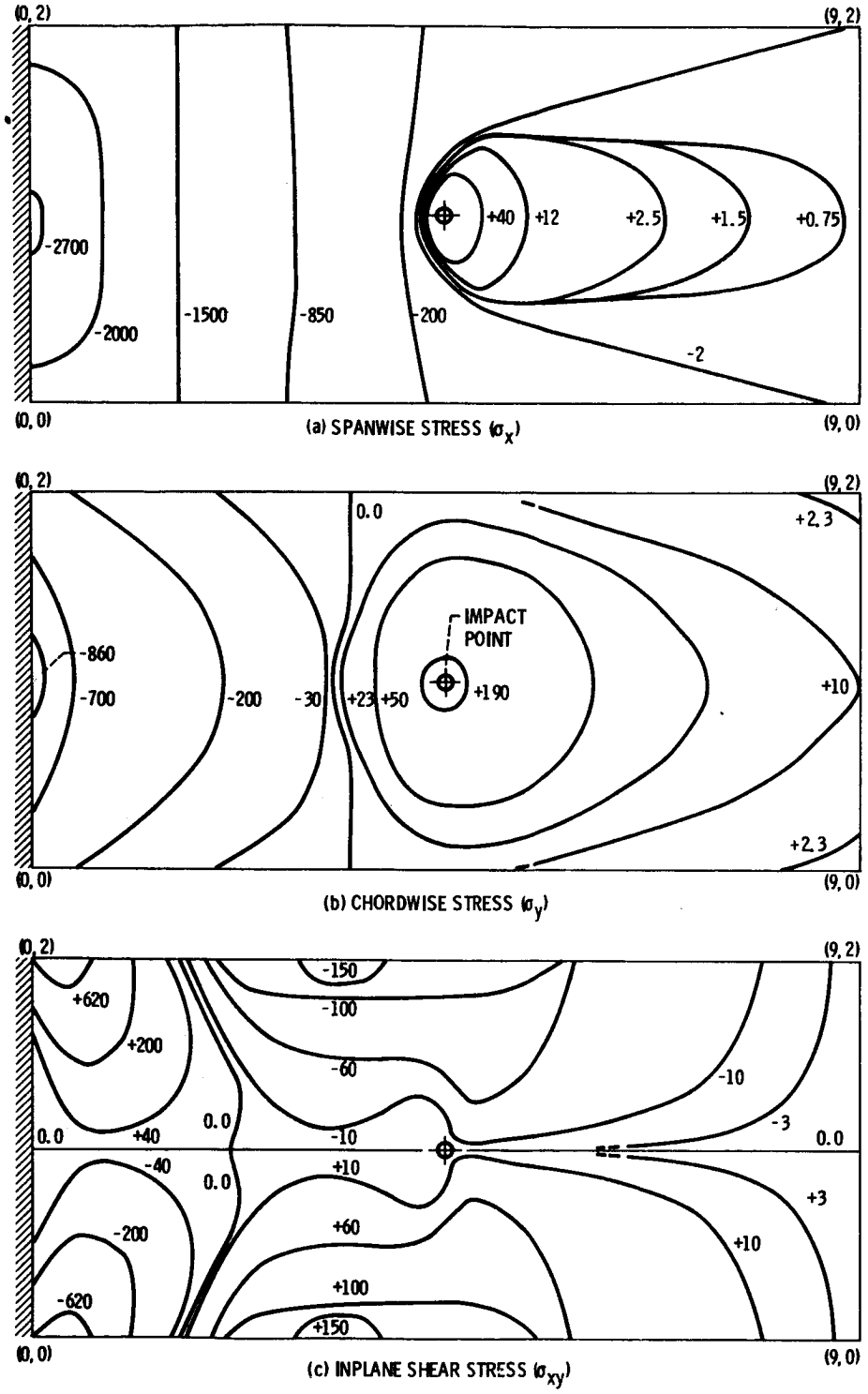

Figure 17. - NASTRAN predicted stress contours due to unit load at impact point (AS/S-GI intraply hybrid $[\pm 40, 0, 10, 0, -10]_s$).

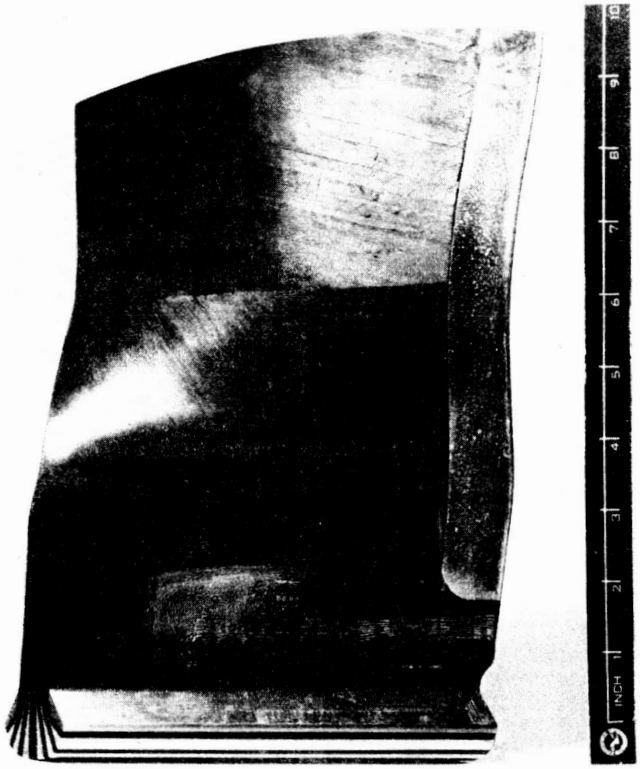

CS-76354

Figure 18. - Photograph of high-tip-speed composite blade. HTS/K601, (±40, ±20, 0).

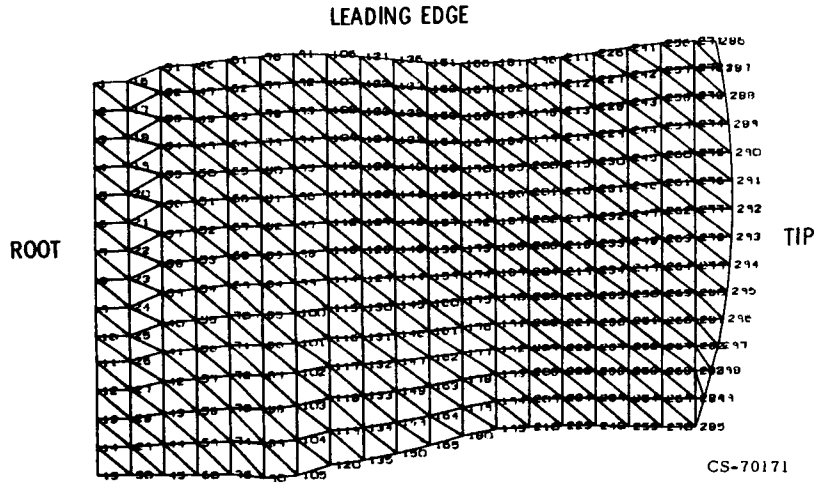

Figure 19. - NASTRAN finite element representation for fiber composite blade.

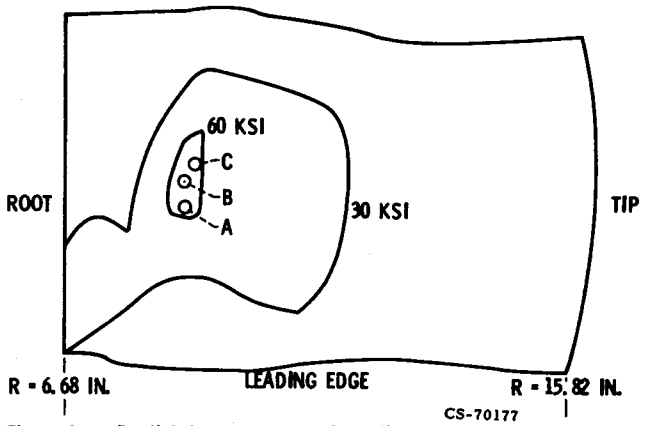

Figure 20. - Predicted average composite radial stress contours on pressure surface.

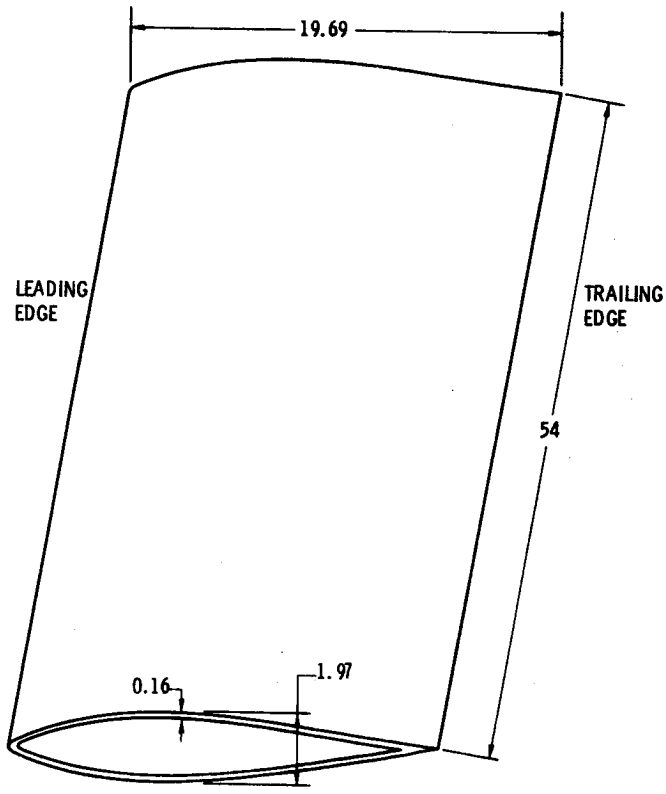

Figure 21. - Schematic of airfoil geometry (NACA 64A010; Dimensions in inches; laminate AS/E; $[(\pm 45)_2, 90_2, 0_{10}]_s$; attack angle $\approx 15^0$).

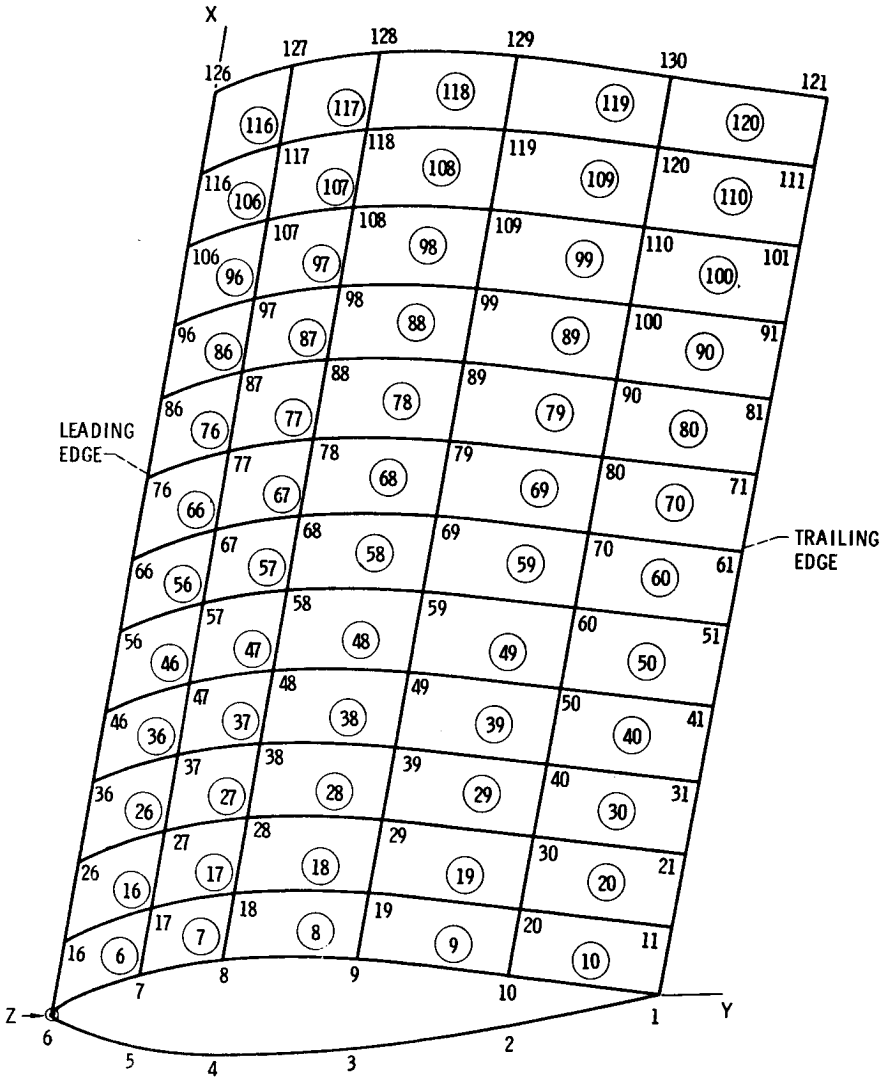

(a) SUCTION SURFACE.

Figure 22. - Airfoil NASTRAN model (130 nodes; 120 CQUAD2 elements).

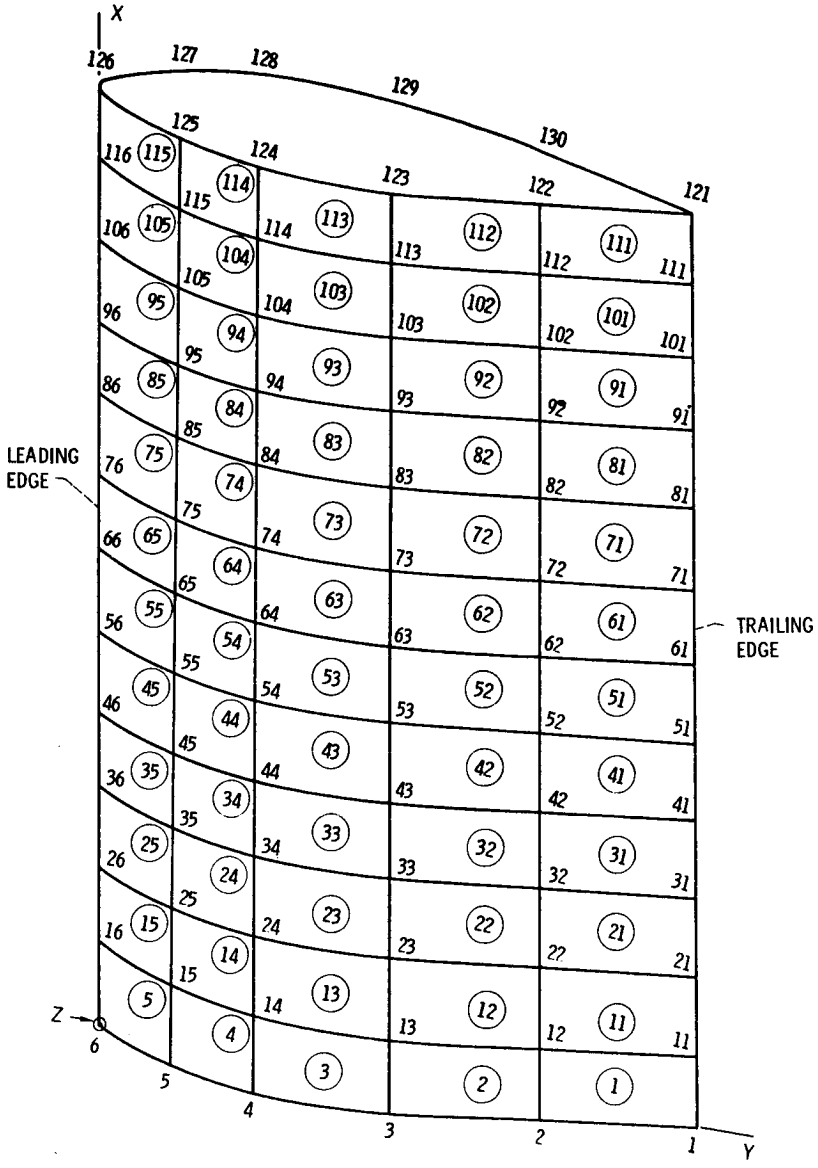

(b) PRESSURE SURFACE

Figure 22. - Concluded.

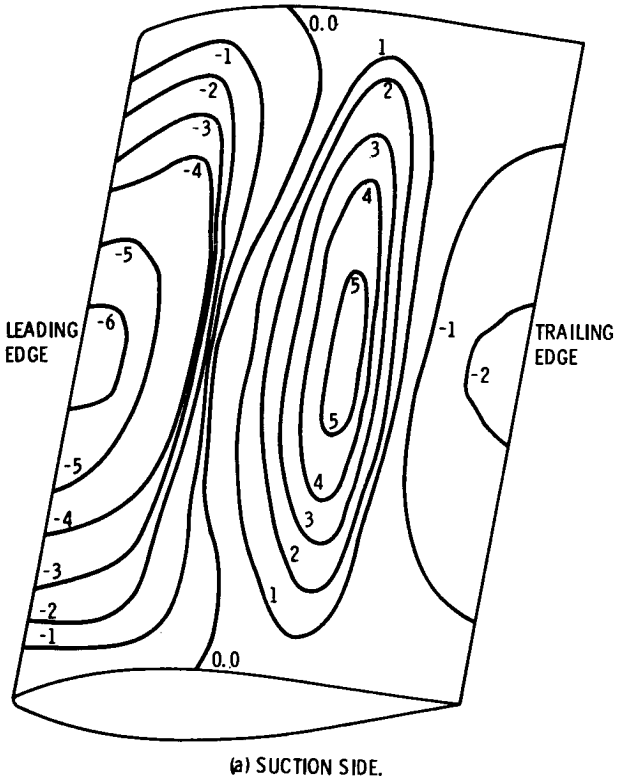

(a) SUCTION SIDE.

Figure 23. - NASTRAN predicted stress contour plots (ksi) in the spanwise direction on the outer surface of a composite airfoil (NACA 64A010).

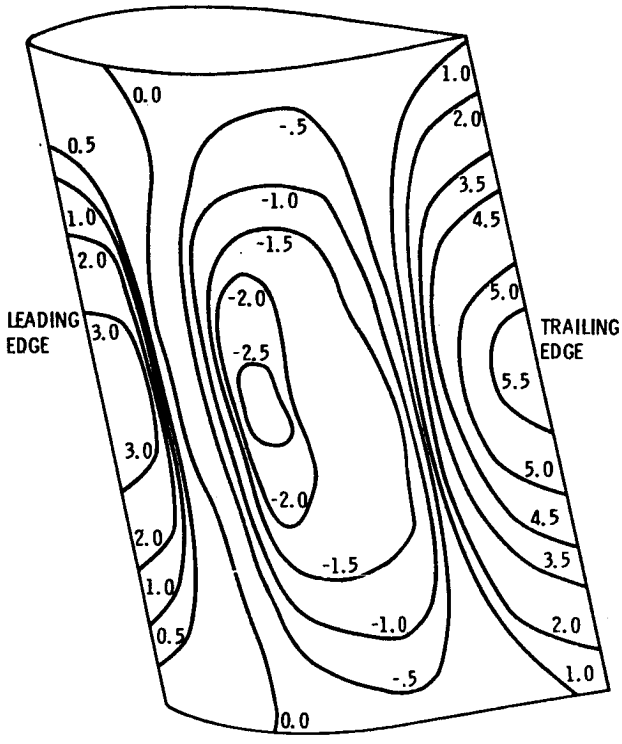

(b) PRESSURE SIDE.

Figure 23. - Concluded.

THE QUARTER-POINT QUADRATIC ISOPARAMETRIC ELEMENT AS A SINGULAR ELEMENT FOR CRACK PROBLEMS

M.A. Hussain, W.E. Lorensen and G. Pflegl
Department of the Army
Watervliet Arsenal
Watervliet, New York 12189

SUMMARY

The quadratic isoparametric elements which embody the inverse square root singularity are used for calculating the stress intensity factors at tips of cracks. The strain singularity at a point or an edge is obtained in a simple manner by placing the mid-side nodes at quarter points in the vicinity of the crack tip or an edge. These elements are implemented in NASTRAN as dummy elements. The method eliminates the use of special crack tip elements and in addition, these elements satisfy the constant strain and rigid body modes required for convergence.

INTRODUCTION

In "Crack Tip Finite Elements are Unnecessary", Henshell and Shaw (ref. 1) reported that the inverse of the Jacobian associated with the coordinate transformation becomes singular at a point when the mid-side nodes for two-dimensional eight-point quadrilateral elements are placed at quarter points. Interestingly enough, the same singularity was discovered independently by Barsoum (ref. 2) for two-dimensional, as well as, three-dimensional quadratic isoparametric elements. It was then natural to investigate the order of the singularity and it was found that the singularity was precisely of the order one-half for the strains, a phenomenon encountered in linear fracture mechanics. This remarkable phenomenon completely eliminates the necessity of incorporating special crack-tip elements (ref. 3, 4 and 5) and has additional advantages over the special crack-tip elements, namely; it satisfies constant strain and rigid body modes. The special crack-tip elements were introduced in the literature to avoid the extremely fine grid mesh required in the vicinity of the crack and the cumbersome extrapolation needed when using regular finite elements (ref. 6 and 7).

Advanced versions of NASTRAN (ref. 8), as well as some general purpose programs have such isoparametric elements. Hence, by judicious choice of nodes, accurate crack-tip elements can be formulated and stress intensity factors for cracks and flaws can be computed.

In this paper, after a brief review of the two and three-dimensional formulation, we discuss the implementation of the two-dimensional quadrilateral and three-dimensional brick elements as NASTRAN dummy user elements.

Lastly, test problems are done to assess the accuracy. Stress intensity factors are computed for a C-shaped specimen. The C-shaped fracture toughness method has been accepted by ASTM as a standard test for thick-walled cylinders.

SYMBOLS

(x,y)	Cartesian coordinates
(ξ,η)	Curvilinear coordinates
x_i,y_i,ξ_i,η_i	Grid point coordinates
N_i	Shape function at grid point i
u,v	Cartesian displacements
$\{\varepsilon\}$	Strain vector
$[J]$	Jacobian matrix
$\{\sigma\}$	Stress vector
$[D]$	Stress-strain matrix
$[K]$	Element stiffness matrix
E,G,ν	Elastic constants
K_I,K_{II}	Stress intensity factors
r,θ	Local cylindrical coordinates
$\{F\}^e$	Equivalent nodal forces

THE TWO-DIMENSIONAL CASE

Following the notation of Zienkiewicz (ref. 9) the eight node element in Cartesian coordinates (x,y) is formulated by mapping its geometry into the curvilinear space (ξ,η) of the normalized square $(-1 \leq \xi \leq 1,\ -1 \leq \eta \leq 1)$ by quadratic shape functions of the 'Serendipity' family (ref. 9):

$$x = \sum_{i=1}^{8} N_i(\xi,\eta)x_i \ ,$$

$$y = \sum_{i=1}^{8} N_i(\xi,\eta)y_i \ ,$$

$$N_i = [(1+\xi\xi_i)(1+\eta\eta_i) - (1-\xi^2)(1+\eta\eta_i) - (1-\eta^2)(1+\xi\xi_i)]\ \xi_i^2\ \eta_i^2/4 + (1-\xi^2)(1+\eta\eta_i)(1-\xi_i^2)\eta_i^2/2 + (1-\eta^2)(1+\xi\xi_i)(1-\eta_i^2)\ \xi_i^2/2 \ , \tag{1}$$

where N_i is the shape function at node i whose Cartesian and curvilinear coordinates are (x_i,y_i) and (ξ_i,η_i) respectively. The details of the shape functions and the numbering sequence are given in figure 1. The same shape functions are used to interpolate the displacements within the element, hence the name isoparametric:

$$u = \sum_{i=1}^{8} N_i(\xi,\eta)u_i \ ,$$

$$v = \sum_{i=1}^{8} N_i(\xi,\eta)v_i \ . \tag{2}$$

The stiffness matrix is found in the usual way as follows:

$$\{\varepsilon\} = \begin{Bmatrix} \varepsilon_x \\ \varepsilon_y \\ \gamma_{xy} \end{Bmatrix} = \begin{bmatrix} \frac{\partial}{\partial x} & 0 \\ 0 & \frac{\partial}{\partial y} \\ \frac{\partial}{\partial x} & \frac{\partial}{\partial y} \end{bmatrix} \begin{Bmatrix} u \\ v \end{Bmatrix} . \tag{3}$$

Substituting from equation (2) into equation (3) we have:

$$\{\varepsilon\} = [B] \begin{Bmatrix} \vdots \\ u_i \\ v_i \\ \vdots \end{Bmatrix} = [\ldots\ B_i\ \ldots] \begin{Bmatrix} \vdots \\ u_i \\ v_i \\ \vdots \end{Bmatrix} , \tag{4}$$

where

$$[B_i] = \begin{bmatrix} \frac{\partial N_i}{\partial x} & 0 \\ 0 & \frac{\partial N_i}{\partial y} \\ \frac{\partial N_i}{\partial x} & \frac{\partial N_i}{\partial y} \end{bmatrix} . \tag{5}$$

By the rules of partial differentiation we obtain

$$\begin{Bmatrix} \dfrac{\partial N_i}{\partial x} \\ \\ \dfrac{\partial N_i}{\partial y} \end{Bmatrix} = [J]^{-1} \begin{Bmatrix} \dfrac{\partial N_i}{\partial \xi} \\ \\ \dfrac{\partial N_i}{\partial \eta} \end{Bmatrix} \tag{6}$$

where [J], the Jacobian matrix, by virtue of equation (1) is given by

$$[J] = \begin{bmatrix} \dfrac{\partial x}{\partial \xi} & \dfrac{\partial y}{\partial \xi} \\ \\ \dfrac{\partial x}{\partial \eta} & \dfrac{\partial y}{\partial \eta} \end{bmatrix} = \begin{bmatrix} - - - & \dfrac{\partial N_i}{\partial \xi} & - - - \\ \\ - - - & \dfrac{\partial N_i}{\partial \eta} & - - - \end{bmatrix} \begin{bmatrix} | & | \\ | & | \\ x_i & y_i \\ | & | \\ | & | \end{bmatrix} . \tag{7}$$

The stress components are given by

$$\{\sigma\} = \begin{Bmatrix} \sigma_x \\ \sigma_y \\ \tau_{xy} \end{Bmatrix} = [D]\ \{\varepsilon\} \tag{8}$$

where [D] is the stress-strain matrix and for the case of plane stress is given by

$$[D] = \frac{E}{1-\nu^2} \begin{bmatrix} 1 & \nu & 0 \\ \nu & 1 & 0 \\ 0 & 0 & (1-\nu)/2 \end{bmatrix} . \tag{9}$$

The element stiffness matrix is then:

$$[K] = \int_{-1}^{1} \int_{-1}^{1} [B]^T[D][B]\ \det|J|\, d\xi d\eta\ . \tag{10}$$

The integration in equation (10) is done numerically by nine-point Gaussian quadrature as explained in reference 9.

THE CRACK TIP ELEMENT

It is clear from equations (4) and (6) that we need the inverse of Jacobian matrix [J] before the strains can be computed. Hence, whenever the inverse of [J] is singular or, equivalently, the determinant of [J] is zero, the strains and stresses become singular. This is simply accomplished by placing the mid-side nodes (e.g., nodes 5 and 8 of figure 1) at quarter points

from node 1 in Cartesian coordinates.

This can be illustrated by investigating the singularity along line 1-2 (η=-1) of figure 1. Evaluating the shape functions given in figure 1 at η=-1, we have the transformation

$$x = -1/2\ \xi(1-\xi)\ x_1 + 1/2\ \xi(1+\xi)\ x_2 + (1-\xi^2)\ x_5\ . \tag{11}$$

Choosing x_1=0, x_2=L and the quarter point x_5=L/4, equation (11) becomes

$$x = 1/2\ \xi(1+\xi)L + (1-\xi^2)\ L/4 \tag{12}$$

Solving for ξ we have

$$\xi = -1 + 2\sqrt{x/L}\ . \tag{13}$$

In this case the reduced Jacobian becomes

$$\frac{\partial x}{\partial \xi} = \frac{L}{2}\ (1+\xi) = \sqrt{xL}\ . \tag{14}$$

Equation (14) clearly indicates the singularity for the inverse of the Jacobian at x=0, ξ=-1. The order of singularity can be obtained from the displacement along line 1-2 (fig. 1). From equation (2) we have

$$u(\xi,-1) = -1/2\ \xi(1-\xi)u_1 + 1/2\ \xi(1+\xi)u_2 + (1-\xi^2)u_5\ ,$$

and writing in terms of x from equation (13) we have

$$u = -1/2(-1+2\sqrt{\tfrac{x}{L}})(2-2\sqrt{\tfrac{x}{L}})u_1 + 1/2(-1+2\sqrt{\tfrac{x}{L}})(2\sqrt{\tfrac{x}{L}})u_2+4(\sqrt{\tfrac{x}{L}} - \tfrac{x}{L})u_5\ . \tag{15}$$

Differentiating equation (15) we obtain the strains in the x-direction:

$$\varepsilon_x = \frac{\partial u}{\partial x} = -1/2[\frac{3}{\sqrt{xL}} - \frac{4}{L}]u_1+1/2[\frac{1}{\sqrt{xL}} + \frac{4}{L}]u_2+[\frac{2}{\sqrt{xL}} - \frac{4}{L}]u_5\ , \tag{16}$$

indicating the singularity of order one-half ($\frac{1}{\sqrt{x}}$), precisely the singularity needed for crack problems. It can be seen that equation (16) also incorporates constant strain terms.

We have only investigated the singularity at node 1 along line 1-2 of figure 1. However, the singularity at node 1 along any other ray emanating from node 1 is weaker than one-half. The singularity of order one-half can simply be achieved by collapsing grid points 1, 4 and 8 and placing grid points 5 and 7 at the quarter points in Cartesian coordinates as shown in figure 2. Without loss of generality we take the Cartesian coordinates as shown. Using equations (1) and (7) it can be shown that

$$\det.|J| = 1/16\ (1+\xi)^3\sin\alpha\ , \tag{17}$$

which vanishes for ξ=-1 for all η (i.e., along any ray from node 1). The

displacement, using polar coordinates ($x = r\cos\theta$, $y = r\sin\theta$) is given by:

$$u = 2r^{1/2}\frac{\cos^{1/2}(\theta-\alpha/2)}{\cos^{1/2}(\alpha/2)}\left[2\left(1-\frac{\cos^{1/2}(\theta-\alpha/2)}{\cos^{1/2}(\alpha/2)}r^{1/2}\right)\left\{-1/4(1-\eta)u_2 -1/4(1+\eta)u_3 + 1/2(1-\eta)u_5 + 1/2(1+\eta)u_7\right\} -1/4\eta(1-\eta)u_2 +1/4\eta(1+\eta)u_3 +1/2(1-\eta^2)u_6\right] \tag{18}$$

with

$$\eta = \frac{\tan(\theta-\alpha/2)}{\tan(\alpha/2)} . \tag{19}$$

Equation (18) indicates that the strains will have the necessary singularity of order one-half ($\frac{1}{\sqrt{r}}$) at the crack tip.

The stress intensity factors K_I and K_{II} are computed at the quarter points using the Westergaard near field displacements which, for plane stress, are given by (ref. 10).

$$\begin{aligned} u &= \frac{K_I}{G}\left(\frac{r}{2\pi}\right)^{1/2}\cos\theta/2\left[\frac{1-\nu}{1+\nu} + \sin^2\theta/2\right] + \frac{K_{II}}{G}\left(\frac{r}{2\pi}\right)^{1/2}\sin\theta/2\left[\frac{2}{1+\nu} + \cos^2\theta/2\right] \\ v &= \frac{K_I}{G}\left(\frac{r}{2\pi}\right)^{1/2}\sin\theta/2\left[\frac{2}{1+\nu} - \cos^2\theta/2\right] + \frac{K_{II}}{G}\left(\frac{r}{2\pi}\right)^{1/2}\cos\theta/2\left[-\frac{1-\nu}{1+\nu} + \sin^2\theta/2\right] \end{aligned} \tag{20}$$

Solving for K_I, K_{II} we have:

$$\begin{aligned} K_I &= G\left(\frac{2\pi}{r}\right)^{1/2}\frac{u\cos\theta/2\left[-\frac{2\nu}{1+\nu} + \cos^2\theta/2\right] + v\sin\theta/2\left[\frac{2}{1+\nu} + \cos^2\theta/2\right]}{\left[\frac{2}{1+\nu} - \cos^2\theta/2\right]\left[\frac{2}{1+\nu} - \cos^2\theta/2\right]} \\ K_{II} &= G\left(\frac{2\pi}{r}\right)^{1/2}\frac{u\sin\theta/2 - v\cos\theta/2}{\left[\frac{2}{1+\nu} - \cos^2\theta/2\right]} \end{aligned} \tag{21}$$

THE THREE-DIMENSIONAL CASE

The three-dimensional twenty-point isoparametric quadratic 'Brick' element is formulated in much the same way, by mapping the geometry into curvilinear space (ξ,η,ζ) of a normalized cube ($-1 \leq \xi,\eta,\zeta \leq 1$) by the quadratic shape function (ref. 9),

$$x = \sum_{i=1}^{20} N_i(\xi,\eta,\zeta)x_i \ ,$$

$$y = \sum_{i=1}^{20} N_i(\xi,\eta,\zeta)y_i \ ,$$

$$z = \sum_{i=1}^{20} N_i(\xi,\eta,\zeta)z_i \ ,$$

$$\begin{aligned} N_i = {} & 1/8(1+\xi\xi_i)(1+\eta\eta_i)(1+\zeta\zeta_i)(\xi\xi_i + \eta\eta_i + \zeta\zeta_i -2)\ \xi_i^2\ \eta_i^2\ \zeta_i^2 \\ & + 1/4(1-\xi^2)(1+\eta\eta_i)(1+\zeta\zeta_i)(1-\xi_i^2) \\ & + 1/4(1-\eta^2)(1+\xi\xi_i)(1+\zeta\zeta_i)(1-\eta_i^2) \\ & + 1/4(1-\zeta^2)(1+\xi\xi_i)(1+\eta\eta_i)(1-\zeta_i^2) \ , \end{aligned} \tag{22}$$

where N_i is the shape function at node i (i=1 to 20) whose Cartesian and curvilinear coordinates are (x_i, y_i, z_i) and (ξ_i, η_i, ζ_i) respectively. It should be noted that the shape function given in equation (22) is obtained by superposition of those given in reference 9. The geometry of the unit cube and the numbering sequence, as suggested by reference 11, is shown in figure 3.

For the isoparametric formulation and displacements are given by

$$\begin{aligned} u &= \sum_{i=1}^{20} N_i(\xi,\eta,\zeta)u_i \ , \\ v &= \sum_{i=1}^{20} N_i(\xi,\eta,\zeta)v_i \ , \\ w &= \sum_{i=1}^{20} N_i(\xi,\eta,\zeta)w_i \ . \end{aligned} \tag{23}$$

The rest of the analysis follows in a similar fashion that given for the two-dimensional case with appropriate augmentation to the three-dimensional quantities.

The singularity element is obtained by collapsing one face, 2376, and placing the midside nodes 9, 13, 11, 15 of figure 3 at quarter points. The singular element is shown in figure 4, in Cartesian coordinates. Since the elements are isoparametric they automatically satisfy inter-element compatibility and continuity in their regular or singular forms. It should be noted that the displacements are not singular. Further, it is easily shown that $\sum_i N_i=1$. Hence, by theorems given in reference 9 the elements satisfy the constant strain and rigid body modes. The above conditions are necessary for the 'patch test' mentioned in reference 2.

NASTRAN IMPLEMENTATION

The isoparametric quadratic quadrilateral and brick elements have been implemented using the NASTRAN dummy user element facility as outlined in Section 6.8.5 of reference 12. This involved coding element stiffness and stress data recovery subroutines using the analysis outlined above and relinking the affected NASTRAN Links. Additional modifications were required to some of the Output File Processor (OFP) routines. These changes are detailed below.

The quadrilateral element was implemented as a DUM1 element. Figure 5 shows the formats for the ADUM1, CDUM1 and PDUM1 cards. KDUM1, the element stiffness matrix subroutine, obtains material and grid point information from the element connection and property table (ECPT) and builds the matrices required to perform the integration in equation (10). The integration is performed numerically using compound 3-point Gaussian quadrature as explained in reference 9. This results in 9 evaluations of the integrand. Once the 16 by 16 stiffness matrix is complete, the appropriate 2 by 2 submatrices corresponding to the given pivot point are entered into the upper left of the 6 by 6 submatrices required by SMA1B, the stiffness matrix insertion subroutine. SMA1B is called 8 times for each pivot point. The time for element stiffness generation is 14 seconds per element on an IBM 360 model 44.

NASTRAN stress data recovery is accomplished in two phases. During phase I, SDUM11 calculates [D][B] from equations (5) and (9) for each grid point and passes the resultant 24 by 16 matrix to SDUM12 for final stress calculations. SDUM11 also checks for singularities in the inverse of the Jacobian (eq.(7)) and flags those grid points which have a singularity. Information passed to SDUM12 from SDUM11 includes the element id, grid point numbers, grid point singularity flag, coordinates of the eight grid points and the material constants E, G and ν. SDUM12, phase II of the stress recovery, locates the displacements associated with a given element and multiplies [D][B] times these displacements (eq. (4) and (8)) to give the stress components at each of the eight grid points. Grid point flags are checked for singular grid points and, if singularities exist, Mode I and Mode II stress intensity factors are calculated using equation (21). These stress intensity factors at the quarter points are output at the corner nodes of the collapsed side while the corresponding mid-side node stress output is set to zero. The point ids of the singular corner nodes are negated and the mid-side id is set to overflow the integer field specification, thus flagging the point with asterisks.

OFP has been modified to output the eight sets of stress components for each element. These modifications were implemented by adding heading formats to OFP1A and changing the appropriate pointers and format specifications in OFP1BD, OFP5BD and OF1PBD. Although the ADUM cards allow sufficient flexibility to implement the element stiffness subroutine, changes were required to GPTA1 which describes the connection and property characteristics of each element (see Section 2.5.2.1 in ref. 12). These changes were required to handle the expanded stress requirements. The number of words SDR2 passes from phase I to phase II was changed from 100 to 430 while the count of words SDR2 outputs for real stresses was increased from 10 to 33.

The implementation of the twenty node brick element was not as straightforward as that of the quadrilateral element. The brick was implemented as a DUM2 element. Figure 6 shows formats for the ADUM2, CDUM2 and PDUM2 cards. DIMENSION changes were required in TA1A and TA1B since NASTRAN assumes a maximum of 10 grid points per element. KDUM2 was initially implemented similarly to KDUM1. However, in this case, the integration using 3-point Gaussian quadrature requires 27 integrand evaluations with a stiffness matrix of order 60. The size of the KDUM2 subroutine necessitated a change to the overlay structure of LINK3, placing KDUM2 in its own overlay segment. Also, since NASTRAN calls the stiffness routines based upon the pivot point concept, the same brick element stiffness matrix is built twenty times in an analysis. This technique results in a 20 minute stay in SMA1 for a one element problem on an IBM 360 model 44. Changes are being made to KDUM2 to build each element stiffness matrix once and save it on auxiliary storage. When a request for an element stiffness matrix is made, KDUM2 will check auxiliary storage for a copy of the matrix. If it is not there, KDUM2 will build the matrix and add it to the file. If it is there, the matrix will be retrieved and not recalculated. Using this procedure, stiffness matrix generation should not exceed 2 minutes per element.

Stress data recovery is also non-standard for the brick element. Due to the size of the arrays used in stress recovery for the brick, phase I has a limited function of assembling arrays dependent on parameters not available to phase II. The majority of calculations for stress recovery are accomplished during phase II, saving storage but increasing stress recovery times. Quantities passed from phase I to phase II are the stress-strain matrix [D], the element id, grid point ids, grid point coordinates and the material constants E, G and ν. Phase II locates the displacements, calculates the stress components for each grid point, checks for singular Jacobians and calculates stress intensity factors as required. Stress intensity factors are displayed in a manner similar to that employed for the quadrilateral element.

OFP has been modified to output the twenty sets of stress components for each element. A DIMENSION change was also required in OFP to allow twenty grid points per element. OFP1A, OFP1BD, OFP5BD and OF1PBD were updated to produce the required heading and output formats. GPTA1 was changed to increase the number of words to 120 that SDR2 passes from phase I to phase II. The count of words SDR2 outputs for real stresses was increased to 141.

Both element implementations were checked independent of NASTRAN via dummy driver routines for SMA1 and SDR2. The coding for the element stiffness subroutines was verified by multiplying the stiffness matrix for one element times the known displacements for a uniform stress field. The resultant nodal loading was compared to that found analytically from (for the two-dimensional case)

$$\{F\}^e = \int_{-1}^{1}\int_{-1}^{1} [B]^T \{\sigma\}\, d\xi\, d\eta \tag{24}$$

Figure 7 illustrates equivalent nodal forces for $\sigma_y = 1$ on the normalized square $(-1 \leq x,y \leq 1)$. The stress recovery coding was checked by passing the known

displacements for a uniform stress field to the stress recovery subroutines and observing the constant stress results.

Implementation of the quadrilateral element was complete within a week of the completion of the analysis while the brick element implementation took 2 weeks because of the length of coding, overlay changes and NASTRAN changes to support more than 10 grid points.

NUMERICAL RESULTS

To assess the accuracy of the method, three test problems with fairly a coarse grid (68 elements and approximately 239 grid points) were run. The problems are the single edge crack, double edge crack and center crack. These three problems can be done in a single run as subcases with different single point constraints as shown in figures 8a, 8b, 8c. The solutions of above problems, by various methods, have been well documented (ref. 12). It was found that the finite element solutions were accurate to within 2-3%. Graphically, this is illustrated in figure 9 for the double edge crack by using the Westergaard near field solution (ref. 10) for σ_y.

ASTM has stringent requirements for the size of specimens for fracture toughness testing. However, in many applications of thick-walled cylinders these requirements are not easily met. The C-shaped specimen, which is easily obtained from thick-walled cylinders, was suggested (ref. 13) and is now accepted as a standard test for such cylindrical material. The stress intensity factors for such a section, shown in figure 10, were computed for different crack lengths and the finite element results, experimental results, and the collocation results of reference 13 are shown in figure 11. It is seen that remarkable agreement is obtained with just 48 elements and 171 grid points. The results have also been compared with those in reference 16 and similar correspondence was observed.

CONCLUSIONS

Quadratic isoparametric elements have been used to form a singular element for fracture mechanics analysis. These elements provide excellent results even with coarse grids as long as the singular elements strictly conform to the geometries of figures 2 and 4. The elements have been successfully implemented on NASTRAN Level 15.0 as dummy user elements.

REFERENCES

1. Henshell, R. D., and Shaw, K. G.: Crack Tip Elements are Unnecessary. Int. J. Num. Meth. Engrg, vol. 9, 1975, pp. 495-507.

2. Barsoum, Roshdy S.: On the Use of Isoparametric Finite Elements in Linear Fracture Mechanics. Int. J. Num. Meth. Engrg., vol. 10, 1976, pp. 25-76.

3. Tracey, D. M.: Finite Elements for Determination of Crack Tip Elastic Stress Intensity Factors. Eng. Fract. Mech., vol. 3, 1971, pp. 255-265.

4. Wilkinson, R. F., and Kelley, J. W.: A Failsafe Analysis Using NASTRAN's Piecewise Linear Analysis and a Nine Node Linear Element. NASTRAN: Users' Experiences, NASA TM X-3278, 1975, pp. 181-200.

5. Aberson, J. A. and Anderson, J. M.: Cracked Finite Elements Proposed for NASTRAN. NASTRAN: Users' Experiences, NASA TM X-2893, 1973.

6. Anderson, G. P., Ruggles, V. L., and Stibor, G. S.: Use of Finite Element Computer Programs in Fracture Mechanics. Int. J. Fract. Mech., vol. 7, March 1971, pp. 63-76.

7. Chan, S. K., Tuba, I. S., and Wilson, W. K.: On the Finite Element Method in Linear Fracture Mechanics. Eng. Fract. Mech., vol. 2, no. 1, 1970, pp. 1-17.

8. McDonough, J. R.,: A Survey of NASTRAN Improvements Since Level 15.5. NASTRAN: Users' Experiences, NASA TM X-3278, 1975, pp. 11-22.

9. Zienkiewicz, O. O.: The Finite Element Method in Engineering Science. McGraw Hill, London, 1971.

10. Fracture Toughness Testing and Its Applications. ASTM, STP 381, pp. 32-33.

11. Wahlstron, Stig: Solid Element Requirements for NASTRAN. NASTRAN Users' Experiences, NASA TM X-2378, 1971, pp. 797-811.

12. The NASTRAN Programmer's Manual. NASA SP-223(01), Sept. 1972.

13. Tada, H., Paris, C. P. and Irwin, G. R.: The Stress Analysis of Cracks Handbook. Del Research Corporation, 1973, pp. 2.1-2.11.

14. Kendall, D. P. and Hussain, M. A.: A New Fracture-Toughness Test Method for Thick-Walled Cylinder Material. Experimental Mechanics, April 1972, pp. 184-189.

15. Hussain, M. A., Lorensen, W. E., Kendall, D. P., and Pu, S. L.: A Modified Collocation Method for C-Shaped Specimens. Watervliet Arsenal Tech. Report, R-WVT-X-6-73, 1973.

16. Gross, B. and Srawley, J. E.: Analysis of Radially Cracked Ring Segments Subject to Forces and Couples. NASA TM X-71842, 1976.

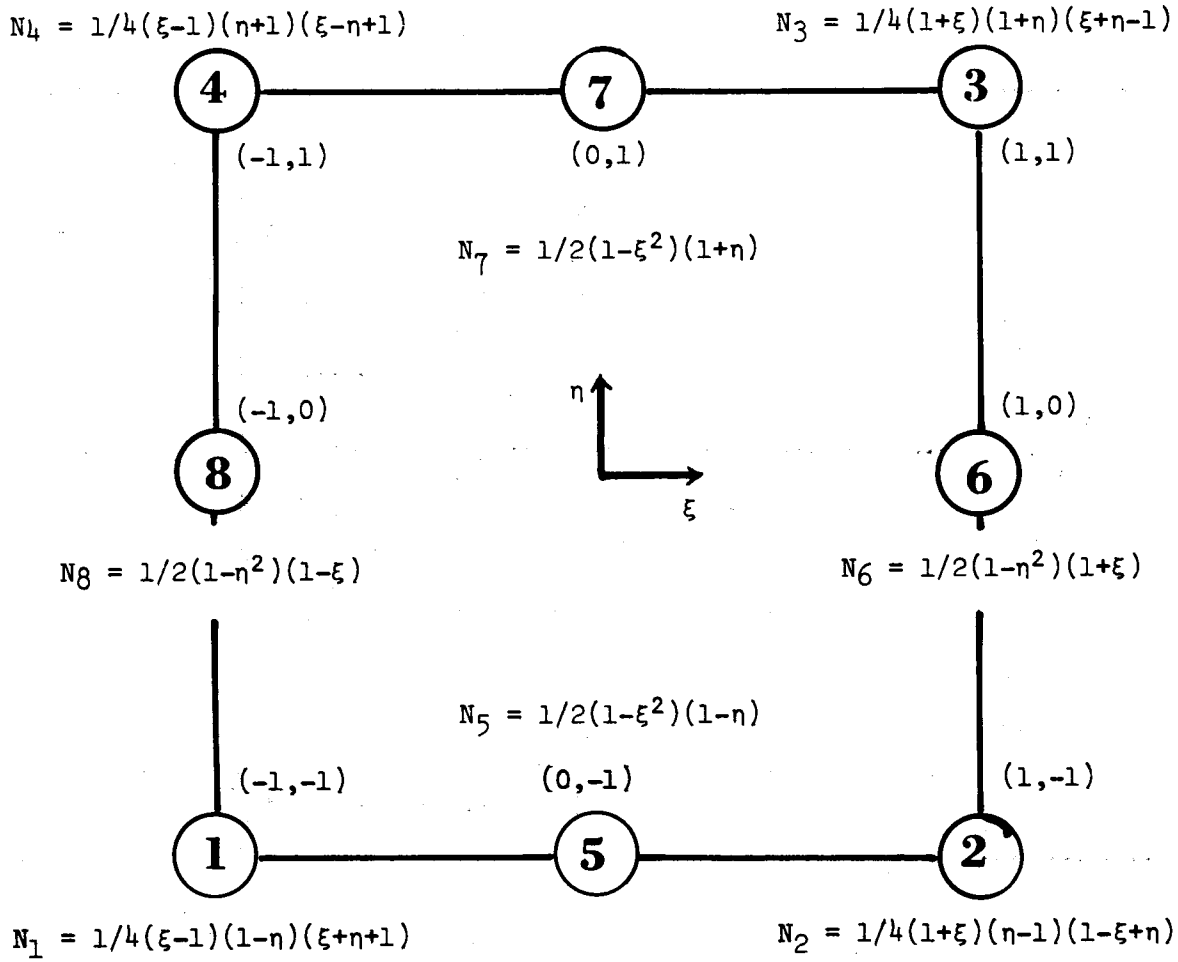

Figure 1. - Shape Functions and Numbering Sequence for Quadrilateral Element.

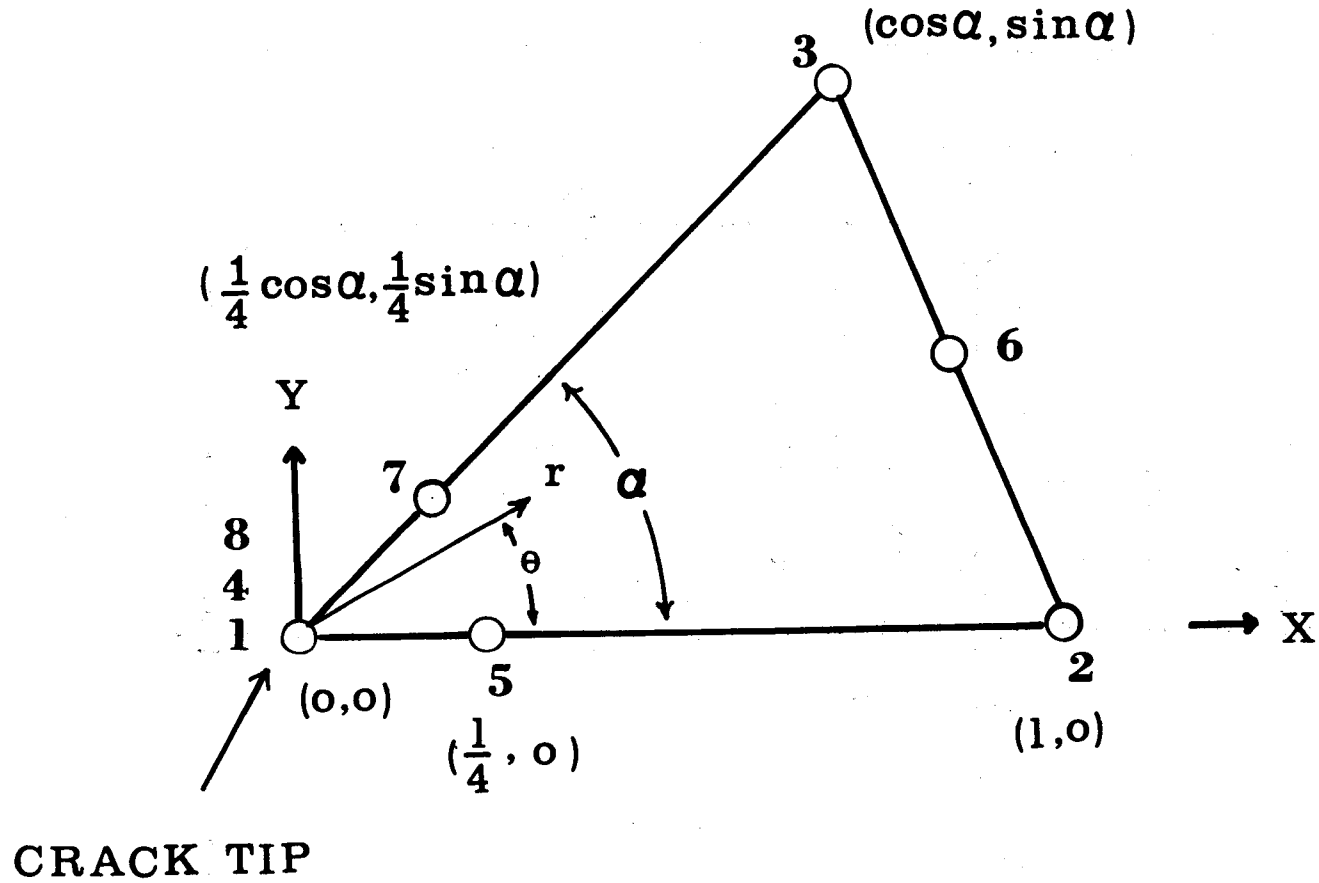

Figure 2. - Singularity Element Obtained by Collapsing 1, 4 and 8 and placing 5 and 7 at Quarter Points.

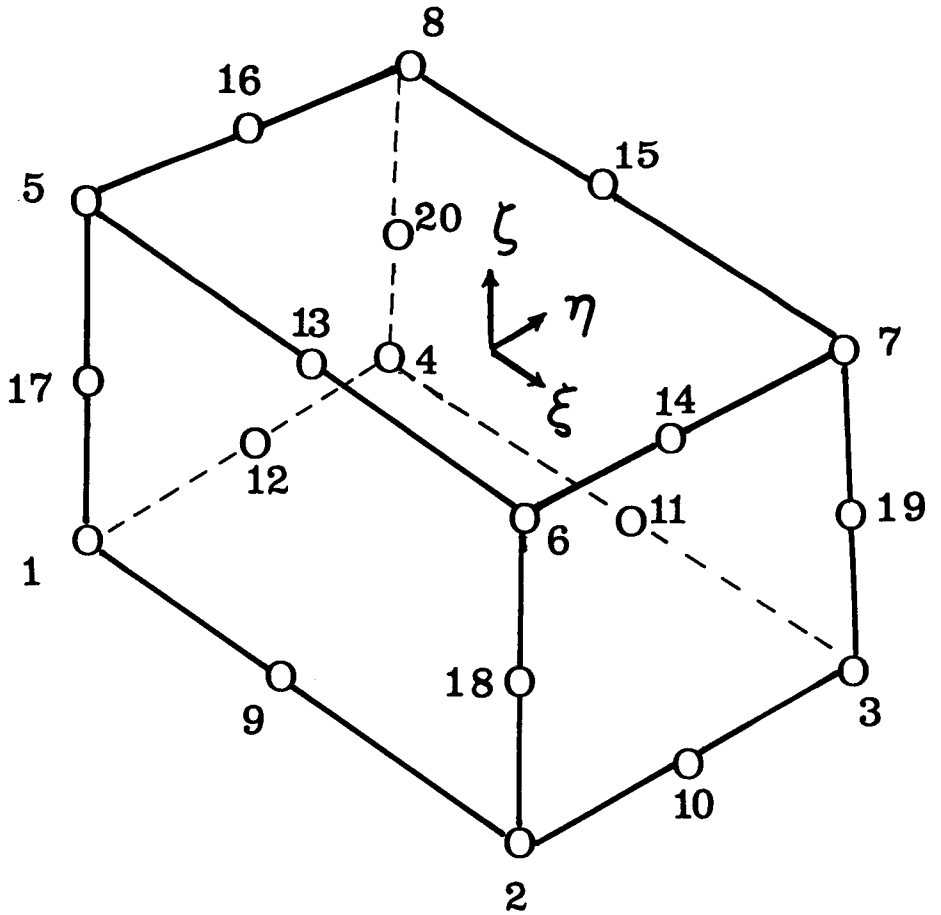

Figure 3. - Numbering Sequence of Isoparametric Quadratic 'Brick' Element.

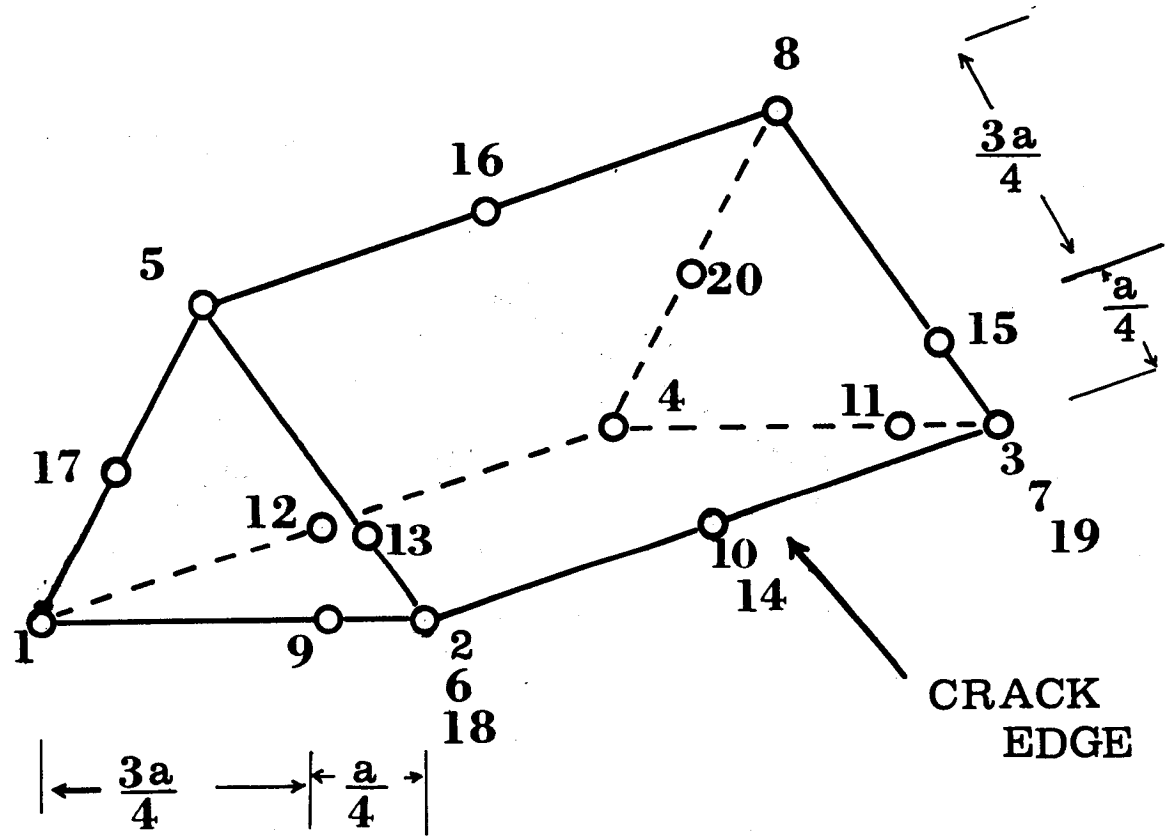

Figure 4. - Singularity Element Obtained by Collapsing the Face 2376 and Placing the Nodes 9, 13, 11 and 15 at Quarter Points.

ADUMi	NG	NC	NP	ND					
ADUM1	8	0	1	3					

CDUMi	EID	PID	G1	G2	G3	G4	G5	G6	abc
CDUM1	1	10	1	2	3	4	5	6	abc

+bc	G7	G8							
+bc	7	8							

PDUMi	PID	MID							
PDUM1	10	20							

Figure 5. Bulk Data Cards for Quadrilateral Element.

ADUMi	NG	NC	NP	ND					
ADUM2	20	0	1	3					

CDUMi	EID	PID	G1	G2	G3	G4	G5	G6	abc
CDUM2	1	10	1	2	3	4	5	6	abc

+bc	G7	G8	G9	G10	G11	G12	G13	G14	def
+bc	7	8	9	10	11	12	13	14	def

+ef	G15	G16	G17	G18	G19	G20			
+ef	15	16	17	18	19	20			

PDUMi	PID	MID							
PDUM2	10	20							

Figure 6. Bulk Data Cards for Brick Element.

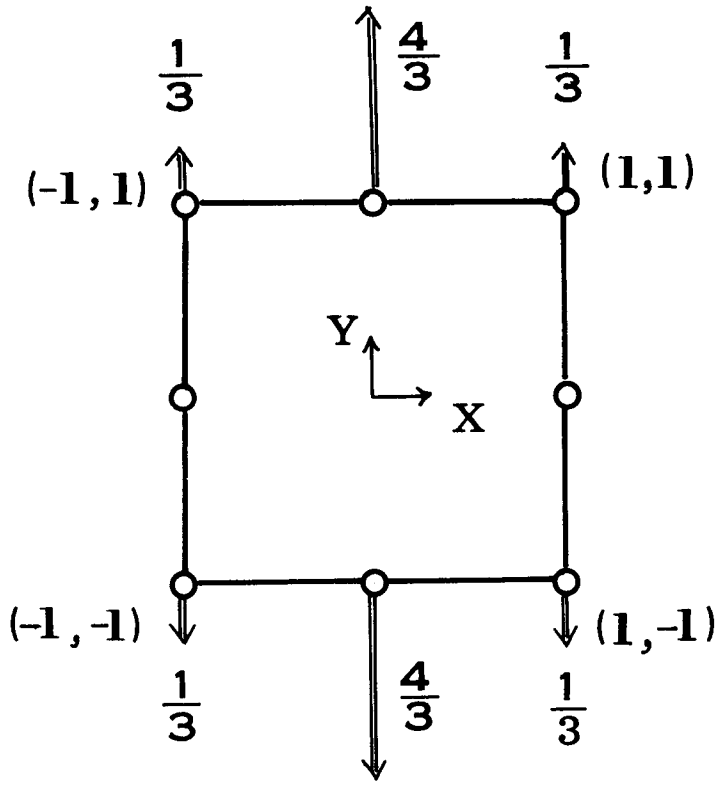

Figure 7. - Equivalent Nodal Forces Required for $\sigma y=1$.

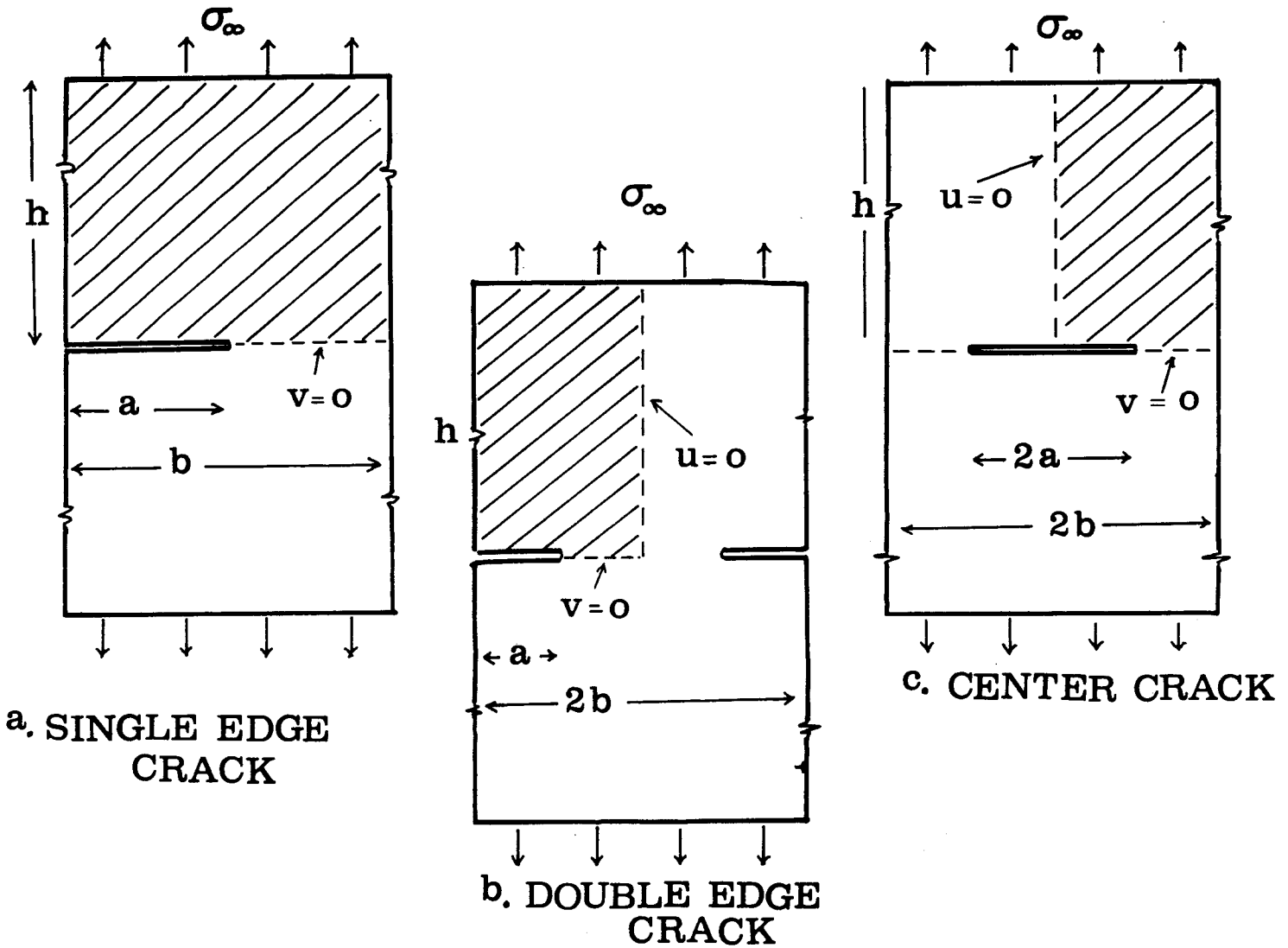

Figure 8. - Test Problem: Shaded Area Analysed by Finite Elements. ($\frac{a}{b} = \frac{1}{2}, \frac{h}{b} = 4$)

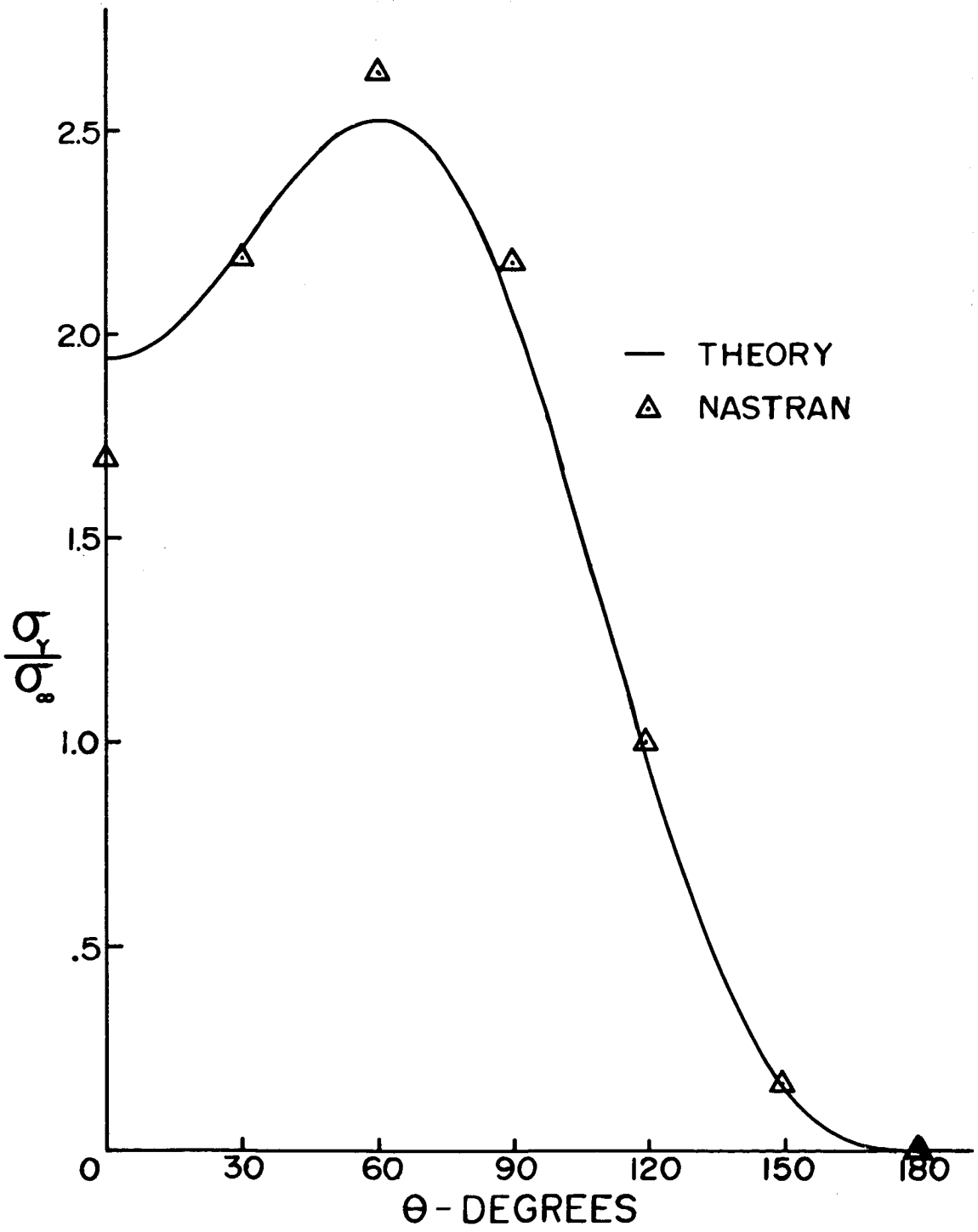

Figure 9. - Comparison of NASTRAN Results With the Theoretical Solution for Double-Edge Crack.

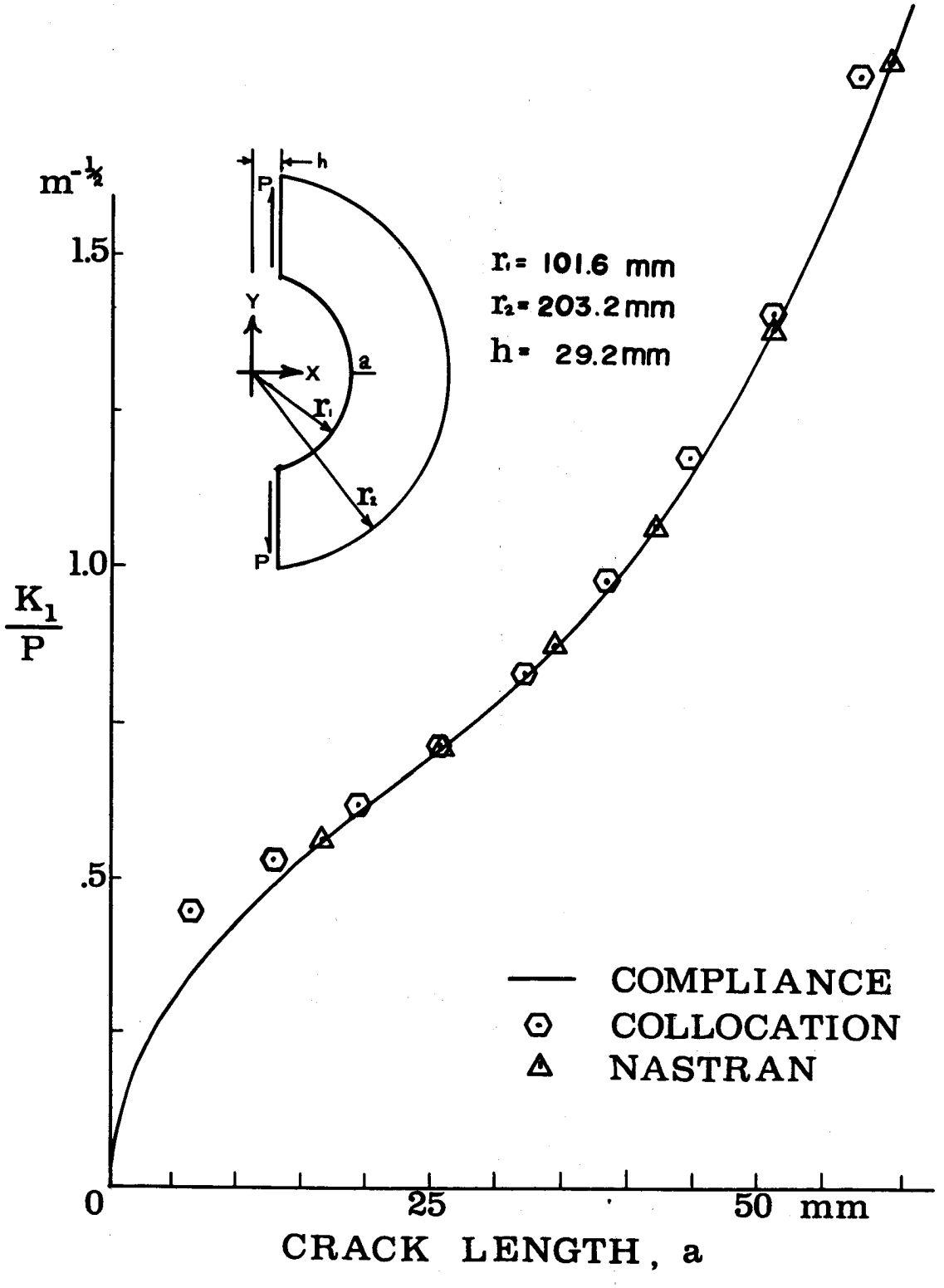

Figure 10. - Comparison of NASTRAN Results With Those Obtained Experimentally and by Collocation.

ADDITION OF HIGHER ORDER PLATE ELEMENTS TO NASTRAN

by

R. Narayanaswami
Department of Mechanical Engineering and Mechanics
Old Dominion University, Norfolk, Virginia

and

Chuh Mei
Vought Corporation, Hampton, Virginia

SUMMARY

Two plate elements, the linear strain triangular membrane element CTRIM6 and the higher order plate bending element CTRPLT1, have been added to NASTRAN Level 16.0. This paper describes the theoretical formulation, programming details, and bulk data information pertaining to the addition of these elements. Sample problems illustrating the use of these elements have been presented.

A triangular shallow shell element, CTRSHL, formulated from the above mentioned plate elements utilizing shallow shell theory, is under development. Details of formulation of the element are given.

With the addition of these elements, NASTRAN has excellent capability for solving plate and shell problems using the statics, normal modes, and buckling analyses rigid formats.

INTRODUCTION

NASTRAN presently (Level 16.0) has, in all, a total of ten different forms of plate elements in two different shapes (triangular and quadrilateral). The present NASTRAN triangular membrane element TRMEM, uses a linear displacement field and is found to be overly stiff; the basic bending element, TRBSC, the basic unit from which the bending properties of the other plate elements are formed, is also found to be very stiff due to the constraint of normal slope having to vary linearly on the exterior edges of the element. The higher order membrane and bending plate elements (given the mnemonic of TRIM6 and TRPLT1, respectively) available in the literature (refs. 1 and 2) are found to be more accurate and computationally more efficient than the existing NASTRAN plate elements. In this paper, the addition of these elements into the Level 16 version of NASTRAN is described.

A triangular shallow shell element formulated from the above mentioned elements utilizing shallow shell theory (mnemonic: TRSHL) is also being added into the Level 16.0 version of NASTRAN. Addition of this element is nearing completion; details of the use of this element are also given in this paper.

LIST OF SYMBOLS

a,b	lengths
a_i, c_i, d_i, h_i	coefficients
C_i	constants
D	bending rigidity
E	Young's modulus
I	moment of inertia
L	length
m, n	number of nodal lines
M	moment forces
N	membrane force
P	applied load

SYMBOLS (CONT'D)

R	radius
T	temperature
t	thickness
X, Y, Z	global coordinates
x, y, z	element coordinates
u, v, w	displacements
α, β	rotations
δ	deflection
ε	strain
κ	rate of taper
λ	buckling factor
υ	Poisson's ratio
ρ	mass density
Ω	frequency parameter
ω	circular frequency

Special Symbols

,	denotes derivative

Subscripts

o	denotes value at end of beam
mn	number of nodal lines
1,2	denotes value at top and bottom of column
x,y	in x and y direction
cr	critical

TRIANGULAR MEMBRANE ELEMENT, TRIM6

The present development is based on the derivation in reference 1. The important characteristics of the element are that

1. The stresses and strains vary linearly within the element.
2. Bilinear variation in the planar co-ordinates for the thickness of the element is permitted.
3. Bilinear variation in the planar co-ordinates for the temperature in the element is provided.
4. Currently the use of the element is limited to solving problems using Rigid Formats 1 and 3.

Element Geometry and Derivation of Matrices

The geometry of the element is shown in figure 1. The element has six grid points, three at the vertices and three at the mid-points of the sides. u and v are components of displacements parallel to the x and y axes of the element co-ordinate system and are assumed to vary quadratically with position on the surface of the element.

$$u = a_1 + a_2x + a_3y + a_4x^2 + a_5xy + a_6y^2 \tag{1}$$

$$v = a_7 + a_8x + a_9y + a_{10}x^2 + a_{11}xy + a_{12}y^2 \tag{2}$$

The undetermined coefficients a_1 to a_{12} can be related to the 12 components of the element displacement vector.

The thickness t of the element, and also the temperature T, at any point (x,y) within the element are given by

$$t = c_1 + c_2x + c_3y \tag{3}$$

$$T = d_1 + d_2x + d_3y \tag{4}$$

The coefficients c_1, c_2, and c_3, as also d_1, d_2, and d_3, can be evaluated from the user specified values for t and T, respectively, at the three vertices of the element.

The derivation of the element stiffness matrix, consistent mass matrix and consistent thermal load vector follows familiar lines (see, for example, ref. 3) and will not be described here. The stresses are evaluated at the three vertices and the centroid of the element. Execution time to evaluate the stiffness matrix is 0.16 sec. per element in single precision and 0.23 sec. per element in double precision on the CDC 6600 machine.

Two new bulk data cards have been added to the NASTRAN bulk data deck for using the TRIM6 element. They are the connection and property cards for the element, viz, the CTRIM6 and PTRIM6 cards, and are given in Appendix A. Some examples of the application of the element are given in Appendix B. Excellent agreement with plane stress elasticity and experimental solutions is shown even for coarse mesh subdivisions.

TRIANGUALR PLATE ELEMENT, TRPLT1

The mnemonic of TRPLT1 will be used to refer to this element. The important characteristics of the element are:

1. Bilinear variation in the planar co-ordinates for the thickness of the element is permitted.
2. Bilinear variation in the planar co-ordinates for the temperature in the element is provided for in the element dependent subroutine for the calculation of the thermal load vector. However, this capability can be operational in NASTRAN only after provision for specification of grid point temperature gradients is made.
3. Transverse shear flexibility is taken into account in the element stiffness formulation.
4. Currently, the use of the element is limited to solving problems using Rigid Formats 1 and 3.

Element Geometry and Derivation of Matrices

The geometry of the element is shown in figure 2. The element has six grid points, three at the vertices and three at the mid-points of the sides. The deflection w(x,y) within the element is assumed to vary as a quintic polynomial in the local co-ordinates, i.e.,

$$
\begin{aligned}
w(x,y) = {} & a_1 + a_2 + a_3 y + a_4 x^2 + a_5 xy + a_6 y^2 + a_7 x^3 \\
& + a_8 x^2 y + a_9 xy^2 + a_{10} y^3 + a_{11} x^4 + a_{12} x^3 y \\
& + a_{13} x^2 y^2 + a_{14} xy^3 + a_{15} y^4 + a_{16} x^5 + a_{17} x^4 y \\
& + a_{18} x^3 y^2 + a_{19} x^2 y^3 + a_{20} xy^4 + a_{21} y^5
\end{aligned}
\tag{5}
$$

The element has 18 d.o.f., viz, the transverse displacement w, rotation about x-axis, α, and rotation about y-axis, β, at the six grid points of the element. Three constraints among the coefficients of eq. (5) are now introduced so that the normal slope varies cubically along each edge. Thus the 18 independent coefficients of eq. (5) can be related to the 18 d.o.f. of the element. The thickness, t, of the element, and the temperature, T, in the element, at any point (x,y) within the element are given by equations (3) and (4), respectively.

Examples of the application of the element for classical plate bending problems are given in reference 4 and show the excellent accuracy of the element for such problems. Additional problems showing the use of the element for variable thickness plates are given in Appendix C. Two new bulk data cards have been added to the NASTRAN bulk data deck for using the TRPLT1 element. They are the connection and property cards for the element, viz , the CTRPLT1 and PTRPLT1 cards, and are given in Appendix A. Execution time to evaluate the stiffness matrix is 0.987 sec. per element in single precision and 1.579 sec. per element in double precision on the CDC 6600 machine.

TRIANGULAR SHALLOW SHELL ELEMENT, TRSHL

The mnemonic of TRSHL will be used to refer to this element. The important characteristics of the element are:

1. Bilinear variation in the planar co-ordinates for the thickness of the element is permitted.
2. Bilinear variation in the planar co-ordinates for the temperature in the element is provided for in the element dependent subroutine for calculation of the thermal load vector. However, only the calculations for membrane effect utilize this feature at present; the calculations for the bending effect will be operational only after provision for specification of grid point temperature gradients is made.

Element Geometry and Derivation of Matrices

The geometry of the element is shown in fig. 3. The shell shape is defined by the height, $z(x,y)$, above the base plane in which x,y are taken as local co-ordinates and X,Y,Z are the global co-ordinates. The shell surface over each element is approximated as a quadratic polynomial

$$z(x,y) = h_1 + h_2x + h_3y + h_4x^2 + h_5xy + h_6y^2 \tag{6}$$

The membrane displacements u and v are assumed to vary as quadratic polynomials as in equations (1) and (2). The normal displacement w is assumed to vary as a quintic polynomial as in equation (5). From the shallow shell theory of Novozhilov (ref. 5), the membrane strains are given by

$$\left.\begin{aligned} \varepsilon_{xx} &= u_{,x} - z_{,xx}w \\ \varepsilon_{yy} &= v_{,y} - z_{,yy}w \\ \varepsilon_{xy} &= u_{,y} + v_{,x} - 2z_{,xy}w \end{aligned}\right\} \tag{7}$$

The element has 6 grid points and 5 d.o.f. per grid point in the element co-ordinate system. As in the case of TRPLT1, the three constraint equations are introduced so that the normal slope varies cubically along each edge. Additional details of formulation of the element and application of the element to solve shell problems are given in reference 6. Two new bulk data cards for the element, viz , CTRSHL and PTRSHL cards, that have been added to the NASTRAN bulk data deck are given in Appendix A. Two example problems illustrating the use of the shell element is given in Appendix D.

CONCLUDING REMARKS

Two plate type elements, a linear strain membrane element (TRIM6) and a higher order bending element (TRPLT1), have been added to a proprietary version of NASTRAN Level 16.0. The addition of a triangular shallow shell element is in advanced stages of completion. The theoretical formulation, bulk data information and example problems pertaining to these elements are discussed in this paper. The example problems illustrate the excellent accuracy of these elements for solution of plate and shell problems for statics, vibration and buckling rigid formats.

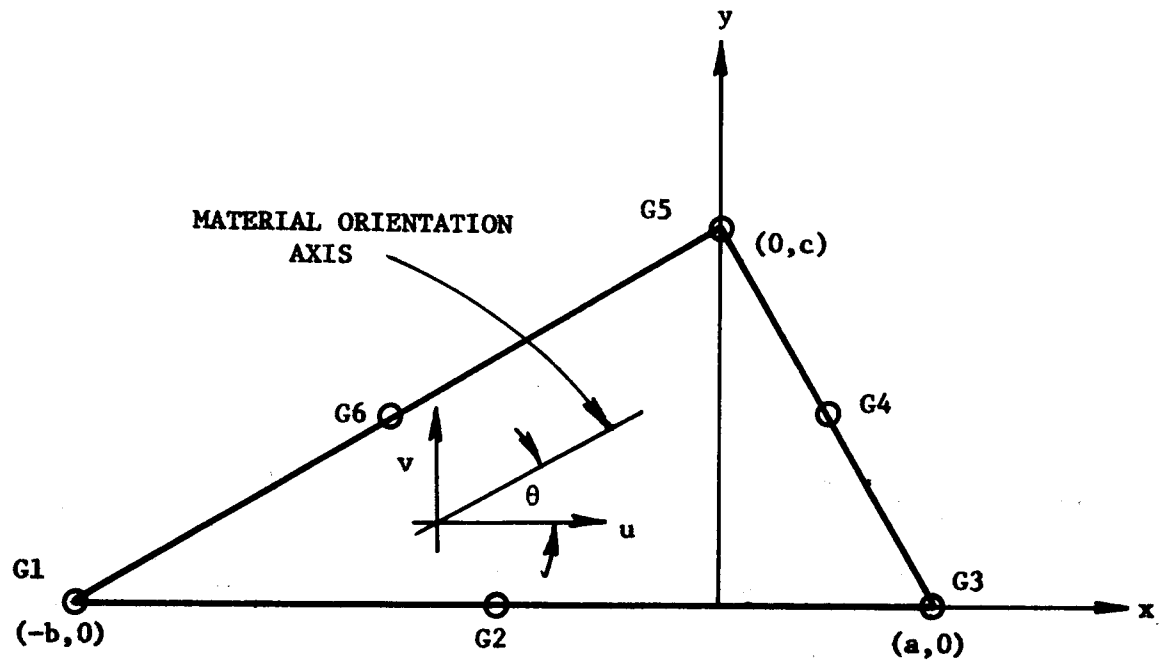

Figure 1. TRIM6 membrane element in element coordinate system.

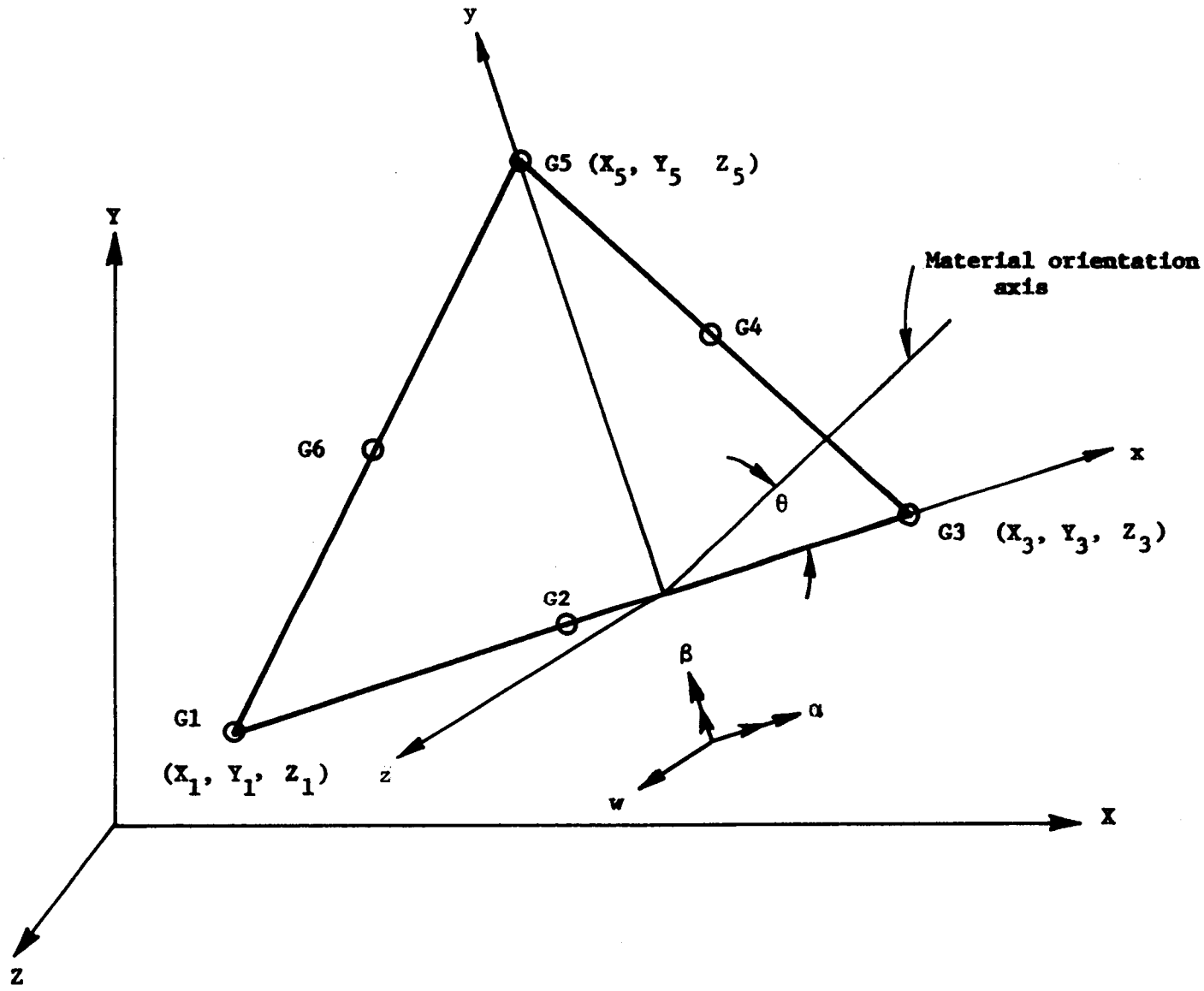

Figure 2. TRPLT1 triangular bending element geometry.

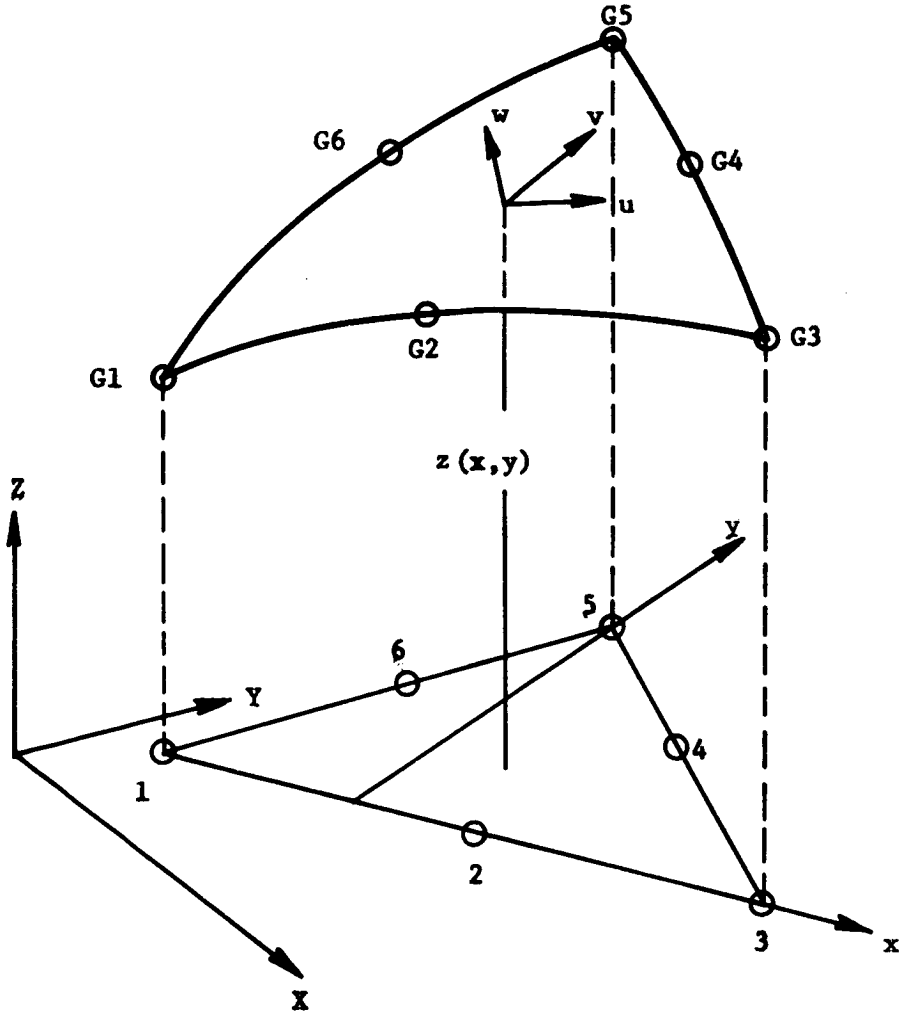

Figure 3. TRSHL shell element geometry and coordinate systems.

BULK DATA DECK

Input Data Card CTRIM6 Triangular Element Connection

Description: Defines a linear strain triangular membrane element (TRIM6) of the structrual model.

Format and Examples:

1	2	3	4	5	6	7	8	9	10
CTRIM6	EID	PID	G1	G2	G3	G4	G5	G6	+abc
CTRIM6	220	666	100	110	120	210	220	320	+C3

+abc	TH								
+C3	1.2								

Field	Contents
EID	Element identification number (Integer > 0)
PID	Identification number of PTRIM6 property card (Default is EID) (Integer > 0)
G1, G2, G3, G4, G5, G6	Grid point identification numbers of connection points (Integers > 0; G1 ≠ G2 ≠ G3 ≠ G4 ≠ G5 ≠ G6)
TH	Material property orientation angle in degrees (Real) The sketch below gives the sign convention for TH.

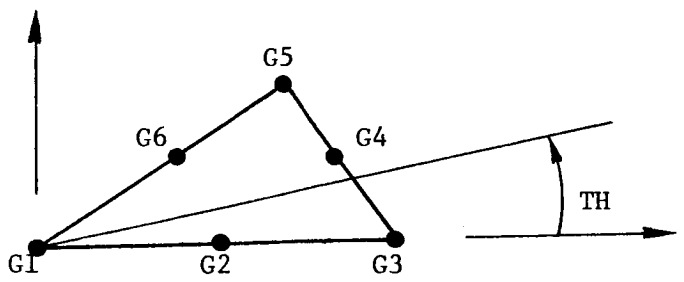

Remarks:

1. Element identification numbers must be unique with respect to all other element identification numbers.
2. Interior angles must be less than 180°.
3. The gridpoints must be listed consecutively going around the perimeter in an anticlockwise direction and starting at a vertex.

4. G2, G4, and G6 are assumed to lie at the midpoints of the sides. The locations of these gridpoints (on GRID Bulk Data cards) are used only for global coordinate system definition, GPWG (weight generator module), centrifugal forces, and deformed structure plotting.
5. Continuation card must be present.

Input Data Card PTRIM6 Triangular Membrane Property

Description: Used to define the properties of a linear strain triangular membrane element. Referenced by the CTRIM6 card. No bending properties are included.

Format and Example:

1	2	3	4	5	6	7	8	9	10
PTRIM6	PID	MID	T1	T3	T5	NSM			
PTRIM6	666	999	1.17	2.52	3.84	8.3			

Field	Contents
PID	Property identification number (integer > 0)
MID	Material identification number (integer > 0)
T1, T3, T5	Membrane thickness at the vertices of the element (Real)
NSM	Nonstructural mass per unit area (Real)

Remarks:

1. All PTRIM6 cards must have unique property identification numbers.

2. For structural problems, the material may be MAT1 or MAT2.

3. The thickness varies linearly over the triangle. If T3 or T5 is specified 0.0 or blank, it will be set equal to T1.

Input Data Card CTRPLT1 Triangular Element Connection

Description: Defines a triangular bending element (TRPLT1) of the structural model.

Format and Example:

1	2	3	4	5	6	7	8	9	10
CTRPLT1	EID	PID	G1	G2	G3	G4	G5	G6	+abc
CTRPLT1	160	20	120	10	30	40	70	110	+ABC

+abc	TH								
+ABC	16.2								

Field	Contents
EID	Element identification number (Integer > 0)
PID	Identification number of PTRPLT1 property card (Default is EID) (Integer > 0)
G1, G2, G3, G4, G5, G6	Grid point identification numbers of connection points (integer > 0: G1 ≠ G2 ≠ G3 ≠ G4 ≠ G5 ≠ G6)
TH	Material property orientation angle in degrees (Real)- The sketch below gives the sign convention for TH.

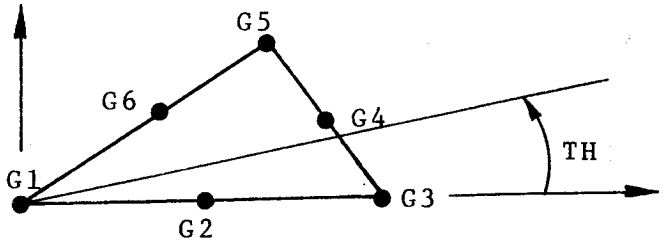

Remarks:

1. Element identification numbers must be unique with respect to all other element identification numbers.

2. Interior angles must be less than 180°.

3. The grid points must be listed consecutively going around the perimeter in an anticlockwise direction and starting at a vertex.

4. Continuation card must be present.

Input Data Card PTRPLT1 Triangular Plate Property

Description: Used to define the bending properties of a triangular plate element. Referenced by the CTRPLT1 card. No membrane properties are included.

Format and Example:

1	2	3	4	5	6	7	8	9	10
PTRPLT1	PID	MID1	I1	I3	I5	MID2	TS1	TS3	+abc
PTRPLT1	15	25	20.0	30.0	40.0	35	3.0	1.15	+PQR

+abc	TS5	NSM	Z11	Z21	Z13	Z23	Z15	Z25	
+PQR	1.0	9.0	1.5	-1.5	2.0	-2.0	2.5	-2.5	

Field	Contents
PID	Property identification number (Integer > 0)
MID1	Material identification number for bending (Integer > 0)
I1, I3, I5	Bending area moment of inertia per unit width at the grid points G1, G3, G5, respectively (Real > 0.0) ; $I1 = T_1^3/12$, $I3 = T_3^3/12$, $I5 = T_5^3/12$ where T_1, T_3, T_5 are the thickness of the element at the vertices, respectively.
MID2	Material identification number for transverse shear (Integer > 0)
TS1, TS3, TS5	Transverse Shear thickness at the grid points G1, G3, G5, respectively.
NSM	Nonstructural mass per unit area (Real)
Z11, Z21, Z13 Z23, Z15, Z25	Fiber distances for stress computation at grid points G1, G3, G5, respectively, positive according to the right-hand sequence defined on the CTRPLT1 card (Real)

Remarks:

1. All PTRPLT1 cards must have unique property identification numbers.

2. If TS1 is zero, the element is assumed to be rigid in transverse shear.

3. If TS3 or TS5 is 0.0 or blank, it will be set equal to TS1.

4. IF I3 or I5 is 0.0 or blank, it will be set equal to I1.

5. The stresses at the centroid are computed at the top and bottom fibers.

Input Data Card CTRSHL **Triangular Shell Element Connection**

Description: Defines a triangular thin shallow shell element (TRSHL) of the structural model.

Format and Example:

1	2	3	4	5	6	7	8	9	10
CTRSHL	EID	PID	G1	G2	G3	G4	G5	G6	+abc
CTRPLT	160	20	120	10	30	40	70	110	+ABC

+abc	TH								
+ABC	16.2								

Field	Contents
EID	Element identification number (Integer > 0)
PID	Identification number of PTRSHL property card (Default is EID) (Integer > 0)
G1, G2, G3, G4, G5, G6	Grid point identification numbers of connection points (integer > 0: G1 ≠ G2 ≠ G3 ≠ G4 ≠ G5 ≠ G6)
TH	Material property orientation angle in degrees (Real) - The sketch below gives the sign convention for TH.

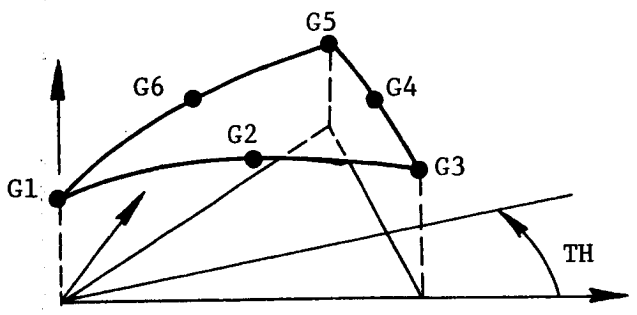

Remarks:

1. Element identification numbers must be unique with respect to all other element identification numbers.

2. Interior angles must be less than 180°.

3. The grid points must be listed consecutively going around the perimeter in an anticlockwise direction and starting at a vertex.

4. Continuation card must be present.

Input Data Card PTRSHL Triangular Shell Property

Description: Used to define the bending properties of a triangular shell element. Referenced by the CTRSHL card.

Format and Example:

1	2	3	4	5	6	7	8	9	10
PTRSHL	PID	MID1	T1	T3	T5	MID2	I1	I3	+abc
PTRSHL	10	20	3.0	6.0	4.0	30	2.25	18.0	+PQR

+abc	I5	MID3	TS1	TS3	TS5	NSM	Z11	Z21	+def
+PQR	5.33	40	2.5	5.0	3.5	50	1.5	-1.5	+STU

+def	Z13	Z23	Z15	Z25					
+STU	3.0	-3.0	2.0	-2.0					

Field	Content
PID	Property Identification number (Integer > 0)
MID	Material identification number for membrane effect (Integer > 0)
T1, T3, T5	Thickness for membrane action at vertices 1,3,5 of the elements (Real > 0.0)
MID2	Material identification number for bending effects (Integer > 0)
I1, I3, I5	Area moments of inertia of the element at the vertices 1,3,5 of the element. (Real > 0.0)
MID3	Material identification number for transverse shear (Integer > 0)
TS1, TS3, TS5	Transverse shear thickness (Real > 0.0) at the vertices 1, 3, 5, of the element.
NSM	Non-structural mass per unit area (Real)
Z11, Z12, Z13, Z23, Z15, Z25	Fiber distances for stress computation at grid points G1, G3, G5, respectively, positive according to the right-hand sequence defined on the CTRSHL card (Real > 0.0)

Remarks:

1. All PTRSHL cards must have unique property identification numbers.

2. If T3 or T5 equal to 0.0, or blank, they will be set equal to T1.

3. If I3 or I5 equal to 0.0, or blank, they will be set equal to I1.

4. If TS3 or TS5 equal to 0.0, or blank, they will be set equal to TS1.

5. If TS1 is 0.0, or blank, the element is assumed to be rigid in trasnverse shear.

6. The stresses at the centroid will be computed at the top and bottom fibers.

APPENDIX B

RESULTS OF TRIANGULAR MEMBRANE ELEMENT

The triangular membrane element is used to solve two static beam problems. The first one is a cantilever beam subjected to linear thermal gradient over the depth as shown in figure B1(a). The temperature is 188.71°K (-120°F) at the top surface, and 322.04°K (120°F) at the bottom surface of the beam. This problem was analyzed in reference 7 for demonstration of the isoparametric solid elements. The same material properties which were given in reference 7 are used in the analysis. The beam was modeled with eight TRIM6 elements. Results for the tip displacement using TRIM6, IHEXi and theoretical solution are shown in table B1. It is demonstrated that excellent accuracy has been obtained using TRIM6 with as few as eight elements.

The second problem is a cantilever beam of variable cross section under a concentrated force of 133.85 lb. (595.39 N) at the free end as shown in figure B1(b). The exact deflection is given by

$$\left.\begin{aligned} \delta y &= 3.2727 \frac{P}{E} \left\{ \frac{1}{b^2} \left[ax + \frac{bx^2}{2} - \frac{a}{b} \left\{ (a + bx) \log (a + bx) - (a + bx) \right\} \right] + C_1 x + C_2 \right\} \\ &\text{where} \\ a &= 100.0 \\ b &= 1.0 \\ C_1 &= -(150.0 - 100 \log 150) \\ C_2 &= -(6250.0 - 100.0 (150 \log 150 - 150)) - 50\, C_1 \end{aligned}\right\} \text{(B1)}$$

Four TRIM6 elements were used to model the beam. NASTRAN and theoretical results for lateral deflections along the length of the beam are shown in table B2.

TABLE B1. TIP DEFLECTIONS FOR A CANTILEVER BEAM SUBJECTED TO LINEAR THERMAL GRADIENT

	Tip deflection δ_y, cm
IHEX1 (216 Elements)	3.668
IHEX2 (36 Elements)	3.932
IHEX3 (8 Elements)	3.894
TRIM6 (8 Elements)	3.858
Theoretical Solution	3.762

TABLE B2. DEFLECTIONS FOR A CANTILEVER BEAM OF VARIABLE CROSS SECTION UNDER A CONCENTRATED FORCE AT THE FREE END

$\frac{x}{L}$	Deflection, inch (cm)	
	NASTRAN TRIM6	Exact
0.25	.006722 (0.0171)	.006878 (0.0175)
0.50	.025601 (0.0650)	.025658 (0.0652)
0.75	.053129 (0.1349)	.053141 (0.1350)
1.00	.085662 (0.2176)	.085410 (0.2169)

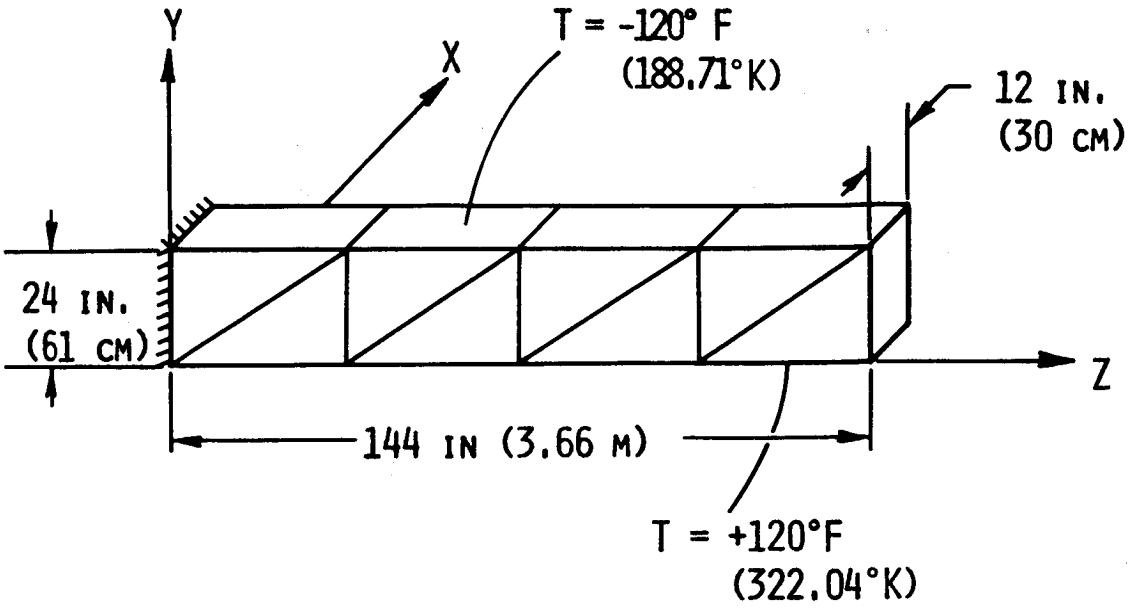

(A) UNIFORM CANTILEVER BEAM UNDER THERMAL LOADING.

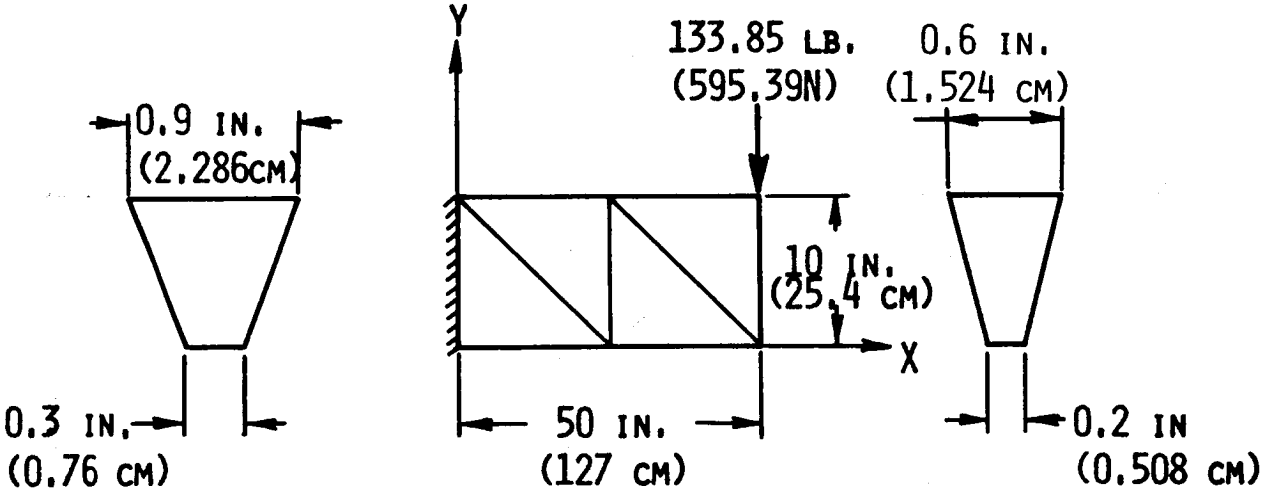

(B) TAPERED CANTILEVER BEAM UNDER CONCENTRATED LOAD.

FIGURE B1. BEAM GEOMETRY AND FINITE ELEMENT IDEALIZATION FOR THE MEMBRANE ELEMENT (TRIM6) TEST PROBLEMS.

APPENDIX C

RESULTS OF TRIANGULAR PLATE ELEMENT

The triangular bending element is used to solve problems in vibration and buckling of thin isotropic plates.

Vibration Problems

Two vibration problems were analyzed. The first one is a linearly tapered simply supported rectangular plate shown in figure C1 (a). The plate thickness is given by

$$t = t_o \left(1 + \kappa \frac{x}{a}\right) \tag{C1}$$

where κ is a constant determining the rate of taper. Two different mesh sizes of the finite element model, 1 x 2 and 2 x 4, are used. Due to symmetry, only half of the plate is used in the analysis. Nondimensional fundamental frequencies for rectangular plates for three different aspect ratios $\frac{a}{b}$ and κ = 0.5 and 0.8 are presented in table C1. The frequency parameter is defined as:

$$\Omega = \omega a^2 \sqrt{\frac{\rho t_o}{D_o}} \tag{C2}$$

where ω is the circular frequency, a is the length, ρ is the mass density, t_o is thickness and D_o is the bending rigidity. Analytical results from reference 8 are also shown for comparison.

The second problem is vibration of a linearly tapered rectangular cantilever plate. The plate is idealized with a mesh size of 2 x 4, or 16 elements, as shown in figure C1 (b). Results of frequency parameters Ω_{mn} as defined in equation (C2), where m and n represent the number of nodal lines perpendicular and parallel to the support, respectively, using TRIA2 and TRPLT1 are shown in table C2. Constant thicknesses of 0.0405 in (0.1029 cm) and 0.1215 in (0.3086 cm) was used when modeling with TRIA2 element. Experimental data obtained by Plunkett in reference 9 are also given. Tables C1 and C2 showed that very good results have been obtained using the higher order plate element. For lower modes, NASTRAN TRIA2 also gave good results.

Buckling Problems

The out-of-plane buckling of plate elements is evaluated from the differential stiffness matrix of bending plate element TRPLT1 due to membrane prestress effects obtained from a membrane analysis using TRIM6 elements. To solve out-of-plane buckling of plates, a membrane-bending combination element is necessary. TRSHL is such a combination element with the added feature of membrane bending coupling for shell problems. For pure plate problems, where the curvature is zero, there is no coupling between membrane and bending effects and for such cases TRSHL reduces to a combination element. The results of plate buckling in this section are obtained using TRSHL elements. Since the addition of TRSHL into the NASTRAN program is not yet complete, the results for problems in this section have been obtained from a stand-alone version.

Three buckling problems were investigated using the triangular plate and membrane elements. The first one is buckling of a tapered column or truncated pyramid shown in figure C2 (a). The area moment of inertia at any cross section can be expressed in the form

$$I_x = I_1 \left(\frac{x}{a}\right)^4 \tag{C3}$$

where I_1 is the moment of inertia at the top of the column ($x = a$). Results for the buckling factor for a tapered column of $\frac{I_1}{I_2} = 0.2$ from NASTRAN using TRIA2 and TRPLT1, and an analytical solution from reference 10 are given in table C3 for comparison. Monotonic convergence characteristics of the buckling factor are observed with TRSHL element although quite slow. Results given by NASTRAN TRIA2 elements appear to diverge from the exact solution. The slow convergence of TRSHL results and the apparent divergence of TRIA2 results may be due to the modeling of the beam using these plate elements instead of using beam type finite elements. The buckling factor is defined by the expression:

$$P_{cr} = \lambda \frac{EI_2}{L^2} \tag{C4}$$

where I_2 is the moment of inertia at the lower end of the column.

The second problem is a simply supported square plate subjected to uniform compression in one direction. Owing to symmetry, only one

quarter of the plate (modeled with 2 x 2 mesh size) is used as shown in figure C2 (b). Results of the buckling factor from NASTRAN TRIA2 and TRSHL elements and the exact solution are shown in table C4. The nondimensional buckling factor λ is represented by the formula

$$N_{cr} = \lambda \frac{\pi^2 D}{b^2} \tag{C5}$$

The third problem considered is buckling of a simply supported rectangular plate of aspect ratio $\frac{a}{b} = 0.8$ under inplane bending loading shown in figure C2 (c). Due to symmetry, only half of the plate is used in the analysis. NASTRAN results using TRIA2 and TRSHL with different mesh sizes are shown in table C5, along with analytical results from reference 10. Table C5 clearly shows that the TRSHL elements gave a much better prediction of the critical buckling load than the TRIA2 elements.

TABLE C1. FUNDAMENTAL FREQUENCY FOR LINEARLY TAPERED RECTANGULAR PLATES SIMPLY SUPPORTED ON ALL EDGES: $\nu = 0.3$

Aspect ratio $\frac{a}{b}$	NASTRAN TRPLT1 Finite element layout	Frequency parameter $\Omega = \omega a^2 \left(\frac{\rho t_0}{D_0}\right)^{1/2}$	
		Taper rate $\kappa = 0.5$	Taper rate $\kappa = 0.8$
0.5	1 x 2	14.662	16.242
	Theory	15.304	16.994
1.0	1 x 2	24.171	26.901
	2 x 4	24.454	—
	Theory	24.556	27.354
2.0	1 x 2	58.560	64.770
	2 x 4	60.346	—
	Theory	60.982	67.500

TABLE C2. FREQUENCY PARAMETERS FOR A LINEARLY TAPERED RECTANGULAR CANTILEVER PLATE; $\nu = 0.3$

Mode		Frequency parameter $\Omega_{mn} = \omega_{mn} a^2 \left(\frac{\rho t_0}{D_0}\right)^{1/2}$		
		NASTRAN		Experiment
m	n	TRIA2	TRPLT1	
0	0	2.28	2.25	2.47
1	0	9.8	10.0	10.6
0	1	14.5	13.6	14.5
1	1	23.8	27.0	28.7
0	2	35.9	32.8	34.4
0	3	51.5	47.3	47.4
2	0	31.0	53.3	52.5
1	2	64.0	57.7	54.0

TABLE C3. BUCKLING FACTOR FOR A TAPERED COLUMN

	Buckling factor $\lambda = \frac{P_{cr}L^2}{EI_2}$		
	Finite Element layout		
		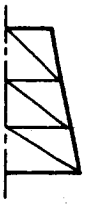	
TRIA2	1.4242	1.3618	1.3420
TRSHL	1.6437	1.6050	1.5853
Theory	1.505		

TABLE C4. BUCKLING FACTOR FOR SIMPLY SUPPORTED SQUARE PLATE UNIFORMLY COMPRESSED IN ONE DIRECTION; $\nu = 0.3$

	Buckling factor $\lambda = \frac{N_{cr}b^2}{\pi^2 D}$
TRIA2	4.0356
TRSHL	3.9779
Exact	4.0000

TABLE C5. BUCKLING FACTOR FOR A SIMPLY SUPPORTED RECTANGULAR PLATE OF ASPECT RATIO 0.8 UNDER INPLANE BENDING; $\nu = 0.3$

	Buckling factor $\lambda = \frac{(N_o)_{cr} b^2}{\pi^2 D}$		
	Finite element layout		
	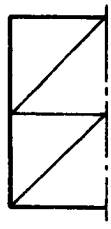	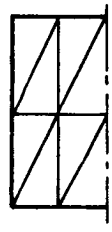	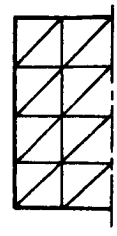
TRIA2	29.7815	35.3289	23.8702
TRSHL	24.5507	24.1103	24.1708
Theory	24.4		

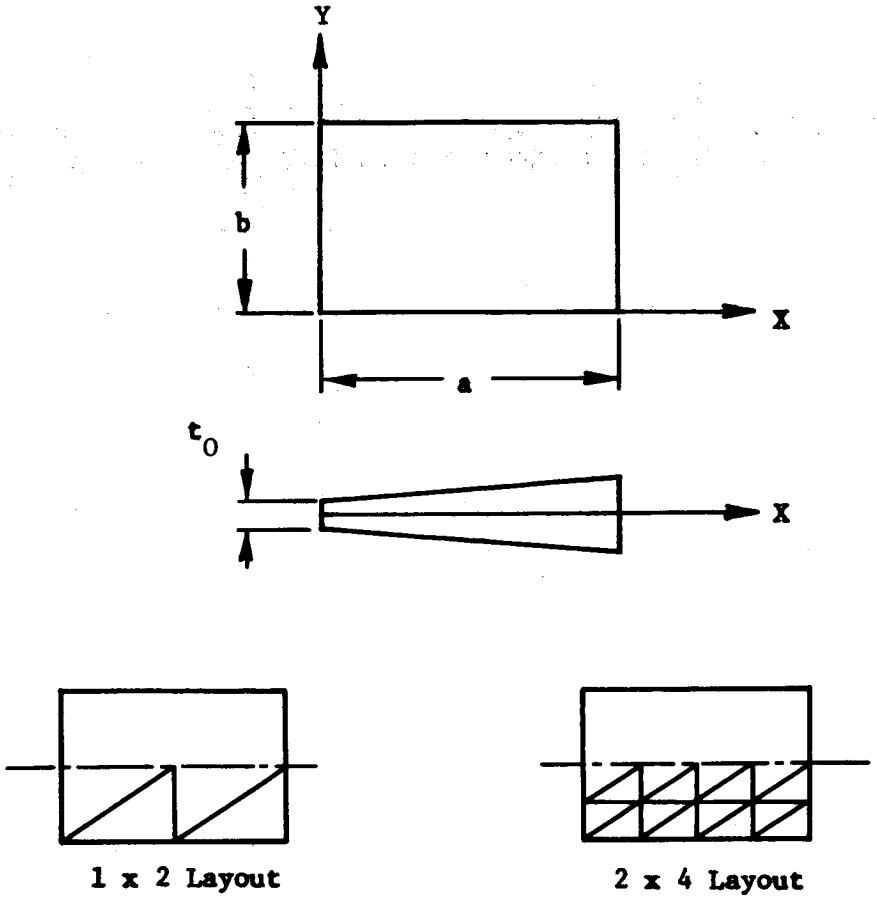

(a) Simply supported plate.

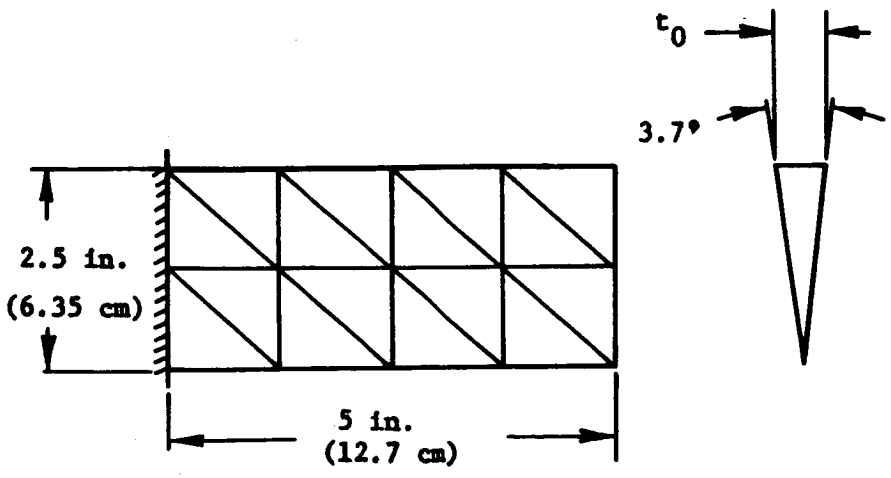

(b) Cantilever plate.

Figure C1. Plate geometry and finite element idealization for the TRPLT1 element test problems.

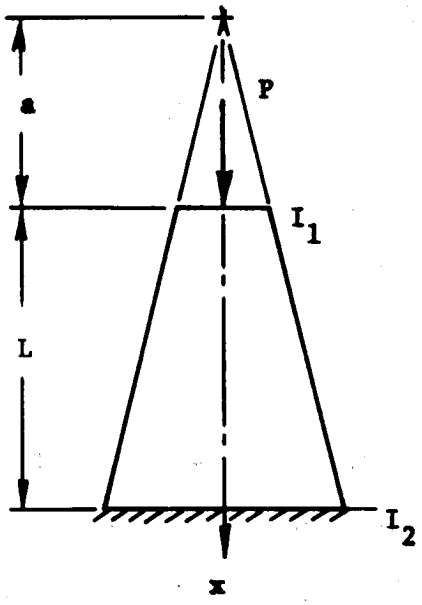

(a) Tapered column.

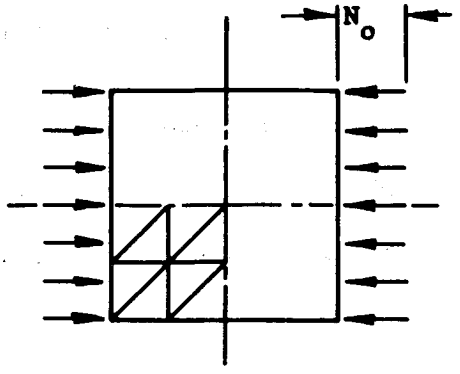

(b) Simply supported square plate under uniform compression.

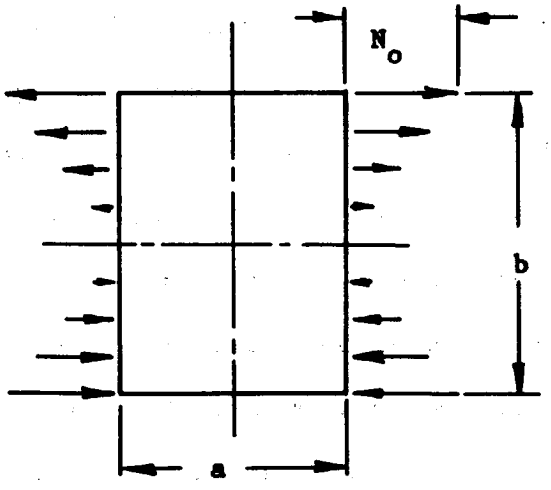

(c) Simply supported plate under inplane bending.

Figure C2. Column and plate geometry for TRSHL element buckling test problems.

APPENDIX D

RESULTS OF TRIANGULAR SHALLOW SHELL ELEMENT

Two problems, (1) that of a spherical cap, and (2) that of a cylindrical shell roof, are considered. These are the same two example problems analyzed in reference 11.

Good agreement in deflections at the center of the cap is obtained even with relatively coarse mesh sizes as shown in table D1. Even though the results appear to be oscillating about the exact value, the percentage error in the converged solution is very negligible.

The geometry and the finite element idealization of the cylindrical shell roof used in the analysis is shown in figure D1. Results for the shell roof problem and the exact solution reported by Cowper et. al. (ref. 11) are given in table D2. Reasonable agreement is seen between the finite element and the exact solutions in u_A, w_B and N_{xxB}. The convergence of the deflection at the central point C appears to be very slow; this, in turn affects the convergence of M_{xxC} and M_{yyC}. A non-uniform finer mesh near the center of the shell, C, is likely to yield converging value to the deflection w_C; the moments M_{xxC} and M_{yyC} may then approach the exact values.

TABLE D1. CENTER DEFLECTIONS FOR SPHERICAL CAP

Finite Element Grids	Spherical Cap Problem	
	$Rt/L^2 = 0.02$	$Rt/L^2 = 0.005$
	Values of $\frac{Etw_c}{P_o R^2}$	Values of $\frac{Etw_c}{P_o R^2}$
1 x 1	1.151069	1.139514
2 x 2	1.007740	0.991776
3 x 3	1.004518	1.001766
4 x 4	1.004365	1.000842
Exact	1.009785	1.000429

TABLE D2. RESULTS FOR A CYLINDRICAL SHELL ROOF

Finite Element Grids	$10u_A$ (in.)	w_B (in.)	$10v_B$ (in.)	$10w_C$ (in.)	$10^{-3}N_{xxB}$ (lb./in.)	$10^{-3}M_{yyC}$ (lb. in./in.)	$10^{-2}M_{xxC}$ (lb. in./in.)
1 x 1	-0.45168	-0.29100	-2.48424	-4.0700	2.4659	0.7685	2.8520
2 x 2	-0.7812	-12516	-4.77312	-2.1344	4.2801	-0.9395	-0.8896
3 x 3	-1.09590	-2.49876	-7.12872	-1.3606	5.4948	-2.0283	-1.1136
4 x 4	-1.2939	-3.4332	-8.57580	2.2224	6.0277	-2.3828	-1.7912
5 x 5	-1.4160	-3.88152	-9.29000	2.8182	6.3279	-2.3538	-1.9770
6 x 6	-1.4733	-4.09176	-9.76992	3.0900	6.4444	-2.3242	-2.0638
Exact	-1.51325	-4.09916	-8.76147	5.2494	6.4124	-2.0562	-0.9272

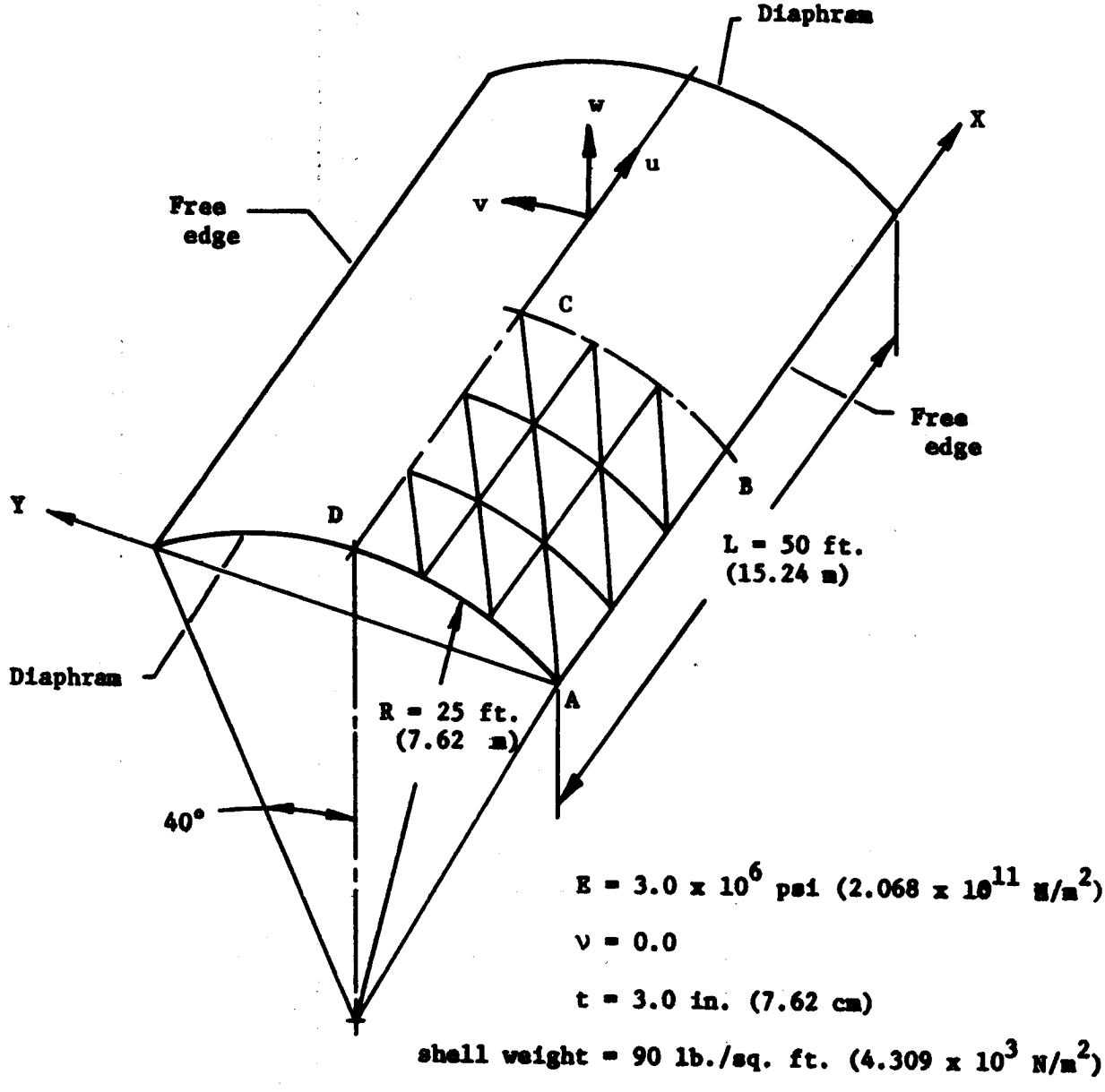

Figure D1. Geometry of cylindrical shell roof and finite element idealization.

References

1. Argyris, J. H., "Triangular Elements with Linearly Varying Strain for the Matrix Displacement Method", J. Royal Aero Society Tech. Note 69, pp. 711-713, October 1965.

2. Narayanaswami, R., "New Plate and Shell Elements for NASTRAN", In NASTRAN: Users' Experiences, NASA TM X-2893, pp. 455-485, Sept. 1973.

3. Zienkiewicz, O. C., "The Finite Element Method in Engineering Science" McGraw Hill Book Co., 1971.

4. Narayanaswami, R., "New Triangular Plate Bending Finite Element With Transverse Sheer Flexibility", J. AIAA, Vol. 12, pp. 1761-1763, 1974.

5. Novozhilov, V. V., "The Theory of Thin Shells" 2nd Edition, Noordhoff, 1964 .

6. Narayanaswami, R., "New Triangular Shallow Shell Finite Element", Technical Report 74-77, Old Dominion University, Norfolk, VA, Nov. 1974.

7. Johnson, S. E. and Field, E. I.: NASTRAN Users' Experiences, "Three Isoparametric Solid Elements for NASTRAN", NASA TM X-2893, pp. 423-437, 1973.

8. Leissa, A. W.: "Vibration of Plates. NASA SP-160, pp. 285-297, 1969.

9. Plunkett, R.: "Natural Frequencies of Uniform and Non-uniform Rectangular Cantilever Plates", J. Mech. Engr. Sci., Vol. 5, pp. 146-156, 1963.

10. Timoshenko, S. P. and Gere, J. M.: "Theory of Elastic Stability", McGraw Hill, pp. 125-132, and 372-379, 1961.

11. Cowper, G. R. Lindberg, G. M. and Olson, M. D.: "A Shallow Shell Finite Element of Triangular Shape", Int. J. Solids and Structures, Vol. 6, pp. 1133-1156 , 1970.

IMPLEMENTATION ON A NONLINEAR CONCRETE CRACKING ALGORITHM IN NASTRAN

David N. Herting, David L. Herendeen and Richard L. Hoesly
Universal Analytics, Inc.

H. Chang
Ebasco Services Incorporated

SUMMARY

A computer code for the analysis of reinforced concrete structures has been developed using NASTRAN as a basis. Nonlinear iteration procedures were developed for obtaining solutions with a wide variety of loading sequences. A direct access file system was used to save results at each load step to restart within the solution module for further analysis. A multi-nested looping capability was implemented to control the iterations and change the loads. The basis for the analysis is a set of multi-layer plate elements which allow local definition of materials and cracking properties.

INTRODUCTION

Faced with an ever-growing need to ensure environmental safety, the nuclear industry must develop analytical tools to determine the physical integrity of reactor structures. These structures, typically layers of concrete interspersed with reinforcing materials, must withstand severe emergency loading conditions. Resulting high stresses due to these loads are expected to cause the formation and propagation of cracks within the concrete. Once this process begins, the structural characteristics change. Thus, a nonlinear solution algorithm is required with the capability of subjecting the structure to an arbitrary sequence of loadings -- thermal, pressure, gravitational and equivalent dynamics. Also, the algorithm designed must be efficient for the solution of large-order and complex structural models.

Although the present NASTRAN (NASA Structural Analysis) computer program system contains a limited elasto-plastic analysis capability in Rigid Format 6 (Piecewise Linear Analysis), it was unacceptable for simulating the three-dimensional concrete cracking phenomena. The present NASTRAN stress-strain rules for nonlinear materials do not allow for a decrease in stress with increasing strain. This effect is certainly evidenced by the behavior of concrete where the internal loads disappear due to cracking. Furthermore, the present analysis is limited to a stepwise application of a single load vector and requires large amounts of computer time.

This paper presents the implementation in Level 15.5 NASTRAN of a nonlinear concrete analysis capability. The effort, performed by Universal Analytics, Inc. (UAI) and Ebasco, involved the addition of nonlinear elements, new functional modules, a DMAP (Direct Matrix Abstraction Program) alter package, and modifications to the NASTRAN executive system. This project illustrates the practicality of modifying NASTRAN for a specialized problem in contrast to the development of general capabilities as implemented in the standard NASA versions.

The basic computational methods were chosen to provide efficient solutions to a wide variety of concrete cracking problems. Multi-layer quadrilateral and triangular plate elements with independent layer-by-layer material definition were implemented to calculate both linear and nonlinear stiffness matrix and load effects.

A nonlinear iteration system was implemented to obtain solutions for large-order problems from efficient vector processing techniques. The system, controlled by DMAP, is controlled by a new module which performs nonlinear loading functions, convergence testing, and automated property updates (for design optimization).

For user convenience in the practical solution of complex structural problems, several modifications were implemented in the NASTRAN Executive system. A restart capability for re-analysis of a problem starting at any previous solution was performed with the addition of a random access storage file independent of the NASTRAN file system. New DMAP language modifications, currently in Level 16 NASTRAN, were installed to provide data block control for multi-nested DMAP looping.

In the following discussion, the physical characteristics of the expected structures are described, followed by separate descriptions of the major items.

PHYSICAL PROBLEM

Many types of composite steel/concrete construction methods are used in the fabrication of high-strength structures. The hypothetical example shown in figure 1 illustrates the nature of a containment vessel used in nuclear power plant construction. Each layer represents a different property which may contain one or more types of materials. For example, a layer of closely spaced thin rods is imbedded in a concrete matrix and the stress-strain properties represent the effects of both materials as a composite. The combination of bending and membrane forces in the structure contribute nonuniform stresses through the depth of the plate and therefore require a layer-by-layer analysis of the nonlinear effects.

The nonlinear effects of concrete cracking are significantly different physically from the effects of plastic strains in metal structures. Classical elasto-plastic analysis methods use one or more plastic "flow rules" which assume a continuous transition between elastic and plastic behavior with stresses always increasing with increasing strains (refs. 1 and 2). However,

the concrete stresses can be assumed linear until cracking occurs, at which point the stresses normal to the crack must be completely removed, leading to problems with discontinuities in the general solution.

The theoretical limits for the principal strains in concrete are shown in figure 2, along with the actual approximations used. Also shown in the stress-strain diagram for a principal strain. The stresses, and therefore the resulting internal forces, will be discontinuous and may lead to difficulties in the solution algorithm. This problem is discussed in a subsequent section.

REINFORCED CONCRETE ELEMENTS

New triangular and quadrilateral plate elements were developed to represent the layered properties of the reinforced concrete. The generalized displacements and element geometry are identical to the existing NASTRAN TRIA1 and QUAD1 plate elements. However, the nonlinear, multi-layered properties required a reformulation of the basic equations to account for the resulting coupling between the in-plane membrane and bending forces. A basic approach similar to the method used in reference 3 was adapted for use with NASTRAN-type element formulations.

Each layer of the new triangular element (TRCA) illustrated in figure 3 corresponds to a unique concrete or steel property which may be defined independently. The grid point locations may be off-set from the element reference coordinate system and the mean bending plane of the element does not require user calculation.

In existing NASTRAN plate elements the membrane and bending properties are calculated independently. However, the coupling terms occurring in the layered elements require their simultaneous calculations. For these new elements, the existing NASTRAN bending routines have been expanded to include in-plane displacements and strains for each component basic triangle. Since the triangle and quadrilateral elements in NASTRAN are comprised of component triangles, the combination process also was expanded to include the coupled in-plane terms.

During solution, the basic element calculations are used for several purposes. These include:

1. Generation of a new stiffness matrix K to represent the current cracked condition.

2. Generation of loads due to thermal expansion with forces across cracked layers removed.

3. Generation of corrective forces P for each element representing the change in forces due to new cracks at a particular deformed shape.

4. Calculation of stresses in the cracked layers for output processing.

5. If requested, the thicknesses of cracked layers may be automatically modified to eliminate the cracking strains. This option is used for design optimization.

The finite elements which may include the standard NASTRAN elements are assembled into stiffness and mass matrices. Multipoint and single-point constraints may be used to define boundaries. The static solution to applied loads, enforced displacements and temperatures is described in the next section.

SOLUTION METHOD

With finite elements, the general form of the static nonlinear equation of state is

$$\{\Phi(u,T)\} = \{P_e\} \tag{1}$$

where $\{\Phi\}$ is the generalized load vector resulting from element stresses

u are the set of node point displacements

T is the temperature field

$\{P_e\}$ is the vector of externally applied loads at the node points

The load function vector, Φ, may be obtained from the total energy of the system, U, and Lagrange's equation, or:

$$\Phi_i = \frac{\partial U}{\partial u_i} \tag{2}$$

For the concrete cracking problem, the system may be reduced to a bounded linear problem. At any cracking condition, i, the generalized loads are:

$$\{\Phi\} = [K_i]\{u_i\} - \{Q_i(T)\} \tag{3}$$

where $[K_i]$ is the stiffness matrix and $\{Q_i\}$ is the thermal load vector.

To be valid, the displacements $\{u_i\}$ in the above equation must be compatible with the cracking state used in $[K_i]$. To find the displacements, the following procedure is used. Equation (1) may be so structured as to produce the iteration equation below:

$$[K_a]\{u_{i+1}\} = \{P_e\} - \{\Phi(u_i)\} + [K_a]\{u_i\} \tag{4}$$

where the index i indicates each step of the iteration and each vector $\{u_{i+1}\}$ is a new estimate of the displacement.

Two choices for the matrix $[K_a]$ are available in the iteration process. In the Newton-Raphson method (ref. 4) the matrix $[K_a]$ is updated at each step using the new displacement vector, $\{u_{i+1}\}$. In the so-called perturbation method, a constant stiffness matrix $[K_a]$ may be used, thereby eliminating the need to decompose a new matrix at each time step. The perturbation method is used initially. If the measured convergence rate is too slow, the matrix is updated to speed up the convergence.

If $[K_a]$ is the matrix corresponding to the initial cracking condition $\{u_i\}$, the vector $\{\Phi\}$ from equation (3) may be substituted into equation (4) to produce the equation:

$$[K_a]\{u_{i+1}\} = \{P_e\} + \{Q_i(T)\} + [K_a - K_i]\{u_i\} \tag{5}$$

Note that the stiffness matrix $[K_a]$ is constant, and no matrix decompositions are required except for the first step.

For calculation purposes, equation (5) is rearranged to produce the actual iteration equation:

$$[K_a]\{u_{i+1}\} = \{P_e\} + \{Q_a\} + \{\delta P_i\} \tag{6}$$

where

$$\{\delta P_i\} = [K_a - K_i]\{u_i\} + \{Q_i - Q_a\} \tag{7}$$

Note that the variable quantity on the right-hand side is the "corrective load" $\{\delta P_i\}$. This is a function only of the elements which have changed in stiffness between states a and i. An exact solution is obtained when a displacement vector is found which satisfies equation (1), or if $\{u_{i+1}\} = \{u_i\}$.

In the above method, the initial stiffness matrix $[K_a]$ may be obtained from any previous cracking condition or may be updated in the iteration procedure. The starting vector (i = a) must be chosen such that no additional cracks will be formed with respect to state a. For this reason, the initial starting vector (u_i at i = a) is always null.

The iteration procedure is illustrated in figure 4 for a single degree of freedom problem with several layers of steel and concrete. The sawtooth curve represents the force-displacement function, Φ. Each peak represents the limit of each layer and the dashed line represents the applied load. Note that several solutions exist (where the dotted line intersects the solid lines). If the structure was initially uncracked, the iterations would follow the dotted lines. However, once a layer is cracked, the unloading curve follows a different path, i.e., corresponding to the stiffness matrix of the cracked structure. New applied loads will also use this path.

Both convergence and divergence of the system may be tested after each iteration. The loading error vector $\{\delta_i\}$ is defined as:

$$\{\delta_i\} = \{\Phi_i\} - \{P_e\} \tag{8}$$

and from equations (3) and (7):

$$\begin{aligned}\{\delta_i\} &= [K_i]\{u_i\} - \{Q_i\} - \{P_e\} \\ &= -\{\delta P_i\} + [K_a]\{u_i\} - \{Q_a\} - \{P_e\}\end{aligned} \tag{9}$$

Substituting equation (6) for the second term on the right side, we obtain:

$$\{\delta_i\} = \{\delta P_{i-1}\} - \{\delta P_i\} \tag{10}$$

The energy error of the system is obtained from the vector products of displacement and loads. As shown in figure 4 ($i = 3$), the load error may diverge for one step, yet the process may still converge. In practice, however, for large-order problems, the curves Φ become more continuous and the temporary type of divergence is rarely encountered.

Many of the above matrix operations could be processed by existing NASTRAN DMAP as with the similar Level 16 differential stiffness procedure. However, because nonlinear element routines may be designed to directly calculate the corrective loads defined in equation (7), and because most of the vector operations may be performed more efficiently in core, the basic iterations are performed in a new NASTRAN module. Described below is the basic organization of the NASTRAN implementation.

NASTRAN IMPLEMENTATION

The implementation of the concrete analysis (CA) algorithm in NASTRAN required only isolated interfaces to the program due to NASTRAN's modular design. The interfaces of the new elements were straightforward due to the organization of the element table processing. Most of the new solution iteration procedure code was isolated to six new modules which used many of the existing NASTRAN matrix subroutines.

The cracking analysis solution algorithm was implemented using the NASTRAN DMAP (Direct Matrix Abstraction) control language. The Level 16 DMAP compiler (ref. 5), available in Level 16 NASTRAN, was used to take advantage of its improved capabilities and constructs not available in the previous compiler. The most important of these features are the utility module SWITCH and the freedom to use Data Blocks before they are defined. SWITCH allows Data Block names to be interchanged so that two successive iterates may be SWITCHed and a branch made back to the iteration module.

The initial framework for the cracking analysis DMAP used the Piecewise Linear DMAP of Rigid Format 6. DMAP ALTERs were inserted as required to

implement the new technique. The overall logical flow of the DMAP, paying particular attention to the relationship of the new modules and loop controls, is shown in figure 5. The basic computational procedures for the cracking analysis are carried out by the six new modules that were implemented. A brief description of each appears below.

1. Functional Module CASMG (Strain Matrix Generator)

   Generates the cracking analysis strain matrix which will transform grid point idsplacements into generalized element strain of the element. This strain matrix is stored to be used within the iteration loop to compute:

   a. Thermal loads
   b. Element stress
   c. Corrective load vectors

2. Functional Module CAUTIL (Cracking Analysis Utilities)

   Performs several utility functions for the cracking analysis. These include:

   a. Extracting data from the CAØF (defined in a later section) for previous material states
   b. Appending interpolated element temperatures to the EST
   c. Reorganizing property change specification Bulk Data
   d. Assembling partitioning vectors for CAITER (described below)

3. Functional Module CASMA (Element Stiffness Assembler)

   Calculates the variable stiffness matrix for the cracking analysis. This matrix is assembled for each element on the initial pass, and only for updated elements on subsequent passes.

4. Functional Module CAECPT (Cracking Analysis ECPT)

   Generates the updated ECPTCA data block with all element property updates for the current iteration. The updated ECPTCA is also saved on the CAØF. In addition, if DIAG 25 is set, a summary of all elements that cracked in the last stiffness iteration will be printed.

5. Functional Module CAITER (Crack Analysis Iteration)

   Iterates to an equilibrium state solution for the nonlinear cracking analysis.

6. Functional Module CAØUTP (Cracking Analysis Output Processor)

   Formats and prints the output data for a cracking analysis, including stresses, forces and property updates.

Module CAITER is the primary iteration module. It controls the corrective load iteration, property updates, convergence testing, and setting of parameters to control DMAP execution. The logical flow is shown in figure 5.

In order to implement the desired solution paths of the cracking analysis, a random access 'Cracking Analysis Operating File' (CAØF) was integrated into the solution methodology. The standard NASTRAN data base, GINØ, could not adequately handle the required procedures. The CAØF is a stylized version of the Automated Multi-Stage Substructuring Operation File (SØF) (ref. 6) found in standard Level 16 NASTRAN. This file allows the user maximum versatility during solution, the capability to use previous subcases as initial conditions for subsequent cases, and the cost effectiveness of internal restart.

Data for each cracking element and each subcase is stored on the CAØF until deleted by the user. For elements, the stiffness and strain matrices are stored on the CAØF to allow rapid assembly of system matrices similar to Level 16 NASTRAN. For each subcase, the current element summary (EST) and connection (ECPT) tables are stored. Also stored are the most recent load and displacement vectors which may represent a final or some intermediate stage in the iteration cycle. Current iteration parameters are also saved at each step. In the event that convergence has not been obtained, or a system failure has occurred, these parameters may be used to reinitiate the solution. This particular powerful tool allows an 'internal' restart to be performed either at some stage in the solution DMAP or within the CAITER module itself, outside the standard NASTRAN restart framework.

CONCLUSIONS

The nonlinear concrete cracking analysis described above has been implemented in a Level 15.5 version of NASTRAN. Although extensive testing has been performed using moderate size problems, the program is still being tested with large-order problems to provide experimental correlations. With the basic cracking analysis capabilities and the additional user conveniences for multiple cases, the program is expected to become a powerful tool for the analysis of reinforced concrete structures.

Many of the program techniques used in the concrete analysis modifications may be adapted to other types of NASTRAN analyses. A capability to perform automatic internal restarts inside a module, which could be implemented in other NASTRAN modules, has been proven. New methods of processing nonlinear elements have been implemented to provide additional efficiencies. New, highly efficient iteration techniques have been installed which combine core-held vector iterations in a module with out-of-core matrix iterations using DMAP. These operations could be adapted to perform more general types of nonlinear structure analysis such as elasto-plastic analysis combined with crack elements and nonlinear geometry behavior.

REFERENCES

1. Swedlow, J. L.: The Thickness Effect and Plastic Flow in Cracked Plates. Aerospace Research Laboratories, Wright Patterson Air Force Base, Ohio, ARL 65-216, October 1965.

2. Hutchinson, J. W.: Finite Strain Analysis of Elastic-Plastic Solids and Structures, Numerical Solution of Nonlinear Structure Problems. ASME-AMD-Vol. 6, R. F. Hartung, Ed., November 1973.

3. Hand, F. R.; Pecknold, D. A.; and Schnobrick, W. C.: Nonlinear Analysis of RC Plates and Shells. ASCE Journal of the Structure Division, July 1973.

4. Stricklin, J. A., et al.: Survey of Static Geometric and Material Nonlinear Analysis by the Finite Element Method. Proceedings of 2nd U.S.-Japan Seminar on Matrix Methods in Structure Mechanics, University of Alabama Press, 1972.

5. Herendeen, D. L.: An Improved DMAP Capability. NASTRAN: Users' Experiences, NASA TM X3278, 1975.

6. Field, E. I., et al.: The Automated Multi-Level Substructuring System for NASTRAN. NASTRAN: Users' Experiences, NASA TM X3278, 1975.

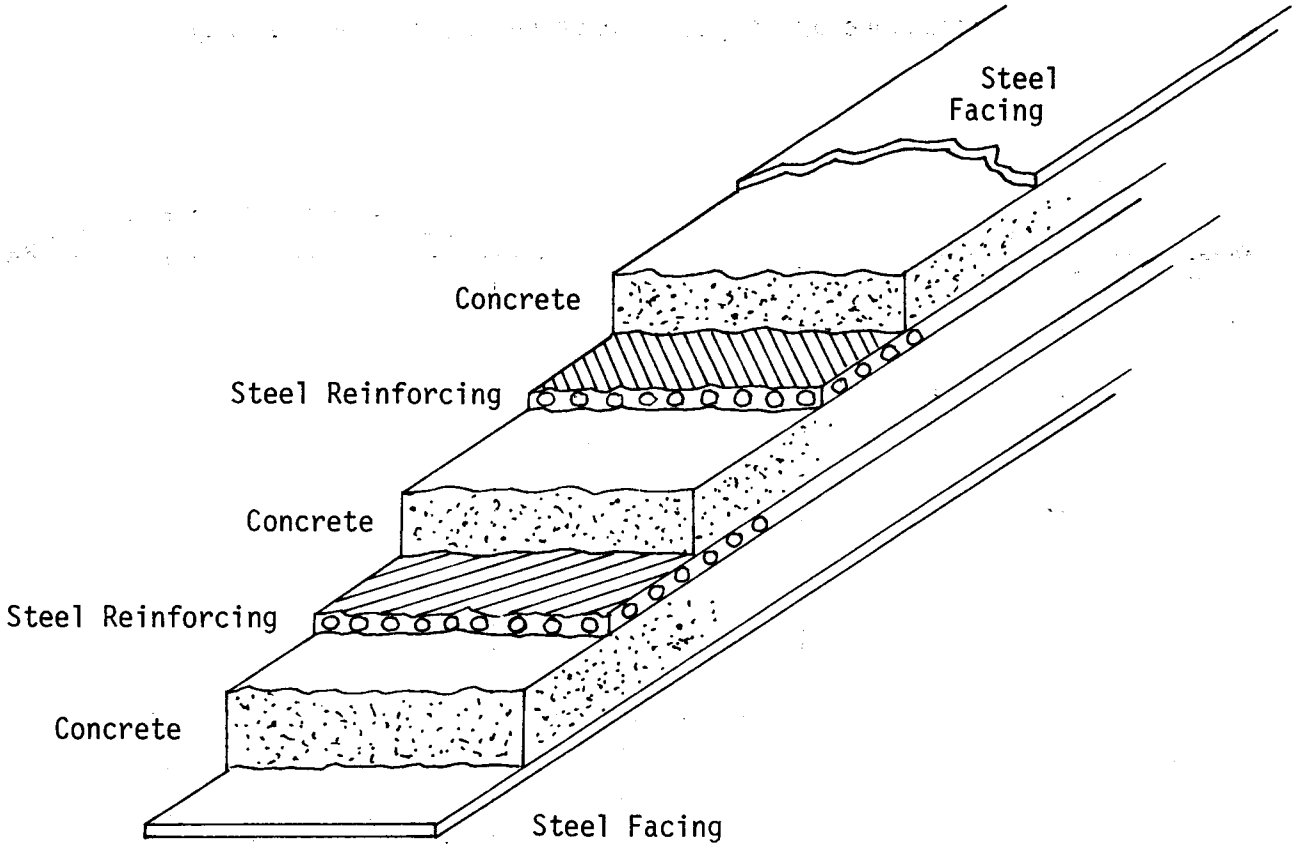

Figure 1.- Sample multi-layer reinforced concrete.

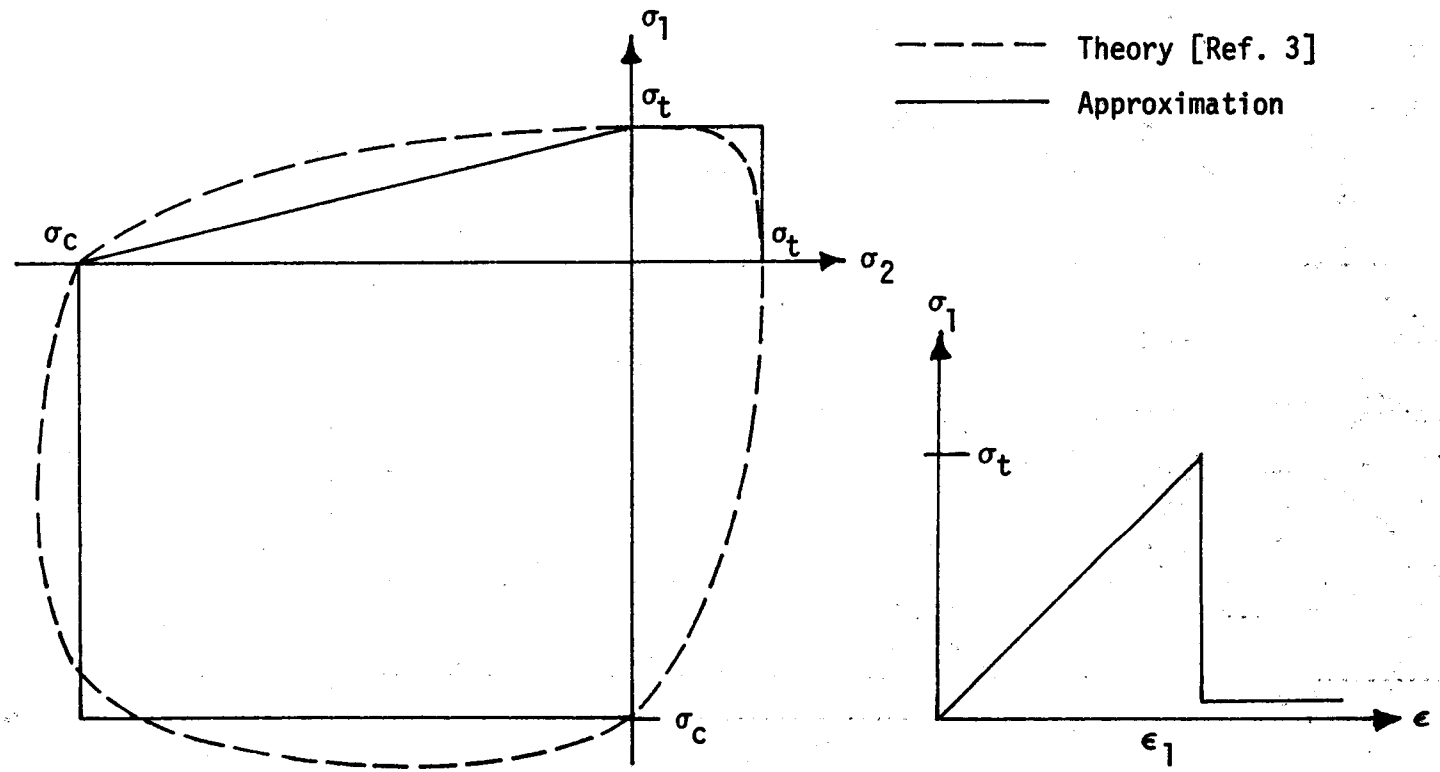

Figure 2.- Stress and strain limits for concrete.

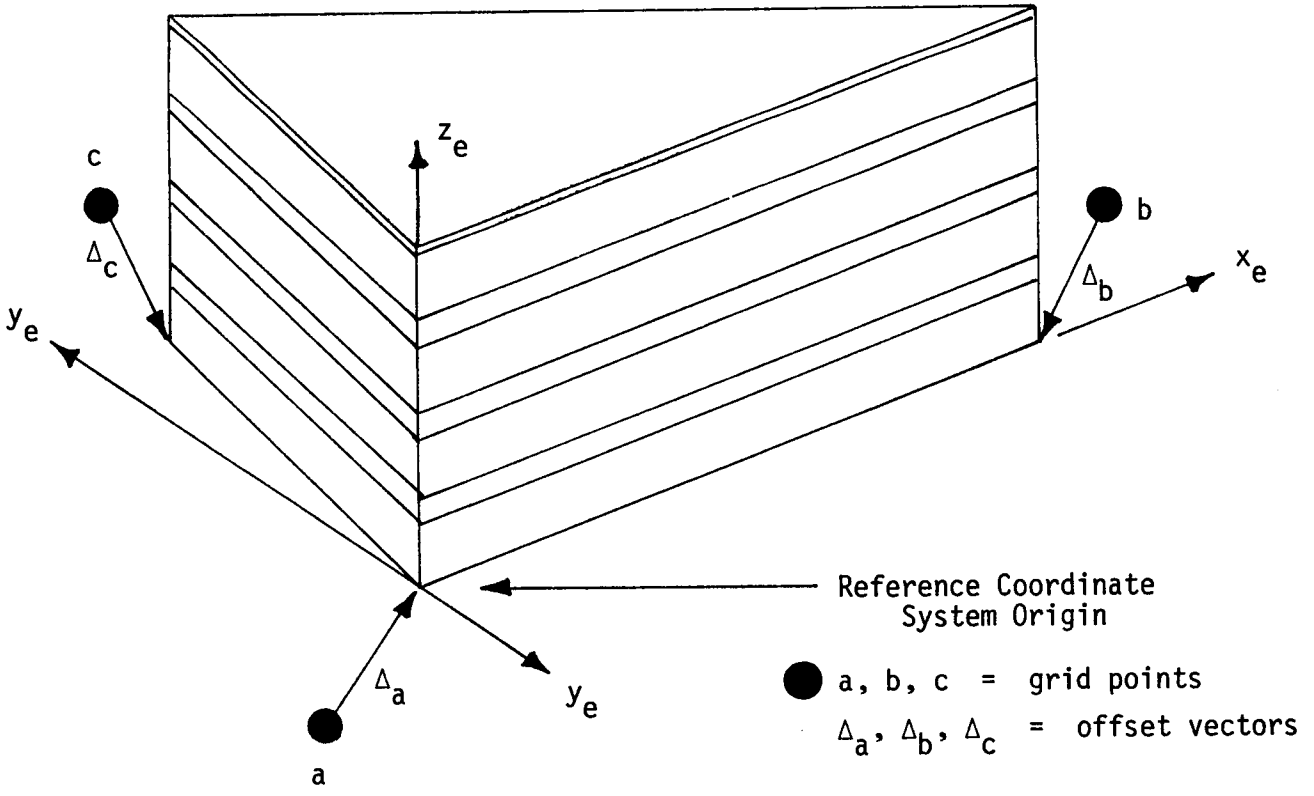

Figure 3.- Triangular crack analysis plate element.

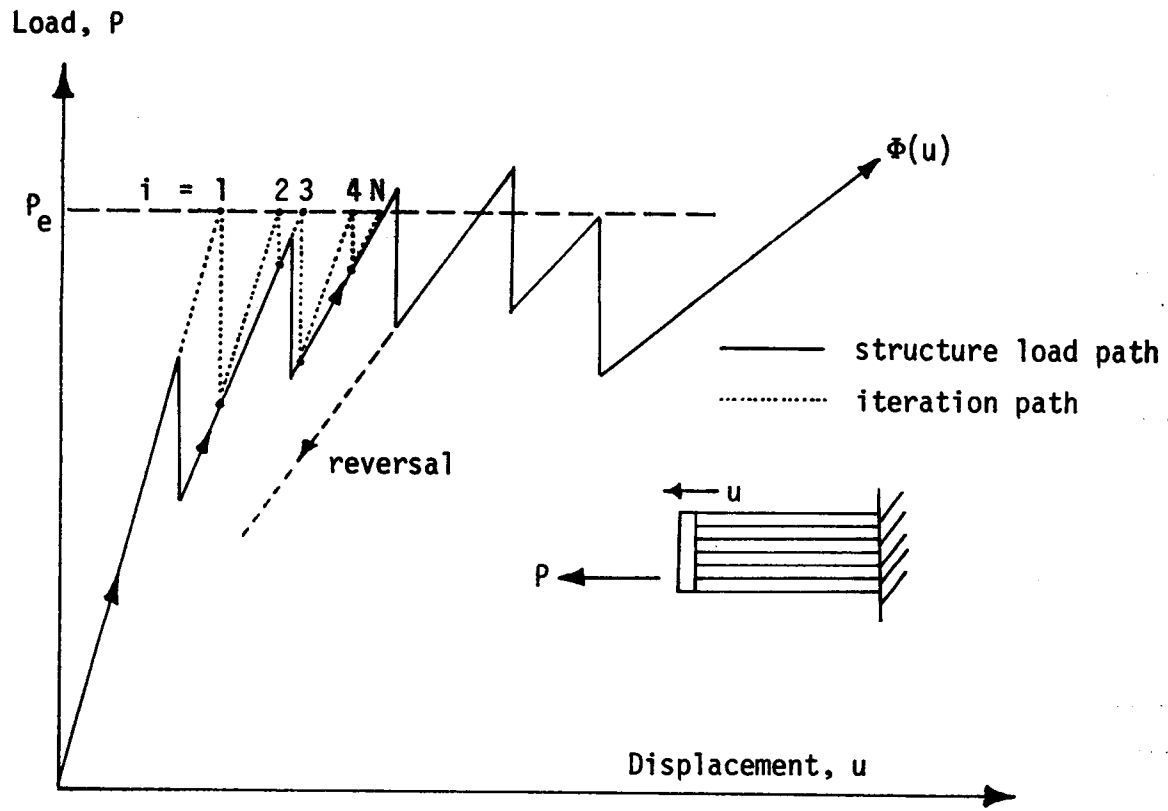

Figure 4.- Load functions for single multi-layer element.

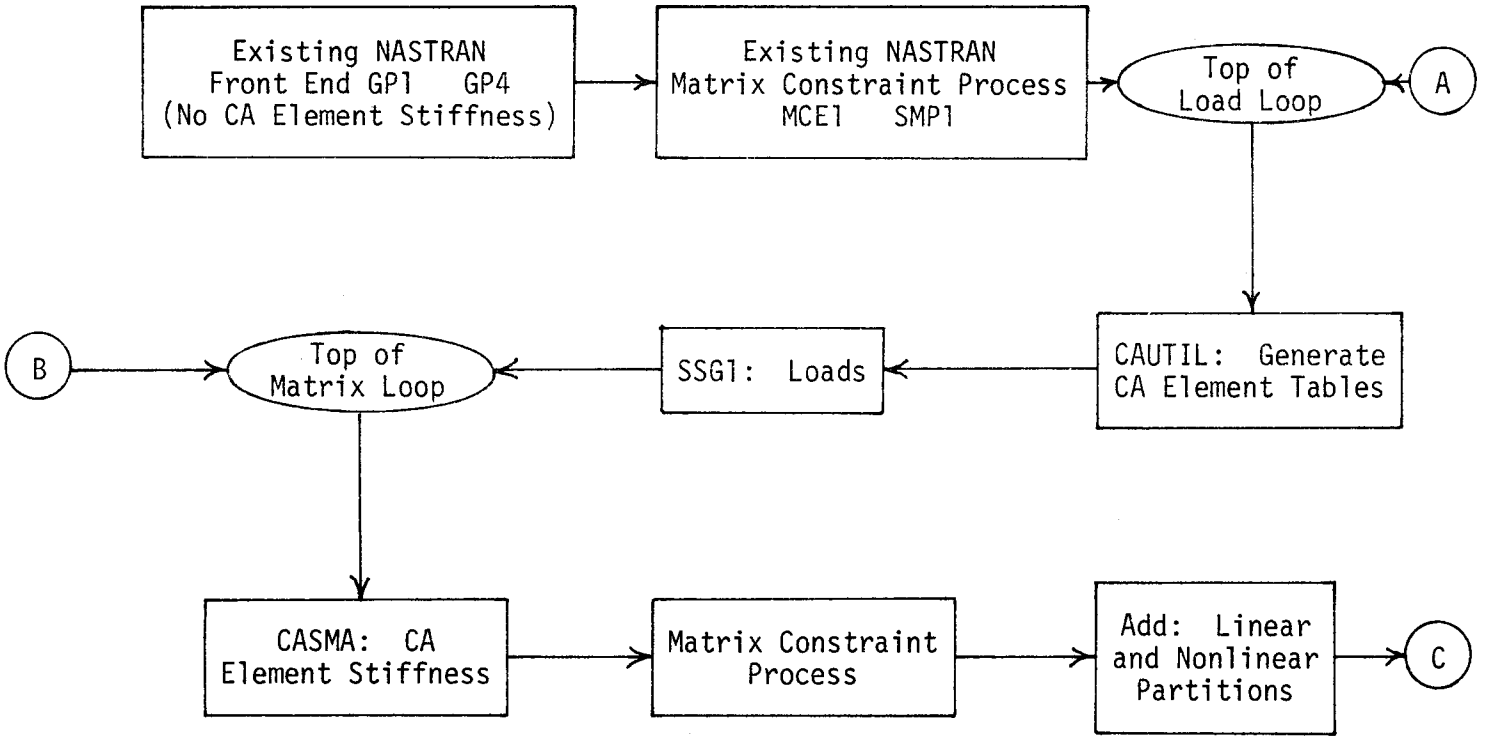

Figure 5.- Logical flow for concrete analysis in NASTRAN.

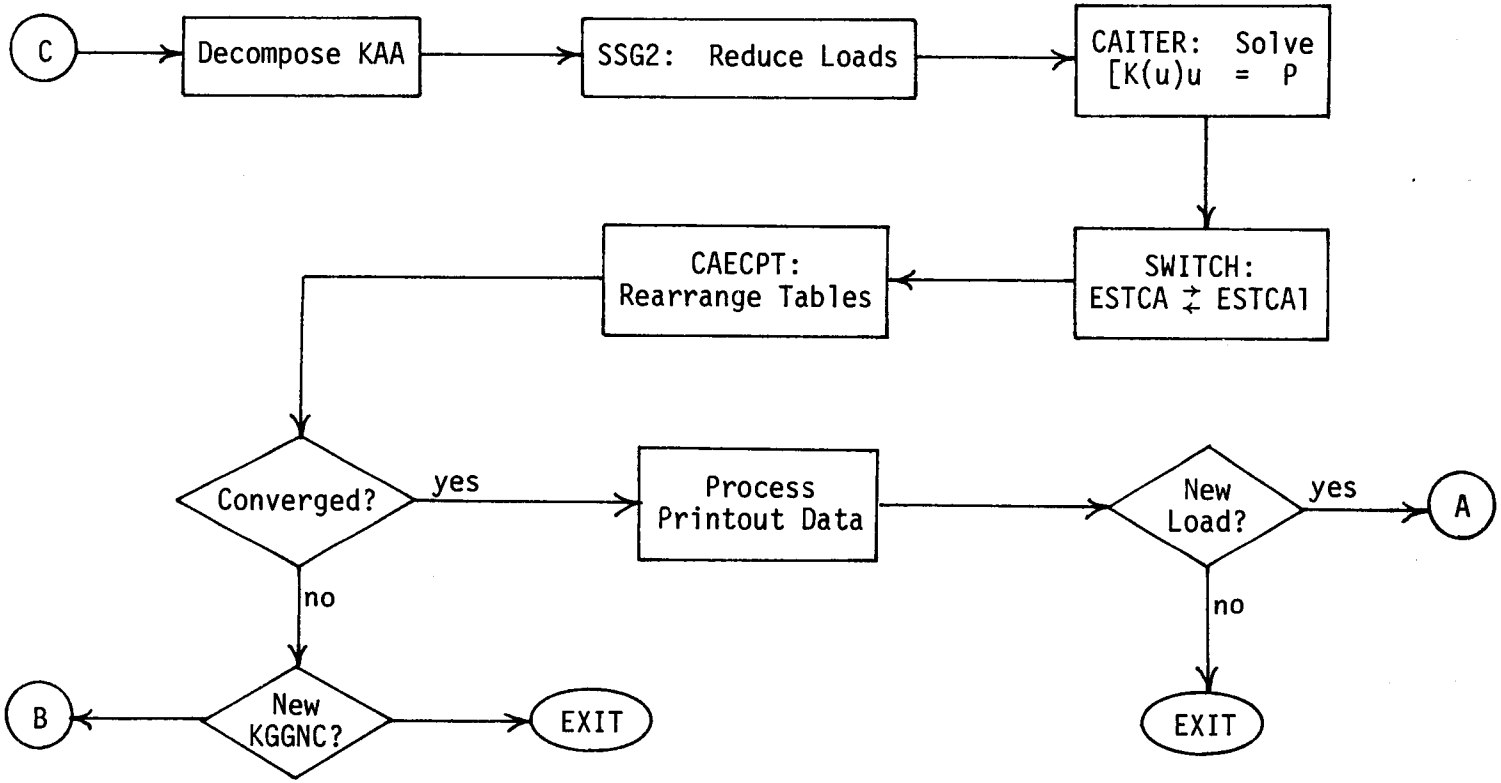

Figure 5.- Logical flow for concrete analysis in NASTRAN. (Cont'd)

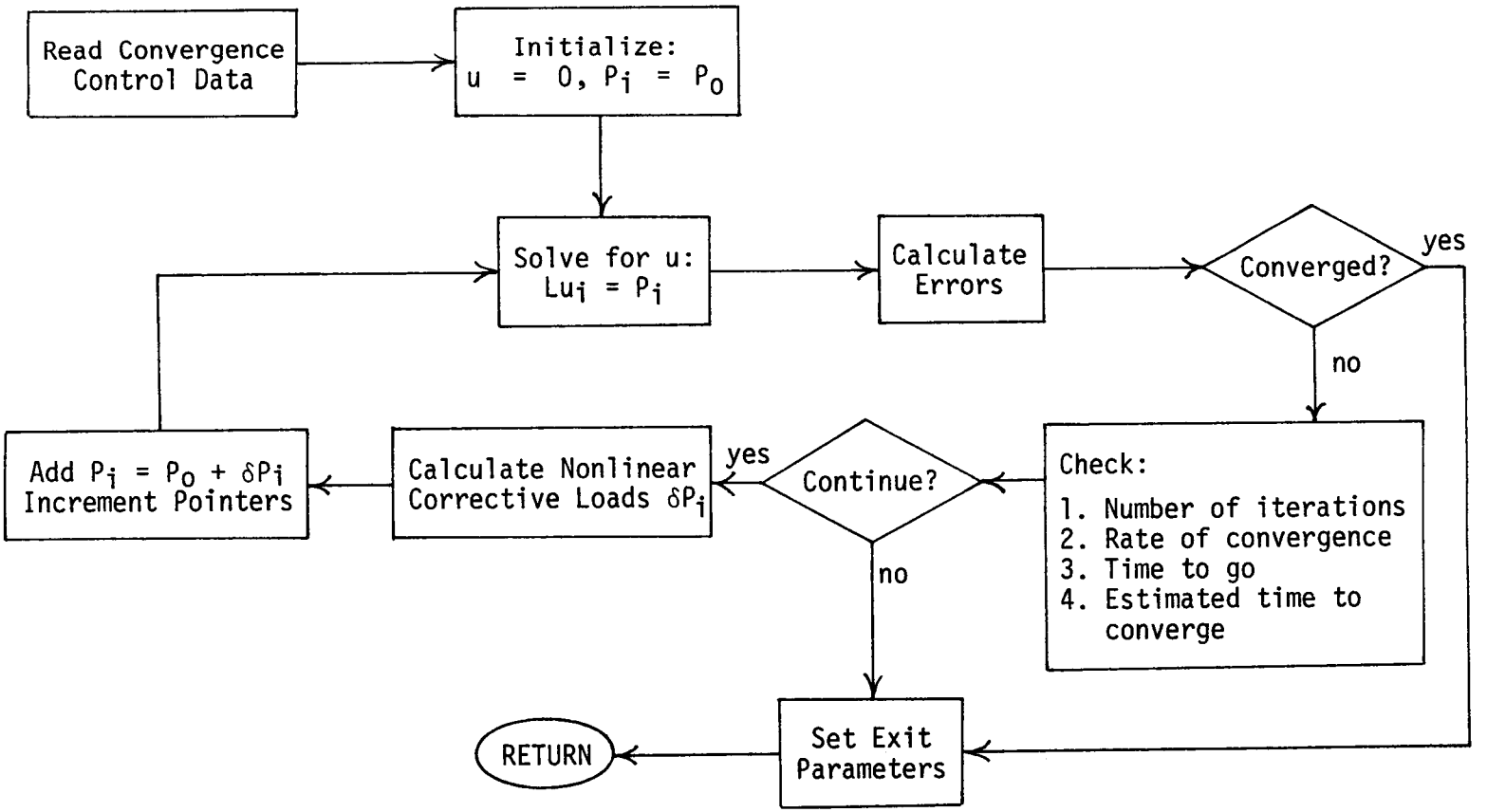

Figure 6.- Logical flow for module CAITER.

SOME APPLICATIONS OF THE NASTRAN LEVEL 16 SUBSONIC FLUTTER ANALYSIS CAPABILITY

Robert V. Doggett, Jr., and Herbert J. Cunningham
NASA Langley Research Center

ABSTRACT AND SUMMARY

Results are presented that were obtained by applying the new Level 16 flutter analysis capability to an aspect-ratio-6.8 subsonic-transport-type wing, an aspect-ratio-1.7 arrow wing, and an aspect-ratio-1.3 all-movable horizontal tail with a geared elevator. The transport wing and arrow-wing results are compared with experimental results obtained in the Langley transonic dynamic tunnel and with other calculated results obtained using subsonic lifting surface (kernel function) unsteady aerodynamic theory.

INTRODUCTION

Improvements in the NASA structural analysis computer program (NASTRAN) have been made continuously since the first public release of the program in 1970. These improvements have included both the upgrading of capability that was included in the initial public version and the addition of new analysis capabilities that were not included previously. One new capability that is generally available in a standard level for the first time with the release of Level 16 is subsonic flutter analysis. The flutter analysis is organized into a new rigid format, APP AERO, SOL 10. The features and capabilities of the Level 16 flutter analysis are the same as those of the analysis originally installed in a nonstandard Level 15.1 version (see refs. 1 and 2). As presently implemented, the analysis is applicable to multiple, nonplanar, mutually interfering lifting surfaces. The analysis is of the modal type. That is, the flutter equations are formulated in terms of generalized modal coordinates using a finite number of the natural modes of the structure. These modes and frequencies are determined using a conventional NASTRAN finite-element structural model. The solution of the flutter equations is accomplished by the traditional k-method. The generalized unsteady aerodynamic forces are determined using doublet lattice unsteady aerodynamic theory which requires that the lifting surface be divided into an array of trapezoidal boxes. As implemented in NASTRAN, there is an aerodynamic grid point located at the center of each of these boxes. The interconnection of the aerodynamic and structural models is accomplished by using one-dimensional and surface spline functions to interpolate the modal displacements determined at the structural grid points to displacements and slopes required at the aerodynamic grid points. The generality of this structural-aerodynamic interface allows the user to select a structural model that is best suited from structural considerations alone and an aerodynamic model that is dictated by aerodynamic considerations alone. Capability is provided for interpolating the generalized aerodynamic forces determined at

specific values of the independent aerodynamic parameter, Mach number, or reduced frequency, to forces at intermediate values of these parameters.

The purpose of this paper is to present NASTRAN flutter results for three different configurations; namely, an aspect-ratio-6.8 subsonic-transport-type wing, an aspect-ratio-1.7 arrow wing, and an aspect-ratio-1.3 all-movable horizontal tail with a geared-elevator control surface. The NASTRAN flutter results for the transport wing and arrow wing are compared with wind-tunnel model experimental results obtained in the Langley transonic dynamics tunnel and with other calculated results obtained by using subsonic lifting surface (kernel function) unsteady aerodynamic theory. The kernel function results were obtained using NASTRAN calculated modes and frequencies and flutter analysis methods similar to those contained in NASTRAN, such as surface spline interpolation, generalized aerodynamic force interpolation, and the k-method of solution. All NASTRAN flutter results presented were obtained using standard Level 16 as installed on the CDC 6000 series computers at the Langley Research Center.

APPLICATIONS

Subsonic Transport Wing

The subsonic-transport wing for which NASTRAN flutter results were obtained was one of two wind-tunnel models tested in the Langley transonic dynamics tunnel to study possible supercritical-airfoil-section effects on flutter (see ref. 3). A photograph of the swept, tapered, aspect-ratio-6.8 cantilever-mounted wing installed on a fuselage half-body in the wind tunnel is presented in figure 1. The wing geometry, the structural model, and one of the aerodynamic models used (doublet lattice box arrangement) are presented in figure 2. Although the model construction was rather complex (fiberglass skins stabilized by a full-depth honeycomb core with ballasting weights inserted in the core), the wing was essentially a beamlike structure so NASTRAN BAR elements were used in the structural model. The aerodynamic model shown in figure 2 contains 100 doublet lattice boxes, five boxes along the chord at each of 20 span stations. The aerodynamic model in the figure was the basic one used in the flutter analysis, but additional calculations were made using 50 boxes, five per chord at 10 span stations, and also 200 boxes, five per chord at 40 span stations. Note that the aerodynamic planform is slightly different from the actual planform near the wing root and tip since curved planform edges are approximated by the straight line segments of the doublet lattice boxes.

The first six calculated natural modes and frequencies of the wing were used in the flutter analysis. Oblique projections of the calculated mode shapes and the corresponding natural frequencies are shown in figure 3. Also included in the figure are the measured natural frequencies. The measured and calculated natural frequencies are in good agreement and, although not shown in this figure, the calculated mode shapes are very similar to the measured mode shapes. One-dimensional spline functions were used to interpolate the modal displacements in the flutter analysis.

The flutter results are presented in figure 4 as the variations of the flutter frequency and dynamic pressure with Mach number. The NASTRAN results are indicated by the symbols in this figure. Also included are the experimental flutter results (from ref. 3) and calculated results obtained using subsonic lifting surface (kernel function) theory (ref. 4). A six-by-six collocation point arrangement was used for the kernel function calculations. Both sets of calculated results predict higher flutter frequencies and dynamic pressures than were found experimentally. Although the kernel function results are in better agreement with the experiment than the NASTRAN results, the differences between the two calculations are not considered to be large and are not untypical of differences that occur in flutter analyses using different unsteady aerodynamic theories. The NASTRAN results at Mach number 0.934 using 50, 100, and 200 doublet lattice boxes show that the 100-box and 200-box results are virtually the same, and that the 50-box results are only slightly higher.

Arrow Wing

The arrow-wing configuration was another wind-tunnel model and is shown mounted in the wind tunnel in figure 5. The aspect-ratio-1.7, cantilever-mounted model is a simplified 0.02-size version of the Supersonic Cruise Aircraft Research (SCAR) arrow-wing design. The experimental flutter data obtained for this model will be used in validating flutter analysis methods applicable to the arrow-wing configuration. The model geometry, structural model, and aerodynamic model are presented in figure 6. The arrow-wing model was of simple construction, being an aluminum-alloy plate covered with balsa wood to give the desired airfoil shape. The structural model consisted of NASTRAN QUAD2 and TRIA2 plate-bending elements. The basic aerodynamic model shown in figure 6 consisted of 108 doublet lattice boxes, nine along the chord at each of 12 span stations. Some calculations were made using 60 boxes, 5 by 12, and 189 boxes, 9 by 21. Note that the aerodynamic model planform is slightly different from the geometric planform.

The first five calculated natural modes were used in the flutter analysis. Oblique projections of the calculated mode shapes along with the corresponding natural frequencies are presented in figure 7. Also included in the figure are the measured natural frequencies. The calculated and measured frequencies are in reasonably good agreement. Surface-spline functions were used to interpolate the modal displacements at the structural grid points to displacements and slopes required for each doublet lattice box.

The flutter results are presented in figure 8 as the variations of the flutter frequency and dynamic pressure with Mach number. Also included in the figure are calculated results obtained using kernel function unsteady aerodynamic theory (ref. 4) and some previously unpublished experimental flutter results obtained in the Langley transonic dynamics tunnel by the first author and Rodney H. Ricketts of the Vought Corporation, Hampton Technical Center. A six-by-six collocation point arrangement was used in the kernel function analysis. The NASTRAN results are in good agreement with the experiment. The kernel function results indicate a flutter boundary lower than NASTRAN and the experimental results. The NASTRAN results at 0.9 Mach number using 60, 108,

and 189 doublet lattice boxes show that the 108-box and 189-box results are virtually the same, and that the 60-box results are slightly higher.

All-Movable Horizontal Tail

The third configuration which was studied is the aspect-ratio-1.3 all-movable horizontal tail with geared elevator shown in the upper left sketch in figure 9. This configuration is being used in a study to provide a better understanding of the effects of elevator-gear ratio on flutter. Some initial results from this study are presented here. Elevator gear ratio as used herein is defined by the sketch shown at the lower left in figure 9. Also included in figure 9 is the basic aerodynamic model used. This model is a purely analytical representation, that is, no physical model exists for which experimental flutter data have been obtained.

The configuration consists of a stabilizer portion which can translate and rotate about the stabilizer pitch axis which is located at 40 percent of the root chord. A full-span elevator with unswept hinge line is hinged to the stabilizer. The elevator hinge line is at 75 percent of the root chord. Since the stabilizer and elevator were analyzed as rigid surfaces, there are no camber or bending deformations. The horizontal tail was modeled structurally using spring (CELAS2) elements to represent the translational, pitch, and elevator-rotational stiffnesses. The mass and inertia of the stabilizer and elevator were modeled using concentrated masses (CONM2). The elevator gearing was effected by using multipoint constraints (MPC's). Oblique projections of the calculated mode shapes for the 2 to 1 gear-ratio configuration are shown in figure 10. It should be pointed out that since the elevator rotational stiffness spring was in series with the gearing mechanism, the elevator rotational angles in the mode shapes are not simply the stabilizer pitch angle times the gear ratio. The calculated natural frequencies for all gear ratios studied are tabulated on this figure. Note that the mode shapes are composed of varying combinations of vertical translation, stabilizer pitch, and elevator rotation. The mode shapes for the other gear ratios studied are similar to those shown in the figure, the primary differences being in relative angular rotation between the stabilizer and elevator. Also note that increasing the elevator gear ratio had little effect on the first-mode frequency while the second-mode frequency systematically decreased and the third-mode frequency systematically increased as the gear ratio was increased.

To meet the purposes of the present study, it was not only necessary to have a simple structural model to facilitate the changing of structural parameters, but it was also desired to have a simple aerodynamic model (minimum number of doublet lattice boxes) in order to keep computational costs low since the CPU time required for the unsteady aerodynamic forces is approximately proportional to the square of the number of boxes. Since the 25-box arrangement shown in figure 9 gave results essentially the same as a large 100-box arrangement, this admittedly coarse model was used as the basic aerodynamic model. Surface spline functions were used to interpolate the modal displacements. A separate spline function was used for the stabilizer and elevator in order to account properly for the geometric discontinuity in the downwash that occurs at the elevator hinge line.

The calculated flutter results are presented in figure 11 as the variation of flutter frequency and dynamic pressure with elevator gear ratio. All calculations were made for a density of 0.515 kg/m^3 (42 percent of sea-level standard air density) at a Mach number of 0.80. Both the flutter dynamic pressure and frequency increase as the gear ratio is increased indicating that gearing the elevator is mildly favorable from a flutter point of view. The trend of these data is consistent with that presented in reference 5 where wind-tunnel flutter results are presented for a relatively complex geared-elevator model having a planform similar to the one used here.

CONCLUDING REMARKS

Results from applying the NASTRAN Level 16 subsonic flutter analysis (which uses doublet lattice unsteady aerodynamic theory) to three configurations have been presented. The three configurations studied were (1) a swept, tapered, aspect-ratio-6.8 subsonic-transport-type wing, (2) an aspect-ratio-1.7 arrow wing which is representative of supersonic cruise aircraft configurations of current interest, and (3) an aspect-ratio-1.3 all-movable horizontal tail with a geared-elevator control surface. The NASTRAN results for the subsonic-transport wing and the arrow wing were in good agreement with wind-tunnel model experimental flutter results and were consistent with other calculated flutter results obtained using subsonic lifting surface (kernel function) unsteady aerodynamic theory. The NASTRAN results for the horizontal-tail configuration with geared elevator indicated a gradual increase in flutter frequency and dynamic pressure with increasing gear ratio. Although no experimental and other calculated results are available for the specific horizontal tail studied here, the trends of the NASTRAN results are the same as those determined in reference 5 for a similar, but more complex, configuration.

REFERENCES

1. Doggett, Robert V., Jr.; and Harder, Robert L.: Subsonic Flutter Analysis Addition to NASTRAN. NASTRAN: User's Experiences. NASA TM X-2893, September 1973, pp. 507-529.

2. Jew, Howard: Delta Wing Flutter Based on Doublet Lattice Method in NASTRAN. NASTRAN: User's Experiences. NASA TM X-3278, September 1975, pp. 603-613.

3. Farmer, Moses G.; and Hanson, Perry W.: Comparison of Supercritical and Conventional Wing Flutter Characteristics. Proceedings AIAA/ASME/SAE 17th Structures, Structural Dynamics, and Materials Conference (King of Prussia, PA), May 5-7, 1976, pp. 308-614. (Also available as NASA TM X-72837.)

4. Watkins, Charles E.; Woolston, Donald S.; and Cunningham, Herbert J.: A Systematic Kernel Function Procedure for Determining Aerodynamic Forces on Oscillating or Steady Finite Wings at Subsonic Speeds. NASA TR R-48, 1959.

5. Ruhlin, Charles L.; Doggett, Robert V., Jr.; and Gregory, Richard A.: Geared-Elevator Flutter Study. Proceedings AIAA/ASME/SAE 17th Structures, Structural Dynamics, and Materials Conference (King of Prussia, PA), May 5-7, 1976, pp. 598-607.

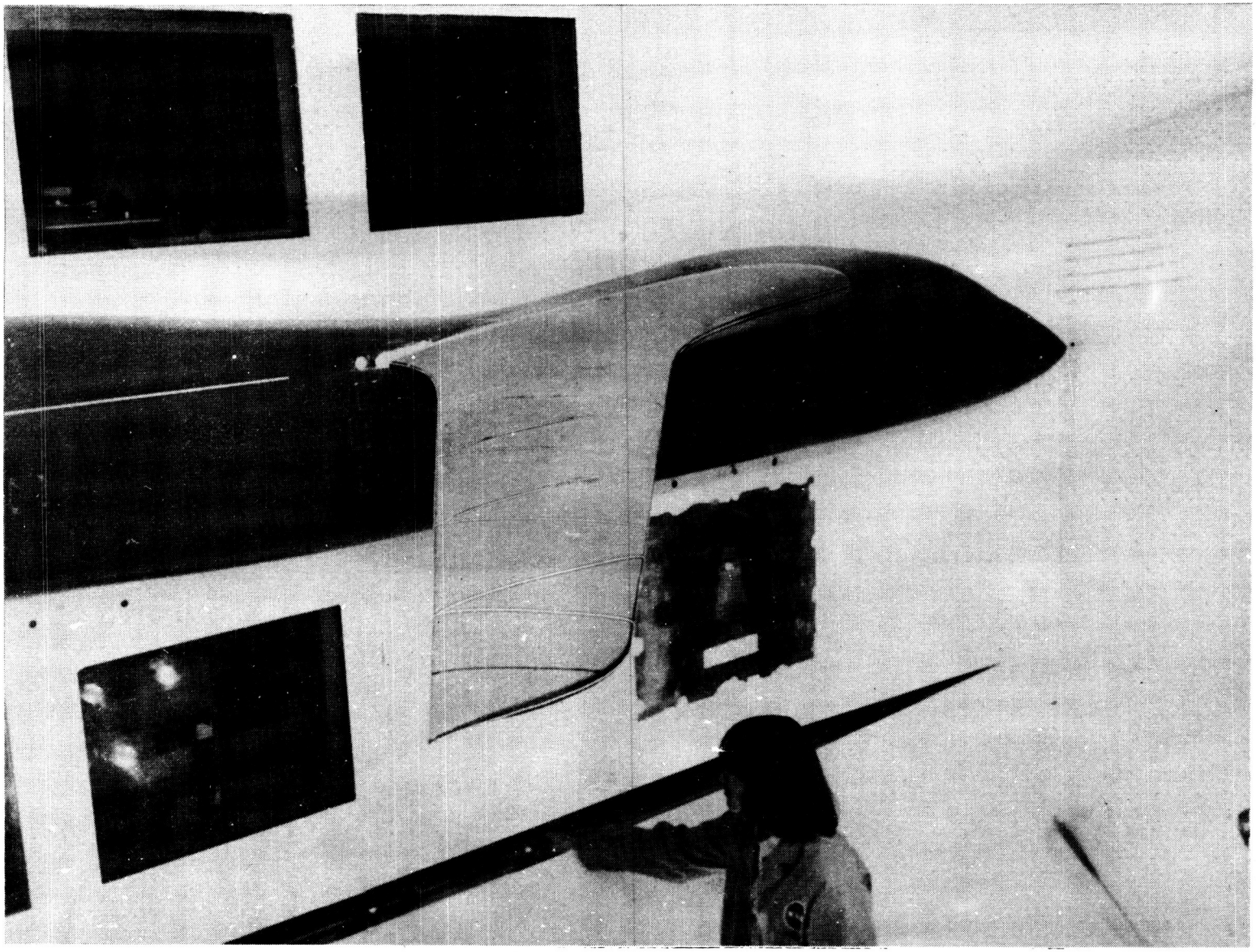

Figure 1. Subsonic-transport wing mounted in transonic dynamics tunnel.

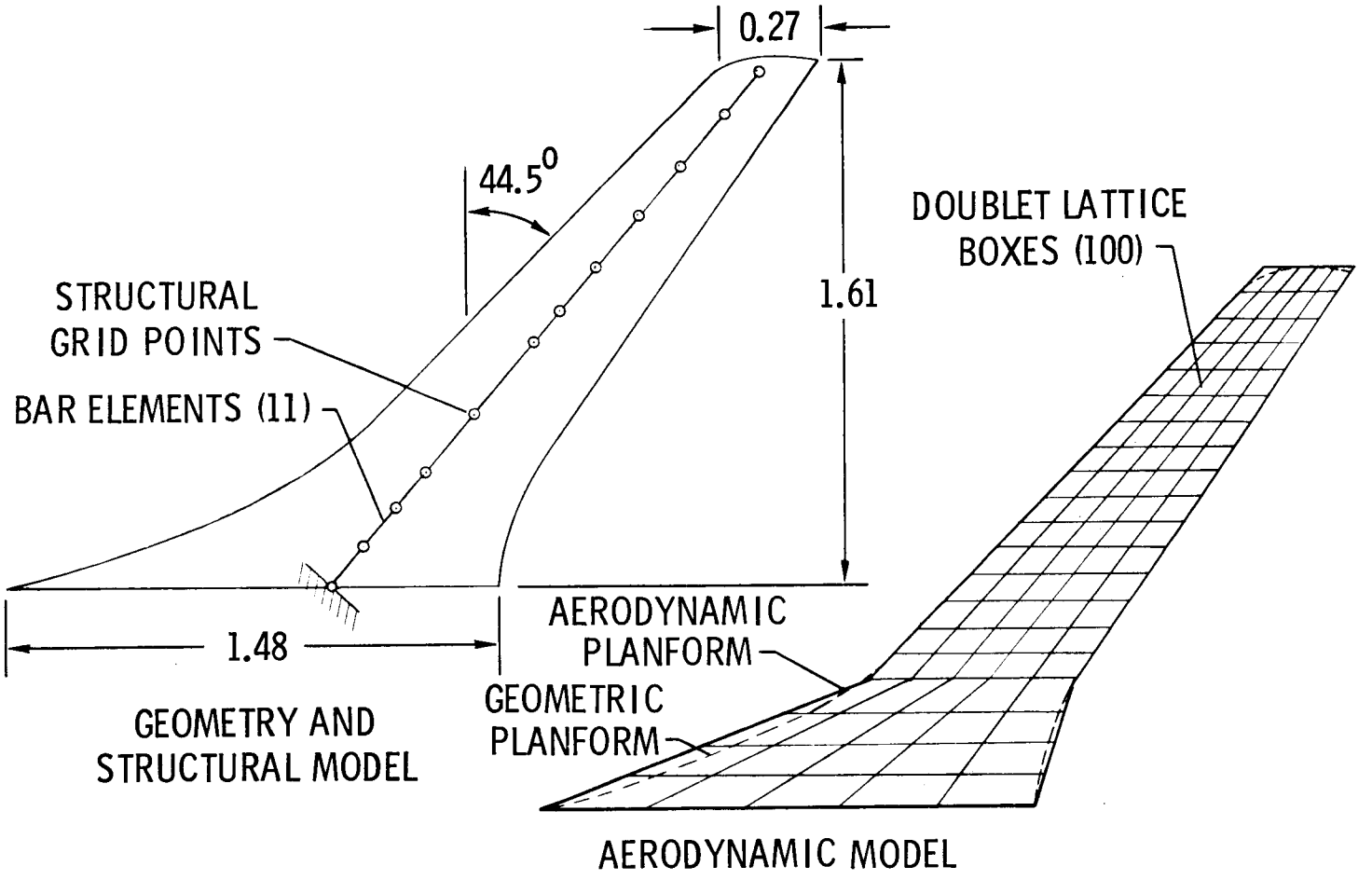

Figure 2. Subsonic-transport-wing geometry, structural model, and aerodynamic model. All dimensions are in meters.

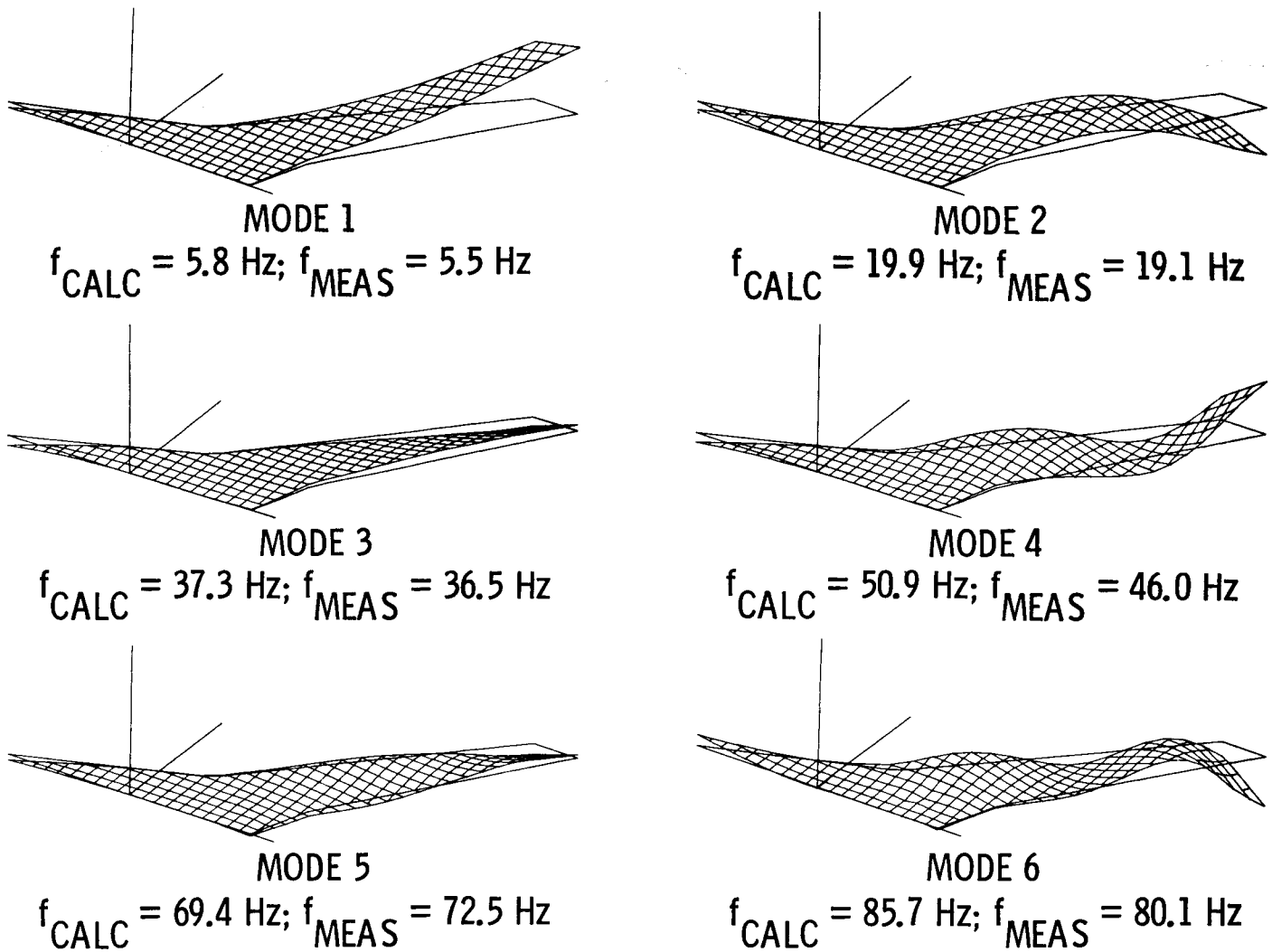

Figure 3. Subsonic-transport-wing mode shapes and frequencies.

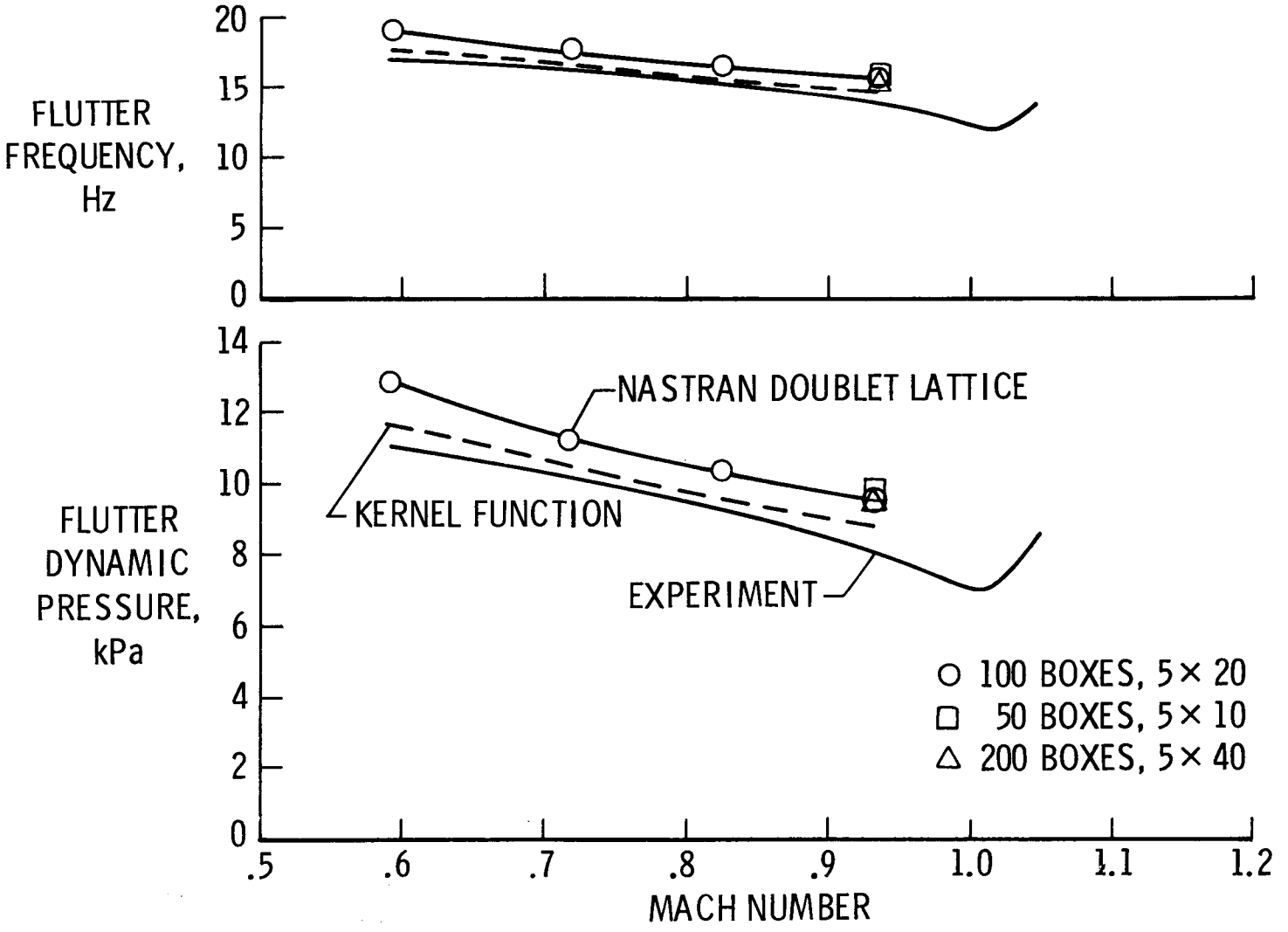

Figure 4. Subsonic-transport-wing flutter results.

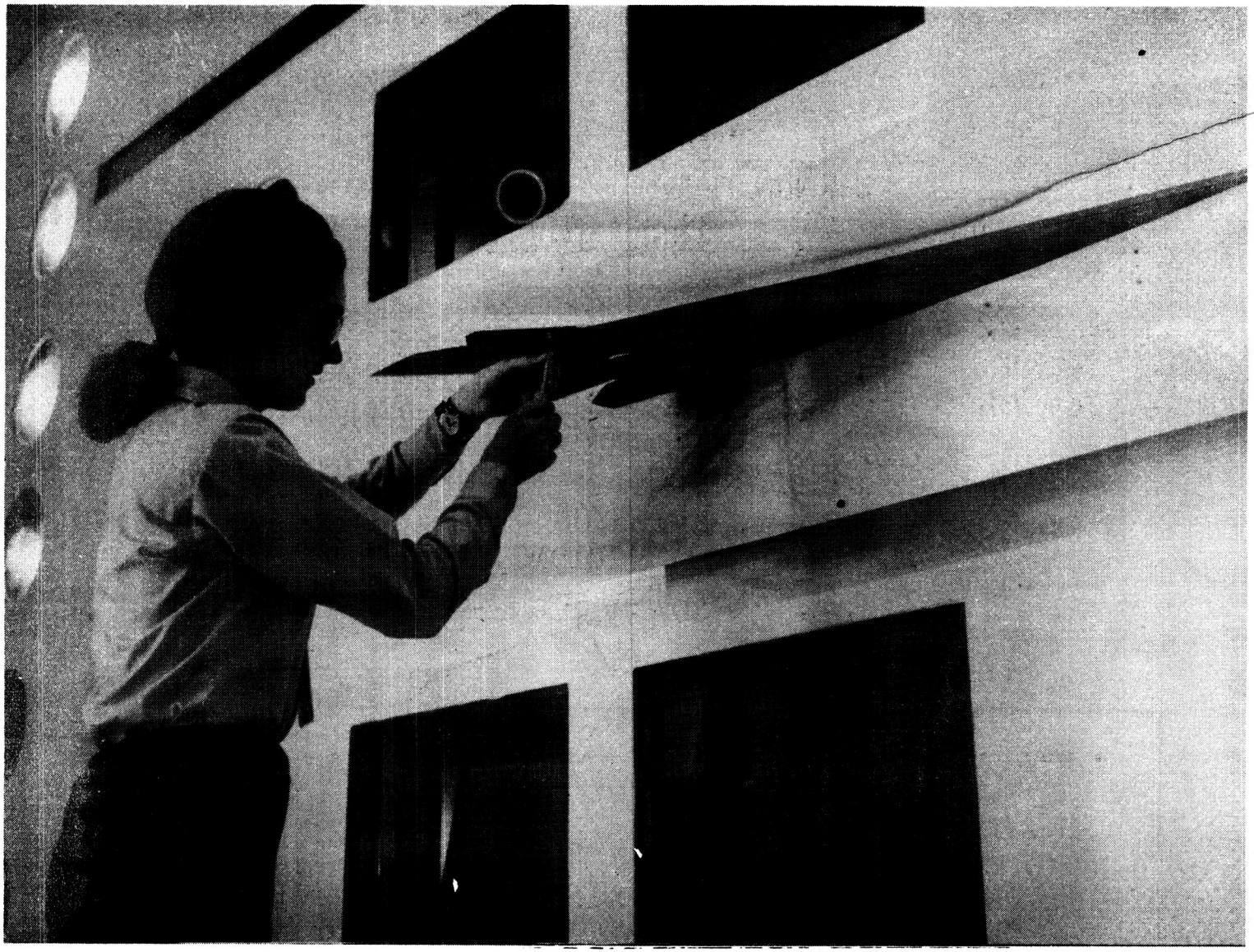

Figure 5. Arrow wing mounted in transonic dynamics tunnel.

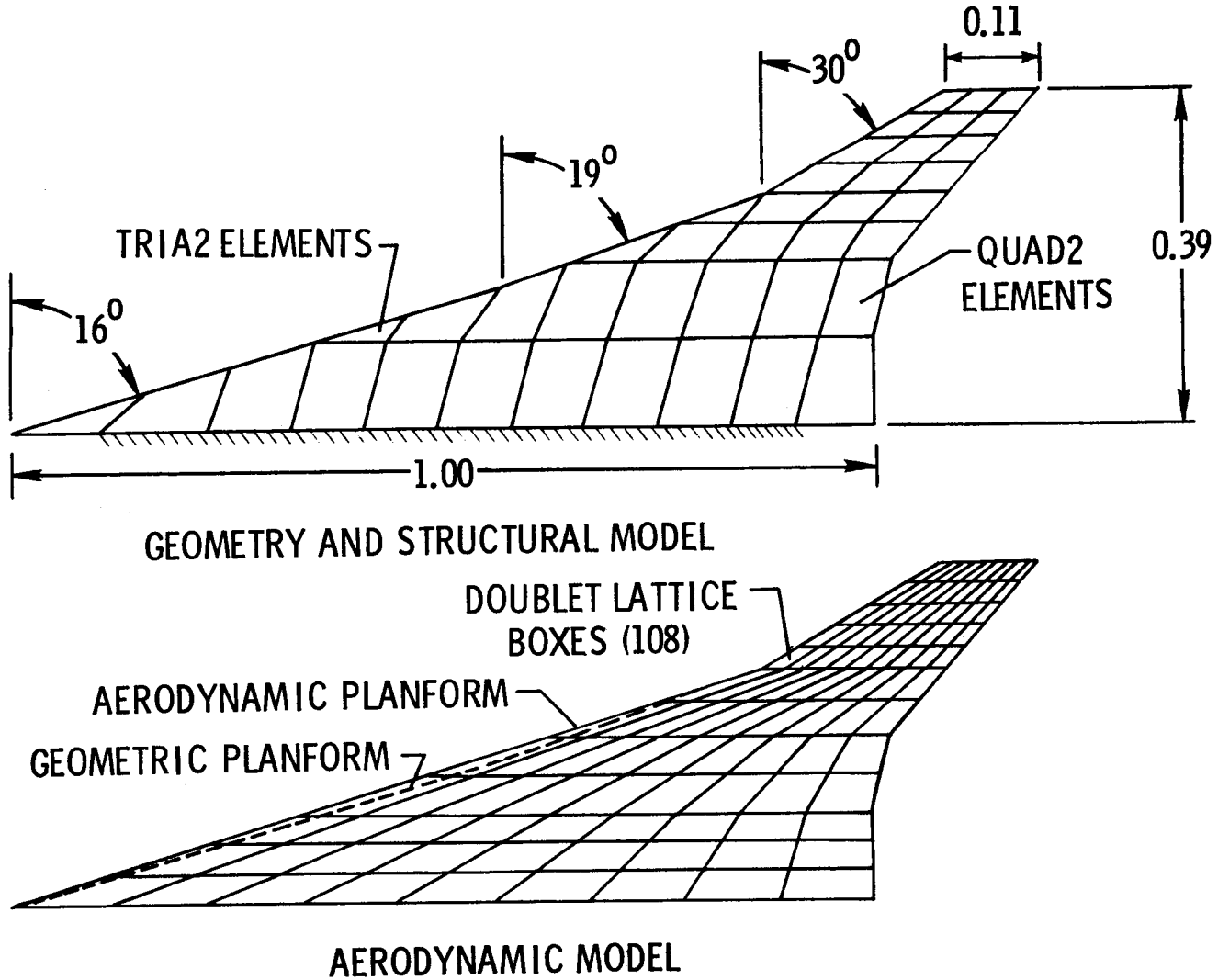

Figure 6. Arrow-wing geometry, structural model, and aerodynamic model. All dimensions are in meters.

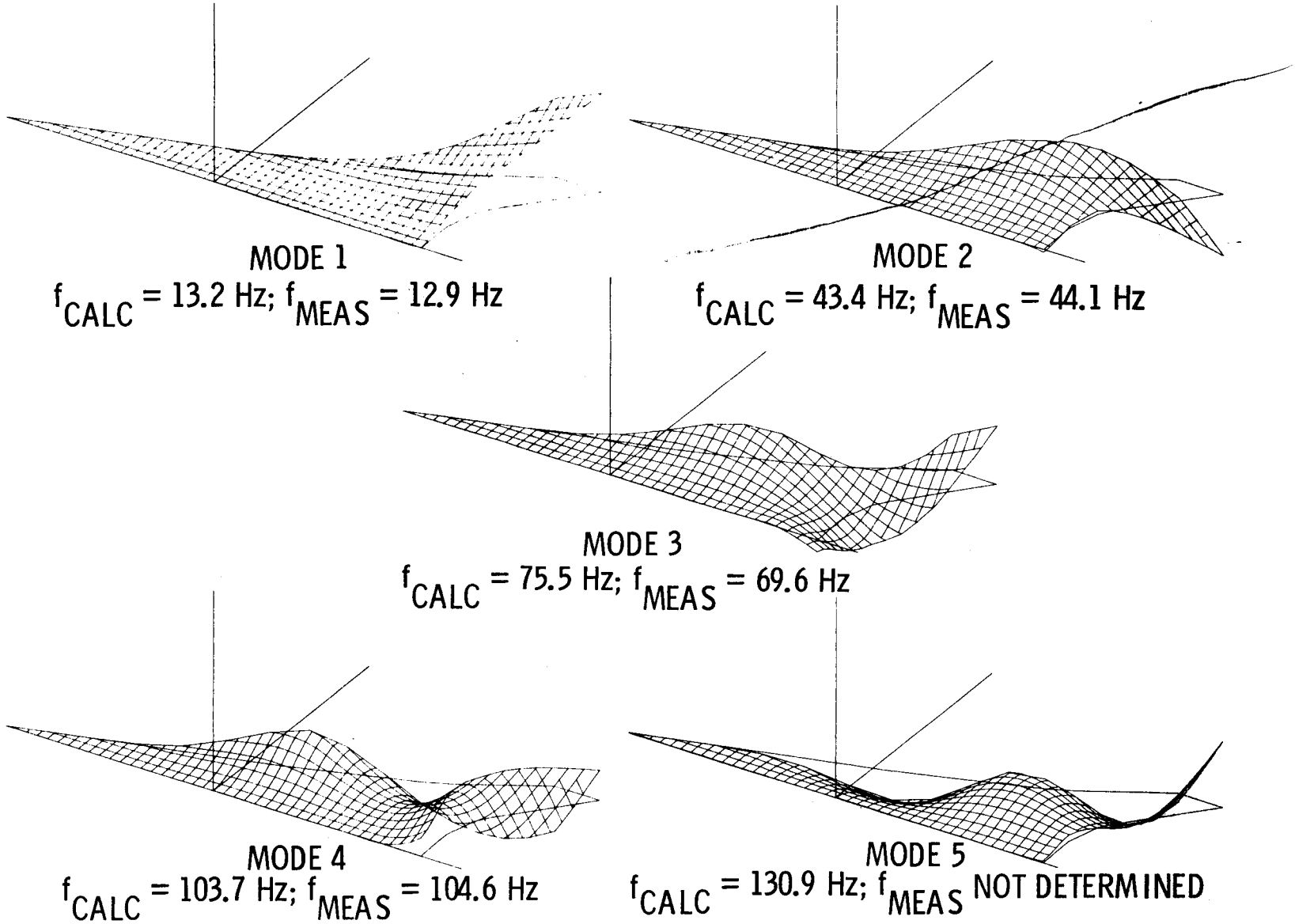

Figure 7. Arrow-wing mode shapes and frequencies.

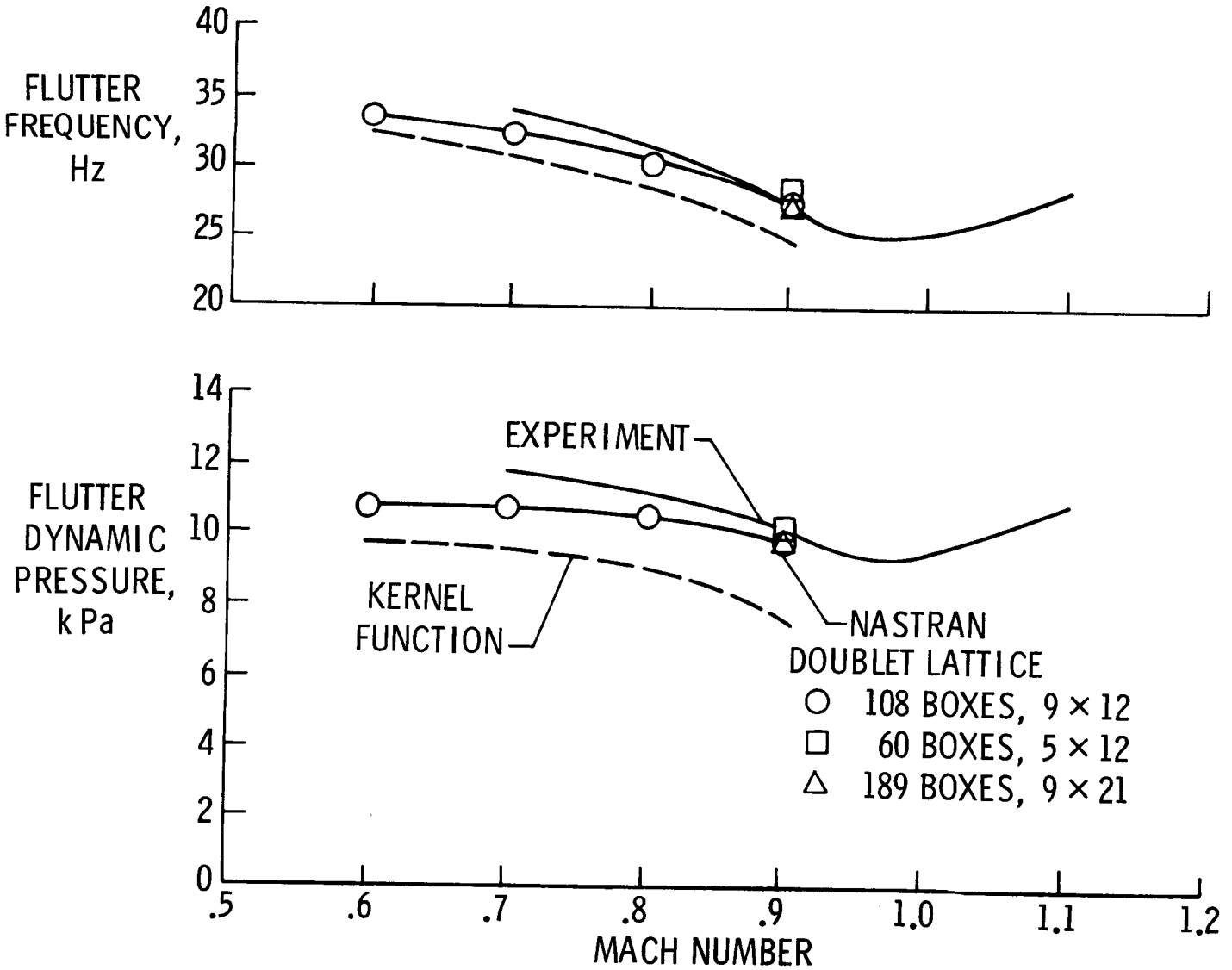

Figure 8. Arrow-wing flutter results.

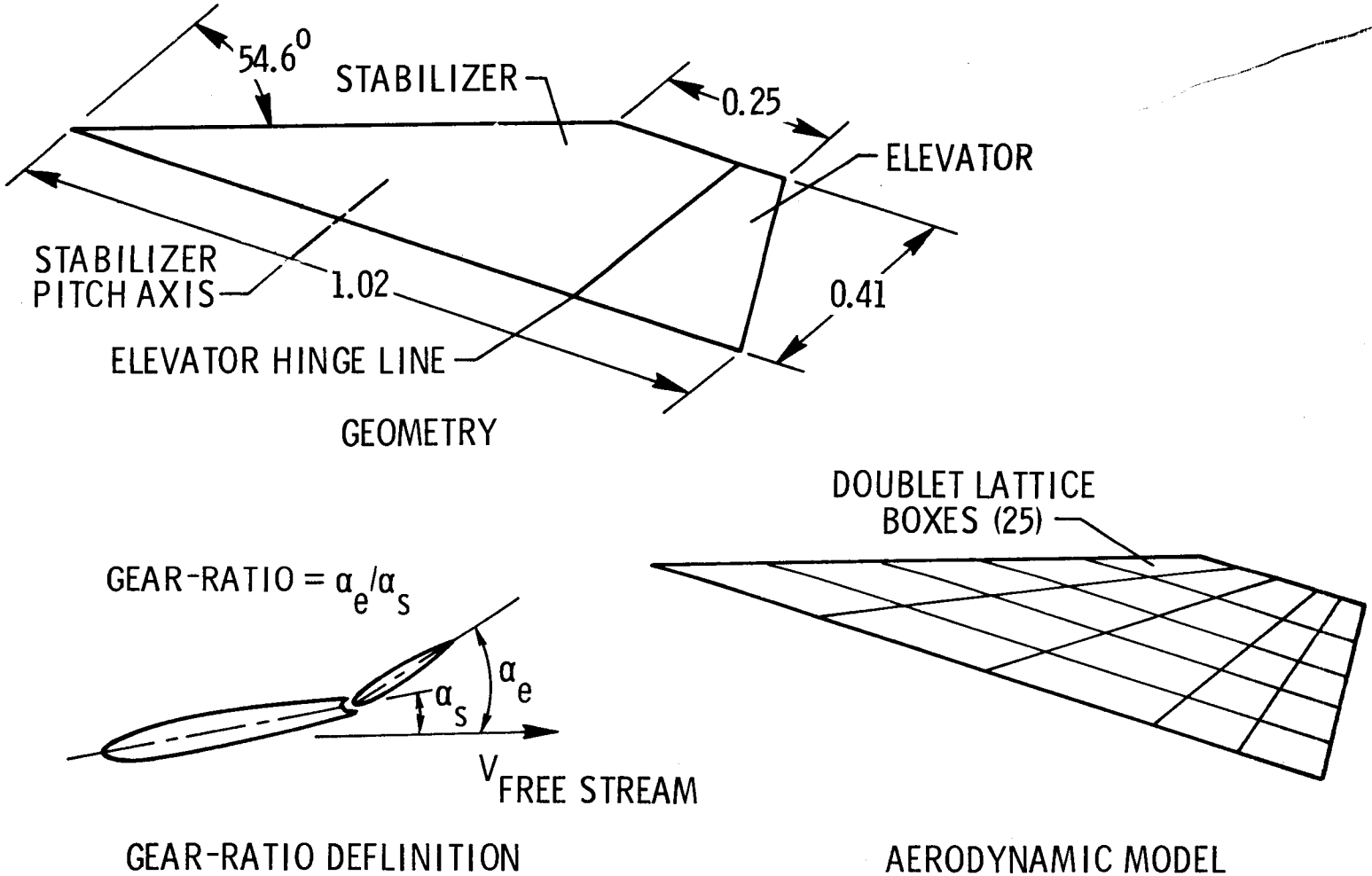

Figure 9. All-movable horizontal tail geometry, aerodynamic model, and gear-ratio definition. All dimensions are in meters.

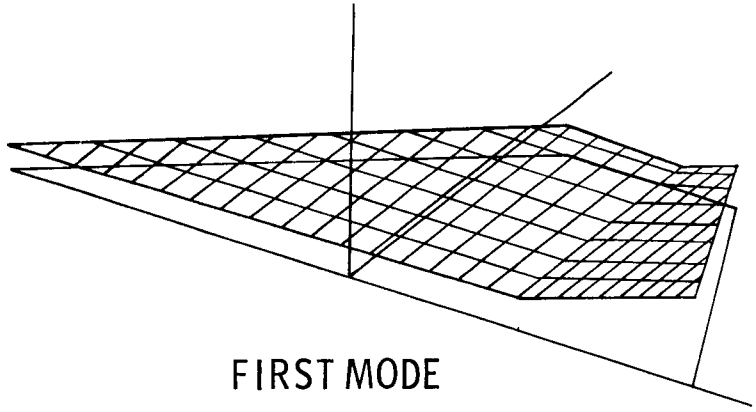

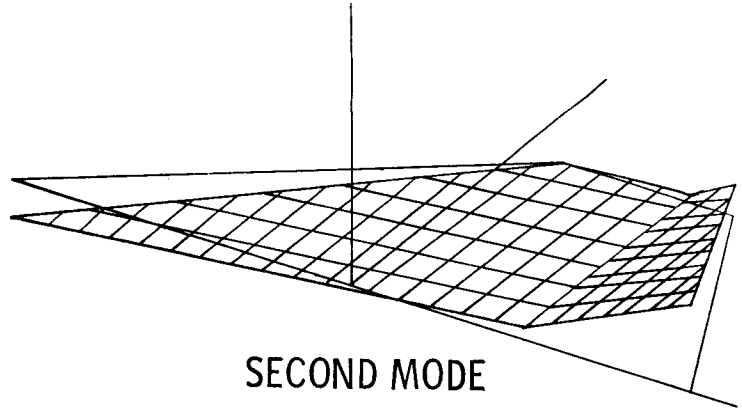

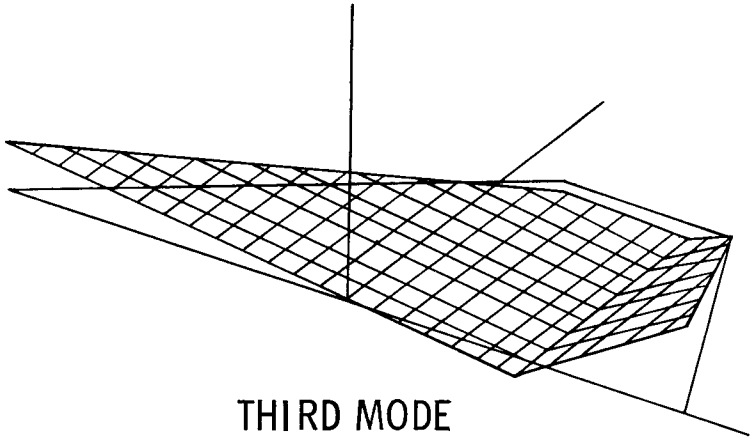

	CALCULATED NATURAL FREQUENCIES, Hz		
GEAR-RATIO	FIRST MODE	SECOND MODE	THIRD MODE
1.0 : 1	6.9	21.6	35.6
1.5 : 1	6.9	20.4	37.6
2.0 : 1	6.9	19.4	39.7
2.5 : 1	6.9	18.4	41.9
3.0 : 1	6.9	17.5	44.2

Figure 10. All-movable horizontal tail mode shapes and frequencies.

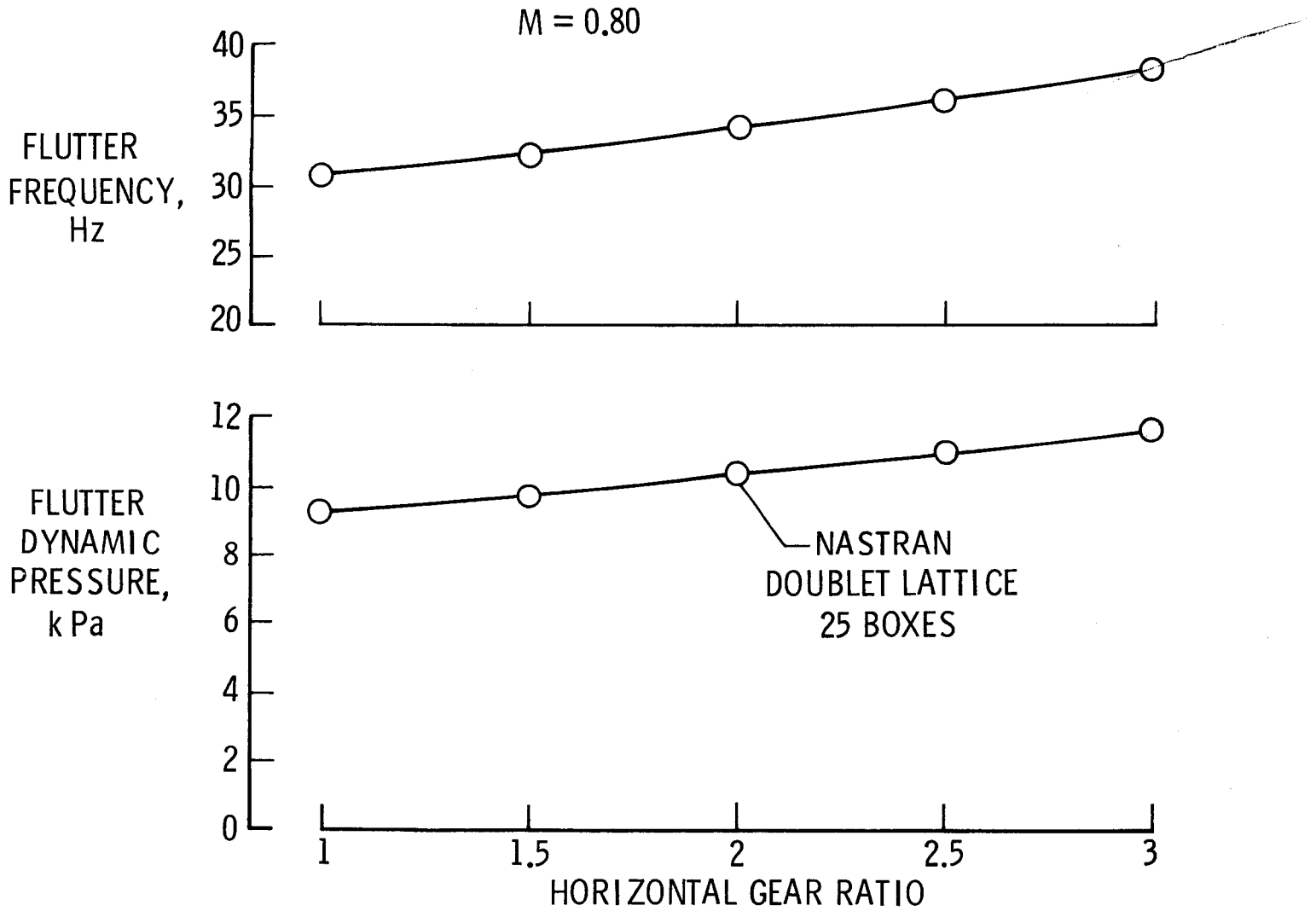

Figure 11. All-movable horizontal tail flutter results.

AUTOMATED MULTI-STAGE SUBSTRUCTURING ANALYSIS COMPARED WITH SUPERELEMENT ANALYSIS

by

Lalit C. Shah
Rockwell International

ABSTRACT

Two large NASTRAN models for static analysis have been built by use of two different automated substructuring techniques currently available. The first model consists of about 30,000 degrees of freedom representing the Space Shuttle Crew Module. The second model consists of about 20,000 degrees of freedom representing the B-1 Nacelle. The automated multistage substructuring capability added to the Level 15.5 was applied to the first model and some interesting lessons were learned from that experience. The superelement capability, available in MacNeal-Schwendler version of NASTRAN (CDC Level 28), was applied to the second model. User convenience (automation) becomes increasingly important for large finite-element models. There are some significant differences between the two approaches in this area even though the basic matrix operations carried out are identical. In conclusion, some practical suggestions are presented that may be beneficial to other users.

MODAL SEISMIC ANALYSIS OF A NUCLEAR POWER PLANT CONTROL PANEL AND COMPARISON WITH SAP IV

by

M. R. Pamidi
Sargent and Lundy Engineers
Chicago, Illinois

and

P. R. Pamidi
Computer Sciences Corporation
Hampton, Virginia

SUMMARY

This paper deals with the application of NASTRAN to seismic analysis by considering the example of a nuclear power plant control panel. A modal analysis of a three-dimensional model of the panel, consisting of beam and quadrilateral membrane elements, is performed. Using the results of this analysis and a typical response spectrum of an earthquake, the seismic response of the structure is obtained. ALTERs required to the program in order to compute the maximum modal responses as well as the resultant response are given. The results are compared with those obtained by using the SAP IV computer program.

INTRODUCTION

Current government and industry regulations [References 1 and 2] require that the safety-related systems, structures and components of nuclear power plants be designed to withstand specified seismic excitations without loss of capability to perform their safety functions. This requirement is necessary in order to ensure

(a) continued operation of the reactor without undue risk to the health and safety of the public during an Operating Base Earthquake (OBE), and,

(b) shutdown of the reactor and its maintenance in a safe shutdown condition following a Safe Shutdown Earthquake (SSE).

The design of such equipment to withstand seismic disturbances involves dynamic analysis, testing or a combination of both. Seismic qualification by analysis alone is deemed sufficient provided the safety function of a structure or component is assured by its structural integrity. Thus, for instance, most mechanical equipment, such as heat exchangers, tanks, pressure vessels, etc., are usually qualified by analysis. Qualification by testing is recommended

in those cases where functional operability is not necessarily assured by structural integrity. Thus, most electrical equipment, such as switchgears, motor control centers, control panels, etc., are usually qualified by testing. However, in many instances, testing is impractical either due to the size of the equipment involved or due to the prohibitive cost entailed by such testing. In such cases, a detailed dynamic analysis of the equipment, such as a control panel, is performed and the various associated electrical instrumentation and devices are then tested to acceleration levels determined by the analysis.

In this study, the application of NASTRAN to seismic analysis has been discussed by considering the example of a nuclear power plant control panel. A modal analysis of a three-dimensional model of the panel, consisting of beam and quadrilateral membrane elements, is performed. Using the results of this analysis and a typical response spectrum of an earthquake, the seismic response of the structure is obtained. The results are compared with those obtained by using the SAP IV computer program.

FORMULATION OF THE SEISMIC ANALYSIS PROBLEM

Obtaining the Modal Responses

The dynamic behavior of a system having multiple (n) degrees of freedom and subjected to seismic excitation is described by a set of differential equations represented by

$$[M]\{\ddot{u}\} + [C]\{\dot{u}\} + [K]\{u\} = -[M][D]\{\ddot{u}_f\} \tag{1}$$

where [M], [C] and [K] are the (n x n) mass, damping and stiffness matrices respectively of the system; {u} is the (n x 1) displacement vector of interest; $\{\ddot{u}_f\}$ is a (3 x 1) vector that represents the time-dependent floor acceleration in the three component (X, Y and Z) directions; and [D] is an (n x 3) direction cosine matrix consisting of ones and zeroes that selects the masses that are involved in the motion in the three directions. The negative sign in this equation merely indicates that the effective load due to the seismic disturbance is opposite to that of the floor acceleration.

The displacement vector {u} in Eq. (1) may be expressed in terms of the normal coordinates as

$$\{u\} = \sum_{i=1}^{n} \{\phi_i\} w_i = [\phi]\{w\} \tag{2}$$

where {w} is an (n x 1) vector that represents the normal (or generalized) coordinates w_i and $[\phi]$ is an (n x n) matrix whose columns $\{\phi_i\}$ are the n eigenvectors of the free, undamped system given by

$$[M]\{\ddot{u}\} + [K]\{u\} = 0 \tag{3}$$

By using the orthogonal properties of the eigenvectors and utilizing the relationships that exist among the generalized mass, damping and stiffness quantities at any mode, Eqs. (1) and (2) can be combined to give a set of n uncoupled equations in the normal coordinates as follows [Ref. 3]:

$$\ddot{w}_i + 2\,\xi_i\,\omega_i\dot{w}_i + \omega_i^2\,w_i = -\,\{F_i\}^T\{\ddot{u}_f\},\ i = 1, 2, \ldots\ldots, n \tag{4}$$

where ξ_i is the damping ratio and ω_i is the natural frequency of the ith mode. $\{F_i\}$ is a (3 x 1) vector whose elements represent the so-called modal participation factors in the three component directions for the ith mode and is given by

$$\{F_i\}^T = \begin{Bmatrix} F_{ix} \\ F_{iy} \\ F_{iz} \end{Bmatrix}^T = \frac{\{\phi_i\}^T\,[M]\,[D]}{\{\phi_i\}^T\,[M]\,\{\phi_i\}} \tag{5}$$

The denominator on the right hand side of the above equation is the generalized mass for the ith mode.

Equations (4) can be solved for significant modes by direct integration if the time-history of the floor acceleration $\{\ddot{u}_f\}$ is known. The solutions for the various significant modes can then be superimposed as per Eq. (2) to obtain the total solution. However, from a design point of view, it is simpler and often more convenient and economical to obtain the maximum displacements in any given mode by response spectrum analysis. This approach involves the use of design spectra derived from past earthquake data.

Let $\{S_{di}\} = \begin{Bmatrix} S_{dix} \\ S_{diy} \\ S_{diz} \end{Bmatrix}$ represent the spectral displacements for the ith mode for excitations in the X, Y and Z directions. The corresponding spectral velocities $\{S_{vi}\}$ and spectral accelerations $\{S_{ai}\}$ are related to the spectral displacements by

$$\{S_{di}\} = \frac{\{S_{vi}\}}{\omega_i} = \frac{\{S_{ai}\}}{\omega_i^2} \tag{6}$$

The maximum response for the ith mode due to the individual spectral displacements S_{dix}, S_{diy} and S_{diz} in the X, Y and Z directions respectively is

given by [Ref. 3]:

$$\{u_i\}_{x_{max}} = \{\phi_i\}\ F_{ix}\ S_{dix} \tag{7a}$$

$$\{u_i\}_{y_{max}} = \{\phi_i\}\ F_{iy}\ S_{diy} \tag{7b}$$

$$\{u_i\}_{z_{max}} = \{\phi_i\}\ F_{iz}\ S_{diz} \tag{7c}$$

The maximum response for the ith mode due to simultaneous seismic excitations in the three component directions is obtained by combining Eqs. (7a), (7b) and (7c) and is represented by[1]

$$\{u_i\}_{max} = \{u_i\}_{x_{max}} + \{u_i\}_{y_{max}} + \{u_i\}_{z_{max}} \tag{8}$$

or

$$\{u_i\}_{max} = \{\phi_i\}\ G_i \tag{9}$$

where G_i is a scalar quantity given by the product

$$G_i = \{F_i\}^T\{S_{di}\} \tag{10}$$

Eq. (9), which gives the maximum response for the ith mode, can be generalized to give the maximum response for any of m modes ($1 \leq m \leq n$) by the single matrix equation

$$[u']_{max} = [\phi']\ \mathrm{diag}\left[[F']^T[S'_d]\right] \tag{11}$$

where

$$[u']_{max} = [\{u_1\}_{max}\ \{u_2\}_{max}\ \ldots\ldots\ \{u_m\}_{max}] \tag{12a}$$

---

[1] Eq. (8) gives a conservative estimate for the maximum response for the ith mode. It is acceptable to the regulatory authorities to compute this response by taking the square root of the sum of the squares of the maximum responses in the three component directions [Ref. 4].

$$[\phi'] = [\{\phi_1\}\ \{\phi_2\}\ \ldots\ldots\ \{\phi_m\}] \tag{12b}$$

$$[F'] = [\{F_1\}\ \{F_2\}\ \ldots\ldots\ \{F_m\}] \tag{12c}$$

and

$$[S_d'] = [\{S_{d1}\}\ \{S_{d2}\}\ \ldots\ldots\ \{S_{dm}\}] \tag{12d}$$

Eq. (11) can be rewritten as

$$[u']_{max} = [\phi']\,[G'] \tag{13}$$

where $[G'] = \mathrm{diag}[F']^T[S_d'] = \begin{bmatrix} G_1 & 0 & \ldots\ldots & 0 \\ 0 & G_2 & \ldots\ldots & 0 \\ \vdots & \vdots & \ddots & \vdots \\ 0 & 0 & \ldots\ldots & G_m \end{bmatrix}$ (14)

The elements of the (m x m) diagonal matrix [G'] are given by Eq. (10).

Combining the Modal Responses

The total response of the system can be obtained by combining the maximum responses of the individual modes involved as given by Eq. (13). The exact manner in which these modal responses are combined is, however, a matter of judgment and there is no one way for obtaining the total response. When the modes are not closely spaced,[2] current regulatory practice [Ref. 4] requires that the resultant response (whether it be displacement, stress or other quantity) be obtained by taking the square root of the sum of the squares (SRSS) of the corresponding maximum responses for the individual modes involved. When the modes are closely spaced, it is required that the total response be computed by any one of three methods acceptable to the regulatory authorities. Referred to as the Grouping Method, the Ten Percent Method and the Double Sum Method, the details of these methods are given in Reference 4.

---

[2] Two modes are said to be closely spaced if their frequencies differ from each other by 10% or less of the lower frequency.

ANALYSIS

Analysis by NASTRAN Program

NASTRAN cannot directly perform seismic analysis, but can be adapted for the purpose. The procedure employed here corresponds to the theoretical development presented in the previous section. The method essentially involves two major steps as indicated below[3]:

Step 1. Perform a normal mode analysis using Rigid Format 3 and obtain the significant modes.[4]

Step 2. Once the significant natural frequencies are known, input the appropriate spectral displacement matrix $[S_d']$ [see Eq. (12d)] and the direction cosine matrix [D] [see Eq. (1)] via DMI bulk data cards and repeat the normal mode analysis using the following ALTERs to Rigid Format 3 (Level 16) and employing NØRM = MASS (normalization to unit value of the generalized mass) on the EIGR bulk data card [Ref. 7]:

```
ALTER 106 $
MPYAD     PHIA,MAA,/DUMMYA/C,N,1 $
MPYAD     DUMMYA,DIRCØS,/MØDEPF/C,N,0 $
MPYAD     MØDEPF,SEISMIC,/DUMMYB/C,N,0 $
DIAGØNAL  DUMMYB/DUMMYC/C,N,SQUARE $
MPYAD     PHIA,DUMMYC,/PHIASS/C,N,0 $
ALTER 108 $
SDR1      USET,,PHIASS,,,GØ,GM,,KFS,,/PHIG,,QG/C,N,1/C,N,REIG $
ALTER 121 $
TRNSP     PHIASS/PHIASST $
MPYAD     PHIASS,PHIASST,/DUMMYD/C,N,0 $
DIAGØNAL  DUMMYD/SRSSDISP/C,N,CØLUMN/C,N,0.5 $
MATPRN    SRSSDISP,,,,// $
ENDALTER  $
```

---

[3] The adaptation of NASTRAN for seismic analysis has also been discussed by other users [Refs. 5 and 6].

[4] For seismic analysis purposes, a mode is considered significant if its frequency is less than or equal to 33 Hz.

The data blocks used in the above ALTER package have the following correspondences to the matrices mentioned in the previous section:

$$
\begin{aligned}
\text{PHIA} &\equiv [\phi'] \\
\text{MAA} &\equiv [M] \\
\text{DIRCØS} &\equiv [D] \\
\text{MØDEPF} &\equiv [F']^T \\
\text{SEISMIC} &\equiv [S'_d] \\
\text{DUMMYC} &\equiv [G'] \\
\text{PHIASS} &\equiv [u']_{max}
\end{aligned}
$$

The so-called eigenvectors printed out by the above analysis actually represent the maximum modal responses (displacements) as given by Eq. (13). The stresses obtained correspond to these displacements.

The output data block SRSSDISP in the above ALTER package is an (n x 1) vector that represents the resultant response obtained by taking the square root of the sum of the squares (SRSS) of the maximum modal displacements. The corresponding SRSS stresses can be obtained by combining the individual modal stresses.

Analysis by SAP IV Program

SAP IV can perform seismic analysis directly without the need for a separate intermediate run just to obtain the significant modes. The proportions of the seismic excitations in the three directions are specified and the spectral information (displacements or accelerations) is input as a table of spectral values versus period. The maximum modal displacements and the resultant (SRSS) displacements and stresses are automatically output. The details of the method are explained fully in Reference 8.

FINITE ELEMENT MODEL

The basic details of the finite element model of the control panel considered are shown in Figures 1, 2 and 3. Beam elements of three different cross sections and quadrilateral membrane elements of two different thicknesses are used to model the structure. The beam elements are represented by the CBAR elements in NASTRAN and by the three-dimensional beam elements (element type 2) in SAP IV; the membrane elements are represented by the CQDMEM elements in NASTRAN and by the plane stress quadrilateral membrane elements (element type 3) in SAP IV. A total of 265 active degrees of freedom are involved in the analysis. The complete details of the model can be obtained from the authors.

RESULTS

Using essentially identical input data, the finite element model described above was analyzed by both NASTRAN and SAP IV programs following the procedure outlined earlier. Seismic excitations of equal magnitude in the three component directions were assumed. The spectral data used was based on the El Centro (Calif.) earthquake of 1940. A damping of 2% (see Reference 9 for guidelines in this regard) was assumed.

The results of the analysis are presented in Tables 1, 2 and 3. Table 1 lists the significant natural frequencies obtained by the two programs. Table 2 gives the corresponding modal participation factors. Table 3 shows some representative resultant (SRSS) displacements of significant magnitude.

It can be seen from Table 1 that the agreement between the significant natural frequencies obtained by the two programs is excellent. The modal participation factors given in Table 2 agree well too, except when their magnitudes are small; this is due to small differences that exist in the various eigenvector components (not shown) obtained by the two programs. The representative resultant (SRSS) displacements of significant magnitude shown in Table 3 also agree well, but the same is not true when they are of smaller magnitude. This is due not only to the small differences in the modal participation factors involved, but also to the different manner in which the spectral data is input to the two programs. The agreement in the results, on the whole, is quite good.

SUMMARY AND CONCLUSIONS

The application of NASTRAN to seismic analysis has been discussed by considering the example of a nuclear power plant control panel. A modal analysis of a three-dimensional model of the panel, consisting of beam and quadrilateral membrane elements, is performed. Using the results of this analysis and a typical response spectrum of an earthquake, the seismic response of the structure is obtained. ALTERs required to the program in order to compute the maximum modal responses as well as the resultant (SRSS) response are given. The results are compared with those obtained by using the SAP IV program. The agreement, on the whole, is quite satisfactory.

The paper demonstrates the adaptability and suitability of NASTRAN for seismic analysis. The greater choice of elements offered by NASTRAN as well as the availability of such desirable features as the CNGRNT capability (which can result in significant reductions in running times particularly for large problems) [Ref. 7] and Guyan reduction [Ref. 10] make this versatile program an attractive tool for seismic analysis of large structures.

REFERENCES

1. Regulatory Guide 1.29, Seismic Design Classification, U. S. Atomic Energy Commission, Directorate of Regulatory Standards, Washington, D. C., Revision 1, August 1973.

2. IEEE STD 344-1975, IEEE Recommended Practices for Seismic Qualification of Class 1E Equipment for Nuclear Power Generating Stations, IEEE, New York, 1975.

3. Wiegel, R. L., (ed.), Earthquake Engineering, Prentice-Hall, Englewood Cliffs, N. J., 1970.

4. Regulatory Guide 1.92, Combining Modal Responses and Spatial Components in Seismic Response Analysis, U. S. Nuclear Regulatory Commission, Office of Standards Development, Washington, D. C., Revision 1, February 1976.

5. Go, J. C., "Seismic Analysis of Nuclear Power Plant Structures", NASTRAN: Users' Experiences, NASA TM X-2893, September 1973, pp. 243-249.

6. Setlur, A. V. and Valathur, M., "Some Studies on the Use of NASTRAN for Nuclear Power Plant Structural Analysis and Design", NASTRAN: Users' Experiences, NASA TM X-2893, September 1973, pp. 585-594.

7. The NASTRAN User's Manual, (Level 16.0), NASA SP-222(03), March 1976.

8. Bathe, K. J., Wilson, E. L., and Peterson, F. E., SAP IV: A Structural Analysis Program for Static and Dynamic Response of Linear Systems, University of California, Earthquake Engineering Research Center, Berkeley, California, June 1973.

9. Regulatory Guide 1.61, Damping Values for Seismic Design of Nuclear Power Plants, U. S. Atomic Energy Commission, Directorate of Regulatory Standards, Washington, D. C., October 1973.

10. The NASTRAN Theoretical Manual, (Level 16.0), NASA SP-221(03), March 1976.

Table 1. Natural Frequencies of Significant Modes

Mode no.	Natural frequencies (Hz)	
	NASTRAN results	SAP IV results
1	0.6352E+01	0.6352E+01
2	0.6563E+01	0.6563E+01
3	0.6699E+01	0.6700E+01
4	0.1013E+02	0.1013E+02
5	0.1180E+02	0.1180E+02
6	0.1401E+02	0.1401E+02
7	0.1648E+02	0.1649E+02
8	0.1652E+02	0.1652E+02
9	0.1665E+02	0.1665E+02
10	0.1706E+02	0.1706E+02
11	0.2371E+02	0.2370E+02
12	0.2578E+02	0.2579E+02
13	0.3082E+02	0.3082E+02

Table 2. Modal Participation Factors for Significant Modes

Mode no.	Modal participation factors					
	NASTRAN results			SAP IV results		
	X-direction	Y-direction	Z-direction	X-direction	Y-direction	Z-direction
1	0.4692E-04	0.2313E-01	0.6498E+00	0.4879E-04	0.2316E-01	0.6524E+00
2	0.1033E-03	-0.1002E-01	-0.4356E+00	0.1305E-03	-0.9960E-02	-0.4348E+00
3	0.1467E-03	0.1909E-01	0.5135E+00	0.1679E-03	0.1902E-01	0.5128E+00
4	-0.2529E-03	-0.1750E-01	0.4024E+00	-0.3235E-03	-0.1755E-01	0.4035E+00
5	0.3132E+00	0.1331E-02	0.3729E-03	0.3132E+00	0.1340E-02	0.4287E-03
6	-0.1957E-03	0.5041E-01	-0.2872E+00	-0.1730E-03	0.5043E-01	-0.2885E+00
7	0.2507E+00	-0.6438E-02	0.3732E-03	0.2507E+00	-0.6425E-02	0.2668E-03
8	-0.1324E-02	-0.2445E-01	0.1439E-01	-0.1446E-02	-0.2465E-01	0.1291E-01
9	0.1969E-02	0.3657E-01	-0.5804E-01	0.1849E-02	0.3639E-01	-0.5702E-01
10	-0.7096E-03	0.1421E-01	-0.3724E-01	-0.7052E-03	0.1409E-01	-0.3580E-01
11	-0.3842E+00	0.2454E-01	-0.2009E-02	-0.3844E+00	0.2452E-01	-0.2307E-02
12	-0.5905E-03	-0.1363E+00	0.1533E+00	-0.6860E-03	-0.1363E+00	0.1564E+00
13	-0.1407E+00	-0.2246E-01	-0.2920E-02	-0.1407E+00	-0.2247E-01	-0.3697E-02

Table 3. Representative Values of Resultant (SRSS) Displacements

Grid point no.	Direction of motion	Resultant (SRSS) displacements (cm.)	
		NASTRAN results	SAP IV results
19	Z	0.53861E+00	0.54059E+00
20	Z	0.65093E+00	0.65283E+00
30	X	0.16941E+00	0.17834E+00
34	Z	0.67732E+00	0.68189E+00
35	Z	0.85773E+00	0.86271E+00
45	X	0.26523E+00	0.26662E+00
49	Z	0.44626E+00	0.44775E+00
50	Z	0.56609E+00	0.56746E+00

FINITE ELEMENT MODEL
(Numbers Designate Nodes)

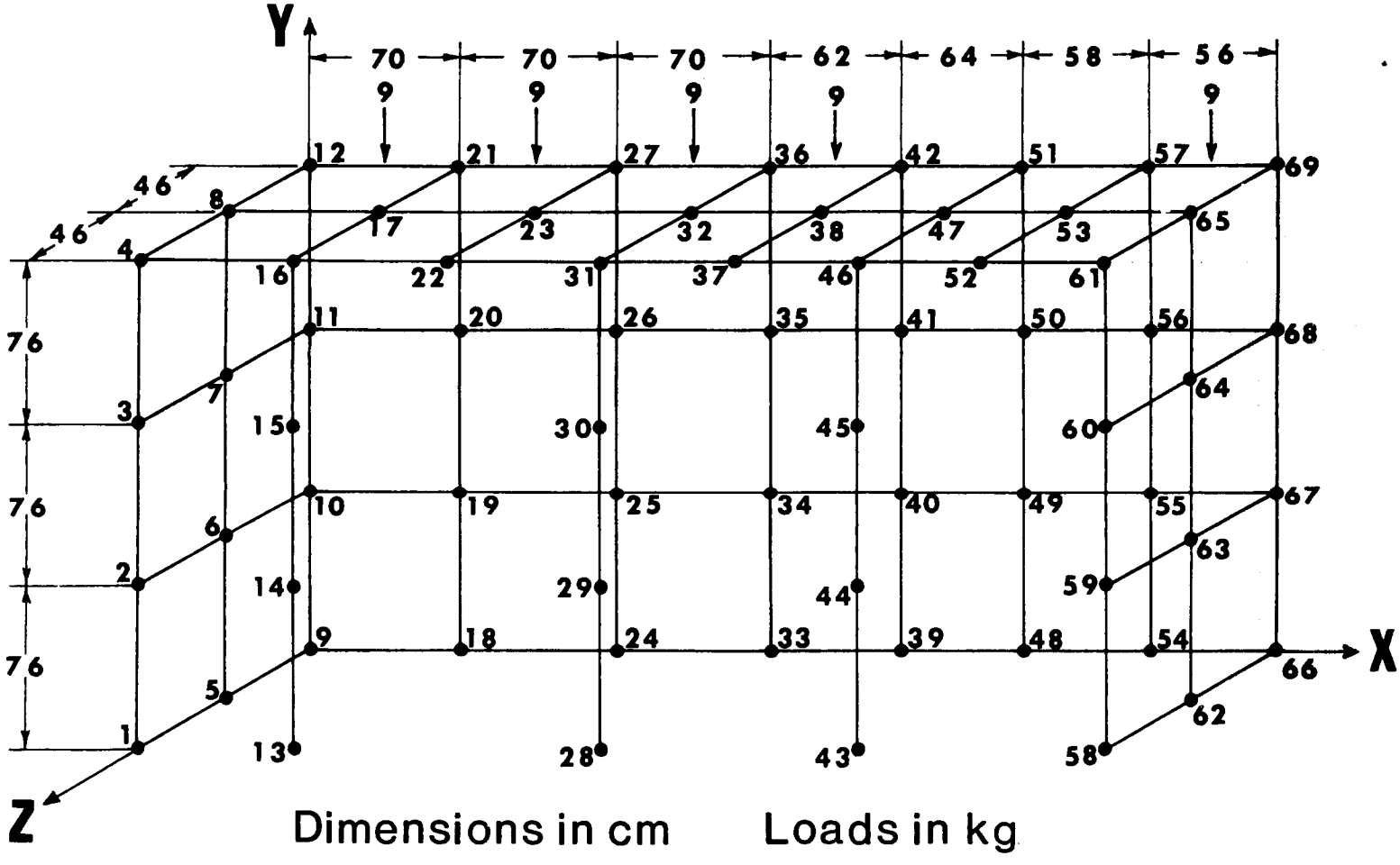

FIGURE 1

FINITE ELEMENT MODEL
(Numbers Designate Beam Elements)

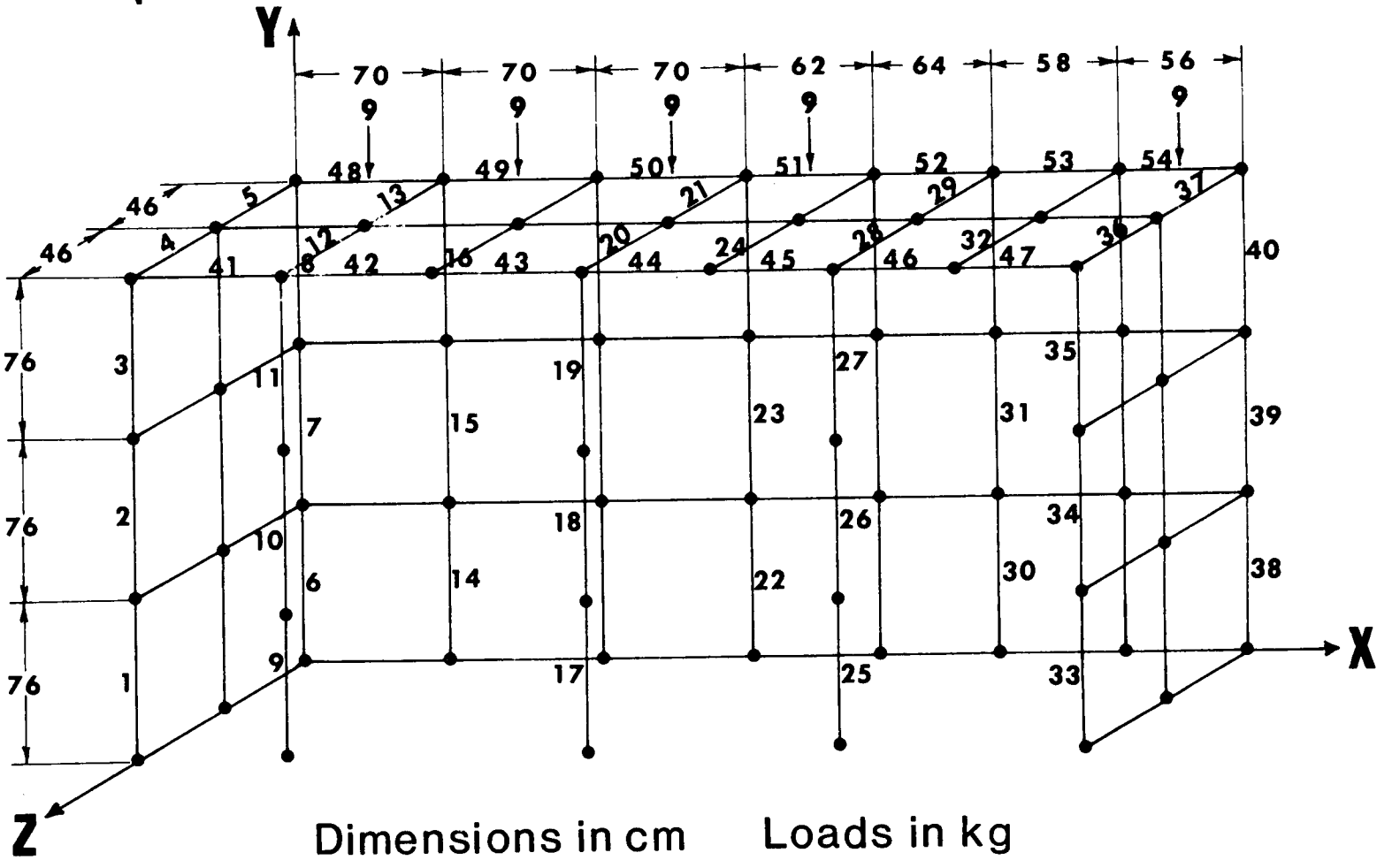

FIGURE 2

FINITE ELEMENT MODEL
(Numbers Designate Membrane Elements)

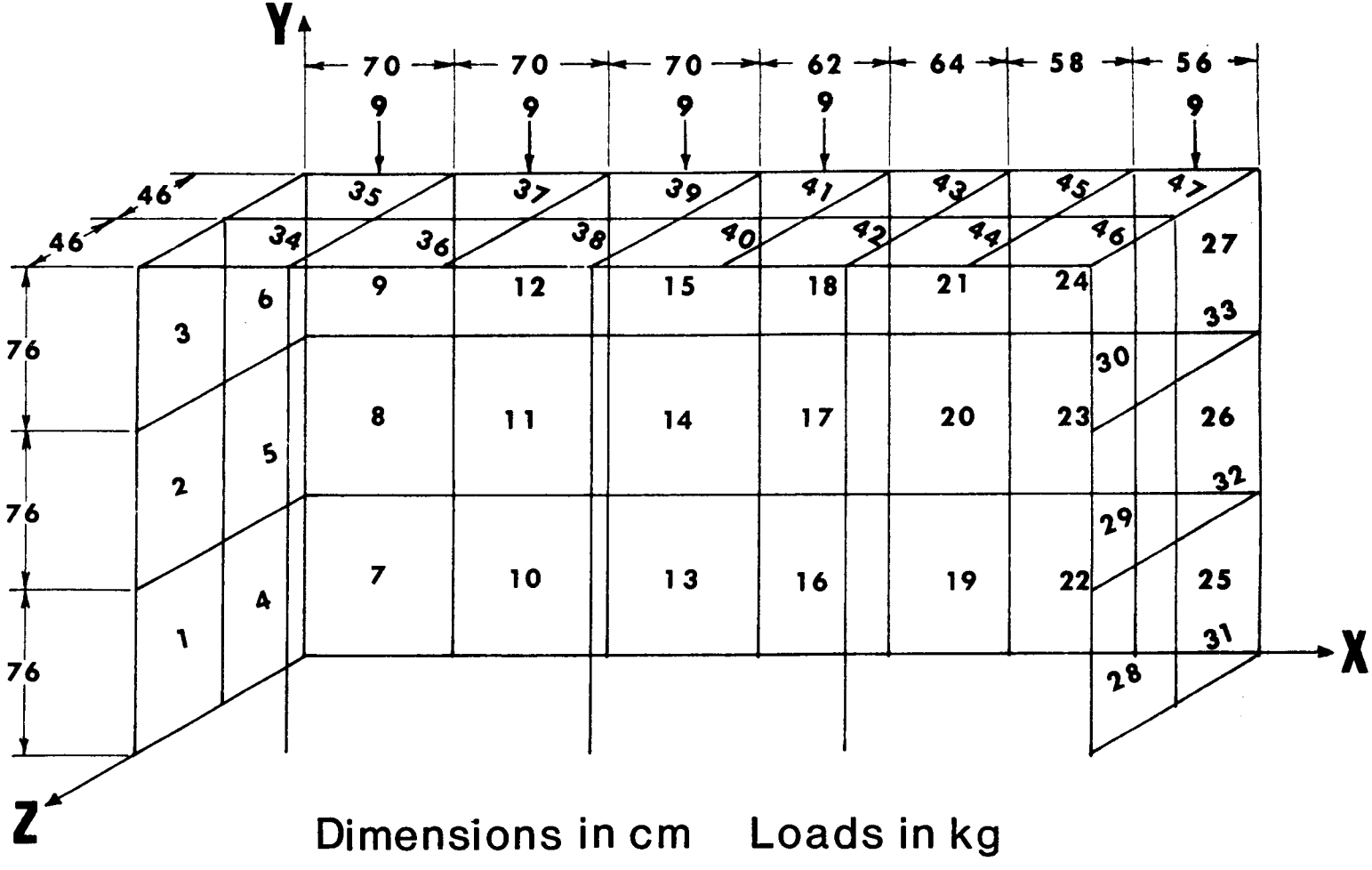

Dimensions in cm Loads in kg

FIGURE 3

NASTRAN USED IN A PRODUCTION ENVIRONMENT

R. F. Wilkinson, J. W. Kelley, and N. K. Snead

Lockheed-Georgia Company

SUMMARY

This paper describes a finite element analysis procedure built around the NASTRAN system. It describes a number of support programs that have either been written or modified to interface with NASTRAN and some improvements that have been made to NASTRAN itself. It shows some typical models that are being analyzed and an actual schedule that is being followed for constructing and analyzing the models to support a large design program.

INTRODUCTION

NASTRAN is the main finite element analysis tool used in the C-5A project stress office at the Lockheed-Georgia Company (Gelac). It was first used in June '72 on an analysis which required an idealization using plate bending elements (CQUAD2). The in house program FAMAS was not used because it did not have a similar type of element. Upon using the system it became evident that NASTRAN had most of the capabilities that existed in FAMAS plus many more. One big draw back, however, to adopting NASTRAN in place of FAMAS as Gelac's main finite element analysis tool was that a number of support programs existed that specifically interfaced with FAMAS. Since then these have all been modified to interface with NASTRAN which has led to a very efficient static finite element analysis capability. This capability is currently playing an important part in a program to redesign the C-5A wing.

FINITE ELEMENT ANALYSIS PROCEDURE AT THE LOCKHEED-GEORGIA COMPANY

An engineer at the Lockheed-Georgia Company has available to him three modes in which to execute his computer runs on two UNIVAC 1106 machines. Twenty-three UNIVAC DCT (Data Communications Terminals), which are

asynchronous key board/print devices, allows the engineer to execute jobs and edit data files in an interactive, DEMAND, mode. Jobs executed in this manner are limited to 32K and a CPU time of 10 minutes. A UNIVAC 1557/1558 display system, SCOPE, is used in a similar mode with the additional capability of displaying data on the 1558 console. Finally jobs can be executed in a batch mode which has a turn around time of between 2 and 24 hours.

The standard procedure by which an engineer concerned with making a finite element analysis uses this system is shown in Figure 1. This has been partitioned into the three main tasks involved in a finite element analysis namely "Model Construction", "Model Check Out", and "Analysis". Models are constructed thru a computer program called NABDAG (NASTRAN Bulk Data Generator). The input to this program can be as much as an order of magnitude less than the bulk data that it generates. The input can be either typed in at the DEMAND terminals or key punched and read into a mass storage file. The program is executed in the DEMAND mode, the output being saved in a mass storage BULK DATA FILE. When all the bulk data has been generated NASTRAN is executed to form the element connectivity tables and grid point coordinate tables. These tables are copied into mass storage files which are then read into an interactive graphics program executed from the SCOPE console. The interactive graphics program displays the model on the console enabling the engineer to identify any errors. These can then be corrected by editing the bulk data file in the DEMAND mode. The cycle of plotting the model and editing the file is repeated until all errors have been eliminated. Once a checked out BULK DATA FILE is available NASTRAN is again run to form the element connectivity tables. These are read into a banding program, BANDIT, which forms the necessary SEQGP card images and edits them into the BULK DATA FILE. The actual analysis, which is executed in the batch mode, is often interfaced with post processing programs. A typical such program, Loose Fit, simulates effects like the pull away of a plate from a bolt in a hole. These programs are similarly interfaced with NASTRAN by writing the necessary tables and matrices into mass storage files.

BULK DATA GENERATOR (NABDAG)

The NASTRAN bulk data format, by its nature, requires large quantities of input data cards. As the utilization of NASTRAN increased at Gelac the need for a condensed input format became evident. Since the inhouse finite element program, FAMAS, utilizes a very efficient input system, its subroutines have been utilized in a NASTRAN bulk data generator program, NABDAG.

The FAMAS read subroutine, RETAK, reads unformatted data records which are delineated by a minus (-) in Column 1 of the last card of the record. The words in a record, which are read as real numbers starting in Column 4, are delineated by commas. Each record read by RETAK is stored in a single dimensional array and returned to the calling program for appropriate manipulation. The unique feature in RETAK which lends itself to generating bulk data for a finite element model is the ability to repeat or bump data words. This is accomplished thru the use of the following two special data words:

- nR — Repeat.
- nB, J, b_1,----,b_J — Bump.

The 'nR' indicates that the previous word should be repeated n times. The nB indicates that the previous J words should be repeated, as a block, n times, each time adding the increments b_1 thru b_J to the respective words. As an example consider the RETAK record:

10,4R,2B,5,10,4R

This would be returned to the calling program as the array

10 10 10 10 10 20 20 20 20 20 30 30 30 30 30

The main features of the NABDAG program are:

- The card image output format is defined as input data, hence the program can in fact be used for any finite element system.
- A single RETAK record is used to input, for all bulk data cards of the same type, the data for each output field. For example in inputting the GRID data a single RETAK record would be used to specify say all the X2 coordinates.
- If two data fields are identical then only a single RETAK record is required. For example, if all input and output coordinate systems on a GRID card are identical then only one need be input.

The input to the program consists of three parts. The first part defines the type of each RETAK record i.e. whether it is real or integer,

and it specifies in which output field each of the records go. The second part defines the output format and the third part consists of the actual RETAK records. Specific input definitions are given in Table 1.

As an example consider a simple swept wing surface. The NABDAG input data to idealize this surface by quadrilateral membrane elements, CQDMEM, is shown in Figure 2. These 9 card images became 54 BULK DATA card images after being processed by NABDAG. Although this example is for an ideally regular model, a savings of 10 to 1 can be achieved on complicated models.

BANDING PROGRAM

The Lockheed-Georgia Company has a program called BANDIT which will automatically resequence the grid point numbers for a model in such a way that the semi-band width of the stiffness matrix tends towards a minimum. The program requires the grid points to be numbered sequentially and works with a grid point connectivity table which lists, for each pivotal grid point, the grid points that are connected to it by elements. The details of the algorithm will not be presented here as the object of this section is only to demonstrate how simple it was to interface NASTRAN with BANDIT.

The external grid point numbering for a NASTRAN model, as constructed at the Lockheed-Georgia Company, are in general non-sequential. NASTRAN however works internally with grid point numbers that are sequential and in fact generates connectivity tables in terms of these internal grid numbers. The two NASTRAN tables that can be used to create the desired connectivity table are GPCT and EQEXIN, reference 1. The GPCT table gives the grid point connectivity in terms of the SIL number (Scalar Index List). The EQEXIN table gives the external grid number in terms of the internal grid numbers and the external grid number in terms of the SIL numbers. It was therefore a simple task to modify the BANDIT program to accept these two tables and generate the desired connectivity table in terms of internal grid numbers. The program resequences these numbers and then used the EQEXIN table to determine the resequencing for the external grid numbers. These are output to a mass storage file as SEQGP bulk data card images for direct input to NASTRAN. The DMAP instructions for generating the GPCT and EQEXIN tables and writing them out into a mass storage file is shown in Table 2.

INTERACTIVE GRAPHICS

An interactive graphics program has been developed at Gelac which is used to check finite element models prior to making an analysis, reference 2. This program is executed from a UNIVAC 1558 graphics display console which has a 12-inch square viewing area, see Figure 3. The program was initially developed to plot models coded for the in house FAMAS system. It was found that the simplest way to plot a model coded for the NASTRAN system was to modify the program to accept the EST, BGPDT, MPT, SIL, and EQEXIN tables generated in a NASTRAN run, see reference 1. The EST table gives the element connectivity data in terms of SIL numbers. The BGPDT table gives the grid point coordinate data. The MPT table gives the element material data. The SIL and EQEXIN tables give the external grid point numbers in terms of the SIL numbers and the internal grid point numbers. The DMAP instructions for generating these tables and writing them on a file for input to the interactive graphics program are shown in table 3.

The interactive graphics program plots the following three basic shapes:

- A two node line element
- A three node triangular element
- A four node quadrilateral element

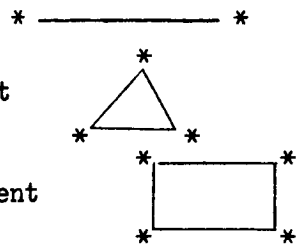

It was therefore necessary to associate each of the NASTRAN elements to one of these shapes. The interactive graphics program also uses the concept of element groups where a group consists of a set of elements all of the same type. This feature is convenient for selecting various model views especially when idealizations overlap each other.

An engineer working in real time at the scope console first selects the groups he desires to plot. He may then further partition his model by specifying a plane, box, sphere, cylinder, or a specific quadrant. Then only those elements within the defined region will be displayed. Once the desired partition is displayed he is able to rotate it about any of the 3 axis, translate it, or zoom in on a specific detail. The advantage of an interactive graphics system over plots generated in a batch mode is

illustrated in figure 4. View 'a' shows how the model first appears on the console. Upon rotating the view 30° about the vertical axis then 30° about the horizontal axis an error became apparent, view 'b'. Zooming in on the region of the error allows the engineer to identify exactly what the problem is, view 'c'. Hence, where a single sitting at the console identifies the error, it would take at least two batch runs to do the same.

LOOSE FIT PROGRAM

This program is used to simulate a loose fit in the joint of a structure. For example two coincidental grid points may be able to displace independently within a fixed tolerance before they become locked and transmit load to one another. Another example is a beam with sunken supports. The grid points would be able to displace freely within fixed limits before they become grounded and react loads.

The algorithm used to simulate this effect is to solve the equation.

$$\{R\} = \{P\} - [K] \times \{U\} \tag{1}$$

where

$[K]$ is the relative stiffness matrix for the joints that have a loose fit.

$\{P\}$ is the loads matrix for the joints when they are rigidly connected.

$\{u\}$ is the relative displacement of the joints.

The equation is solved for $\{u\}$ subject to the following constraints.

$$\begin{aligned} & u\ \min \leqslant u \leqslant u\ \max \\ & \text{If } u_{min} < u < u_{max},\quad R = 0 \\ & \text{If } u = u_{min},\ R \leqslant 0 \\ & \text{If } u = u_{max},\ R \geqslant 0 \end{aligned} \tag{2}$$

Where u_{min} and u_{max} are the tolerances for the displacements $\{u\}$. The solution is an iterative process which is accomplished by the following steps.

1. Initially $\{R\}$ is assumed to be zero and equation (1) is solved for $\{u\}$.

2. $\{U\}$ is inspected and any displacements outside the tolerances are fixed to be equal to the respective tolerance. These are then partitioned out of equation (1) and the remaining equations again solved for $\{R\} = 0$.

3. The residuals $\{R\}$ are now solved, thru equation 1, for the freedoms that were eliminated in step 2. These are inspected and any that violate the last two constraints in equation (2) are freed from having these displacements fixed at a tolerance. The displacements $\{u\}$ are also reexamined and any additional ones that are outside the tolerance are likewise fixed to be equal to the respective tolerance.

4. The new partition of equation (1) is again solved for $\{u\}$. Stages 3 and 4 are repeated until all constraints in (2) are satisfied.

To illustrate how this program is interfaced with NASTRAN consider the problem of a beam on sunken supports shown in Figure 5. First the problem is analyzed using rigid format 1. The vertical displacements for the grid points are included in the "A" set and the rigid format is altered to output the reduced "A" set stiffness and load matrices, (KLL) and (PL), onto a file immediately after they have been formed and terminate. These matrices are read into the Loose Fit Program together with the tolerance

$$0 \leqslant u_a \leqslant 0.00009$$

Loose fit solves for the "A" set displacements, ULV, and generates the DMI cards for direct input back into NASTRAN. Rigid format 1 is then restarted using these "A" set displacements and completes the analysis. Table 4 shows the executive control decks for both NASTRAN analysis and the DMI cards specifying the ULV displacements.

GELAC IMPROVEMENTS TO NASTRAN

Improvements have been made to the NASTRAN system at Gelac by way of including additional elements. The two elements that have so far been added are a Nine Node Crack Element and a Fastener Element. The nine node crack element is used to calculate the stress intensity at the tip of a crack for crack growth and stability studies. The formulation for this element and how it was incorporated into NASTRAN as a dummy element was presented at the last colloquium, reference 3. The fastener element is simply two orthogonal CELASI elements which have the same stiffness. This is a desirable element for representing a fastener attaching two plates. The advantage of using this element over two CELASI elements is of course that it halves the amount of input data but more important it is able to directly output the resultant load on the fastener. Currently this element is limited to an elastic material property. Plans are underway to include plasticity so that it can truly represent the nonlinear load deflection curve for a fastener.

C-5A WING REDESIGN SUPPORT

The C-5A wing redesign program requires the analysis of nineteen finite element models. The models represent local areas in the wing where cracks developed during the cyclic testing of a full scale fatigue article. The purpose of the analyses is to find an optimum design that minimizes the concentrations that causes the cracks. The models are also used to generate stress intensity factors, using the crack element, for crack growth studies.

The analysis for these models are spread over an eight month period as shown in Figure 6. The models vary in complexity, and require between four and eight weeks to construct and analyze. The construction phase takes between one and three weeks, the check out phase between one and two weeks, and the analysis phase between two and three weeks. The analysis phase generally includes a number of iterations involving geometry and property changes. Three models, which are typical of the nineteen shown in Figure 6 will now be described in detail.

The model shown in Figure 7 represents a typical stringer run out at a chordwise splice. The initial configuration was designed such that the skin tab lined up with the centroid of the skin stringer combination. Strain gage measurements indicate that with this configuration there are

large bending stresses in the tab, also cracks developed at the holes in the tab on the test article. The purpose of the analysis is therefore to investigate the effect of varying the joggle of the tab in order to find a configuration which minimizes the bending stresses. The model idealizes one half of a skin/stringer combination and has boundary constraints which represent an infinite panel. The splice plates and the skin are idealized by plate bending and membrane elements. The riser web is idealized by membrane elements and the riser flange by axial elements. The fasteners are idealized by bar elements with constraint equations written to equate the rotations at the ends of the bar. The moment of inertia for the bars are then calculated from the equation

$$\frac{P\,l^3}{12EI} = \frac{P}{K}$$

where K is the fastener stiffness obtained from test.

The model shown in Figure 8 represents a tab out in the skin panel at the front spar which picks up the leading edge structure. Cracks originated in the fatigue article at the hole adjacent to the tab out radius. The model was set up so that the location of the hole relative to the radius could be varied in order to find the configuration that gave the minimum concentration effect. The results of the analysis were intended to be used directly in a fatigue analysis, so the actual hole was modeled in both the skin and the leading edge structure. The effect of the bolt on the distribution was included by modeling the bolt and simulating the pull away effect by the Loose Fit Program. The way this was done is illustrated in Figure 9. Scalar points were defined for each grid point on the skin and leading edge structure around the hole. Multi point constraint equations were then written such that these scalar points defined the relative radial displacement between the skin and the bolt and the leading edge structure and the bolt. These freedoms were then defined in the A set and the procedure previously described used to interface with the Loose Fit Program. The constraints on the relative displacement used in the Loose Fit program were:

$$0 \leqslant Ua < \infty$$

The resulting relative displacements are shown in Figure 9.

The region modeled in the third example, shown in Figure 10, represents a main joint in the rear spar of the wing. The model is split into two substructures representing the center and inner wing sides of the joint. Details are shown for the idealization of the inner wing substructure only. The various components, web, fitting, and cap are idealized individually and connected together by fastener elements. The purpose of the model is to size the fitting and web in such a way that the concentration effects caused by the web dumping load into the cap at the joint is minimized. The two substructures were initially analyzed and iterated with rigid restraints imposed at their interface to obtain an approximate sizing. They were then coupled together and again iterated to obtain the final sizing. The coupling analysis was divided into three phases. Phase 1 involved an individual analysis for each substructure to obtain the boundary stiffness and loads matrices. The coupling freedoms were included in the "A" set and the "A" set stiffness and loads matrices written out onto a user tape. The alters to rigid format 1 to do this are identical to those shown in table 4 for the Loose Fit program. Phase 2 involves the actual coupling analysis which solves the equilibrium equations for the boundary displacements. The DMAP instructions for the coupling analysis are shown in table 5. Finally Phase 3 solves for the element stresses. Here again the alters to rigid format 1 are the same as those shown in table 4 for the Loose Fit program.

CONCLUSION

The intent of this paper has been to demonstrate how effectively NASTRAN can be used in a production environment. The key to accomplishing this was in being able to interface NASTRAN with existing finite element support programs. We at Lockheed-Georgia Company credit our success to the excellent documentation provided with NASTRAN.

REFERENCES

1. The NASTRAN Programmers Manual. NAS SP-223(01), Sept. 1972.

2. Batdorf, W. J., Holliday, J.F., Peed, J. L.: A Graphics Program for Aircraft Design - GPAD System. AIAA Thirteenth Aerospace Sciences Meeting. 75-136.

3. Wilkinson, R. F., Kelley, J.W.: A Failsafe Analysis Using NASTRAN's Piecewise Linear Analysis and a Nine Node Linear Crack Element. NASTRAN User's Experience. NAS TM X-3278, 1975.

TABLE 1 Input Instructions for NABDAG

RECORD	FORMAT	VARIABLE	DESCRIPTION
1	10I5	M	OUTPUT UNIT #
		NFOR	# OF A6 WORDS NEEDED FOR THE OUTPUT FORMAT
		NWPC	# OF DATA FIELDS ON A BULK DATA CARD
		NRECS	# OF INPUT RECORDS
		INT(1) ⋮ INT(NRECS)	INPUT RECORD TYPE SPECIFICATION 0 INDICATES INTEGER DATA 1 INDICATES REAL DATA
		MSEQ(1) ⋮ MSEQ(NWPC)	SPECIFY A NUMBER FOR EACH OUTPUT FIELD INDICATING WHICH INPUT RECORD IS TO BE USED
2	12A6	IFOR(1) ⋮ IFOR(NFOR)	OUTPUT FORMAT
3 ⋮ 2 + NRECS	RETAK ⋮ RETAK	DATA ⋮ DATA	INPUT DATA

TABLE 2 DMAP Listing for Interfacing NASTRAN With BANDIT

```
ID BANDIT,TABLES
APP DMAP
TIME 10
DIAG 1,14
BEGIN$
GP1 GEOM1,GEOM2,/GPL,EQEXIN,GPDT,CSTM,BGPDT,SIL/V,N,LUSET/C,N,
    123/V,N,NOGPDT $
SAVE LUSET $
GP2  GEOM2,EQEXIN/ECT $
GP3  GEOM3,EQEXIN,GEOM2/SLT,GPTT/C,N,123/V,N,NOGRAV/C,N,123 $
TA1, ,ECT,EPT,BGPDT,SIL,GPTT,CSTM/EST,,GEI,ECPT,GPCT/V,N,LUSET/C,N,
     123/V,N,NOSIMP/C,N,0/V,N,NOGENL/V,N,GENEL $
OUTPUT2 GPCT,EQEXIN,,,//C,N,0/C,N,12 $
END$
CEND
TITLE = DATA TABLES NECESSARY FOR BANDING THE STIFFNESS MATRIX
BEGIN BULK
$  * * * BULK DATA DECK * * *
ENDDATA
```

TABLE 3 DMAP Listing for Interfacing NASTRAN and 3-D Graphics

```
ID GRAPHICS,PLOTS
APP DMAP
TIME 10
DIAG 1,14
BEGIN$
GP1 GEOM1,GEOM2,/GPL,EQEXIN,GPDT,CSTM,BGPDT,SIL/V,N,LUSET/C,N,
    123/V,N,NOGPDT $
SAVE LUSET $
GP2  GEOM2,EQEXIN/ECT $
GP3  GEOM3,EQEXIN,GEOM2/SLT,GPTT/C,N,123/V,N,NOGRAV/C,N,123 $
TA1, ,ECT,EPT,BGPDT,SIL,GPTT,CSTM/EST,,GEI,ECPT,GPCT/V,N,LUSET/C,N,
     123/V,N,NOSIMP/C,N,0/V,N,NOGENL/V,N,GENEL $
OUTPUT2 SIL,BGPDT,EQEXIN,EST,MPT//C,N,0/C,N,12 $
END$
CEND
TITLE = DATA TABLES NECESSARY FOR PLOTTING ON THE SCOPE
BEGIN BULK
$  * * * BULK DATA DECK * * *
ENDDATA
```

TABLE 4 DMAP Listings for a Loose Fit Analysis

```
ID LOOSE,FIT
CHKPNT YES
APP DISPLACEMENT
SOL 1,1
ALTER 103,126
OUTPUT2 KLL,PL,,,//C,N,-1/C,N,12/C,N,LABEL $
ALTER 136,137
ENDALTER
TIME 20
DIAG 1,14
CEND
TITLE = LOOSE FIT ANALYSIS EXAMPLE
OUTPUT
DISPLACEMENT = ALL
ELSTRESS = ALL
SPCFORCE = ALL
MPC = 1
SPC = 1
SUBCASE 1
LOAD = 1
BEGIN BULK
$ * * * BULK DATA DECK * * *
ENDDATA
```

Initial Analysis to Form the A Set Stiffness and Loads Matrices

```
ID LOOSE,FIT
RESTART  LOOSE    ,FIT      , 6/28/76,    14106,
         1,   XVPS     ,   FLAGS = 0,    REEL =  1,   FILE =      6
         2,   REENTER AT DMAP SEQUENCE NUMBER      7
         3,   GPL      ,   FLAGS = 0,    REEL =  1,   FILE =      7
                              .
                              .
                              .
                              .
$ END OF CHECKPOINT DICTIONARY
APP DISPLACEMENT
SOL 1,1
ALTER 103,105
FBS      LOO,UOO,PO/UOOV $
MPYAD    KLL,ULV,PL/RULV/C,N,0/C,N,-1 $
MPYAD    KOO,UOOV,PO/RUOV/C,N,0/C,N,-1 $
CKHPNT   UOOV,RULV,RUOV $
ENDALTER
TIME 20
DIAG 1,14
CEND
TITLE = LOOSE FIT ANALYSIS EXAMPLE
OUTPUT
DISPLACEMENT = ALL
ELSTRESS = ALL
SPCFORCE = ALL
MPC = 1
SPC = 1
SUBCASE 1
LOAD = 1
BEGIN BULK
DMI      ULV              0        2        2        2                 9        1
DMI*     ULV                                1                 1-.4401316000D-04*  1    1
*  1   1-.7508772000D-04-.8861842000D-04-.9000000000D-04-.9000000000D-04*  5    1
*  5   1-.9000000000D-04-.8861842000D-04-.7508772000D-04-.4401316000D-04
PARAM    IRES             1
ENDDATA
LINES TO EOF     37
```

Final Restart Analysis to Form the Displacements and Stresses

TABLE 5 DMAP Instructions for Coupling

```
ID JOB100N,KELLEY $
TIME 10
DIAG 1,14
APP DMAP
BEGIN $
INPUTT1 /,,,,/C,N,-1/C,N,0/C,N,M8300S $
INPUTT1 /B1,E1T,KLL1P,PL1PPP,PG1PP/ $
INPUTT1 /B2,E2T,KLL2P,PL2PPP,PG2PP/ $
MPYAD E1T,KLL1P,/X1/C,N,1 $
MPYAD E2T,KLL2P,/X2/C,N,1 $
MPYAD X1,E1T,/KLL1/C,N,0 $
MPYAD X2,E2T,/KLL2/C,N,0 $
MPYAD E1T,PL1PPP,/X4/C,N,1 $
MPYAD E2T,PL2PPP,/X5/C,N,1 $
MPYAD X4,B1,/PL1/C,N,0 $
MPYAD X5,B2,/PL2/C,N,0 $
ADD5 KLL1,KLL2,,,/KLL/ $
ADD5 PL1,PL2,,,/PL/ $
MPYAD PG1PP,B1,/PG1/C,N,0 $
MPYAD PG2PP,B2,/PG2/C,N,0 $
DECOMP KLL/LLL,ULL $
FBS LLL,ULL,PL/ULV $
MPYAD E1T,ULV,/ULV1P/C,N,0 $
MPYAD E2T,ULV,/ULV2P/C,N,0 $
MPYAD KLL1,ULV,PL1/RULV1/C,N,0/C,N,-1 $
MPYAD KLL2,ULV,PL2/RULV2/C,N,0/C,N,-1 $
MPYAD E1T,RULV1,/RULV1P/C,N,0 $
MPYAD E2T,RULV2,/RULV2P/C,N,0 $
ADD5 RULV1,RULV2,,,/RULV/ $
OUTPUT1 PG1,ULV1P,RULV1P,,// $
OUTPUT1 PG2,ULV2P,RULV2P,,// $
MATPRN PG1,PG2,,ULV,ULV1P// $
MATPRN ULV2P,,RULV1P,RULV2P,// $
MATPRN RULV,,,,// $
END $
CEND
TITLE = PHASE 2 COUPLING ANALYSIS
BEGIN BULK

ENDDATA
```

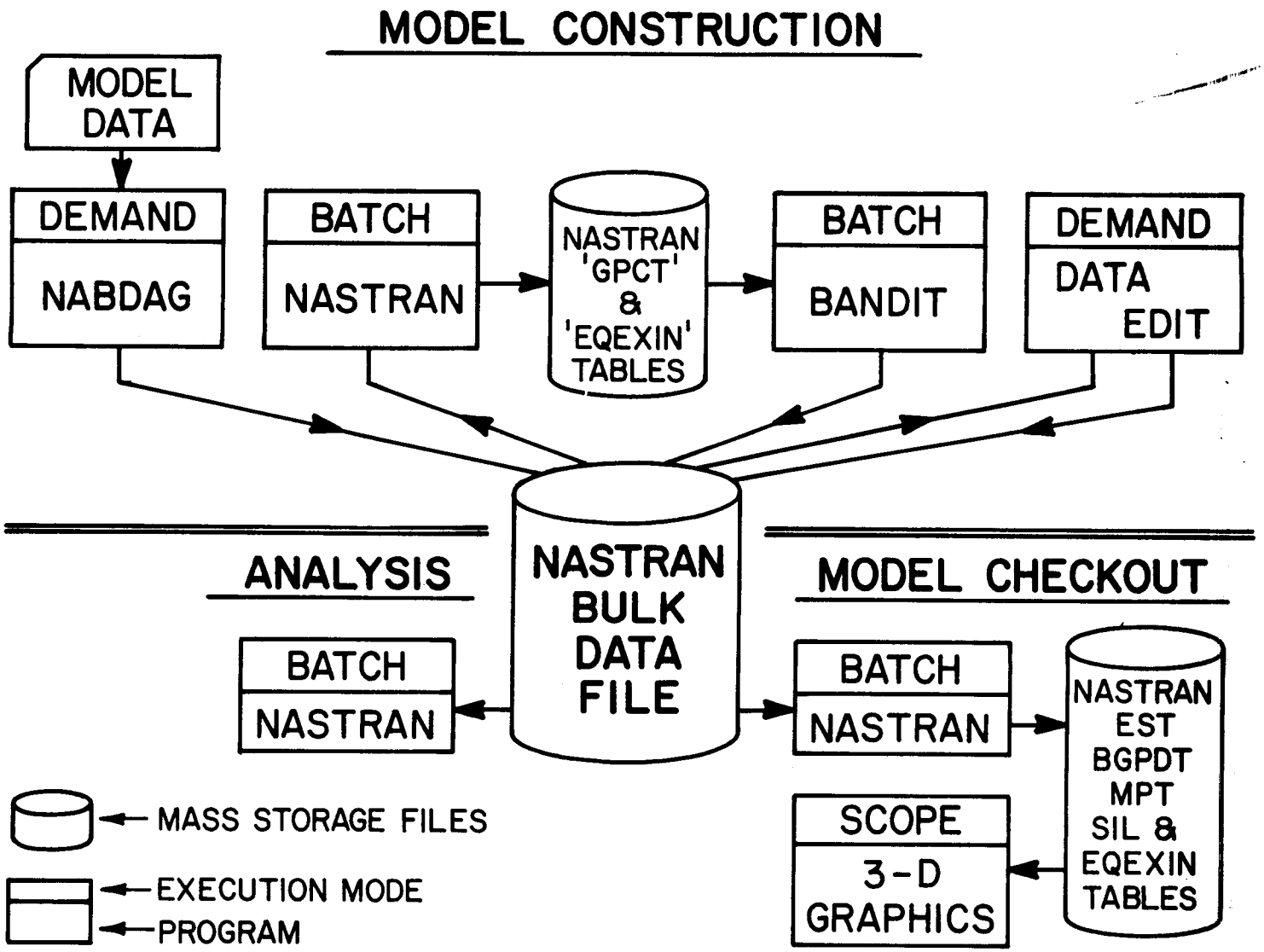

FIGURE 1 Gelac Standard Finite Element Analysis Procedure.

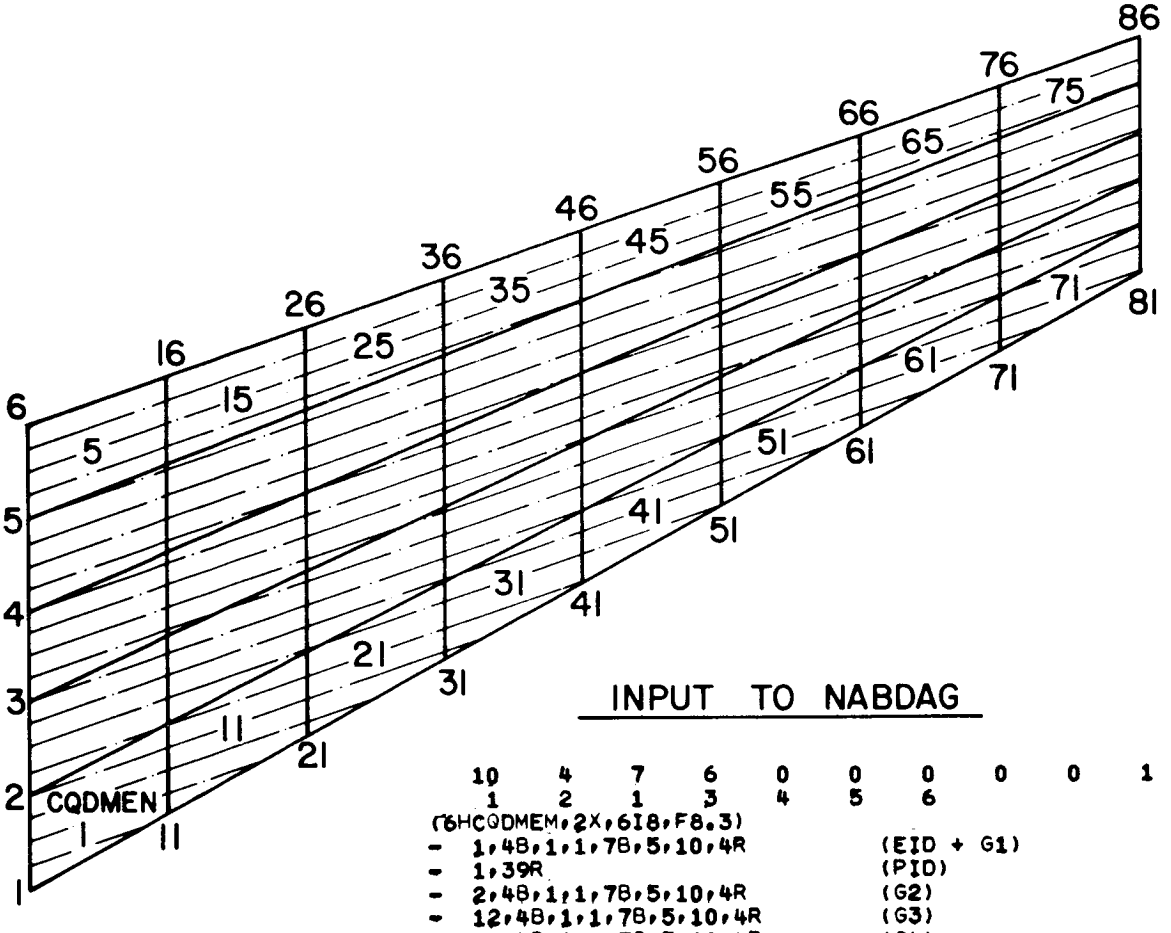

INPUT TO NABDAG

```
  10    4    7    6    0    0    0    0    0    1
   1    2    1    3    4    5    6
(6HCQDMEM,2X,6I8,F8.3)
-  1,4B,1,1,7B,5,10,4R          (EID + G1)
-  1,39R                        (PID)
-  2,4B,1,1,7B,5,10,4R          (G2)
-  12,4B,1,1,7B,5,10,4R         (G3)
-  11,4B,1,1,7B,5,10,4R         (G4)
-  70.0,39R                     (TH)
```

OUTPUT FROM NABDAG

CQDMEM	1	1	1	2	12	11	70.000
CQDMEM	2	1	2	3	13	12	70.000
CQDMEM	3	1	3	4	14	13	70.000
⋮	⋮	⋮	⋮	⋮	⋮	⋮	⋮
CQDMEM	73	1	73	74	84	83	70.000
CQDMEM	74	1	74	75	85	84	70.000
CQDMEM	75	1	75	76	86	85	70.000

FIGURE 2 NABDAG Data For Specifying the CQDMEM Elements of a Swept Wing Surface

Figure 3 UNIVAC 1558 Graphics Display Console

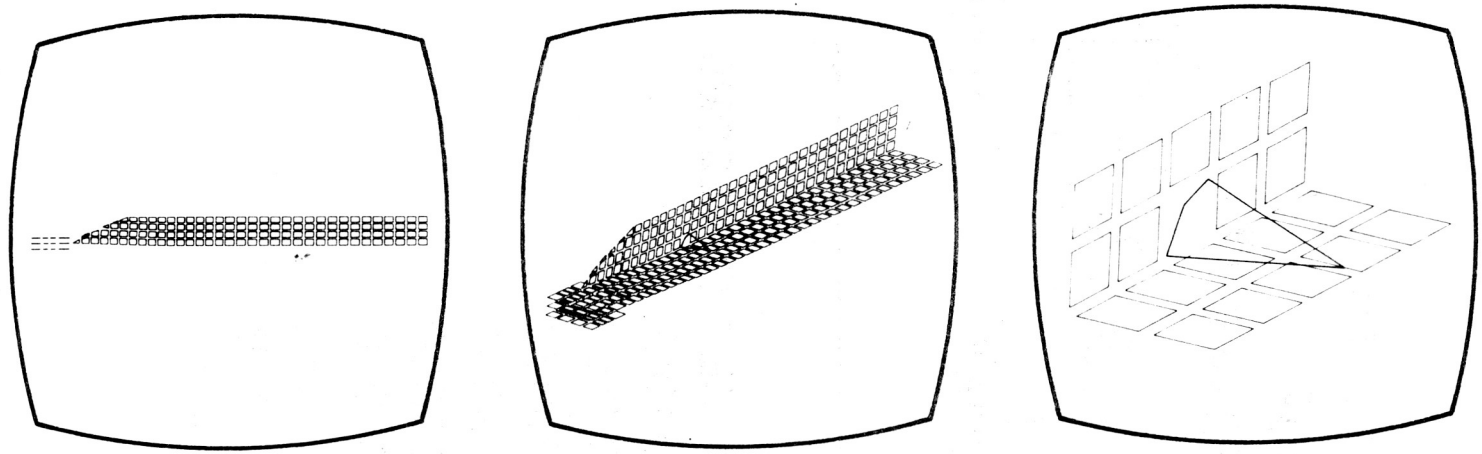

View a View b View c

FIGURE 4 The Advantages of an Interactive Graphics System

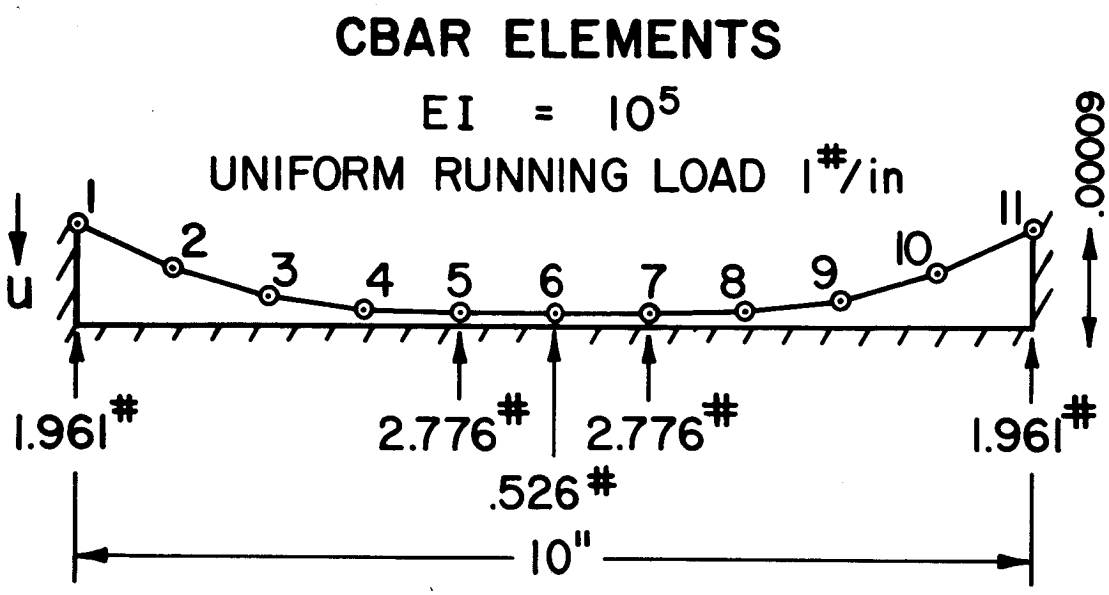

DISPLACEMENTS FOR A SET FREEDOMS

u_2 = .00004013
u_3 = .00007509
u_4 = .00008862
u_5 = .00009000
u_6 = .00009000
u_7 = .00009000
u_8 = .00008862
u_9 = .00007509
u_{10} = .00004013

FIGURE 5 Loose Fit Analysis for a Beam on Sunken Supports.

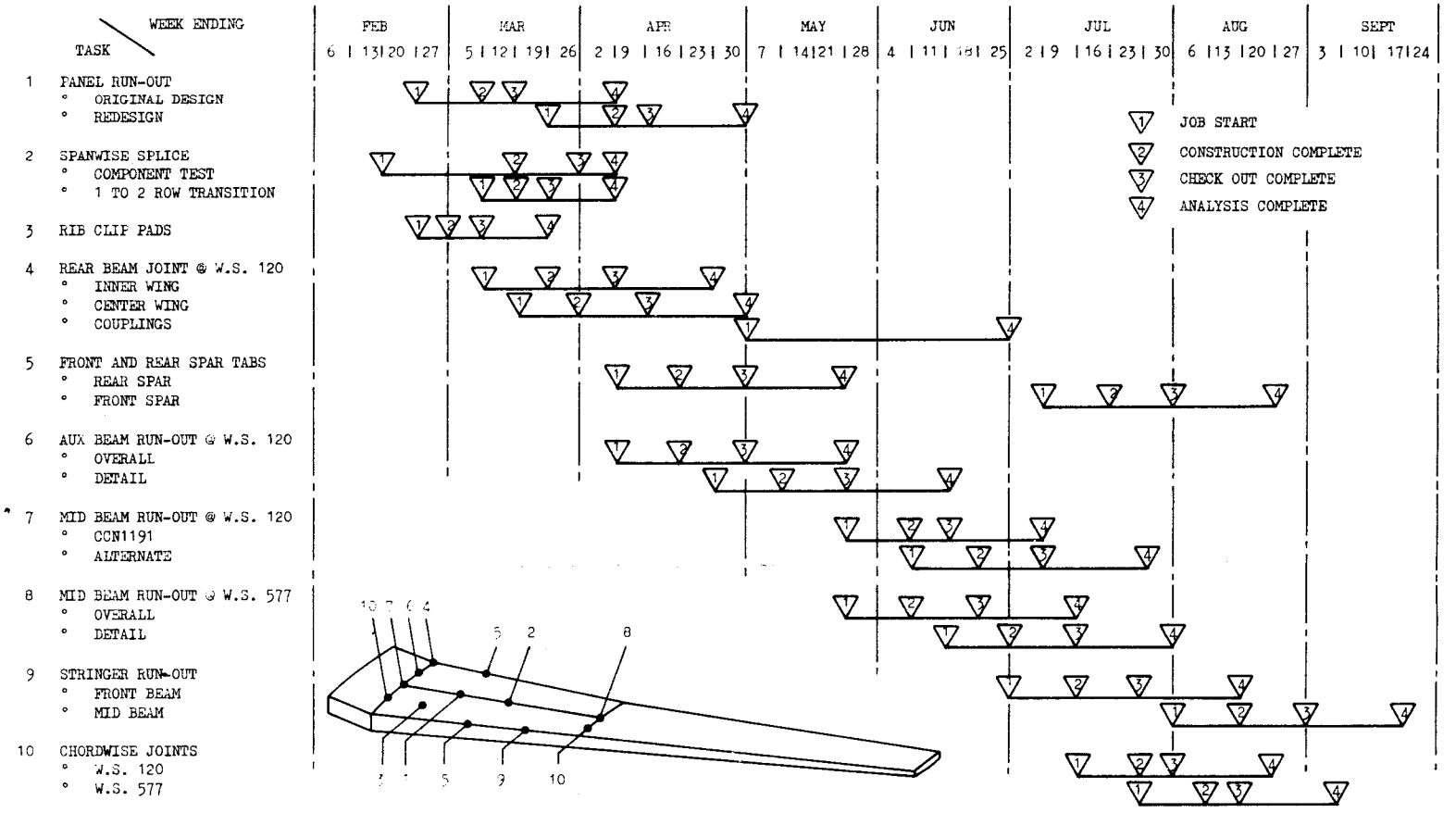

FIGURE 6 NASTRAN Finite Element Analysis Schedule For the C-5A Wing Redesign.

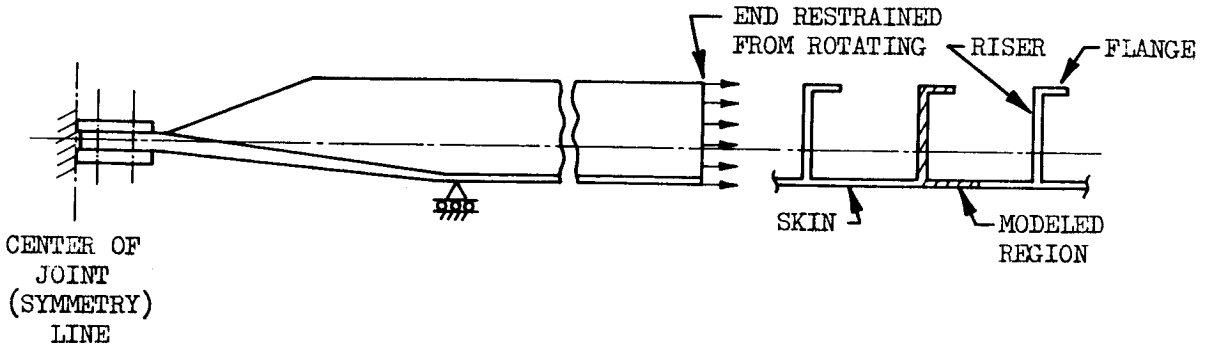

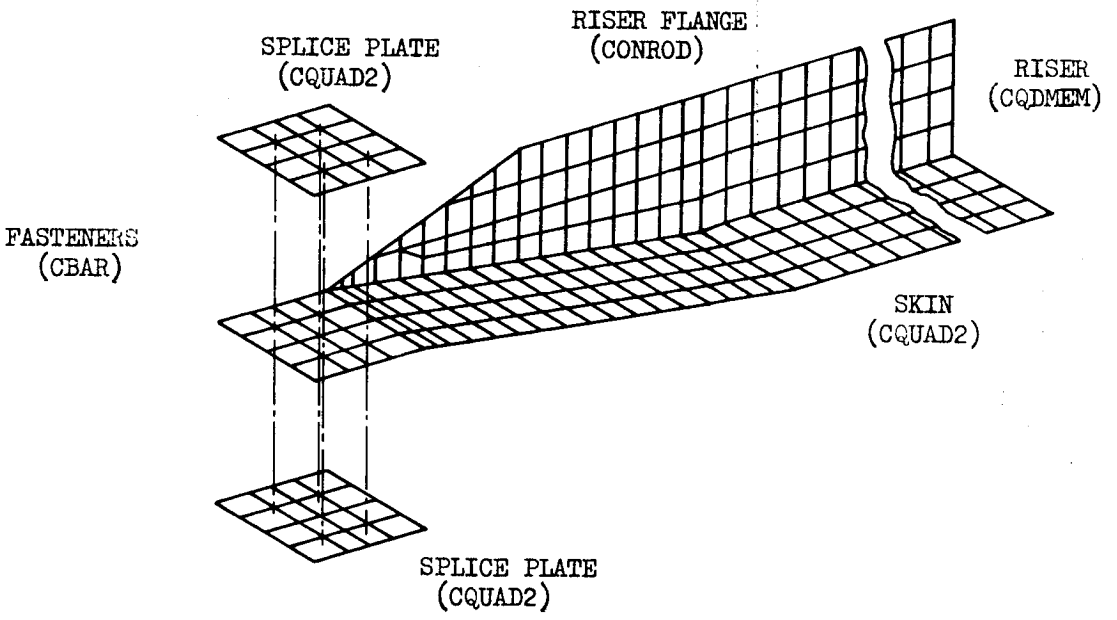

FIGURE 7 Chordwise Joint Model.

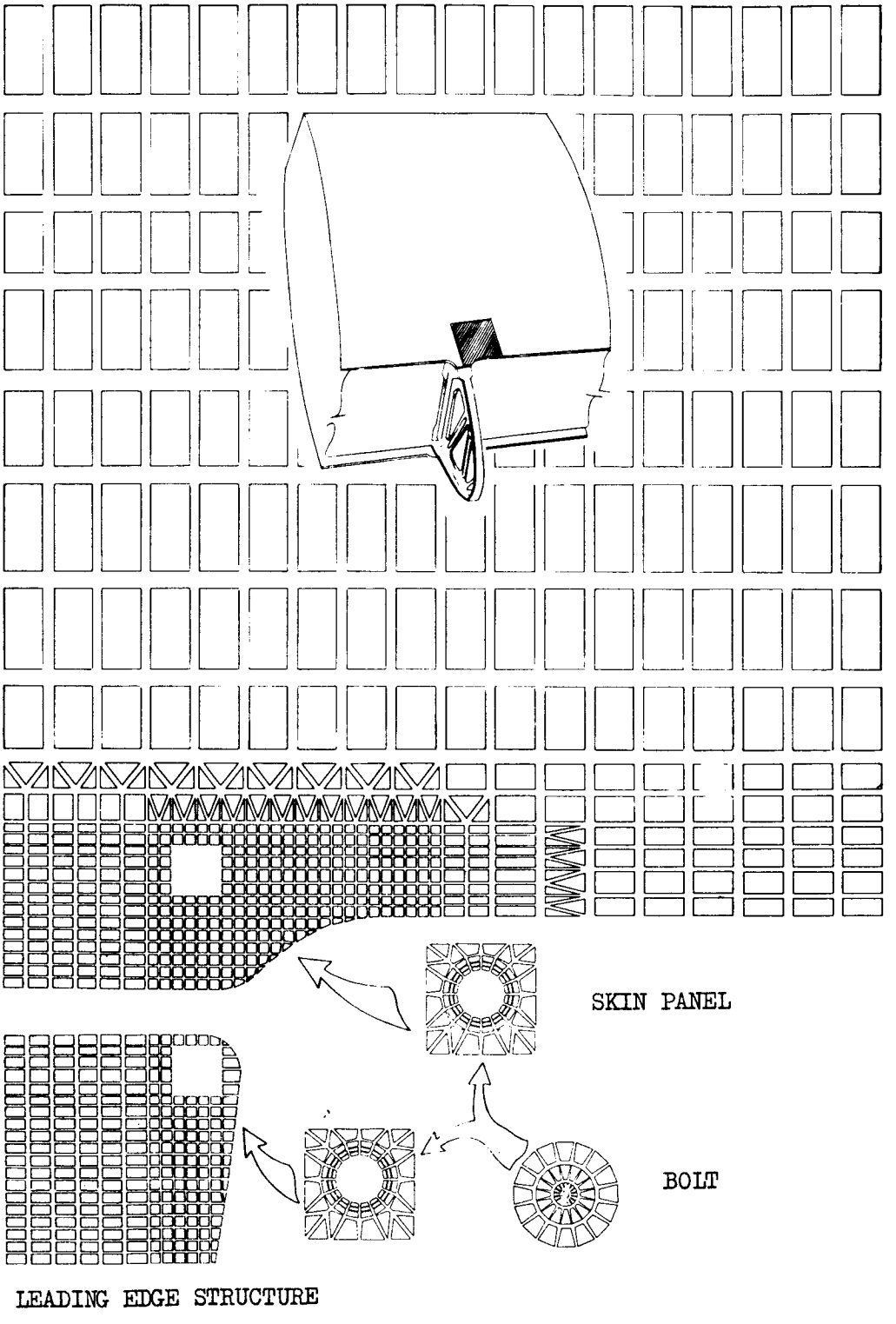

FIGURE 8 Finite Element Model of the Leading Edge Tab Out

CONSTRAINT EQUATIONS TO DEFINE THE RELATIVE DISPLACEMENT u(E) BETWEEN THE SKIN AND BOLT AND u(F) BETWEEN THE LEADING EDGE STRUCTURE AND THE BOLT.

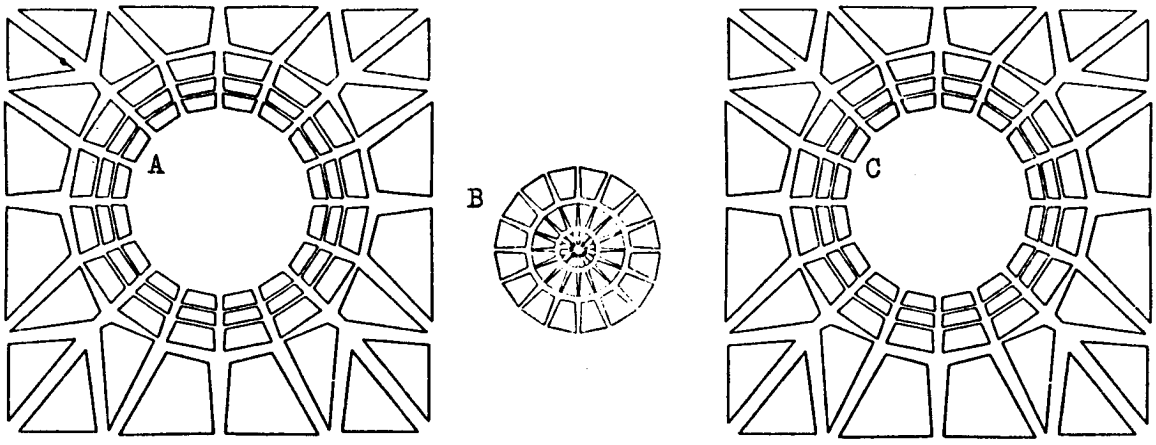

$$uR(A) - uR(B) = u(E)$$
$$uR(C) - uR(B) = u(F)$$

Where E & F are Scalar Points

RELATIVE DISPLACEMENTS u(E) AND u(F) FROM LOOSE FIT

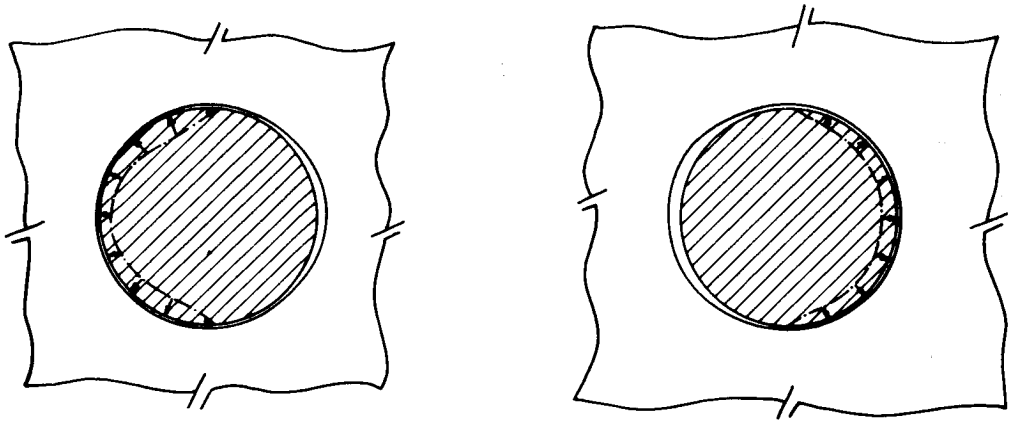

FIGURE 9 Loose Fit Used To Simulate Bolt Pull Away

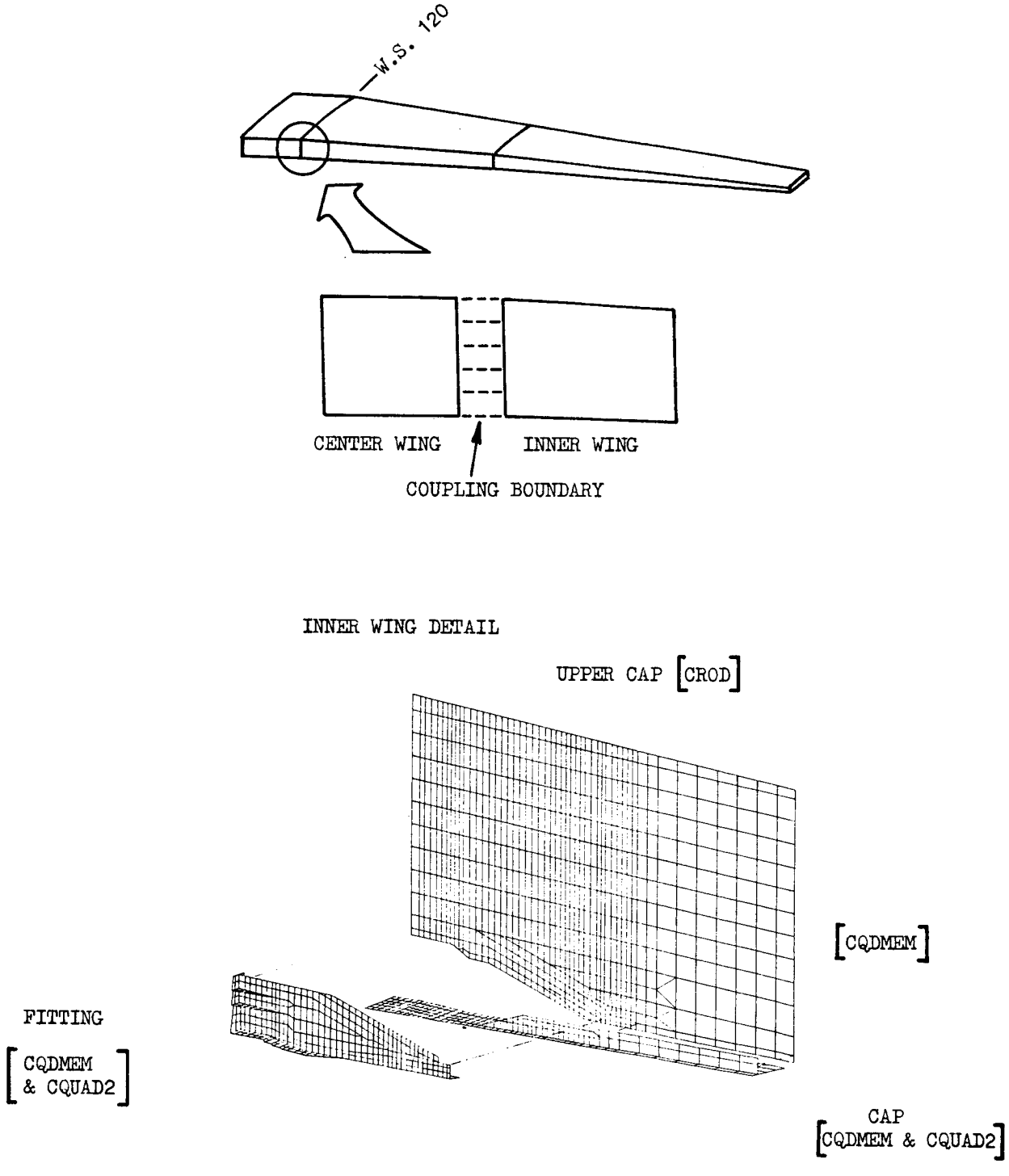

FIGURE 10. Rear Spar Joint On W.S. 120 Model

A POSTPROCESSOR SYSTEM FOR THE DATA REDUCTION AND POST ANALYSIS OF NASTRAN RESULTS

A. I. Raibstein, S. Emil and A. Pipano
Israel Aircraft Industries Ltd.

SUMMARY

A post-processor system for the data reduction and post analysis of NASTRAN results is described. NASTRAN analysis results are scanned to determine maximum and minimum displacements, forces and stresses. Allowables and margins of safety are computed, and in the case of multiple loading conditions, envelopes for displacements, forces, stresses and margins of safety are also produced for specified element sets. Graphical plots of the reduced or the regular NASTRAN results may be obtained superimposed either on a developed fuselage strip or on a projection of any specified part of the finite element model. The use of the data reduction, post analysis and graphical plotting capabilities provide the analyst with a fast and convenient tool for the study of NASTRAN analysis results and their presentation for project documentation.

INTRODUCTION

The high computational speed and large storage capacity of modern computers have enabled the analysis of large and complex structures subjected to multiple loadings and various boundary conditions. As a consequence, the structural engineer is bound to devote a substantial portion of his time in scanning and interpreting a large amount of output data, a process which is time consuming, error prone and hence inefficient. The way to alleviate this problem is to automate, wherever possible, the scanning and interpretation of the results, and to give the analyst the option to reduce the amount of computer output according to his engineering requirements. For further efficiency, this should be done in conjunction with graphical display of the reduced finite element analysis results. Additional help for the analyst can be obtained through the automation of certain standard post analysis procedures such as the computations of allowable stresses and margins of safety for the structural elements used in the finite element analysis.

The need for these capabilities has been felt for some time and as a result a large number of post-processors have been developed. However, most of these satellite programs are generally limited in scope, usually serving one particular purpose only, such as plotting (reference 1), or scanning (reference 2). At Israel Aircraft Industries an attempt has been made to integrate data reduction, post analysis, and graphic visualization into one package which has been especially devised to be engineering oriented.

This paper describes two interrelated software modules for the post processing, post analysis and graphical presentation of NASTRAN analysis results. Emphasis is put on the fact, that both

modules are easy to apply, demanding a minimum of information from the user, yet leaving him with enough options to answer his design oriented requirements. The first of the two modules, NASDAT (reference 3) performs the post-processing and post analysis of the NASTRAN results; the second module, GRAS, plots any of the regular or reduced results in a graphical form.

DESCRIPTION OF MAIN MODULES

Description Of The NASDAT Module

The execution of the NASDAT module, illustrated in figure 1, may be subdivided into three main phases.

a) In phase one, regular NASTRAN output data blocks are sorted and stored in a compact form on a disk file for subsequent use. This file may be saved after termination of NASDAT execution. Thus, a restart file, which contains all necessary I/O information of the NASTRAN analysis, is created to be used in phases 2 and 3.

b) In phase two, the packed and sorted NASTRAN output is scanned, and efficient data reduction performed in accordance with the user's requirements.

c) Finally, in phase three, post analysis of results including computations of allowables and margins of safety are performed.

NASDAT may be run either in conjunction with NASTRAN as a single job, or as a separate run following a NASTRAN analysis for which the necessary output data blocks have been saved. NASDAT may be restarted as many times as required.

NASDAT Capabilities

Presently, using NASDAT capabilities, the user may obtain:

* Maxima and minima values
* Envelopes of displacements, forces, stresses and/or margins of safety
* Output in preferred sequence and format
* Computations of allowables and margins of safety

The following is a brief description of the different options mentioned above:

a) *Maximum and Minimum Values*

The user may define a given set of elements and/or gridpoints from which the program will single out and identify those elements and grid points bearing extreme values of

force, stress and displacement; the magnitude of these extrema is also produced. In addition, it is possible to specify the upper and lower bounds beyond which the search for maximum and minimum values is to begin.

b) *Envelopes of Displacements, Forces, Stresses and Margins of Safety*

When analyzing several loading cases or checking various boundary condition configurations, the user has the option of obtaining envelopes of displacements, forces, stresses and margins of safety for a specified set of grid points and elements.

c) *Output In A Preferred Sequence And Format*

In some cases the user may require the results in a certain region of interest to be printed out separately in a specified sequence. In addition, if upper and lower bounds on the output values are also defined, then only those elements of the set with results above these bounds are printed.

d) *Computations Of Allowables And Margins Of Safety*

The margins of safety of any Rod, Shear Panel or Membrane element can be computed using allowables either defined by the user or automatically computed by the program. For the latter option the user may either define the section properties via manual input or allow the program to retrieve the geometrical and mechanical properties of these sections from tables generated in the NASTRAN analysis.

The NASDAT Input

In order to generate the main input for NASDAT the following DMAP statements for static analysis, must be included into the Executive Control Deck of the NASTRAN deck:

```
1.  ALTER 121
2.  OUTPUT2     CASECC, EST, MPT, GPL,/C,N,-1/C,N,11/C,N,UTAPE   $
3.  OUTPUT2     OUGV1, OQG1, OEF1, OES1,/C,N,0/C,N,11   $
4.  ENDALTER
```

Statement 2 saves the necessary geometrical and mechanical properties of the structure on NASTRAN Fortran file UT1 and Statement 3 saves all the analysis results.

As can be noted, the main input to NASDAT comes from the above mentioned data blocks stored on file. However, additional input is required to specify the user's request for data reduction, post analysis and graphical presentation of results. This is prepared in a form similar to the NASTRAN input (reference 4). The NASDAT data deck consists therefore of an Executive Control Deck, a Case Control Deck and a Bulk Data Deck.

The Executive Control Deck contains that information required by NASDAT to decide if the NASTRAN output files are to be sorted and/or checkpointed for restart purposes.

The Case Control Deck consists only of SET cards needed to define the element and grid sets referred to in the Bulk Data Deck, and TITLE cards which produce output labels for the preferred sequence option.

The Bulk Data Deck contains the main information required for the data reduction and post analysis. The format and order of input is similar to that of NASTRAN, i.e. data is input in 8 column fields with freedom to arrange the input cards in any sequence. Facsimiles of input cards for the data reduction and definition of lower and upper bounds are shown for Bar and Shear elements in figures 2, 3 and 4 respectively. Facsimiles of input cards for the automatic computation of margins of safety for Rod and Shear elements are shown in figures 5 and 6 respectively.

Description Of The GRAS Module

This is the off-line graphical postprocessing module, which is used to display graphically either the reduced results produced by NASDAT or the regular NASTRAN output. Input for the GRAS module is generated by NASDAT.

At present, GRAS is run in a batch mode environment and uses a Calcomp drum plotter. The plotting capabilities can take one of the following forms:

a) *Developed Fuselage Strip*

Using this option, a segment of the fuselage of an aircraft is developed into a flat strip upon which the values of the reduced or regular results are plotted.

b) *Bulkhead Plots*

Using this option graphical displays of bending moments, bending stresses and transverse shear forces in Bar elements may be obtained.

c) *Projection Plots*

The user may obtain a graphical display of the projection of any specified part of the structure on any one of the three principal planes. The stress values are then plotted on this projection. Figure 7 shows stresses in Rods plotted on a projected view of an aircraft delta wing in the XY plane.

NUMERICAL APPLICATIONS

The NASDAT and GRAS modules were first utilized in the data reduction and post analysis of the results obtained from the NASTRAN analysis of the IAI Westwind 1124 aft fuselage (reference 5). The structure was idealized using Shear Panels to represent the skins, Rod elements to represent the stringers and Bar elements offset from the skins to represent the bulkheads. The complete mathematical model, shown in figure 8, consisted of 460 BAR elements, 1670 ROD elements, 1030 SHEAR elements and 1250 GRID points representing a total of 3650 unconstrained degrees of freedom. The structure was subjected to 18 loading conditions. Because of the size of the structure a substructuring technique (reference 6) was employed, subdividing the aft-fuselage into 5 substructures.

Based on engineering considerations related to the structural configuration and loading conditions the analyst has asked for (presented here as an example) information relative to extreme values of average shear stresses, data relative to critical regions affected by shear buckling of skin panels, and margins of safety of Rod elements. In order to get the full picture of the internal load distribution in a bulkhead of interest, the preferred sequence option has been used to output results in this region. In addition, graphical capabilities have also been employed to display moments, shear stresses and axial stresses. Finally, a plot to represent the envelope of shear stresses has been required.

A listing of the complete input required to perform this type of data reduction and post analysis for substructure 1 (figure 9), is given in figure 10. Based on the user's request, the following data was obtained:

(i) Twenty extreme absolute values for average stresses in Shear Panels and axial stresses in Rod elements (figure 11).

(ii) Buckling stresses, diagonal tension factors and related margins of safety for Shear Panels located in the left hand side of the fuselage structure.

Since the actual skin panels between bulkheads were represented in the idealization as a mesh of NASTRAN Shear Panels, it should be noted that the aspect ratio (a/b) referred to the *actual* skin panels and not to the dimensions of an idealized element. Therefore, in this case, the user had to input the aspect ratio manually. The critical stresses, diagonal tension factors and margins of safety, shown in figure 12 were computed using criteria defined in references 7 and 8.

(iii) Euler buckling stresses, ultimate tensile stresses and related margins of safety for Rod elements located in the left hand side of the fuselage structure.

In this case the necessary geometric material and cross section properties of the rod elements were retrieved from the NASTRAN tables using the automatic procedure (via the FLAG=2 option). Computer output is shown in figure 13.

Note that this output is presented for illustration only. Usually, the user will request

only a print-out for those elements having negative margins of safety.

(iv) A table of the internal load distribution for a bulkhead as requested via the preferred sequence option. Computer output is shown in figure 14.

(v) Graphical display needed for project documentation including (a) plot of bending stresses for a bulkhead as shown in figure 15; (b) presentation of envelopes for maximum and minimum shear stresses as shown in figure 16 and 17 respectively, (c) presentation of stresses in Rod elements and Shear Panels as shown in figures 18 and 19 respectively.

Since the original height of the Calcomp plots was 29 inches (73.6 cm) only a part of the plot (the left hand side) is presented.

The total amount of computer output for the complete NASTRAN finite element analysis consisted of about 5000 pages. Scanning, hand reduction, post analysis and drawing of results would have required several man months of engineering work. In contrast, meaningful engineering-oriented output and data reduction as presented above could be accomplished in the span of a few days.

CURRENT DEVELOPMENTS

Current developments of NASDAT include the expansion of the options which deal with computations of the allowables. These will incorporate bending elements as well as stiffened panels.

The NASDAT/GRAS modules are presently converted to operate in a time-sharing mode using low cost graphic display terminals, and together with NASTRAN will be included as modules in Israel Aircraft Industries' ISSAS, (Interfaced Software System for Sizing and Analysis of aircraft Structures) (reference 9).

CONCLUSION

Scanning of analysis results and computations of allowables and margins of safety, which are especially error prone and time consuming, may be performed with the aid of NASDAT and results graphically displayed by GRAS in an automated fashion, thus freeing the analyst to devote a larger portion of his time to engineering decision-making based upon results which are obtained in an organized form.

The use of the presented data reduction, post analysis and graphical plotting capabilities provide the analyst with an efficient and convenient tool for the study of NASTRAN analysis results and their presentation for project documentation.

REFERENCES

1. Herness, E. D., and Kriloff, H. Z.: NASTRAN Pre- and Postprocessors Using Low-Cost Interactive Graphics. NASTRAN: Users' Experiences, NASA TM X-3278, Sept., 1974.

2. Walker, D.C.: Scanning NASTRAN Output Data For Maximum And Minimum Values. NASTRAN: Users' Experiences, NASA TM X-3278, Sept., 1974.

3. Raibstein, A. I.: The NASDAT User and Application Manual. IAI TR 10623, July, 1976.

4. McCormick, C.W. (ed.): The NASTRAN User's Manual. NASA SP-222(01), June, 1972.

5. Raibstein, A. I., and Emil, S.: Finite Element Analysis of the Westwind 1124 Aft Fuselage. IAI TR 4842/8533, Oct., 1975.

6. Raibstein, A. I., and Pipano, A.: Substructuring in NASTRAN. IAI TR 4842/8527, March, 1975.

7. Timoshenko, S.P., and Gere, J. M.: Theory of Elastic Stability. Second ed., McGraw - Hill Book Co., Inc., 1961.

8. Kuhn, P., Peterson, J. P., and Levin, L. R.: A Summary of Diagonal Tension, Part I, NACA TN 2661, May, 1952.

9. Bendavid, D., Somekh, E., Pipano, A. and Raibstein, A. I.: Interactive Computer Graphics System for Sizing and Analysis of Aircraft Structures. NASA SP-390, Application of Computer Graphics in Engineering. Oct., 1975, pp. 233-256.

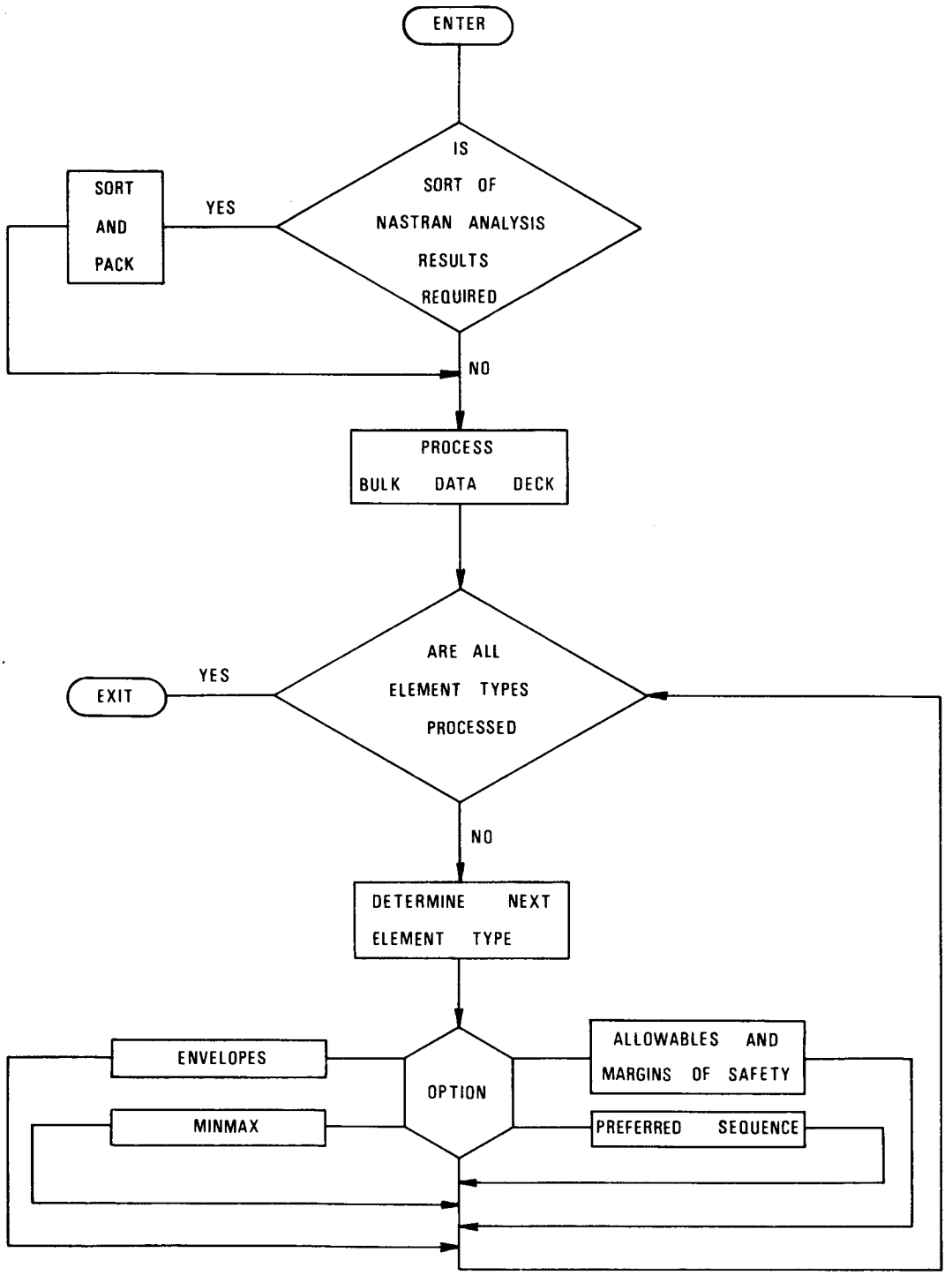

FIGURE 1: FLOW DIAGRAM FOR THE NASDAT MODULE

Bulk Data Card — BAR Data reduction for CBAR elements

Description: Defines the option and the element set for which data reduction is requested.

Format and Example

1	2	3	4	5	6	7	8	9	10
BAR	SID	COMPON	SUBCASE	SSID	OPTION	MINSET	MAXSET	NMINMAX	PLOT
BAR	16	15678	4		PREFSEQ				YES

Alternate Form

BAR	SID	COMPON	SUBCASE	SSID	OPTION	MINSET	MAXSET	NMINMAX	PLOT
BAR	ALL	ALL		ALL	ENVEL				

Field		Contents
SID		Element set identification number (Integer > 0)
COMPON		Component number for which data reduction is requested. Any unique combinations of the digits 1-8 (with no imbedded blanks)
SUBCASE		Single Subcase identification number for which data reduction is requested (Integer > 0 or blank)
OPTION		Data reduction option; one of the BCD values "ENVEL", MINMAX", "MS" or "PREFSEQ"
	ENVEL	Stress or force envelope
	MINMAX	Scan for minimum (negative) or maximum (positive) values per Subcase.
	MS	Margin of Safety computations
	PREFSEQ	Preferred sequence in output set
MINSET, MAXSET		Identification number of a BARMIN or BARMAX (Integer > 0 or blank).
NMINMAX		Number of minimum or maximum extreme stress or force values required (Integer > 0 or blank)
PLØT		Generate input for the plot modules "YES" - generate "NO" - do not generate (Default)

Remarks:

1. The element set identification number must be defined in the Case Control Deck (SET SID = ...) to be used by NASDAT

2. In order to reduce the NASTRAN output for CBAR elements the user has the option to define the following output components to be output or plotted.

Component	Value
1	Moment in plane 1 at end A and B
2	Moment in plane 2 at end A and B
3	Transverse shear in plane 1 and 2
4	Torsional moment
5	Axial force
6	Axial stress
7	Maximum normal stress at end A and B
8	Minimum normal stress at end A and B

FIGURE 2: NASDAT BULK DATA CARD BAR

Bulk Data Cards — BARMIN: BARMAX

Negative (BARMIN) or positive (BARMAX) bounds for force and stress values of CBAR elements.

Description: Defines the smallest negative (BARMIN) or largest positive (BARMAX) stress or force value for CBAR elements. Output consists of negative values or positive values larger than those defined on the BARMIN or BARMAX card.

Format and Example

1	2	3	4	5	6	7	8	9	10
BARMIN	SID	M1A	M1B	M2A	M2B	SF1	SF2	MT	ABCD
BARMIN	5	-100.0	-100.0			-50.0			CØN1
+BCD	AF	AS	SMAXA	SMAXB	SMINA	SMINB			
+ØN1	-1000.	-2500.			-3000.	-3500.			

Field	Contents
Type	One of the BCD values "BARMIN" or "BARMAX"
SID	MINSET (BARMIN) OR MAXSET (BARMAX) identification number (Integer > 0)
M1A; M1B	Extreme value of moment in plane 1 at end -A- and -B- (Real ≥ 0.0 (BARMAX); Real ≤ 0.0 (BARMIN))
M2A; M2B	Extreme value of moment in plane 2 at end -A- and -B- (Real ≥ 0.0 (BARMAX): Real ≤ 0.0 (BARMIN))
SF1; SF2	Extreme value of transverse shear in plane 1 and plane 2 (Real ≥ 0.0 (BARMAX); Real ≤ (BARMIN))
MT	Extreme value of torsional moment (Real ≥ 0.0 (BARMAX), Real ≤ 0.0 (BARMIN))
AF	Extreme value of axial force (Real ≥ 0.0 (BARMAX); Real ≤ 0.0.(BARMIN))
AS	Extreme value of axial stress (Real ≥ 0.0 (BARMAX); Real ≤ 0.0 (BARMIN))
SMAXA: SMAXB	Extreme value of maximum combined normal stress at end -A- and -B- (Real ≥ 0.0 (BARMAX); Real ≤ 0.0 (BARMIN))
SMINA: SMINB	Extreme value of minimum combined normal stress at end -A- and -B- (Real ≥ 0.0 (BARMAX); Real ≤ 0.0 (BARMIN))

Remarks:

1. The values defined on the BARMIN and BARMAX are used in the following manner:

   a. If the related BAR card defines OPTION ="MS" then the values defined are considered to be critical ones and the margins of safety is computed.

   b. If the related BAR card defines OPTION = "ENVEL", "MINMAX" or "PREFSEQ" then the values are considered as criteria to output values larger than those defined on the BARMIN or BARMAX card.

FIGURE 3: NASDAT BULK DATA CARD BARMIN

Bulk Data Card — SHEAR Data reduction for CSHEAR elements

Description: Defines the option and element set for which data reduction is requested.

Format and Example

1	2	3	4	5	6	7	8	9	10
SHEAR	SID		SUBCASE	SSID	OPTION	SMIN	SMAX	NMINMAX	PLOT
SHEAR	18		4		MINMAX		3000	20	

Alternate Form

SHEAR	SID		SUBCASE	SSID	OPTION	SMIN	SMAX	NMINMAX	PLØT
SHEAR	ALL			21	ENVEL				YES

Field	Contents
SID	Element set identification number (Integer > 0)
SUBCASE	Single Subcase identification number for which data reduction is requested (Integer > 0 or blank)
SSID	Subcase set identification number (Integer > 0 or blank).
OPTIØN	Data reduction option ; one of the BCD values "ENVEL", "MINMAX", "MS" or PREFSEQ"
	"ENVEL" - Stress envelope
	"MINMAX" - Scan for minimum (negative) or maximum (positive) values per subcase
	"MS" - Computes margin of safety
	"PREFSEQ" - Set output in preferred sequence
SMIN: SMAX	Define the negative (SMIN) and positive (SMAX) boundary values for the average shear stresses Output consists of negative values or positive values larger than those defined by SMIN or SMAX (Real ≥ 0.0 (SMAX); Real ≤ 0.0 (SMIN)).
NMINMAX	Number of minimum and maximum extreme stress values required (Integer > 0 or blank)
PLØT	Generate input for the plot modules, YES - Generate; NØ - do not generate (Default)

Remarks:

1. The element set identification number must be defined in the Case Control Deck (SET SID =.....) to be used by NASDAT.
2. If OPTION = "MS" then the entry for SMAX is considered to be the critical stress for the shear panels defined in the element set.

FIGURE 4: NASDAT BULK DATA CARD SHEAR

Bulk Data Card — ALRØD Computations of Allowables and related margins of safety for Rod elements.

Description — Defines the properties of CROD and CONROD elements needed to compute their Euler buckling and ultimate tensile stresses and to evaluate their margins of safety.

Format and Example:

1	2	3	4	5	6	7	8	9	10
ALROD	SID	I	L	E	A	R	FTU	FLAG	SUBCASE
ALROD	1	0.132				1.0	63000.	2	4

Field	Contents
SID	Element set identification number (Integer > 0)
I	Minimum moment of inertia (Real > 0.0)
L	Length of rod element (Real > 0.0 or blank; see below)
E	Young's modulus (Real > 0.0 or blank; see below)
A	Cross sectional area of rod element (Real > 0.0 or blank; see below)
R	Flag to specify the support condition of the rod element (Real > 0.0, see remark 2)
FTU	Ultimate stress for rod element material (Real > 0.0)
FLAG	Flag to specify the nature of fields 4-6 as follows:

	4	5	6
FLAG=1	L	A	E
FLAG=2			

If FLAG=1 Then the user defines the values required to perform the computations of the allowables.

If FLAG=2 Then the program takes the data from the appropriate NASTRAN tables

SUBCASE	Single subcase identification number for which data reduction is requested (Integer > 0)

Remarks:

1. The element set identification number must be defined in the Case Control Deck (SET SID = ...) to be used by NASDAT
2. Program assumes uniform cross section and computes the Euler or Ultimate stress and the margins of safety for the rod elements.

   R may have one of the following values

Boundary Condition			R
Simple	-	Simple	1.0
fixed	-	fixed	2.0
fixed	-	free	0.5
fixed	-	simple	1.43

FIGURE 5: NASDAT BULK DATA CARD ALROD

Bulk Data Card — ALSHEAR Computations of Allowables and related margins of safety for Shear elements.

Description: Defines the properties of CSHEAR elements needed to compute the buckling stress of shear panels and to evaluate their margins of safety.

Format and Example:

1	2	3	4	5	6	7	8	9	10
ALSHEAR	SID	A/B	T	E	NU	R		FLAG	SUBCASE
ALSHEAR	5	3.0	0.04	10.5E+6	0.3			1	5

Field	Contents
SID	Element set identification number (Integer > 0)
A/B	Aspect ratio of shear panel (Real > 0.0 or blank; see below)
T	Thickness of shear panel (Real > 0.0 or blank; see below)
E	Young's modulus (Real > 0.0 or blank; see below)
NU	Poisson's ratio (Real > 0.0 or blank; see below)
R	Radius of curvature of portion of skin under investigation (Real > 0.0 or blank)
FLAG	Flag to specify the nature of fields 3-6 as follows:

	3	4	5	6
FLAG=1	A/B	T	E	NU
Flag=2				

If FLAG=1 Then the user defines the values required to perform computations for the allowables of the shear panels.

If FLAG=2 Then the program takes the data from the appropriate NASTRAN tables.

SUBCASE — Single Subcase identification number for which data reduction is requested (Integer > 0)

Remarks:

1. The element set identification number must be defined in the Case Control Deck (SET SID =.....) to be used by NASDAT

2. Presently, the program assumes that the panel is simply supported on four sides.

FIGURE 6: NASDAT BULK DATA CARD ALSHEAR

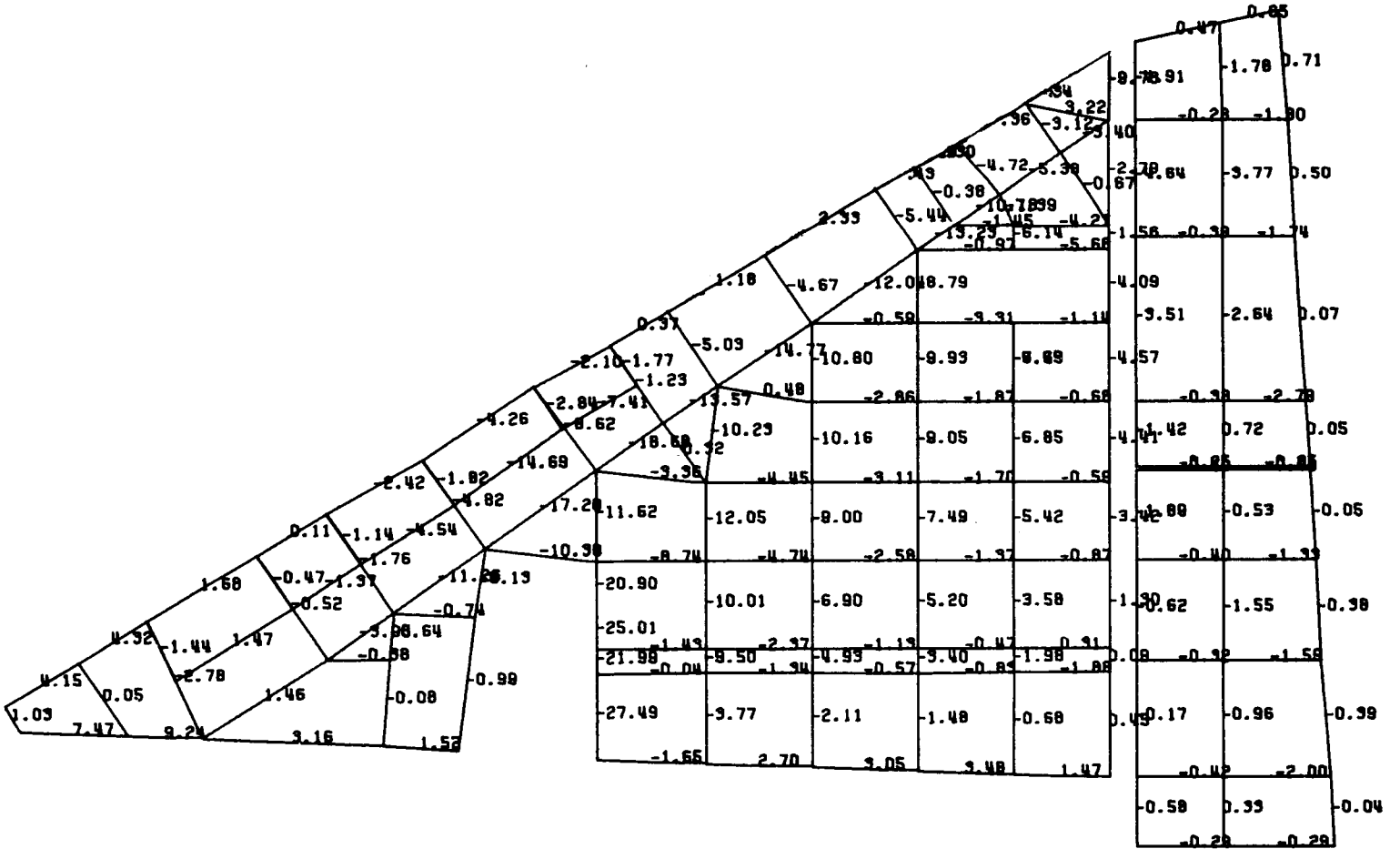

FIGURE 7: ROD STRESSES DISPLAYED ON A PROJECTED VIEW OF A DELTA WING

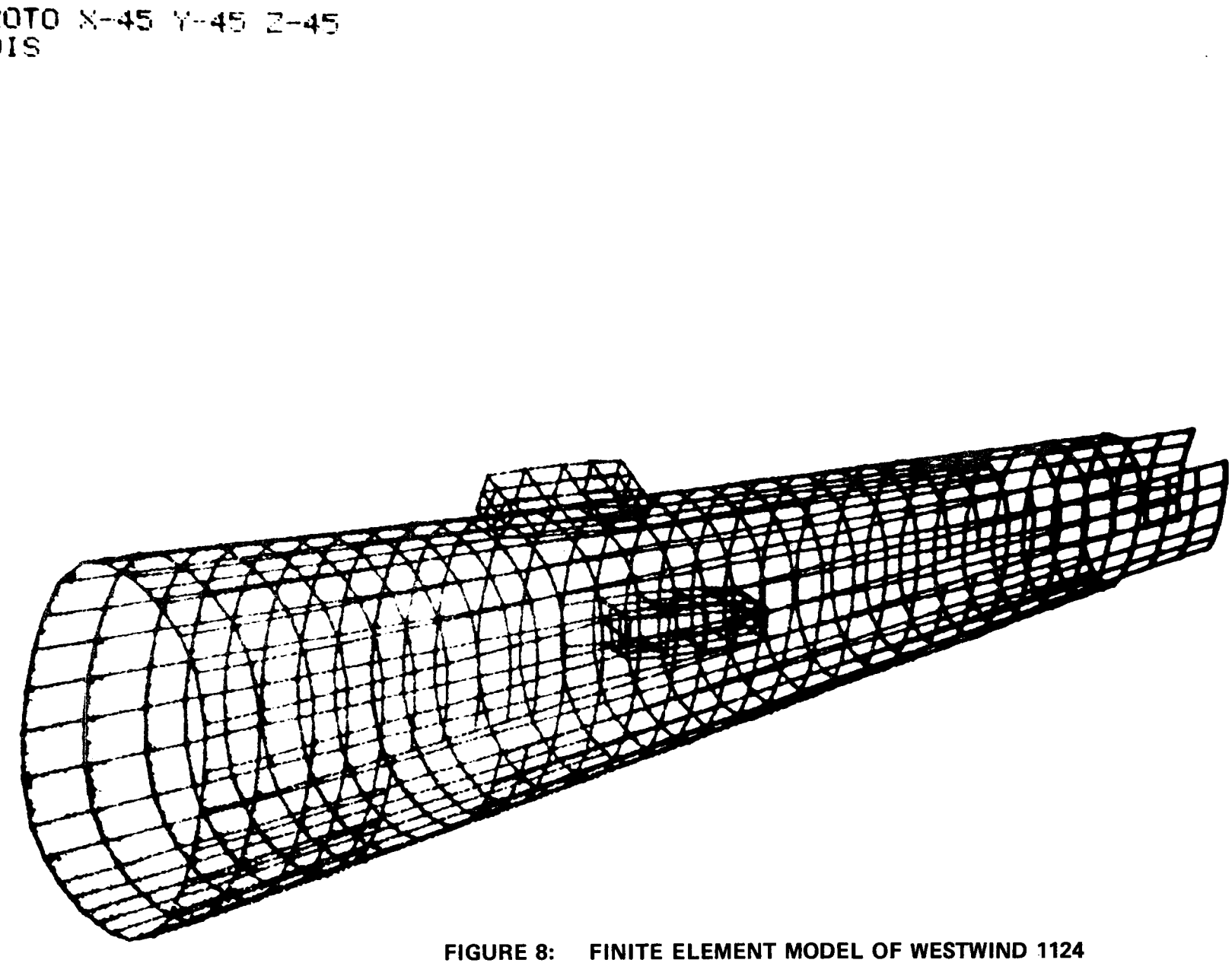

FIGURE 8: FINITE ELEMENT MODEL OF WESTWIND 1124 AFT FUSELAGE (COMPLETE MODEL)

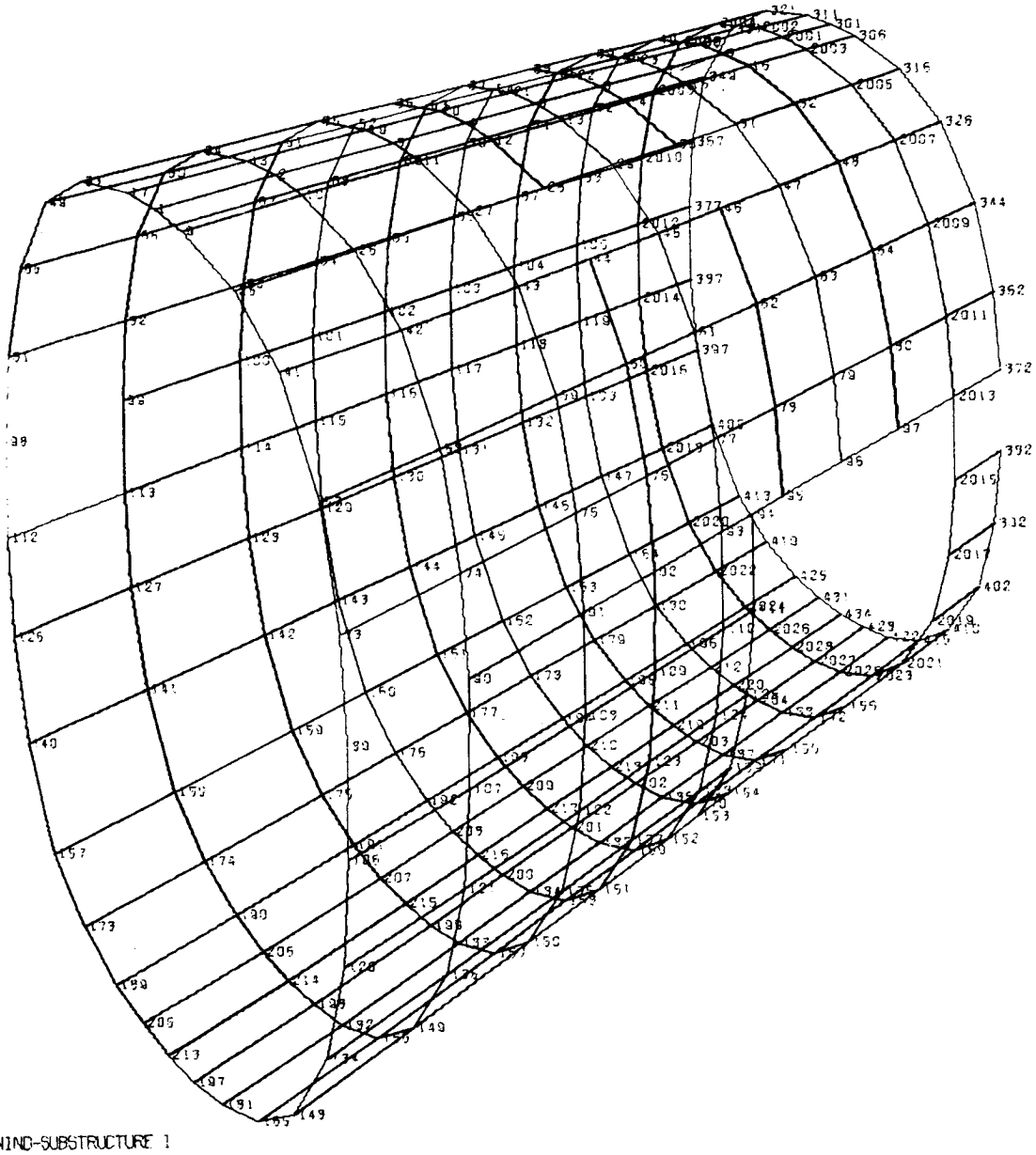

WESTWIND-SUBSTRUCTURE 1

UNDEFORMED SHAPE

FIGURE 9: FINITE ELEMENT MODEL OF WESTWIND 1124 AFT FUSELAGE (SUBSTRUCTURE 1)

N A S D A T E X E C U T I V E C O N T R O L D E C K E C H O

```
ID POST,PROCESSOR
SORT YES
CHKPNT YES
CEND
```

N A S D A T C A S E C O N T R O L D E C K E C H O

```
SET 1=1121 THRU 1162 EXCEPT 1143,1144,1151,1152,1160,1170,1174,1175,
      1179 THRU 1184,1199 THRU 1206,1495,1557
SET 2=1143,1144,1151,1152,1160,1168,1169,1172,1173,1176,1177,1178,
      1287,1501,1507,1521,1527,1541,1545,1549
SET 3=1165,1166,1167,1185 THRU 1190
SET 4=1191 THRU 1198,1553
SET 5=3113,3114
SET 6=3115 THRU 3118,3181,3182,3189,3190,3199 THRU 3212 EXCEPT 3205,3206,
      3557,3561
SET 7=3120
SET 8=3121,3122,3129,3130,3166,3167,3171,3172,3176,3177,3187,3188,3195,
      3196,3549,3553,3557,3561
SET 9=3123 THRU 3128,3135,3136,3164,3168,3169,3491,3545
SET 10=3138,3146,3191 THRU 3194
SET 11=3139 THRU 3151 EXCEPT 3145,3146,3503,3517,3523,3529,3539
SET 12=3154,3162
SET 13=3197,3198,3205,3206
SET 14=3152 THRU 3162,3173 THRU 3175,3178 THRU 3180
SET 15=3183 THRU 3188
TITLE=FRAME AT STATION 340  - SUBSTRUCTURE 1 -
SET 25=2 THRU 11
SET 21=57 THRU 84
BEGIN BULK
```

N A S D A T S O R T E D B U L K D A T A E C H O

CARD COUNT										
1	ALROD	1	0.132						2	4
2	ALROD	2	0.167						2	4
3	ALROD	3	0.488						2	4
4	ALROD	4	0.452						2	4
5	ALSHEAR	5	6.0	0.04	10.5E+6	0.3			1	5
6	ALSHEAR	6	3.8	0.04	10.5E+6	0.3			1	5
7	ALSHEAR	7	3.4	0.04	10.5E+6	0.3			1	5
8	ALSHEAR	8	3.0	0.04	10.5E+6	0.3			1	5
9	ALSHEAR	9	2.0	0.04	10.5E+6	0.3			1	5
10	ALSHEAR	10	1.5	0.04	10.5E+6	0.3			1	5
11	ALSHEAR	11	1.0	0.04	10.5E+6	0.3			1	5
12	ALSHEAR	12	1.0	0.04	10.5E+6	0.3			1	5
13	ALSHEAR	13	5.0	0.04	10.5E+6	0.3			1	5
14	ALSHEAR	14	2.5	0.072	10.5E+6	0.3			1	5
15	ALSHEAR	15	1.5	0.072	10.5E+6	0.3			1	5
16	BAR	21	15678	4		PREFSEQ				YES
17	ROD	ALL	2	4		MINMAX		1	20	
18	ROD	ALL	2	4		PREFSEQ		1	20	
19	ROOMIN	1		-40000.						
20	SWEAR	ALL		4		MINMAX			20	
21	SWEAR	ALL		4		PREFSEQ				YES
22	SWEAR	ALL			25	ENVEL				YES
23	ENDDATA									

FIGURE 10: TYPICAL INPUT DATA DECK FOR NASDAT

THE FOLLOWING LIST PRESENTS THE EXTREME STRESSES IN C S H E A R ELEMENTS FOR S U B C A S E 4

20 EXTREME VALUES ARE REQUESTED - 10 VALUES ARE FOUND TO BE POSITIVE, 10 ARE NEGATIVE

****
MAXIMUM (POSITIVE) STRESSES
****

ELEMENT ID.	AVG STRESS	ELEMENT ID.	AVG STRESS
3151	1.1645E+04	3150	1.0372E+04
3196	1.0367E+04	3158	1.0170E+04
3149	9.9385E+03	3195	9.8036E+03
3194	9.5829E+03	3193	8.9942E+03
3166	8.9071E+03	3188	8.5570E+03

****
MINIMUM (NEGATIVE) STRESSES
****

ELEMENT ID.	AVG STRESS	ELEMENT ID.	AVG STRESS
3049	-9.4084E+03	3066	-8.4594E+03
3073	-7.7787E+03	3048	-7.6788E+03
3040	-7.6418E+03	3060	-7.4885E+03
3056	-7.3720E+03	3032	-7.3580E+03
3036	-7.3221E+03	3047	-7.3046E+03

THE FOLLOWING LIST PRESENTS THE EXTREME AXIAL STRESSES IN C R O D ELEMENTS FOR S U B C A S E 4

20 EXTREME VALUES ARE REQUEST - 20 VALUES ARE FOUND TO BE POSITIVE, -0 ARE NEGATIVE

****
MAXIMUM (POSITIVE) STRESSES
****

ELEMENT ID.	AXIAL STRESS	ELEMENT ID.	AXIAL STRESS
1139	4.9660E+04	1097	4.8070E+04
1138	4.7072E+04	1089	4.6432E+04
1113	4.6383E+04	1090	4.6018E+04
1121	4.5952E+04	1129	4.5700E+04
1091	4.5455E+04	1114	4.5029E+04
1122	4.4157E+04	1134	4.4011E+04
1115	4.3012E+04	1123	4.2808E+04
1105	4.2489E+04	1133	4.1843E+04
1102	4.1757E+04	1140	4.1635E+04
1124	4.0831E+04	1135	4.0641E+04

FIGURE 11: MAXIMUM AND MINIMUM STRESSES IN SHEAR PANELS AND ROD ELEMENTS

AVERAGE STRESSES, CRITICAL STRESSES, DIAGONAL TENSION FACTOR AND MARGINS OF SAFETY FOR C S H E A R ELEMENTS

SUBCASE 5

ELEMENT ID.	AVG SHEAR	CRITICAL SHEAR	DIAG TENSION FACTOR	MARGIN OF SAFETY	ELEMENT ID.	AVG SHEAR	CRITICAL SHEAR	DIAG TENSION FACTOR	MARGIN OF SAFETY
3113	1.4250E+03	3.9474E+03	0.	1.77E+00	3114	1.1210E+03	4.3999E+03	0.	2.92E+00
3115	2.7490E+03	5.3184E+03	0.	9.35E-01	3116	2.9340E+03	5.6291E+03	0.	9.19E-01
3117	1.1490E+03	6.0665E+03	0.	4.28E+00	3118	1.2330E+03	6.4194E+03	0.	4.21E+00
3119	1.3400E+02	6.8070E+03	0.	4.98E+01	3120	1.4300E+02	7.2341E+03	0.	4.96E+01
3121	2.7150E+03	1.4025E+03	1.42E-01	-4.83E-01	3122	1.4480E+03	1.4812E+03	0.	2.29E-02
3123	3.7670E+03	1.8252E+03	1.56E-01	-5.15E-01	3124	4.0130E+03	1.9281E+03	1.58E-01	-5.20E-01
3125	2.0300E+03	2.0805E+03	0.	2.49E-02	3126	2.1620E+03	2.2000E+03	0.	1.76E-02
3127	1.2290E+03	2.3294E+03	0.	8.95E-01	3128	1.3220E+03	2.4660E+03	0.	8.65E-01
3129	3.7220E+03	1.6792E+03	1.71E-01	-5.49E-01	3130	7.8540E+03	1.6646E+03	3.25E-01	-7.88E-01
3135	7.8000E+03	2.4047E+03	2.50E-01	-6.92E-01	3136	8.2780E+03	2.5285E+03	2.52E-01	-6.95E-01
3137	4.9350E+03	1.1965E+03	2.98E-01	-7.58E-01	3138	1.7160E+03	1.3094E+03	5.87E-02	-2.37E-01
3139	5.3060E+03	1.6320E+03	2.51E-01	-6.92E-01	3140	5.5710E+03	1.7017E+03	2.52E-01	-6.95E-01
3141	6.9690E+03	1.8100E+03	2.85E-01	-7.40E-01	3142	7.3070E+03	1.8854E+03	2.86E-01	-7.42E-01
3143	7.0000E+03	1.9656E+03	2.69E-01	-7.19E-01	3144	4.0860E+03	6.6482E+03	0.	6.27E-01
3145	6.1930E+03	1.2899E+03	3.28E-01	-7.92E-01	3146	2.1820E+03	1.3393E+03	1.06E-01	-3.86E-01
3147	3.3040E+03	1.6084E+03	1.55E-01	-5.13E-01	3148	3.4470E+03	1.6689E+03	1.56E-01	-5.16E-01
3149	1.0800E+04	1.7660E+03	3.74E-01	-8.36E-01	3150	1.1283E+04	1.8306E+03	3.76E-01	-8.38E-01
3151	1.2700E+04	1.8990E+03	3.91E-01	-8.50E-01	3152	7.3250E+03	6.3880E+03	2.97E-02	-1.28E-01
3154	5.6960E+03	5.5935E+03	3.94E-03	-1.80E-02	3155	2.4040E+03	6.6386E+03	0.	1.76E+00
3156	1.3650E+03	6.8423E+03	0.	4.01E+00	3157	5.3450E+03	7.2018E+03	0.	3.47E-01
3158	1.0900E+04	7.4128E+03	8.35E-02	-3.20E-01	3159	7.8460E+03	7.6366E+03	5.88E-03	-2.67E-02
3160	7.9270E+03	7.8700E+03	1.57E-03	-7.19E-03	3162	6.5700E+03	1.5050E+03	3.10E-01	-7.71E-01
3163	4.6760E+03	5.8301E+03	0.	2.47E-01	3164	8.2960E+03	5.9979E+03	7.03E-02	-2.77E-01
3165	5.5000E+03	7.2158E+03	0.	3.12E-01	3166	9.4530E+03	1.4760E+03	3.83E-01	-8.44E-01
3167	6.9300E+03	1.5500E+03	3.14E-01	-7.76E-01	3168	5.0240E+03	6.0835E+03	0.	2.11E-01
3169	5.2300E+03	6.3134E+03	0.	2.07E-01	3170	2.1260E+03	7.7225E+03	0.	2.63E+00
3171	8.7190E+03	1.4167E+03	3.75E-01	-8.38E-01	3172	7.4120E+03	1.4862E+03	3.35E-01	-7.99E-01
3173	3.7770E+03	5.8343E+03	0.	5.45E-01	3174	3.9410E+03	6.0558E+03	0.	5.37E-01
3175	1.7200E+03	7.3807E+03	0.	3.29E+00	3176	7.2890E+03	1.3934E+03	3.45E-01	-8.09E-01
3177	5.2160E+03	1.4702E+03	2.68E-01	-7.18E-01	3178	2.1480E+03	5.7903E+03	0.	1.70E+00
3179	3.0910E+03	6.0505E+03	0.	9.57E-01	3180	1.8620E+03	7.4379E+03	0.	2.99E+00
3181	5.2190E+03	2.2984E+03	1.76E-01	-5.60E-01	3182	3.5710E+03	2.4221E+03	8.41E-02	-3.22E-01
3183	1.0000E+02	9.4659E+03	0.	9.37E+01	3184	1.3140E+03	9.9414E+03	0.	6.57E+00
3185	5.4180E+03	1.0668E+04	0.	9.69E-01	3186	8.1530E+03	1.1228E+04	0.	3.77E-01
3187	8.2340E+03	1.1832E+04	0.	4.37E-01	3188	8.7110E+03	1.2426E+04	0.	4.26E-01
3189	2.9300E+03	2.6419E+03	2.25E-02	-9.83E-02	3190	3.2800E+03	2.7978E+03	3.45E-02	-1.47E-01
3191	2.8180E+03	3.3554E+03	0.	1.91E-01	3192	2.9860E+03	3.5283E+03	0.	1.82E-01
3193	9.2710E+03	3.7871E+03	1.92E-01	-5.92E-01	3194	9.8770E+03	3.9740E+03	1.95E-01	-5.98E-01
3195	1.0305E+04	4.1762E+03	1.94E-01	-5.95E-01	3196	1.0899E+04	4.4098E+03	1.94E-01	-5.95E-01
3197	2.2870E+03	4.0430E+03	0.	7.68E-01	3198	2.0120E+03	4.2991E+03	0.	1.14E+00
3199	2.3770E+03	5.1000E+03	0.	1.15E+00	3200	2.5120E+03	5.3989E+03	0.	1.15E+00
3201	4.2550E+03	5.8246E+03	0.	3.69E-01	3202	4.5200E+03	6.1649E+03	0.	3.64E-01
3203	4.1850E+03	6.5387E+03	0.	5.62E-01	3204	4.5190E+03	6.9528E+03	0.	5.39E-01
3205	1.0670E+03	4.7247E+03	0.	3.43E+00	3206	1.2560E+03	5.0460E+03	0.	3.02E+00
3207	2.3770E+03	5.8886E+03	0.	1.48E+00	3208	2.5510E+03	6.2245E+03	0.	1.44E+00
3209	2.4400E+03	6.6842E+03	0.	1.74E+00	3210	2.5990E+03	7.0616E+03	0.	1.72E+00
3211	2.7040E+03	7.4749E+03	0.	1.76E+00	3212	2.8870E+03	7.9287E+03	0.	1.75E+00
3485	2.6730E+03	7.9805E+03	0.	1.99E+00	3491	5.3510E+03	2.7320E+03	1.45E-01	-4.89E-01
3497	7.4480E+03	2.7835E+03	2.11E-01	-6.26E-01	3503	5.9550E+03	3.4940E+03	1.15E-01	-4.13E-01
3517	3.4310E+03	3.3362E+03	6.09E-03	-2.76E-02	3523	5.5000E+02	8.4831E+03	0.	1.44E+01
3529	5.8030E+03	8.1391E+03	0.	4.03E-01	3539	6.7890E+03	7.7675E+03	0.	1.44E-01
3545	9.5230E+03	8.0738E+03	3.58E-02	-1.52E-01	3549	2.0770E+03	1.3665E+04	0.	5.58E+00
3553	2.5090E+03	4.8658E+03	0.	9.39E-01	3557	3.1500E+02	7.6745E+03	0.	2.34E+01

FIGURE 12: AVERAGE STRESSES, BUCKLING STRESSES, DIAGONAL TENSION FACTORS AND MARGINS OF SAFETY FOR SHEAR PANELS

CRITICAL STRESSES AND SAFETY MARGINS FOR C R O D AND C O N R O D ELEMENTS

SUBCASE 4

ELEMENT ID.	AXIAL STRESS	CRITICAL STRESS	MARGIN OF SAFETY	ELEMENT ID.	AXIAL STRESS	CRITICAL STRESS	MARGIN OF SAFETY
1121	4.5952E+04	6.3000E+04	3.71E-01	1122	4.4157E+04	6.3000E+04	4.27E-01
1123	4.2808E+04	6.3000E+04	4.72E-01	1124	4.0831E+04	6.3000E+04	5.43E-01
1125	3.8921E+04	6.3000E+04	6.19E-01	1126	3.7087E+04	6.3000E+04	6.99E-01
1127	3.5340E+04	6.3000E+04	7.83E-01	1128	3.3674E+04	6.3000E+04	8.71E-01
1129	4.5700E+04	6.3000E+04	3.79E-01	1130	3.7796E+04	6.3000E+04	6.67E-01
1131	3.3243E+04	6.3000E+04	8.95E-01	1132	3.8220E+04	6.3000E+04	6.48E-01
1133	4.1843E+04	6.3000E+04	5.06E-01	1134	4.4011E+04	6.3000E+04	4.31E-01
1135	4.0641E+04	6.3000E+04	5.50E-01	1136	3.1402E+04	6.3000E+04	1.01E+00
1137	4.2424E+04	6.3000E+04	4.85E-01	1138	4.7072E+04	6.3000E+04	3.38E-01
1139	4.9660E+04	6.3000E+04	2.69E-01	1140	4.1635E+04	6.3000E+04	5.13E-01
1141	3.2667E+04	6.3000E+04	9.29E-01	1142	2.2714E+04	6.3000E+04	1.77E+00
1143	1.6800E+04	6.3000E+04	2.75E+00	1144	1.6578E+04	6.3000E+04	2.80E+00
1145	3.1339E+04	6.3000E+04	1.01E+00	1146	2.8888E+04	6.3000E+04	1.18E+00
1147	2.9498E+04	6.3000E+04	1.14E+00	1148	3.2423E+04	6.3000E+04	9.43E-01
1149	3.1210E+04	6.3000E+04	1.02E+00	1150	2.5675E+04	6.3000E+04	1.45E+00
1151	1.7413E+04	6.3000E+04	2.62E+00	1152	9.0450E+03	6.3000E+04	5.97E+00
1153	1.5262E+04	6.3000E+04	3.13E+00	1154	1.7667E+04	6.3000E+04	2.57E+00
1155	1.1765E+04	6.3000E+04	4.35E+00	1156	1.5191E+04	6.3000E+04	3.15E+00
1157	2.0445E+04	6.3000E+04	2.08E+00	1158	1.5263E+04	6.3000E+04	3.13E+00
1159	8.2030E+03	6.3000E+04	6.68E+00	1160	5.9990E+03	6.3000E+04	9.50E+00
1162	4.6000E+02	6.3000E+04	1.36E+02	1165	1.4490E+03	6.3000E+04	4.25E+01
1166	-3.2450E+03	4.1505E+05	1.27E+02	1167	-5.6720E+03	1.2104E+06	2.12E+02
1168	-6.7860E+03	1.3806E+06	2.02E+02	1169	-1.7060E+03	6.3428E+06	3.72E+03
1170	-8.3780E+03	5.4371E+05	6.39E+01	1171	-8.1460E+03	5.1895E+05	6.27E+01
1172	-6.1430E+03	1.4781E+06	2.40E+02	1173	-2.2900E+03	1.3746E+06	5.99E+02
1174	-1.7244E+04	5.4106E+05	3.04E+01	1175	-1.2869E+04	5.1644E+05	3.91E+01
1176	-6.4970E+03	1.4717E+06	2.26E+02	1177	-2.0160E+03	1.3686E+06	6.78E+02
1178	-2.3700E+02	6.2843E+06	2.65E+04	1179	-2.4851E+04	5.3919E+05	2.07E+01
1180	-2.1027E+04	5.1453E+05	2.35E+01	1183	-2.8673E+04	5.3949E+05	1.78E+01
1184	-2.5788E+04	5.1427E+05	1.89E+01	1185	-1.6496E+04	1.4180E+06	8.50E+01
1186	-2.0531E+04	1.4180E+06	6.81E+01	1187	-2.2884E+04	1.6280E+06	7.01E+01
1188	-2.0475E+04	1.6280E+06	7.85E+01	1189	-1.6220E+04	1.6277E+06	9.94E+01
1190	-1.1795E+04	1.6277E+06	1.37E+02	1191	-3.1848E+04	6.0624E+05	1.80E+01
1192	-2.4863E+04	5.5245E+05	2.12E+01	1193	-2.6296E+04	1.3578E+06	5.06E+01
1194	-2.5676E+04	1.3578E+06	5.19E+01	1195	-2.4067E+04	1.5587E+06	6.38E+01
1196	-2.1399E+04	1.5587E+06	7.18E+01	1197	-1.8456E+04	1.5587E+06	8.35E+01
1198	-1.5254E+04	1.5587E+06	1.01E+02	1199	-3.1835E+04	5.4082E+05	1.60E+01
1200	-2.8743E+04	5.1463E+05	1.69E+01	1201	-2.7402E+04	1.2464E+06	4.45E+01
1202	-2.7234E+04	1.2464E+06	4.48E+01	1203	-2.5667E+04	1.4309E+06	5.47E+01
1204	-2.2585E+04	1.4309E+06	6.24E+01	1205	-1.9922E+04	1.4308E+06	7.08E+01
1206	-1.7654E+04	1.4308E+06	8.00E+01	1287	-2.2800E+02	6.3117E+06	2.77E+04
1489	3.0985E+04	6.3000E+04	1.03E+00	1495	2.5233E+04	6.3000E+04	1.50E+00
1501	1.7339E+04	6.3000E+04	2.63E+00	1507	7.5840E+03	6.3000E+04	7.31E+00
1521	6.9690E+03	6.3000E+04	8.04E+00	1527	-1.4130E+03	2.1482E+06	1.52E+03
1541	-3.4710E+03	2.1384E+06	6.15E+02	1549	-1.7532E+04	2.1254E+06	1.20E+02
1553	-1.3834E+04	2.1694E+06	1.56E+02	1557	-1.7866E+04	1.9475E+06	1.08E+02

FIGURE 13: AXIAL STRESSES, EULER/ULTIMATE STRESSES AND MARGINS OF SAFETY FOR ROD ELEMENTS

FRAME AT STATION 340 - SUBSTRUCTURE 1 - SUBCASE 4

CBAR	M1(A)	M1(B)	AXIAL FORCE	AXIAL STRESS	SIGMAX(A)	SIGMAX(B)	SIGMIN(A)	SIGMIN(B)
57	-2.972E+02	+.817E+02	1.056E+03	2.080E+0[illegible]	2.907E+03	1.728E+03	2.898E+03	1.572E+02
58	2.087E+02	1.125E+03	7.458E+02	1.469E+0[illegible]	1.824E+03	6.364E+02	3.380E+03	-3.020E+03
59	7.185E+02	1.360E+03	2.870E+02	5.654E+0[illegible]	1.786E+03	-2.302E+03	2.875E+03	-4.861E+03
60	6.332E+02	1.054E+03	-5.055E+02	-9.959E+0[illegible]	7.977E+01	-3.523E+03	7.955E+02	-5.204E+03
61	1.633E+03	-[illegible].283E+02	1.563E+02	2.404E+0[illegible]	2.497E+03	-2.654E+03	1.354E+03	-6.279E+02
62	-3.094E+02	+.937E+02	4.034E+02	6.125E+0[illegible]	1.161E+03	1.849E+02	1.170E+03	-1.032E+02
63	-8.870E+02	-1.361E+03	-5.255E+02	-7.205E+0[illegible]	2.549E+02	-1.459E+03	7.761E+02	-1.869E+03
64	-8.122E+02	-1.591E+03	-2.402E+02	-3.092E+0[illegible]	3.798E+02	-8.402E+02	1.125E+03	-1.415E+03
65	-1.480E+03	-1.959E+03	-1.499E+02	-2.004E+0[illegible]	1.210E+03	-1.193E+03	1.695E+03	-1.534E+03
66	-1.603E+03	-[illegible].590E+03	2.945E+01	2.527E+01	1.728E+03	-1.006E+03	2.775E+03	-1.640E+03
67	-1.353E+03	-1.914E+03	7.376E+02	1.120E+0[illegible]	3.519E+03	-7.507E+02	4.512E+03	-1.525E+03
68	-2.606E+03	[illegible].725E+02	-4.449E+01	-6.764E+01	1.031E+04	-4.515E+03	1.395E+03	-3.570E+03
69	2.840E+02	1.297E+03	-7.599E+02	-1.497E+0[illegible]	-1.015E+03	-2.630E+03	7.069E+02	-6.675E+03
70	1.565E+03	1.707E+03	-4.930E+02	-9.712E+0[illegible]	1.687E+03	-7.216E+03	1.928E+03	-7.783E+03
71	1.681E+03	1.668E+03	-5.211E+02	-1.027E+0[illegible]	1.829E+03	-7.736E+03	1.807E+03	-7.683E+03
72	1.315E+03	+.715E+02	-8.812E+02	-1.736E+0[illegible]	4.996E+02	-6.988E+03	-9.349E+02	-3.618E+03
73	1.191E+03	-[illegible].263E+03	-2.370E+01	-4.669E+01	1.976E+03	-4.799E+03	8.984E+03	-3.890E+03
74	-1.634E+03	-1.155E+03	7.460E+02	1.132E+0[illegible]	4.029E+03	-1.126E+03	3.180E+03	-4.636E+02
75	-2.052E+03	-1.176E+03	7.338E+01	6.296E+01	2.241E+03	-1.256E+03	1.312E+03	-6.933E+02
76	-9.744E+02	-1.129E+02	1.633E+02	2.183E+0[illegible]	1.147E+03	-4.350E+02	3.259E+02	1.425E+02
77	-1.934E+02	1.164E+03	1.179E+02	1.518E+0[illegible]	3.158E+02	2.536E+01	9.130E+02	-8.357E+02
78	-4.259E+02	[illegible].151E+02	-5.500E+02	-7.541E+0[illegible]	-2.858E+02	-1.113E+03	-6.644E+01	-1.650E+03
79	4.517E+02	+.445E+02	-7.510E+02	-1.140E+0[illegible]	-5.158E+02	-1.941E+03	-5.257E+02	-1.928E+03
80	1.144E+03	-[illegible].680E+02	-1.982E+02	-3.009E+0[illegible]	1.280E+03	-2.328E+03	6.832E+02	-1.224E+03
81	4.214E+02	-1.267E+03	6.527E+02	1.286E+03	2.002E+03	-3.958E+02	6.343E+03	-8.666E+02
82	-7.904E+02	-7.912E+02	1.210E+03	2.383E+03	5.538E+03	1.041E+03	5.541E+03	1.039E+03
83	-7.109E+02	-5.172E+02	1.292E+03	2.546E+03	5.383E+03	1.338E+03	4.610E+03	1.667E+03
84	-5.666E+02	-5.479E+01	1.230E+03	2.423E+03	4.685E+03	1.460E+03	2.642E+03	2.330E+03

FIGURE 14: INTERNAL LOAD DISTRIBUTION IN A BULKHEAD

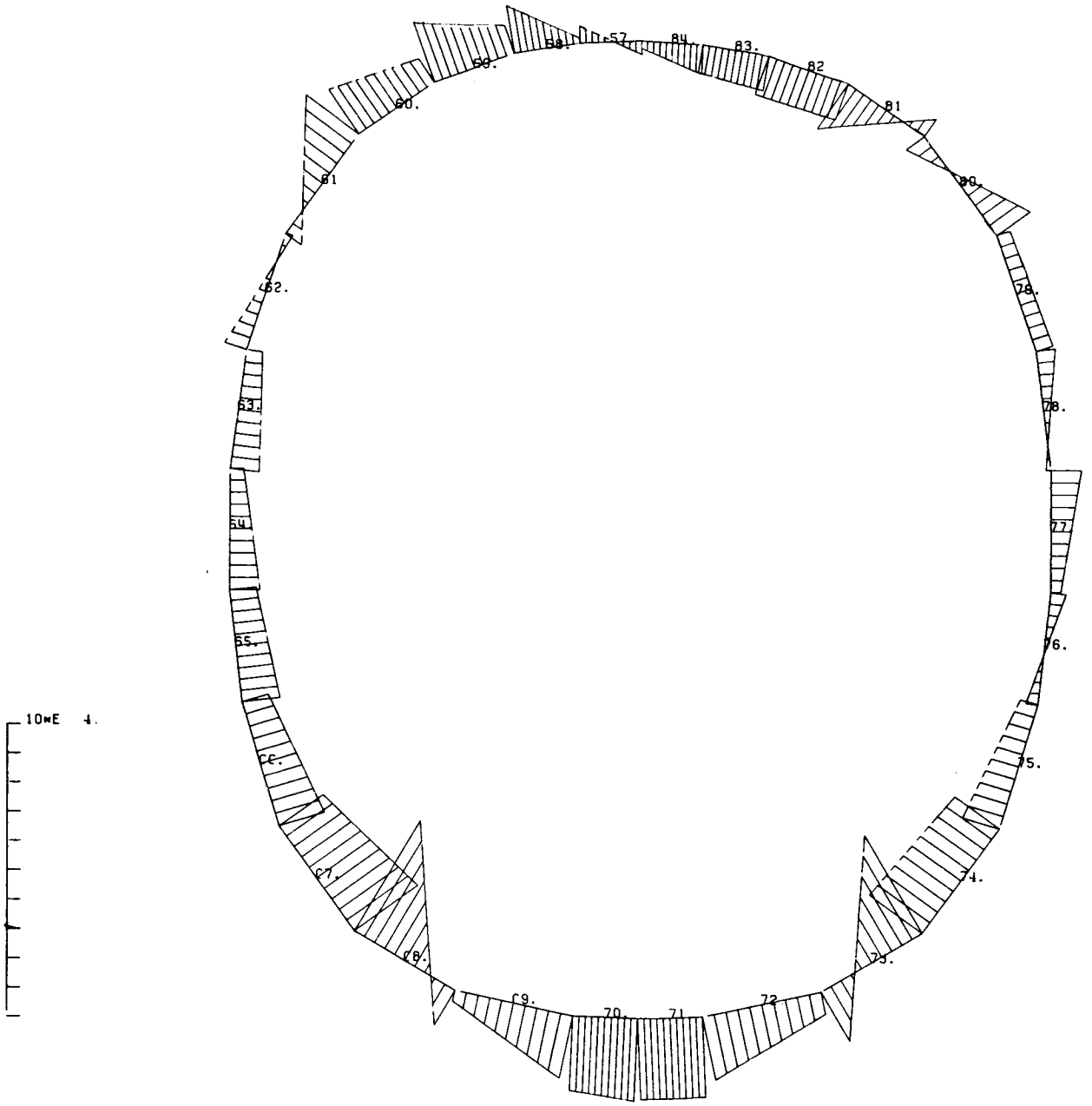

STRESSES IN BAR ELEMENTS
BULKHEAD AT STATION = 340.00

FIGURE 15: BENDING STRESSES DIAGRAM FOR A BULKHEAD

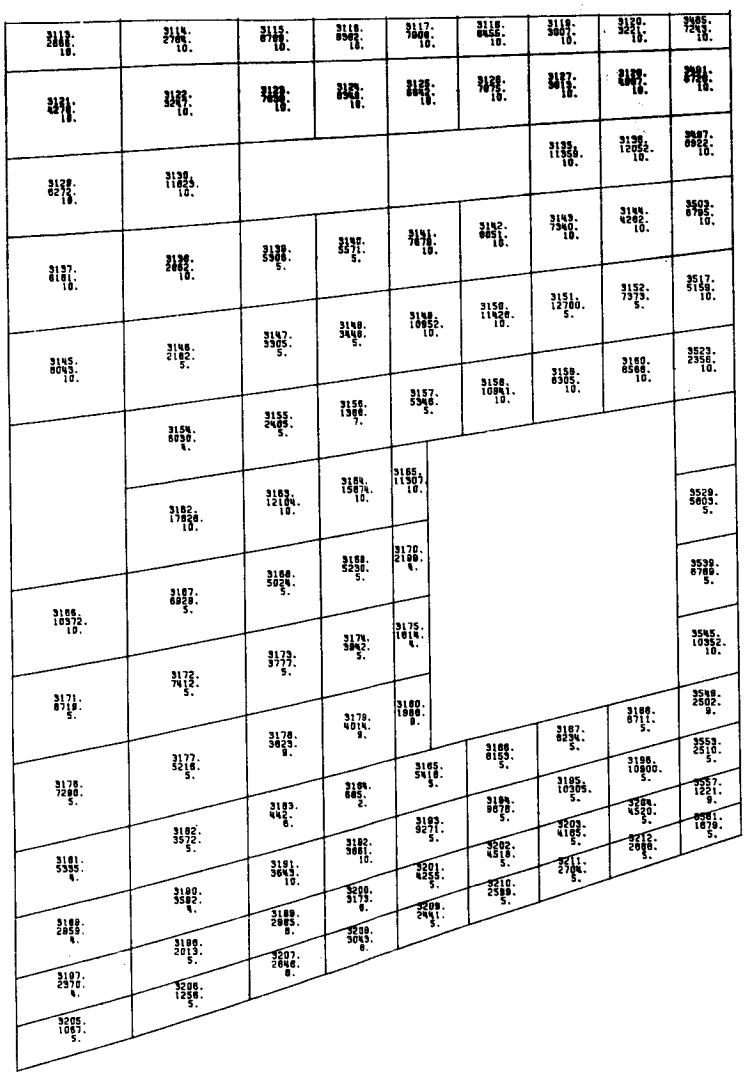

WESTWIND SUBSTRUCTURE 1
ENVELØPE FØR MAXIMUM
SHEAR STRESS IN PANELS

FIGURE 16: POSITIVE SHEAR STRESSES ENVELOPE DISPLAYED ON A DEVELOPED STRIP OF THE FUSELAGE

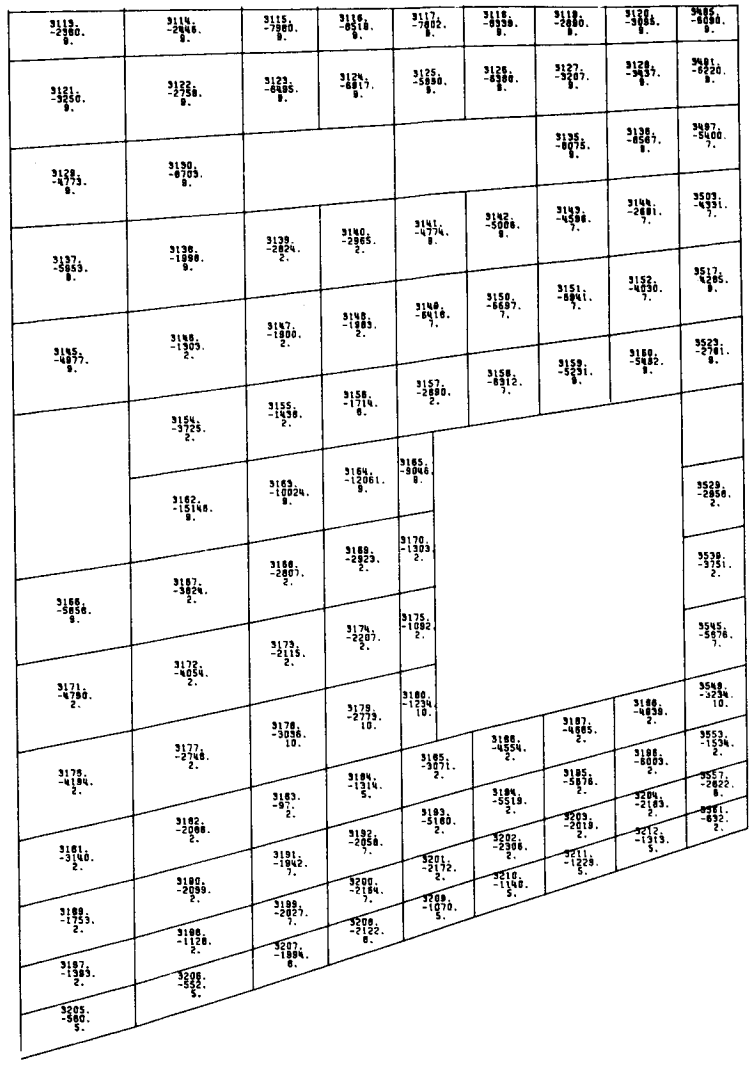

WESTWIND SUBSTRUCTURE 1
ENVELØPE FØR MINIMUM
SHEAR STRESS IN PANELS

FIGURE 17: NEGATIVE SHEAR STRESSES ENVELOPE DISPLAYED ON A DEVELOPED STRIP OF THE FUSELAGE

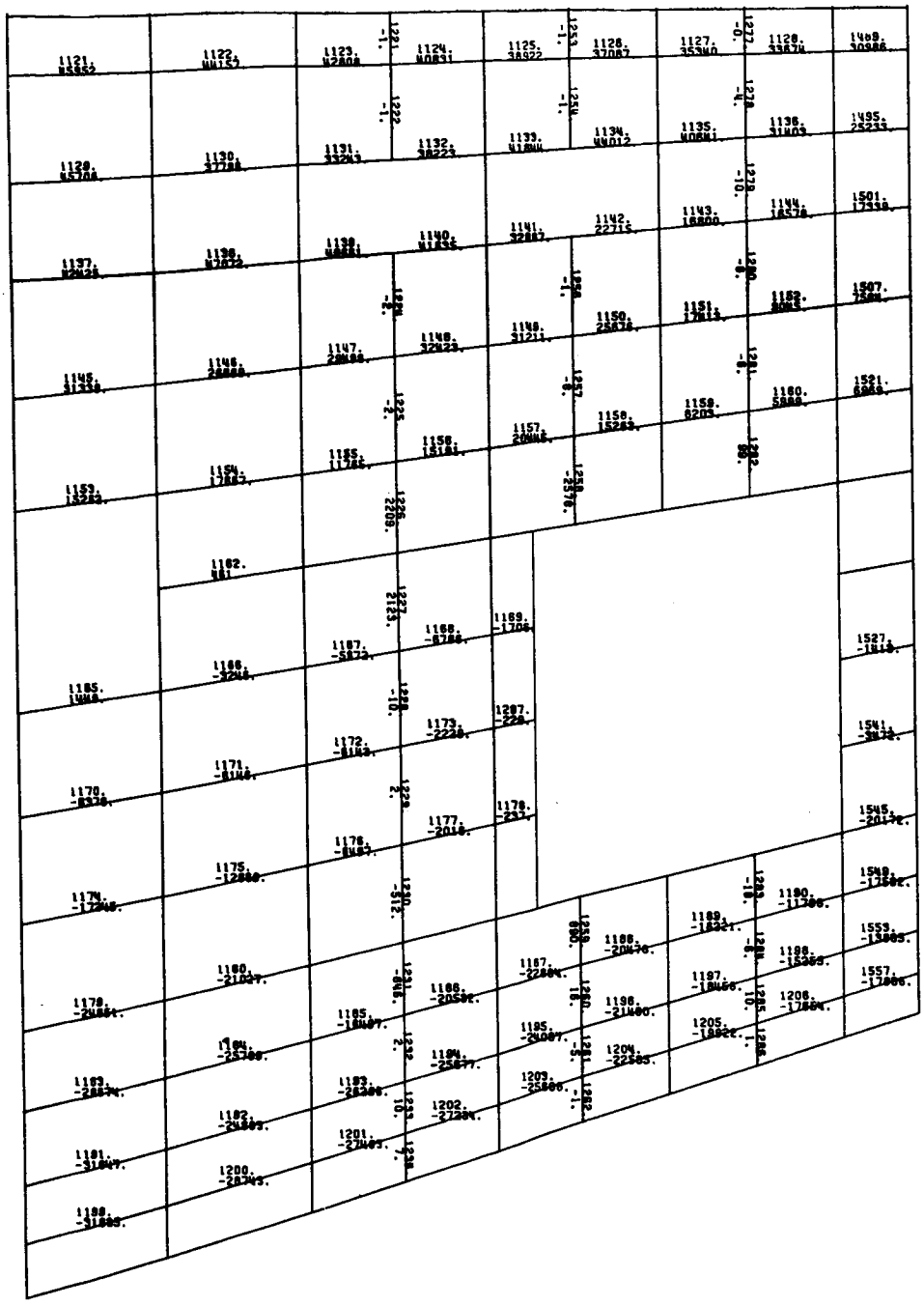

WESTWIND SUBSTRUCTURE 1
SUBCASE 4 -UPGUST CONDITION CONFIG. 5-
STRESSES IN ROD ELEMENTS

FIGURE 18: ROD STRESSES DISPLAYED ON A DEVELOPED STRIP OF THE FUSELAGE

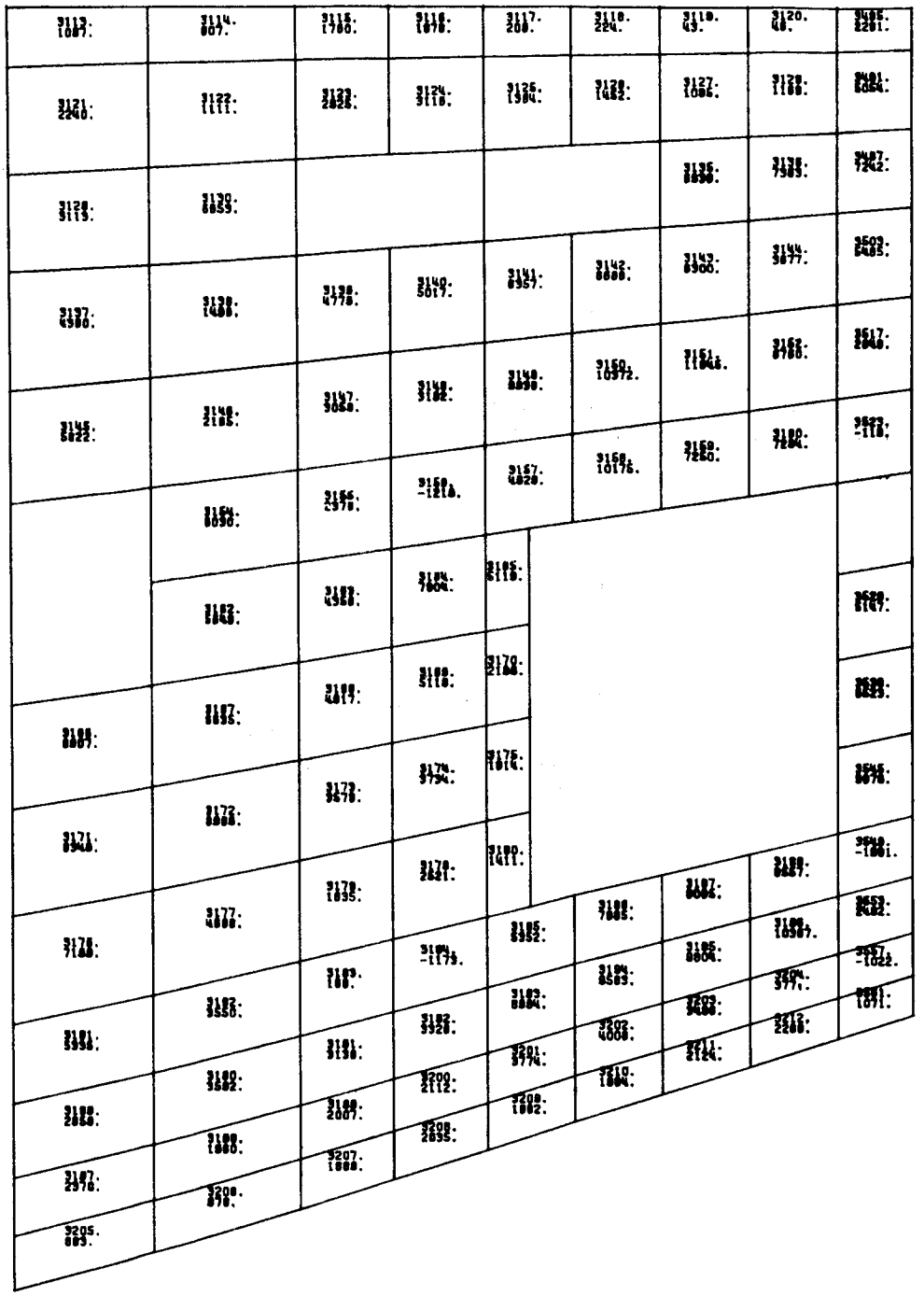

WESTWIND SUBSTRUCTURE 1
SUBCASE 4 -UPGUST CONDITION CONFIG. 5-
SHEAR STRESS IN PANELS

FIGURE 19: SHEAR STRESSES DISPLAYED ON A DEVELOPED STRIP OF THE FUSELAGE

APPLICATION OF LEVEL 15.9 NASTRAN TO A LARGE MODEL OF B-1 WING

by

Lalit C. Shah and Ronald Breznak
Rockwell International

ABSTRACT

The use of Level 15.9 NASTRAN for a large model of B-1 wing is described. Significant cost savings were experienced compared to the previous versions of NASTRAN. Computer support programs for modeling and post processing NASTRAN output are discussed. Sample output from max/min search program and contour plotter program is presented.

*U.S. GOVERNMENT PRINTING OFFICE: 1977 - 735-004/28